

Marco Ceccarelli  
*Editor*

# Proceedings of EUCOMES 08

The Second European Conference on  
Mechanism Science

 Springer

# Proceedings of EUCOMES 08

Marco Ceccarelli  
Editor

# Proceedings of EUCOMES 08

The Second European Conference  
on Mechanism Science

 Springer

*Editor*

Prof. Marco Ceccarelli  
LARM: Laboratory of Robotics and Mechatronics  
DiMSAT at University of Cassino  
Via Di Biasio 43, 03043 Cassino (Fr)  
Italy  
ceccarelli@unicas.it

ISBN: 978-1-4020-8914-5

e-ISBN: 978-1-4020-8915-2

DOI 10.1007/978-1-4020-8915-2

Library of Congress Control Number: 2008934049

© Springer Science+Business Media B.V. 2009

No part of this work may be reproduced, stored in a retrieval system, or transmitted in any form or by any means, electronic, mechanical, photocopying, microfilming, recording or otherwise, without written permission from the Publisher, with the exception of any material supplied specifically for the purpose of being entered and executed on a computer system, for exclusive use by the purchaser of the work.

Printed on acid-free paper

9 8 7 6 5 4 3 2 1

springer.com

# Preface

The EUCOMES08, Second European Conference on Mechanism Science is the second event of a series that has been started in 2006 as a conference activity for an European community working in Mechanism Science. The first event was held in Obergurgl, Austria in 2006. This year EUCOMES08 Conference has come to Cassino in Italy taking place from 17 to 20 September 2008.

The aim of the EUCOMES Conference is to bring together European researchers, industry professionals and students from the broad ranges of disciplines referring to Mechanism Science, in an intimate, collegial and stimulating environment.

In this second event we have received an increased attention to the initiative, as can be seen by the fact that the EUCOMES08 Proceedings will contain contributions by authors even from all around the world. This means also that there is a really interest to have not only a conference frame but even a need of aggregation for an European Community well identified in Mechanism Science with the aim to strengthen common views and collaboration activities among European researchers and institutions.

I believe that a reader will take advantage of the papers in these Proceedings with further satisfaction and motivation for her or his work. These papers cover the wide field of the Mechanism Science. The program of EUCOMES08 Conference has included technical sessions with oral presentations, which, together with informal conversations during the social program, have enabled to offer wide opportunities to share experiences and discuss scientific achievements and current trends in the areas encompassed by the EUCOMES08 conference.

We received 80 papers, and after review 72 papers have been accepted both for presentation and publication in the Proceedings. These papers cover several aspects of the wide field of Mechanism Science. The contributions have been grouped in sessions on Theoretical and Computational Kinematics, History of Mechanism Science, Design Algorithms, Mechanism Designs, Mechanical Transmissions, Gearing Systems, Manipulators, Linkages, Mechanics of Robots, Experimental Mechanics, Dynamics of Multibody Systems, Industrial Applications, and Non Industrial Applications. But they cover more subjects than those expressed in the above-mentioned session titles.

We would like to express grateful thanks to the members of the International Steering Committee for EUCOMES Conference for co-operating enthusiastically

for the success of the EUCOMES08 event: Bob Bicker (Newcastle University, UK), Marco Ceccarelli (Univ. Cassino, Italy), Burkhard Corves (Univ. Aachen, Germany), Manfred Husty (Univ. Innsbruck, Austria), Jean-Pierre Merlet (INRIA, France), Doina Pisla (Tech. Univ. Cluj-Napoca, Romania), Fernando Viadero (Univ. Cantabria, Spain), Teresa Zielinska (Warsaw Tech. Univ., Poland).

We thank the authors who have contributed with very interesting papers in several subjects, covering many fields of Mechanism Science. We are grateful to the reviewers for the time and effort they spent evaluating the papers. I thank the University of Cassino for hosting the EUCOMES08 event. I would like to thank my colleagues at the LARM, Laboratory of Robotics and Mechatronics of University of Cassino for their help, namely Dr Chiara Lanni, Dr Erika Ottaviano, and particularly Dr Giuseppe Carbone, who has served also as Secretary for EUCOMES08.

I am grateful to my wife Brunella, my daughters Elisa and Sofia, and my son Raffaele. Without their patience and comprehension it would not have been possible for me to organize EUCOMES08, Second European Conference on Mechanism Science.

University of Cassino  
June 2008

Marco Ceccarelli

# Contents

<b>Automatic Weapons of the Roman Empire</b> .....	1
Flavio Russo, Cesare Rossi and Ferruccio Russo	
<b>“DEUS-EX-MACHINA” in Phlius Theatre</b> .....	11
Argyris S. Papadogiannis, Marilena C. Tsakoumaki and Thomas G. Chondros	
<b>Archimedes and the Origins of Mechanisms Design</b> .....	21
Thomas G. Chondros	
<b>The Mirror Weapon in Archimedes Era</b> .....	29
A.S. Papadogiannis, N.S. Papadogianni, A. Carabelas, S. Tsitomeneas, P. Kyraggelos and T.G. Chondros	
<b>The Creation of the Site About the Historical Part of Collection of Mechanisms Bauman MSTU</b> .....	37
Theodor Vitiukov and Valentin Tarabarin	
<b>Using Computer Spreadsheets in Teaching Mechanisms</b> .....	45
Eres Söylemez	
<b>Hinged Frameworks with Unusual Geometrical Properties</b> .....	55
Mikhail Kovalev	
<b>A Comparison Between Line Geometries of Point and Line Displacements</b>	61
Chintien Huang	
<b>A Kinematic Approach to Calculate Protein Motion Paths</b> .....	69
Mikel Diez, Víctor Petuya, Mónica Urizar and Alfonso Hernández	
<b>Solutions of the Equation of Meshing for Planar Gear Profiles</b> .....	77
Giovanni Bonandrini, Giovanni Mimmi and Carlo Rottenbacher	

<b>A Numerical Method for the Second-Order Mobility Analysis of Mechanisms</b> .....	87
Igor Fernández de Bustos, Josu Agirrebeitia and Rafael Avilés	
<b>Mathematical Models of Mechanisms with Essentially Elastic Links</b> .....	95
G. Ualiyev and Assylbek Jomartov	
<b>Design and Simulation of a New Hybrid Mobile Robot for Overpassing Obstacles</b> .....	101
Gianni Castelli and Erika Ottaviano	
<b>Evolving Four-Bars for Optimal Synthesis</b> .....	109
Hans-Peter Schröcker, Bert Jüttler and Martin Aigner	
<b>A New Family of Overconstrained 6R-Mechanisms</b> .....	117
Martin Pfurner	
<b>Development of a Spherical Linkage Mechanism with the Aid of the Dynamic Spatial Geometry Program “GECKO”</b> .....	125
G. Lonij, Mathias Husing, S.W. Choi and Burkhard Corves	
<b>Elastic and Safety Clutch with Radial Disposed Elastic Lamellas</b> .....	133
Ioan Stroe	
<b>Computational Multi-Objective Optimization to Design Service Robots</b> ..	139
Cristina Castejón, Giuseppe Carbone, Juan Carlos García Prada and Marco Ceccarelli	
<b>An Optimal Design for a New Underactuated Finger Mechanism</b> .....	149
Shuangji Yao, Marco Ceccarelli, Giuseppe Carbone and Zhen Lu	
<b>Synthesis of a Spatial Five-Link Mechanism with Two Degrees of Freedom According to the Given Laws of Motion</b> .....	159
Nodar Davitashvili and Otar Gelashvili	
<b>Synthesis of Mechanisms with Evolutionary Techniques</b> .....	167
J.A. Cabrera, J.J. Castillo, F. Nadal, A. Ortiz and A. Simón	
<b>Optimal Synthesis of Steering Mechanisms Including Transmission Angles</b> .....	175
Ana de-Juan, Ramon Sancibrian and Fernando Viadero	
<b>Workspace Fitting and Control for a Serial-Robot Motion Simulator</b> .....	183
Andrés Kecskeméthy, Ismar Masic and Martin Tändler	



**Operation Features of Milli-CaTraSys** . . . . . 191  
 Eusebio Hernandez-Martinez, Giuseppe Carbone and Carlos Lopez-Cajun

**Design of an Actuation System for a Fatigue Test RIG** . . . . . 201  
 Luca Pugi, Andrea Rindi, Benedetto Allotta and Giuseppe Gori

**The Influence of Motion Mode and Friction on the Dynamics of a Parallel Robot Used for Orientation Applications** . . . . . 209  
 Doina Pisla and Tiberiu Itul

**Elastohydrodynamic Models for Predicting Friction in Point Contacts Lubricated with Polyalphaolefins** . . . . . 219  
 J. Echávarri Otero, P. Lafont Morgado, J.B. Sánchez-Peñuela, J.L. Muñoz Sanz, J.M. Munoz-Guijosa, A. Díaz Lantada and H. Lorenzo Yustos

**An Integrated Differentiation-Projection Approach for the Kinematic Data Consistency of Biomechanical Systems** . . . . . 229  
 F.J. Alonso, J. Cuadrado and P. Pintado

**Design of Simple Humanoid Dedicated to the Research on the Gait Synthesis** . . . . . 237  
 Teresa Zielinska, Krzysztof Mianowski and Przemyslaw Kryczka

**A Comparison of Algorithms for Path Planning of Industrial Robots** . . . . . 247  
 Francisco Rubio, Francisco Valero, Josep Lluís Suñer and Vicente Mata

**Stiffness Analysis of Parallel Manipulator Using Matrix Structural Analysis** . . . . . 255  
 Rogério Sales Gonçalves and João Carlos Mendes Carvalho

**Modelling of Robot’s Motion by Use of Vibration of Internal Masses** . . . . . 263  
 Jatsun Sergey, Dyshenko Vyacheslav, Yatsun Andrey and Malchikov Andrey

**Mechanical Design of a 3-dof Parallel Robot Actuated by Smart Wires** . . . 271  
 Terenziano Raparelli, Pierluigi Beomonte Zobel and Francesco Durante

**A Multicriteria Approach for Optimal Trajectories in Dynamic Parameter Identification of Parallel Robots** . . . . . 279  
 Xabier Iriarte, Miguel Díaz-Rodríguez and Vicente Mata

**Reinforcement Neural Network for the Stabilization of a Furuta Pendulum** . . . . . 287  
 Benedetto Allotta, Luca Pugi and Fabio Bartolini

<b>A Technique for Vibration Suppression of a 2 DOF Compliant Manipulator</b> .....	295
Giovanni Incerti	
<b>Investigation on the Baumgarte Stabilization Method for Dynamic Analysis of Constrained Multibody Systems</b> .....	305
Paulo Flores, Rui Pereira, Margarida Machado and Eurico Seabra	
<b>Cornering Stability and Dynamic Analysis of a Four Steering Wheels Vehicle Driven by “In Wheel” Engines</b> .....	313
Massimo Callegari, Andrea Gabrielli and Matteo-Claudio Palpacelli	
<b>Dynamic Modelling of a Single – Link Flexible Arm to be Used as a Sensing Antenna</b> .....	321
Javier Guerra Fernández, Vicente Feliu Batlle and Miguel Ángel Caminero Torija	
<b>Method of Dynamic Analysis of Mechanisms of Variable Structure</b> .....	329
Assylbek Jomartov and Z.G. Ualiyev	
<b>A Contribution to the Synthesis of a Trihedral Conjugate Cam</b> .....	337
Miroslav Václavík and Zdeněk Koloc	
<b>Experimental and Theoretical Research of Cams Wearing of Cams Mechanism</b> .....	343
Alexander Golovin, Alexey Lafitsky and Alexey Simuskhin	
<b>Dynamic Features of Speed Increaseers from Mechatronic Wind and Hydro Systems. Part I: Structure Kinematics</b> .....	351
C. Jaliu, D.V. Diaconescu, M. Neagoie and R. Săulescu	
<b>Dynamic Features of Speed Increaseers from Mechatronic Wind and Hydro Systems. Part II: Dynamic Aspects</b> .....	361
C. Jaliu, D.V. Diaconescu, M. Neagoie and R. Săulescu	
<b>A Computer Aided Method for Cam Profile Design</b> .....	369
A. Petropoulou, S. Dimopoulos, D. Mourtzis and T.G. Chondros	
<b>On the Power Transmission and Running Quality of Micro-Mechanisms</b> .	377
Hanfried Kerle	
<b>Probable Simulating Models of Wear for Open Gearing with High-Ratio Gear</b> .....	387
Alexander Golovin and Tamara Milevskaya	

**Alternative in Harmonic Train Design** ..... 397  
 Valentin Tarabarin and Zinaida Tarabarina

**On the Position of the Single Pair Tooth Segment Relative to the Pitch Point, for Internal Gears, with Effect on Contact Stress Calculus** ..... 405  
 Radu Velicu, Gheorghe Moldovean and Cristina A. Bozan

**Gears and Belt Drives for Non-Uniform Transmission** ..... 415  
 Hellmuth Stachel

**Fulleroid-Like Linkages** ..... 423  
 Gökhan Kiper

**On the Classification of Compliant Mechanisms** ..... 431  
 Lena Zentner and Valter Böhm

**Comparative Kinematics of Mobile Transversal Coupling, as Multibody System** ..... 439  
 Cornel Cătălin Gavrilă

**The Synthesis of a Linkage with Linear Actuator for Solar Tracking with Large Angular Stroke** ..... 447  
 Ion Visa, Dorin Diaconescu, Valentina Popa, Bogdan Burduhos and Radu Saulescu

**Dynamics of Heel Strike in Bipedal Systems with Circular Feet** ..... 455  
 Josep Maria Font and József Kövecses

**Parallel Manipulators with Simple Geometrical Structure** ..... 463  
 Adolf Karger

**Analysis of Wire Elasticity for Wire-driven Parallel Robots** ..... 471  
 Jean-Pierre Merlet

**Kinematic Analysis of a Compliant, Parallel and Three-Dimensional Meso-Manipulator Generated from a Planar Structure** ..... 479  
 Cinzia Amici, Alberto Borboni, Pier Luigi Magnani and Diego Pomi

**Dynamic Analysis of a Compliant, Parallel and Three-Dimensional Meso-Manipulator Generated from a Planar Structure** ..... 487  
 Cinzia Amici, Alberto Borboni, Pier Luigi Magnani and Diego Pomi

<b>Modelling of the Orientation Error of a 3-DOF Translational Parallel Manipulator</b> .....	495
Zouhaier Affi and Lotfi Romdhane	
<b>Sensitivity Analysis of Degenerate and Non-Degenerate Planar Parallel Manipulators</b> .....	505
Nicolas Binaud, Stéphane Caro and Philippe Wenger	
<b>3D Object Reconstruction Using a Robot Arm</b> .....	513
Cesare Rossi, Sergio Savino and Salvatore Strano	
<b>Considerations on Process Performance in Incremental Forming by Inducing High Frequency Vibration</b> .....	523
D. Mundo, G. Gatti, G. Ambrogio, L. Filice and G. A. Danieli	
<b>Scheduling and Verification of Micro Assembly Processes</b> .....	531
Kerstin Schöttler, Arne Burisch, Annika Raatz and Jürgen Hesselbach	
<b>Cambio – A Miniaturized Tool Changer for Desktop Factory Application</b> .	541
Arne Burisch, Christian Loechte, Annika Raatz and Adriano Fabrizi	
<b>Tensegrity Concept – From Natural Systems to Robots</b> .....	549
Simona-Mariana Cretu	
<b>Laser-Based Structuring of Piezoceramics for Mobile Microrobots</b> .....	559
Christoph Edeler and Daniel Jasper	
<b>Evaluation of Spatial Vibrations Using a Platform with 6 Degrees of Freedom</b> .....	567
Jiri Blekta, Josef Mevald and Iva Petrikova	
<b>Mechanical Design and Optimization of a Microsurgical Robot</b> .....	575
M. Miroir, J. Szewczyk, Y. Nguyen, S. Mazalaigue, A. Bozorg Grayeli and O. Sterkers	
<b>Multy Mirror Adjustable Space Reflector as the Mechanism with Many Degrees of Freedom</b> .....	585
Viktor I. Bujakas	
<b>Dynamic Modeling of a Parallel Robot Used in Minimally Invasive Surgery</b> .....	595
N. Plitea, D. Pislă, C. Vaida, B. Gherman and A. Pislă	

**Controlling the Traditional Rigid Endoscopic Instrumentation Motion . . . 603**  
D. Moschella and G.A. Danieli

**Use of Substitute of Mechanisms for Tolerance Investigation of Guidance  
Mechanisms . . . . . 613**  
Mathias Husing and Burkhard Corves

**Index . . . . . 623**

# Contributors

**Zouhaier Affi** Laboratoire de Génie Mécanique, Ecole Nationale d'Ingénieurs de Monastir, e-mail: [zouhaier.affi@enim.rnu.tn](mailto:zouhaier.affi@enim.rnu.tn)

**Josu Agirrebeitia** Departamento de Ingeniería Mecánica, Escuela Superior de Ingenieros de Bilbao, Alda. de Urquijo s/n 48013 Bilbao (Vizcaya), Spain

**Martin Aigner** Institute of Applied Geometry, University of Linz, Linz, Austria

**Benedetto Allotta** Sezione di Meccanica Applicata alle Macchine, Dipartimento di Energetica “Sergio Stecco”, Università di Firenze, Via Santa Marta 3, 50100 Firenze (FI), Italy, e-mail: [ben@mapp1.de.unifi.it](mailto:ben@mapp1.de.unifi.it), web page: <http://mapp1.de.unifi.it>

**F.J. Alonso** Departamento de Ingeniería Mecánica, Energética y de los Materiales, Universidad de Extremadura, Avda. de Elvas s/n, 06071 Badajoz, Spain, e-mail: [fjas@unex.es](mailto:fjas@unex.es)

**G. Ambrogio** Dipartimento di Meccanica, Università della Calabria, Via P. Bucci, 87036, Arcavacata di Rende (Cs), Italy

**Cinzia Amici** Dipartimento di Ingegneria Meccanica e Industriale (DIMI), Università degli Studi di Brescia, Via Branze 38, 25123 Brescia (BS), Italy, e-mail: [cinzia.amici@ing.unibs.it](mailto:cinzia.amici@ing.unibs.it)

**Malchikov Andrey** Mechatronical Department, Kursk State Technical University, Kursk, Russia

**Yatsun Andrey** Mechatronical Department, Kursk State Technical University, Kursk, Russia

**Rafael Avilés** Departamento de Ingeniería Mecánica, Escuela Superior de Ingenieros de Bilbao, Alda. de Urquijo s/n 48013 Bilbao (Vizcaya), Spain

**Fabio Bartolini** Sezione di Meccanica Applicata alle Macchine, Dipartimento di Energetica “Sergio Stecco”, Università di Firenze, Via Santa Marta 3, 50100 Firenze (FI), Italy, e-mail: [bartolini@mapp1.de.unifi.it](mailto:bartolini@mapp1.de.unifi.it), web page: <http://mapp1.de.unifi.it><sup>TM</sup>

**Vicente Feliu Batlle** Departamento de Ingeniería Eléctrica, Electrónica y Automática, ETS Ing. Industriales, Universidad de Castilla – La Mancha Avda. Camilo José Cela, s/n 13071 Ciudad Real, Spain

**Nicolas Binaud** Institut de Recherche en Communications et Cybernétique de Nantes, UMR CNRS n° 6597, 1 rue de la Noë, 44321 Nantes, e-mail: France, binaud@irccyn.ec-nantes.fr

**Jiri Blekta** Department of Applied Mechanics, Technical University of Liberec, Studentská 2, 46117 Liberec, Czech Republic

**Valter Böhm** Fakultät für Maschinenbau, Technische Universität Ilmenau, PF 100565, 98684 Ilmenau, Germany

**Giovanni Bonandrini** Dipartimento di Meccanica Strutturale, Università di Pavia, Via Ferrata 1, I-27100 Pavia, Italy

**Alberto Borboni** Dipartimento di Ingegneria Meccanica e Industriale (DIMI), Università degli Studi di Brescia, Via Branze 38, 25123 Brescia (BS), Italy

**Cristina A. Bozan** Department of Product Design and Robotics, Transilvania University of Braşov, Bdul Eroilor 27, 500036 Braşov, Romania, e-mail: crissy\_ro@yahoo.com

**A. Bozorg Grayeli** Inserm, Unit-M 867, Paris; AP-HP Hôpital Beaujon, Service d'ORL, Clichy; Université Denis-Diderot, France

**V.I. Bujakas** P.N. Lebedev Physical Institute, Russian Academy of Science, Moscow, Russia, e-mail: bujakas@yandex.ru.

**Bogdan Burduhos** Department of Product Design and Robotics, Transilvania University of Brasov, Eroilor Boulevard 29, 500036 Brasov, Romania, e-mail: bogdan.burduhos@unitbv.ro

**Arne Burisch** Institute of Machine Tools and Production Technology; Institut für Werkzeugmaschinen und Fertigungstechnik, Technische Universität Braunschweig, Langer Kamp 19 B, 38106 Braunschweig, Germany, e-mail: a.burisch@tu-bs.de

**J.A. Cabrera** Department of Mechanical Engineering, University of Málaga, Campus El Ejido, 29013 Málaga, Spain

**Massimo Callegari** Dipartimento di Meccanica, Università Politecnica delle Marche, Via Brecce Bianche s/n, 60131 Ancona, Italy, e-mail: m.callegari@univpm.it

**Miguel Ángel Caminero Torija** Departamento de Ingeniería Eléctrica, Electrónica y Automática, ETS Ing. Industriales, Universidad de Castilla – La Mancha Avda, Camilo José Cela, s/n 13071 Ciudad Real, Spain

**A. Carabelas** University of Patras, Department of Mechanical Eng & Aeronautics, 265 00 Patras, Greece

**Giuseppe Carbone** LARM: Laboratory of Robotics and Mechatronics, DiMSAT, University of Cassino, Via Di Biasio 43, 03043 Cassino (Fr), Italy, e-mail: carbone@unicas.it

**Stéphane Caro** Institut de Recherche en Communications et Cybernétique de Nantes, UMR CNRS n° 6597, 1 rue de la Noë, 44321 Nantes, France, caro@irccyn.ec-nantes.fr

**C. Castejón** MAQLAB Group, Mechanical Dept. Carlos III University, Av. De la Universidad 30, 28911 Madrid, Spain, e-mail: castejon@ing.uc3m.es

**G. Castelli** LARM: Laboratory of Robotics and Mechatronics, DiMSAT, University of Cassino, Via G. Di Biasio 43, 03043 Cassino, Italy, e-mail: g.castelli@unicas.it

**J.J. Castillo** Department of Mechanical Engineering, University of Málaga, Campus El Ejido, 29013 Málaga, Spain

**Marco Ceccarelli** LARM: Laboratory of Robotics and Mechatronics, DiMSAT, University of Cassino, Via Di Biasio 43, 03043 Cassino (Fr), Italy, ceccarelli@unicas.it, cecca@unicas.it

**S.W. Choi** Department of Mechanism Theory and Dynamics of Machines, RWTH-Aachen University, Aachen, 52056 Germany

**Thomas G. Chondros** University of Patras, Department of Mechanical Eng. & Aeronautics, 265 00 Patras, Greece, e-mail: chondros@mech.upatras.gr

**B. Corves** Department of Mechanism Theory and Dynamics of Machines, RWTH-Aachen University, Aachen, 52056 Germany

**J. Cuadrado** Departamento de Ingeniería Industrial II, Universidad de La Coruña, Mendizábal s/n, 15403 Ferrol, Spain, e-mail: javicquad@cdf.udc.es

**G.A. Danieli** Dipartimento di Meccanica, Università della Calabria, Via P. Bucci, 87036, Arcavacata di Rende (Cs), Italy, e-mail: d.mundo@unical.it

**Nodar Davitashvili** Georgian Technical University, 77, M. Kostava Str., 0175, Tbilisi, GA, e-mail: nodav@geo.net.ge

**Ana de-Juan** Department of Structural and Mechanical Engineering, University of Cantabria, ETSIT, Avda. De los Castros s/n. Santander (Spain), e-mail: dejuanam@unican.es, url: <http://personales.unican.es/sancibr>

**Dorin V. Diaconescu** Department of Product Design and Robotics, Transilvania University of Brasov, Eroilor Boulevard 29, 500036 Brasov, Romania, e-mail: dvdiaconescu@unitbv.ro

**A. Díaz Lantada** División de Ingeniería de Máquinas, Universidad Politécnica de Madrid, José Gutiérrez Abascal 2, 28006 Madrid, Spain

**Miguel Díaz-Rodríguez** Departamento de Tecnología y Diseño, Universidad de Los Andes, Merida, Venezuela, e-mail: dmiguel@ula.ve



**Mikel Diez** Department of Mechanical Engineering, University of the Basque Country, Bilbao, 48013, Spain, e-mail: mikel.diez@ehu.es

**S. Dimopoulos** University of Patras, Department of Mechanical Engineering & Aeronautics, 265 00 Patras, Greece

**Francesco Durante** Dipartimento di Ingegneria Meccanica, Energetica e Gestionale – DIMEG, Università dell’Aquila, Roio Poggio, L’Aquila, Italy

**J. Echávarri Otero** División de Ingeniería de Máquinas, Universidad Politécnica de Madrid, José Gutiérrez Abascal 2, 28006 Madrid, Spain, e-mail: jechavarri@etsii.upm.es

**Christoph Edeler** Division Microrobotics and Control Engineering, University of Oldenburg, Uhlhornsweg 84, 26111 Oldenburg, Germany, e-mail: christoph.edeler@kisum.uni-oldenburg.de

**Adriano Fabrizi** Laboratory of Robotics and Mechatronics at DiMSAT, University of Cassino, Cassino, Via Di Biasio 43, 03043 Cassino (Fr), Italy

**Javier Guerra Fernández** Departamento de Ingeniería Eléctrica, Electrónica y Automática, ETS Ing. Industriales, Universidad de Castilla – La Mancha Avda. Camilo José Cela, s/n 13071 Ciudad Real, Spain, e-mail: Javier.Guerra@uclm.es

**Igor Fernández de Bustos** Departamento de Ingeniería Mecánica, Escuela Superior de Ingenieros de Bilbao, Alda. de Urquijo s/n 48013 Bilbao (Vizcaya), Spain, e-mail: igor.fernandezdebustos@ehu.es

**L. Filice** Dipartimento di Meccanica, Università della Calabria, Via P. Bucci, 87036, Arcavacata di Rende (Cs), Italy

**Paulo Flores** Departamento de Engenharia Mecânica, Universidade do Minho, Campus de Azurém, 4800-058 Guimarães, Portugal, e-mail: pfflores@dem.uminho.pt

**Josep Maria Font** Department of Mechanical Engineering, Centre for Intelligent Machines, McGill University, 817 Sherbrooke Street West, H3A 2K6 Montréal, Québec, Canada, e-mail: josep.font@mcgill.ca

**Andrea Gabrielli** Dipartimento di Meccanica, Università Politecnica delle Marche, Via Breccia Bianche s/n, 60131 Ancona, Italy, e-mail: andrea.gabrielli@univpm.it

**G. Gatti** Dipartimento di Meccanica, Università della Calabria, Via P. Bucci, 87036, Arcavacata di Rende (Cs), Italy

**Cornel Cătălin Gavrilă** Product Design and Robotics Department, Transilvania University of Brasov, Eroilor 29, 500036 Braşov, România, cgavrila@unitbv.ro

**Otar Gelashvili** Georgian Technical University, 77, M. Kostava Str., 0175, Tbilisi, GA

**A. Gherman** Technical University of Cluj-Napoca, Constantin Daicoviciu 15, RO-400020 Cluj-Napoca, Romania

**Alexander Golovin** Department of Theory Mechanisms & Machines, Bauman Moscow State Technical University, 2nd Baumanskaya Str., 5, 105005 Moscow, Russia, e-mail: aalgol@rambler.ru

**Rogério Sales Gonçalves** School of Mechanical Engineering, Federal University of Uberlândia, Campus Santa Mônica, CEP 38400-902, Uberlândia, MG, Brasil, e-mail: ufursgoncalves@yahoo.com.br

**Giuseppe Gori** Servindustria SRL Pistoia, Italy

**Alfonso Hernández** Department of Mechanical Engineering, University of the Basque Country, Bilbao, 48013, Spain

**E. Hernandez-Martinez** Facultad de Ingeniería, Universidad Autónoma de Querétaro, Qro, México, e-mail: e.hernandez@unicas.it

**Jürgen Hesselbach** Institute of Machine Tools and Production Technology, Technische Universität Braunschweig, Langer Kamp 19 B, 38106 Braunschweig, Germany

**Chintien Huang** Department of Mechanical Engineering, National Cheng Kung University, No. 1, University Road, Tainan 701, Taiwan, e-mail: chuang@mail.ncku.edu.tw

**M. Husing** Department of Mechanism Theory and Dynamics of Machines, Eilfschornestrestinstr. 18, RWTH-Aachen University, Aachen, 52056 Germany, e-mail: huesing@igm.rwth-aachen.de

**Giovanni Incerti** Dipartimento di Ingegneria Meccanica e Industriale, Università di Brescia, Via Branze 38, 25123 Brescia, Italy, e-mail: giovanni.incerti@ing.unibs.it

**Xabier Iriarte** Departamento de Ingeniería Mecánica, Energética y de Materiales, Universidad Pública de Navarra, 31006, Pamplona, España, e-mail: xabier.iriarte@unavarra.es

**Tiberiu Itul** Technical University of Cluj-Napoca, Constantin Daicoviciu 15, RO-400020 Cluj-Napoca, Romania

**C. Jaliu** Department of Product Design and Robotics, Transilvania University of Brasov, Bdul Eroilor 29, 500036 Brasov, Romania, e-mail: cjaliu@unitbv.ro

**Daniel Jasper** Division Microrobotics and Control Engineering, University of Oldenburg, Uhlhornsweg 84, 26111 Oldenburg, Germany

**A.A. Jomartov** Institute of Mechanics and Machine Sciences, Valikhanov st. 106, 050010 Almaty, Republic Kazakhstan, e-mail: legsert@mail.ru

**Bert Jüttler** Institute of Applied Geometry, University of Linz, Linz, Austria

**Adolf Karger** Charles University Praha, Faculty of Mathematics and Physics, Czech Republic, e-mail: Adolf.Karger@mff.cuni.cz

**Andrés Kecskeméthy** Chair of Mechanics, University Duisburg-Essen, Lotharstraße 1, 47057 Duisburg, Germany, e-mail: andres.kecskemethy@uni-due.de

**Hanfried Kerle** Institut für Werkzeugmaschinen und Fertigungstechnik, Technische Universität Braunschweig, Langer Kamp 19b, D-38106 Braunschweig, Germany, e-mail: h.kerle@t-online.de

**Gökhan Kiper** Mechanical Engineering Department, Middle East Technical University, İnönü Bulvarı, 06531 Ankara, Turkey, e-mail: kiper@metu.edu.tr

**Zdeněk Koloc, Ph.D.** Research Institute of Textile Machines Liberec, Plc., U Jezu 525/4, 46119 Liberec, Czech Republic

**Mikhail Kovalev** Bauman Moscow State University, 105005, Moscow, 2-ya Baumanskaya, 5, Russia, e-mail: mdkovalev@mtu-net.ru

**József Kövecses** Department of Mechanical Engineering, Centre for Intelligent Machines, McGill University, 817 Sherbrooke Street West, H3A 2K6 Montréal, Québec, Canada, e-mail: jozsef.kovecses@mcgill.ca

**Przemyslaw Kryczka** Faculty of Power and Aeronautical Engineering, ul.Nowowiejska 24, Warsaw University of Technology, 00-665 Warsaw, Poland

**P. Kyraggelos** University of Patras, Department of Mechanical Eng. & Aeronautics, 265 00 Patras, Greece

**Alexey Lafitsky** Mechanical-Technological Department, Bauman Moscow State Technical University, 2nd Baumanskaya Str., 5, 105005 Moscow, Russia, e-mail: lexxx\_13.87@mail.ru

**Christian Loechte** Institut für Werkzeugmaschinen und Fertigungstechnik, Technische Universität Braunschweig, Langer Kamp 19 b, 38106 Braunschweig, Germany

**G. Lonij** Department of Mechanism Theory and Dynamics of Machines, RWTH-Aachen University, Aachen, 52056 Germany, e-mail: lonij@igm.rwth-aachen.de

**C. Lopez-Cajun** Facultad de Ingeniería, Universidad Autónoma de Querétaro, Qro, México, e-mail: cajun@uaq.mx

**Zhen Lu** School of Automation Science and Electrical Engineering, Beihang University, Beijing P.R., China

**Margarida Machado** Departamento de Engenharia Mecânica, Universidade do Minho, Campus de Azurém, 4800-058 Guimarães, Portugal, e-mail: margarida@dem.uminho.pt

**Pier Luigi Magnani** Dipartimento di Ingegneria Meccanica e Industriale (DIMI), Università degli Studi di Brescia, Via Branze 38, 25123 Brescia (BS), Italy

**Ismar Masic** Chair of Mechanics, University Duisburg-Essen, Lotharstraße 1, 47057 Duisburg, Germany, e-mail: ismar.masic@uni-due.de

**Vicente Mata** Departamento de Mecánica y Materiales, Universidad Politécnica de Valencia, Camino de Vera, 46020, Valencia, España, e-mail: vmata@mcm.upvnet.upv.es

**S. Mazalaigue** Collin SA, Bagneux, France

**João Carlos Mendes Carvalho** School of Mechanical Engineering, Federal University of Uberlândia, Campus Santa Mônica, CEP 38400-902, Uberlândia, MG, Brasil, e-mail: jcmendes@mecanica.ufu.br

**Jean-Pierre Merlet** COPRIN project-team, INRIA Sophia Antipolis, France, e-mail: Jean-Pierre.Merlet@sophia.inria.fr

**Josef Mevald** Department of Applied Mechanics, Technical University of Liberec, Studentská 2, 46117 Liberec, Czech Republic

**Krzysztof Mianowski** Faculty of Power and Aeronautical Engineering, ul.Nowowiejska 24, Warsaw University of Technology, 00-665 Warsaw, Poland

**Tamara Milevskaya** Mechanical-Technological Department, Bauman Moscow State Technical University, 2nd Baumanskaya Str., 5, 105005 Moscow, Russia, e-mail: cherryjoy@yandex.ru

**Giovanni Mimmi** Dipartimento di Meccanica Strutturale, Università di Pavia, Via Ferrata 1, I-27100 Pavia, Italy, e-mail: giovanni.mimmi@unipv.it

**M. Miroir** Université Pierre et Marie Curie-Paris 6, FRE-2507, Institut des Systèmes Intelligents et Robotique (ISIR), Paris, France; Collin SA, Bagneux, France, e-mail: miroir@isir.fr

**Gheorghe Moldovean** Department of Product Design and Robotics, Transilvania University of Braşov, Bdul Eroilor 27, 500036 Braşov, Romania, e-mail: ghmoldovean@unitbv.ro

**P. Lafont Morgado** División de Ingeniería de Máquinas, Universidad Politécnica de Madrid, José Gutiérrez Abascal 2, 28006 Madrid, Spain

**D. Moschella** Dipartimento di Meccanica, Università della Calabria, Via P. Bucci, 87036, Arcavacata di Rende (Cs), Italy, e-mail: d.mundo@unical.it

**D. Mourtzis** University of Patras, Department of Mechanical Engineering & Aeronautics, 265 00 Patras, Greece

**D. Mundo** Dipartimento di Meccanica, Università della Calabria, Via P. Bucci, 87036, Arcavacata di Rende (Cs), Italy, e-mail: d.mundo@unical.it

**J.L. Muñoz Sanz** División de Ingeniería de Máquinas, Universidad Politécnica de Madrid, José Gutiérrez Abascal 2, 28006 Madrid, Spain

**J.M. Munoz-Guijosa** División de Ingeniería de Máquinas, Universidad Politécnica de Madrid, José Gutiérrez Abascal 2, 28006 Madrid, Spain

**F. Nadal** Department of Mechanical Engineering, University of Málaga, Campus El Ejido, 29013 Málaga, Spain

**M. Neagoe** Department of Product Design and Robotics, Transilvania University of Brasov, Bdul Eroilor 29, 500036 Brasov, Romania

**Y. Nguyen** Inserm, Unit-M 867, Paris; AP-HP Hôpital Beaujon, Service d'ORL, Clichy; Université Denis-Diderot, France

**A. Ortiz** Department of Mechanical Engineering. University of Málaga, Campus El Ejido, 29013 Málaga. Spain

**E. Ottaviano** LARM: Laboratory of Robotics and Mechatronics, DiMSAT, University of Cassino, Via G. Di Biasio 43, 03043 Cassino, Italy, e-mail: ottaviano@unicas.it

**Matteo-Claudio Palpacelli** Dipartimento di Meccanica, Università Politecnica delle Marche, Via Breccie Bianche s/n, 60131 Ancona, Italy, e-mail: m.palpacelli@univpm.it

**N.S. Papadogianni** University of Patras, Department of Mechanical Eng. & Aeronautics, 265 00 Patras, Greece

**Argyris S. Papadogiannis** University of Patras, Department of Mechanical Eng. & Aeronautics, 265 00 Patras, Greece, e-mail: papadog@mech.upatras.gr

**Rui Pereira** Departamento de Matemática, Universidade do Minho, Campus de Azurém, 4800-058 Guimarães, Portugal, e-mail: rmp@mct.uminho.pt

**Iva Petrikova** Department of Applied Mechanics, Technical University of Liberec, Studentská 2, 46117 Liberec, Czech Republic, e-mail: iva.petrikova@tul.cz

**Petropoulou A.** University of Patras, Department of Mechanical Engineering & Aeronautics, 265 00 Patras, Greece

**Víctor Petuya** Department of Mechanical Engineering, University of the Basque Country, Bilbao, 48013, Spain

**Martin Pfulner** Unit Geometry and CAD, Technikersrt. 13, University of Innsbruck, 6020 Innsbruck, Austria, email: martin.pfulner@uibk.ac.at

**P. Pintado** Departamento de Mecánica Aplicada, Universidad de Castilla La Mancha, Camilo J Cela s/n, 13071 Ciudad Real, Spain, e-mail: Publio.Pintado@uclm.es

**A. Pisla** Technical University of Cluj-Napoca, Constantin Daicoviciu 15, RO-400020 Cluj-Napoca, Romania

**Doina Pisla** Technical University of Cluj-Napoca, Constantin Daicoviciu 15, RO-400020 Cluj-Napoca, Romania, e-mail: Doina.Pisla@mep.utcluj.ro

**N. Plitea** Technical University of Cluj-Napoca, Constantin Daicoviciu 15, RO-400020 Cluj-Napoca, Romania

**Diego Pomi** Dipartimento di Ingegneria Meccanica e Industriale (DIMI), Università degli Studi di Brescia, Via Branze 38, 25123 Brescia (BS), Italy

**Valentina Popa** Department of Product Design and Robotics, Transilvania University of Brasov, Eroilor Boulevard 29, 500036 Brasov, Romania, e-mail: valentina.popa@unitbv.ro

**J.C. García Prada** MAQLAB Group, Mechanical Dept. Carlos III University, Av. De la Universidad 30, 28911 Madrid, Spain, e-mail: jcgprada@ing.uc3m.es

**Luca Pugi** Sez., Meccanica Applicata Dip. Energetica Sergio Stecco, Università di Firenze, Via Santa Marta 3, 50100 Firenze (FI), Italy; Corso di laurea in Ingegneria dei Trasporti, Università di Firenze, Via Santa Marta 3, 50100 Firenze (FI), Italy, e-mail: luca@mapp1.de.unfi.it

**Dominik Raab** Chair of Mechanics, University Duisburg-Essen, Lotharstraße 1, 47057 Duisburg, Germany, dominik.raab@uni-due.de

**Annika Raatz** Institute of Machine Tools and Production Technology; Institut für Werkzeugmaschinen und Fertigungstechnik, Technische Universität Braunschweig, Langer Kamp 19 B, 38106 Braunschweig, Germany

**Terenziano Raparelli** Dipartimento di Meccanica, Politecnico di Torino, Corso Duca degli Abruzzi 24, Torino, Italy

**Andrea Rindi** Sez., Meccanica Applicata Dip. Energetica Sergio Stecco, Università di Firenze, Via Santa Marta 3, 50100 Firenze (FI), Italy

**Lotfi Romdhane** Laboratoire de Génie Mécanique, Ecole Nationale d'Ingénieurs de Sousse, Sousse, Tunisia, e-mail: lotfi.romdhane@enim.rnu.tn

**Cesare Rossi** University of Napoli "Federico II", via Claudio, 21 – 80125 Napoli Italy, e-mail: cesare.rossi@unina.it

**Carlo Rottenbacher** Dipartimento di Meccanica Strutturale, Università di Pavia, Via Ferrata 1, I-27100 Pavia, Italy

**Francisco Rubio** Dpt. of Mechanical Engineering, Politechnic University of Valencia, Camino de Vera s/n Valencia 46023, Spain, e-mail: frubio@mcm.upv.es

**Ferruccio Russo** Free Lance Journalist, Napoli, Italy

**Flavio Russo** USSME Historical Bureau HQ Italian Army, Napoli, Italy

**J.B. Sánchez-Peñuela** División de Ingeniería de Máquinas, Universidad Politécnica de Madrid, José Gutiérrez Abascal 2, 28006 Madrid, Spain

**Ramon Sancibrian** Department of Structural and Mechanical Engineering, University of Cantabria, ETSIT, Avda. De los Castros s/n. Santander, (Spain), url: <http://personales.unican.es/sancibr>

**Radu Săulescu** Department of Product Design and Robotics, Transilvania University of Brasov, Eroilor Boulevard 29, 500036 Brasov, Romania, e-mail: rsaulescu@unitbv.ro

**Sergio Savino** University of Napoli “Federico II”, via Claudio, 21 – 80125 Napoli, Italy

**Kerstin Schöttler** Institute of Machine Tools and Production Technology, Technische Universität Braunschweig, Langer Kamp 19 B, 38106 Braunschweig, Germany, e-mail: k.schoettler@tu-bs.de

**Hans-Peter Schröcker** Unit Geometry and CAD, Technikersrt. 13, University Innsbruck, 6020 Innsbruck, Austria

**Eurico Seabra** Departamento de Engenharia Mecânica, Universidade do Minho, Campus de Azurém, 4800-058 Guimarães, Portugal, e-mail: eseabra@dem.uminho.pt

**Jatsun Sergey** Mechatronical Department, Kursk State Technical University, Kursk, Russia, e-mail: jatsun@kursknet.ru

**A. Simón** Department of Mechanical Engineering, University of Málaga, Campus El Ejido, 29013 Málaga, Spain

**Alexey Simuskhin** Mechanical-Technological Department, Bauman Moscow State Technical University, 2nd Baumanskaya Str., 5, 105005 Moscow, Russia, e-mail: simuskhin@mail.ru

**Eres Söylemez** Mechanical Engineering Department, Middle East Technical University, İnönü Bulvarı, 06531 Ankara, Turkey, e-mail: eres@metu.edu.tr

**Hellmuth Stachel** Institute of Discrete Mathematics and Geometry, Vienna University of Technology, Wiedner Hauptstr. 8-10/104, A 1040 Wien, Austria, e-mail: stachel@dmg.tuwien.ac.at

**O. Sterkers** Inserm, Unit-M 867, Paris; AP-HP Hôpital Beaujon, Service d’ORL, Clichy; Université Denis-Diderot, France

**Salvatore Strano** University of Napoli “Federico II”, via Claudio, 21 – 80125 Napoli, Italy

**Ioan Stroe** Department Design of Products and Robotics, Faculty of Technologic Engineering University, “Transylvania” of Brasov, B-dul. Eroilor nr. 29, 500036 Brasov, Romania, e-mail: stroei@unitbv.ro

**Josep Lluís Suñer** Departamento de Mecánica y Materials, Universidad Politécnica de Valencia, Camino de Vera, 46020, Valencia, España

**J. Szewczyk** Université Pierre et Marie Curie-Paris 6, FRE-2507, Institut des Systèmes Intelligents et Robotique (ISIR), Paris, France

**Martin Tändl** Chair of Mechanics, University Duisburg-Essen, Lotharstraße 1, 47057 Duisburg, Germany, e-mail: martin.taendl@uni-due.de

**Valentin Tarabarin** The “Theory of Machines and Mechanisms” Department, The Bauman Moscow State Technical University, 2nd Baumanskaya Str., 5, 105005, Moscow, Russia, e-mail: vtarabarin@gmail.com

**Zinaida Tarabarina** The “Theory of Machines and Mechanisms” Department, The Bauman Moscow State Technical University, 2nd Baumanskaya Str., 5, 105005, Moscow, Russia

**Marilena C. Tsakoumaki** University of Patras, Department of Mechanical Eng. & Aeronautics, 265 00 Patras, Greece

**S. Tsitomeneas** University of Patras, Department of Mechanical Eng. & Aeronautics, 265 00 Patras, Greece

**G. Ualiyev** Institute of Mechanics and Machine Sciences, Valikhanov St. 106, 050010 Almaty, Republic Kazakhstan, e-mail: legsert@mail.ru

**Z.G. Ualiyev** Institute of Mechanics and Machine Sciences, Valikhanov St. 106, 050010 Almaty, Republic Kazakhstan, e-mail: legsert@mail.ru

**Mónica Urizar** Department of Mechanical Engineering, University of the Basque Country, Bilbao, 48013, Spain

**Prof. Miroslav Václavík, Ph.D.,** Research Institute of Textile Machines Liberec, Plc., U Jezu 525/4, 46119 Liberec, Czech Republic, e-mail: miroslav.vaclavik@vuts.cz

**C. Vaida** Technical University of Cluj-Napoca, Constantin Daicoviciu 15, RO-400020 Cluj-Napoca, Romania

**Francisco Valero** Departamento de Mecánica y Materiales, Universidad Politécnica de Valencia, Camino de Vera, 46020, Valencia, España

**Radu Velicu** Department of Product Design and Robotics, Transilvania University of Braşov, Bdul Eroilor 27, 500036 Braşov, Romania, e-mail: rvelicu@unitbv.ro

**Fernando Viadero** Department of Structural and Mechanical Engineering, University of Cantabria, ETSIT, Avda. De los Castros s/n., Santander (Spain), url: <http://personales.unican.es/sancibr>

**Ion Visa** Department of Product Design and Robotics, Transilvania University of Brasov, Eroilor Boulevard 29, 500036 Brasov, Romania, e-mail: visaion@unitbv.ro

**Theodor Vitiukov** Student, Dept. Theory Machines and Mechanisms, Bauman Moscow State Technical University, Moscow, Russia, e-mail: vietfed7@gmail.com

**Dyshenko Vyacheslav** Mechatronical Department, Kursk State Technical University, Kursk, Russia

**Philippe Wenger** Institut de Recherche en Communications et Cybernétique de Nantes, UMR CNRS n° 6597, 1 rue de la Noë, 44321 Nantes, France, e-mail: wenger@ircyn.ec-nantes.fr



**Shuangji Yao** School of Automation Science and Electrical Engineering, Beihang University, Beijing P.R., China, e-mail: buaayaoshuangji@163.com

**H. Lorenzo Yustos** División de Ingeniería de Máquinas, Universidad Politécnica de Madrid, José Gutiérrez Abascal 2, 28006 Madrid, Spain

**Lena Zentner** Fakultät für Maschinenbau, Technische Universität Ilmenau, PF 100565, 98684 Ilmenau, Germany, e-mail: lena.zentner@tu-ilmenau.de

**Teresa Zielinska** Faculty of Power and Aeronautical Engineering, ul.Nowowiejska 24, Warsaw University of Technology, 00-665 Warsaw, Poland, e-mail: teresaz@meil.pw.edu.pl

**Pierluigi Beomonte Zobel** Dipartimento di Ingegneria Meccanica, Energetica e Gestionale – DIMEG, Università dell’Aquila, Roio Poggio, L’Aquila, Italy, e-mail: zobel@ing.univaq.it

# Automatic Weapons of the Roman Empire

Flavio Russo, Cesare Rossi and Ferruccio Russo

**Abstract** In the present paper the mechanics and the mechanisms that were used in some military weapons of the Roman Army are presented. In particular it is shown that both automatic weapons and pneumatic weapons were invented and used at that ages.

These military devices and in particular the design and construction of their components can show us that mechanical knowledge were much more advanced than one can commonly think.

**Keywords** Kinematics · Mechanism design · Manipulators

## Introduction

Certainly the Roman Empire was conquered and hold not only by the army itself but also by the Roman technology and modernity. This modernity was not only in the field of the Right and Literature but also (and perhaps mostly) in the field of Engineering and Science.

The Engineering, in particular was more advanced than one can commonly think; this is certainly true in the field of architectural works but probably even more true in the field of Hydraulics and Mechanics. This last field is probably less known than the other because the archaeological finds are less evident, smaller and sometimes unrecognised.

The weapons of the Roman Army presented in this paper contribute to show that the Mechanics and Mechanisms Science were very advanced and also the surprising modernity of some mechanical constructions and conceptions of those ages.

---

C. Rossi (✉)  
University of Napoli “Federico II”, via Claudio, 21–80125 Napoli Italy  
e-mail: cesare.rossi@unina.it

## The Repeating Catapult

The word catapult comes from the Greek (κατα = through and πέλτη = shield). During the Roman Empire this word was used for a machine that throws darts, while the word *ballista* (that also comes from the Greek word βαλλω = to throw) was used for a machine that throws balls. During the Middle Age the words were used with the opposite meaning: ballista for a dart throwing machine and catapult for a ball throwing one.

The Roman catapult was one of the most important weapons of the light artillery of the Roman Army. It is similar to a large crossbow and throws darts. In his conception the ballista is considered the most complex and scientifically evolved weapon before the industrial revolution. Few centuries after the fall of the Roman Empire it was no more built as it was very expensive and difficult to built.

## The Working Principles of a Catapult

To describe the working principle of a “normal” catapult, we must start from the motor. This last term, in the Hellenistic Age, was adopted to indicate the reason of a kinematic event. The ballistae were moved by two different kinds of elastic motors: the flexion motor and the torsion motor. The first one was used in the crossbows and small ballistae and was made first by a combination of wood, horns and sinews and later by steel or bronze leaves. For larger and more powerful catapults (and also for other launching machines) it was necessary a small and powerful motor: the torsion motor. According to sources, this last appeared around the middle of the 4th century BC in the same period torsion artillery appeared on the scene and replaced flexion artillery in just a few decades.

In Fig. 1 the torsion motor of a catapult is shown.

How it can be seen, a torsion motor consisted of a strong square wooden frame, reinforced by iron straps, divided into three separate sections. The central section was used to insert the frame of the weapons, while the sides were for the two coils of twisted rope. Inside were the arms to which the rope was affixed, like the ends of an archery bow.

The coils were made of twisted bovine sinews, horsehair or women’s hair. Keratinous formations were preferred for their superior resistance, excellent for elastic motors that worked by repeated cycles of torsion and immediate return. Since the kinetic power of a weapon depended on the diameter of the coils, the diameter became the dimensional module, just like the calibre in modern artillery.

Preparation for firing consisted of applying an initial torsion to the coils by means of special levers, almost up to the yield point. By effecting an additional rotation of approximately 50°/60° using the arms of the weapon rather than the levers, rotating them by pulling the cord with the crank, a tremendous amount of potential elastic energy was stored. When the restraint was released and the weapon fired, the coil would rotate rapidly in the opposite direction, pulling the arms to fire or hurl the projectile.

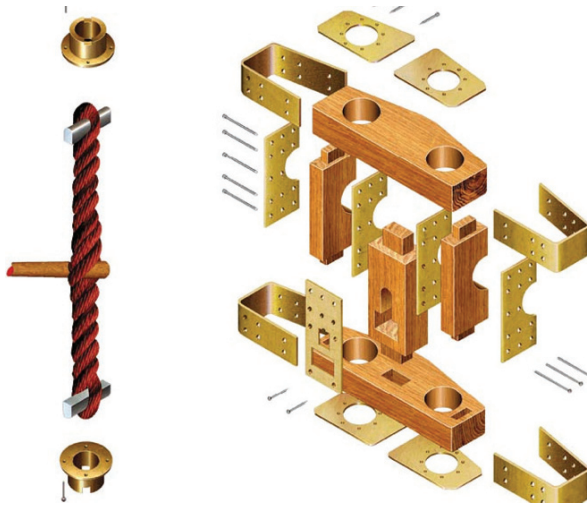


**Fig. 1** Torsion motor of a catapult

The dart was about 450 mm and weighted about 200 g or 850 mm long and its weighted about 250 g; the range was up to 550 m.

## The Repeating Catapult Working Principle

A pictorial drawing and an orthogonal technical drawing of our reconstruction of the repeating catapult is shown in Fig. 2; it is possible to observe the arrow magazine, the chain and the crank handles.

The repeating catapult is described by Philon of Byzantium [3, 4] and can be considered as a futuristic automatic weapon that throws 481 mm long darts. This machine was attributed to Dionysius of Alexandria and, apparently, it was used around the 1st century BC; it was as a part of the arsenal of Rhodes that may be considered as a concentration of the most advanced mechanical kinematic and automatic systems of the time, many of which are still widely used [5].

Essentially, it consisted of a container holding within it a number of arrows, a cylinder feeding device and movement chain.

The description left to us by Philon, as is easily understandable, was not written to eliminate all doubt, as it lacks a technical glossary and an analytic style. In Fig. 3 some details of the mechanism are shown.

According to Philon, the arrows were located in a vertical feeder (see Fig. 4) and were transferred one at a time into the firing groove by means of a rotating drum activated alternatively by a guided cam, in turn activated by a slide. A simple rotation of the crank was sufficient to move the drum, the slide, the coupling mechanism and the release mechanism. The cycle repeated automatically without interruption

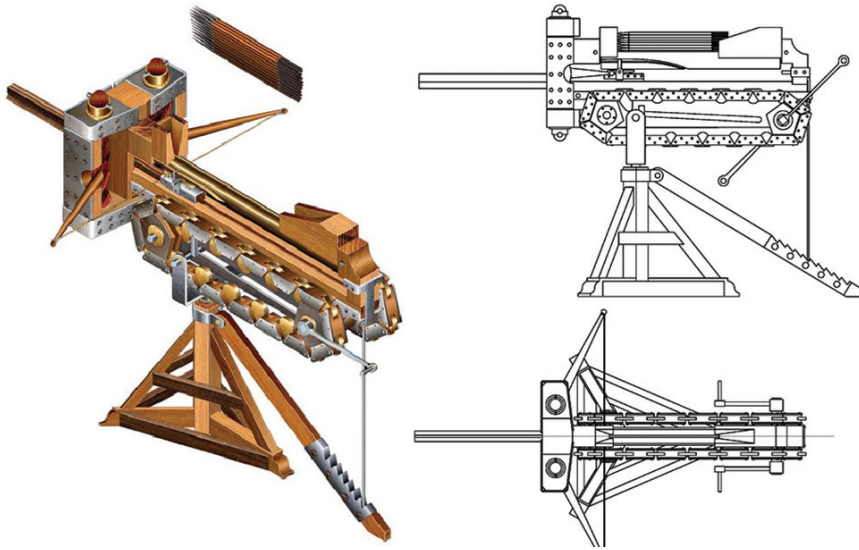


**Fig. 2** Reconstruction of the repeating catapult

or inverting the rotation of the sprocket until the charger was empty, a charger that could be re-loaded without suspending firing.

It is interesting to note that the motion from the crank shaft to the other parts occurred by means of two flat link chains pulled by pentagonal sprockets, as shown also in Fig. 4. These, similar to modern electrical saws, had interior teeth that were inserted into the spaces of the pentagonal motor sprocket and the return sprocket, preventing them from exiting. Similar types of chains, called *Galle*, are attributed to Leonardo da Vinci and transmit motion in bicycles and motorcycles.

One of the longer interior teeth (see Fig. 4) pulled the slide which in turn pulled the cord, loading the coils of the motor. When in motion, an attached cam caused a 180° rotation in the direction of the loaded cylinder, drawing an arrow from the loader and placing it in the channel in front of the rope (see Fig. 6). When the slide reached the rear of the weapon, the cog released it, while another opened the release mechanisms. An instant later, upon completion of sprocket rotation, the same cog coupled with the slide from underneath, pulling in the opposite direction. Near the top of the weapon, the second device closed the hook after it had retrieved the cord, while the feeder picked up another arrow from the feeder. A half rotation in the sprocket and the cycle was repeated. In Fig. 4 is also shown the feed mechanism compared with the one of the Gatling machine gun; this last is considered as the first (1862 U.S. patent) machine gun and its working principle is still used for actual aircraft automatic weapons.

From a ballistic perspective, the rate of fire must have been about of five stroke per minute: very little when compared to our automatic weapons, but certainly impressive for the era. Paradoxically, this very reason made it useless as it concentrated

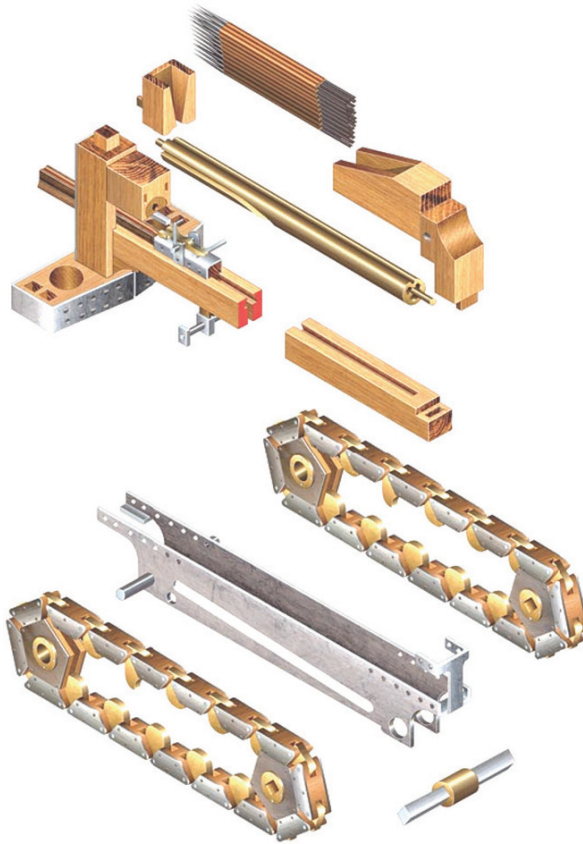


**Fig. 3** Details of the mechanism

all the arrows in the same location in such a short period of time that it continued to strike the same target.

An unquestionable demonstration of its potential was confirmed in the early 1900s, when a life size reproduction was made in Germany: during the testing performed in front of the Kaiser, one of its arrows split a another arrow exactly in two!

## The Pneumatic Ballista

The only and not insignificant drawback of torsion motors was the strongly hygroscopic nature of the coils, which were weakened when they came into contact with water or a humid environment. Rain or even a prolonged exposure to humidity or fog drastically decreased its potential. When they wanted to use torsion artillery in Nordic climates or in naval contexts, the motors had to be carefully protected in

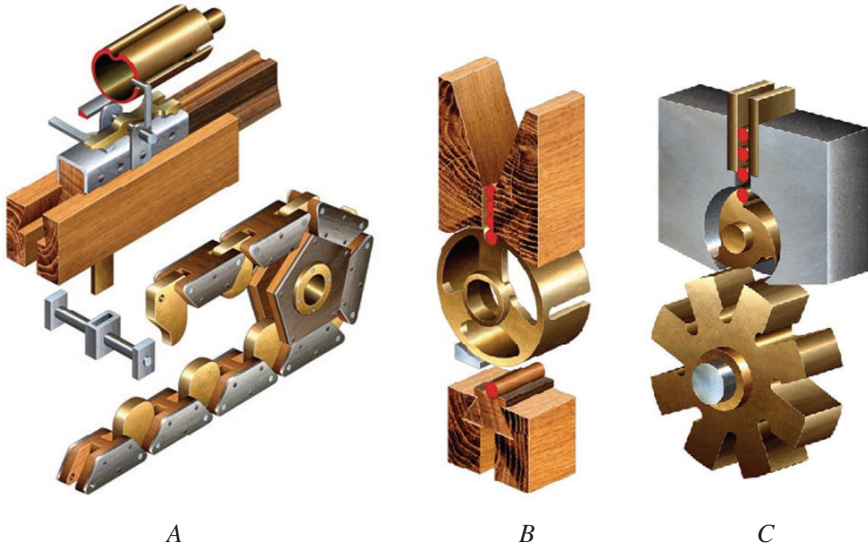


**Fig. 4** Chain and trigger mechanism (A); repeating catapult (B) and Gatling machine gunfeeding mechanisms (C)

hermetically sealed housings. These solutions were not completely satisfying, so a new invention in this field was made in the same ages.

During the Hellenistic Age, many scientists and engineer invented a number of devices that make use of pneumatics, so the knowledge of this academic discipline should have been very advanced. In particular, Philon of Byzantium was perfectly (2nd century BC) described a weapon in his work *Belopica*, that he defined as an *air spring ballista*. In this weapon he makes only minimum modifications to the usual (already at that ages) cylinder-piston device.

A pictorial reconstruction of this device is shown in Fig. 5 and some particulars in the lower part of the figure.

The ballista is essentially made up by two cylinder-piston devices that substitute the usual torsion motor. The pistons are fixed to the catapult's frame while the pistons are linked to a rack and pinion system; the catapult's arms are moved by the pinions; these last are obviously confined to a sector gear.

In Fig. 6 an orthogonal design is reported.

Although even one cylinder would have been sufficient, in order to reach the correct volume it would have required a larger diameter and stroke; this was difficult to achieve at the time with any degree of precision.

In his description Philon stated that the cylinders were first hammered externally to increase their resistance, bored internally with a drill and then polished. As for the pistons, he mentions the geometric precision of the lathe enhanced by polishing. Since even the smallest tolerances cannot prevent loss of compression, recourse to gaskets is inevitable: Philon mentions two, one at the mouth of the cylinders and the

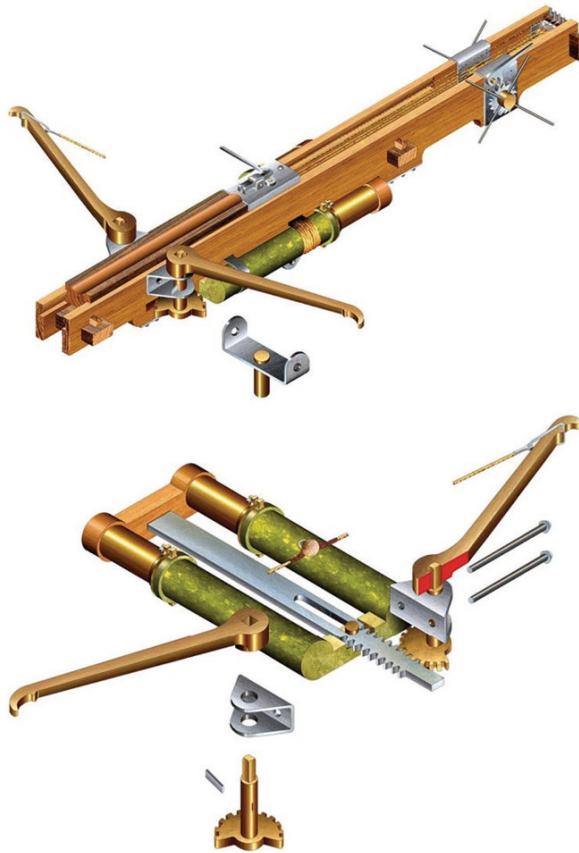


**Fig. 5** A reconstruction of the Pneumatic Ballista

other on the heads of the pistons, to prevent the escape of air. These were achieved by using an abundant layer of fish glue, which maintained its elasticity even when dry.

It is interesting to report that Philon tells that during the tests carried out by Ctesibius, he forced the cylinder's piston to violently release by applying a vigorous blow with a mallet. When it came out he was astonished to see that its internal gasket was on fire! But neither he nor his followers, almost up to engineer Rudolf Diesel, could know that a gas subjected to rapid decompression heats rapidly and abundantly. No one in the 2nd century BC had sufficient knowledge to describe such a prodigious event without having seen it personally!

Finally it must be said that the working principle is essentially similar to the pre-compressed air guns proposed in the last few decades in the field of air shooting competitions as the last and most effective novelty.



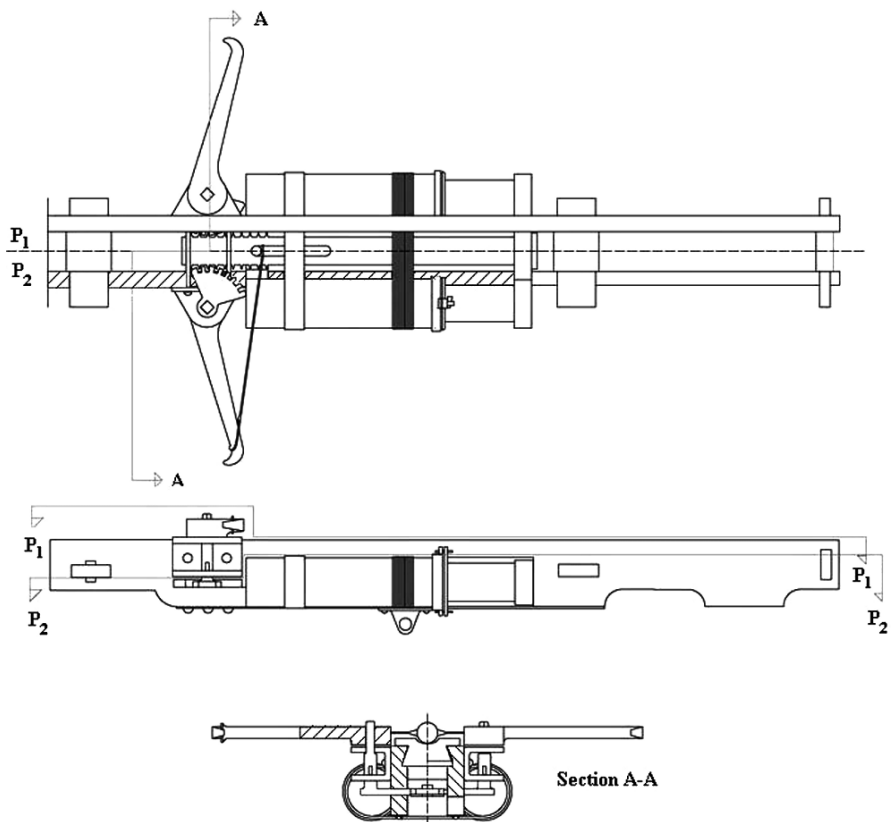


Fig. 6 Orthogonal design of the pneumatic catapult

### Conclusions

The reconstructions of two less-known ordnance of the Roman Army have been presented; unfortunately, during the centuries, many inventions and technological innovations have been conceived starting from military applications. Anyway these devices show that engineers and craftsmen, who existed millenniums before us, solved problems using the devices of their era, making machinery and equipment whose concept is of such a surprising modernity that we must rethink our image of the past.

Reconstruction of ancient devices are often difficult. The one of the repeating catapult, for instance is based on old texts (e.g. [6]), on the work made by Schramm [7] that is also reported by Marsden [3, 4] with the original description by Philon of Byzantium. As for this last description it has to be pointed out that ancient Greek hasn't technical terms: for instance in "Ta Filonos Belopoika 75, 33-34" the chainmail is called "πλιυθια" = little brick and the teeth of the chain are called "περονας" = fin. The difference between our reconstruction of this device and

the previous ones mainly consist in the reload sequence: the other Authors suppose that the crank handles had to reverse the rotation each strike, while we suppose the direction of rotation was always the same. This seems to us more believable also because, in his way, the ratchet could have worked correctly and the rate of fire could have been maintained quasi constant.

## References

1. Russo F. and Russo F., *POMPEI Course Toward Transformation – the Forgotten Contributions of Roman Naval Technology*, NATO, CCMAR Naples, 2007. ISBN 978-88-95430-05-8.
2. *79 A.D. Course for Pompeii, Inquiry on the Death of an Admiral*, NATO, CCMAR Naples, lecture notes 2006.
3. Marsden E. W., *Greek and Roman Artillery Historical Development*, Oxford University Press II Ed. 1969.
4. Marsden E. W., *Greek and Romana Artillery. Technicacal Treatises*, Oxford, 1971, pp. 106–184.
5. *Tormenta Navalia. L'artiglieria navale romana*, USSM Italian Navy, Roma, 2007.
6. Baldi B., *Heronis Ctesibii Belopoiika, hoc est, Telifactiva*. Augusta Vindelicorum, typu Davidu Frany, 1616.
7. Schramm E., *Die antike Geschütze del Saalburg*, Berlin, Weidmannsche Buchandlung, 1918.

# “DEUS-EX-MACHINA” in Phlius Theatre

Argyris S. Papadogiannis, Marilena C. Tsakoumaki and Thomas G. Chondros

**Abstract** The stage machine used to bring the gods or the heroes of the tragedy on stage, known with the Latin term *Deus ex machina* was used in some ancient Greek drama, for the solution of an apparently insoluble crisis. This intervention of a god or a hero brought on stage was possible by this elaborate piece of equipment, the *mechane*. Archaeological evidence in the ancient Greek theatre of *Phlius* (Corinthia) was reappraised in an attempt to reconstruct the *mechane*.

**Keywords** *Deus Ex Machina* · Kinematics · Mechanism design · Dynamics · Machine reconstruction · Ancient Greek theatre

## Introduction

The ancient Greek theatre was born in the 6th century BC out of a form of a single actor dance drama that flourished in the Dorian parts of Greece. It reached a period of maturity by the 5th century BC, following the victorious wars against the Persian Empire and the rise of Greek Drama, Aeschylus, who was himself a war hero, won his first literary victory in the dramatic festival of 484 in Athens. In 472 he presented the *Persians*, where he introduced the second actor besides himself, and thus created the multi actor theatrical play. Sophocles, Euripides and Aristophanes made great contributions to the Greek theatre of the 5th century [1]. Aristotle [2, 3] provides a chronological statement of the various steps in the evolution of Attic Tragedy.

Aeschylus introduced the idea of a god, which would emerge suddenly from behind the skene building, over the roof and (perhaps) into the Orchestra area to conclude the drama. The preparation and pick-up of the actors (and in some cases of horses and chariots too) was done from behind the skene building. The instrument for this operation was called *mechane* equivalent to the Latin term machine [4, 5]. The first known written record of the word machine appears in Homer and Herodotus to describe political manipulation [1]. The word was not used with its

---

A.S. Papadogiannis (✉)

University of Patras, Department of Mechanical Eng. & Aeronautics, 265 00 Patras, Greece

modern meaning until Aeschylus used it to describe the theatrical device used to bring the gods or the heroes of the drama on stage; whence the Latin term *Deus ex machine* prevailed. *Mechanema* (mechanism), in turn, as used by Aristophanes, means “an assemblage of machines”. None of these theatrical machines, made of perishable materials, is extant. However, there are numerous references in extant plays, which will yield information about its design and operation. Very few details are known about the *mechane*, but it is certain that they were substantial mechanisms for path and motion generation. They were probably several meters high and operated above the stage and roof of the theatre. In a fully retracted position a *mechane* was hidden behind the stage, so it would have to have more than one moving link and it could carry substantial load.

Detailed information on stage scenery and machinery in the ancient theater are given by Vitruvius [6] and Pollux [7]. It is described by Pollux as follows “The mechane shows gods or heroes – Bellerophons or Perseuses – in the air”. It is situated by the left parodos at a height above the skene Parodos (side walk) is the narrow pass to the Orchestra on each side. This defines the position of the main body of the *mechane*, though it is not known at which side. It defines also the range of operation since “Deus ex Machina” appeared at about the middle of the *skene* building.

Most authorities agree that the *mechane* was first used in Aeschylus times. In *Eumenides* (403) Athena flies in on a chariot, which means that a load of about 4,000 N was transported. Wilamowitz [8] however, suggested that the entrance of Athena was on foot and that the respective line was added later when the mechane was available.

There is further evidence that the *mechane* was used by Aeschylus: in *Prometheus Bound* the entrance of the chorus of the Oceanids by a flying chariot is introduced by Prometheus by thirteen lines, while in Euripides plays the respective introductions are 6–7 lines [1]. One explanation is the substantial load to be transported: Since the number of the chorus members at this time was fifteen, it can be estimated that the load transported would have been about 10,000 N. The door is open, however, for a different interpretation: A double entry using two mechanes as suggested by the scholiast Lucianus (2nd century AD) one on each side. This reduces the load on each to 5,000 N still a formidable one for that time. Pollux describes the *mechane* as a crane, which comes from above and grabs the body of Memnon in the Aeschylus tragedy.

Aristophanes used the *mechane* too. In *Peace* Trygaios flies to heaven on a dung beetle and appeals to the mechanic not to let him fall (line 173) “. . . engineer be careful, for if you are not, I will become food for the dung beetle . . .” and he further complains that he is dizzy from the swinging motion. He recites eighteen lines (154–172) during which time he is swung violently enough to convey a sense of space travel and then lowered back to the point where he had started. In *Daedalus* Aristophanes mentioned that the *mechanopoios* – machine maker operates the wheel. The fact that the designer himself operates the machine could only point to a complex mechanical device. Further, in *Gerytades* he moves the crane fast using the word *periagon*, which means general rotation about a pivot. In *Clouds*

he describes Socrates is coming from the air in a net hanging from the *mechane*. In *Birds* there are references to flight.

Several conclusions can be drawn from these:

- (a) The machine could provide vertical motion in addition to horizontal.
- (b) The operator could control the vertical position of the load.
- (c) A wheel was used by the operator for some control function.
- (d) A pivoted beam was probably the main party of the *mechane*.
- (e) In some cases the load should move fast.

Although there are numerous illustrations of plays involving the *mechane* in vase paintings there is a very little information about the *mechane* itself, which seems to be invisible. In an Apulian vase in the Metropolitan Museum of Art in New York we can see the body of *Sharpedon*, son of *Europa*, carried through the air by *Sleep* (*Ypnos*) and *Death* (*Thanatos*) most probably from Aeschylos’ *Europa* (Fig. 1). There is an important piece of information in this, however, since it indicates that the *mechane* was not very visible. This also agrees with aesthetic considerations, since a highly visible mechanism would not be in tune with the scenery, costumes and masks they were using.

Another vase painting illustrates a scene from Euripides’ *Medea* (Fig. 2). *Medea* is ready to drive off to Athens in a snake drawn chariot of the Sun, which would have been on the *mechane* while below there are her dead children, on the left is Jason and on the right the teacher and, probably *Aphrodite*. Again the *mechane* seems invisible.

It is important to note that *Prometheus Bound*, where the most powerful *mechane* on record appears to have been used, is a hymn to democracy and technology [1]. Product of Aeschylos age of maturity, it was produced in 458, shortly before his



**Fig. 1** Sharpedon, son of Europa, carried through the air by Sleep and Death, Aeschylos’ *Europa*. Apulian vase



**Fig. 2** Medea in a snake drawn chariot of the Sun, Euripides' *Medea*. Early Lucanian hydria, ca. 400 BC

death in 456, in Sicily. This tragedy has a powerful symbolism: Prometheus taught the people the science, the technology and the use of the fire. With them, they could tame the natural powers and make their life better. Antiphanes, making fun of the tragedy poets, said that "... they move the *machane* as they raise their finger, when they have nothing to say ...". This indicates that mechanical advantage and load balancing was used. Platon in *Cratylus* has a similar reference to the tragic poets.

Other pieces of stage machinery were the *periaktos* and the *ekkyklema*. *Periaktos* was a revolving piece of scenery, which was used as today's revolving stage for quick change of scenery. It had three faces, and was supported on a vertical shaft, which was itself pivoted on the floor in a stone bearing. The *ekkyklema* was a wheeled low-profile vehicle used to carry to and from the stage heavy scenery. From the circular holes found on the ground of many theaters it appears that such poles were in wide use for the *periaktos* and probably for the *mechane*. Since bearings and lubrication were well-known at that time [9] it seems that those vertical poles were rotating.

Dimarogonas [1] and Chondros [10] suggested a reconstruction of the *mechane* capable for operation in the theatre of Dionysus consisting of a pivoted beam with ropes and pulleys forming a four-bar spatial mechanism for generation of a curved path of the end of the beam coupler, located behind the skene building and near the left *parodos* of the theatre of Athens. This *mechane* is capable for lifting weights up to 10,000 N and its range of operation permitted loading and unloading from behind the skene building to the orchestra area in front of the skene building. Kinematic and dynamic analysis of the *mechane* showed that this design was feasible.

A twin facing stone base was found in the theatre of Phlius (Corinthia) behind the skene building [11, 12]. This evidence was analyzed in an attempt for the reconstruction of *Deus Ex Machina* used in the theatre of Phlius. The existence of similar foundations in the theatres of Megalopolis and Eretria [13, 14] indicating their use for specific purposes connected with the needs of the drama, makes the twin facing stone base in the theatre of Phlius unique. Based on the archaeological evidence of this twin stone foundation. An attempt was made to interpret its superstructure based on archaeological evidence and proper static and kinematics analysis, and literary descriptions.

## Ancient Greek Theatres

A substantial number of ancient Greek theatres have survived the time to the extent that their architecture can be reconstructed with some precision. A reconstruction by Bulle [15] of the typical 5th century Athens theatre of *Dionysus Eleuthereus*, on the southeast slope of Acropolis is shown in Fig. 3. Performances were given throughout the day and lasted for several days. In earlier times, the skene building of the Athens theatre was about 4 m high and 27 m wide. At later times the skene was a two-story building, according to some authors. The skene building had an almost flat roof on which the actors performed in some plays. Otherwise the play was performed in the circular area called Orchestra.

The ancient theatre of Phlius was discovered in 1924 by Bleyen and in the years 1970–1973 after extended excavations most of its architectural characteristics were revealed [11]. An important piece of archaeological evidence found behind the skene building indicates a direct relation with the operation of the *mechane*. A pair of stone foundations is located at the right part of the skene and behind the skene building [12]. These foundations are rectangular in shape with overall dimensions of approximately  $800 \times 1,300$  mm, open on one short side. The space left open by the slabs measures  $300 \times 340$  mm. The foundations are facing each other with a distance of approx. 1,200 mm. The side walls meet the short walls at right angles and are secured by iron hook clamps set in lead. All four of these clamps have survived in situ. Rectangular cuttings exist in the upper surfaces of the side walls. The open ends of each construction are partially blocked by a rectangular slab which provides an angled floor between the two side walls positioned at a  $30^\circ$  angle sloping inwards, ending at the level of the cuts of the side blocks and facing the short side of the rectangle.

In Fig. 4, the pair of stone foundations situated behind the west side of the rear wall of the skene building is shown at the lower left end of the theatre plan. The open ends of each construction are partially blocked by a rectangular slab which provides an angled floor between the two side walls positioned at a  $30^\circ$  angle sloping inwards, ending at the level of the cuts of the side blocks and facing the short side of the rectangle. The vertical line to the longitudinal axis connecting the two pairs of stone foundations is heading to the *skene* centre.

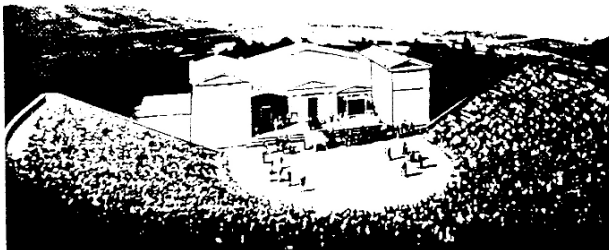


Fig. 3 Reconstruction of the Athens theater by Bulle [15]

THE THEATER AT PHLIUS: EXCAVATIONS 1973

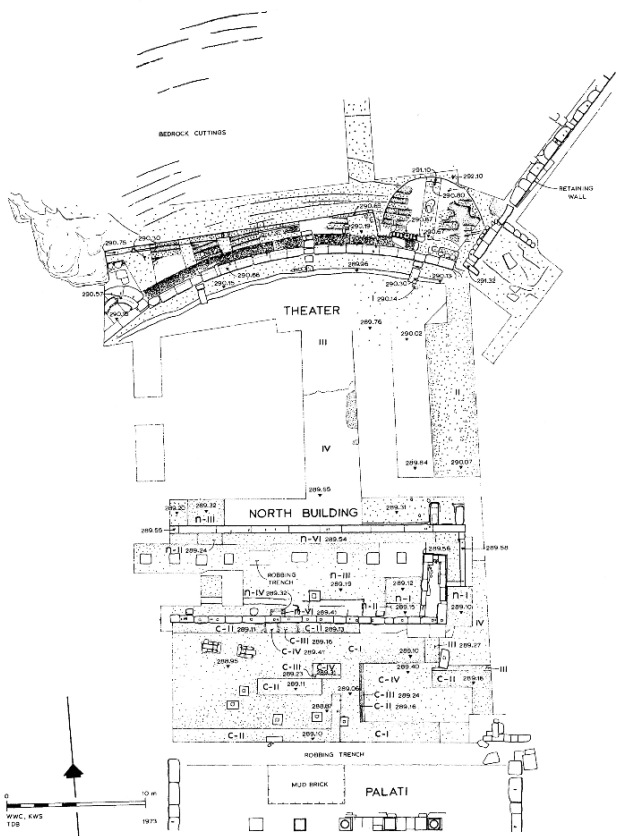
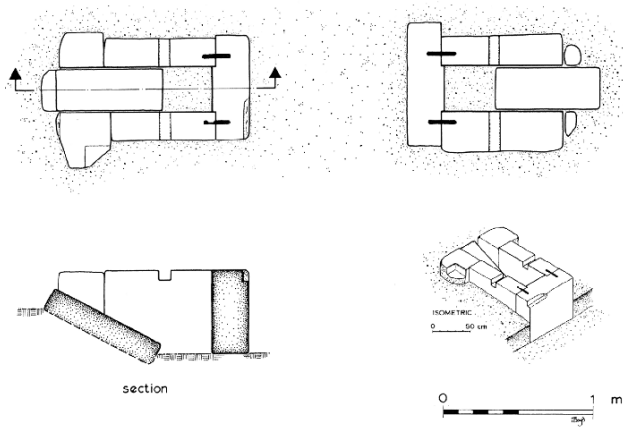


Fig. 4 The stone foundation, and Plan of the Phlius theatre in the 1st century BC, Biers [12]



The foundations in Phlius are unique, they are located directly behind the line of the skene and on its west side, placed closely together and not oriented with the present skene building but more southeast-northwest. Based on the dimensions of the skene building in the theatre of Phlius and the spatial envelope in which the *mechane* would operate, an attempt to reconstruct *Deus ex Machina* is presented here. It will be assumed here that this pair of stone foundations was used for windlass operation. Kinematic and dynamic analysis was performed for the design and reconstruction of the *mechane*.

## ***Mechane* Reconstruction**

The problem of lifting heavy architectural members is considered mainly in terms of the various cranes and hoists based on compound pulley systems which are described by Vitruvius and Hero of Alexandria [6, 7]. The simple pulley, used not to gain mechanical advantage but just to change the direction of pull, is first known from the 9th century BC and may well have been known to the Greeks before they began to build in megalithic masonry in the late 7th century BC; but the earliest indisputable evidence for a knowledge of compound pulley systems is referred in the *Mechanical Problems* attributed to Aristotle.

Load handling machines in antiquity [1, 16] were equipped with ropes to provide a specific path of a point of the beam, usually circular. In the reconstructed *mechane*, the main beam is connected with two links between the beam upper end at the hook pulley and the ground (Fig. 5), giving circular motion to this point and a curved motion of the hook on a plane containing the beam. This configuration for the *mechane* results in a four-bar plane mechanism for generation of a curved path of the end of the beam coupler, in this case the carriage hanging point. The beam has two supports, one at the pivot point and the other at about 150 mm far from the beam's end for the rope pulley as shown in Figs. 5 and 6. Static and Dynamic analyses were performed to evaluate the feasibility of the reconstructed *mechane*.

Moreover, since the load had to be lowered only with the winch, the rope friction at the drum and the pulley at the beam end would help the operator during unloading. For the usual 2,000–4,000 N loads one operator would suffice for the lower 2,000 N load while two operators were required for the 4,000 N. With the two lateral links the operator could have precise control of the motion, this leading to path control.

It is impossible to time exactly the motion of the *mechane*. We can safely assume, however, in view of the above observations and contemporary theatrical interpretations that it would be in the order of a few seconds. If 15 s were assumed for raising the load from the skene roof to the higher point above it, i.e. 4 m, 6 revolutions of the drum would be required for 21 mm drum diameter. Then the mast had to be retrieved by an angle of  $16^\circ$ , this requiring 1.5 turns of the horizontal drum or 3 s. Then, another 10 s were required to lower the load beneath the back wall and the total time to hide the load from the spectators and lower it to the ground beneath the skene building is summed up to 30 s. After that the main beam had to lean

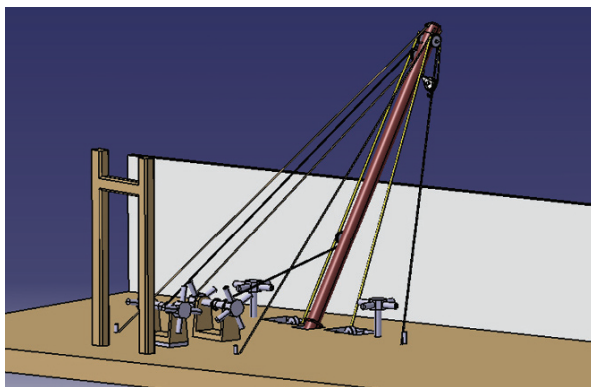


**Fig. 5** The mechane in operation position, back view

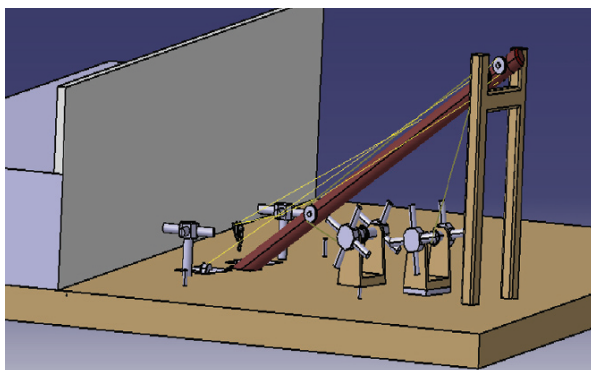


**Fig. 6** The mechane in rest position, hidden behind the skene

backwards on a vertical support as shown in Fig. 6, this requiring another 5 s. Thus, the total required time to hide the *mechane* is 35 s.

## Conclusion

*Deus-X-Machina* was the achievement of engineering (intelligence) in response to specifications imposed by the needs of the stage production. The *mechane* together with other mechanical devices such as the *periaktos* and the *ekkyklema*, used as stage machinery in the ancient Greek theatre, are the very early heritage of mechanical engineering. Mechanical engineering has its roots in the *mechanopoioi* of Aristophanes, the pioneers who designed, built and operated the *mechane*. The twin facing machine base in the theatre of Phlius were analyzed in an attempt for the reconstruction of *Deus Ex Machina* used in the theatre of Phlius. The existence of similar foundations in the theatres of Megalopolis and Eretria, indicating their use for specific purposes connected with the needs of the drama makes the twin facing

stone base in the theatre of Phlius unique. An attempt was made to interpret its superstructure based on archaeological evidence and proper static and kinematics analysis, and literary descriptions. The reconstructed mechanism comprised of a spatial single beam, a sidle twin lifting system, and a beam lowering system, designed for path generation. This *mechane* does not appear to have any close predecessor and its development is of great engineering significance since it appears that it was designed to meet very close requirements of the play, it was different from other similar devices in other theatres, and it was not arrived at by long evolution.

## References

1. Dimarogonas, A. D. 1992, *Mechanisms of the Ancient Greek Theater*, ASME Design Conference, Phoenix Arizona.
2. Aristotle, *Poetic*, iii. 3.
3. Ridgeway, W. 1915, The Origin of Tragedy: Introduction. *The Dramas and Dramatic Dances of Non-European Races*. Cambridge University Press, Cambridge.
4. Mastronarde, D. J. 1990, *Actors at High: The Scene Roof, the Crane and the Gods in Attic Drama*, Classical antiquity, Univ. of California – Berkeley Press.
5. Dimarogonas, A. D. 1986, *History of Technology*, Symmetry publ. Athens.
6. Vitruvius, M. P. *De Architectura*, V. 7, 1st Century A.D. (republished by Barbaro D., I Dieci Libri dell'Architettura di M. Vitruvio, Venezia, 1584.)
7. Julius, P. 1890, *Onomastikon*, Edited by Bethe, *Pollucis Onomastikon*, Stuttgart.
8. Wilamowitz-Moellendorf, U. 1907, *Einleitung in der GriechischenTragoedie*, Weidmann Buchhandlung, Berlin.
9. Dimarogonas, A. D. 1991, The Origins of the Theory of Machines and Mechanisms. *Proceedings 40 Years of Modern Kinematics: A Tribute to Ferdinand Freudenstein Conference*. Minneapolis.
10. Chondros, T. G. 2004, Deus-Ex-Machina Reconstruction and Dynamics, Edited by Marco Ceccarelli, *International Symposium on History of Machines and Mechanisms, Proceedings HMM2004*, Kluwer Academic Publishers, pp. 87–104.
11. Biers, W. R. 1972, Excavations at Phlius, *Hesperia*, Vol. 42, No. 1. (Jan.–Mar., 1973), pp. 102–120.
12. Biers, W. R. 1975, The Theater at Phlius: Excavations 1973, *Hesperia*, Vol. 44, No. 1. (Jan.–Mar., 1975), pp. 51–68.
13. Fiechter, E. 1931, *Das Theater in Megalopolis (Antike Griechische Theaterbauten, IV)*, Stuttgart.
14. Fiechter, E. 1937, *Das Theater in Eretria (Antike Griechische Theaterbauten, VIII)*, Stuttgart.
15. Bulle, H. 1928, *Untersuchungen an Griechischen Theatern*. Abhandlungen, Bayrischen Akademie der Wissenschaften, Munich.
16. Coulton, J. J. 1974, Lifting in Early Greek Architecture, *The Journal of Hellenic Studies*, Vol. 94, pp. 1–19.

# Archimedes and the Origins of Mechanisms Design

Thomas G. Chondros

**Abstract** Archimedes (ca. 287–212 BC) was born in Syracuse, in the Greek colony of Sicily. He studied mathematics at the Museum in Alexandria. He is the founder of statics and of hydrostatics, Archimedes discovered fundamental theorems concerning the center of gravity of plane geometric shapes and solids and his machine designs fascinated subsequent writers. Archimedes systematized the design of simple machines and the study of their functions and developed a rigorous theory of levers and the kinematics of the screw. His works contain a set of concrete principles upon which design can be developed as a science using mathematics and reason.

**Keywords** Archimedes · Kinematics · Mechanisms design · Design methodology

## Introduction

Archimedes (ca. 287–212 BC) was born in Syracuse, in the Greek colony of Sicily. His father was the astronomer and mathematician Phidias, and he was related to King Hieron II (308–216 BC) [1, 2]. The name of his father – Pheidias – suggests an origin, at least some generations back, in an artistic background [3] (Fig. 1).

At the time of Archimedes, Syracuse was an independent Greek city-state with a 500-year history. The colony of Syracuse was established by Corinthians, led by Archias in 734 BC. The city grew and prospered, and in the course of the 5th century BC the wealth, cultural development, political power and victorious wars against Athenians and Carthaginians ensured for a long time the dominance of Syracuse as the most powerful Greek city over the entire south-western Mediterranean basin. Archimedes went to Alexandria about 250–240 BC to study in the Museum under Conon of Samos, a mathematician and astronomer (the custodian of the Alexandrian library after Euclid’s death), Eratosthenes and other mathematicians who had been

---

T.G. Chondros (✉)

University of Patras, Department of Mechanical Eng. & Aeronautics, 265 00 Patras, Greece  
e-mail: chondros@mech.upatras.gr

**Fig. 1** Archimedes portrait  
courtesy of the MacTutor  
History of Mathematics  
Archive run by the School of  
Mathematics and Statistics at  
the University of St.  
Andrews, Fife, Scotland



students of Euclid. Archimedes later settled in his native city, Syracuse, where he devoted the rest of his life to the study of mathematics and the design of machines.

Archimedes' books concentrated on applied mathematics and mechanics and rigorous mathematical proofs [4–6]. He established the principles of plane and solid geometry. Some of Archimedes' accomplishments were founded with mathematical principles, such as his calculation of the first reliable value for  $\pi$  to calculate the areas and volumes of curved surfaces and circular forms. He also created a system of exponential notation to allow him to prove that nothing exists that is too large to be measured [6–8].

In addition to his mathematical studies, Archimedes was both a great engineer and a great inventor. He invented the field of statics, enunciated the law of the lever, the law of equilibrium of fluids, and the law of buoyancy, and he contributed to knowledge concerning at least three of the five simple machines – winch, pulley, lever, wedge, and screw – known to antiquity. He discovered the concept of specific gravity and conducted experiments on buoyancy. He is credited with inventing the compound pulley, the catapult, and the Archimedes Screw, an auger-like device for raising water. He conducted important studies on gravity, balance, and equilibrium that grew out of his work with levers and demonstrated the power of mechanical advantage [3, 9] (Fig. 2).

Archimedes was also known as an outstanding astronomer; his observations of solstices were used by other astronomers of the era. As an astronomer, he developed an incredibly accurate self-moving model of the Sun, Moon, and constellations, which even showed eclipses in a time-lapse manner. The model used a system of screws and pulleys to move the globes at various speeds and on different courses [3, 9].

During Archimedes' lifetime the first two of the three Punic Wars between the Romans and the Carthaginians were fought. During the Second Punic War (218–201 BC) – the great World War of the classical Mediterranean, Syracuse allied itself with Carthage, and when the Roman general Marcellus began a siege on the city in 214 BC, Archimedes was called upon by King Hieron to aid in its defence and later worked as a military engineer for Syracuse (Plutarch ca. 45–120 AD).

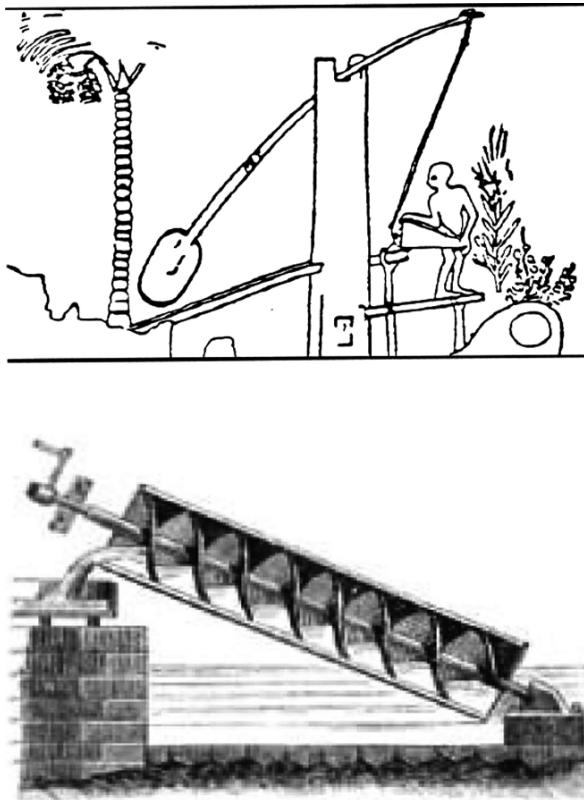


**Fig. 2** The shaduf, first used in Mesopotamia in about 3000 BC and Archimedes' screw machine [10]

Archimedes, either invented or improved upon a device that would remain one of the most important forms of warfare technology for almost two millennia: the catapult. Plutarchos and Polybios (201–120 BC) describe giant mechanisms for lifting ships from the sea, ship-burning mirrors and a steam gun designed and built by Archimedes. The latter fascinated Leonardo da Vinci, however the validity of these stories is questionable.

According to Netz [11] in the most expansive sense, bringing in the Arabic tradition in its entirety, 31 works may be ascribed to Archimedes. The corpus surviving in Greek – where Eutocius' commentaries are considered as well – includes the following works:

1. *On the Sphere and the Cylinder. The First Book*, 2. *Eutocius' commentary on the First Book*, 3. *On the Sphere and the Cylinder. The Second Book*, 4. *Eutocius' commentary on the Second Book*, 5. *Spiral Lines*, 6. *Conoids and Spheroids*, 7. *Measurement of the Circle (Dimensio Circuli)*, 8. *Eutocius' commentary to the above*, 9. *The Sand Reckoner (Arenarius)*, 10. *Planes in Equilibrium*, 11. *Eutocius' commentary to the above*, 12. *Quadrature of the Parabola*, 13. *The Method*, 14. *The first*

book *On Floating Bodies (de Corporibus Fluztantzbus)*, 15. The second book *On Floating Bodies (de Corporibus Fluztantzbus)*, 16. *The Cattle Problem (Problems Bovinum)*, 17. *Stomachion*.

Additionally, there are 13 works ascribed to Archimedes by Arabic sources, five are paraphrases or extracts of 1, 3, 7, 14 and 17, four are either no longer extant or, when extant, can be proved to have no relation to Archimedes, while four may have some roots in an Archimedean original [12, 3, 9]. These four are:

1. *Construction of the Regular Heptagon*, 2. *On Tangent Circles*, 3. *On Lemmas*, 4. *On Assumptions*. None of these works seems to be in such textual shape that we can consider them, as they stand, as works by Archimedes, even though some of the results there may have been discovered by him. Finally, several works by Archimedes are mentioned in ancient sources but are no longer extant. These are listed by Heiberg as “fragments,” collected at the end of the second volume of the second edition:

*On Polyhedra, On the Measure of a Circle, On Plynths and Cylinders, On Surfaces and Irregular Bodies, Mechanics, Catoptrics, On Sphere-Making, On the Length of the Year.*

From extant works whose present state seems to be essentially that intended by Archimedes, ten works mentioned above as: 1, 2, 5, 6, 9, 10, 12, 13, 14, and 15 are attributed in great probability to Archimedes.

## Archimedes and the Design of Mechanisms and Machines

The problem of lifting heavy architectural members is considered mainly in terms of the various cranes and hoists based on compound pulley systems which are described by Vitruvius and Hero of Alexandria [13, 14]. The simple pulley, used not to gain mechanical advantage but just to change the direction of pull, is first known from the 9th century BC and may well have been known to the Greeks before they began to build in megalithic masonry in the late 7th century BC; but the earliest indisputable evidence for a knowledge of compound pulley systems is referred in the *Mechanical Problems* attributed to Aristotle.

Rapid advancement in natural sciences was followed by systematic attempts to organize the knowledge in engineering and, in particular, in Mechanical Design, developing it beyond the level of a mere craft. Heraclitus of Ephesus (ca. 550–475 BC) appears to have been the first to separate the study of motion itself from dynamics, the forces causing the motion, and introduced the principle of retribution, or change, in the motion of celestial bodies.

Kinematics and machine design have a distinct place in the history of engineering because they comprised the very first of its divisions to receive a mathematical foundation [1]. The first known written record of the word *machine* appears in Homer and Herodotus to describe political manipulation [1, 15]. The word was not used with its modern meaning until Aeschylus used it to describe the theatrical device used to bring the gods or the heroes of the drama on stage; whence the Latin term

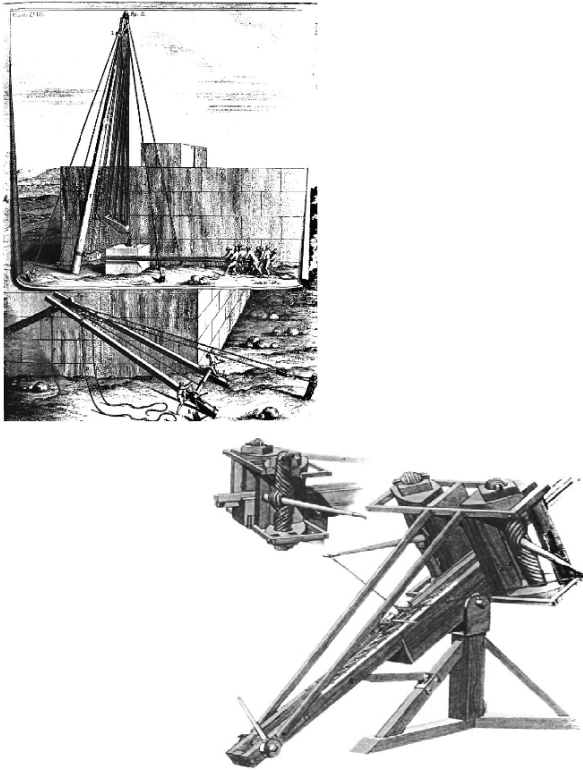


**Fig. 3** Lifting machine (trispaston) from Archimedes times, drawing from Vitruvius book, and reconstruction of Catapult from Alexander the Great times [10]

*deus ex machina*. Mechanema (mechanism), in turn, as used by Aristophanes, means “an assemblage of machines.” None of these theatrical machines, made of perishable materials, is extant. The designers and builders of these mechanisms were called by Aristophanes *mechanopoioi* (machine-makers), meaning “machine designers” in modern terminology (Fig. 3).

Archimedes systematized the simple machines and the study of their functions. The lever and the wedge are our technology heritage from the paleolithic era. Archimedes first designed in a systematic way those machines and mechanisms and developed a rigorous theory of lever and the kinematics of the screw. His contribution separates engineering science from technology and crafts, often confused for matters arrived at empirically through a process of long evolution.

“Give me a place to stand, and I shall move the Earth,” Archimedes is said to have promised [8]. Archimedes was referring to the law of the lever, which (in the variant form of the law of the balance) he had proved in his treatise, *Planes in Equilibrium*. One can say that Archimedes moved the Earth – in principle – without standing anywhere. Also, Archimedes figured out that the Earth and a pebble are the same kind of thing, differing only in size. Despite the familiar lever law this concept gave



rise to the question of the need to think about time from a new viewpoint outside time. This atemporal perspective of time has been distinguished by modern philosophers as the “Archimedean view from nowhere” leading to the four-dimensional “block universe,” of which time is simply a part [16]. Purely mechanical treatises on machinery go back to the 4th century BC. One of Plato’s contemporaries and friends and a student of Pythagoras, Archytas of Tarentum (ca. 400–365 BC), is said to have written the first systematic treatise on machines based on mathematical principles. This, too, is lost. It is known, however, that Archytas built an air-propelled flying wooden dove (Aulus Gellius, ca. 150 AD). Details about Archytas’s dove are not known but it seems to be the first flying machine.

Some fragments of and references to an extensive treatise, *Machine Syntaxis* (synonymous with *synthesis*), by Philo of Byzantium (ca. 250 BC) [1]. He was a student of Ctesibius at the Museum, and his treatise dealt among other things with the idea of *machine elements*, a small number of simple elements that constitute every machine. Most of this treatise is also lost. However, a comprehensive mechanical treatise by Hero of Alexandria (1st century AD) is extant in an Arab translation. Its title, *Mechanica* (the same as that of Aristotle’s treatise) is generally known as *Mechanics* (*Mechanike*), but the correct meaning of the title is *Problems of Machines*. The Greek word *Mechane* means “Machine.” It should be noted that *Mechanica* is not a guide for the design of mechanical devices, because Hero wrote such texts for particular categories of devices, such as pneumatic machines, automata, optical instruments, balances, and artillery machines. *Problems of Machines* is really a study of design methodology. Hero separated the study of particular machines and the general concepts of machines from the study of standardized elements. He introduced five simple mechanical elements for the solution of the general problem of moving a weight with a given force: wheel and axle, lever, windlass, wedge, and screw. In fact, he asserted that all five solutions are physical devices embodying the lever principle, a simple function module in terms of contemporary literature. Hero’s *Problems of Machines* gave the first systematic development of design solutions to a given mechanism problem. It is to be noted that a substantial part of Hero’s work is probably based on earlier (lost) works of Philo and Ctesibius.

Commentators on the classics flourished in Rome. They not only preserved most of the classical culture but made substantial advances of their own. Most notable was the architect Marcus Vitruvius Pollio, whose ten books *De Architecture* (on Architecture) contained important material on the history of technology and on the design of machinery. Vitruvius defined a machine as “a combination of timbers fastened together, chiefly efficacious in moving great weights” [1].

The Arabs played an important role in the preservation of the Greek science and engineering and made substantial contributions of their own. They devised ingenious mechanisms with a high degree of automation and control. One of the Arabic writers of this era was Ibn al-Razzaz Jazari, who in his extensive and beautifully illustrated treatise on machines, *Book of Knowledge of Ingenious Mechanical Devices* (1206), described a great number of ingenious mechanisms and automata.

The early modern era is highlighted by the works of Galileo and Newton and includes the early stages of mechanization and the Industrial Revolution. The contemporary development of calculus and continuum mechanics led to the rapid development of mechanics by the mid 19th century. The fundamental contribution of Galileo and Newton is the revival and redefinition of classical physics and mechanics just as greater progress was being demanded from natural science.

Design of machines and mechanisms in modern times were established in 1794 when The 'Ecole Polytechnique in Paris established the separate study of kinematics from the study of machinery [1, 2]. Hachette, a colleague of L.N.M. Carnot one of the founders of the 'Ecole Polytechnique, in his book *Traité élémentaire des machines* (1811) proposed the classification of the machine elements into six orders: *recepteurs*, receiving the motion from prime movers; *communicateurs*, passing on the motion; *modificateurs*, changing the type of the motion; *supports*; *regulateurs*, transmission ratio regulators; and *opérateurs*, performing the machine function. Releaux in 1875 published *Theoretische Kinematik* on an attempt to systematize and classify a great number of different machines and mechanisms, a "mechanical alphabet".

Archimedes earned the honorary title "father of experimental science" because he not only discussed and explained many basic scientific principles, but he also tested them in a three-step process of trial and experimentation [1, 17]. The first of these three steps is the idea that principles continue to work even with large changes in size. The second step proposes that mechanical power can be transferred from "toys" and laboratory work to practical applications. The third step states that a rational, step-by-step logic is involved in solving mechanical problems and designing equipment. His works contain a set of concrete principles upon which design can be developed as a science using mathematics and reason.

The aforementioned mechanical design principles can be traced to Filippo Brunelleschi, a Renaissance architect famed for designing the cupola for Santa Maria del Fiore in Florence in the 1420s [18]. He introduced a method of design based on a six-step design process, identical in essence to the design principles of Archimedes, consisting of (1) analyzing the design requirements, (2) making a concept design, (3) making a detailed design, (4) planning the manufacturing process, (5) manufacturing the parts and (6) assembling the parts. Brunelleschi's six-step design process is considered the first systematic design process in engineering history and was carried out for 500 years. In 1964 Sandor [1] proposed a seven steps strategy for machine design that is similar to that of Brunelleschi. The seven steps proposed by Sandor are: formulation of the problem, design concepts, synthesis, analyzable model, analysis-experiment-optimization, presentation.

Similar sequential design procedures were in use until the 1970s, when the notion of engineers working on product design in teams manufacturing and mechanical engineers took hold, and by the 1980s many engineering firms adopted this concept, called concurrent engineering [1]. This switch to concurrent engineering has changed the way engineers do their work, and around that time the advent of computer aided design has revolutionized engineering design. It appears that certain fundamental ideas return with some regularity to the methodology of machine

design. Design rules and concepts were practiced extensively by the engineers of ancient times leading to machine design from machine elements to the design of a machine as a system.

## Conclusion

Archimedes studies greatly enhanced knowledge concerning the way things work, and established major design principles. Mathematical rigor was used by Archimedes for the design of his mechanisms. His practical applications remain vital today. Archimedes earned the honorary title “father of experimental science” because he not only discussed and explained many basic scientific principles, but he also tested them in a process of trial and experimentation providing engineering rationality that was achieved again in the times of Renaissance and the Industrial Revolution. His works contain a set of concrete principles upon which design of machines and mechanisms was developed as a science using mathematics and reason.

## References

1. Dimarogonas, A.D., 2001 *Machine Design A CAD Approach*, John Wiley and Sons, New York.
2. Dimarogonas, A.D., 1991 *The Origins of the Theory of Machines and Mechanisms. Proceedings 40 Years of Modern Kinematics: A Tribute to Ferdinand Freudenstein Conference*. Minneapolis, Minn.
3. Stamatias, E., 1973 *Archimedes–Apanta*, Vols. 1–3. Technical Chamber of Greece, Athens, (in Greek).
4. Heath, T.L., *History of Greek Mathematics*, The Clarendon Press, Oxford, 1921; Dover, New York, 1981.
5. Netz, R., 2004 *The Works of Archimedes*, Cambridge University Press, UK.
6. Netz, R., 1999 *The Shaping of Deduction in Greek Mathematics*, Cambridge University Press, UK.
7. Bell, E.T., 1965 *Men of Mathematics*, Penguin, London.
8. Dijksterhuis, E.J., 1987 *Archimedes*, Princeton University Press, Princeton, NJ.
9. Heath, T.L., 2002 *The Works of Archimedes*, Dover Publications, New York.
10. Lazos, C.D., *Archimedes: The Ingenious Engineer*, Aiolos Publishers, Athens, 1995 [in Greek].
11. Netz, R., 2004 *The Works of Archimedes*, Cambridge University Press, UK.
12. Heiberg, I.L., 1972 *Archimedis Opera Omnia*, I–III CVM COMMENTARIIS EVTOCII, STVGARDIAE IN AEDIBVS B.G. TEVBNERI MCMLXXII, Stuttgart.
13. Vitruvius, M.P., *De Architectura*, V. 7, 1st Century A.D.
14. Julius, P., 1890 *Onomastikon*, edited by Bethe, *Pollucis Onomastikon*, Stuttgart.
15. Chondros, T.G., 2004 “Deus-Ex-Machina” Reconstruction and Dynamics, *International Symposium on History of Machines and Mechanisms, Proceedings HMM2004*, edited by Marco Ceccarelli, Kluwer Academic Publishers, pp 87–104.
16. De Solla Price, D., 1975 *Gears from the Greeks the Antikythera Mechanism – A Calendar Computer from ca. 80 B.C.*, Science History Publications, New York.
17. Bendick, J., 1995 *Archimedes and the Door of Science*, Bethlehem Books, Ignatius Press, Warsaw, ND San Francisco.
18. Mechanical Engineering, 2004 The American Society of Mechanical Engineers magazine *Mechanical Engineering Design*. Editorial Note Salustri.

# The Mirror Weapon in Archimedes Era

A.S. Papadogiannis, N.S. Papadogianni, A. Carabelas, S. Tsitomeneas,  
P. Kyraggelos and T.G. Chondros

**Abstract** The historical accounts of Archimedes' war-faring inventions are vivid and possibly exaggerated. It is claimed that he devised catapult launchers that threw heavy beams and stones at the Roman ships, burning-glasses that reflected the sun's rays and set ships on fire. It is said that Archimedes prevented one Roman attack on Syracuse by using a large array of mirrors (speculated to have been highly polished shields) to reflect sunlight onto the attacking ships causing them to catch fire. In this paper the parameters of irradiation intensity produced by burning glasses or mirrors are investigated and compared with experimental results from the literature.

**Keywords** Burning glass · Mirrors weapons · Solar irradiation · War machines · Experiments

## Introduction

The first known written record of the word "machine" appears in Homer and Herodotus to describe political manipulation [1, 2]. A remarkable mechanism, the first device for which the name mechane (machine, in Greek, Deus ex machine in Latin) is used, is the one used extensively in the ancient Greek theatre in Aeschylus times (4th century BC) as a stage device to lift actors, chariots or flying horses in the air, as though flying, portraying the descent of gods from the sky and similar purposes. They were large mechanisms consisting of booms, wheels, and ropes that could raise weights perhaps as great as one ton and, in some cases depict space travel [3].

Archimedes systematized the design of simple machines and the study of their functions. He invented the entire field of hydrostatics with the discovery of the Archimedes' Principle. Archimedes studied fluids at rest, hydrostatics, and it was nearly 2000 years before Daniel Bernoulli took the next step when he combined

---

A.S. Papadogiannis (✉)  
University of Patras, Department of Mechanical Eng. & Aeronautics, 265 00 Patras, Greece  
e-mail: papadog@mech.upatras.gr

Archimedes' idea of pressure with Newton's laws of motion to develop the subject of fluid dynamics [4–6]. He made many other discoveries in geometry, mechanics and other fields and introduced step-by-step logic combined with analysis and experiments in solving mechanical problems and design of machinery procedures.

Archimedes was also known as an outstanding astronomer; his observations of solstices were used by other astronomers of the era. As an astronomer, he developed an incredibly accurate self-moving model of the Sun, Moon, and constellations, which even showed eclipses in a time-lapse manner. The model used a system of screws and pulleys to move the globes at various speeds and on different courses [7].

At the time of Archimedes Syracuse was an independent Greek city-state with a 500-year history. The colony of Syracuse was established by Corinthians, led by Archias in 734 BC. The city grew and prospered, and in the course of the 5th century BC the wealth, cultural development, political power and victorious wars against Athenians and Carthaginians, ensured for a long time the dominance of Syracuse as the most powerful Greek city over the entire southwestern Mediterranean basin [4].

During Archimedes' lifetime the first two of the three Punic Wars between the Romans and the Carthaginians were fought. The series of wars between Rome and Carthage were known to the Romans as the "Punic Wars" because of the Latin name for the Carthaginians: Punici, derived from Phoenici, referring to the Carthaginians' Phoenician ancestry.

During the Second Punic War (218–201 BC) – the great World War of the classical Mediterranean, Syracuse allied itself with Carthage, and when the Roman general Marcellus began a siege on the city in 214 BC, Archimedes was called upon by King Hieron to aid in its defence and Archimedes worked as a military engineer for Syracuse [4].

The historical accounts of Archimedes' war-faring inventions are vivid and possibly exaggerated. It is claimed that he devised catapult launchers that threw heavy beams and stones at the Roman ships, burning-glasses that reflected the sun's rays and set ships on fire, and either invented or improved upon a device that would remain one of the most important forms of warfare technology for almost two millennia: the catapult. Plutarchos and Polybios (201–120 BC) describe giant mechanisms for lifting ships from the sea, ship-burning mirrors and a steam gun designed and built by Archimedes [4].

Archimedes discoveries in catoptrics are reported [7, 8]. It is said that Archimedes prevented one Roman attack on Syracuse by using a large array of mirrors (speculated to have been highly polished shields) to reflect sunlight onto the attacking ships causing them to catch fire. This popular legend has been tested many times since the Renaissance and often discredited as it seemed the ships would have had to have been virtually motionless and very close to shore for them to ignite, an unlikely scenario during a battle. Tests were performed in Greece by engineer Sakas in 1974 [8] and by another group at MIT [4] in 2004 and concluded that the mirror weapon was a possibility.

The solar irradiation is photon energy  $W$ , is inversely proportional to the wave length  $\lambda$  in vacuum:

$$W = \frac{h.c}{\lambda} \cong \frac{2}{\lambda(nm)} \cdot 10^{-16} \tag{1}$$

Optical wave energy is subject to high degradation during reflection on materials or during diffusion in the atmosphere. Mirrors possibly consisting of polished shields made of bronze, capable of reflecting sun-rays provided a warfare mechanism in classical antiquity [4]. The dimensions and the optical parameters of the mirror surfaces as well as the degrees of freedom for targeting were crucial factors for their configuration and arrangement according to the specific needs, sufficiently determining the effectiveness of the mechanism. Knowledge of the solar irradiation parameters is an important factor, for the design of the mechanism and the the mirror’s surface characteristics. In Fig. 1 the solar radiation vs. the wave length is shown.

Then a supervising practical medium should be set up to ascertain its effectiveness, and thus the investigation and analytical knowledge of the local parameters will proceed. The relevant procedure should have been supported with data for the adequate calculation of the direct sun irradiance that will fall on the mirror. In the past experimental observation must have been used. The sun’s irradiance  $E$  on the mirror depends on the sunlight spectral irradiance  $E_\lambda$  at wavelength  $\lambda$  as:

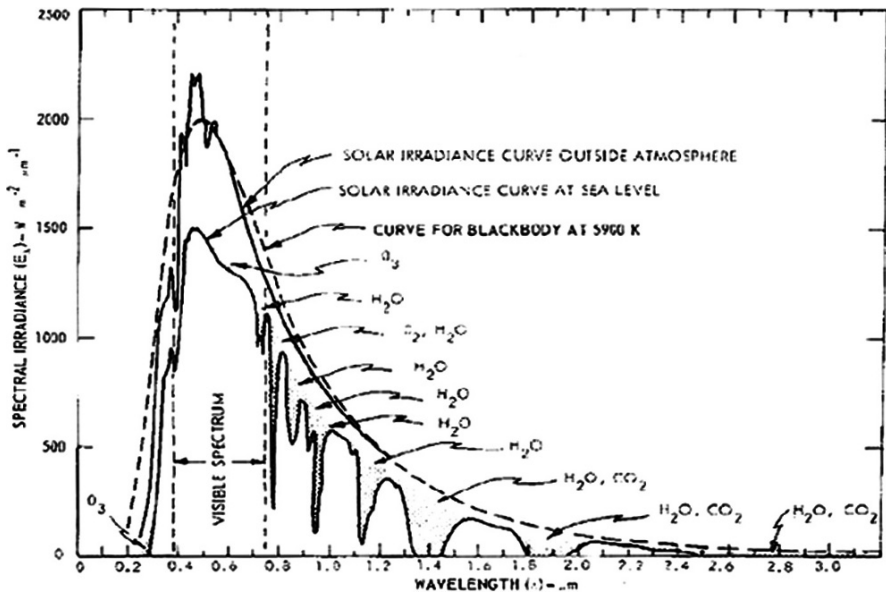


Fig. 1 Solar radiation on Earth’s surface (NASA/ASTM standard)

$$E = \int_0^{\infty} E_{\lambda} d\lambda \quad (2)$$

Outside the earth's atmosphere the solar irradiance is:  $E \cong 1400 \text{ W/m}^2$  at perihelion.  $E = 1353 \text{ W/m}^2$  is accepted by NASA [9, 10] as the solar constant at the mean Earth–Sun distance. Therefore, this value may be used as the level of the optical input energy unfiltered by the atmosphere. Under the same conditions the mean  $E_{\lambda}$  curve given by NASA/ASTM standard is more useful (Fig. 1). The influence of the atmospheric absorption on the sun's irradiance over the earth's atmosphere, is given by the Bouguer-Lambert law, yielding the mean  $S_{\lambda}$  intensity of the immediate irradiation on the earth's surface at wavelength  $\lambda$  as:

$$S_{\lambda} = S_{0\lambda} p_{\lambda}^m \quad (3)$$

where  $S_{0\lambda} = \mathbf{H}$ , the solar irradiation intensity entering the earth's atmosphere,  $P_{\lambda} = 0$  the (spectral) atmospheric absorption coefficient depending on the molecular absorption and diffusion in the atmosphere, and  $m=H$  the atmospheric optical air mass depending on the angle  $\beta$  of the solar rise (Fig. 2), as:

$$m = 1 / \sin \beta \quad (4)$$

As a result, the direct sun irradiation will be at its minimum in the morning and maximum at noon time, while during the rest hours of the day the average values will depend on the atmospheric optical mass. This general daily course will also be

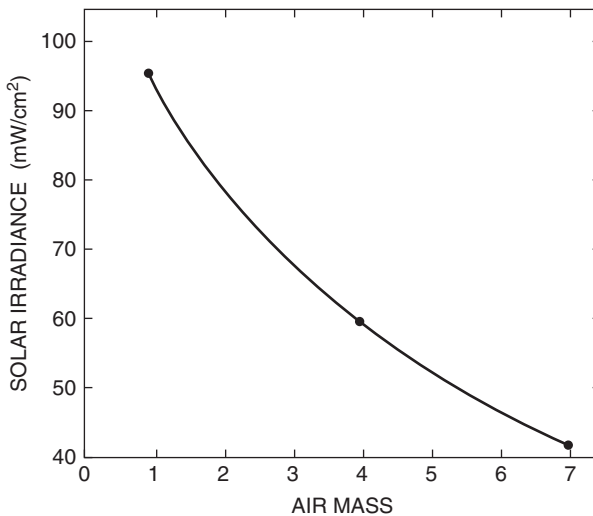


**Fig. 2** Air mass and solar radiation

shaped by the local light diffusion or absorption by the clouds, suspension of dust particles etc., which have a share in the atmosphere transparency.

## Solar Beam Irradiation Properties

Intensity is the main feature of the solar beam, ensuring controllable applications on a target, with maximal impact on the tissue of a body or flammable organic object. Biological effects from optical irradiation also depend on wavelength; therefore, the results depend on the surface material of the mirror and the reflection value of solar spectrum from the near – IR through to the UV. Main parameters influencing solar beam irradiation are: (i) the irradiation duration, (ii) the relaxation time (the duration over which the tissue or organic object loses half of the absorbed energy). Therefore, interaction depends on the irradiation type, the mechanical and thermal characteristics (emissivity and conductivity) and the size of a target. The optimal use of solar beam with maximal damage (trauma to tissue, flame on objects) depends on the relation between duration and relaxation time.

The radiation absorption of a target depend mainly on its water content (skin 70%, bone 10–30% etc.), modified by the content of blood, chromophores etc. Light absorption depth  $L$  is the inverse of the absorption coefficient  $a$  ( $L = 1/a$ ). Water has several absorption ( $a = 13000 \text{ cm}^{-1}$  at  $2.8 \text{ }\mu\text{m}$ ,  $a = 50 \text{ cm}^{-1}$  at  $2.1 \text{ }\mu\text{m}$ ,  $a = l \text{ cm}^{-1}$  at  $1.06 \text{ }\mu\text{m}$ ) and transmission peaks (the largest almost  $400 \text{ nm}$ ). Blood is a strong absorber of visible light (several peaks in  $400\text{--}600 \text{ nm}$ ). Chromophores modulate absorption in the visible spectral region (melanin's  $a = 1000 \text{ cm}^{-1}$  at  $400 \text{ nm}$  and  $a = 80 \text{ cm}^{-1}$  at  $1 \text{ }\mu\text{m}$ ), followed by the protein's absorption ( $a = 27000 \text{ cm}^{-1}$  at  $\lambda < 200 \text{ nm}$ ). Therefore, the final impact is mainly based on the wavelength and duration time combination. Thus, the mirror type (wavelength, power output) is constructed to optimize the interaction with the targeted tissue/object and the beam-target interaction. In any given case, the optical radiation optimization depends strongly upon the reflection characteristics of the mirror which is being used [9].

The solar radiation beam effects upon a target may be categorized as (i) non-thermal (tissue is photo-stimulated or heated to approximately  $62^\circ\text{C}$ ) in a photomechanical process, and to (ii) thermal (tissue/object is heated to approximately above  $62^\circ\text{C}$ ) in a coagulation, vaporization, and carbonization process. Photomechanical interaction to the tissue is produced by a high power moving beam focused into a small spot. An optical breakdown may occur with the production of momentary localized ionized plasma in multiphoton processes. The hydrodynamic shock wave following the plasma formation can disrupt tissues (semitransparent membranes etc.). If a tissue is heated below  $62^\circ\text{C}$  (reversible warming at  $35\text{--}55^\circ\text{C}$ , fuse of collagen fibers at  $55\text{--}62^\circ\text{C}$ ) the thermal damage is confined to the mechanical disruption region. The photochemical interaction is the optically triggered-accelerated chemical process in the tissue, with final ult a different chemical structure. Coagulation is the blanching of the photo-irradiated tissue caused by the structure change which leads to an increased scatter and multiple refraction/reflection of illumination light, as the temperature is raised up to  $62\text{--}100^\circ\text{C}$ . The main coagulation mechanism is



protein (collagen etc.) denaturation, when the molecular form the ubiquitous protein becomes unstable and the chains unfold. In the vaporization process, the tissue is heated to 100°C, thus cell water boils and steam escapes from the ruptured explosive cell walls. The tissue/object damage, by the steam spread of heat, is limited in the absorption area of an optical beam. Once water has completely evaporated from a cell and irradiation is continued, any debris remaining in the ruptured structure and the residual material is rapidly raised to a higher temperature. At 300–400°C the tissue/object becomes carbonized (blackens) with outgas and smoke, and at over 500°C it burns and evaporates in the atmospheric oxygen.

The quantification of the solar beam potential harm is done according to Laser beam impacts [9] depending on the wavelength and power output. The beam is non-harm, inherently, due to the low output beam power by which it cannot exceed the ocular Exposure Limit level [11, 12]. If a mirror emits low power ( $\max P_o < 1\text{mW}$ ) in the 400–700 nm region, human aversion to bright light will protect the enemy personnel. Thus a protection mechanism is the eye’s 0.25 s “blink reflex”. If a mirror emits slightly higher-power ( $1\text{mW} < \max P_o < 5\text{mW}$ ) in the 400–700 nm region, then the direct viewing of the beam dangerous, and the blink reflex is the primary protection. If a mirror emits medium power ( $\max P_o < 500\text{mW}$ ) and does not belong to the previous cases, then it produces direct hazardous emissions, and the diffused beam reflection is not hazardous unless a person stares on it intentionally. If the mirror emits high power ( $\max P_o > 500\text{mW}$ ), it produces direct and diffuse, irradiation.

Any exposure above the Exposure Limits expressed as irradiance  $E$  (in  $\text{W}/\text{m}^2$  or  $\text{mW}/\text{cm}^2$ ) or radiant exposure  $H$  (in  $\text{J}/\text{m}^2$  or  $\text{mJ}/\text{cm}^2$ ) would be a damage risk [13]. The simplest over-exposure of the eye to a solar beam reflected by a mirror for  $400 < \lambda < 1400\text{nm}$  may cause retina damage. Since there may be no pain or even discomfort when a beam strikes the retina, the victim may not be aware of any injury until several burns have been infected and vision has been impaired. The injury effects are thermal and/or non-thermal [7, 9]. Beams with wavelength beyond the 400–1400 nm region and not focusing onto the retina, are absorbed at the cornea or skin with other damage mechanisms involved.

The nominal hazard zone ( $R_{\text{NHZ}}$ ) gives the possible over-exposure range. Numerical examples of optical radiation hazard given in the next table with the use of the formula [15–17].

$$R_{\text{NHZ}} = -\frac{1}{\tan(\frac{\phi}{2})} \sqrt{\frac{knP_o}{\pi S_{EL}}} \tag{5}$$

**Table 1** Nominal hazard zone range ( $R_{\text{NHZ}}$ ) in a beam from  $n$  mirrors with concentration  $k$  & divergence 0,05 rad reflected at  $n$  elements with appropriate mirror surface of  $1\text{m}^2$

Wavelength band nm	Reflectivity	Power output W	Exposure duration s	Personnel $R_{\text{NHZ}}$ m	Wood $R_{\text{NHZ}}$ m
400–520	0,4	$\text{Kn}.66,7$	0,25	$36,5 \sqrt{kn}$	$3,65 \sqrt{kn}$
750–1400	0,9	$\text{Kn}.292,1$	10	$121,4 \sqrt{kn}$	$12,14 \sqrt{kn}$

where  $\Phi$  = the beam divergence (rad),  $P_o$  = the power output from one mirror (Watts),  $n$  = the number of mirrors with concentration  $k$ , and  $S_{EL}$  the appropriate exposure limit ( $W/m^2$ ).

It is clear that in all these cases of caustic mirrors the exposure must be higher than the exposure limits. Thus the nominal hazardous zone ( $R_{NHZ}$ ) gives the possible over-exposure range.

## Conclusion

Archimedes discoveries in catoptrics are reported [8, 18, 19]. The historical accounts of Archimedes' war-faring inventions are vivid and possibly exaggerated. It is claimed that he devised catapult launchers that threw heavy beams and stones at the Roman ships, burning-glasses that reflected the sun's rays and set ships on fire, and either invented or improved upon the catapult. It is also said that Archimedes prevented one Roman attack on Syracuse by using a large array of mirrors (speculated to have been highly polished shields) to reflect sunlight onto the attacking ships causing them to catch fire. This popular legend has been tested many times since the Renaissance and often discredited as it seemed the ships would have had to have been virtually motionless and very close to shore for them to ignite, an unlikely scenario during a battle. But, recently tests were performed in Greece by engineer Sakas in 1974 [8] and by another group at MIT in 2004 and concluded that the mirror weapon was a possibility. A theoretical investigation on the sun-rays properties presented here may be used as an evaluation tool for supporting this theory and can be further extended to various mirror and sunglass configurations.

## References

1. Dimarogonas A.D., 2001 *Machine Design A CAD Approach*, John Wiley and Sons, New York.
2. Dimarogonas A.D., 1991 "The origins of the theory of machines and mechanisms" *Proceedings 40 Years of Modern Kinematics: A Tribute to Ferdinand Freudenstein Conference*. Minneapolis, MN.
3. Dimarogonas A.D. 1997 *Journal of Integrated Design and Process Science*, **1**, 54–75, Philosophical Issues in Engineering Design.
4. Chondros T.G. 2007 *Archimedes (287–212 BC) History of Mechanism and Machine Science I, Distinguished Figures in Mechanism and Machine Science, Their Contributions and Legacies*, Part 1. Edited by Marco Ceccarelli, University of Cassino, Italy, Springer, The Netherlands. ISBN 978-1-4020-6365-7. pp 1–30.
5. Dijksterhuis E.J. 1987 *Archimedes*, Princeton University Press, Princeton, NJ.
6. Stamatias E., 1973 *Archimedes–Apanta*, Vols. 1–3. Technical Chamber of Greece, Athens, (in Greek).
7. Archimedes–Apanta, 2002 *The Works of Archimedes*, Vols. 1–6, Kaktos Publications, Athens, (in Greek).
8. Lazos C.D., 1995 *Archimedes: The Ingenious Engineer*, Aiolos Publishers, Athens, (in Greek).
9. Duffie J.A., 1980 *Solar Engineering of Thermal Processes*, John Wiley & Sons, USA.
10. National Aeronautics and Space Administration, 1971 *Solar Electromagnetic Radiation*, ASA SP-8005.

11. World Health Organization, 1982 *Non-Ionizing Radiation Protection*, World Health Organization Regional Publications, European Series No. 10, Suss M. J. (ed), Copenhagen, Denmark.
12. The IRPA Non-Ionizing Radiation Committee, 1991 *IRPA "Guidelines on Protection Against Non-Ionizing Radiation"*, Pergamon Press, New York.
13. Carruth J.A.S., McKenzie A.L., 1986 "Safety with surgical lasers", *Medical Lasers: Science and Clinical Practice*, Adam Hilger Ltd., Bristol and Boston, 233–261.
14. McKenzie L.A., 1990 "Physics of Thermal Processes in Laser-Tissue Interaction" *Phys. Med Biol.* 35 1175–1209.
15. Tsitomeneas S., Carabelas A., 1998 "The use of laser pointers and the related hazards" *Proceedings Series of SPIE (International Society for Optical Engineering)* 3(2) 459–463.
16. Tsitomeneas S., 1998 "Optoelectronic indicator/warning circuit for detecting & observing the high values of the incident optical radiation" *Proceedings Series of SPIE (International Society for Optical Engineering)* 3423 112–116.
17. Tsitomeneas S., Petropoulos B., "Intensity/frequency indicator for application of maximum permissible exposure to solar or Laser optical radiation in space flights" *Astronautica*
18. Netz R., 2004 *The Works of Archimedes*, Cambridge University Press, UK.
19. Ceccarelli M., 2006 "Early TMM in Le Mecaniche by Galileo Galilei in 1593" *Mechanism and Machine Theory* 41 1401–1406.

# The Creation of the Site About the Historical Part of Collection of Mechanisms Bauman MSTU

Theodor Vitiukov and Valentin Tarabarin

**Abstract** This paper devotes the creation of the site about a historical part of the collection of models mechanisms Bauman MSTU. This collection has started to be formed in 40 years of 19th centuries. The greatest contribution to its creation was brought in by A. Ershov, F. Orlov, N. Mertsalov, L. Smirnov, L. Reshetov and A. Gavrilenko. Now the collection includes more than 600 models of which approximately 120 refers to the 19th century.

**Keywords** Collection of models of mechanisms · Virtual museum · Site · Internet · History of mechanics

## Introduction

The beginning of creation of Applied mechanics room and mechanic models collection in Moscow Industrial Educational Institution (MIEI) was initiated by I. Balashov, a general and practical mechanics teacher, in 1940s of the 19th century [1]. The room contained a small amount of models made in MIEI. The collection was essentially broadened by the efforts of A. Ershov, a practical mechanics teacher and director of MIEI. Then a teaching process appreciably changed. Substantially, new educational mechanical workshops were founded, the apprenticeship was increased, more attention was devoted to theoretical training as well as practical. Besides educational workshops in MIEI there was a machine building factory, which manufactured and sold steam engines, pumps, turbines, engineering tools, etc. [2]. In the senior years of study the factory gave students practical skills in real business (industrial, administrative and economic). At first students of the first years of education studied the methods of working with tools. Then the teaching

---

T. Vitiukov (✉)

Dept. Theory Machines and Mechanisms, Bauman Moscow State Technical University,  
Moscow, Russia

e-mail: vietfed7@gmail.com



Fig. 1 Models with represented author's surnames and years of manufacturing

continued in educational workshops (model, foundry, blacksmith's and mechanical) and in drawing classes. It might be supposed that at the end of studying at workshops classes students carried out a final work—making a model of a rather difficult mechanism. Two models made in 1861 by Ivan Naumov and by Pavel Ivanov in 1862 corroborate this supposition (Fig. 1). The lists of graduating students, who were taught in MIEI from 1845 till 1912 were brought in book [3]. In this book on pages 94 and 163 we can find a dedication “Naumov Ivan Naumovich, foreman, 1866 year”, and on pages 55 and 163—“Ivanov Pavel Ivanovich scientist-foreman, 1868”. The apprenticeship in MIEI was then about 8–10 years. From 1861 year Naumov studied in 1–2 class of foreman rank, approximately the same thing was about Ivanov in 1862.

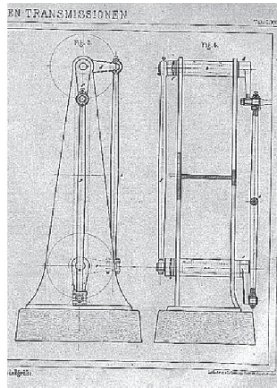
These models from BMSTU are very close in their structure to the models given in F. Redtenbacher's book [4]. As authors found out, the only copies of Redtenbacher's models had been made in Polytechnic school in Karlsruhe (Germany) not for sale. It was corroborated by the fact of Redtenbacher's book publication with detailed models drawings. This book were destined for those, who wanted to make the same models. It was useful in exercises fulfillment in drawing constructions of mechanisms.

The research and comparing of BMSTU models with drawings from Redtenbacher's book and original Karlsruhe models photos (from *kmoddl.library.cornell.edu* web-site) revealed a great number of structure differences, which shows that models are made in different workshops. The photos of similar models from BMSTU and Karlsruhe models collection and drawing from [4] are shown on Fig. 2. There are about 40 saved models from Ershov-Redtenbacher collection. Some of them have structure elements similar to Redtenbacher models, but there are no drawings in [4]. A models collection made by Ershov was successively demonstrated on industrial exhibitions in Russia and on Universal exhibition in Paris in 1867 year.

After A. Ershov the collection was generally filled up with models from Germany and France [5]. Sixty seven F. Reuleaux models, made by G. Voight in Berlin [6, 7], 1 Shreuder's model (Germany), 8 models of A. Clair, made in Paris, at alias were preserved in collection. Some of 19th century models lost their specialty plates and authors could only suppose where are that models from.



Model of collection of BMSTU



Original model of Redtenbacher and its draft



**Fig. 2** Comparing BMSTU model with Redtenbacher model

Our days the interest to educational models, made in the age of a high engineering education generation, is increasing. This models take an important place in expositions of various museums, like Useful Arts Conservatory in Paris, German museum in Munich, Polytechnic museum in Moscow. Many technological universities of the world create real and virtual museums of mechanisms [8–11]. Similar works are made on Theory of machines and Mechanisms (TMM) department in BMSTU.

The first information about BMSTU models collection in Internet was published in 1998 on the TMM department educational web-site *tmm-umk.bmstu.ru* [12] (Fig. 3). That time systematization of models collection with descriptive operations, photography and video filming started. Beginning that work authors had incomplete imagination about difficulties, that could appear in work process. Practically total absence of archival materials (lost in 2nd World War), absence of necessary equipment and financing became a cause of still unfinished work. Though some results are achieved.

In 2003 students R. Tokarev and V. Tkachenko made a test release of web-site which was constructed like a virtual mechanisms museum (Fig. 4). Web-pages de-



**Fig. 3** Fragments from models category of 1998 web-site



Fig. 4 Fragments from models web-site made in 2003

sign, information cards forms for models descriptions were developed. Also photos and video movies with some models were made. But the main part of models descriptions wasn't prepared for that moment, and that's why that web-site release was remained as one of possible work variants. After that the main efforts were aimed at the making of models descriptions. More than 10 students were assigned for this work, but received results were inadequate. For the main part of students the task was too difficult, because they didn't have general knowledge in theory of mechanisms and mechanic history.

Literature, necessary for descriptions making, wasn't available or it was written on foreign languages, which students didn't know.

New dynamic release of the web-site was developed in 2006 by students A. Kostin, A. Demina and N. Evsukova (Fig. 5). With creation of this web-site release the main aim was a creation of program shell, which could permit to make changes and additions to the web-site. For this moment that web-site release is available on *tmmcolmech.bmstu.ru*.

Unfortunately, an absence of a reliable server was a reason of a partially prepared version of a web-site loss, because a backup of a web-site wasn't made. The information presented on a web-site contains misprints and inexactitude, and for correction making it's necessary to attract the specialists for this work. Thereto there is a need to solve the problem of financial support of a web-site.

The last web-site release was developed in 2007 by students Th. Vitiukov, A. Pushkarev and A. Mikhailov (Fig. 6). The main targets of this web-site release were: returning to a static web-site version, because of it's better conditions for material storage, adding structure schemes to the mechanism descriptions, repeating models photographing for photos quality improvement. Short time constraints, which executors had (about 3 months), made impossible a full work fulfillment. The main web-pages design and structure, construction schemes and photos for the majority of mechanisms were developed. The photographing of models was a very difficult task, because they have a lot of glared surfaces. Most models structures are

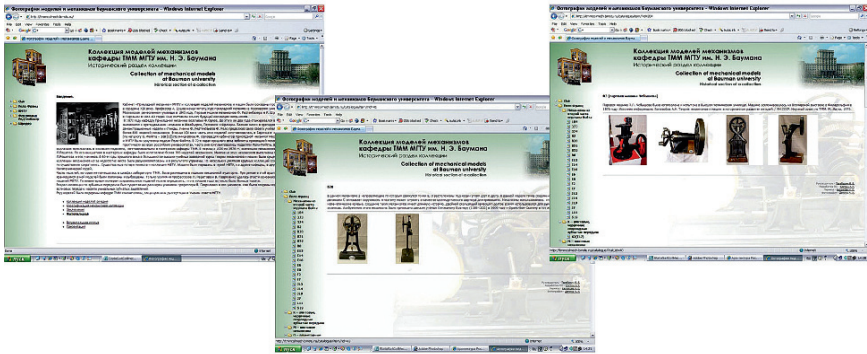


Fig. 5 Fragments from dynamical web-site made in 2006

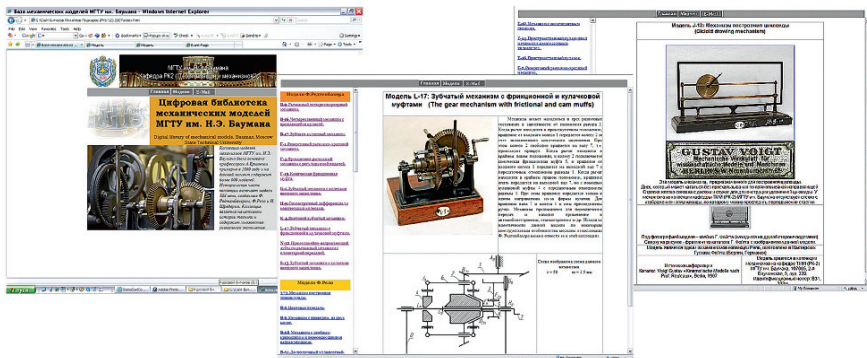


Fig. 6 Fragments from static web-site made in 2006

sophisticated that's why it was difficult to choose a right angle, those could make visible all the important mechanism's parts.

Many models were photographed in various positions, particular parts and details were enlarged on photos (Fig. 7). Sometimes problems with models descriptions appeared. Not always mechanism purpose or some of its parts could be precisely recognized. Unfortunately, there is only a part of descriptions of researched mechanisms in TMM literature. Many of models are the complex spatial mechanisms, that's why structural schemes making was attended by some difficulties. Pictures from catalogue [5] included to this Ruleaux-Voigt collection models descriptions. Models descriptions, which prototypes were Redtenbacher models, contained the drawings from book [4]. Copies of this books had not a large value, that's why the quality of this illustrations isn't high.





**Fig. 7** Old (*left*) and new (*right*) photos of model D-14

Autumn 2007 students O. Ivanov and I. Saveljev fulfilled the recording of video movies, which demonstrate models in motion. The following method was chosen for video filming. In the beginning the photographing fulfilled for a several phases of mechanism motion (about 50 in a cycle). The photographing of each model carried out from the different positions with varied zoom. Obtained photos transformed with help of Macromedia Flash program into the video file. For using this files on web-site they were recorded in  $320 \times 240$  definition. In all there were created 60 files (Fig. 8), for their producing more than 6,500 photos were made. In the final version a general volume of video files appeared 275 Mb (60 files with volume from 1 to 8 Mb) or about 30 min. of demonstration. This method of video creation was chosen because mobile sections imagery after usual video filming often became fuzzy, there were outside objects in a frame (for example, a hand of an assistant, that made the models moving), often it was difficult to get even rotating (models get stuck in some positions). But the method has some shortcomings: in the photography process the lighting can be changed, and it causes to unnatural video blinking.

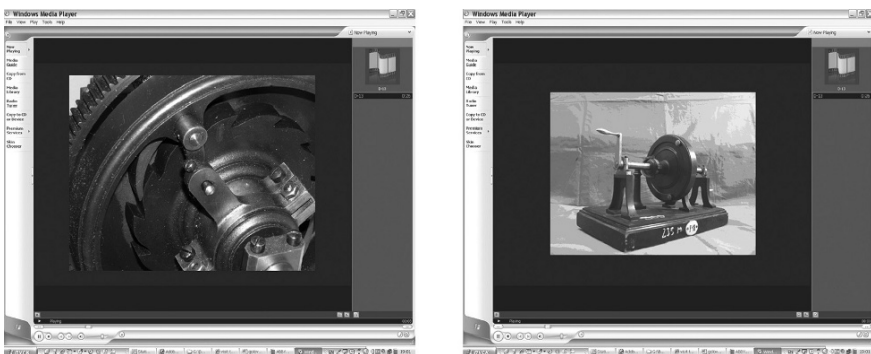


**Fig. 8** Video fragments with mechanic models

## Conclusion

The development of web-sites devoted to the monuments of science history and technology is one of the main directions of technical museums activity. They make valuable (but in ordinary conditions not easily accessible) monuments of culture open to students, scientists and other internet users. Authors trust, that their work in the nearest future will be completed, and all of interested people will be able to see mechanic models from BMSTU collection.

**Acknowledgments** Authors thank students from RK6, RK9, RK10 groups, who collaborated in web-sites development and prepared the working materials. They also thank developers of *kmoddl.library.cornell.edu* and *www.acmf.org.tw/antique* web-sites, that served like examples in TMM department web-site creation.

## References

1. Tiulina I., Chinenova V., Some aspects of lecturing on mechanisms and machines theory at Moscow University (19th – the first third of 20th century). Proceeding of Third International Workshop on History of Machines and Mechanisms. Edited by M. Ceccarelli and A. Golovin. – Moscow, BMSTU, May 17–19, 2005. –21–33pp.
2. Experimental plant of MHTS name after N.E. Bauman 1832–1952. The prospectus. Under edited of G.A., Nikolaev L.E., Zinoviev – M.: Publishing house MHTS, 1982.–47 c.
3. Imperial Moscow Technical School. The alphabetical list ended MHTS with 1845–1912 M.: – 1913.–223pp.
4. Redtenbacher F., Die Bewegungs-Mechanismen: Darstellung und Beschreibung eines Theiles der Maschinen-Modell-Sammlung der polytechnischen Schule in Carlsruhe. Edited by F. Redtenbacher. Heidelberg: F. Bassermann, – 1866.
5. Tarabarin V., Golovin A., Tarabarina Z. The historical part of collection models of machines and mechanisms of TMM’ s department of the Bauman Moscow State Technical University. Proceedings of 12th International Symposium on Theory of Machines and Mechanisms, Besanson, 2007.
6. Voigt G. Kinematic models after reuleaux. Catalog, Berlin. – 1907.
7. Golovin A., Tarabarin. The Collection models of machines and mechanisms of TMM’s Department of BMSTU. IFToMM Workshop-Lectures. History of machines and mechanisms 2006. Edited by Prof. F.C. Moon. Cornell University. College of Engineering. 9–10 September 2006. Ithaca. New York.
8. Politecnico di Torino. Museo Virtuale. Meccanica. Cinematismi. ([www2.polito.it/strutture/cemed/001/museovirtuale.htm](http://www2.polito.it/strutture/cemed/001/museovirtuale.htm)).
9. Kinematic Models for Design. Digital Library. Cornell University College of Engineering ([kmoddl.library.cornell.edu](http://kmoddl.library.cornell.edu)).
10. Tiwan’s Antique Mechanisms Teaching Models. Digital Museum ([www.acmf.org.tw/model](http://www.acmf.org.tw/model)).
11. The Digital Mechanism and Gear Library (short DMG-Lib). Technische Universität Ilmenau, Technische Universität Dresden and RWTHAachen ([www.dmg-lib.org](http://www.dmg-lib.org)).
12. Tarabarin V., Tarabatina Z. The electronic a learning-methodical complex at the course the Theory of machines and mechanisms. Proceeding of the China-Russian symposium on problems of development and use of the information technology in engineering education, HPU, China, Harbin, on November, 3rd 2007 – 139pp.

# Using Computer Spreadsheets in Teaching Mechanisms

Eres Söylemez

**Abstract** In this paper the use of widely available user friendly spreadsheet programs such as Microsoft® Excel in teaching mechanisms is explained and its advantages over off-the-shelf programs are shown. Instead of using specific costly programs for the analysis and synthesis of different mechanisms, the students are first thought certain features of Excel and later starting with the analysis of single loop mechanisms, the solution of more complex problems in the analysis and synthesis of mechanisms are attempted. The simulation of mechanisms can be achieved by using the Chart and control toolbox features of Excel. Students are able to prepare their own spreadsheets for the solution of different mechanism problems. In this article different examples using spreadsheet program will be explained and its benefits as an educational tool will be demonstrated.

**Keywords** Spreadsheets in mechanisms · Analysis and synthesis of mechanisms · Spreadsheet in teaching

## Introduction

With the advance in computer technology, mechanism analysis and synthesis using computers is a continually developing process. The first program “KAM – Kinematic Analysis Method” was developed by IBM in 1964 [1]. In later years kinematic and dynamic analysis programs such as ADAMS®, WorkingModel® and synthesis programs such as KINSYN and LINCAGES, and many others developed at the universities some of which are free and some are commercially available [2, 3]. These programs are well written programs and the students can learn on how to define an input and then how to interpret the output. They cannot interfere with the program nor identify the algorithm used for the solution. A considerable time must be spent in the use of such programs.

---

E. Söylemez (✉)

Mechanical Engineering Department, Middle East Technical University,  
İnönü Bulvarı, 06531 Ankara, Turkey  
e-mail: eres@metu.edu.tr

Noting the drawback of an executable file in education, some lecturers and textbook authors have switched to the use of mathematical packages such as MathCad<sup>®</sup> Matlab<sup>®</sup> or Mathematica<sup>®</sup> as a tool in solving machine theory problems. These general purpose mathematical packages have been found to be very useful [4–6].

Another alternative in teaching with the computers is the use of spreadsheet programs. Starting with VisiCalc in 1979 for Apple II platform, spreadsheet programs are being used very effectively for repetitive tabular calculations. Although several spreadsheet programs such as OpenOffice.OrgCalc (as a freeware) are available, since the mid 1990s Microsoft<sup>®</sup> Excel commands a big share of the market. The spread-sheet programs are so easily available at no extra cost and are so versatile, use of these programs in all fields of engineering is becoming an essential tool [7, 8].

Basically in all spreadsheet programs relations between the cells arranged as an array of rows and columns can be defined by the user. The cells are automatically updated and results are displayed when a value in a cell is changed by the user. All types of mathematical, logical, statistical, etc. functions are available Matrix inversion and multiplication can be performed easily. In addition, graphic interface and charting in Excel is simple and versatile to use. All these features can also be extended by add-ins such as Microsoft<sup>®</sup> Excel Solver, or by writing custom codes such as functions, subroutines using Microsoft's Visual Basic for Applications<sup>®</sup> (VBA) editor which is embedded in Excel. Hence all these features make spreadsheet program a very important tool in teaching mechanisms.

## Kinematic Analysis

As a first example consider the kinematic analysis of a four-bar mechanism (Fig. 1). The necessary analysis equations can be derived by using one of the well known approaches such as solving for Theta4 using the loop equation or by dividing the quadrilateral  $A_0ABB_0$  into two triangles and solving for these two triangles  $A_0AB_0$  and  $AB_0B$  in sequence [9]. The fixed link length values can be placed into cells B1 to B4 and these cells can be labelled as "Crank, Coupler, Rocker, Fixed" for later use as shown in Fig. 2. Now, starting from the first column of a row (row 8, in row 7 the formulas typed are shown), we enter the necessary formulas in sequence to solve for the unknown position variables Theta3 and Theta4. In ten cells (A8 to J8) the position analysis of the four-bar for the given crank angle (cell A8, in degrees) is performed. By changing the value typed in cell A8, position analysis for a different crank angle can be obtained. The analysis can be performed for the whole cycle by first tabulating the input crank angle on one column (say Column A) and then copying cells B8 to J8 to the corresponding rows. If the mechanism is to be drawn at a given Theta2 input angle, selecting a Cartesian reference frame with center  $A_0$  and the x axis coincident with the fixed link, than the coordinates of the joint axes are  $A_0(0,0)$ ,  $A(\text{Crank}*\cos(\text{Theta}2))$ ,  $\text{Crank}*\sin(\text{Theta}2)$ ,  $B_0(\text{Fixed}, 0)$  and

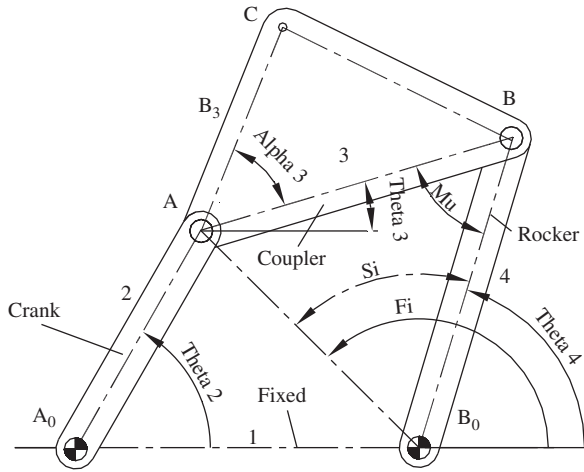


Fig. 1 Four-bar mechanism

	A	B	C	D	E	F	G	H	I	J
1	CRANK	35	B3	126.6						
2	COUPLER	62,3	ALFA3	35,538	0,620					
3	ROCKER	56								
4	FIXED	70								
5										
6	Theta2	Theta2 (Rad)	Xs	Ys	S	Fi	Si	Mu	Theta4	Theta3
7	10	=B8*PI()/180	=-FIXED + CRANK*COS(B7)	=CRANK*SIN(B7)	=SQRT(C7^2+D7^2)	=ATAN2(C7;D7)	=ACOS(ROCKER^2+E7^2-COUPLER^2)/(2*ROCKER*E)	=ACOS(ROCKER^2+COUPLER^2-E7^2)/(2*ROCKER*COUPLE	=F7-G7	=I7-H7
8	10,000	0,175	-35,532	6,078	36,048	2,972	1,433	0,610	1,539	0,929

Fig. 2 Excel sheet for the analysis of a four-bar

B(Fixed +Rocker\*cos(Theta4), Rocker\*sin(Theta4)). Using the Chart Wizard, we can select x–y scatter, line and select the x and y coordinates of the joint axes as the series to be drawn, we can draw the four-bar mechanism as shown in Fig. 3a. Using the control tool-box available in Excel, a “Spin botton” or “Control bar” can be linked to cell A8 and the value of input angle can be incremented by any preset amount. Thus the motion of the mechanism can be simulated.

For the coupler point C, its coordinates relative to the fixed Cartesian frame can be readily determined as C(x<sub>c</sub>,y<sub>c</sub>) where:

$$x_c = Crank * \cos(\Theta_2) + B3 * \cos(\text{Alfa}3 + \Theta_3),$$

and

$$y_c = Crank \sin(\Theta_2) + B3 * \sin(\text{Alfa}3 + \Theta_3)$$

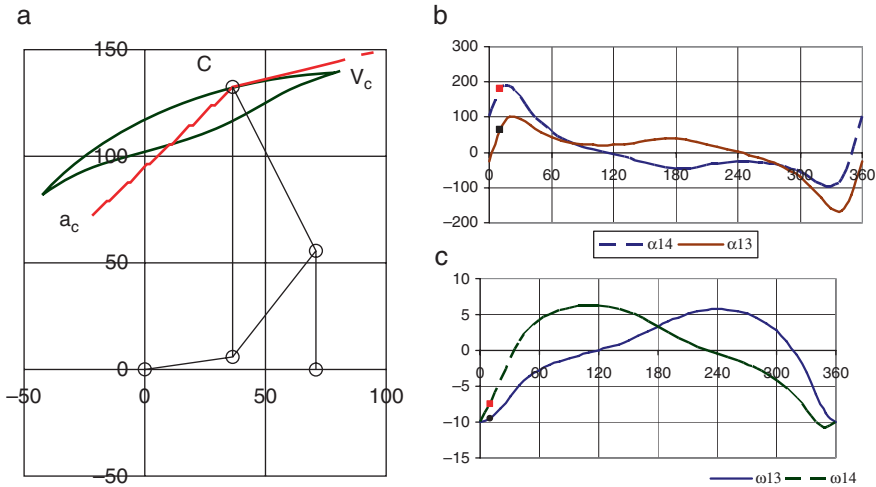


**Fig. 3** (a) Four-bar with coupler path, (b,c) angular velocity and acceleration diagrams of the coupler and rocker

Using a few more cells in the row, one can easily write the necessary equations for the coupler point coordinates, for the angular velocity and accelerations of the coupler and rocker and the linear velocity and acceleration of point C, and show these entities graphically as shown in Fig. 3a, 3b and 3c. The mechanism can be simulated and, as important as the simulation, one can ask “what if” question in engineering, such as “what happens if the link lengths are changed, or a different coupler point is selected”.

Similar approach can be used for the analysis of all single loop planar mechanisms such as slider-crank, inverted slider-crank, conchoidal motion mechanisms. Usually these are given as homework or tutorial assignments so that the students can derive the necessary equations for the analysis and master the Excel commands.

The capabilities of Excel is not limited to computation that can be performed in between the cells. For example, in several problems solution of a triangle for an angle or a side using cosine theorem repeats itself. One can write simple function routines using VBA editor. For example for the cosine theorem we can write two functions in the form **AngCos**(Side1, Side2, Opposite) and **MagCos**(Side1, Side2, Angle) to determine the angle or the length of the opposite side to the angle when the three parameters for a triangle are given. On the Excel sheet these “User defined” functions can be used as if they are sine or cosine functions. Similarly, one can write simple function routines for the four-bar, slider-crank, inverted slider-crank mechanisms. For the four-bar mechanism (Fig. 1):

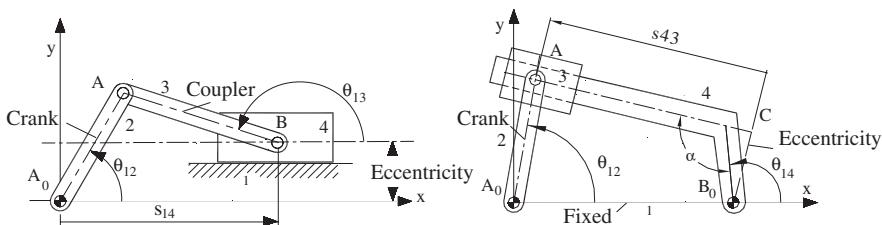


Fig. 4 Slider Crank and inverted slider crank mechanisms

$$[\Theta_{3}, \Theta_{4}] = \mathbf{FourBar2}(\text{Crank}, \text{Coupler}, \text{Rocker}, \text{Fixed}, \text{Config}, \Theta_{2})$$

$$\Theta_{4} = \mathbf{FourBar}(\text{Crank}, \text{Coupler}, \text{Rocker}, \text{Fixed}, \text{Config}, \Theta_{2})$$

where Config = ±1 depending whether the four-bar mechanism is assembled in open or crossed form. For Slider-Crank and Inverted-Slider Crank mechanisms similar equations can be written in the form (refer to Fig. 4):

$$[\theta_{13}, s_{14}] = \mathbf{SliderCrank2}(\text{Crank}, \text{Coupler}, \text{Eccentricity}, \text{Config}, \theta_{12})$$

$$[s_{43}, \theta_{14}] = \mathbf{InvSliderCrank2}(\text{Crank}, \text{Fixed}, \text{Eccentricity}, \text{Config}, \theta_{12})$$

A big class of mechanisms that do not require an iterative solution for the position analysis are made up of four-link loops. Hence multiple loop mechanisms can now be solved using the user defined functions. For example the position variables of the six link mechanism shown in Fig. 5 can be solved for a given input crank angle using the equations and user defined functions as (let the link lengths be denoted by  $a_i$  and  $b_i$ ):

$$[\theta_{13}, s_{14}] = \mathbf{SliderCrank2}(a_2, a_3, a_1, 1, \theta_{12})$$

$$S = |D_0C| = \sqrt{(a_1^2 + (b_1 - s_{14})^2)}$$

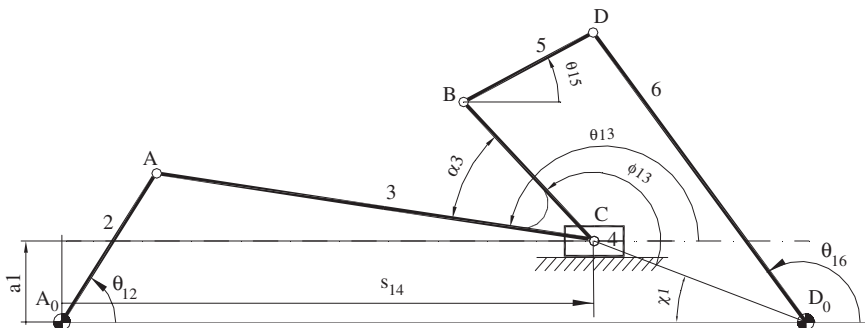


Fig. 5 A six link mechanism

$$\chi_1 = \tan^{-1}((b_1 - s_{14}), a_1)$$

$$[\theta_{15}, \theta_{16}] = [\mathbf{FourBar2}(b_3, a_5, a_6, s, 1, (\theta_{13} - \alpha_3 + \chi_1)) - \chi_1]$$

Using the spreadsheet, the students can be asked to analyze and simulate complex planar mechanisms which do not require iterative solutions, such as the walking sculpture of Theo Jansen [10] or a double press mechanism by R. F. Dehn (US patent #3,052,200) (Fig. 6). In Excel, iterative solution is also possible by using the Solver Add-in function. In such a case, the loop closure equations are written and with an initial guess, the value of the dependent parameters are found.

The use of Excel in mechanisms is not limited to the position analysis. Depending on the topics thought, the students can use Bobillier’ construction to determine the moving and fixed centrodes and the center of curvature of a coupler point C (C<sub>0</sub>) (Fig. 7), draw the cubic of stationary curvature, or perform static or dynamic force analysis of complex mechanisms, such as the loader, coupled with the motion simulation (Fig. 8).

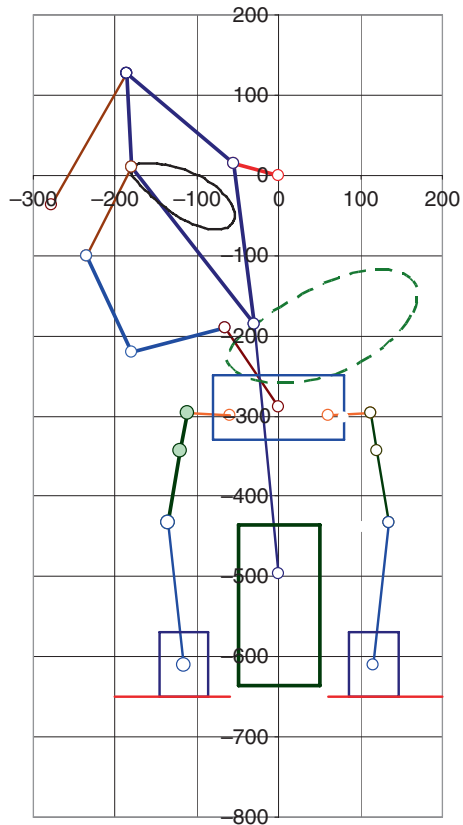


**Fig. 6** Double press (R.F. Dehn US patent #3 052 200)



Fig. 7 Centroides of a FourBar

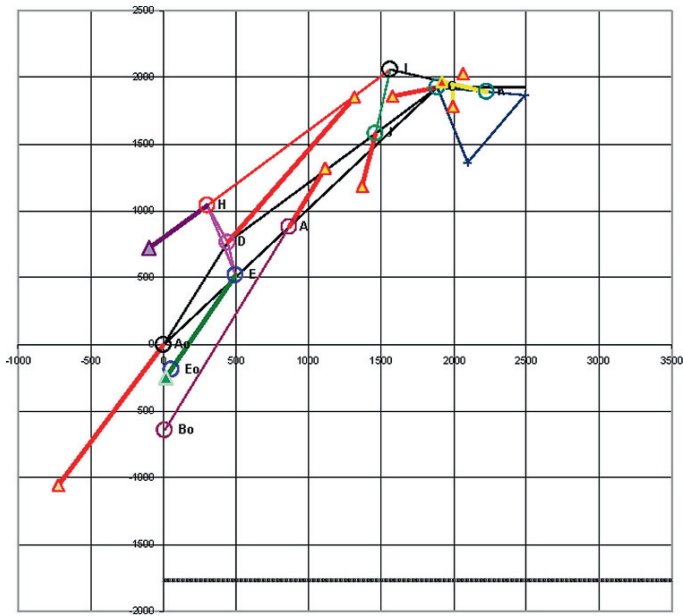
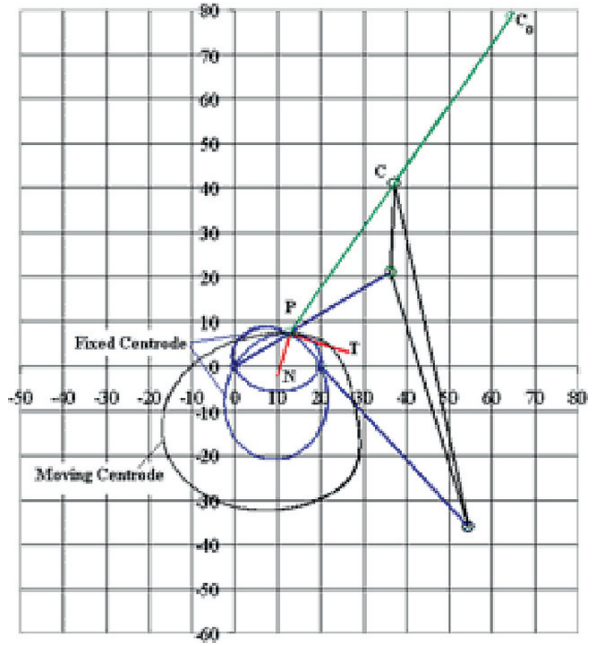


Fig. 8 Force Analysis of a loader

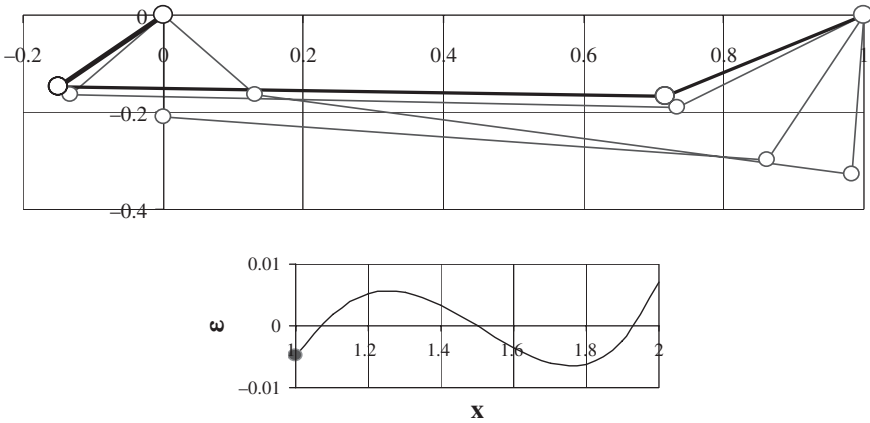


Fig. 9 Four bar to generate  $y = \ln x$   $1 < x < 2$  and its error curve

### Kinematic Synthesis

There are several design problems that can be solved using a spreadsheet. For example for the generation of a function  $y = f(x)$  within the range  $x_{in} < x < x_{fin}$ , one can use Chebyshev spacing for three precision points; correlate  $x$  and  $y$  with the rotation of the cranks of a four-bar and use Freudenstein's equation for the synthesis. By changing initial crank angles, different solutions can be found. In Fig. 9 result for generating  $y = \ln x$  within the range  $1 < x < 2$  is shown.

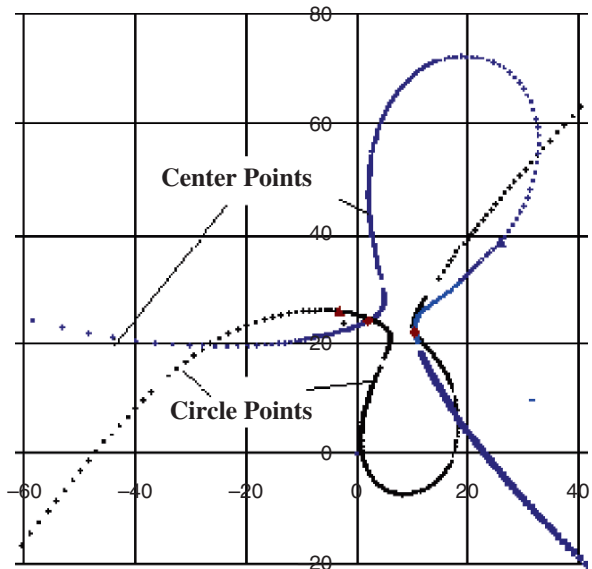


Fig. 10 Burmester curves as an Excel chart

Design for dead centers can also be effectively implemented using an Excel sheet. For four position synthesis the Burmester curves can be drawn (Fig. 10); the four-bar mechanism constructed by selecting two pairs of Burmester points can be checked for movability, transmission angle and simulated on the screen.

## Conclusion

Spreadsheet programs provide a very versatile, easy to use, readily available and a cheap platform for the analysis and synthesis of mechanisms. With some programming in VBA, they can perform tasks such as the solution of a set of nonlinear differential equations (For dynamic motion analysis). Since most of the engineering students have some knowledge about office programs it is very easy to use Excel as a teaching material in courses. The emphasis throughout the course is not on programming but on the topics covered in mechanisms courses. Excel is a tool and if it is mastered by the students, it can be used in a similar fashion in all of the technical topics both as a student and as an engineer. As in the quotation: “Give a man a fish, he will eat for a day, teach a man to fish, he will eat forever”, using a spreadsheet program we are teaching a student how to solve problems in an algorithmic structure, we are not giving a solution to a problem.

## References

1. Cooper, D.W., Frayne, D.N., Bitonti, F., Hansen, H.H., “Kinematic Analysis method” SP-272, Society of Automotive Engineers, 1965.
2. Corves, B., “Computer-Aided Lectures and Exercises: Graphical Analysis and Synthesis in Mechanism Theory”, Proceedings 11. World Congress in Mechanisms and Machine Science, Tianjin, China, April 2004.
3. Petuya, V., Diez, M., Pinto, Ch., Hernandez, A., “An Educational Software for the Analysis and Synthesis of Planar Four Bar Linkages”, Proceedings 12. World Congress in Mechanism-sand Machine Science, Besancon, France, June 2007.
4. Wilson, E.W., Sadler, J.P., “Kinematics and Dynamics of Machinery”, Prentice Hall Pearson Education, 2003.
5. Freeman, R., “An Asynchronous Approach to Teaching Math and Engineering Software with the Context of a Course in Mechanisms”, Proceedings of the American Society for Engineering Education (CD-ROM DEStech Publications) Session 1365: 15pp., 2003.
6. Egelhoff, C.J., Blackketter, D.M., Beyerlein, S., “Software Compliments Structured Learning for Kinematics of Mechanisms” Frontiers in Education (FIE) Conference IEEE Catalog Number: 96CH35946 <http://www.eng.auburn.edu/users/marghdb/MECH6710/mech5710.html>, 1996.
7. Baker, J.E., Sugden, S.J., “Spread Sheets in Education – The First 25 Years”, eJSiE, Vol. 1, No. 1, 18–43, July 24, 2003.
8. Mokheimer, E.M.A., Antar, M.A., “On the Use of Spreadsheets in Heat Conduction Analysis”, International Journal of Mechanical Engineering Education, Vol. 28, No. 2, 118–139.
9. Norton, R.L., “Design of Machinery”, McGrawHill, 2003.
10. <http://www.loekvanderklis.com/EN/BeachAnimals/BeachAnim02.html>.

# Hinged Frameworks with Unusual Geometrical Properties

Mikhail Kovalev

**Abstract** Examples of bar and joint frameworks in the plane having unusual geometrical properties are presented. The first of them is a linkage with the varying number of degrees of freedom, depending on its position. The second is a geometrically stable hinged truss with all hinges lying on a straight line. The third one is an exotically unstable truss. Some questions concerning geometry of hinged trusses are stated.

**Keywords** Linkages · Degrees of freedom · Hinged trusses

## Introduction

We examine ideal flat constructions made of absolutely rigid rectilinear levers, having hinges on the ends. Some hinges may be fixed in the plane; these fastened hinges are marked on the figures by crosses. Small circles designate not fastened hinges. Levers can rotate across the hinges arbitrarily in the plane. From the point of view of the theory of mechanisms our hinge can be usual rotary pair, or so-called combined hinge, if it belongs to more than two levers. In our model we do not take into account, that the crossing of levers can prevent the motion of linkage. The author has find some constructions of this kind with exotic properties, and he hopes that these constructions may be of interest for specialists in kinematic geometry.

## A Linkage with Variable Number of Degrees of Freedom

It is often assumed that a linkage has the quite certain number of degrees of freedom. This assumption is certainly valid, if the configuration space of the linkage is a

---

M. Kovalev (✉)

Bauman Moscow State University, 105005, Moscow, 2-ya Baumanskaya, 5, Russia  
e-mail: mdkovalev@mtu-net.ru

manifold. However, it may be not a manifold. For example, it may be a connected union of torus and circle. Let's describe a similar example given by the author in [1, 2].

This mechanism (Fig. 1) contains 13 levers, 7 free and 3 fixed hinges. It consists of two hinged parallelograms  $\Pi_1$   $\nu_8\nu_1\nu_3\nu_9$ , and  $\Pi_2$   $\nu_8\nu_4\nu_6\nu_9$ . The hinges  $\nu_2$  and  $\nu_5$  also lay in the middle of levers  $\nu_1\nu_3$  and  $\nu_4\nu_6$  accordingly. It can be achieved by fastening them by levers  $\nu_1\nu_2$ ,  $\nu_2\nu_3$  and  $\nu_4\nu_5$  and  $\nu_5\nu_6$ . The lengths of the additional levers  $\nu_2\nu_7$  and  $\nu_5\nu_7$  are equal to the lengths of the side levers of the parallelograms. The length of the lever  $\nu_{10}\nu_7$  is chosen so, that the hinge  $\nu_7$  can move to the middle of the segment  $\nu_8\nu_9$ , as shown in Figs. 1, 2a. When the hinge  $\nu_7$  is in the indicated position, the parallelograms  $\Pi_1$  and  $\Pi_2$  can move independently one from another with 1 degree of freedom everyone, and consequently the local number of degrees of freedom of the mechanism in such positions is equal to 2. If the mechanism is brought to the position with the lever  $\nu_{10}\nu_7$  on the lever  $\nu_1\nu_2$  and the lever  $\nu_7\nu_5$  on the continuation of the lever  $\nu_{10}\nu_7$ , the hinge  $\nu_7$  can be moved from its place (Fig. 2b). In those positions when the hinge  $\nu_7$  does not lay in the midpoint of the segment  $\nu_8\nu_9$  (Fig. 2b), the number of degrees of freedom of the mechanism is equal to 1.

The latter number of degrees of freedom is also given by the Tchebycheff-Grübler formula. In the positions when  $\nu_7$  lies in the midpoint of  $\nu_8\nu_9$ , one of connections  $\nu_2\nu_7$  or  $\nu_5\nu_7$  appears to be false or passive. After publication of this example the author has learned from V.I. Bujakas that similar called by K. Wohlhart kinematotropic mechanisms were already described in the literature [3]. The first planar mechanism of this kind was given by Wunderlich [4] in 1954. But these publications do not contain the described above example. Wohlhart has developed this example. Combining our mechanisms he constructed a mechanism with the number of degrees of freedom varying from 1 up to any natural number.

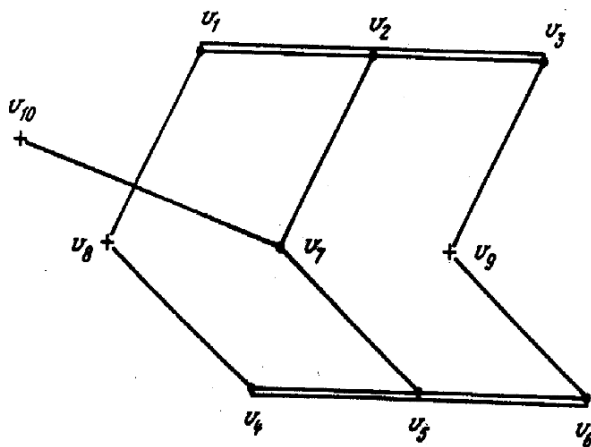
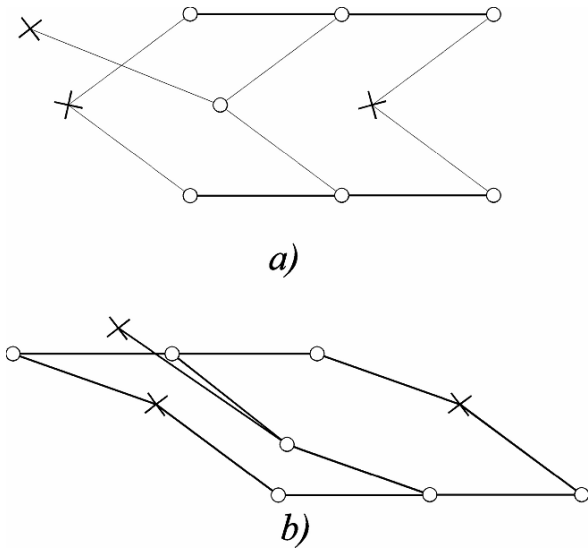


Fig. 1 Kinematotropic linkage

**Fig. 2** Two positions of kinematotropic linkage with different local degrees of freedom



### Straightened Hinged Frameworks

A straightened planar hinged framework is a framework with all hinges lying on a straight line. The following theorem is valid [5, 6]:

**THEOREM.** Any two distinct straightened reassemblings of a hinged framework are different positions of the same planar hinged mechanism.

We call a hinged truss geometrically stable (or briefly stable) [7], if one could put it together despite of any small mistakes in the lengths of levers, and this disturbed truss will be close to the undisturbed one. For example, the elementary planar truss of Fig. 3 with two fastened and one free hinge is (geometrically) stable, if the free hinge does not lie on the straight line connecting fastened hinges. A statically determined truss is always stable.

The author constructed [5] an example of straightened geometrically stable hinged truss. The structural scheme of this truss is shown in Fig. 4. And the example

**Fig. 3** Geometrically stable hinged truss

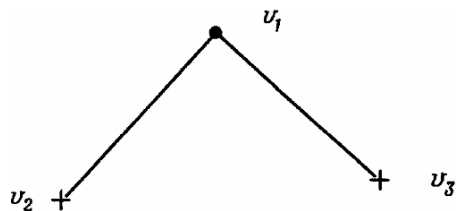
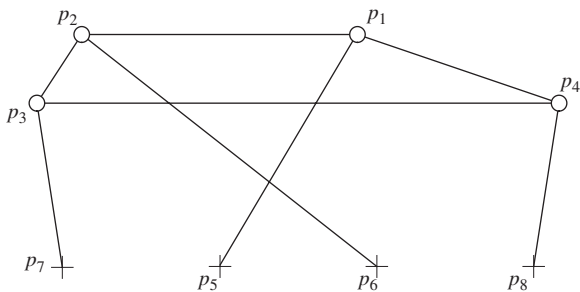


**Fig. 4** Structural scheme of the straightened hinged trusses with unusual properties



is presented in Fig. 5a (free hinge  $p_3$  coincide with the fastened hinge  $p_8$ ). In Fig. 5b another reassembling of this truss is shown. Naturally, according to the theorem above, it is not straightened.

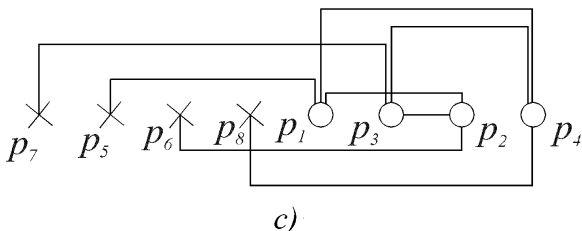
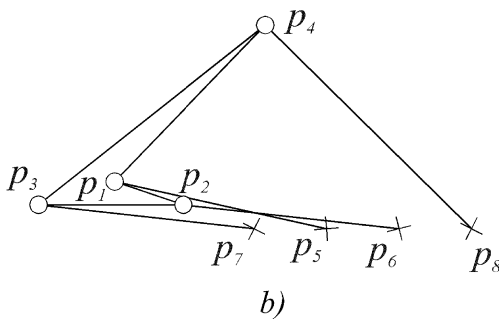
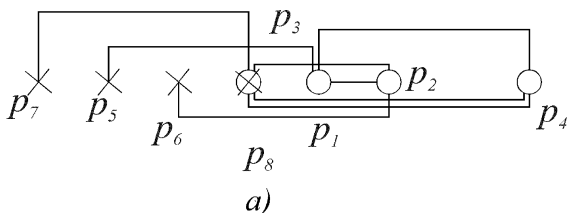


**Fig. 5** Straightened stable and curiously unstable hinged trusses

In Fig. 5c a straightened truss with the same structural scheme but distinct lengths of levers is presented. This truss is unstable and has to some extent a curious property [5]. Namely it is stable under arbitrary but enough small change of the length of every one lever separately. Note that there are arbitrarily small simultaneous changes of several levers, after that one could not put it together near the initial position. These trusses are the first examples of such kind in the literature.

The proof of these properties of the hinged trusses is rather complicated. It is based on the consideration of mapping of multidimensional Euclidean spaces, which coordinate functions are squares of the lengths of levers. The author calls it the edge mapping, but in English literature it is often called the rigidity mapping [8, 9]. In last examples this is the mapping between eight-dimensional spaces. The proof of the geometrical stability essentially uses the concept of a topological degree of a mapping.

Still there are unsolved fundamental questions concerning geometrical stability of hinged frameworks [10]. Let's mention even two of them.

QUESTION 1. If a hinged truss is geometrically stable when its fastened hinges are immobile, will it be necessarily stable with respect to small disturbance of the positions of fastened hinges?

QUESTION 2. Are there any geometrically stable hinged trusses, which can be put together in only one way?

These questions caused by the theory of mechanisms and trusses seem to be rather difficult geometrical problems. They demonstrate that the mechanisms and trusses theory still can be a source of significant mathematical problems.

## References

1. Kovalev M.D., Geometric Theory of Hinged Devices. In Russian Acad. Sci. *Izv. Math.* 44(1), 1995, pp. 43–67.
2. Kovalev M.D., To Geometrical Aspects of Hinged Devices and Configurations. *Vestnik MGTU. Mashinostroenie* 4(45), 2001, pp. 33–51 (Russian).
3. Wohlhart K., *Kinematotropic Linkages*. Recent Advances in Robot Kinematics. Kluwer Academic Publishers, 1996, pp. 359–368.
4. Wunderlich W., Ein merkwürdiges Zwölfstabgetriebe. *Österreichisches Ingenieurarchiv*. Band 8, Heft 2/3, 1954, pp. 224–228.
5. Kovalev M.D., Stability of Hinged Frameworks and Hinged Schemes. *Results of Science and Engineering*. Series of Modern Mathematics and Applications. V. 68. Works of the International Conference Devoted to 90 Anniversary of L.S. Pontryagin v. 7. *Geometry and Topology*. Moscow, VINITI, 1999, pp. 65–86 (Russian).
6. Bezdek K., Connelly R., Pushing Disks Apart – the Kneser – Poulsen Conjecture in the Plane, *J. Reine Angew. Math.* 553, 2002, pp. 221–236.
7. Kovalev M.D., Straightened Hinged Frameworks *Sbornik. Mathematics* 195(6), 2004, pp. 833–858.



8. Asimow L., Roth B., The Rigidity of Graphs. *Trans. Amer. Math. Soc.*, 245, 1978, pp. 279–289.
9. Connelly R., *Handbook of Convex Geometry*. Vol. A, B, North-Holland, Amsterdam, 1993, pp. 223–271.
10. Kovalev M.D, Results and Problems of Geometry of Hinged Devices. The Report on 12 World Congress IFTOMM, Besancon, France, June 18–21, 2007 (Russian).

# A Comparison Between Line Geometries of Point and Line Displacements

Chintien Huang

**Abstract** This paper deals with the comparison between the line geometries of point and line displacements. The central concept is that two linear complexes of different pitches are associated to a displacement screw. One is pertaining to point displacements, while the other to line displacements. Similarities between the two linear complexes in their construction, elements, properties, and relations to the displacement screw are investigated. This study shows that all of the recently developed theorems and properties in the line geometry of line displacements resemble those in the well-developed line geometry of point displacements. The results provided in this paper can help bridge the gap between point and line displacements in both theoretical treatments and practical applications.

**Keywords** Line geometry · Point displacement · Line displacement · Linear complex · Screw · Regulus

## Introduction

The two positions theory in kinematics accounts for the relations between two positions of point, plane, and line elements of a rigid body. Line geometry pertaining to the two positions theory has been developed for over a century [1, 2]; however, most of them had focused on the line geometries of point and plane displacements. The line geometry of line displacements, on the other hand, had not been thoroughly investigated. Based on recent developments [3, 4] in the line geometry of line displacements, this paper conducts a comparative study on the line geometries of point and line displacements.

The line geometry of point displacements is the foundation for the development of screw theory [2, 5–7]. It is known that there is a one-to-one correspondence between a linear line complex (LLC) and a screw. An LLC contains  $\infty^3$  lines whose

---

C. Huang (✉)

Department of Mechanical Engineering, National Cheng Kung University, No. 1, University Road, Tainan 701, Taiwan  
e-mail: chuang@mail.ncku.edu.tw

Plücker coordinates are constrained by a linear equation. In instantaneous kinematics and statics, an LLC can be thought of as containing  $\infty^3$  zero-pitch screws, which are reciprocal to the screw corresponding to the LLC. In finite kinematics, an LLC is best described by using the notion of null-planes, which are planes through midpoints of homologous points and perpendicular to line segments connecting the homologous points. Therefore, the notion of helicoidal vector fields can be depicted for statics and instantaneous kinematics, as well as finite displacements of points.

However, the LLC associated with homologous lines is lesser known. It was described in literature as follows: there is a unique pair of homologous lines intersecting at an arbitrary point in space, and the line through the point and perpendicular to both of the intersecting homologous lines belongs to an LLC [2]. Until recently, the notion of the helicoidal vector field of the LLC of line displacements was not clearly depicted. Then, it was shown [3] that the internal bisector of the intersecting homologous lines at each point in space indeed belongs to a helicoidal vector field. Based upon the finding, it followed that the notion of null-planes was also established for the LLC of line displacements.

The concept of null-planes is helpful not only in the description of an LLC, but also in the representation of a pair of homologous points. This is, however, not true in the LLC of line displacements because a pair of general homologous lines does not correspond to a null plane. Recent research results [4] showed that a regulus, rather than a null-plane, uniquely corresponded to a pair of general (non-intersecting) homologous lines. The regulus of lines resides on the hyperbolic paraboloid whose central axis is the internal bisector of the pair of homologous lines.

These recent findings in the LLC of line displacements suggest that the two LLCs of point and line displacements, except for their pitches, are similar in many aspects when perceived using line geometry. This paper aims to summarize and bring forth similarities between the line geometries of point and line displacements.

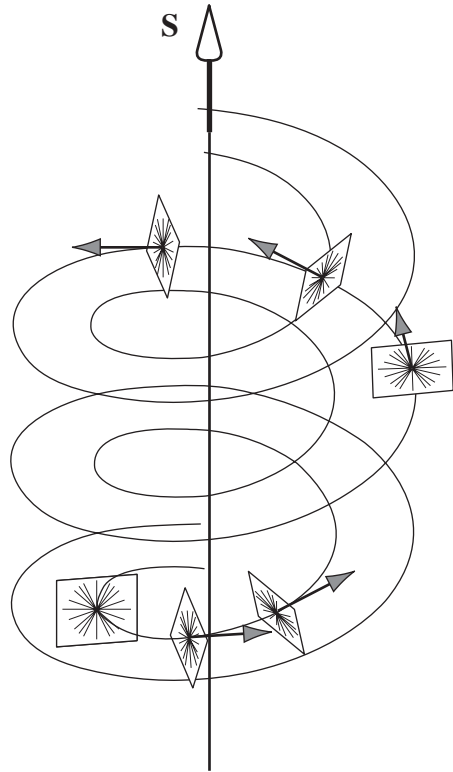
## Theoretical Background for the Line Geometry of Line Displacements

Let a line be represented by Plücker coordinates  $(\mathbf{q}, \mathbf{q}')$ , where  $\mathbf{q} = (q_1, q_2, q_3)$  and  $\mathbf{q}' = (q'_1, q'_2, q'_3)$  are Cartesian 3-vectors. A linear line complex (LLC) is a set of lines constrained by a linear equation of the following form:

$$\mathbf{c} \cdot \mathbf{q}' + \mathbf{c}' \cdot \mathbf{q} = 0 \quad (1)$$

where the coefficients  $\mathbf{c} = (c_1, c_2, c_3)$  and  $\mathbf{c}' = (c'_1, c'_2, c'_3)$  are Cartesian 3-vectors, and  $(\mathbf{c}, \mathbf{c}')$  can be thought of as the coordinates of a screw, whose pitch is  $(\mathbf{c} \cdot \mathbf{c}')/(\mathbf{c} \cdot \mathbf{c})$ , provided  $\mathbf{c} \neq \mathbf{0}$ . A line can be thought of as a zero-pitch screw, and it fulfills the

**Fig. 1** LLC and helicoidal vector field in instantaneous kinematics



Plücker identity:  $\mathbf{q} \cdot \mathbf{q}' = 0$ . In terms of screw algebra, Eq. (1) is the reciprocal condition between a screw  $\mathbf{S}$  and a zero-pitch screw  $\mathbf{L}$ , where  $\mathbf{S} = (\mathbf{c}, \mathbf{c}')$  and  $\mathbf{L} = (\mathbf{q}, \mathbf{q}')$ . It is obvious that there is a one-to-one correspondence between a screw and an LLC.

The best way to illustrate the lines of an LLC is probably by using the notion of a helicoidal velocity field [5–7]. Consider an instantaneous screw of a rigid body. The velocity of an arbitrary point belongs to a helicoidal vector field, whose pitch is the velocity divided by the angular velocity of the screw, as shown in Fig. 1. The pencil of lines on the plane normal to the velocity and through the point belongs to an LLC. One can interpret the lines in the LLC as the pure forces (zero-pitch wrenches) that do no work on the rigid body undergoing such an instantaneous motion.

An LLC can also be illustrated within the context of finite kinematics [1, 2]. Consider two finitely separated positions of a body. A point of the body at one position and its corresponding point at the other position are called homologous points. The null-plane corresponding to a pair of homologous points is the plane through their midpoint and perpendicular to the line joining them. All lines on the normal plane and through the midpoint of a pair of homologous points form a pencil of lines, and the pencils of lines corresponding to all pairs of homologous points constitute an LLC.

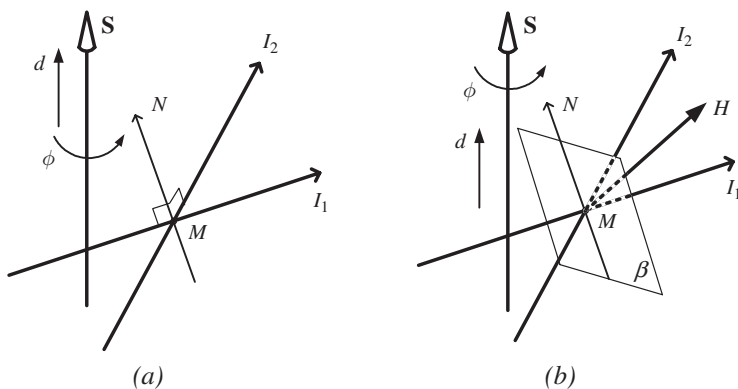


Fig. 2 LLC and helicoidal vector field of line displacements

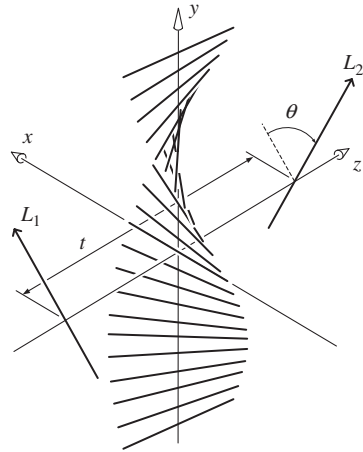
The description of the LLC of homologous lines can be found in [2], in which the two positions theory in kinematics was discussed in detail by using line geometry. As shown in Fig. 2a, given two positions of a rigid body, one can determine the screw axis and corresponding rotation and translation parameters,  $\phi$  and  $d$ , respectively, of the displacement. For any point  $M$  in space, there exists a pair of homologous lines,  $I_1$  and  $I_2$ , intersecting at  $M$ . The line through  $M$  and perpendicular to  $I_1$  and  $I_2$  is denoted by  $N$ . For all the  $\infty^3$  points in space, there exist  $\infty^3$  such normal lines like  $N$ , which form a linear line complex [3]. The pitch of the screw corresponding to the LLC is  $(d / \sin \phi)$

### Recent Developments in the Line Geometry of Line Displacements

Based on the discussion in [2], one can see that the LLC of homologous lines differs from that of homologous points because the notion of null-planes and helicoidal vector fields were not clearly depicted. Recent research results [3, 4] have provided a better insight into the LLC of homologous lines.

As illustrated in Fig. 2b, given two positions of a rigid body, for every point in space, there exists a corresponding null-plane  $\beta$  that consists of a pencil of lines of the LLC of homologous lines. The normal of the null-plane is the internal bisector  $H$  of the two intersecting homologous lines. Furthermore, for any finite displacement screw, there exists a helicoidal vector field associated with intersecting homologous lines, and the pitch of the helicoidal vector field is the translation divided by the sine of the rotation. With regard to the set of lines corresponding to a pair of general homologous lines, recent research results [4] demonstrated that a regulus residing on a hyperbolic paraboloid uniquely corresponded to the pair of homologous lines, as shown in Fig. 3.

**Fig. 3** Regulus corresponding to a pair of homologous lines



To determine the displacement of a rigid body, one has to specify three pairs of homologous points or two pairs of homologous lines. If we are concerned with only a line element of the body, there will be only one pair of specified homologous lines. In that case a unique displacement screw cannot be determined. This is one of the so-called incompletely specified displacements [8]. There are  $\infty^2$  possible screws for displacing the line. Furthermore, it has been discovered [9] that these  $\infty^2$  screws can form a screw system of the third order (a 3-system). The regulus associated with the 3-system of a pair of homologues lines was discovered [4] by using the intersection of three LLCs corresponding to basis screws of the 3-system. This regulus contains lines residing on a hyperbolic paraboloid. Figure 3 shows a pair of homologous lines ( $L_1, L_2$ ) and its corresponding regulus. The distance and angle between and  $L_2$  are  $t$  and  $\theta$ , respectively. We set up a coordinate system whose origin is the midpoint on the common perpendicular of  $L_1$  and  $L_2$ . The  $x$ -axis and  $y$ -axis are, respectively, the external and internal bisectors of  $L_1$  and  $L_2$ . Consequently, the  $z$ -axis coincides with the common perpendicular of  $L_1$  and  $L_2$ . The Plücker coordinates of this regulus are [4]:

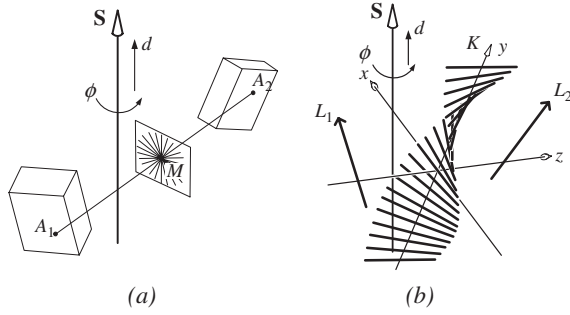
$$q_1 = -t, q_2 = 0, q_3 = -Y \sin \theta; q'_1 = -Y^2 \sin \theta, q'_2 = 0, q'_3 = tY \quad (2)$$

where  $Y$  is an arbitrary scalar, the parameter for generating the regulus. As illustrated in Fig. 3, the regulus can be visualized as a ruled surface with lines perpendicular to and twisting along the  $y$ -axis.

### A Comparative study of Point and Line Displacements

According to the discussion heretofore, we can see that there are many similarities between line geometries of point and line displacements. In what follows, we

**Fig. 4** Pencil of lines vs. regulus of lines



summarize the theorems regarding point and line displacements in separate columns for comparison purposes.

As shown in Fig. 4, each of the  $\infty^3$  different points ( $\infty^4$  different lines) in the Cartesian 3-space is the midpoint (internal bisector) of a unique pair of homologous points (lines).

*An arbitrary point  $M$  is the midpoint of a unique pair of homologous points,  $A_1$  and  $A_2$ .*

*An arbitrary line  $K$  is the internal bisector of a unique pair of homologous lines,  $L_1$  and  $L_2$ .*

Another similarity can be drawn for the case in which the pair of homologous lines intersects. (See Figs. 4a and 2b.)

*An arbitrary point  $M$  is the midpoint of a unique pair of homologous points,  $A_1$  and  $A_2$ .*

*An arbitrary point  $M$  is the intersection of a unique pair of intersecting homologous lines,  $I_1$  and  $I_2$ .*

Also illustrated in Fig. 4, there is a parallel between the pencil of lines on a null-plane and the regulus of lines residing on a hyperbolic paraboloid.

*The pencil of lines on the null-plane through  $M$  and perpendicular to the line  $A_1A_2$  uniquely corresponds to the point displacement of  $A_1$  to  $A_2$ .*

*The regulus of lines residing on a hyperbolic paraboloid, whose axis is  $K$ , uniquely corresponds to the line displacement of  $L_1$  to  $L_2$ .*

Figure 5 illustrates the following similarities in the existence of linear complexes and helicoidal vector fields.

*The pencil of lines belongs to a linear complex, whose pitch is  $(\frac{d}{2} / \tan \frac{\phi}{2})$ . The vector  $A_1A_2$  belongs to a helicoidal vector field of pitch  $(\frac{d}{2} / \tan \frac{\phi}{2})$ .*

*The regulus of lines belongs to a linear complex, whose pitch is  $(d / \sin \phi)$ . The internal bisector of  $I_1$  and  $I_2$  belongs to a helicoidal vector field of pitch  $(d / \sin \phi)$ .*

It is a common practice to specify three pairs of homologous points to determine a unique displacement. When considering line displacements, only two pairs of homologous lines are required to determine a displacement. As shown in Fig. 6, in terms of linear complexes, the following similarity can be drawn.

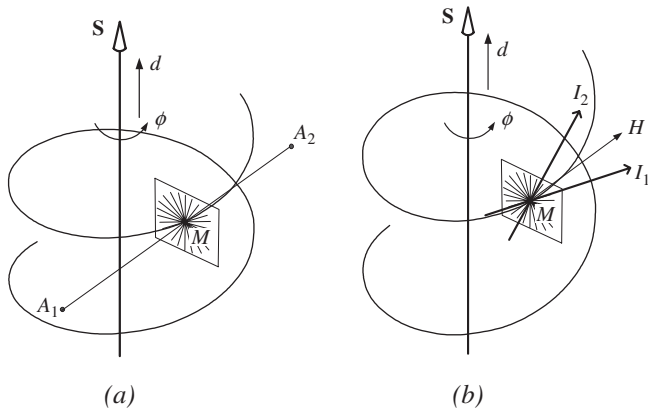


Fig. 5 Midpoint vs. internal bisector, for helicoidal vector fields

*Three pencils of lines, corresponding to three pairs of homologous points, determine a unique linear complex.*

*Two regulii, corresponding to two pairs of homologous lines, determine a unique linear complex.*

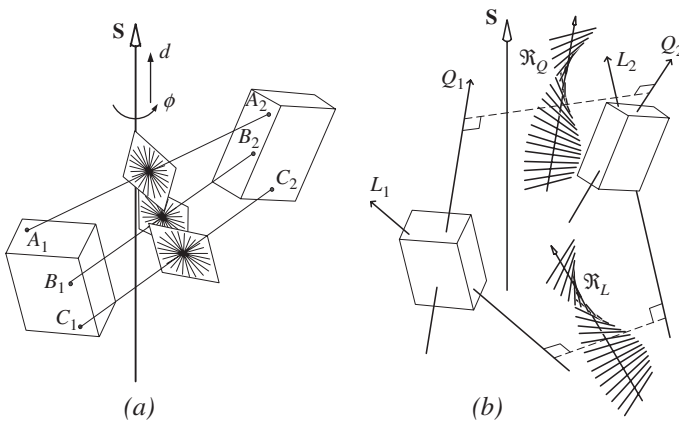


Fig. 6 Three pencils vs. two regulii, for determining a displacement

### Conclusion

This paper summarizes recent developments in the line geometry of line displacements and conducts a comparative study to draw the similarities between line geometries of point and line displacements. Two linear complexes with different pitches are associated with point and line displacements. Homologous points and lines uniquely correspond to different entities in line geometry: pencils and regulii,



respectively. Three pencils of lines of homologous points, or two regulii of homologous lines uniquely fit a linear complex, which corresponds to a unique spatial displacement.

As illustrated in this paper, recent developments in the line geometry of line displacements can help bridge the gap between theories pertaining to point and line displacements. As a result, line displacements can be treated equally as the extensively studied point displacements, in both theoretical and application aspects.

**Acknowledgments** The author would like to express his gratitude to Mr. Wuchang Kuo for assistance with the figures. The financial support of the National Science Council of Taiwan, ROC (Grant No.: NSC 96-2923-I-006-001-MY2) is gratefully acknowledged.

## References

1. Study, E., Von den Bewegungen und Umlegungen, *Mathematische Annalen*, 39, 1891, pp. 441–564.
2. Bottema, O., and Roth, B., *Theoretical Kinematics*, North-Holland Publishing Company, Amsterdam, 1979.
3. Huang C., Kuo W., and Ravani B., On the Linear Line Complex and Helicoidal Vector Field Associated with Homologous Lines of a Finite Displacement, 12th IFToMM World Congress, Besançon, France, June 18–21, 2007.
4. Huang C., Kuo W., and Ravani B., On the Regulus Associated with the Displacement of a Line, *Proceedings of the 2007 ASME International Design Engineering Technical Conferences and Computer and Information in Engineering Conference*, Las Vegas, USA, September 4–7, 2007.
5. Phillips, J., *Freedom in Machinery*, Volumes 1 and 2, Cambridge University Press, Cambridge, 1984, 1990.
6. Hunt, K. H., *Kinematic Geometry of Mechanisms*, Clarendon, Oxford, 1978.
7. Pottmann H., and Wallner J., *Computational Line Geometry*, Springer-Verlag, Berlin, 2001.
8. Tsai, L. W., and Roth, B., Incompletely Specified Displacements: Geometry and Spatial Linkage Synthesis, *ASME Journal of Engineering for Industry*, Vol. 95(B), 1973, pp. 603–611.
9. Huang, C., and Wang, J. C., The Finite Screw System Associated with the Displacement of a Line, *Journal of Mechanical Design*, *Trans. ASME*, Vol. 125, 2003, pp. 105–109.

# A Kinematic Approach to Calculate Protein Motion Paths

Mikel Diez, Víctor Petuya, Mónica Urizar and Alfonso Hernández

**Abstract** Proteins play an essential role in biochemical processes. Recently, a new viewpoint has arisen within protein researches, based on the parallelisms between proteins and mechanism. In this paper the authors present a new approach to obtain protein motion paths based in computational kinematic considerations. Finally, simulation results for an specific protein are presented.

**Keywords** Biokinematics · Protein motion · Motion Paths · Peptide plane · Dihedral angles

## Introduction

Thanks to Humane Genome discovery great progress has been made within genetic science, specially in proteins field. Human Genome has provided us with a powerful tool capable of coming across new sorts of proteins, therefore giving us a lot of information about biological processes that proteins carry out in the human body. For example, enzymes actuate as catalysts in chemical reactions, antigens protect the organism from external agents and fibred proteins provide mechanical functions and participate in spun bonds formation [1]. Currently, numerous researches deal with proteins analysis. *Protein folding* problem comes from amino acids sequence or initial structure to achieve the protein steady configuration, also called protein native structure, which states the protein function. *Protein docking* outlines the problem between two proteins joining. *Molecular dynamic* studies protein motion based on atomic force analysis. Finally, *Loop closure* problem investigates the unfilled gaps within protein chains.

For studying protein structure there can be found diverse methods which can be classified into experimental and analytical methods [2]. *Nuclear Magnetic Resonance* and *X-ray Crystallography* are experimental methods that obtain photographs

---

M. Diez (✉)

Department of Mechanical Engineering, University of the Basque Country, Bilbao, 48013, Spain  
e-mail: mikel.diez@ehu.es

of the protein structure. Analytical methods focus on different approaches. *Ab initio Methods* and *Homology Modeling* deals with protein folding problem. *Ab initio Methods* search the protein minimum potential energy, which corresponds to its native structure. *Homology modeling*, otherwise, models the protein through primary structure comparison. *Molecular Dynamics*, *Lattice Models* and *Statistical Models*, as well as some adaptations of *ab initio methods*, try to simulate the proteins motion, since every protein has a certain motion in its folding process, and some of them need to modify their native configuration when carrying out their function.

Recently, a new viewpoint has arisen among protein investigation. This novel perspective, which could be designated *Biokinematics*, treats the proteins as if they were about mechanisms. In [3] it is proposed a new procedure that instead of the potential function, minimizes equivalent torques in each protein degree of freedom. As well, in [4] the angular momentum conservation is used to simulate the protein folding process. Also, in [5], inverse kinematic principles are proposed for solving *Loop closure* problem.

In this paper, it is presented a new approach for obtaining the motion paths of the protein movement as a result of the *ligand docking* process, which causes large conformational changes due to the presence of the target ligand.

## Protein Kinematic

Proteins have specific biochemical characteristics. A protein consists of several amino acids joined together making up a chain. The amino acids constitute a structure, illustrated in Fig. 1a, formed by one nitrogen atom and two carbon atoms linked between them. The central carbon atom is designated as  $C\alpha$ , and in each amino acid, the  $C\alpha$  possesses a different radical. The amino acids are joined one to each other by a bond named *peptide bond*, formed by the last  $C$  atom of one amino acid and the  $N$  atom of the next amino acid. The relative angle between the atoms in the peptide bond,  $\omega$ , has a constant value of  $0^\circ$  or  $180^\circ$ . The links between  $N - C\alpha$  and  $C\alpha - C$  possess certain rotation motion and the relative angles located in these links, namely *dihedral angles*, are designated as  $\phi$  y  $\psi$  respectively (see Fig. 1). These angles must satisfy the Ramachandran plot [1] to guarantee no collision between atoms.

Focusing on these structural characteristics, it can be observed some parallelisms between proteins and mechanisms [6], so several hypothesis can be formulated to model and analyze proteins using computational kinematics considerations. Since the angles and length of the peptide bond are considered constant [7], the substructure  $C\alpha_{i-1} - C_{i-1} - N_i - C\alpha_i$  remains permanently in a plane, called the peptide plane  $\pi$  (see Fig. 1a). Thus, the peptide plane can be considered as a rigid element, as shown in Fig. 1b. Consequently, the links  $N - C\alpha$  and  $C\alpha - C$  can be modeled as links joined by revolute joints with an axis pointing along the link direction. The *dihedral angles* will be considered as the protein degrees of freedom (dof). Therefore, the proteins movement is defined by the rotation of the peptide planes produced by the variation of the dihedral angles. Thus, the protein motion shares

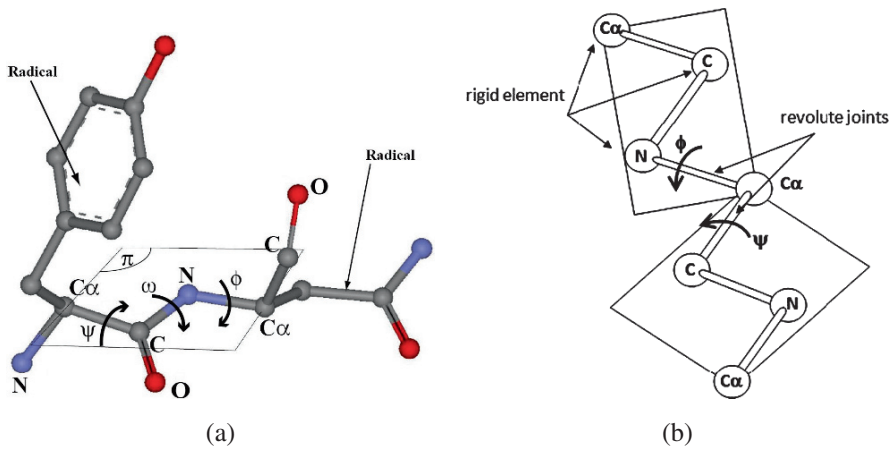


Fig. 1 (a) Biochemical model. (b) Kinematic model

similar characteristics to that in serial manipulators, although proteins number of dof is much more higher, ranging between 100 and 3,000.

### Calculation of Protein Motion Paths

In general, each protein has a small movement in its equilibrium state. However, some kinds of proteins suffer large conformational changes, such as those produced by “target ligand” presence in *ligand docking* process, or those changes that occur in transport proteins due to the ATP reaction. These movements throw some light on how proteins execute their biological processes.

Considering the protein kinematics described in the previous section, it will be approached the calculation of the motion paths that take place into the movements due to large conformational changes, by adapting the principles of computational kinematics to this problem. For that purpose, it will be used the proteins data of the initial and final position of the protein’s movement obtained experimentally.

To evaluate the procedure, it has been chosen the protein Inorganic Pyrophosphatase (in the Protein Data Bank, PDB, it corresponds to the entry 1k20 [8]). The protein under study is an enzyme that takes part in the hydrolysis process of pyrophosphate. The protein initial and final positions are shown in Fig. 2 (ribbon representation of the protein chain). This protein possesses 304 amino acids with a total amount of 4,732 atoms. Overall, the protein dof rises to 606.

The analysis has been done using a software under development, named GIM-PRO, capable of simulating protein motion. Taking advantage of the fact that all protein dof are of angular type, the calculation has been done working only with angular parameters. In the ensuing analysis, the values of each amino acid  $i$  dihedral angles,  $\phi_i$  and  $\psi_i$ , are calculated in the both start (0) and final positions ( $f$ ). Intermediate positions will be used only for error evaluation throughout the process. Next,

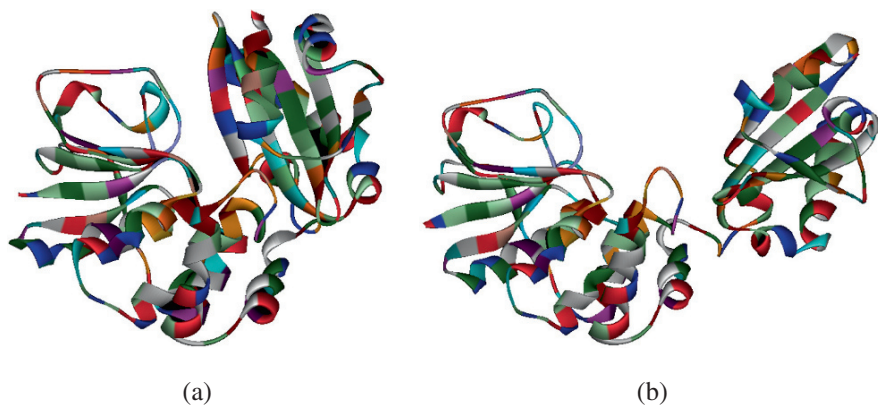


**Fig. 2** (a) 1K20 protein start position. (b) 1K20 protein final position

simulation is done by applying the increments gradually to each dof, according to Eq. (1), until the final configuration is reached, obtaining throughout the progress the protein motion paths,

$$\Delta\phi_i = \frac{\phi_i^f - \phi_i^0}{n}; \quad \Delta\psi_i = \frac{\psi_i^f - \psi_i^0}{n} \quad (1)$$

where  $n$  is the number of steps in the simulation. The process progresses from the first amino acid to the last one, by rotating all the  $\mathbf{r}_j$  around their axis  $\mathbf{e}_i$  in each dof of the protein ( $\Delta\phi_i, \Delta\psi_i$ ), where vectors  $\mathbf{r}_j$  are defined between the atom which is origin of the rotation axis  $\mathbf{e}_i$  and every atom which will be rotated (see Fig. 3). The rotations of the peptide planes are evaluated by Rodrigues rotation formula used in mechanism analysis and simulation [9]:

$$\mathbf{r}_j^{k+1} = \mathbf{u} + \mathbf{v} \cdot \cos \Delta\phi_i + \mathbf{d} \cdot \sin \Delta\phi_i \quad (2)$$

Where  $k$  is the actual position. The rotated vector  $\mathbf{r}_j^{k+1}$  is decomposed into three vectors:  $\mathbf{v}$  is its component in the plane defined by  $\mathbf{r}_j^k$  and  $\mathbf{e}_i$ ,  $\mathbf{d}$  is its normal component to that plane and  $\mathbf{u}$  will be the projection of  $\mathbf{r}_j^k$  on  $\mathbf{e}_i$ :

$$\mathbf{v} = \mathbf{r}_j^k - (\mathbf{e}_i \cdot \mathbf{r}_j^k) \cdot \mathbf{e}_i; \quad \mathbf{d} = \mathbf{e}_i \times \mathbf{r}_j^k; \quad \mathbf{u} = (\mathbf{e}_i \cdot \mathbf{r}_j^k) \cdot \mathbf{e}_i \quad (3)$$

Vectors  $\mathbf{v}$  and  $\mathbf{d}$  are multiplied by  $\cos \Delta\phi_i$  and  $\sin \Delta\phi_i$  respectively, thus vector  $\mathbf{r}_j^{k+1}$  is obtained by Eq. (2) depicted in Fig. 4.

The relative error between the simulated and experimental protein structures (including protein motion intermediate structures) is obtained calculating the root mean square error ( $rmsd_i$ ) between the equivalent atoms of two structures overlapped. Theoretically is impossible to achieve models with a rmsd value smaller

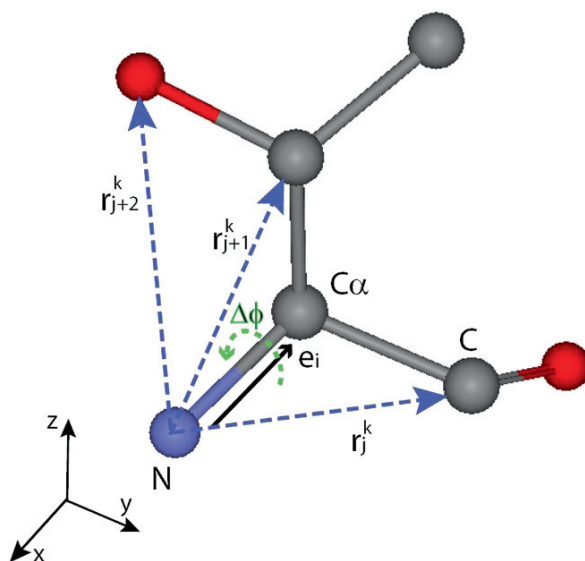


Fig. 3 Location of vectors  $r_j^k$  in a protein chain section

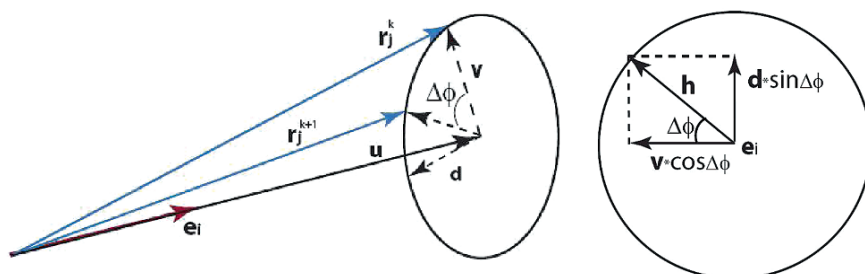
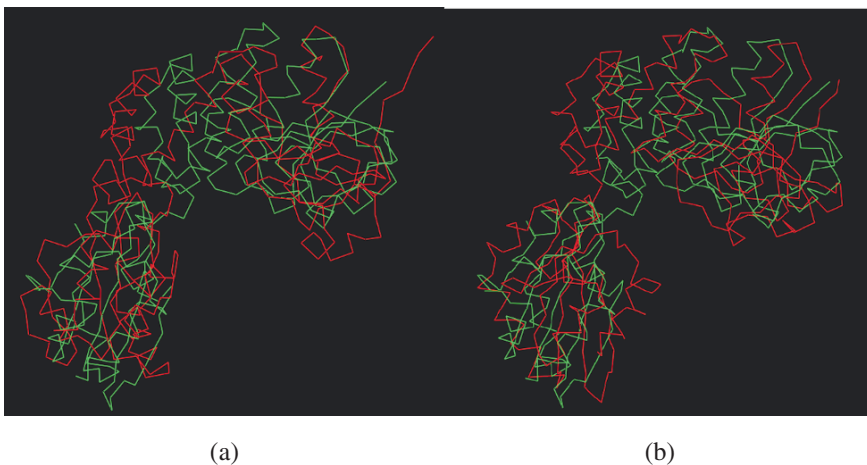


Fig. 4 Graphical construction for  $r_j^k$  rotation

than 1–2 Å, due to the vibration of the atoms around their position. In Fig. 5a it can be observed the experimental protein final configuration (in green) and the one obtained via simulation (in red). As can be observed, there exist marked differences between both structures. The relative error at the final position is equal to 10.82Å. In Fig. 6 the error evolution through the simulation progress is shown. Analysing the experimental initial and final positions, it can be observed that the dihedral angles values of the peptide bonds are not 0° or 180°, as they should be. This fact also occurs with the distances and the interatomic angles. These errors are caused by the inaccuracies of the experimental methods. In this way, the positions obtained experimentally do not verify the biochemical structural requirements. Therefore, the final position obtained via simulation is substantially altered with respect to the experimental one. Consequently, if the calculation uses the data



**Fig. 5** (a) Protein without peptide bond angle modification. (b) Simulation results including peptide bond angles variation

from the PDB, the peptide angles can not be considered constant and they must be taken into account as *virtual degrees of freedom*. Thus, similarly to Eq. (1), the variation of the peptide angle  $\Delta\omega_i$  must be calculated. Eq. (2) is also applied to every peptide bond of the protein. Now, the  $rmsd_i$  relative error decreases to a maximum of  $6.88 \text{ \AA}$  at the final position (see Fig. 6). In Fig. 5b it is shown the final position obtained by taking into consideration  $\omega$  variation, overlapped to the experimental final configuration. However, our assumption of  $\omega$  variation defers from the own nature of the bond. In addition, this fact has the consequence of increasing the protein dof, causing an extra computational cost.

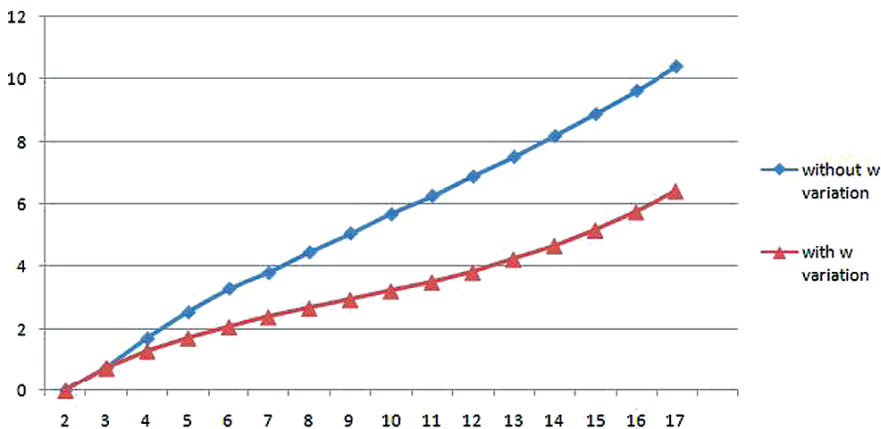


**Fig. 6**  $rmsd_i$  error evolution without and with  $\omega$  variation

This calculation allow us to simulate the entire movement of the protein between the initial and final positions obtaining all the atoms' motion paths. To further minimize the maximum relative error, it could be used experimental intermediate positions as data. Because the protein movements are carried out by angular variations, it would be convenient to use angular relative errors.

## Refinement Algorithm for Protein Structures

The limitations of experimental methods not only increases the dof of the proposed approach, but also brings in errors in the structures. For this purpose, a refinement method is being currently developed to enhance the initial and final protein structures.

Initially, each peptide plane atoms are projected to a common plane, so that  $\omega$  yields the value of  $0^\circ$  or  $180^\circ$  (see Fig. 7a). Secondly, geometrical constraints are applied iteratively in each amino acid, adapting the bases of a procedure developed for position analysis of mechanisms [10] (see Fig. 7b).

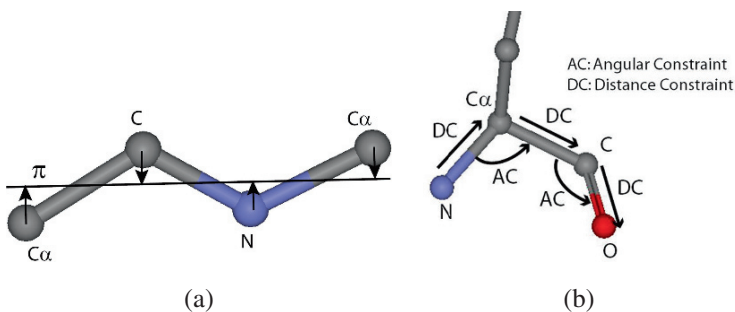


**Fig. 7** (a) Projection of the peptide plane atoms into a common plane. (b) Geometric constraints defined in an amino acid

## Conclusion

A new approach has been presented for simulating the protein movement as a result of the *ligand docking* process. This new method has a low computational cost and allows to carry out simulations rapidly. Thus, the protein motion paths are obtained. Currently, a refining procedure is being developed that, basing on the iterative application of geometrical constraints, attempts to minimize the errors in the selected initial and final reference positions used in our method. Future work will consider the evaluation of a potential energy function throughout the simulation process in order to improve the obtained motion paths.



## References

1. Arthur Lesk. *Introduction to Protein Science*. Oxford University Press, 2006.
2. Tamar Schlick. *Molecular Modeling and Simulation*. Springer, 2006.
3. Kazem Kazerounian, Khalid Laif, and Carlos Alvarado. Prototfold: A successive kinetostatic compliance method for protein conformation prediction. *Journal of Mechanism Design*, 127:712–717, 2005.
4. Sean Cahill, Michael Cahill, and Kevin Cahill. On the kinematics of protein folding. *Journal of Computational Chemistry*, 24:1364–1370, 2003.
5. Rachel Kolodny, Leonidas Guibas, Michael Levitt, and Patrice Koehl. Inverse kinematics in biology: The protein loop closure problem. *International Journal of Robotics Research*, 24:151–163, 2005.
6. Kazem Kazerounian. From mechanism and robotics to protein conformation and drug design. *Journal of Mechanism Design*, 126:40–45, 2004.
7. Linus Pauling and Robert B. Corey. Atomic coordinates and structure factors for two helical configurations of polypeptide chains. *Proceedings of the National Academy of Sciences*, 37, 1951.
8. Protein Data Bank. PDB. <http://www.wwpdb.org/index.html>.
9. Eric W. Weisstein. Roation formula. *MathWorld-A Wolfram Web Resource*, <http://mathworld.wolfram.com/RoationFormula.html>.
10. V. Petuya, J.M. Gutierrez, A. Alonso, O. Altuzarra, and A. Hernandez. A numerical procedure to solve non-linear kinematic problems in spatial mechanisms. *International Journal for Numerical Methods in Engineering*, 73:825–843, 2008.

# Solutions of the Equation of Meshing for Planar Gear Profiles

Giovanni Bonandrini, Giovanni Mimmi and Carlo Rottenbacher

**Abstract** This paper illustrates the possibility of obtaining an explicit solution for the equation of meshing for any type of regular two-dimensional curve of a planar gearing, in order to compute the conjugate profile of the curve. The analysis of the equation of meshing permits to express its explicit solution when the relative motion between the considered reference systems occurs with a constant transmission ratio (for example internal or external gears and rack). The solution is expressed with the general conventions of the theory of gearing. In this way, when we have a generating curve in homogeneous coordinates, and the transformation matrixes which define the relative motion between the profiles considered, we can directly find the solution of the equation of meshing, and consequently the profile conjugated to the generating one by a simple coordinate transformation. The method here presented can be successfully applied to the profiles of planar gears and rotary machines.

**Keywords** Theory of gearings · Conjugate profile · Pumps · Compressors

## Introduction

The theory of gearing is widely used for the computation of the profiles in mechanisms and machines with curves or surfaces in mesh. Usually the practice in defining the profiles is to choose a generating curve and then to compute the conjugate profile by the combination of the equation of meshing and the coordinate transformation. When the equation of meshing is resolved, the computation of the contact line becomes possible. An advantage in the use of the theory of gearing is its general validity, which allows to apply it for every type of profile. It only requires the hypothesis of regularity of the generating profile geometry. Besides its formulation, based on vectors and matrixes, can be suitably applied in computer program languages. The reference textbook on the theory of gearing has been written by Litvin [1]. The theory of gearing for planar curves has been deeply analyzed in [2],

---

G. Bonandrini (✉)

Dipartimento di Meccanica Strutturale, Università di Pavia, Via Ferrata 1, I-27100 Pavia, Italy  
e-mail: giovanni.mimmi@unipv.it

especially focused on the generation of the envelope to a parametric family of curves and on the determination of its singularities. The theory of gearing is often used to calculate the profile of the rotors of rotary machines with conjugate profiles, such as gerotors (some interesting papers are [3–5]), external lobe pumps and blowers [3, 6, 7] and screw compressors [8–10]. Besides, other mechanisms characterized by conjugate profiles are the cycloidal speed reducers [11, 12]. Almost in all the papers in literature that use the theory of gearing, the equation of meshing and the coordinate transformation are applied in order to obtain the conjugate profiles. Some of them present the solution of the equation of meshing, when the generating curve is not complex (circular arc, ellipse, trochoid).

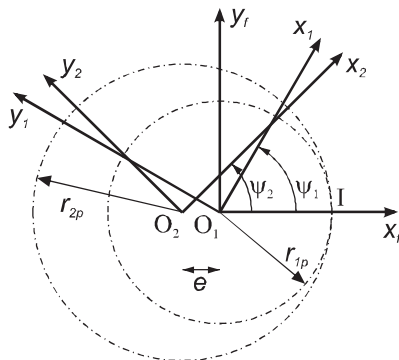
When used in planar cases, the theory of gearing results particularly simple and its application can be systematic. Nevertheless, it is necessary to find an analytical solution of the equation of meshing or to solve it numerically. The first option allows to avoid dedicated and sophisticated calculations, that on the contrary are required in the second case. Those calculations can generate computing errors and sometimes need extended computing time. However, in literature one can not find any technique to obtain a systematic solution for the equation of meshing.

In this paper an explicit solution is pointed out, valid for every generating regular profile, suitable for mechanisms and machines with conjugate profiles and constant gear ratio. In this way, from the equation of the generating profile and the position of the relative instantaneous center of rotation, it is possible to obtain in an explicit form the profile conjugated to any regular curve. The formulation of the explicit solution of the equation of meshing is derived from the work of Bär [13], and adapted herein to the theory of gearing. This paper presents the procedure used to obtain the explicit formulation and some examples of its application.

## Nomenclature

$C_1$	conic curve parameter
$e$	eccentricity ( $e = r_{2p} - r_{1p}$ )
$I$	instantaneous rotation center
<b>M</b>	transformation matrix
$m_{12}$	transmission ratio
$n_1$	rotor-1 lobe number
$n_2$	rotor-2 lobe number
$r_{1p}$	rotor-1 pitch radius
$r_{2p}$	rotor-2 pitch radius
$r_B$	involute base radius
$r_C$	conic curve radius
<b>r</b>	profile position vector
$\Gamma$	rotor profile
$\phi$	generating curve parameter
$\psi_{1,2}$	motion parameters
1, 2	generating, conjugate profile

**Fig. 1** Internal gears reference systems



Let us consider a planar mechanism characterized by two conjugate rotors which rotate with a constant transmission ratio. In order to study the profiles in mesh, we use the theory of gearing, considering three reference systems,  $S_1$ ,  $S_2$  and  $S_f$ , rigidly connected to rotor 1, rotor 2 and to the frame respectively. Let us consider, for example, an internal gear mechanism, where the coordinate systems and the pitch circumferences are represented as in Fig. 1.

Assuming that we have a given regular profile  $\mathbf{r}_1$  on rotor 1, defined in  $S_1$  as a function of the parameter  $\phi$ , we can write:

$$\mathbf{r}_1^{(1)}(\phi) = \begin{bmatrix} x_1^{(1)}(\phi) \\ y_1^{(1)}(\phi) \\ 0 \\ 1 \end{bmatrix} \quad \mathbf{r}_1^{(1)}(\phi) \in C^2, \quad \frac{\partial \mathbf{r}_1^{(1)}(\phi)}{\partial \phi} \neq 0 \quad (1)$$

where the superscript (1) indicates the coordinate system in which the profile  $\mathbf{r}_1$  is considered. Assumed  $\psi_1$  as the angle of rotation of the rotor 1, the transmission ratio between the rotors is given by:

$$m_{12} = \frac{n_2}{n_1} = \frac{\psi_1}{\psi_2} \quad (2)$$

The conjugated profile  $\mathbf{r}_2$  is given by the equation of meshing (3) and the coordinate transformation (4):

$$f(\phi, \psi_1) = 0 \quad (3)$$

$$\mathbf{r}_2^{(2)}(\phi, \psi_1) = \mathbf{M}_{21}(\psi_1) \cdot \mathbf{r}_1^{(1)}(\phi) \quad (4)$$

The equation of meshing represents the tangency condition between the profiles during the motion. It may be written as:

$$\mathbf{N}_1^{(1)}(\phi) \cdot \mathbf{v}_1^{(12)}(\phi, \psi_1) = f(\phi, \psi_1) = 0 \quad (5)$$

where  $\mathbf{N}_1^{(1)}$  is the normal to the profile and  $\mathbf{v}_1^{(12)}$  is the sliding velocity of the contact point on rotor 1 in respect to the one on rotor 2.

For planar gears, where rotor 1 and 2 perform rotation about parallel axes, considering the instantaneous center of rotation  $I_1(X_1, Y_1)$  in  $S_1$ , the equation of meshing may be represented in the following way:

$$f(\phi, \psi_1) = \frac{X_1^{(1)}(\psi_1) - x_1^{(1)}(\phi)}{N_{x_1}^{(1)}(\phi)} - \frac{Y_1^{(1)}(\psi_1) - y_1^{(1)}(\phi)}{N_{y_1}^{(1)}(\phi)} = 0 \quad (6)$$

The equation of meshing is the necessary condition of existence of the envelope to the family of planar curves  $\mathbf{r}_1^{(2)}(\phi, \psi_1)$ , i.e. the profile conjugated to  $\mathbf{r}_1(\phi)$  in  $S_2$ .

For the computing of the conjugate profile, we find, by means of the equation of meshing, the relation between the parameter of the generating curve  $\phi$  and the generalized parameter of motion  $\psi_1$ . Then the coordinate transformation can be applied, using an explicit formulation of  $\phi$  as a function of  $\psi_1$  or vice-versa. In the equation of meshing the terms relating to the generating profile are defined as a function of the parameter  $\phi$ , whilst the position of the instantaneous rotation center is a function of the generalized parameter of motion  $\psi_1$ . The relative motion between the conjugate gears is generally characterized by a constant transmission ratio. The aim of this work is to calculate the explicit solution of the equation of meshing in this case.

Considering  $Z_1$  as the profile  $\mathbf{r}_1$  in  $S_1$ , we can write it in complex form:

$$\begin{aligned} Z_1 &= x_1^{(1)}(\phi) + iy_1^{(1)}(\phi) = \rho_1(\phi)e^{i\theta_1(\phi)} \\ \rho_1(\phi) &= |Z_1| = \sqrt{(x_1^{(1)}(\phi))^2 + (y_1^{(1)}(\phi))^2} \\ \theta_1(\phi) &= \arg(Z_1) \end{aligned} \quad (7)$$

where  $i$  is the imaginary unit. The tangent vector  $Z_1'$  can be defined as:

$$\begin{aligned} Z_1' &= \frac{dx_1^{(1)}}{d\phi_1}(\phi) + i \frac{dy_1^{(1)}}{d\phi_1}(\phi) = \lambda_1(\phi) e^{i\alpha_1(\phi)} \\ \lambda_1(\phi) &= |Z_1'| = \sqrt{\left(\frac{dx_1^{(1)}}{d\phi_1}(\phi)\right)^2 + \left(\frac{dy_1^{(1)}}{d\phi_1}(\phi)\right)^2} \\ \alpha_1(\phi) &= \arg(Z_1') \end{aligned} \quad (8)$$

The position of the instantaneous center of rotation  $I$  is given in  $S_1$  by:

$$I^{(1)} = \begin{bmatrix} X^{(1)}(\psi_1) \\ Y^{(1)}(\psi_1) \\ 0 \\ 1 \end{bmatrix} = \begin{bmatrix} r_{1p} \cos \psi_1 \\ -r_{1p} \sin \psi_1 \\ 0 \\ 1 \end{bmatrix} \quad (9)$$

In the same way, the instantaneous center of rotation  $I$  can be given in  $S_1$  by the complex number  $I_1$  defined as follows:

$$I_1 = X^{(1)}(\psi_1) + iY^{(1)}(\psi_1) = r_{1p} e^{-i\psi_1} \quad (10)$$

The equation of meshing in two dimensions expresses the condition that the normal to the profile  $\mathbf{r}_1$  passes through the instantaneous center of rotation  $I$ . Since the common normal of the profiles in the contact point is perpendicular to the tangent vector to the profiles, the same condition is expressed by imposing that the direction vector  $Z_1 - I_1$  is normal to the tangent vector  $Z'_1$ , that is:

$$(Z_1 - I_1)\bar{Z}'_1 + (\bar{Z}_1 - \bar{I}_1)Z'_1 = 0 \quad (11)$$

By substituting, we obtain:

$$r_{1p} (e^{i(\psi_1 + \alpha_1(\phi))} + e^{-i(\psi_1 + \alpha_1(\phi))}) = \rho_1(\phi) (e^{i(\theta_1(\phi) - \alpha_1(\phi))} + e^{-i(\theta_1(\phi) - \alpha_1(\phi))}) \quad (12)$$

Remembering with Bär [13] that

$$Z_1 = x_1^{(1)}(\phi) + iy_1^{(1)}(\phi) = \rho_1(\phi) \cos \theta_1(\phi) + ip_1(\phi) \sin \theta_1(\phi) \quad (13)$$

By some simple mathematical passages we obtain the final form of the equation of meshing:

$$r_{1p} \cos(\psi_1 + \alpha_1(\phi)) = x_1(\phi) \cos \alpha_1(\phi) + y_1(\phi) \sin \alpha_1(\phi) \quad (14)$$

The Eq. (14) allows the *explicit solution*:

$$\psi_1 = \pm \arccos \left( \frac{x_1^{(1)}(\phi) \cos \alpha_1(\phi) + y_1^{(1)}(\phi) \sin \alpha_1(\phi)}{r_{1p}} \right) - \alpha_1(\phi) + 2\pi N \quad (15)$$

where  $N = 1, 2, \dots$

Considering the unit vector  $\mathbf{t}_1$  tangent to the profile  $\mathbf{r}_1$  in the contact point, the explicit solution can be written as:

$$\psi_1 = \pm \arccos \left( \frac{x_1^{(1)}(\phi) t_{x_1}^{(1)}(\phi) + y_1^{(1)}(\phi) t_{y_1}^{(1)}(\phi)}{r_{1p}} \right) - \arg(\mathbf{t}_1^{(1)}) + 2\pi N \quad (16)$$

In order to have a solution, the absolute value of the argument of the first term must be lower than one:

$$\left\{ \phi \in \Phi_H : |x_1(\phi) \cos \alpha_1(\phi) + y_1(\phi) \sin \alpha_1(\phi)| \leq |r_{1p}| \right\} \quad (17)$$

**Fig. 2** External gears reference systems

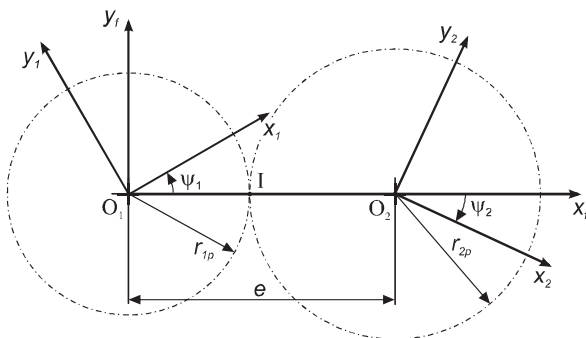
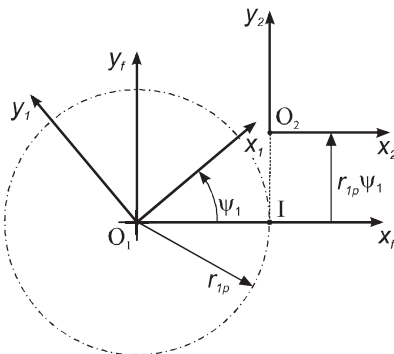


**Fig. 3** Gear and rack reference systems



Using the Eq. (16) under the conditions defined in (17) we can always define an explicit parameterization of the conjugate profile as a function of the parameter of the generating curve  $\phi$ . The conjugate profile can be obtained applying the coordinate transformation. For internal gears, referring to Fig. 1, the coordinate transformation matrix from  $S_1$  to  $S_2$  is:

$$M_{21,int} = \begin{bmatrix} \cos(\psi_1 - \psi_2) & -\sin(\psi_1 - \psi_2) & 0 & e \cdot \cos \psi_2 \\ \sin(\psi_1 - \psi_2) & \cos(\psi_1 - \psi_2) & 0 & e \cdot \sin \psi_2 \\ 0 & 0 & 1 & 0 \\ 0 & 0 & 0 & 1 \end{bmatrix} \quad (18)$$

Figures 2 and 3 show the reference system configurations for external gears and gear and rack respectively.

The corresponding transformation matrixes from  $S_1$  to  $S_2$  can be simply calculated.

### Application Examples

In the following we present an application example to the conic curve, in order to illustrate how easily and simply we can apply the explicit solution of the equation

of meshing. In polar coordinates, a conic section with one focus at the origin and, if any, the other on the x-axis, is given by the equation:

$$\rho = \frac{r_C}{1 + C_1 \cos \phi} \quad (19)$$

where  $r_C$  and  $C_1$  are the conic curve radius and the conic curve parameter respectively.

For the conic curve parameter  $C_1 = 0$  we obtain a circle, for  $0 < C_1 < 1$  we obtain an ellipse, for  $C_1 = 1$  a parabola, and for  $C_1 > 1$  a hyperbola. The generating profile is defined in  $S_1$  as follows:

$$\Gamma_1^{(1)} : \mathbf{r}_1^{(1)} = \begin{bmatrix} x_1^{(1)}(\phi) \\ y_1^{(1)}(\phi) \\ 0 \\ 1 \end{bmatrix} = \begin{bmatrix} x_C^{(1)} + \frac{r_C}{1+C_1 \cos \phi} \cos \phi \\ y_C^{(1)} + \frac{r_C}{1+C_1 \cos \phi} \sin \phi \\ 0 \\ 1 \end{bmatrix} \quad (20)$$

where  $x_C^{(1)}$  and  $y_C^{(1)}$  are the coordinates in  $S_1$  of the center of the conic curve C. The vector  $\mathbf{T}_{\Gamma_1}$  tangent to the profile  $\Gamma_1$  and its argument  $\alpha_1$  result as follows:

$$\mathbf{T}_{\Gamma_1}^{(1)} : \mathbf{r}'_1^{(1)} = \begin{bmatrix} -\frac{r_C}{1+C_1 \cos \phi} \sin \phi + \cos \phi \frac{C_1 r_C \sin \phi}{(1+C_1 \cos \phi)^2} \\ \frac{r_C}{1+C_1 \cos \phi} \cos \phi + \sin \phi \frac{C_1 r_C \sin \phi}{(1+C_1 \cos \phi)^2} \\ 0 \\ 1 \end{bmatrix} \quad (21)$$

$$\alpha_1 = \arg \left( \frac{\partial x_1^{(1)}}{\partial \phi}(\phi) + i \frac{\partial y_1^{(1)}}{\partial \phi}(\phi) \right)$$

The first application example can be performed with a circular profile ( $C_1 = 0$ ): in this case the equation of meshing admits the *explicit solution*:

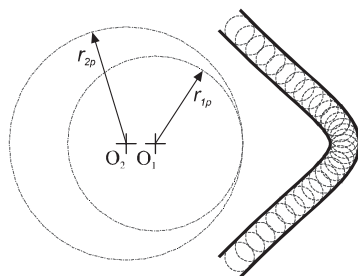
$$\psi_1 = \pm \arccos \left( \frac{-x_C^{(1)} \sin \phi + y_C^{(1)} \cos \phi}{r_{1p}} \right) - \frac{\pi}{2} - \phi + 2\pi N \quad (22)$$

For circular profile the solution can be written in an explicit form of the parameter  $\phi$  too:

$$\phi = \arctan \left( \frac{\frac{y_C^{(1)}}{r_{1p}} + \sin \psi_1}{\frac{x_C^{(1)}}{r_{1p}} - \cos \psi_1} \right) + N\pi \quad (23)$$



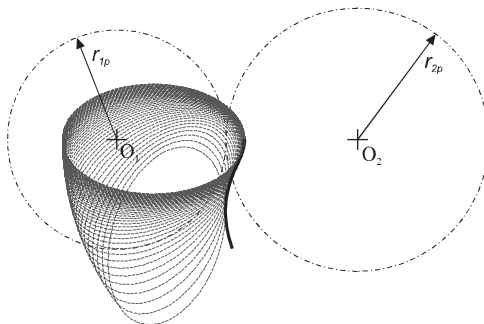
**Fig. 4** Circular arc conjugate profile, internal gear



The circular profile is widely used in internal gears, in which it generates trochoidal curves: Fig. 4 shows the obtained conjugate profiles, internal and external, for an internal gear.

When  $e \neq 0$  the explicit solution of the equation of meshing is more complex, and in general it can not be written in an explicit form of the generating curve parameter  $\phi$ . In Fig. 5 the conjugate profile of an ellipse in external gears is presented: conic curve profiles are often used in machines and mechanisms with conjugate rotors, such as lobe pumps, Roots and twin-screw compressors.

**Fig. 5** Elliptical arc conjugate profile, external gear



## Conclusion

In this paper a method to obtain an explicit solution of the equation of meshing for any type of regular two-dimensional curve is presented.

Once the solution is known in explicit form, it is very simple to compute the conjugate profile of the curve by a simple coordinate transformation. The hypotheses and the procedure to obtain the explicit solution are presented here. In particular we have always an explicit solution of the equation of meshing for the generalized parameter of motion when the transmission ratio between the gears is constant (for example internal or external gears and rack).

In the end, some examples of solutions for typical generating and conjugated profiles are presented.

The results obtained permit to implement computer codes for the computation of the planar mechanism profiles in analytical form with particularly simple and affordable routines.

## References

1. Litvin, F. L., Fuentes, A., *Gear Geometry and Applied Theory*, Cambridge University Press, 2004.
2. Argyris, J., Litvin, F. L., Lian, Q., Lagutin, S. A., 1999, "Determination of envelope to family of planar parametric curves and envelope singularities", *Computer Methods in Applied Mechanics and Engineering*, Vol. 175 (1–2), pp. 175–187.
3. Litvin, F. L., Feng, P-H., 1996, "Computerized design and generation of cycloidal gearings", *Mechanism and Machine Theory*, Vol. 31 (7), pp. 891–911.
4. Mimmi, G., Pennacchi, P., 2000, "Non undercutting conditions in internal gears", *Mechanism and Machine Theory*, Vol. 35 (4), pp. 477–490.
5. Vecchiato D., Demenego A., Litvin F. L., Nervegna N., Mancò S., 2002, "Design and simulation of meshing of a cycloidal pump", *Mechanism and Machine Theory*, Vol. 37 (3), pp. 311–332.
6. Mimmi, G., Pennacchi, P., 1999, "Analytical model of a particular type of positive displacement blower", *Proceedings of the I MECH E Part C Journal of Mechanical Engineering Science*, Vol. 213 (5), pp. 517–526.
7. Chen, C-K., Yang, S-C., 2000, "Geometric modelling for cylindrical and helical gear pumps with circular arc teeth", *Proceedings of the I MECH E Part C Journal of Mechanical Engineering Science*, Vol. 214 (4), pp. 599–607.
8. Litvin, F. L., and Feng, P., 1997, "Computerized design, generation, and simulation of meshing of rotors of screw compressor", *Mechanism and Machine Theory*, Vol. 32 (2), pp. 137–160.
9. Su, S., Tseng C., 2000, "Synthesis and optimization for rotor profiles in twin rotor screw compressors", *ASME Journal of Mechanical Design*, Vol. 122 (4), pp. 543–552.
10. Wu, Y-R., Fong, Z-H., 2007, "Improved rotor profiling based on the arbitrary sealing line for twin-screw compressors", *Mechanism and Machine Theory*, doi:10.1016/j.mechmachtheory.2007.05.008 (in press)
11. Shin, J., Kwon S., 2006, "On the lobe profile design in a cycloid reducer using instant velocity center", *Mechanism and Machine Theory*, Vol. 41 (5), pp. 487–616.
12. Hwang, Y-W., Hsieh, C-F., 2007, "Geometric design using hypotrochoid and nonundercutting conditions for an internal cycloidal gear", *ASME Journal of Mechanical Design*, Vol. 129, pp. 413–420.
13. Bär, G., 2003, "Explicit calculation methods for conjugate profiles", *Journal for Geometry and Graphics*, Vol. 7 (2), pp. 201–210.

# A Numerical Method for the Second-Order Mobility Analysis of Mechanisms

Igor Fernández de Bustos, Josu Agirrebeitia and Rafael Avilés

**Abstract** The second order mobility analysis of mechanisms is a complicated problem that can be approached in a direct way via the analysis of the compatibility of the acceleration field. This paper will present a simple, numerical approach to retrieve the restrictions imposed to the movement that are derived from the second order (curvature) restrictions. This algorithm can be easily applied to bi and three dimensional mechanisms and delivers a good degree of efficiency. The results of this analysis can be employed to improve the efficiency of other algorithms which present lack of convergence in the vicinity of singular configurations.

**Keywords** Kinematics · Mechanism analysis · Manipulators

## Introduction

The singular configurations of mechanisms is a phenomenology which is getting an increasing degree of interest in the last years. While former investigations were related to the avoidance of these configurations, more recent developments try to deliver an insight of the restrictions which define the real behaviour of the mechanism in those configurations.

This is not unexpected, however, because the increase in the degree of complexity of the currently employed kinematic chains, leads to an increase of the amount of singular configurations in these chains. Moreover, some interesting phenomena arise in singular configurations, which are of interest for the designer. An example of these is the kinematotropy.

But in order to analyse the behaviour of a mechanism in singular configuration, it is necessary to resort to a second or even higher order analysis. Although this kind of analysis can be performed directly via analytical approaches, this possibility requires an independent analysis for each mechanism. In order to implement an

---

I. Fernández de Bustos (✉)

Departamento de Ingeniería Mecánica, Escuela Superior de Ingenieros de Bilbao,

Alda. de Urquijo s/n 48013 Bilbao (Vizcaya), Spain

e-mail: igor.fernandezdebustos@ehu.es

algorithm capable to deal with any mechanism, a numerical approach needs to be developed.

Most of the papers related to singularities are dedicated to the problem of its detection and classification via geometrical considerations (see [1–4]), being their aim the avoidance of these configurations. With this idea, a second order analysis is performed by Karger in [5], being the aim of this analysis to detect how the singularity evolves in its vicinity. This approach allows one to identify the real possibilities of avoiding a singularity when going from one non-singular configuration to another. Other kinds of second-order analysis include all the acceleration problem analysis (See for example [6]), being few the second order analysis related to the discovery finite second order motions of a mechanism in a singular configuration. A relevant work is shown in [7], where this second order analysis is applied to several mechanisms in an analytical way. Another work related to this subject is shown in [8], where the problem is solved in an approach suitable to both numerical and analytical methodologies.

This paper employs this acceleration-based formulation to tackle the second order analysis in a numerical way. The basis of this formulation is exposed in [8]. In order to expose the algorithm, firstly a numerical method to solve the velocity and acceleration problems is exposed, and afterwards, the aforementioned formulation is applied. Here the generalization of the method exposed in [8] to problems including input values will be addressed.

## Base Algorithm for Velocity and Acceleration

The proposed method to solve velocity and acceleration problems is an straightforward one, which is specially well suited to computer algorithms of general application, where mechanism kinematics are only one of the problems to solve. All the links in the kinematic chain are represented by a moving reference frame, and the joints in this link are referred to that system, as represented in Fig. 1.

In order to obtain the velocity equations imposed by each joint, one writes the absolute velocity of each joint as measured from each link. This way the restrictions are obtaining via equaling these absolute values. For example, for the case of the simplest R-joint (see Fig. 2), one can write:

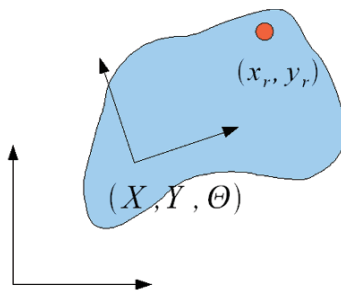
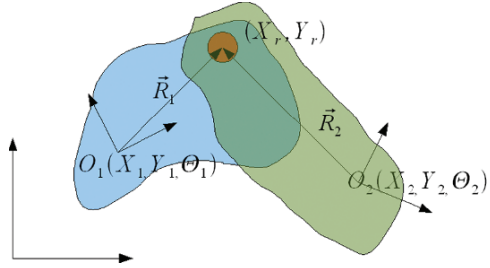


Fig. 1 Link definition

**Fig. 2** Relationship imposed by R-joint



$$\vec{V}_r = \vec{v}_1 + \dot{\Theta}_1 \wedge \vec{R}_1 = \vec{v}_2 + \dot{\Theta}_2 \wedge \vec{R}_2 \tag{1}$$

Which can be written in the form:

$$\vec{v}_1 + \dot{\Theta}_1 \wedge \vec{R}_1 - \vec{v}_2 + \dot{\Theta}_2 \wedge \vec{R}_2 = \vec{0} \tag{2}$$

Other joints equations are developed in a similar way, and the three dimensional problem case is also obtained following the same steps.

Writing all the equations of all of the joints in that way, one can write an equation in the form:

$$[J]\{\dot{x}\} = \{0\} \tag{3}$$

Where  $[J]$  is a rectangular  $m \times n$  matrix, being  $n$  the number of links multiplied by the number of coordinates defining its position (3 for bi-dimensional problems and 6 for three dimensional) and  $m$  the number of restrictions imposed by the joints. In the event of input values, each of them can be added to the equations, leading to an equation in the form:

$$[\vec{J}]\{\dot{x}\} = \{b\} \tag{4}$$

Thus, in the case of the existence of input values the system turns to be non-homogeneous, and the number of equations are increased.

To solve the acceleration problem, the same procedure applies. In the case of the R-joint, one can write:

$$\vec{A}_r = \vec{a}_1 + \dot{\Theta}_1 \wedge \vec{V}_1 - \dot{\Theta}_1^2 = \vec{a}_2 + \dot{\Theta}_2 \wedge \vec{V}_2 - \dot{\Theta}_2^2 \vec{R}_2 \tag{5}$$

Or:

$$\vec{a}_1 + \dot{\Theta}_1 \wedge \vec{V}_1 - \vec{a}_2 - \dot{\Theta}_2 \wedge \vec{V}_2 = \dot{\Theta}_1^2 \vec{R}_1 - \dot{\Theta}_2^2 \vec{R}_2 \tag{6}$$

Which, including the relevant equations for all the joints and the input values, if any, can be rewritten in the form:

$$[J]\{\ddot{x}\} = -[\dot{J}(\{\dot{x}\})]\{\dot{x}\} \quad (7)$$

Now the velocity and acceleration problem can be solved for any mechanism by assembling and solving Eqs. (4) and (7). The next step is employing the Jacobian matrix and its derivative to solve the second order analysis. In order to solve (4), recommended methods include LU generalized LU factorization (capable of dealing with non-definite non-rectangular matrices), SVD or QR decompositions. While LU is faster, SVD usually leads to a lower error, being QR a compromise alternative.

## Second Order Analysis

The second order analysis is only needed if there is evidence that the configuration is a singular one or if in doubt. In this last case, it is important to note that a second order analysis is not able to find third order restrictions, but these kind of situations are rarely found in usual kinematic chains.

Usually, for a given configuration, the velocity problem is solved. This allows one to find one or more vectors which are a possible solution to Eq. (4). If this information comes from a mechanism whose permanent number of degrees of freedom is known, and the number of obtained vectors is bigger than this, a singular configuration might have been found, and the restrictions to the movement obtained via the second order analysis will deliver interesting information. Again, here must be remembered that in some conditions, even higher order analysis should be performed to reach the full set of restrictions. Although the presented algorithm can be easily extended to higher order analysis, here only the second order analysis will be tackled.

As exposed in [8], the algorithm requires the solution of the velocity field, which has been obtained via factorization of the Jacobian Matrix. Let the obtained solutions be written in the form.

$$\{\dot{x}\} = \{\dot{x}\}_p + a_1\{\dot{x}\}_{h1} + a_2\{\dot{x}\}_{h2} + \dots + a_k\{\dot{x}\}_{hk} = \{\dot{x}\}_p + [\dot{X}]_h\{\dot{a}\} \quad (8)$$

Where  $k$  denotes the dimension of the nullspace of  $[\bar{J}]$  and  $\{\dot{x}\}_{hi}$  is the  $i$ -th eigenvector of  $[\bar{J}]$ . The difference with the formulation exposed in (1) is that now we include a particular solution  $\{\dot{x}\}_p$  required because of the input velocities, and related to normal accelerations. For the acceleration equation, (7), one can write:

$$-[\dot{J}(\{\dot{x}\})]\{\dot{x}\} = -\left([\dot{J}(\{\dot{x}\}_p)] + [\dot{J}(\{\dot{x}\}_{h1})] + \dots + [\dot{J}(\{\dot{x}\}_{hk})]\right) (\{\dot{x}\}_p + \{\dot{x}\}_{h1} + \dots + \{\dot{x}\}_{jk}) \quad (9)$$

Now it is necessary to introduce the compatibility requirement in the acceleration equation. This requirement can be introduced via a simple analysis of the image subspace of,  $[\bar{J}]$ , as exposed in [8], so that (10) is verified:

$$[S] \left[ \dot{J}(\{\dot{x}\}) \right] \{\dot{x}\} = \{0\} \tag{10}$$

This equation will lead to the second order restrictions required, each of them in the form exposed in (11).

$$b_{11}^j a_1^2 + \dots + b_{13}^j a_1 a_k + b_{22}^j a_2^2 + \dots + b_{2k}^j a_2 a_k + \dots + b_{kk}^j a_k^2 \tag{11}$$

Which can be written as a quadratic form, (12):

$$\{a\}^T [B]_j \{a\} = 0 \tag{12}$$

In order to obtain the solutions to this system, we resort to Takagis factorization, also known as symmetrical espectral decomposition (13):

$$[B]_j = [T]^T [D] [T] \tag{13}$$

Which allows one to obtain an alternate system of reference where the equations are written in the form (14):

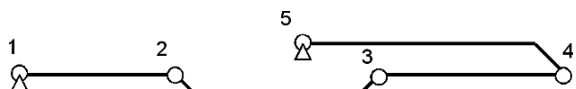
$$b_1^j a_{1j}^2 + b_2^j a_{2j}^2 + \dots + b_k^j a_{kj}^2 \tag{14}$$

Much easier to deal with.

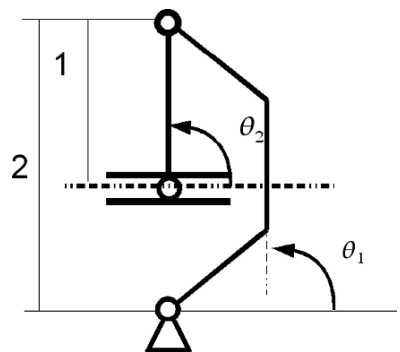
### Examples

The exposed algorithm has been programmed in C and verified with several mechanisms. Some of them are shown in the following images.

**Fig. 3** Five bar in singular configuration



**Fig. 4** Slider-crack in singular configuration



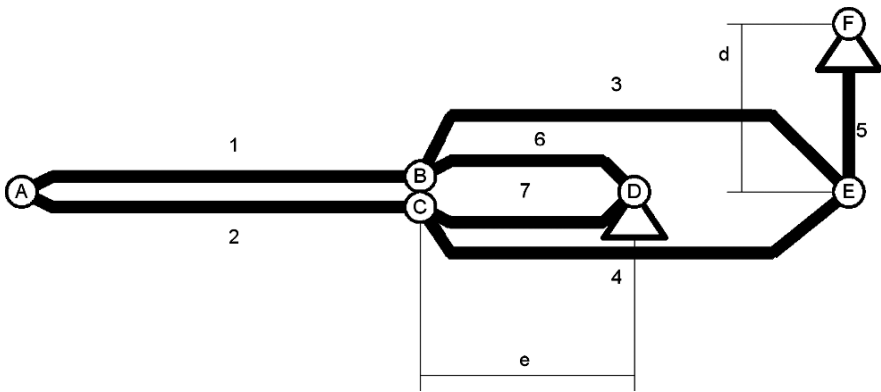


**Fig. 5** Peaucellier linkage in singular configuration

## Conclusions

A numerical algorithm for the second order mobility analysis has been exposed. This algorithm allows one to automatically generate for a given mechanism its Jacobian matrix and derivative, and afterwards apply the acceleration compatibility condition to find the quadratic restrictions that are required for a given motion not being infinitesimal. The algorithm is easy to implement and has little overhead when compared to the velocity analysis, because it is able to employ the same matrix factorization. In order to solve the quadratic restrictions in a simple way, the authors propose the use of the Takagi transformation (also known as symmetric SVD) to the restrictions written in matricial form, this transformation includes some additional work, but is only needed in the event of a restriction, so it does not penalize the algorithm in a non-singular configuration. Moreover, the associated cost of Takagi factorization is small due to the small size of the involved matrices.

## References

1. Fernández-Bustos, I. Agirrebeitia, J. Avilés, R. A general procedure for the mobility and singularity analysis of kinematical chains including branch identification. Proceedings of the 12th IFToMM World Congress, Besançon (France), June 18–21, 2007.
2. Altuzarra, O. Pinto, C. Avilés, R. Hernández, A. A practical procedure to analyze singular configurations in closed kinematic chains. *IEEE Transactions on Robotics*, 20(6) December 2004.
3. Nokolby, S.B. Podhorodeski, R.P. Reciprocity-based resolution of velocity degeneracies (singularities) for redundant manipulators. *Mechanism and Machine Theory*, 36 397–409 2001.
4. Zlatanov, D. Fenton, R.G. Benhabib, B. Identification and classification of the singular configurations of mechanisms. *Mechanism and Machine Theory*, 33(6) 743–760, 1998.
5. Park, F.C. Kim, J.W. Singularity analysis of closed kinematic chains. *Transactions of the ASME Journal of Mechanical Design*, 121 32–38, March, 1999.
6. Karger, A. Singularity analysis of serial robot-manipulators. *Transactions of the ASME Journal of Mechanical Design*, 118, 1996.



7. Müller, A. Geometric characterization of the configuration space of rigid body mechanisms in regular and singular points. Proceedings of the IDETC/CIE 2005 ASME 2005 International Design Engineering Technical Conferences & Computers and Information in Engineering Conference, Long Beach, California USA, September 24–28, 2005.
8. Rico, J.M. Gallardo, J. Duffy, J. Screw theory and higher order kinematic analysis of open serial and closed chains. *Mechanism and Machine Theory*, 34 559–586, 1999.

# Mathematical Models of Mechanisms with Essentially Elastic Links

G. Ualiyev and Assylbek Jomartov

**Abstract** In this report it is presented some principles of construction of mathematical models of transfer mechanisms with essentially elastic links. In different driving phases the elastic links are presented both as connections and as driving source, i.e. driving is realized at the expense of potential energies of elastic links. It was examined definition problems of elastic forces longitudinally to the deformable connecting rod of the mechanism with four links, and the problem of equation setting up of double-lever mechanism driving taking into account a mass of the elastic connecting rod.

**Keywords** Transfer mechanisms · Elastic links · Multi-mass torsional system

## Introduction

The mathematical modeling of complex mechanical systems, especially of multi-mass torsional oscillatory systems with concentrated and distributed masses, in which we have many settlement circuits of technological machines and automatic transfer lines, is connected with constructions of general dynamic models and local models of the executive or transfer camlever mechanisms with nonlinear state functions.

Constructing mathematical models of multi-mass mechanical systems with concentrated parameters we usually start from the proposals, that the inertial properties of system are displayed in masses  $m_{ij}$  or moments of inertia  $J_{ij}$ , concentrated in sections, which are connected with non-inertial elastic dispersion  $c_{ij}$  connections. The movement of such multi-mass torsional system is described by system of the equations in this way [1],

$$\| a_{ij} \| \{ \ddot{q}_j \} + \| b_{ij} \| \{ \dot{q}_j \} + \| c_{ij} \| \{ q_{ij} \} = \{ Q_j \} \quad (1)$$

---

G. Ualiyev (✉)  
Institute of Mechanics and Machine Sciences, Valikhanov St.  
106, 050010 Almaty, Republic Kazakhstan  
e-mail: legsert@mail.ru

where  $\| a_{ij} \|$ ,  $\| c_{ij} \|$  – are matrices of inertial and quasielastic coefficients,  $q_j$  are generalized coordinates.

At drawing up the equations of movement of such systems there is a necessity connected with experimental calculated settlement of the given inertial parameters of many transfer and executive mechanisms. In the given work some principles of drawing up of mathematical models of transfer and executive mechanisms of independent movement with elastic parts are resulted. In mechanisms with considerable elastic parts the complete cycle of their movement is supposed to be considered as separate periods. In the various periods of movement the elastic parts are represented both as communication, and as source of movement, i.e. movement is carried out at the expense of the potential energies of elastic parts (2).

The questions of drawing up of mathematical models of resulted executive mechanisms of independent movement and definition of inertial parameters of separate mechanisms of variable structure with elastic connections are considered.

## Analytical Method of Definition Inertial Parameters

The movement of a link of reduction of the executive and transfer mechanism can be described by elastic parts with 1 degree of freedom by such an Eq. (2):

$$J_n(\varphi)\ddot{\varphi}(t) + 0,5J'_n(\varphi)\dot{\varphi}^2(t) \equiv M_{II}(\varphi) \quad (2)$$

In the period of accumulating, i.e. in process of compression of springs or rotating of the elastic shaft the given moment of forces is represented as the sum of driving  $M_q$  and moment of resistance to elastic deformation  $M_c$ . The latters depend on the statement of a link of reduction. Inertial parameters – the given moment of inertia of the mechanism.  $J_n(\varphi)$  is always a positive function.

The return task of dynamics of mechanisms with considerable elastic parts is formulated. The law of movement of the executive mechanism in the period of accumulation is determined by the speed of rotation of the main shaft, which is possibly approximately to consider as constant  $\alpha(t) = \text{const}$ . In such case the Eq. (2) can be written down concerning the given moment of inertia, as the linear differential equation of the first order.

$$\dot{\varphi}^2(t)J'_n(\varphi) + 2\dot{\varphi}(t)J_n(\varphi) = K\varphi(t), \quad (3)$$

Where  $\dot{\varphi}(t)$ ,  $\ddot{\varphi}(t)$  – are angular speeds and acceleration of entrance link of the executive mechanism. These transfer functions can be determined through functions of the situation between the main shaft of machines – of automatic devices and entrance part of the executive mechanism. From the Eq. (3) at  $\dot{\varphi}(t) \neq 0$ ,  $J_{n0} = J_n(\varphi_0)$  the analytical expression of the given moment of inertia is defined  $J_n = A(\varphi, \dot{\varphi})$ .

The decisions of a return task allows to construct mathematical model of the executive mechanism, and by the decision of the Eq. (2) the law of movement of

the mechanism with elastic parts in process of reaccumulating is defined, i.e. in the period of re-twisting of the elastic shaft or release of springs.

The usage of the equation of movement of the executive mechanisms is convenient for definition of the given moment of inertia at construction of general dynamic model of complex mechanical system at study of movement of so-called mechanisms of independent movement [3]. Such mechanisms, at which the basic movement is carried out at the expense of the moments of elastic forces of the twirled shaft or compressed springs are frequently met in high-speed machines.

### Mathematical Model of the Executive Mechanisms with Essential Elastic Connecting-Rod of Multimass Systems

The mechanisms of making of duck thread of looms tools such as STB, such as the dashing mechanism, 4-color and 6-color mechanisms of change of duck, the mechanisms of braking construction represent cam-lever mechanisms with elastic parts and connections. And movement in these mechanisms is carried out at the expense of potential energy of twirled torso platen or compressed cylindrical springs. In connection with research of movements of such mechanisms there is a necessity to account final elastic movements of its parts. In the given work the questions of definition of elastic forces of longitudinal deformable connecting-rod of 4-part mechanism are considered, also the equation of movement of flat 2-rocker mechanism in view of weight of elastic connecting-rod is drawn up.

In flat 4-part mechanism (Fig. 1) the elastic connecting-rod can be considered as well as non-stationary connection. The mathematical expression of deformation of an elastic link allows to unit in one system equations of movement of firm bodies located till both parties of an elastic link. The task in this case will be shown to search basic movements  $O_1A$  and  $O_2B$  as systems of firm bodies, and additional movement

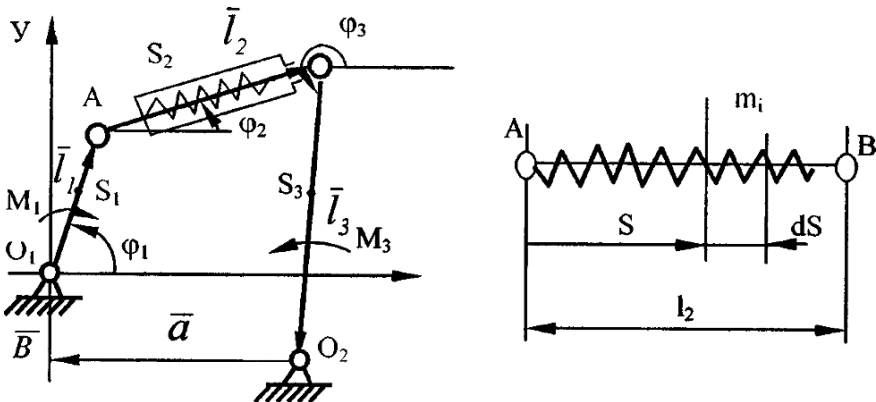


Fig. 1 The mechanism of 4-part machine with elastic connecting-rod

determined by the elastic characteristics of AB. We got differential equation for defining the movement of elastic connecting-rod as following [4]:

$$\frac{d\lambda}{d\varphi_1} - a_1\lambda^2 - b_1\lambda = F(\varphi_1, \dot{\varphi}_2), \quad (4)$$

where  $\lambda = l_2 - l_2^0$  change of length of connecting-rod.

From the Eq. (7), as the special case, the well-known expression for small elastic movements will be got [4].

The system of the equations describing the movement of 2-rocker mechanism with elastic connecting-rod is received [1]:

$$\left. \begin{aligned} I_1\ddot{q}_1 + (I_3\ddot{q}_2 + I_3\ddot{q}_3)\Pi' &= M_1 - M_3\Pi' \\ I_3\ddot{q}_2 + I_3\ddot{q}_3 + c^*q_2 &= -M_3 \end{aligned} \right\}, \quad (5)$$

where  $q_1 = \varphi_1, q_2 = \Delta\varphi_3 = \left(\frac{d\Pi}{d\lambda}\right)^0 \lambda, q_3 = \Pi(q_1), \ll 0 \gg$  is a statement at  $\Delta l_2 = l - l_2 - l_2^0 = 0$

$I_1, I_3, M_1, M_3$  – moments of inertia and moments of forces.

In many systems there is a necessity to account weight of a deformable part. It is connected with that the elastic part has weight of the same order or even more, than rigid parts, and as the consequence, it is a source of inertial stimulating forces. For example, in mechanisms of changing of colour duck of looms tools [5] movements are carried out at the expense of deformation (compression–stretching) elastic connecting-rod, and its weight is more than weight of crank and rocker. It is shown, that kinetic energy of elastic connecting-rod is defined from the expression.

$$2T = m_2(l_1^2\dot{\varphi}_1^2 + \dot{\lambda}^2 + 2l_1^2\dot{\varphi}_1\dot{\lambda}\cos\beta) + I_2(\varphi_1)\dot{\varphi}_2^2, \quad (6)$$

where  $\dot{\lambda} = V_{S_2A}$  – is a component of relative speed of a point  $S_2$  along the connecting-rod;

$\beta$  – angle between vectors and

$I_2$  – variable moment of inertia of connecting-rod.

The system of the equations describing movement of the flat 4-part mechanism in view of weight of elastic connecting-rod is received as following:

$$\left. \begin{aligned} I_{11}\ddot{\varphi}_1 + I_{13}\ddot{\varphi}_3 + c\frac{l_1l_2}{2l_2^2}\cos(\varphi_3 - \varphi_1)\frac{\partial\phi}{\partial\varphi_3} &= M_1, \\ I_{31}\ddot{\varphi}_1 + I_{33}\ddot{\varphi}_3 + c\frac{\varphi_3l_3}{2l_2^2}\cdot\frac{\partial\phi}{\partial\varphi_3}\left(\varphi_3\frac{\partial^2\phi}{\partial\varphi_3^2} + \frac{\partial\phi}{\partial\varphi_3}\right) &= M_3, \end{aligned} \right\} \quad (7)$$

where  $\phi(\varphi_3, l_2)$  – the equation of connection.

The decision of systems of Eq. (5) defines the laws of movement of 2-rocker mechanism at known deformation of a center of gravity of an elastic part determined from the Eq. (4). The specified laws of movement for the periods of compression and re-accumulating are defined from systems of Eq. (7) in view of weight of elastic connecting-rod.

## References

1. Wolfson E.E., Dynamic computations of cyclical machines. 1976: L. 325p.
2. Ualiyev G., Dynamics of mechanisms and machines, Almaty, 2001: 284p.
3. Ualiyev G., Questions of automation of construction of mathematical models of mechanisms of variable structure. NAS RR, series of physical and mathematical sciences, 1993(1): No. 3, 79–81.
4. Bat I., The equation of movement of flat 4-part mechanism with an elastic intermediate link. Works of a seminar on TMM, 1957: No. 3.
5. Djoldasbekov U.A., Ualiyev G. Perfection of mechanisms of weaver's machine tools STB. M., Legpromisdat, 1986: 192p.

# Design and Simulation of a New Hybrid Mobile Robot for Overpassing Obstacles

Gianni Castelli and Erika Ottaviano

**Abstract** In this paper the design and simulation are presented for a 1-DOF leg-wheel walking machine. A dynamic simulation has been proposed for a low-cost robot, which is capable of a straight walking with only one actuator. Suitable simulations have been carried out to verify the operation of the prototype in several environments.

**Keywords** Mobile robots · Hybrid robots · Simulation

## Introduction

Last trends in Robotics show how robots in future will interact with humans for many applications. Mobile robots are a field of great interest in Robotics since close interaction with human environment. They have a wide range of applications such as: inspection, service, defence, manufacturing, cleaning, remote exploration and entertainment. Walking robots, in general, can be divided into two main groups, legged and wheeled robots, with important differences as regarding to mechanical design and control system [1–3].

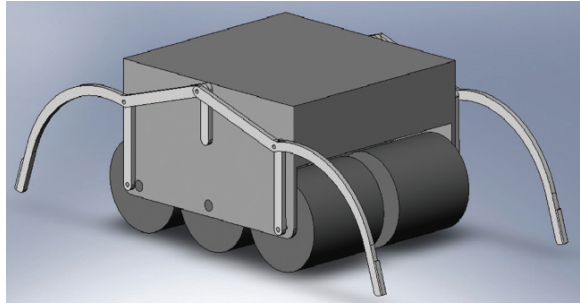
Legged robots have better mobility in rough terrain since they can use isolated foothold that optimizes support and traction, whereas a wheel requires a continuous path of support [4]. Although biped locomotion has been studied for long time, it is only in the past 20 years, that real robots started to walk on two legs. First, there were robots that used static walking [5]. Then dynamic walking was studied [6]. Dynamic walkers can achieve faster walking speeds, running [7], stair climbing, run and execution of flips [8, 9], and even walking with no actuators [10]. The most common walking machines are wheeled and tracked systems, but large interest can

---

G. Castelli (✉)

LARM: Laboratory of Robotics and Mechatronics, DiMSAT, University of Cassino,  
Via G. Di Biasio 43, 03043 Cassino, Italy  
e-mail: g.castelli@unicas.it

**Fig. 1** Mechanical design of the hybrid walking robot



be also focused on legged machines. The combination of leg and wheel can be a good compromise for a walking machine combining the advantages of the both locomotion types.

Hybrid systems have been also developed as combination of wheeled and legged solutions to exploit the advantages of both mobile systems. Prototypes of hybrid robots can be found in [11–22].

The goal of this research and development efforts has been aimed to a robot that can be used in industrial sites, especially in hazardous areas such as nuclear power plants and ocean floors. Most of these robots, however, cannot be easily adapted to environments designed for human beings. If such devices are to be used at industrial sites, they will require special arrangements such as ramps to allow them to move around. Since these places are originally designed for human beings, it is desirable to have robots capable to surpass obstacles and adapt to the environment.

In this paper the design of a new prototype of leg-wheel walking robot is proposed and shown in Fig. 1 with low-cost easy-operation features. In order to obtain a low-cost easy operation walking machine the following requirements have been considered: compactness, modularity, light weight, reduced number of DOFs. The leg structure, shown in Fig. 2, has one DOF (degree of freedom) and it is possible to have one actuator for moving both legs and wheels in order to overcome a large number of obstacle types.

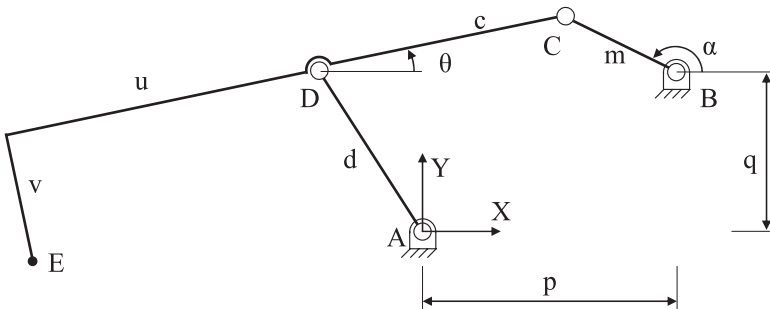


**Fig. 2** A kinematic scheme for the 1-DOF leg



## Design Considerations

The proposed mobile robot is a leg-wheel machine, which can be able to walk on both structured and unstructured terrains. In particular, the basic requirement to possess is to be able to overpass obstacles, which sizes can be greater than the radius of the wheels.

A basic requirement for a mobile robot is to perform the walking without the need of an external control unit. One way to get this goal is to design light and simple architectures with limited number of DOFs, [5]. Furthermore, basic considerations for a leg design can be outlined as follows: the leg end point trajectory should lie on a straight-line; the leg should have a fairly simple mechanical design; the leg should have the minimum number of DOFs to ensure suitable motion capability. In particular, light legs reduce the power consumption of other joints and enable the robot to walk faster. According to those basic requirements a leg has been designed by considering compactness, modularity, light weight, reduced number of DOFs as basic characteristics for an easy-operation walking. Furthermore, the mechanical design has been conceived by using a linkage architecture in order to build a low-cost prototype, as shown in Fig. 1. Aluminium can be selected to build the leg because of its lightness and easy machining. The mechanical design of the hybrid walking robot is the main issue of a project with the aim to obtain a simple system, which is able to walk in several environmental conditions. The designed prototype consists of a chassis on which both wheels and legs are connected to a DC motor for actuation. The actuation system transmits the motion to the leg mechanisms through a T gear, and to the wheels through a gear and gear belts. Consequently, both legs and wheels are actuated by a single motor. The body of the robot can carry batteries and instrumentation, as it shown in Fig. 1. It has been chosen a hybrid solution because of the possibility to overcome obstacles and steps, which are generally inaccessible by wheeled or biped robots.

## Kinematic Analysis of the Leg Mechanism

According to the kinematic scheme of the leg in Fig. 2, the position of point E, with coordinates  $(x,y)$  with respect to  $AXY$  fixed frame, can be evaluated as a function of kinematic parameters of the mechanism ABCDE in the form letters for table footnotes (Table 1).

Since the curve traced by any point of the coupler link of a planar four-bar linkage is algebraic of sixth degree, the coupler curve of a four-bar linkage intersects a line at a maximum of six points. As a consequence, the coupler curve cannot have

**Table 1** Kinematic parameters of the leg in Fig. 2

Parameter	d	m	c	u	v	p	q
Dimension	75.0 mm	45.0 mm	104.0 mm	160.5 mm	63.5 mm	100.0 mm	60.0 mm

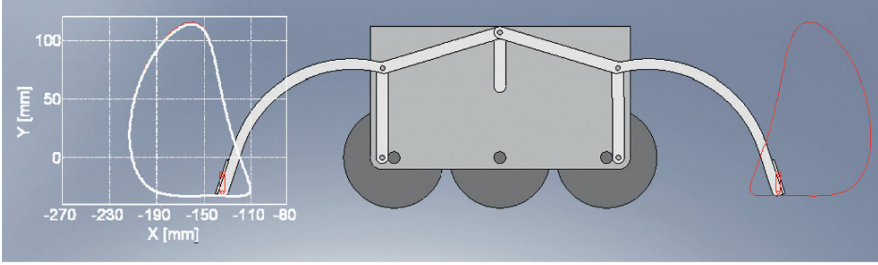


**Fig. 3** A scheme for the hybrid robot with coupler curve traced by point E

straight segments of finite length. Therefore, the required trajectory can have only approximately straight line segments.

In particular links  $\underline{AD}$  and  $\underline{BC}$  can be evaluated with respect to the  $AXY$  frame in the form

$$\underline{AD} = \begin{bmatrix} x + u \cos \theta - v \sin \theta \\ y + u \sin \theta + v \cos \theta \end{bmatrix} \quad \underline{BC} = \begin{bmatrix} x - p + (u + c) \cos \theta - v \sin \theta \\ y - q + (u + c) \sin \theta + v \cos \theta \end{bmatrix} \quad (1)$$

Furthermore, by considering

$$\|\underline{AD}\|^2 = d^2 \quad \|\underline{BC}\|^2 = m^2 \quad (2)$$

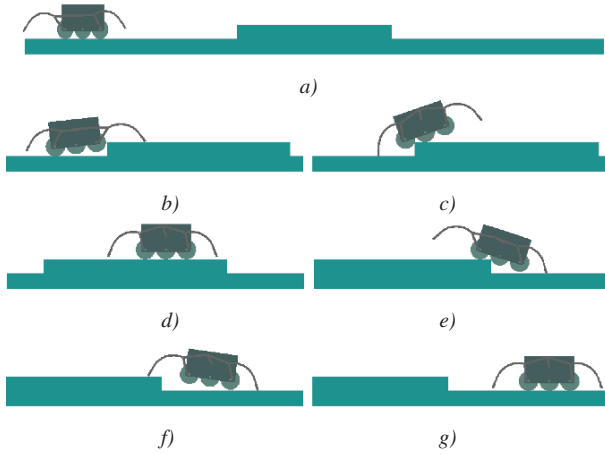
and substituting Eq. (1) in Eq. (2), one can obtain two equations, which are function of design parameters and  $x$ ,  $y$  and  $\theta$ . The desired implicit function can be obtained by eliminating  $\theta$ , and further algebraic manipulations.

A parametric study has been carried out involving design parameters and coupler curve shape. In particular, the trajectory of point E is required to have an approximate straight line trajectory (for the support phase) with a sufficient high to overpassing obstacles. Results of the above mentioned study are reported in Fig. 3 when the kinematic parameters values are reported in Table 1.

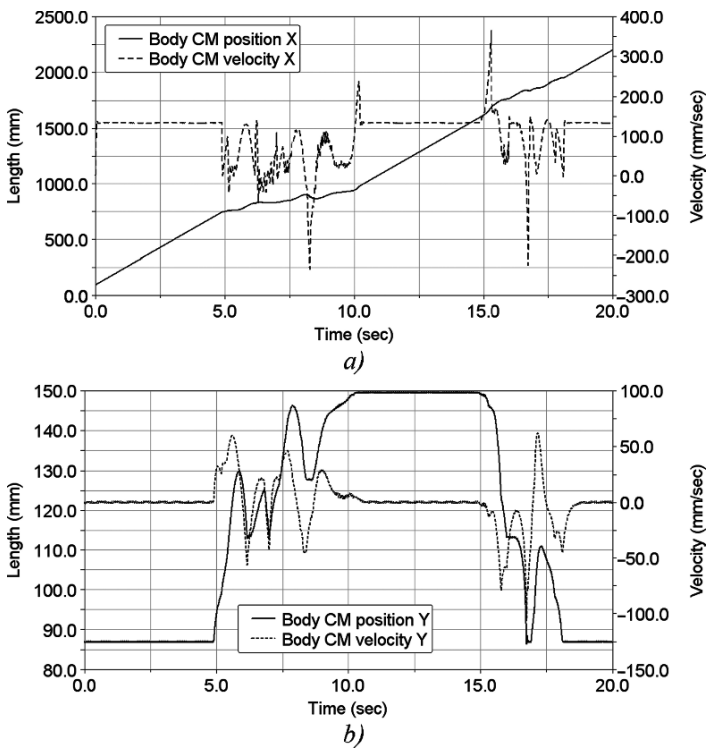
## Dynamic Analysis and Simulation

A suitable 3D model has been developed in ADAMS environment to verify the robot operation in surpassing an obstacle. The body size of the robot is  $220 \text{ mm} \times 210 \text{ mm} \times 120 \text{ mm}$ . The wheels' radii are  $42.5 \text{ mm}$ . The overall mass of the hybrid robot is  $5.5 \text{ kg}$ , batteries not included.

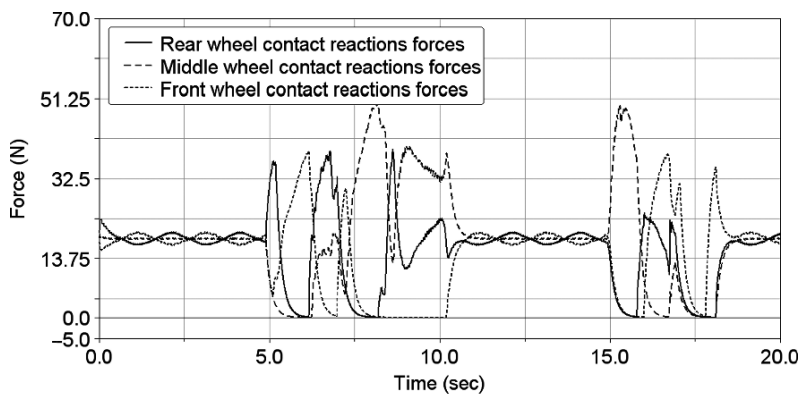
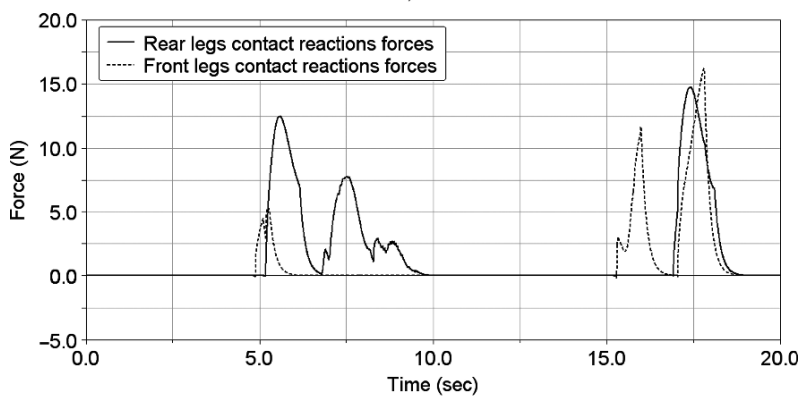
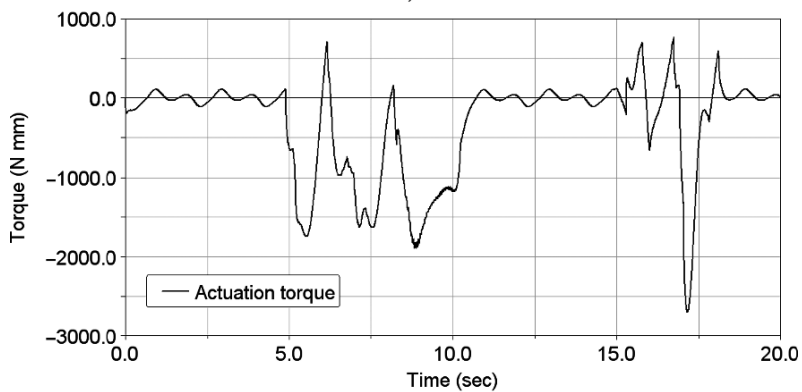
For the proposed numerical simulation the robot has to climb an obstacle of  $62.5 \text{ mm}$  tall (which corresponds to the  $147\%$  of the wheels' radii). The friction coefficient has a great influence on the robot's behaviour because allows to overpass obstacles, in order to perform dynamic simulation. Static friction coefficient



**Fig. 4** Dynamic simulation snapshots for the robot movement in overpassing an obstacle: (a) 0 s; (b) 5 s; (c) 9 s; (d) 13 s; (e) 15 s; (f) 17 s; (g) 18.8 s



**Fig. 5** Numerical results of the dynamic simulation proposed in Fig. 4: (a) body CM horizontal position and velocity; (b) body CM vertical position and velocity

*a)**b)**c)*

**Fig. 6** Numerical results of the dynamic simulation in Fig. 4: (a) wheels contact vertical forces; (b) legs contact vertical forces; (c) motor actuation torque

between ground and wheel has been set equal to 0.5. Furthermore, the static friction coefficient between ground and leg has been set equal to 1.5. These values can be obtained using suitable commercial covering materials for both leg contact surfaces and wheels. Figure 4 shows the snapshots of the reported dynamic simulation for the robot movement during the motion on a straight line and overpassing an obstacle. It is worth to note that the robot has been designed to use wheels in flat terrains and legs in overpassing obstacles that are greater than the wheel's radius. In particular, Fig. 4b and 4c show how the legs allow to climb the obstacle. Moreover, Fig. 4e and 4f show how the legs help the robot to descend the obstacle.

Figures 5 and 6 show numerical results of dynamic simulation in Fig. 4. In particular, the body CM (center of mass) position and velocity are shown in Fig. 5 along horizontal (X) and vertical (Y) directions.

The vertical components have been also reported in Fig. 6 for the reaction forces for both legs and wheels during the robot motion. It is worth to note by observing Fig. 6b the legs' action in helping the robot in surpassing the obstacle. In particular, the vertical components of the reaction forces are identical for front and rear legs respectively. This is related to the symmetrical configuration of both obstacle and robot.

Figure 6c shows the torque that is needed for actuating both legs and wheels. Numerical results show that the robot can surpass the obstacle by keeping its stability during the motion.

## Conclusions

In this paper the design and dynamic simulation are proposed for a new hybrid mobile robot that is able to perform a straight motion but can successfully overpass obstacles which sizes are greater than the wheels radii. Both legs and wheels are actuated by a single motor by a suitable transmission system.

## References

1. Karsten Berns web page: [www.fzi.de/ids/WMC/walking\\_machines\\_katalog/walking\\_machines\\_katalog.html](http://www.fzi.de/ids/WMC/walking_machines_katalog/walking_machines_katalog.html), 2007.
2. Raibert M. H., *Legged Robots That Balance*, MIT Press, pp. 3–14, 1986.
3. Pfeiffer F., Zielinska T., *Walking: Biological and Technological Aspects*, The International Centre for Mechanical Sciences Courses and Lectures n. 467, Springer Wien, pp. 1–29, 2004.
4. Hurmuzlua Y., Genot F., Brogliato B., *Modeling, Stability and Control of Biped Robots – A General Framework*, *Automatica*, Vol. 40, pp. 1647–1664, 2004.
5. Yoneda K., *Design of Non-Bio-Mimetic Walker with Fewer Actuators*, 4th CLAWAR International Conference on Climbing and Walking Robots, Karlsruhe, pp. 115–126, 2001.
6. Benbrahim H., Franklin J. A., *Biped Dynamic Walking Using Reinforcement Learning*, *Robotics and Autonomous Systems*, Vol. 22, pp. 283–302, 1997.
7. Raibert M. H., *Hopping in Legged Systems – Modelling and Simulation for the Two-Dimensional One-Legged Case*, *IEEE Transactions on Systems, Man, and Cybernetics*, Vol. 3, 1993.

8. Hodgins J. K., Raibert M. H., Biped Gymnastics, *Journal of Robotics Research*, Vol. 9, No. 2, 1990.
9. Morrey J.M., Lambrecht B., Horchler A. D., Ritzmann R. E., Quinn R. D., Highly Mobile and Robust Small Quadruped Robots. *IEEE International Conference on Intelligent Robots and Systems (IROS'03)*, Las Vegas, Nevada, 2003.
10. McGeer T., Passive Dynamic Walking, *Journal of Robotic Research*, Vol. 9, No. 2, pp. 62–82, 1990.
11. Yuan J., Hirose S., Zero Carrier: A Novel Eight Leg Wheels Hybrid Stair Climbing Mobile Vehicle, *Journal of Robotics and Mechatronics*, Vol. 17, No. 1, pp. 44–51, 2005.
12. Wellman P., Krovi V., Kumar V., Harwin W., Design of a Wheelchair with Legs for People with Motor Disabilities, *IEEE Transactions on Rehabilitation Engineering*, Vol. 3, No. 4, pp. 343–353, 1995.
13. Morales R., Feliu V., González A., Pintado P., Kinematic Model of a New Staircase Climbing Wheelchair and its Experimental Validation, *The International Journal of Robotics Research*, Vol. 25, No. 9, pp. 825–841, 2006.
14. Tavolieri C., Ottaviano E., Ceccarelli M., Nardelli A., A Design of a New Leg-Wheel Walking Robot, *15th Mediterranean Conference on Control and Automation – MED07*, Paper T30-011, Athens, 2007.
15. Tavolieri C., Ottaviano E., Ceccarelli M., Design and Problems of a New Leg-Wheel Walking Robot, *10th International Conference on Climbing and Walking Robots CLAWAR 2007*, Singapore, pp. 319–328, 2007.
16. Ottaviano E., González A., Ceccarelli M., Un Sistema de Locomocion Híbrida con Capacidad de Giro Para un Robot Movil, *8° Congreso Iberoamericano de Ingeniería Mecánica*, Cusco, paper 185, 2007 (In Spanish).
17. Aarnio P., Koskinen K., Salmi S., Simulation of the Hybtor Robot, *3rd International Conference on Climbing and Walking Robots*, pp. 267–274, 2000.
18. Grand C., Benamar F., Plumet F., Bidaud P., Stability and Traction Optimized of a Reconfigurable Wheel-Legged Robot, *The International Journal of Robotics Research*, Vol. 23, No. 10–11, pp. 1041–1058, 2004.
19. Siegart R., Lamon P., Estier T., Lauria M., Piguat R., Innovative Design for Wheeled Locomotion in Rough Terrai, *Journal of Robotics and Autonomous Systems*, 2002.
20. Hirose S., Takeuchi H., Study on Roller-Walk. Basic Characteristics and its Control, *Proc. IEEE International Conference on Robotics and Automation*, pp. 3265–3270, 1996.
21. González A., Morales R., Feliu V., Pintado P., Improving the Mechanical Design of a New Staircase Wheelchair, *International Journal of Industrial Robots*, Vol. 34, No. 2, pp. 110–115, 2007.
22. Guccione S., Muscato G., The Wheeleg Robot, *IEEE Robotics & Automation Magazine*, Vol. 10, No. 4, pp. 33–43, 2003.

# Evolving Four-Bars for Optimal Synthesis

Hans-Peter Schröcker, Bert Jüttler and Martin Aigner

**Abstract** We present an evolution-based method for optimal mechanism synthesis. It is based on the embedding of the Euclidean motion group in the space of affine displacements upon which an object-oriented Euclidean metric is imposed. This Euclidean structure allows the use of curve and surface evolution techniques from computer aided design and image processing. We demonstrate the algorithm by synthesizing planar four-bar mechanisms and we show how to modify it so that the resulting four-bar is free of circuit defects.

**Keywords** Optimal mechanism synthesis · Curve and surface evolution · Four-bar mechanism · Circuit defect

## Introduction

Optimal mechanism synthesis means finding a mechanism (type, dimension, position of base and end-effector) that *approximately* performs a certain task. It is a well-established field in mechanism science that evolved from the natural need for a more extensive but less accurate task description. In this article we present a novel approach to optimal motion generation.

There exists a wealth of literature on optimal mechanism synthesis and we confine ourselves to just a few references on optimal motion generation. The maybe most direct approaches use numerical techniques for solving an over-constrained system of equations [10, 19, 21]. Mixed numerical and graphical methods for optimal four-bar synthesis have been presented by Yao and Angeles [20]. They allow identification of all critical points of the underlying optimization problem. Finally, we can distinguish genetic algorithms [6, 13, 22] and methods based on evolution techniques, for example Shiakolas, Koladiya and Kebrle [17, 18].

Our approach fits into the last category. Its main distinction from other optimal synthesis schemes is the use of an object-oriented metric that makes the design

---

H.-P. Schröcker (✉)

Unit Geometry and CAD, Technikersrt.13, University Innsbruck, 6020 Innsbruck, Austria

space Euclidean. This allows the advantageous use of geometric techniques from computer aided design and image processing. In particular, we perform closest point computation and curve/surface evolution in this space. Evolution techniques permit great flexibility and control over the mechanism shape during the evolution and can be used to avoid mechanism defects. Moreover, the formulation of the synthesis problem within this framework is independent of the fixed coordinate frame. While our concept is general and can, at least in principle, be used for synthesizing many mechanisms of diverse type and shape, we confine ourselves to the synthesis of planar four-bars. Extensions to further mechanism types will be discussed in a subsequent publication.

In *A Metric for Affine Displacements* we introduce the object-oriented metric used in our approach. It is followed by an outline of a general framework for curve and surface fitting via evolution in *Evolution-Based Fitting of Algebraic Varieties*. In *A Concept for Optimal Four-Bar Synthesis* we explain how to formulate a four-bar synthesis problem within this framework and present a first example. In *Penalty Functions* we discuss how to incorporate additional constraints in order to avoid unwanted defects of the synthesized four-bars and in conclusion we conclude the paper with directions for future research.

## A Metric for Affine Displacements

Measuring the “distance” between two displacements is a fundamental problem of mechanism science with many important applications, in particular in mechanism synthesis. Among the various available concepts (see for example [4, 14]) we choose an approach which leads to an embedding of the Euclidean motion group into the space of affine displacements that is equipped with an *object-oriented* Euclidean metric [5, 9]. This metric has already been used for motion design [11, 12], for computing generalized penetration depths [16], and for defining performance indices of robots [15], but apparently not in mechanism design.

The distance concept is based on the choice of a number of feature points  $m_i \in \mathbb{R}^2$ . These feature points define a positive definite scalar product  $\langle \alpha, \beta \rangle = \sum \langle \alpha(m_i) \beta(m_i) \rangle$  and an associated squared distance  $\text{dist}^2(\alpha, \beta) = \sum \| \alpha(m_i) - \beta(m_i) \|^2$  between  $\alpha$  and  $\beta$  that depends only on the barycenter of the feature points and on their inertia matrix. It endows the space  $\text{GA}^+(2)$  of affine displacements with a *Euclidean metric*. The space  $\text{GA}^+(2)$  contains the Euclidean motion group  $\text{SE}(2)$  as a sub-manifold of dimension three. The feature points  $m_i$  can be replaced by an arbitrary mass distribution  $\mu$  on  $\mathbb{R}^2$ . In this case the formulas for inner product and distance are expressed in terms of integrals [9]. The inner product defined by the feature point  $m_i$  (or by the mass distribution  $\mu$ ) is also generated by four suitable chosen points of equal mass. Hence, the computation of inner product and distance is very efficient. Extensions of this distance concept to higher dimensions are straightforward.



## Evolution-Based Fitting of Algebraic Varieties

Now we describe a general concept for fitting implicitly defined varieties to a number of prescribed feature points (see also [1] and [3]). Its relation to optimal synthesis of four-bars will be explained in the next section.

Consider a system  $F_1(x), \dots, F_m(x)$  of polynomials and its zero set  $C \subset \mathbb{R}^d$ . We assume that the coefficients of  $F_i$  depend on a vector  $s = (s_1, \dots, s_p)$  of *shape parameters*. The vector  $s$  of shape parameters is to be determined such that the zero set  $C$  of the polynomials  $F_i$  approximates a set of target points  $q_0, \dots, q_n$ . By  $p_j$  we denote the point on  $C$  that minimizes the distance to  $q_j$  and by  $\nabla F_i$  we denote the gradient of  $F_i$  with respect to  $x$ .

Now we view  $s$  as depending on a time-variable  $t$ , that is  $s = s(t)$ . As  $s(t)$  varies in time, the points  $p_j = p_j(t)$  move along certain trajectories. Because of  $F_i(p_j(t), s(t)) \equiv 0$  we also have

$$\frac{d}{dt} F_i(p_j(t), s(t)) = \langle \nabla F_i, \dot{p}_j \rangle + \sum_{l=1}^p \frac{\partial F_i}{\partial s_l} \dot{s}_l \equiv 0, \quad (1)$$

where the derivatives of  $F_i$  are evaluated at  $(p_j(t), s_j(t))$  and the dot denotes derivatives with respect to  $t$ . Hence,  $\dot{p}_j$  is the velocity of the closest point  $p_j$ . By  $\{b_{j1}, \dots, b_{jm}\}$  we denote an orthonormal basis of the normal space of  $C$  in  $p_j$ . Ideally, the change of  $s(t)$  should be such that  $q_j - p_j = \dot{p}_j$ , that is,

$$\langle q_j - p_j, b_{jk} \rangle = \langle \dot{p}_j, b_{jk} \rangle \quad \text{for } j = 0, \dots, n \text{ and } k = 1, \dots, m. \quad (2)$$

There exist coefficients  $\beta_{jki}$  such that  $b_{jk} = \sum_{i=1}^m \beta_{jki} \nabla F_i$ . In view of (1), this yields

$$\langle \dot{p}_j, b_{jk} \rangle = \sum_{i=1}^m \beta_{jki} \langle \dot{p}_j, \nabla F_i \rangle = - \sum_{i=1}^m \beta_{jki} \sum_{l=1}^p \frac{\partial F_i}{\partial s_l} \dot{s}_l \quad (3)$$

Hence, (2) leads to an over-constrained system of linear equations in the unknowns  $\dot{s}_j$  that can be solved in least-squares sense. The result is independent of the choice of the basis vectors  $b_{jk}$ . Following the thus defined flow in the manifold of shape parameters leads to a locally optimal solution. It can be shown that the numerical integration of the trajectories via explicit Euler steps is equivalent to a Gauss-Newton method for non-linear least-squares optimization.

## A Concept for Optimal Four-Bar Synthesis

The evolution technique for fitting algebraic varieties to points as described in Section 3 can be used for optimal mechanism synthesis. In principle it is applicable

for arbitrary mechanisms (planar, spherical, spatial, serial, or parallel). We are going to describe the concept for the case of planar four-bar synthesis. Extensions to other classes of mechanisms are postponed to a further publication.

We model a four-bar motion via two *circle constraints*. For  $i = 1, 2$  the point with coordinates  $(a_i, b_i)$  in the moving system is constraint to a circle with center  $(\xi_i, \eta_i)$  and radius  $\rho_i$ . Then the synthesis problems relates to the concept of Section 3 as follows:

- The target points  $q_0, \dots, q_n$  are  $n + 1$  prescribed poses, viewed as points on the Euclidean motion group  $SE(2) \subset GA^+(2) \subset \mathbb{R}^6$ .
- The vector  $s$  of shape parameters has the ten entries  $a_1, b_1, \xi_1, \eta_1, \rho_1, a_2, b_2, \xi_2, \eta_2$ , and  $\rho_i$ .
- The four-bar motion is defined by five algebraic equations  $F_1, \dots, F_5$ . Three of them (the orthogonality conditions on the transformation matrix) define  $SE(2)$  as sub-manifold of  $GA^+(2)$  and remain constant over time. The two remaining equations are the circle constraints  $\| \alpha(a_i, b_i) - (\xi_i, \eta_i) \|^2 = \rho_i^2$ .
- All distances and angles in  $\mathbb{R}^6$  are measured using the inner product  $\langle \cdot, \cdot \rangle$ , which corresponds to the feature-point dependent metric, as described in Section 2. Also, the gradient vectors are computed with respect to that metric.

As a first example we fit a four-bar to eleven prescribed poses, proposed by J. Michael McCarthy on the occasion of the ASME Design Engineering Technical Conference in Montreal in 2002 (see also [8]). Figure 1 shows these poses, the initial configuration, and the results after 15 and 30 iterations. In each picture we display the target poses (dark), the closest poses of the current four-bar motion (white), and the four-bar mechanism in a configuration to reach the third of the prescribed poses. As can be seen, the prescribed poses are particularly amenable to a four-bar approximation.

In all examples of this article we choose the mass distribution by defining a set  $M$  of feature points that roughly represents the shape of the end-effector as depicted in Fig. 1. The total mass distribution is the union of all images of  $M$  under the prescribed poses.

In order to control the step-size in the evolution sequence, we specify a certain maximum allowed displacement  $H$  for the closest points  $p_j$ . The squared length of the displacement vector of  $p_j$  approximately equals  $\delta_j^2 = \sum_{k=1}^m \langle \dot{p}_j, b_{jk} \rangle^2$  and can be computed via Eq. (3). The allowed step size  $h$  for the current step is obtained as  $h = H \min\{\delta_j^{-1}\}$ . Furthermore, we decrease the value of  $H$  once the maximal expected change of the closest points is smaller than  $H$  in order to avoid forcing a large step away from an already good configuration.

Currently, the most time-consuming part of the evolution procedure consists in the computation of the closest points on the constraint variety in  $GA^+(2)$ . The remaining calculations (evaluations of elementary functions and solving a small linear system in the least-squares sense) are relatively cheap. The closest point computation is equivalent to computing the closest pose on a four-bar motion to a given pose. In our implementation we compute these points via standard constrained

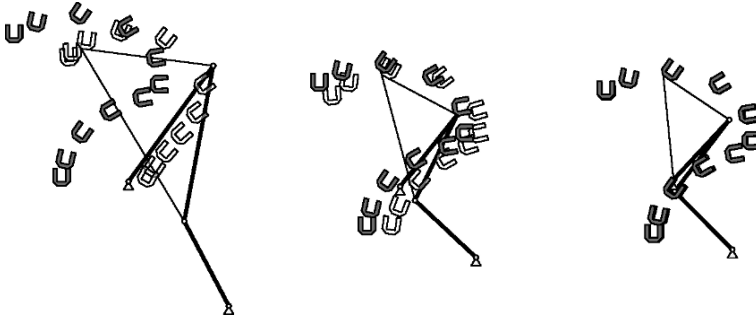


**Fig. 1** Solution to McCarthy’s eleven poses (from *left to right*: initial four-bar, after 15 iterations, after 30 iterations)

optimization routines. This is not completely reliable and we have no guarantee that we really end up in the global minimum. We found, however, that using the closest points from the preceding iteration step as starting values for the new closest points yields a reasonably good performance. A single closest point computations takes about 1–2 ms.

### Penalty Functions

In this section we show how to integrate penalty functions into our evolution framework. We discuss how to avoid singular four-bars and use this technique to produce optimal solutions that are free of circuit defects. Denote the base length of the four-bar by  $g$  and the coupler length by  $h$ . The lengths of driver and follower are the shape parameters  $\rho_1$  and  $\rho_2$ , respectively, while  $g$  and  $h$  are simple functions of the remaining shape parameters. Then a four-bar is singular (folding) if and only if one of the functions

$$C_1 = \frac{(\rho_1 + \rho_2 - g - h)^2}{(\rho_1 + \rho_2 + g + h)^2}, \quad C_2 = \frac{(\rho_1 - \rho_2 + g - h)^2}{(\rho_1 + \rho_2 + g + h)^2}, \quad C_3 = \frac{(\rho_1 - \rho_2 - g + h)^2}{(\rho_1 + \rho_2 + g + h)^2} \quad (4)$$

vanishes. For each of the functions  $C_i$  we choose a minimal permissible value  $\delta_i$ , and an offset  $\sigma_i$ . Using these values, we construct a smooth penalty function  $w_i$  and an activator function  $\alpha_i$  as depicted in Fig. 2. If  $C_i$  falls within  $[\delta_i, \delta_i + \sigma_i]$ , then the evolution pushes the shape parameters away from the zero set of  $C_i$ . This is achieved by adding the equation

$$\alpha(C_i) \cdot \left( \sum_{l=1}^{10} \frac{\partial C_i}{\partial s_l} \dot{s}_l - w_i(C_i) \right) = 0, \quad (5)$$

which is linear in  $\dot{s}$ , to the over-constrained system obtained from Eq. 3.

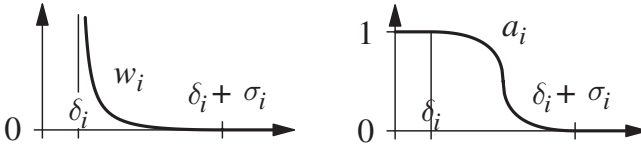


Fig. 2 Penalty function  $w_i$  and activator function  $\alpha_i$

A four-bar mechanism is called circuit defective with respect to a set of poses, if it cannot attain the poses within the same continuous range of motion Chase and Mirth [7]. It needs to be disassembled and re-configured in a different way in order to reach all poses. In our case, the poses are only attained approximately. Therefore, we say that a four-bar exhibits a *circuit defect*, if it is circuit defective with respect to the closest poses.

Assume now that the optimal four-bar obtained via evolution is circuit defective but the initial curve that evolves towards the target was not. Since the closest points  $p_i(t)$  move smoothly during the evolution process, this can only happen if the topology of the four-bar motion – which is seen as a curve on  $SE(2) \subset GA^+(2)$  – changes to two disconnected components (either from one or two components, or from two components via one component back to two components). At the transition between any two stages is a folding four-bar. Therefore, four-bars with circuit defect can be prevented by avoiding folding four-bars. A similar technique can also avoid Grashof defects and mechanism with a bad transmission ratio.

An example avoiding a circuit defect is shown in Fig. 3. The five prescribed poses permit precisely one exact solution that suffers from a circuit defect. The direct application of our algorithm (left-hand side) produces this defective mechanism. The picture in the middle shows an optimal solution, generated from the same initial values, but avoiding the assembly mode defect. The graph on the right-hand side displays the evolution of the square root of the sum of squared distances between target points and closest points over time – dotted for the first (assembly mode defective) solution, and in continuous line-style for the second solution. As opposed to the first solution’s graph, the graph of the second solution comes only close to zero. The kink occurs when the four-bar is pushed away from a singular configuration.

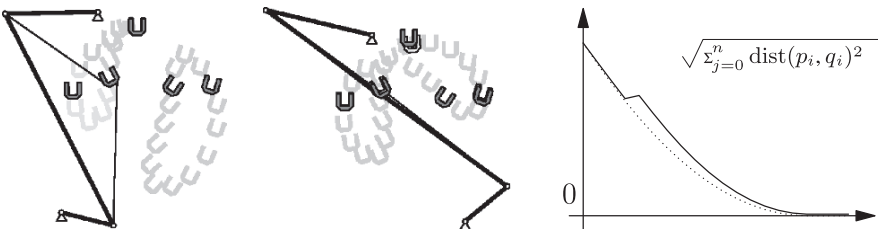


Fig. 3 Avoiding solutions with circuit defect

## Conclusion

We presented an algorithm for optimal mechanism synthesis (motion generation). In this paper we discussed the synthesis of a planar four-bars. The extension to other classes of mechanisms and incorporation of further defect-avoiding constraints is subject of ongoing research.

The evolution viewpoint to numerical optimization – as described in this paper – provides several advantages, including the connection to well-established techniques from image processing, the availability of a geometrically motivated step-size control, the possibility to add constraints via penalty functions, and the invariance with respect to the specific choice of the shape parameters (see [2]). In addition our method provides a geometrically significant solution, due to left-invariance of the used metric and the repeated closest point computation.

## References

1. Aigner, M. Jüttler, B. (2007), “Approximation Flows in Shape Manifolds”, in: *Curve and Surface Design, Avignon 2006*, ed. by Chenin, P., Lyche, T. and Schumaker, L. L., Nashboro Press, pp. 1–10.
2. Aigner, M. and Jüttler, B. (2008), *Gauss-Newton-type Techniques for Robustly Fitting Implicitly Defined Curves and Surfaces to Unorganized Data Points*, FSP Report Industrial geometry 65, To appear in Proc. Shape Modelling International 2008, IEEE; available at <http://www.ig.jku.at>, University Linz.
3. Ainger, M., Šír, Z. and Jüttler, B. (2007), “Evolution-Based Least-Squares Fitting Using Pythagorean Hodograph Spline Curves”, *Comput. Aided Geom. Design* 24:6, pp. 310–322.
4. Angeles, J. (2006), “Is There a Characteristic Length of Rigid-Body Displacements?”, *Mech. Machine Theory* 41:8, pp. 884–896.
5. Belta, C. and Kumar, V. (2002), “An SVD-Based Projection Method for Interpolation on  $SE(3)$ ”, *IEEE Trans. Robotics Automation* 18:3, pp. 334–345.
6. Cabrera, J. A., Simon, A. and Prado, M. (2002), “Optimal Synthesis of Mechanisms with Genetic Algorithms”, *Mech. Machine Theory* 37:10, pp. 1165–1177.
7. Chase, T. R. and Mirth, J. A. (1993), “Circuits and Branches of Single-Degree-of-Freedom Planer Linkages”, *ASME J. Mechanical Design* 115:2, pp. 223–230.
8. Chen, C. and Angeles, J. (2007), “Kinematic Synthesis of an Eight-Bar Linkage to Visit Eleven Poses Exactly”, in: *Proc. CDEN/C2E2 2007 Conference*, Winnipeg, Alberta.
9. Chirikjian, G. S. and Zhou, S. (1998), “Metrics on Motion and Deformation of Solid Models”, *ASME J. Mechanical Design* 120:2, pp. 252–261.
10. Hayes, M. J. D., Luu, T. and Chang, X.-W. (2004), “Kinematic Mapping Application to Approximate Type and Dimension Synthesis of Planar Mechanisms”, in: *Advances in Robot Kinematics*, ed. by Lenarčič, J. and Galletti, C., Kluwer Academic Publishers.
11. Hofer, M. and Pottmann, H. (2004), “Energy-Minimizing Splines in Manifolds”, *Transactions on Graphics* 23:3, Proc. of ACM SIGGRAPH 2004, pp. 284–293.
12. Hofer, M., Pottmann, H. and Ravani, B. (2004), “From curve design algorithms to the design of rigid body motions”, *The Visual Computer* 20:5, pp. 279–297.
13. Kunjur, A. and Krishnamurty, S. (1995), “Genetic Algorithms in Mechanism Synthesis”, in: *Fourth Applied Mechanisms and Robotics Conference AMR 95-068*, Cincinnati, Ohio, pp. 1–7.
14. Larochele, P. M., Murray, A. P. and Angeles, J. (2004), “SVD and PD Based Projection Metrics on  $SE(n)$ ”, in: *On Advances in Robot Kinematics*, ed. by Lenarčič, J. and Galetti, C., Dordrecht, Boston and London: Kluwer Academic Publishers, pp. 13–22.

15. Nawratil, G. (2007), “New Performance Indices for 6R Robots”, *Mech. Machine Theory* 42:11, pp. 1499–1511.
16. Nawratil, G., Pottmann, H. and Ravani, B. (2007), *Generalized Penetration Depth Computation Based on Kinematical Geometry*, Geometry Preprint Series 172, Vienna University of Technology.
17. Shiakolas, P. S., Koladiya, D. and Kebrle, J. (2002), “On the Optimum Synthesis of Four-Bar Linkages Using Differential Evolution and the Geometric Centroid of Precision Positions”, *J. Inversive Problems Engineering* 10:6, pp. 485–502.
18. Shiakolas, P. S., Koladiya, D. and Kebrle, J. (2005), “On the Optimum Synthesis of Six-Bar Linkages Using Differential Evolution and the Geometric Centroid of Precision Positions Technique”, *Mech. Machine Theory* 4:3, pp. 319–335.
19. Smaili, A. A. and Diab, N. A. (2005), “Optimum Synthesis of Mechanisms Using Tabu-Gradient Search Algorithm”, *ASME J. Mechanical Design* 127:5, pp. 917–923.
20. Yao, J. and Angeles, J. (2000), “Computation of All Optimum Dyads in the Approximate Synthesis of Planar Linkages for Rigid-Body Guidance”, *Mech. Machine Theory* 35:8, pp. 1065–1078.
21. Zhang, X., Zhou, J. and Ye, Y. (2000), “Optimal Mechanism Design Using Interior-point Methods”, *Mech. Machine Theory* 35:1, pp. 83–98.
22. Zhou, H. and Cheung Edmund, H. M (2001), “Optimal Synthesis of Crank-Rocker Linkages for Path Generation Using the Orientation Structural Error of the Fixed Link”, *Mech. Machine Theory* 36:8, pp. 973–982.

# A New Family of Overconstrained 6R-Mechanisms

Martin Pfulner

**Abstract** Using algebraic techniques an algorithm to detect new overconstrained 6R-mechanisms is developed. Many of the known overconstrained mechanisms were found rather synthetically or intuitively than by analytical methods. Within the last years analytical methods were used also to find more such mechanisms. With help of this algorithm a whole family of new overconstrained 6R-mechanisms is found. Some members of this family were already known before.

**Keywords** Overconstrained mechanism · Self motion · Movable mechanism

## Introduction

Overconstrained 6R-mechanisms are closed kinematic chains consisting of six rigid bodies, each of them connected to two adjacent ones by revolute joints. In general such chains have, according to the formula of Grübler, Kutzbach and Tschebyscheff (see [10]), zero or less degrees of freedom. But there exist exceptional mechanisms that are mobile because of the special choice of their design parameters. Until now a couple of such overconstrained mechanisms with six revolute joints are known. Some of them contain Bennett linkages like Waldron's [14] or Wohlhart's [16] 6R-linkages. But there exist others which are not combinations of Bennett linkages. A very good overview of nearly all known overconstrained mechanisms can be found in [8] and [1]. A short overview of newer mechanisms is given in [11]. In former times most discoveries of overconstrained six revolute spatial linkages came about synthetically or intuitively rather than by an analytical method. Within the last years analytical methods were used also used to discover more such mechanisms like in [2] or in [5]. Until now there is no complete classification of overconstrained serial closed loop chains with six revolute joints. A complete classification seems to be a difficult problem. The paper at hand gives a promising outlook to a way of handling at least parts of this problem.

---

M. Pfulner (✉)  
Unit Geometry and CAD, Technikersrt.13, University of Innsbruck, 6020 Innsbruck, Austria  
e-mail: martin.pfulner@uibk.ac.at

The paper is organized as follows: *Analysis of Overconstrained Mechanisms* gives an introduction to the analysis of overconstrained mechanisms. *Inverse Kinematics Algorithm* shows the inverse kinematics algorithm which is adapted for the finding of new overconstrained 6R-mechanisms. In *New Overconstrained Mechanisms* the synthesis algorithm is shown and a family of new overconstrained mechanisms is derived.

## Analysis of Overconstrained Mechanisms

From a geometrical point of view a closed loop 6R-chain becomes locally (infinitesimally) mobile when all six revolute axes lie in a linear complex. This mobility can be either configuration dependent, i.e. an instantaneously singular configuration, or configuration independent which then results in a continuous mobility. In order to be mobile the mechanism has to have a special design.

A serial closed kinematic chain can always be seen as an open chain where the end effector is fixed in one pose. Because of this fact one can use the inverse kinematics for the analysis and synthesis of overconstrained mechanisms. If the inverse kinematics of a closed loop 6R-chain yields infinitely many solutions instead of a finite number, then this mechanism is mobile in the prescribed pose of the end effector.

For the computation of the inverse kinematics of serial 6R-chains we will use an algorithm presented in [11] and [9]. A short overview of this algorithm is given in the next section.

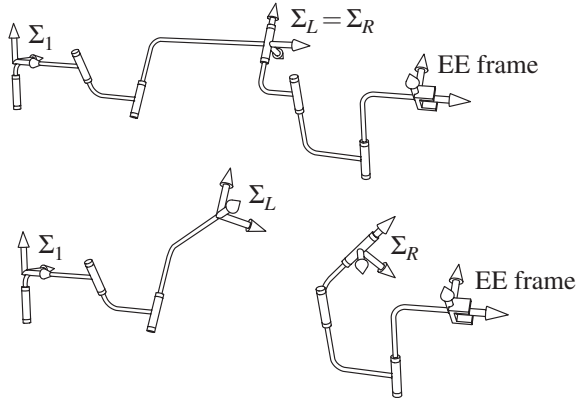
## Inverse Kinematics Algorithm

This algorithm decomposes the serial 6R-chain into two pieces. The chain is opened at the foot point of the common normal of axes three and four on the fourth axis. At the same time two copies of a coordinate frame  $\Sigma_L$  and  $\Sigma_R$  are attached to the common normal of third and fourth axes and to the fourth axis coinciding before the cutting. The resulting mechanisms after this cutting are two open 3R-chains, one is fixed in the base and the other one is fixed in the prescribed and fixed end effector pose of the 6R-chain. These chains have the end effectors  $\Sigma_L$  and  $\Sigma_R$  (see Fig. 1). The task of solving the inverse kinematics of the 6R-chain is now reformulated as the task of finding all poses where the end effector frames of the 3R-chains coincide. This task can be tackled using kinematic mapping. This mapping assigns to every Euclidean transformation  $T$  a point  $\mathbf{t} = (x_0 : x_1 : x_2 : x_3 : y_0 : y_1 : y_2 : y_3)$  in a seven dimensional image space  $P^7$ , the so called kinematic image space. Every transformation  $T$  can be written in matrix description as

$$\mathbf{T} = \begin{bmatrix} 1 & 0 & 0 & 0 \\ -2(x_0y_1 - y_0x_1 - y_2x_3 + y_3x_2) & x_0^2 + x_1^2 - x_3^2 - x_2^2 & -2x_0x_3 + 2x_2x_1 & 2x_3x_1 + 2x_0x_2 \\ -2(x_0y_2 - y_0x_2 - y_3x_1 + y_1x_3) & 2x_2x_1 + 2x_0x_3 & x_0^2 + x_2^2 - x_1^2 - x_3^2 & -2x_0x_1 + 2x_3x_2 \\ -2(x_0y_3 - y_0x_3 - y_1x_2 + y_2x_1) & -2x_0x_2 + 2x_3x_1 & 2x_3x_2 + 2x_0x_1 & x_0^2 + x_3^2 - x_2^2 - x_1^2 \end{bmatrix}. \quad (1)$$



**Fig. 1** Decomposition of the 6R into two 3R serial chains



The entries of these matrix have to fulfill the quadratic identity

$$S_6^2 : \quad x_0y_0 + x_1y_1 + x_2y_2 + x_3y_3 = 0, \quad (2)$$

denoted Study quadric  $S_6^2$ , and at least one  $x_i$  has to be different from zero. Kinematic mapping maps the entries of matrix (1) onto a point in the kinematic image space  $\mathbf{t}$ . To obtain the special form of the transformation matrix in (1) from a general Euclidean transformation matrix one can use the equations of E. Study presented in [9].

Using this mapping all possible poses the end effector of an open 3R-chain can attain are mapped onto a manifold in the kinematic image space. This manifold is called constraint manifold of the serial chain. In [11] it turned out, that this manifold is part of a well known construct in geometry, it is a Segre manifold. This special geometric object can be generated in  $P^7$  as the intersection of four linearly coupled hyperplanes. The constraint manifold of a 3R-chain is then the intersection of the Segre manifold with the Study quadric  $S_6^2$ . This fact is true for both open 3R-chains we have generated by cutting the 6R-chain into two pieces. The intersection of two Segre manifolds with the Study quadric yields then all poses, where the end effector frames of the two open 3R-chains coincide. In these poses the 6R-chain can be reconnected. These configurations are therefore the solutions of the inverse kinematics of the general 6R-chain. For further details on kinematic mapping and Segre manifolds as kinematic images of 3R-serial-chains see [9].

Using this algorithm one obtains eight equations of the type

$$\begin{aligned} H_j : \quad & \sum_{i=0}^3 a_{ij}(v)x_i + \sum_{i=0}^3 b_{ij}(v)y_i = 0 \quad j = 1, \dots, 4 \\ H_j : \quad & \sum_{i=0}^3 a_{ij}(w)x_i + \sum_{i=0}^3 b_{ij}(w)y_i = 0 \quad j = 5, \dots, 8 \end{aligned} \quad (3)$$

which are eight pencils of hyperplanes in  $P^7$  and additionally we have Eq. (2) of the Study-quadric. Equations  $H_j, j = 1, \dots, 4$  resp.  $H_j, j = 5, \dots, 8$  describe the Segre manifolds belonging to the 3R-chain with end effector  $\Sigma_L$  resp.  $\Sigma_R$ . The coefficients  $a_{ij}$  and  $b_{ij}$  in these equations depend on the design parameters of the

robot and on the tangent half of two arbitrary rotation angles of the 6R-chain  $v$  and  $w$ .  $v$  is the algebraic value of one of the rotation angles of the axes one, two or three and  $w$  is the algebraic value of one of the rotation angles of the axes four, five or six of the 6R-chain.

For the solution of the inverse kinematics the design parameters are known. The solution of this system of nonlinear equations given in (3) and (2) with respect to the unknowns  $x_0, \dots, x_3, y_0, \dots, y_3, v$  and  $w$  yields the solution of the inverse kinematics of the 6R-chain. The solution algorithm works in the following way: At first we take seven of the hyperplane equations  $H_j, j = 1, \dots, 7$  from Eq. (3) and solve them linearly for the homogeneous unknowns  $x_i$  and  $y_i, i = 0, \dots, 3$ . Substitution of the solution of this linear system into the remaining two equations  $S_6^2$  and  $H_8$  yield two nonlinear equations in the unknowns  $v$  and  $w$ . These equations are denoted by  $E_1$  and  $E_2$ . The common solutions of these two equations yield directly the solutions of two of the revolute angles in the inverse kinematics of the 6R-chain. The remaining values for the revolute angles can be derived linearly (see [9]).

If the system of equations in (2) and (3) does not yield a finite number of solutions, then the 6R-chain is mobile in the prescribed end effector pose. It is clear, that this can only happen if the mechanism has a special design.

A restriction of this algorithm is, that it is not always possible to use the tangent half of any of the first three rotation angles for  $v$  resp. the tangent half of any of the rotation angles four, five or six for  $w$ . If one decides to take the algebraic value of one of the angles of the first 3R-chain for  $v$  and the remaining two axes have a point of intersection (possibly also a point at infinity) in common for all values of  $v$  then the corresponding Segre manifold lies completely on the Study-quadric. Therefore equation  $E_1$  is equal to zero. In general this would imply that this mechanism is mobile but in this special case this mechanism is not necessarily mobile. Therefore one has to take another angle out of the 3R-chain to obtain a Segre manifold that does not lie completely on the Study quadric. If this is not possible the whole 3R-chain is either a planar or spherical 3R-chain. For more details of these special cases see [11].

In literature only few mechanisms containing – explicitly in their general descriptions – a planar or spherical 3R-chain are known such as Sarrus mechanisms [13] or Waldron's planar Bennett hybrid mechanism [15].

## New Overconstrained Mechanisms

It is obvious that one can use exactly the algorithm for the inverse kinematics to synthesize new overconstrained mechanisms. The only difference is that the design parameters are unknown too. In case of synthesizing a 6R-serial-chain we have 18 design parameters using the Denavit-Hartenberg convention [7]: the distances  $a_i$  and the twist angles  $\alpha_i$  between adjacent axes and the offsets  $d_i$  on the axis, which

are the distances of the foot points of the common perpendiculars of axis  $i$  with the two adjacent axes on the  $i$ -th axis,  $i = 1, \dots, 6$ .

Applying the algorithm described in *Inverse Kinematics Algorithm* an overconstrained mechanism occurs when  $E_1$  and  $E_2$  have a common factor or  $E_1$  or  $E_2$  vanish independently of  $v$  and  $w$ . It is possible to compute equations  $E_1$  and  $E_2$  for arbitrary design parameters. If one can find design parameters such that one of the two items above is true, then we have found an overconstrained mechanism. The first item will be difficult to realize because of the complicated structure of the two equations. The second item means, that all coefficients of all powers of  $v$  and  $w$  in  $E_1$  or  $E_2$  have to vanish identically. In this case the restriction of this inverse kinematic algorithm described in *Inverse Kinematics Algorithm* yields a simplification. Let us consider the case that the 6R-chain is of such a type that one cannot use any Segre manifold for the inverse kinematics solution. If we use exactly this “forbidden” Segre manifold for the synthesis of an overconstrained mechanism, than  $E_1$  is equal to zero. In this case it is a necessary condition, that  $E_2$  has to be equal to zero, so that the whole mechanism can be an overconstrained one. If one uses this forbidden Segre manifold then the condition  $E_2 = 0$  is always shorter than in case of a valid manifold. Therefore in the next steps we will restrict ourselves to a family of mechanisms that contain 3R-chains with at least one associated forbidden Segre manifold. Geometrically this means that we are synthesizing movable 6R-chains having at least one pair of revolute axes being either parallel or intersecting. We will use the “forbidden” manifold to achieve necessary conditions for mobility and we will test the conditions then using valid Segre manifolds. Using the assumptions

$$\alpha_1 = -\alpha_2, \quad a_1 = a_2 = 1 \quad (4)$$

for the following computations will ensure, that the Segre manifold with parameter  $v = v_2 = \tan u_2/2$  ( $u_2$  is the joint parameter of the second revolute joint) will be a “forbidden” Segre manifold. Despite of the restrictions already made it turned out to be impossible to solve the resulting system of nonlinear equations with arbitrary design parameters algebraically. Therefore we made further assumptions on some of the design parameters. In this paper we use the additional restrictions

$$d_1 = d_2 = d_3 = d_4 = d_5 = d_6 = 0. \quad (5)$$

Geometrically these assumptions mean that we are synthesizing mobile 6R-chains having no offsets.

After these simplifications the coefficients of the unknowns  $v_2$  and  $w$  (the tangent half of one of the rotation angles 4, 5 or 6) in the equation  $E_2 = 0$  yield a set of eight nonlinear equations having between 246 and 1,134 operands. The vanishing set  $\mathcal{V}(\mathcal{I})$  of the spanned ideal  $\mathcal{I}$  yields necessary conditions for mobile mechanisms. The remaining unknowns in these equations are  $a_i$ ,  $i = 2, \dots, 6$  (the tangent half of  $\alpha_i$ ) and  $a_i$ ,  $i = 3, \dots, 6$ . It is not possible to solve this system brute force. We used the computer algebra systems Maple and Singular in parallel to compute solutions of this system algebraically. With the help of a step by step

primary decomposition we could split this big system of equations into small parts. Primary decomposition uses the fact, that an ideal can be split into several parts (see [6]):

$$\mathcal{I} = \bigcap_{i=1}^n \mathcal{I}_i \quad \text{with} \quad \mathcal{V}(\mathcal{I}) = \bigcup_{i=1}^n \mathcal{V}(\mathcal{I}_i). \tag{6}$$

That means one can have a look at the vanishing sets of the (usually) smaller ideals  $\mathcal{I}_i$  to obtain all solutions for the whole system. More about primary decomposition and theory of ideals can be found in [6].

After obtaining many sets of solutions we started to unassign the conditions in Eq. (5) and tried to generate more general mechanisms. In Tables 1, 2 and 3 mechanisms derived using this method are listed. The family of mechanisms in Table 1 has the properties of Eq. (4) and furthermore  $a_3 = a_4, a_5 = a_6$ .

All the mechanisms in Table 2 have the common properties of Eq. (4),  $a_4 = a_6$  and  $a_3 = a_5 = |a_4 \sin(\alpha_3) / \sin(\alpha_4)|$ .

The first mechanisms in Tables 1 and 2 were published by Wohlhart in [16]. Mechanism number one in Table 2 was obtained in [16] by applying the theory of “isomerisation” on the first linkage in Table 3 (see also [17]).

The solutions in Table 3 have the common properties of Eq. (4) and furthermore  $a_3 = a_6$  and  $a_4 = a_5$ . Solution number one in this table is the general plane-symmetric Bricard 6R linkage [4].

As Wohlhart showed in [17] “isomerisation” can be used on the mechanisms in Tables 1, 2, 3 to obtain more new overconstrained mechanisms. Of course as members of this family the mechanisms of Sarrus [13] and the plano-spherical hybrid linkage of Bennett [3] are solutions of the prescribing set of equations. This method of synthesizing overconstrained mechanisms yields directly one out of the five input–output equations of the mechanisms algebraically. The remaining ones can be obtained linearly using the method presented in [12]. Figure 2 shows a sketch of one of the new mechanisms.

**Table 1** Mechanisms with restrictions of Eq. (4) and  $a_i = a_{i+1}, i \in \{3, 5\}$

Nr.	$d_1$	$d_2$	$d_3$	$d_4$	$d_5$	$d_6$	$\alpha_3$	$\alpha_4$	$\alpha_5$	$\alpha_6$
1	$d_1$	0	$d_3$	0	$-(d_1 + d_3)$	0	$\alpha_3$	$-\alpha_3$	$\alpha_5$	$-\alpha_5$
2	$d_1$	0	$d_3$	0	$d_1 + d_3$	0	$\alpha_3$	$\pi - \alpha_3$	$\alpha_5$	$\pi - \alpha_5$

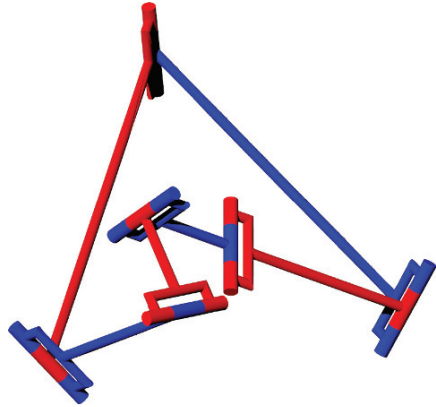
**Table 2** M. w. restr. of Eq. (4),  $a_4 = a_6$  and  $a_3 = a_5 = |a_4 \sin(\alpha_3) / \sin(\alpha_4)|$

Nr.	$d_1$	$d_2$	$d_3$	$d_4$	$d_5$	$d_6$	$\alpha_3$	$\alpha_4$	$\alpha_5$	$\alpha_6$
1	$d_1$	0	$-d_1$	0	0	0	$\alpha_3$	$\alpha_4$	$-\alpha_3$	$-\alpha_4$
2	$d_1$	0	$-d_1$	0	0	0	$\alpha_3$	$\alpha_4$	$-\alpha_3$	$\alpha_4$
3	$d_1$	0	$-d_1$	0	0	0	$\alpha_3$	$\alpha_4$	$\pi - \alpha_3$	$\pi - \alpha_4$
4	$d_1$	0	$-d_1$	0	0	0	$\alpha_3$	$\alpha_4$	$\pi - \alpha_3$	$-(\pi - \alpha_4)$
5	$d_1$	0	$-d_1$	0	0	0	$\alpha_3$	$\alpha_4$	$-(\pi - \alpha_3)$	$\pi - \alpha_4$

**Table 3** Mechanisms with restrictions of Eq. (4),  $a_3 = a_6$  and  $a_4 = a_5$

Nr.	$d_1$	$d_2$	$d_3$	$d_4$	$d_5$	$d_6$	$\alpha_3$	$\alpha_4$	$\alpha_5$	$\alpha_6$
1	$d_1$	0	$-d_1$	$d_4$	0	$-d_4$	$\alpha_3$	$\alpha_4$	$-\alpha_4$	$-\alpha_3$
2	$d_1$	0	$-d_1$	$d_4$	0	$-d_4$	$\alpha_3$	$\alpha_4$	$-\alpha_4$	$\alpha_3$
3	$d_1$	0	$-d_1$	$d_4$	0	$d_4$	$\alpha_3$	$\alpha_4$	$\pi - \alpha_4$	$-(\pi - \alpha_3)$
4	$d_1$	0	$-d_1$	$d_4$	0	$d_4$	$\alpha_3$	$\alpha_4$	$\pi - \alpha_4$	$\pi - \alpha_3$

**Fig. 2** Sketch of a mechanism with dimensions of Nr. 2 in Table 3 with dimensions:  $a_2 = 1, a_4 = 5, a_6 = 2, d_i = 0, i = 1, \dots, 6, al_2 = 1, al_3 = 1/2$  and  $al_4 = 1/3$



## Conclusion

Using the algorithm presented in this paper we are able to find new overconstrained mechanisms. Although this algorithm brings a simplification of the problem description it seems to be a difficult problem to find a classification of all overconstrained 6R-serial closed chains. But the algorithm has the potential to solve at least parts of this problem.

## References

1. J.E. Baker. Displacement-closure equations of the unspecialised double-Hooke’s-joint linkage. *Mechanism and Machine Theory*, 37(10):1127–1144, October 2002.
2. J.E. Baker. A curious new family of overconstrained six-bars. *Transactions of the ASME*, 127:602–606, July 2005.
3. G.T. Bennett. The parallel motion of Sarrut and some allied mechanisms. *Phil. Mag.* (6th series) 9:803–810, 1905.
4. R. Bricard. *Lecons de Cinematique. Tome II Cinématique Appliquée*. Gauthier-Villars, Paris, 1927.
5. Y. Chen and Z. You. Spatial 6R linkages based on the combination of two Goldberg 5R linkages *Mechanism and Machine Theory*, 42(11):1484–1498, November 2007.
6. D. Cox, J. Little, and D. O’Shea. *Ideals, Varieties and Algorithms*. Springer Verlag, New York, third edition, 2007.
7. J. Denavit and R.S. Hartenberg. A kinematic notation for lower-pair mechanisms based on matrices. *Journal of Applied Mechanics*, 77:215–221, 1955.

8. P. Dietmaier. *Einfach übergeschlossene Mechanismen mit Drehgelenken*. Habilitationsschrift, Graz, 1995.
9. H.L. Husty, M. Pfurner, H.P. Schröcker, and K. Brunthaler. Algebraic methods in mechanism analysis and synthesis. *Robotica*, 25:661–675, 2007.
10. M.L. Husty, A. Karger, H. Sachs, and W. Steinhilper. *Kinematik und Robotik*. Springer-Verlag, Berlin, Heidelberg, New York, 1997.
11. M. Pfurner. *Analysis of spatial serial manipulators using kinematic mapping*. PhD thesis, University of Innsbruck, 2006.
12. M. Pfurner and M.L. Husty. A method to determine the motion of overconstrained 6r-mechanisms. In *Proceedings of the 12th World Congress IFToMM*, Besancon, France, June 2007. IFToMM.
13. P.T. Sarrus. Note sur la transformation des mouvements rectilignes alternatifs. *Comptes Rendu*, 36:1036–1038, 1853.
14. K.J. Waldron. A family of overconstrained linkages. *Journal of Mechanisms*, 2:201–211, 1967.
15. K.J. Waldron. Hybrid overconstrained mechanisms. *Journal of Mechanisms*, 3:73–78, 1968.
16. K. Wohlhart. A new 6R space mechanism. In *Proceedings of the 7th World Congress IFToMM*, volume 1, pages 193–198, Sevilla, Spain, 1987.
17. K. Wohlhart. On isomeric overconstrained space mechanisms. In *Proceedings of the Eighth World Congress IFToMM*, pages 153–158, Prague, Czechoslovakia, 1991. IFToMM.

# Development of a Spherical Linkage Mechanism with the Aid of the Dynamic Spatial Geometry Program “GECKO”

G. Lonij, Mathias Husing, S.W. Choi and Burkhard Corves

**Abstract** In this presentation the development of a spherical linkage mechanism for passenger vehicle swivel joint tow coupling is reviewed. The idea for the swivel joint tow coupling emerged after a cooperation between the Department of Mechanism Theory and Dynamics of Machines (IGM) of the RWTH-Aachen University and a market leading manufacturer of tow bar mechanisms. Presently, the swivel joint mechanism has been patented worldwide [1]. Additionally, a prototype of the tow coupling is currently in an advanced design phase, in which the possibilities for cost optimization and suitability for series production are assessed. The dimensions of the spherical mechanism were defined using the dynamic spatial geometry program “GECKO” currently developed at IGM.

**Keywords** Kinematics · Mechanism design · Spherical mechanism · Software development

## Introduction

The tow coupling is in effect the connection of a trailer to a motor vehicle and is usually realized by a ball-and-socket joint. The ball socket located on the trailer frame wraps around a ball head connected to the body of a motor vehicle by means of a bar and a fixed frame. During transport, the socket can move freely around the ball head allowing the trailer to follow the motor vehicle.

Functional features have an increasing role during development and marketing of the tow bar couplings. Improvement of user friendliness, aesthetics and safety as well as a high level of innovation define the products presently on the market.

---

G. Lonij (✉)  
Department of Mechanism Theory and Dynamics of Machines, RWTH-Aachen University,  
Aachen, 52056 Germany  
e-mail: lonij@igm.rwth-aachen.de

## State of the Art

Existing tow couplings can be split into three categories. Firstly, tow couplings which are fixed to the frame and therefore the vehicle body offer a low budget but unsatisfactory solution with regard to the features mentioned above. Secondly, tow couplings which are detachably connected to the frame and therefore the body of the car offer an improvement over the first category. Detaching and storage of several coupling parts must be taken into account when the coupling is not in use.

Recently, a third category of tow couplings has been introduced, which feature a manually or electronically actuated connection of the coupling. When the coupling is not in use it can be simply retracted and hidden from sight behind the bumper of the motor vehicle.

As with the detachable tow couplings the retractable coupling must be locked in place during its use. A form locked solution is generally preferred for safety reasons.

## Literature and Patents

Several solutions of retractable tow couplings are known and some are already on the market. One instance (Fig. 1) shows a tow coupling with a single revolute joint fixed to the frame and vehicle body [2–4]. The curvature of the coupling bar for this solution is limited.

A very cost-effective solution is given by a sliding revolute joint (Fig. 2A) [5–7]. Several other solutions feature a dual driven coupling bar allowing independent vertical and rotary motion (Fig. 2B) [8–10].



Fig. 1 Retractable tow coupling (source Oris)

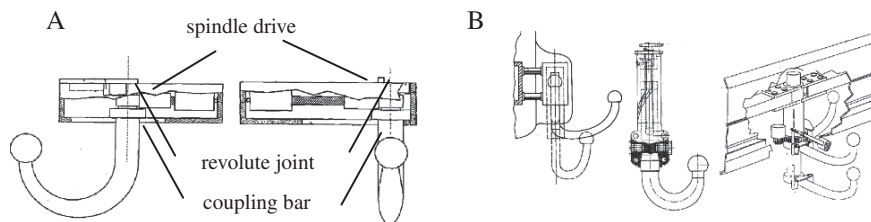


Fig. 2 Retractable tow coupling with sliding revolute joint



## Development of a New Solution

The development of the retractable tow coupling is focused on the realization of desired motion and the retention of the coupling’s position when towing a trailer. In addition the mechanism should feature the following properties:

- Uncomplicated design
- Possibility of manual and electric operation
- Driven by a single actuator
- Direct load transmission [12]
- Invisible when retracted
- No contact on the vehicle body or bumper
- Standardized position of ball head when extended [11]

Possible mechanism solutions can be systematically chosen with the use of the following criteria:

- Function
  - Guiding mechanism
  - Transmission mechanism
  - Planar mechanisms
  - Spherical mechanism
  - Spatial mechanism
- Configuration (Fig. 3)
- Number of linkages (including the base linkage) (Fig. 4)
- Joint types (Fig. 5)
  - Revolute joints
  - Prismatic joints
  - Curve joints
  - Universal joints
  - Ball joints

Resulting from the procedure, a spherical mechanism with four linkages is considered most promising (Fig. 6). Particularly beneficial to this fairly uncomplicated mechanism is the large freedom of motion attainable by the coupler link, which

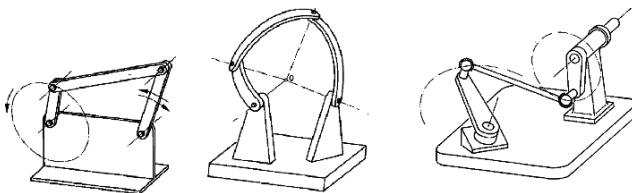


Fig. 3 Mechanism configuration

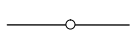
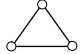
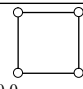
Number of linkages	2	3	4
Kinematische Kette			
	2-0-0	3-0-0	4-0-0

Fig. 4 Number of linkages

Fig. 5 Joint types

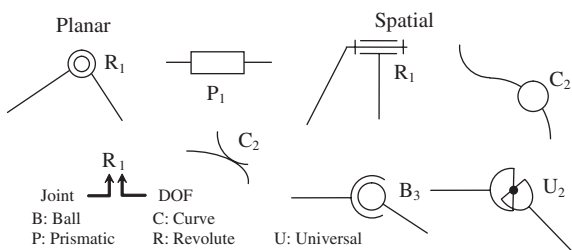
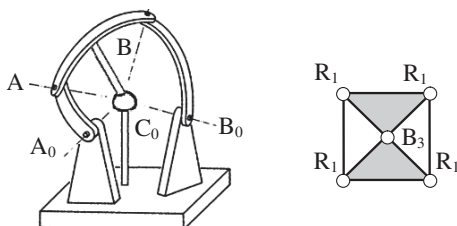


Fig. 6 Spherical mechanism



allows an adaptation of the mechanism to a wide range of motor vehicles as well as the sole use of revolute joints. Furthermore, the mechanism requires only one actuated joint. The additional ball joint connecting the coupler linkage to the base can only be applied to spherical mechanisms due to the specific motion of all points on the individual linkages along concentric spheres. The ball joint allows a direct load transmission to the base.

## Motion Design

The desired motion of the tow coupling is defined by the design space and the required position of the ball head in the extended position. In most vehicles the preferred position of the retracted tow coupling is behind the bumper in the hollow space between bumper and the body of the vehicle in approximately plane P<sub>1</sub> (Fig. 7). The tow coupling's required extended position is behind the vehicle in plane P<sub>2</sub>.

Two different principal solutions can be pursued. On the one hand, the mechanism can be located as low as possible. On the other hand, the installation height can be chosen level with the ball head in extended position. The latter is preferable due to direct load transmission. From the retracted into the extended position the ball head is first lowered (M<sub>1</sub>) than pivoted (M<sub>2</sub>) and then again raised (M<sub>3</sub>). All motions fade into the next resulting in a smooth overall movement (Fig. 8).

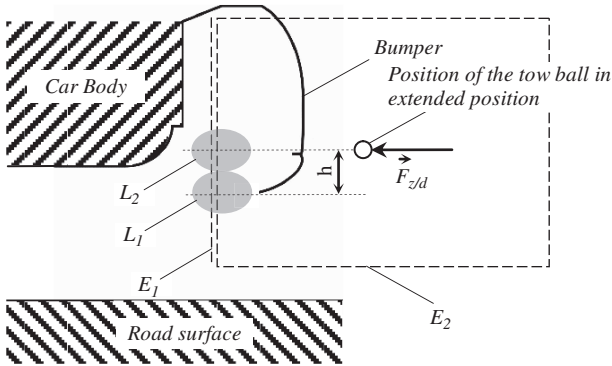


Fig. 7 Side view cross section

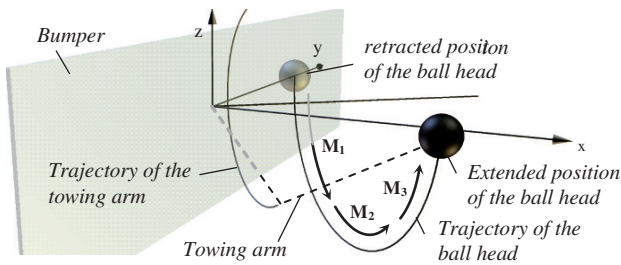


Fig. 8 Motion of the coupling arm and ball head

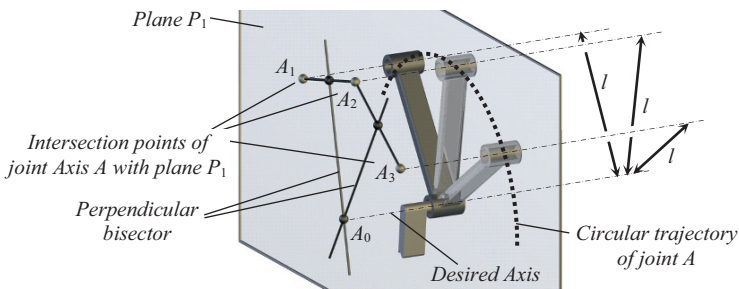
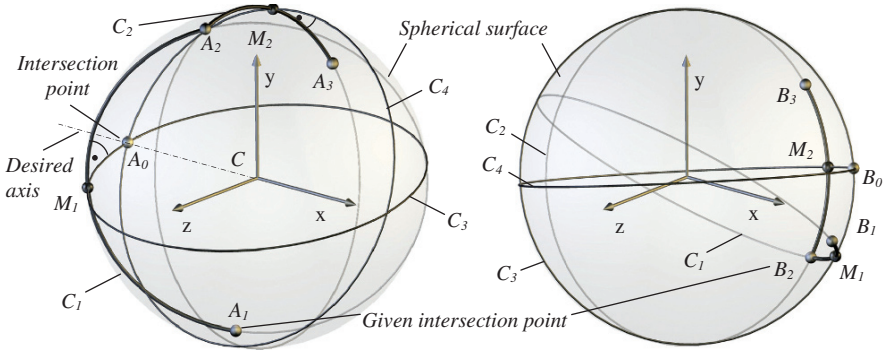


Fig. 9 Procedure defining kinematic dimension “l” of a linkage

## Dimensioning

The use of revolute joints for the connection of two linkages results in a circular motion of all points on the adjacent linkage relative to the joint axis. In effect, all locations of a point on the adjacent link are equidistant to the joint axis (Fig. 9). This property can be used to find an unknown joint axis. Procedures providing the kinematic dimensions of planar linkage mechanisms for a given number of relative joint coordinates are described in [2, 3].



**Fig. 10** Procedure defining the circle centre point

In spherical mechanisms the circular trajectories lie on concentric spherical surfaces around the centre point of the mechanism. However, the mentioned procedures can be easily adapted for this type of mechanism, demonstrated with Fig. 10. The object of the procedure is the determination of the base joint axis represented by the sphere centre point and point  $A_0$  for a given set of positions of joint A.

Two positions  $A_1$  and  $A_2$  (Fig. 10) of the second joint on the linkage are equidistant to circle  $C_3$  representing the perpendicular bisector in Fig. 9. It passes through point  $M_1$  in the middle of arc  $C_1$  defined by  $A_1$ ,  $A_2$  and the centre point of the sphere. Circle  $C_3$  therefore represents all possible positions of a possible axis' intersection point with the sphere. The same construction can be adapted for positions  $A_2$  and  $A_3$ , resulting in the equidistant circle  $C_4$ , again marking the possible positions of the axis' intersection point. Only the joint axis passing through the intersection points of both circles  $C_4$  and  $C_3$  is equidistant to  $A_1$ ,  $A_2$  and  $A_3$ . An identical procedure can be used to find the position of the second base joint axis.

## Dynamic Spatial Geometry Program “GECKO”

When designing mechanisms the engineer can apply many construction methods based on geometric relationships, which can be carried out on paper with the aid of pencil ruler and compasses. However, the imprecision, obscurity, unwieldy and static properties of the graphic procedures have caused numeric methods to gain importance. Especially with the design of spherical and spatial mechanisms the depiction of the numerous graphic procedures is extremely limited. The design of such mechanisms is therefore largely executed using numeric procedures.

From an engineering as well as an educational point of view, the desire for a tool enabling the accurate, fast and adaptable design of mechanisms. In the case of planar mechanisms several software programs have been developed over the last decades providing this. However, spherical and spatial mechanisms still largely rely on numerical procedures.

At the IGM RWTH-Aachen University a dynamic spatial geometry program called “GECKO” is currently being developed. This software, used for research purposes and education of mechanism theory at RWTH-Aachen University provides a platform for design procedures of all types of mechanisms.

For the development of “GECKO” the chosen programming language is Java because the source code can be executed on every system without recompiling provided the availability of a Java Virtual Machine [3]. Additionally it offers many libraries providing useful source code for graphic representation of mechanism elements (Java OpenGL or jogl), user interface (RCP) etc. The object oriented composition of Java contributes to an efficient development whereby common methods of several classes, for instance graphical elements can be programmed solely in the parent class which hands it down to the appropriate subclass.

A main challenge in the development of “GECKO” is the creation of monitoring functions, ascertaining the correct user input. If all conditions, for example pressing a button or selecting an element are met the construction of a new element is started.

The procedure described in the previous chapter will form the bases to demonstrate the application and functionality of “GECKO”.

### Example

The desired motion resulting from the motion design can be substituted by the definition of three characteristic positions of the coupling arm respectively the retracted and extended position as well as the position marking the lowest point of the ball head. After defining two positions of the joints on the coupling arm, “GECKO” allows a fast determination of the desired base joint positions. Given the sets of joint coordinates the circles  $C_1$  to  $C_4$  are constructed using the following sequence:

- Line on sphere between  $A_1$  and  $A_2$
- 1/2 Midpoint on constructed line
- Perpendicular circle to the constructed line in the Midpoint
- Line on sphere between  $A_2$  and  $A_3$
- 1/2 Midpoint on constructed line
- Perpendicular circle to the constructed line in the Midpoint
- AB Intersection point

Subsequently, the same procedure is carried out for  $B_1$  to  $B_3$  resulting in the position of  $B_0$ . A movable mechanism is constructed as follows.

- Definition of the mechanism drive
- Creation of a two link chain

After completion “GECKO” allows an interactive adaptation of the given joint coordinates resulting in a direct adjustment of the construction and kinematic dimensions.

## Conclusion

With the aid of the newly developed software “GECKO”, the engineer gains a powerful tool for the development of spherical and spatial mechanisms. The example of the spherical mechanism in the retractable tow coupling substantiates this. The ongoing development of “GECKO” includes realization of improved analysis capabilities and implementation of curve and cam elements for the near future. In addition the software will be integrated into the mechanism theory course at Aachen University.

## References

1. DE 10 2006 051 096.8 Kompakt bauende schwenkbare Anhängerkupplung, TOW-COP, Anmelder: RWTH Aachen, 2006.
2. Kerle, K., Pittschellis, R., Corves, B., Einführung in die Getriebelehre, Teubner Verlag, Wiesbaden, 2007.
3. Vorlesungsskript Getriebetechnik I, Corves, B., Institut für Getriebetechnik und Maschinendynamik, 2004.
4. Shreiner, D.; u.a.: OpenGL. Programming Guide. 5. Auflage. Upper Saddle River, NJ [u.a.]: Addison-Wesley, 2006.
5. EP 1586470, Anhängerkupplung, WESTFALIA AUTOMOTIVE GMBH & CO, 2005.
6. EP 1586471, Anhängerkupplung, WESTFALIA AUTOMOTIVE GMBH & CO, 2005.
7. DE 1584499, Anhängerkupplung, WESTFALIA AUTOMOTIVE GMBH & CO, 2005.
8. DE 198 26 618, Anhängerkupplung, Rocca, P., 1998.
9. DE 199 44 264, Anhängerkupplung mit axialem Verfahrenweg, Jaeger Cartronix GmbH, 1999.
10. DE 100 04 523, Anhängerkupplung, FAC Frank Abels Consulting & Technology Gesellschaft mbH, 2001.
11. DIN 74058, Kupplungskugel, Maße, Freiräume, Beuth Verlag Berlin, 1988.
12. ISO 3853, Road Vehicles – Towing Vehicle Coupling Device to Tow Caravans or Light Trailers – Mechanical Strength Test, International Organization for Standardization, 1994.

# Elastic and Safety Clutch with Radial Disposed Elastic Lamellas

Ioan Stroe

**Abstract** The paper presents the constructive solution of a new type of clutch. The clutch presented is an elastic and safety clutch with metallic intermediate elements. There are also presented the simple function of the clutch, the operating principle and its specific characteristics. The most combined couplings, in the technical literature, are obtained by the connection of the elastic clutches with safety clutches. The paper presents a new type of clutch named “Elastic and Safety Clutch”, that can accomplish the functions of the elastic clutches and those of the safety clutches, but that is not a combined clutch.

**Keywords** Clutches · Elastic · Safety · Simple function

## Introduction

A condition imposed to the elastic clutches is that, at the breakage of an element, the clutch will not fail immediately. If there is only an elastic element, the total breakage of the clutch has to be inferred, in case of partial fractures or the fissures. Another condition imposed to elastic clutches is that the elastic elements can rapidly be destroyed, to be easily replaced – if it is possible without the clutch disassembling or without the axial displacement of the axle stubs.

The paper presents the constructive solution of a new type of clutch. The presented product is an elastic and safety clutch with metallic intermediate elements. There are also presented the simple function of the clutch, the operating principle and its specific characteristics. The most combined clutches, in the technical literature, are obtained by the connection of the elastic clutches with safety clutches.

The paper presents a new product type named “Elastic and Safety Clutch”, that can accomplish the functions of the elastic and those of the safety clutches, but that

---

I. Stroe (✉)

Department Design of Products and Robotics, Faculty of Technologic Engineering University “Transylvania” of Brasov, B-dul. Eroilor nr. 29, 500036 Brasov, Romania  
e-mail: stroei@unitbv.ro

is not a combined clutch [3, 4]. The relative rotation angle between the two semi-clutches depends on the number of plate spring packet. The strict systematisation of the existent clutches, as well the simple functions' combinations lead to new types of clutches.

## The Structural Scheme of the Elastic and Safety Clutch with Lamellar Bows Radial

Figure 1 presents the structural schemes of the elastic and safety clutch; this clutch is generated from a plane mechanism with degenerate cam and degenerate follower [3, 4].

The clutch has in its structure a cam which is degenerate in an element with multiples lamellar bows, radially disposed (Fig. 1) depending on the torque moment that must be transmitted; the followers are degenerated in multiple roles 2, equiangular disposed [3, 4].

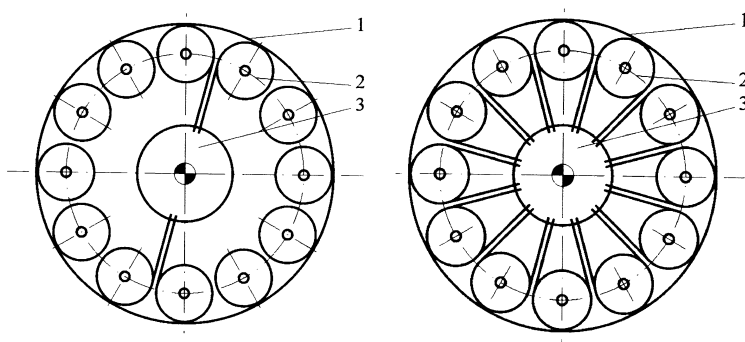


**Fig. 1** The structural scheme of the clutch

## Construction of the Clutch

Starting from the structural schemes and from the representative functions and properties, of the elastic and safety clutch, the next criterions of constructive generation can be formulated:

- the clutch must absorb radial and angular tilts;
- the relative movement between the semi clutches, as well as the releasing must be made without shocks;
- the clutch must have a reduce rigidity; it is suggested a characteristic  $M_t(\varphi)$  with a rising inclination and a big damping capacity;
- the elasticity of the clutch could be modified, by changing or adding constructive elastic elements;



- when the clutch is turning around, big axial forces doesn't appear;
- the clutch must not brake down when an elastic element is destroyed;
- the elastic constructive elements, that can be destroyed fast, must be fastly replace; if it's possible without demount the clutch;
- the changing of the rotation sense must be permitted without duty cycle;
- for the safety enlargement in running the component elements of the clutch mustn't have protuberances.

Baysis on these criterions, for each structural representative scheme, there is generated one constructive variant. One of these schemes is succinctly describe, from constructive and running point of view.

In Fig. 2 is presented the constructive shape of the elastic and safety clutch with lamellar bows – radially disposed. The clutch belongs to the category of derivate clutch from a mechanism with degenerate cam and degenerate follower. The connection between the two semi clutches 1 and 2 is realised with a package of lamellar bows radially disposed 4. The bows have one rigid butt fixed, with the prisms 5, close with screws 7; the other butt is free and introduced in box realised by the disposing of the rolls 3. The hat 6 closes and seals the clutch and the disk plate 8, with the board mountings; cover the fixing butts of the rolls.

At the outrunning of the limit torque moment, which can be transmitted by the clutch, between the semi-clutches appears a relative rotation movement, that permits the load-declutching of the mechanic transmission.

The elastic and safety clutches are characterised by a variable rigidity (nonlinear characteristic), Fig. 3 – relation (1); the security condition of the mechanic transmission is presented by relation (2), [1]:

$$k(\varphi) = \frac{dMt(\varphi)}{d\varphi} \quad (1)$$

$$M_{t \lim}(1 + \Delta) \leq M_{t \max a} \quad (2)$$

where:

$k(\varphi)$  – represents the tangent to the curve of the torsion moment, who is written depending on the relative rotation;  $\varphi$  – the relative rotation angle, between the semi-clutches;  $Mt(\varphi)$  – the torsion moment corresponding to the clutch deformation with the angle  $\varphi$ ;  $M_{t \lim}$  – the torsion moment when the uncoupling produces or ends;  $M_{t \max a}$  – the maximum torsion moment admitted by the strength of the most weak clutch element;  $\Delta$  – the relative error reset inputs in function of the clutch [1, 4].

The torque moment transmitted by the clutch is given by relation (3).

$$M_{t(\varphi)} = \frac{2nz(R + C)EI_z}{C^2}(\alpha + \varphi_{\max}) \quad (3)$$

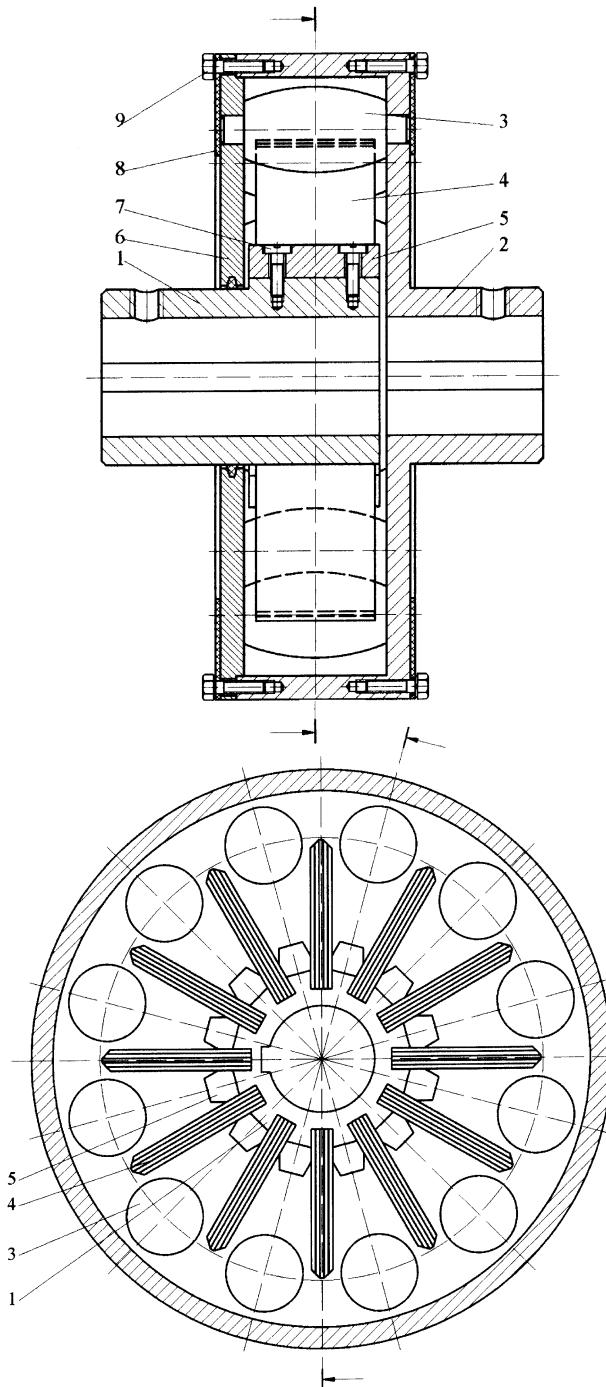
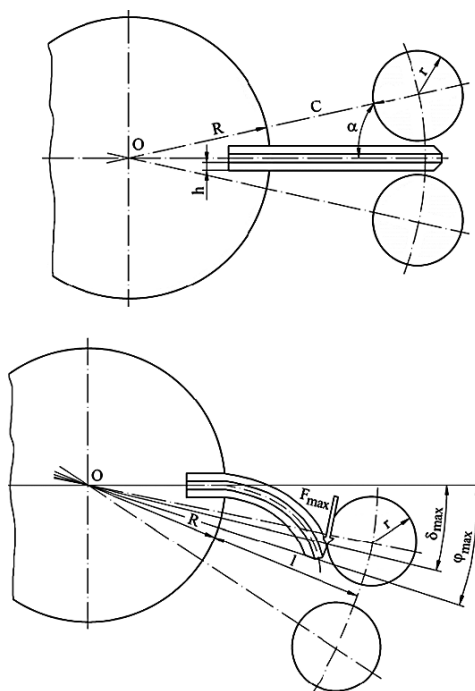


Fig. 2 The design of the elastic and safety clutch



**Fig. 3** The elastic and safety clutch design scheme



**Fig. 4** The picture elastic and safety clutch

where:  $n$  – the number of lamellas package;  $z$  – the number of the elastic lamellas in the package;  $E$  – the longitudinal coefficient of elasticity;  $I_z$  – the inertia moment of the elastic lamellas.

In Fig. 4 is presented the photo of the elastic and safety clutch.

## Conclusion

The elastic and safety clutches with lamellar bows, which are radially disposed, are presenting the next advantages, [2, 4]:

- the clutches have a simple construction, reduced overall size dimension, chip price;
- the clutches ensure the compensation of axial, radial and angular deviation in relative large limits;
- the clutches ensure the relative movement between the semi-clutches, in function of the nature and of the disposing mode of the component elements; above the accepted limits, the elastic clutch becomes a safety one.

## References

1. Draghici, I. Calculul și construcția cuplajelor. Editura Tehnică, București, 1978.
2. Stroe, I., Eftimie, E. Cuplaje elastice și de siguranță. Editura Ecran Magazin, Brașov, 2001.
3. Stroe, I., Diaconescu, D. V. Proceeding of generated of elastic and safety clutches. Proceedings of the International Conference Integrated Engineering C2I 2005. Timisoara–Romania, pp. 99–100.
4. Stroe, I. Design Procedure of Elastic and Safety Clutche Using Cam Mechanisms. World Congress in Mechanism and Machine Science June 17–21 2007. Besancon–France.

# Computational Multi-Objective Optimization to Design Service Robots

Cristina Castejón, Giuseppe Carbone, Juan Carlos García Prada  
and Marco Ceccarelli

**Abstract** In this paper, a multi-objective optimization process is proposed in order to enhance the design of service robots. Main characteristics and peculiarities of service tasks are investigated in order to propose design criteria in the form of computationally efficient objective functions. Then, these design criteria are implemented in a multi-objective optimization algorithm in order to obtain optimal design solutions for service robots. The proposed procedure has been applied to a robotic arm for service tasks that is composed of two modules having altogether four degrees of freedom (dofs).

**Keywords** Robot design · Service robots · Optimal design

## Introduction

In the last few years, service robots have attracted interest of researchers and manufacturers in a wide range of applications including professional use (servicing humans environment) or personal/domestic use (directly servicing of humans) [1]. The close interaction among service robots and humans makes not advisable to use a conventional approach for their design. Some researchers suggest different important aspects to be optimised in order to design a service robot such as its dexterity in the human environment [2], a lightweight design, in order to prevent serious injuries to human beings but also to the robot integrity [3], the stiffness, in order to have a good accuracy with a lightweight design as proposed [4, 5]. On the other hand, power consumption and path planning strategies should be taken into account for improving the autonomy and flexibility as proposed for example in [6, 7].

Optimising a robot with respect to one of the above-mentioned design criteria usually produces a design that is not optimal with respect to other design criteria. A possible solution for overcoming this limit can be the implementation of a

---

C. Castejón (✉)  
MAQLAB Group, Mechanical Dept. Carlos III University, Av. De la Universidad 30,  
28911 Madrid, Spain  
e-mail: castejon@ing.uc3m.es

multi-objective design approach that can take into account several design criteria at the same time [8]. Therefore, in this paper a multi-objective design procedure is proposed specifically for service robots. The proposed procedure is applied to a four-dofs robotic arm for service tasks in order to show feasibility and effectiveness of the proposed design approach.

## Basic Optimization Problem Formulation

The design process for a service robot should take into account simultaneously several design criteria, since each of them can provide contradictory results. Therefore, the design process can be conveniently conceived as multi-objective optimisation problem in order to consider all the design criteria at same time. Thus, the optimum design of manipulators can be formulated with the minimax algorithm in the form

$$\min_{\mathbf{X}} [\mathbf{F}(\mathbf{X})] = \min_{\mathbf{X}} \left\{ \max_{i=1, \dots, N} [w_i f_i(\mathbf{X})] \right\} \quad (1)$$

subjected to;

$$\mathbf{G}(\mathbf{X}) < 0 \quad (2)$$

$$\mathbf{H}(\mathbf{X}) = 0 \quad (3)$$

where min is the operator for calculating the minimum of a vector function  $\mathbf{F}(\mathbf{X})$ ; similarly max determines the maximum value among the  $N$  functions  $[w_i f_i(\mathbf{X})]$  at each iteration;  $\mathbf{G}(\mathbf{X})$  is the vector of constraint functions that describes limiting conditions, and  $\mathbf{H}(\mathbf{X})$  is the vector of constraint functions that describes design prescriptions;  $\mathbf{X}$  is the vector of design variables;  $w_i$  is a weighting factor for the  $i$ -th objective function.

The proposed optimization formulation with min[max[.]] procedure is based on the objective function  $\mathbf{F}(\mathbf{X})$  by choosing at each iteration the worst-case value among all the scalar objective functions for minimizing it in the next iteration, as outlined in [9]. In particular, the worst-case value is selected in Eq. (1) at each iteration as an objective function with maximum value among the  $N$  considered objective functions. This approach for solving multi-objective problems with several objective functions and complex tradeoffs among them is known as “minimax method”. Additionally, it is worth to note that the proposed scalar objective functions  $f_i(\mathbf{X})$  have been formulated to be dimensionless. Moreover, weighting factors  $w_i$  (with  $i = 1, \dots, N$ ) can be properly used to emphasize one aspect over the other as a designer’s guide. In addition, they have been used in order to scale all the objective functions. In particular, weighting factors  $w_i$  are chosen so that each product  $w_i f_i(\mathbf{X})$  is equal to one for an initial guess of a design case. The above-mentioned conditions on the objective functions can be written in the form

$$\sum_{i=1}^N (w_i f_i)_0 = N \quad (4)$$

$$N (w_i f_i)_0 = N \quad (5)$$

where the subscript 0 indicates that the values are computed at an initial guess of the design case. Bigger/lower weighting factors can be chosen in order to increase/reduce the significance of an optimal criterion with respect to others.

There is a wide range of possible solving techniques for Eq. (1). Indeed, a solving technique can be selected among the many available, even in commercial software packages, by looking at a proper fit and/or possible adjustments of the formulation of the objective function to the optimal design problem in terms of number of unknowns, non-linearity type, and involved computations for the optimality criteria and constraints. On the other hand, the formulation and computations for the optimality criteria and design constraints can be conceived and performed by looking also at the peculiarity of a chosen numerical solving technique.

## Numerical Procedure

The first step in the optimisation process consists of selecting the design variables, which could be, for example, geometrical robot properties such as robot link lengths or/and areas. The variables will be included in the vector  $\mathbf{X}$  for Eq. (1). Successively, robot constraints, and upper and lower limits of design variables must be identified in order to reduce the computational cost. In addition, a suitable initial guess solution must be determined. In the work proposed in this paper, the MATLAB toolbox minimax algorithm has been selected as numerical technique to solve the formulated optimisation problem. In this process, preliminary data on the kinematics and physical properties of the robot are needed in order to obtain computationally efficient expressions for the objective functions.

On the other hand, the numerical minimax technique minimizes the worst-case value of a set of multivariable functions, starting at an initial estimate (vector  $\mathbf{X}_0$ ). The minimax technique uses SQP (Sequential Quadratic Programming) to choose a merit function for a line search [10].

## Optimality Criteria for Service Robots

A service robot with manipulative skills should substitute/help human beings in manipulative operations. Therefore, basic characteristics should be referred to human manipulation performance that should be considered as benchmark. A well-trained person is usually characterized for manipulation purpose mainly in terms of arm mobility, positioning skill, arm power consumption, movement velocity, fatigue limits, and safety. Similarly, a robotic arm to be used in service robotics should be designed

and selected for manipulative tasks by looking mainly at workspace, path planning, lightweight design, power consumption efficiency, stiffness, accuracy, and safety performances. Therefore, it is quite reasonable to consider all these aspects together as design criteria.

## Optimality Criteria

### *Workspace*

Position and orientation workspaces are among the most important kinematics properties of service robots, even by practical viewpoint since service robots should share the operation workspace with humans. In order to evaluate the robot workspace as objective function to optimise in the robot design process three aspects should be considered:

- Robot reach. A reasonable and computationally efficient expression of reach performance of a service robot can be given by the following expression

$$f_1(X) = |1 - (R_{\text{robot}}/R_{\text{human}})| \quad (6)$$

in which  $R_{\text{human}}$  stands for the maximum reach of the human arm and  $\|$  stands for absolute value.

- Workspace (WS). The WS can be considered as a suitable design criterion and can be computed by means of a kinematic model of a robot for all the feasible configurations of the actuators. In case of SIDEMAR prototype, due to its configuration, orientation WS has no sense, so position workspace volume performance will be given by

$$f_2(X) = |1 - (V_{\text{pos}}/V_{\text{pos\_max}})| \quad (7)$$

in which  $V_{\text{pos\_max}}$  stands for a maximum reference position WS volume that can be considered as equal to the average workspace volume for a human arm. Information about the calculation of the volume can be found in [10].

- Path planning. The path position of a serial robot is specified in terms of the end-effector position in the Cartesian space. In order to determine a path of the end-effector from a start point to a goal point different trajectories can be performed by the actions of actuators. Path planning optimisation can be carried out by considering the optimal travelling time, which takes the robot to run a trajectory that is defined by two points in Cartesian coordinates. Thus, one can write

$$f_4(X) = |1 - (t_{\text{path}}/t_{\text{straight}})| \quad (8)$$

where  $t_{\text{path}}$  is the time that takes the robot to run the trajectory and  $t_{\text{straight}}$  is the time that the robot will take to run a straight line trajectory.



### ***Lightweight Design***

A service robot should have a lightweight structure even for safety reasons since it interacts with human beings. A large mass of the links produces high inertias that can be the source for injuries to human beings. In addition, the larger is the mass of links the bigger will be the size, power consumption and cost of actuators. Thus, a reasonable and computationally efficient expression of the lightweight design criterion can be given as referring to mass characteristics in the form

$$f_5(\mathbf{X}) = \left| 1 - \frac{M_T}{M_d} \right| \quad (9)$$

where  $M_T$  is the overall mass of a robot and  $M_d$  is the desired overall mass of the same robot than can be the minimum possible value.

### ***Stiffness***

The previous optimal criteria tries to reduce the weight of motors and links. Nevertheless, if links are very thin and lightweight they cannot be considered rigid as in the case of massive industrial robots. But, if they are not enough rigid, their accuracy will be strongly affected by compliant displacements. Therefore, it is necessary to consider the stiffness behaviour of a service robot in order to have good accuracy performance with a light as possible design. A reasonable and computationally efficient expression of the stiffness criterion can be given by [11].

$$f(\mathbf{X}) = 1 - (|\Delta S_{\max}|/|\Delta S_d|) \quad (10)$$

where  $\Delta S_{\max}$  and  $\Delta S_d$  are the maximum and design compliant displacements along X, Y, and Z-axes, respectively. Thus, Eq. (10) can be used to write objective functions  $f_5$ ,  $f_6$  and  $f_7$ .

### ***Safety***

Risks that are derived from a possible collision and subsequent human injuries should be reduced at early design stage yet. In particular, the kinetic energy should be minimal for links and components that could collide with humans while sharing human environment and/or during human–robot interaction. Furthermore, a reduction of the weight and inertia of a robot can improve its inherent safety characteristics since it implies a reduction the effective impedance of the robot as proposed, for example, in [11]. However, reduction of collision effects has been widely exploited in the field of car safety. In particular, crash tests are widely used since several years.

Then, crash test results are used for assessing car safety by means of several criteria, for example, the Head Injury Criterion (HIC) [12]. Based on the above-mentioned considerations one can define an objective function related to the safety issue as

$$f_9 = 1 - (\text{HIC}/\text{HIC}_{sd}) \quad (11)$$

## Constraints

The minimization of the objective function in Eq. (6) gives results that are as close as possible to human arm in terms of maximum reach. Nevertheless, each link length of a service robot cannot be smaller or greater than a given value. The upper and lower bound of link lengths are usually given by manufacturing constraints that can be expressed as

$$L_i - L_{i\max} < 0 \quad (12)$$

$$L_{i\min} - L_i < 0 \quad (13)$$

where  $L_i$  is the link length and  $L_{i\min}$ ,  $L_{i\max}$  are the maximum and minimum design lengths.

On the other hand, one should note that mass of the links can be easily related with their volumes and density. Thus, the minimization process given by Eq. (11) will try to reduce link lengths and cross section sizes. Nevertheless, a constraint should be added in the form

$$A_i - A_{i\min} < 0 \quad (14)$$

where  $A_i$  is the cross section area of  $i$ -th link and  $A_{i\min}$  is the minimum acceptable cross section area for  $i$ -th link. The constraints given by Eq. (14) are needed for obtaining cross sections of links over a minimum area whose value depends on manufacturing constraints and strength limits.

## Numerical Results

The proposed optimisation formulation has been tested as referring to a robotic arm with two 2R modules SIDEMAR [13]. The testing robot has four revolute joints as shown in Fig. 1, as referring to the prototype.

The link lengths  $L_i$ , equivalent cross-section areas  $A_i$  has been chosen as design parameters for the optimisation design problem. An equivalent cross-section area is obtained as sum of link cross-section areas. Links are assumed to have cylindrical shape. Therefore, one can write

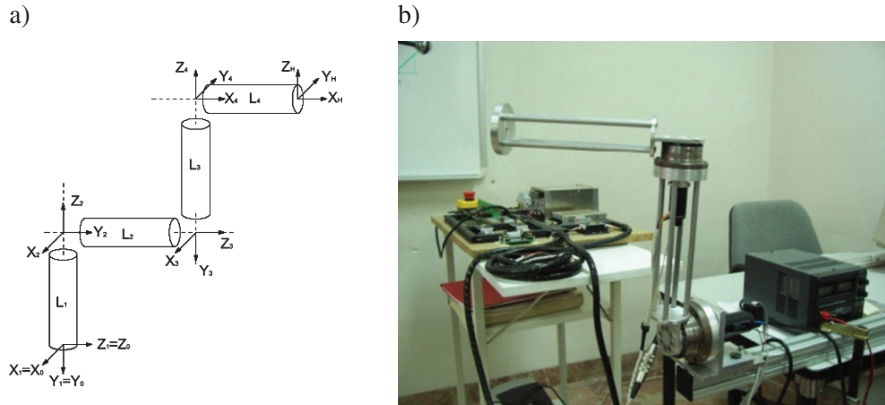


Fig. 1 4R-SIDEMAR: (a) a 3D model; (b) a prototype of a 2R module

$$A_i = n_{bi} \pi \left( \frac{d_i}{2} \right)^2 \tag{15}$$

where  $n_{bi}$  is the number of the link bars and  $d_i$  is the  $i$ -th diameter.

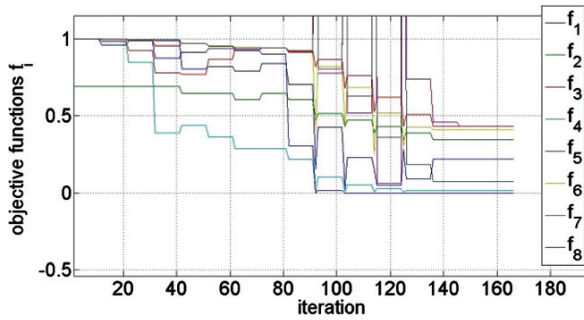
The proposed optimality criteria for 4R SIDEMAR has been implemented using MATLAB<sup>®</sup> optimization toolbox. The numerical procedure takes less than 200 iterations to converge to an optimum solution whose parameters are reported in Table 1.

Figure 2 reports the evolution of the objective functions in the optimisation process. In particular, one can note that the evolution of the objective functions converges to an optimal solution.

The obtained optimal solution gives an increase of the first link length and a reduction of the other lengths. This optimal value let increase the reach and workspace volume without put at risk the accuracy in the movements as can be seen in Table 2 where, design characteristics for the optimum solution are reported. On the other hand, as can be seen in the same table, an important reduction of the equivalent areas is computed for the optimal design as a result that reduces the robot mass three times with respect to the initial design (see Table 2). Summarizing, the numerical example gives an optimal design solution for the SIDEMAR 4R architecture as an illustrative practical example of the soundness and efficiency of the proposed multi-objective optimisation design procedure.

Table 1 Optimal design parameters for 4R-SIDEMAR design

	L1 (mm)	L2 (mm)	L3 (mm)	L4 (mm)	A1 (cm <sup>2</sup> )	A2 (cm <sup>2</sup> )	A3 (cm <sup>2</sup> )	A4 (cm <sup>2</sup> )	F(X)
Initial Guess	221.0	202.2	221.0	202.2	28.00	28.00	28.00	28.00	1.0000
Optimal Value	500.0	388.2	100.0	115.6	0.13	0.13	1.01	1.53	0.2426



**Fig. 2** Evolution of the optimization functions versus number of iterations for the 4R-SIDEMAR optimal design

**Table 2** Design characteristics of optimum solution

	$R_{\text{Robot}}$ (mm)	$V_{\text{pos}}$ ( $\text{m}^3$ )	$t_{\text{path}}$ (s)	$M_{\text{T}}$ (Kg)	$\Delta X_{\text{Max}}$ (mm)	$\Delta Y_{\text{Max}}$ (mm)	$\Delta Z_{\text{Max}}$ (mm)	HIC
Initial Guess	599.1	0.0030	0.91	11.06	$5.7 \cdot 10^{-5}$	$6.3 \cdot 10^{-6}$	$5.2 \cdot 10^{-5}$	7246
Optimal Value	783.4	0.0040	0.40	4.70	$1.4 \cdot 10^{-3}$	$5.9 \cdot 10^{-4}$	$1.4 \cdot 10^{-3}$	0.3388

## Conclusion

In this paper, the methodology to compute a multi-objective optimization problem has been addressed. The minimax algorithm has been chosen as a numerical procedure. This algorithm can be programmed with commercial software packages such as MATLAB. On the other hand main optimal design criteria for service robots have been proposed. These design criteria have been expressed in a mathematical form as objective functions in a multi-objective optimisation design algorithm. The proposed procedure has been applied successfully to SIDEMAR design for service robots. Numerical results of the optimisation process for SIDEMAR arm show the soundness and efficiency of the proposed design procedure.

## References

1. "World's greatest android projects webpage", <http://www.androidworld.com> (March, 2008, last visited).
2. Meng Q., Lee M.H. (2006), Design issues for assistive robotics for the elderly, *Advanced Engineering Informatics*, Vol. 20, pp. 171–186.
3. Gosselin C.M. (1992), The optimum design of robotic manipulators using dexterity indices, *Robotics and Autonomous Systems*, Vol. 9, pp. 213–226.
4. Blanco D., Castejón C., Kadhim S., Moreno L. (2005), *Predesign of an Anthropomorphic Lightweight Manipulator*, 8th Int. Conf. on Climbing and Walking Robots Clawar'05, London.
5. Gao F., Liu X.J., Jin S.L. (2000), Optimum design of 3-dof spherical parallel manipulators with respect to the conditioning and stiffness indices, *Mechanism and Machine Theory*, Vol. 35, N. 9.
6. Zinn M., Khatib O., Roth B., Salisbury J.K. (2004), *Playing it safe*, *IEEE Robotics and Automation Magazine*.

7. Saramago S.F.P., Ceccarelli M. (2004), Effect of numerical parameters on a path planning of robots taking into account actuating energy, *Mechanism and Machine Theory*, Vol. 39, N. 3, pp. 247–270.
8. Ceccarelli M., Carbone G., Ottaviano E. (2005), Multi criteria optimum design of manipulators, *Bullettin of the Polish Academy of Sciences, Technical Sciences*, Vol. 53, N. 1, pp. 9–18.
9. Grace A. (1992), *Optimization Toolbox User's Guide*, The Matlab Works Inc.
10. Castejón C., Carbone G., García-Prada J.C., Ceccarelli M., (2008), A multiobjective optimization of a robotic arm for service tasks. Paper Submitted to *Mechanics Based Design of Structures and Machines*.
11. Carbone G., Lim H.O., Takahashi A., Ceccarelli M. (2003), Optimum Design of a New Humanoid Leg by Using Stiffness Analysis, 12th Int. Workshop on Robotics in Alpe-Andria-Danube Region RAAD 2003, Cassino, paper 045RAAD03.
12. Snyder R.G. (1970), State-of-the-Art – Human Impact Tolerances, SAE 700398, Int. Automobile Safety Conference Compendium.
13. Castejón C., Giménez A., Jardón A., Rubio H., García-Prada, J.C., Balaguer C. (2005), Integrated system of assisted mechatronic design for oriented computer to automatic optimising of structure of service robots (SIDEMAR), 8th Int. Conf. on Climbing and Walking Robots Clawar'05, London.

# An Optimal Design for a New Underactuated Finger Mechanism

Shuangji Yao, Marco Ceccarelli, Giuseppe Carbone and Zhen Lu

**Abstract** In this paper, design problems and requirements for underactuated mechanisms are discussed as related to robotic fingers. Performance characteristics and optimality criteria are analyzed with the aim to formulate a general design algorithm as based on a suitable multi-objective optimization problem. An example of underactuated finger is illustrated as applied to an improvement of LARM Hand with the aim to show the practical feasibility of the proposed concepts and computations.

**Keywords** Underactuated mechanisms · Design · Robotic fingers

## Introduction

Many researchers have studied of robotic hands and fingers. Underactuated finger mechanisms have been also invested to obtain finger with a reduced number of DOFs. A general static model for underactuated fingers is provided in [1] to analyze their behaviors, kinetostatics and grasp stability. In [2] a design of the finger is discussed as based on underactuated linkage mechanism and coupling linkage. A design of compact and bio-mimetic mechanical fingers with contact aided compliant mechanisms has been proposed in [3]. An approach is reported in [4] for computing optimal force distribution for robot hand system.

Linkage-based mechanisms are usually preferred for applications where large grasping forces are requested. Since the early 1990s at LARM, a series of 1-DOF fingers have been developed and prototypes have been built, as reported in [5–8]. A self-adaptation and passive compliance finger has been also proposed in [9]. In this paper, design problems and requirements for underactuated mechanisms are discussed as related to robotic fingers. Particular design considerations are proposed for finger mechanisms. Optimality criteria have been formulated both for evaluation and design purposes. The results of a multi-objective optimality design procedure are presented in this paper for a specific case.

---

S. Yao (✉)

School of Automation Science and Electrical Engineering, Beihang University, Beijing, P.R. China  
e-mail: buaayaoshuangji@163.com

## Underactuated Finger Mechanisms

Three possible approaches for achieving underactuated grasp are discussed in [6]. Namely, one can use flexible links, passive joints or underactuated mechanisms.

Underactuated mechanisms usually have a very large size. Thus, it is difficult to keep them within the finger body.

Flexible links can be used to give a certain extra mobility to mechanism configuration. They can be obtained by suitable design and choice of flexible materials in some link elements of a finger mechanism. Figure 1 shows an example of a solution with flexible links. The deformation of links can be achieved by an actuator input, while links will be stressed by reaction forces. But, the extra motion of flexible elements is very limited.

Passive elements can be used to constrain the kinematics of the finger, such as torsional springs and linear springs. A new type of underactuated finger that is based on linkage mechanism with passive elements has been studied at LARM. Feasible design schemes are shown in Fig. 2. Those kinematic designs for a new underactuated finger are based on four-bar mechanisms with torsional springs and linear springs in different phalanges. They can perform self-adaptation to objects shape and size. Moreover, such underactuated mechanism can remain fully embedded in the finger body. Nevertheless, this result can be only obtained through a careful dimensional synthesis of the mechanism. This dimensional synthesis can be also achieved via a multi-objective optimisation.

**Fig. 1** A design solution for underactuated LARM finger with flexible links

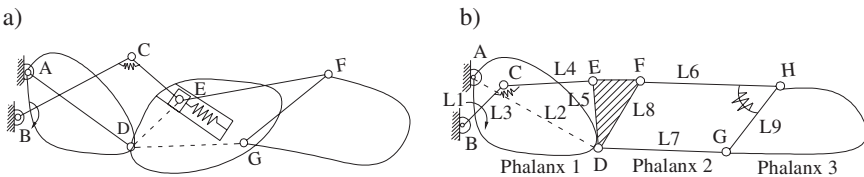
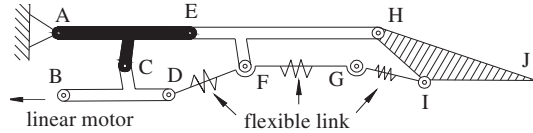


**Fig. 2** Kinematic design schemes for a new linkage underactuated finger mechanism

## A Formulation for Multi-Objective Optimum Design

A design for an anthropomorphic finger must fulfill basic features as human-like contact force, actuation efficiency, grasping capability, underactuation design, compact size, and transmission efficiency.

A human-like finger mechanism should ensure contact forces by three phalanxes according to a human grasping in a final configuration. Characteristics of human grasping can be obtained from human grasping experiments.  $R_{hi}$  is the contact force by each phalanx of a human grasp in a static configuration.  $R_{h2}$  and  $R_{h3}$  can be functions of  $R_{h1}$ . The ratios of contact forces can be described as

$$k_{R, hi} = R_{hi}/R_{h1} \quad (i = 2, 3) \quad (1)$$

in which the coefficients  $k_{R, hi}$  ( $i = 2, 3$ ) are related to characteristic curves for the contact forces.

The contact forces of an underactuated finger mechanism can be described as  $R_{mi}$  ( $i = 1, 2, 3$ ) on each phalanx. The ratio  $k_{R, mi}$  ( $i = 2, 3$ ) is the contact force by phalanx  $i$  ( $i = 2, 3$ ) with respect to the first one, in the form

$$k_{R, mi} = R_i/R_1 \quad (i = 2, 3) \quad (2)$$

Therefore, a criterion for an optimum finger design having human-like grasp forces can be formulated as a function in the form

$$\Delta k_R = \sum |k_{R,hi} - k_{R,mi}| \quad (i = 2, 3) \quad (3)$$

Actuator torque in grasp operation is another aspect to achieve for grasping efficiency. Thus, the maximum input torque  $\tau_{in}$  should be optimized in a design process. The relationship between external force  $\mathbf{f}_e$  on each phalanx and its driving force  $\tau$  can be written as

$$\boldsymbol{\tau} = \mathbf{J}^T \mathbf{f}_e \quad (4)$$

where  $\boldsymbol{\tau}$  is the vector of input torques of the system,  $\mathbf{J}$  is the Jacobian matrix of the proposed mechanism.  $\mathbf{f}_e$  is the vector of contact force. Since  $k_i$  are the coefficients of springs, the acting spring forces can be expressed as

$$\tau_{si} = k_i(\theta_{si} - \theta_{si0}) \quad (5)$$

By including Eq. (5) into Eq. (4), the relation between contact force and driving torque and spring coefficients can be computed as

$$\boldsymbol{\tau} = \mathbf{U} \mathbf{R}_i \quad (6)$$

where  $\boldsymbol{\tau}$  is the vector of torques given as  $[\tau_{in}, \tau_{si}(i = 1, \dots, n)]^T$ ;  $\mathbf{R}_i$  is the vector of contact forces  $[R_1, R_2, R_3]^T$ ;  $\mathbf{U}$  is a matrix containing elements of Jacobian matrix. Therefore, an optimality criterion for the actuator torque can be expressed as  $\min \|\boldsymbol{\tau}\|$  as expressed by Eq. (6).

Grasping capability refers to the size and weight of the object that can be grasped. The maximum dimension of a grasped cylinder is obtained by a condition of static



equilibrium of phalanx contact forces  $R_i$  balancing the object weight  $W$ . The formulation of contact forces and gravity force of object can be described as referring to a frame  $XY$  as

$$\sum R_i \cos(\theta_{pi}) + W = 0 \quad (7)$$

with  $\theta_{pi}$  as angle between  $R_i$  and  $X$ -axis. When the maximum torque  $\tau_{in}$  is obtained in Eq. (6), the optimal criterion of maximum grasped weight of the largest size can be expressed as

$$W_{\max} = \left| \tau_{\max} \left[ \sum U_i^{-1} \cos(\theta_{pi}) \right] \right| \quad (8)$$

$U_i$  is the  $i$ -th row of  $U$ . Friction has been neglected at the design stage since this condition is conservative both for static equilibrium of a grasp and for grasp tasks with low-friction objects. The maximum size  $D$  for a grasped object can be written as

$$D_{\max} = \sum |L_{pi} \cos(\theta_{pi})| + |\Delta X_p| \quad (9)$$

$$D = 2 \left[ \sum |L_{pi} \sin(\theta_{pi})| + \Delta X_p \tan(\theta_{p1}) \right] / [1 + \tan(\theta_{p1})] \quad (10)$$

where  $\Delta X_p$  and  $\Delta Y_p$  are the offsets of a finger frame with respect to palm frame along  $X$  and  $Y$ , respectively.

Springs should be addressed in the design process to consider the energy which is stored by springs for an underactuated grasp operation. The coefficients  $k_i$  can be obtained from Eq. (6) as

$$k_i = \sum U_{j,i} R_i \quad (11)$$

where  $U_{j,i}$  refer to entry at  $j$  row of  $i$  column of the matrix  $U$  in Eq. (6),  $R_i$  is the contact force of the  $i$ -th phalanx. Thus, the amount of energy which is stored in the springs can be formulated as

$$E_{\text{spring}} = 1/2 \sum k_i \Delta \theta_{si}^2 \quad (12)$$

$$\Delta \theta_i = \theta_{si} - \theta_{si0} \quad (13)$$

Thus, an optimality criterion for the springs design can be formulated by using Eq. (12) as  $\min E_{\text{spring}}$  which related to minimize the stored energy.

The compact size of a human finger can be obtained in a robotic finger by imposing size through an optimality criterion. The size  $L_h$  of human finger can be

evaluated as design reference for the finger mechanism size  $L_p$ , so that an optimality criterion for compact design can be expressed as

$$\Delta L = |L_h - L_p| \quad (14)$$

when the overall size is given as

$$L_h = \sum L_{hi}, \quad L_p = \sum L_{pi} \quad (i = 1, 2, 3) \quad (15)$$

for the human finger and robotic design, respectively.

In addition, the link proportion of the second and third phalanxes with respect to the first phalanx should be considered. The proportion of human phalanx  $k_{L, hi}$  and finger mechanism  $k_{L, pi}$  can be described as

$$k_{L, hi} = L_{hi}/L_{h1}, \quad k_{L, pi} = L_{pi}/L_{p1} \quad (i = 2, 3) \quad (16)$$

Thus, an additional optimality criterion for compact design can be expressed in terms of

$$\Delta k_{L, i} = |k_{L, hi} - k_{L, pi}| \quad (i = 2, 3) \quad (17)$$

Transmission efficiency in a finger mechanism should be also considered in a design process. A common rule in engineering practice is that a four-bar linkage should not be used in a range where the transmission angle is less than  $40^\circ$  or larger than  $130^\circ$ , [10].

As shown in Fig. 2b for example, the closure-equations of link polygons ABCED and DFHG can be expressed respectively as

$$\overline{AB} + \overline{BC} + \overline{CE} + \overline{ED} + \overline{DA} = \mathbf{0} \quad (18)$$

$$\overline{DF} + \overline{FH} + \overline{HG} + \overline{GD} = \mathbf{0} \quad (19)$$

The transmission angles can be expressed as the angles between the vectors  $\overline{BE}$  and  $\overline{DE}$  as

$$\lambda_{tr1} = \widehat{DE} - \widehat{BE}; \quad \lambda_{tr2} = \widehat{DE} - \widehat{CE}; \quad \lambda_{tr3} = \widehat{FH} - \widehat{HG} \quad (20)$$

It is worth notice that the choice of transmission angles  $\lambda_{tri}$  is also a function of  $\Delta k_R$  and  $\tau$ . Thus, the transmission angles can be considered as to fixed upper and lower boundary for optimality.

### A Case of Study

The scheme in Fig. 2b has been chosen for further design research at LARM. Figure 3 is a scheme with the design parameters. Referring to Fig. 3, link sizes of a first solution for the proposed finger mechanism are listed in Table 1. Initial values for coefficients of the springs have been determined as  $k_1 = k_2 = 7.7 \times 10^{-2}$  Nm/rad. The design parameters can be considered as angles of the links, and the coefficients of the springs, namely  $L_i, \alpha_i, \delta_i, \theta_i$ , for  $i = 1, 2, \dots, 10$ ;  $\theta_{s1}, s_2, k_1, k_2, c_1, c_2$ .

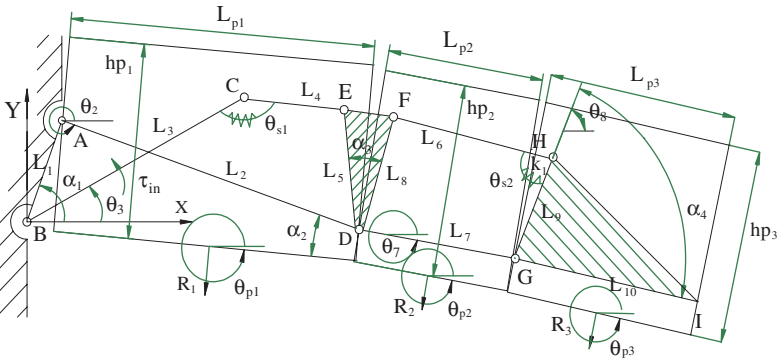


**Fig. 3** The design parameters and phalanx bodies for the underactuated mechanism in Fig. 2b

The above-mentioned evaluation criteria for mechanism design can be used in a multi-objective optimisation problem in the form

$$\min(\mathbf{F}(\mathbf{X})) \text{ subject to } \mathbf{G}(\mathbf{X}) \tag{21}$$

in which  $\mathbf{F}$  is a vector of objective functions as optimality criteria;  $\mathbf{X}$  is the vector of design parameters; and  $\mathbf{G}$  is a vector function of constraints as a limited boundary. The design problems can be numerically solved as outlined in the flowchart of Fig. 4 by using a numerical procedure in commercial software package of MATLAB.

**Table 1** Initial lengths and angle parameters for the underactuated LARM finger mechanism in Fig. 3 as initial guess

$L_i(\text{mm})$	1	2	3	4	5	6	7	8	9	10
Initial guess	11.2	66.5	12.0	51.4	17.8	37.1	33.1	14.3	13.0	41.0
Optimal Solution	7.8	61.1	16.2	54.4	16.8	33.7	35.0	30.0	17.1	23.2

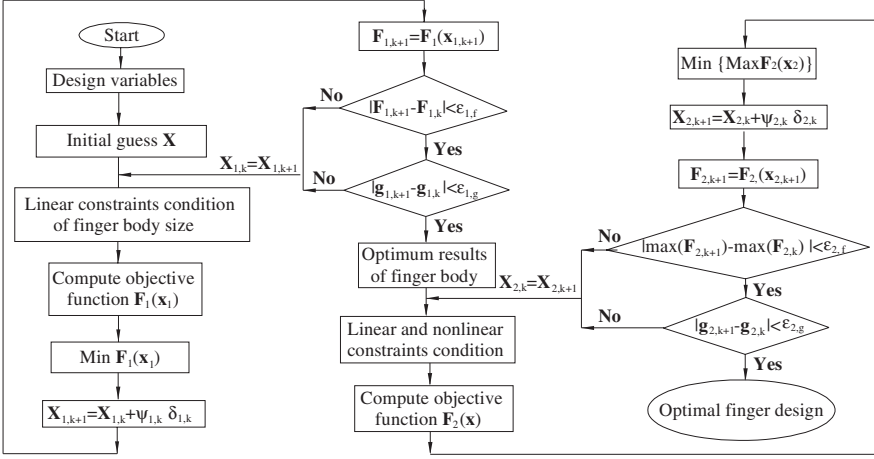


Fig. 4 A numerical procedure for the optimisation problems

### Numerical Results

The optimum design by using weighting factors  $w_i$  ( $i = 1, \dots, 4$ ) for underactuated finger in Fig. 3 can be formulated as

$$\mathbf{F}_1(\mathbf{x}) = w_1 f_1(x) + w_2 f_2(x); \mathbf{F}_2(\mathbf{x}) = w_3 f_3(x) + w_4 f_4(x) \quad (22)$$

subject to

$$g_1(\mathbf{x}) = L_i > 0 (i = 1, \dots, 10); g_2(\mathbf{x}) = 0 \leq \alpha_i \leq 180^\circ (i = 1, \dots, 4)$$

$$g_3(\mathbf{x}) = 0 \leq \theta_{si} \leq 180^\circ; g_4(\mathbf{x}) = 0 \leq \theta_3 \leq 120^\circ \quad (23)$$

$$g_5(\mathbf{x}) = 0.5\Delta K_R \leq \Delta K_R \leq 2\Delta K_R; g_6(\mathbf{x}) = 40^\circ < \lambda_{tri} < 130^\circ \quad (i = 1, \dots, 3)$$

with the objective function given by

$$f_1(\mathbf{x}) = \Delta L; f_2(\mathbf{x}) = k_{L,2} + \Delta k_{L,3}; f_3(\mathbf{x}) = \tau_{in}; f_4(\mathbf{x}) = E_{spring} \quad (24)$$

Two objective function are implemented as Eqs. (24) since computational efficiency in problem solving is obtained by considering combined criteria through suitable weighting factors whose values are given in general as function of designer's experience and task aims. In the numerical example we have chosen  $w_1 = w_2 = w_4 = 1, w_3 = 2$ .

For a numerical example, the data have been assumed as referred to Table 1 with  $h_{pi} = 20.0$  mm,  $\theta_{pi} = 0^\circ$  ( $i = 1, 2, 3$ ) and to a grasped cylindrical object with a diameter 60 mm. Results of an optimal solution are shown in Figs. 5 and 6 and are listed in the Tables 1, 2, and 3. An optimal solution is obtained after 81 iterations for  $F_1$  and 363 iterations for  $F_2$ , with total 168 s of CPU computation with standard PC Genuine Intel (T2050).

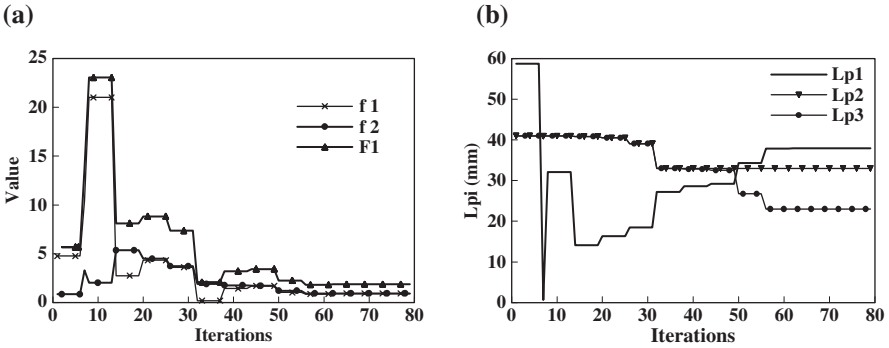


Fig. 5 Evolution of  $F_1$  optimization: (a) objective functions; (b) phalanx size

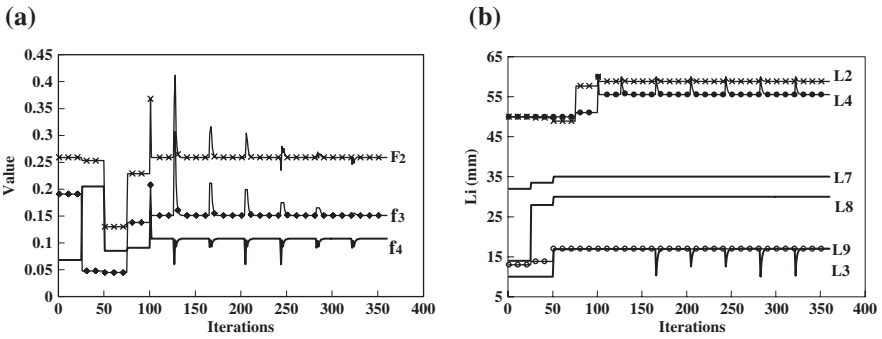


Fig. 6 Evolution of  $F_2$ : (a) objective function; (b) link lengths

Table 2 Design parameters of the computed optimal design for the underactuated finger mechanism in Fig. 3

Parameters	$L_{p1}$	$L_{p2}$	$L_{p3}$	$\alpha_1$	$\alpha_2$	$\alpha_3$	$\alpha_4$
Initial Guess	60.0	41.5	41.0	64.4	22.7	23.1	123.1
Optimal solution	37.9	33.1	23.2	78.7	62.8	25.5	76.4

**Table 3** Design parameters before and after optimality

Parameters	$\lambda_{tr1}/\lambda_{tr2}/\lambda_{tr3}$ (deg)	$k_1/k_2$ ( $10^{-2}$ Nm/rad)	$c_1/c_2$ (Nms/deg)	$h_{pi}/D$ (mm)	$\tau_{in}/E_{spring}$ (N/m)
Guess solution	140/153/85	0.210/0.008	0.25/0.25	20.0/89.8	0.19/0.07
Optimal solution	97/113/79	0.150/0.011	0.05/0.05	20.0/113.2	0.15/0.10

## Conclusion

In this paper we have presented design considerations for underactuated mechanisms of robotic fingers. The design problems have been formulated as a multi-objective optimization problem. The numerical procedure is characterized by formulations for optimality criteria. An example of optimality design has been reported as applied to an enhancement of the underactuated finger mechanisms for the LARM Hand.

**Acknowledgments** Part of this work has been developed within the project No. 27 of the Italy–China program 2006–2009 during a period of study of first author at LARM in 2007–2008 that has been supported by state scholarship program of China Scholarship Council (CSC).

## References

1. Birglen L. and Gosselin C. M., Grasp-state plane analysis of two-phalanx underactuated fingers, *Mechanism and Machine Theory*, Vol. 41, 2006, pp. 807–822.
2. Liu H., et al. The modular multisensory DLR-HIT-Hand, *Mechanism and Machine Theory*, Vol. 42, 2007, pp. 612–625.
3. Yong-Mo M., Bio-mimetic design of finger mechanism with contact aided compliant mechanism, *Mechanism and Machine Theory*, Vol. 42, 2007, pp. 600–611.
4. Al-Gallaf E., Multi-fingered robot hand optimal task force distribution neural inverse kinematics approach, *Robotics and Autonomous Systems*, Vol. 54, 2006, pp. 34–51.
5. LARM homepage. Available from: <http://webuser.unicas.it/webfarm/>, 2008.
6. Ceccarelli M., Tavolieri C., Lu Z. Design considerations for underactuated grasp with a one D.O.F. anthropomorphic finger mechanism, *Proc. of the 2006 IEEE/RSJ International Conference on Intelligent Robots and Systems (IROS 2006)*, Beijing, 2006, pp. 1611–1616.
7. Rodriguez N. E. N., Carbone G., Ceccarelli M., Optimal design of driving mechanism in a 1-DOF anthropomorphic finger, *Mechanism and Machine Theory*, Vol. 41, 2006, pp. 897–911.
8. Civitillo R. Design and experimental validation of an antropomorphic finger with one d.o.f., Master thesis, LARM, University of Cassino, 2001, (in Italian).
9. Licheng W., Carbone G., Ceccarelli M., Designing an underactuated mechanism for a 1 dof finger operation, *Mechanism and Machine Theory*. 2008, DOI 10.1016/j.mechmachtheory.2008.03.011.
10. John J. Uicker, Jr., *Theory of Machines and Mechanisms*, Oxford University Press, 2003.

# Synthesis of a Spatial Five-Link Mechanism with Two Degrees of Freedom According to the Given Laws of Motion

Nodar Davitashvili and Otar Gelashvili

**Abstract** In this work, we offer the synthesis of a RSSRR type spatial five-link mechanism with two degrees of freedom according to the given laws of motion. It is set the equation of a trajectory of the central connective hinge of connecting rods, which order, besides the sizes of links, depends on the value of gear ratio between input links taking into account their direction of motion and on the phase angle between input links. The methods of solution of the problem of synthesis of spatial five-link mechanisms by the given laws of motion are presented.

**Keywords** Spatial mechanism · Synthesis · Trajectory

## Introduction

Five-link hinged mechanisms with two degrees of freedom can accomplish complex given laws of motion. The distinguishing feature of these mechanisms is the possibility of change in the process of work of the trajectory of motion of the point of connecting rod in the space, on a sphere and on a plane, from the simple to the complex, with a change in angular velocities of input links and their initial positions, for constant lengths of links.

These circumstances are directly connected with selection of the lengths of output links of mechanisms and they predetermine the necessary conditions of creating compact, light mechanisms.

Solution of the problem on the positions of spatial mechanisms with several degrees of freedom and spherical five-link mechanism with two degrees of freedom is considered in the work of Ovakimov [1]. Solution of this problem is realized by the method of closed vector contour.

Questions of the kinematic study of a RCRCR type spatial mechanism are examined in the work of Duffy and Habib-Olahi [2]. Dual equations, received for

---

N. Davitashvili (✉)

Georgian Technical University, 77, M. Kostava St., 0175, Tbilisi, GA  
e-mail: nodav@geo.net.ge

determination of displacements for a spatial five-link mechanism, are used in the analysis of spherical five-, six- and seven-link mechanisms in the work of Duffy [3].

Recently appeared works with investigations of plane five-link hinged mechanisms with two degrees of freedom as parallel manipulators. In this connection it is necessary to note the works of Kemal Ider [4] and Zhou, Kwun-Lon Ting [5].

To the problems of study of hinged mechanisms with two degrees of freedom considerable attention was given by Georgian scientists, who carried out the in-depth analysis of mechanisms indicated. In this connection it is necessary to note the works of the author [6–11].

In this work it is set the equation of the trajectory of the connective center of connecting rods of output links of a RSSRR type spatial five-link mechanism with two degrees of freedom. The ways of solution of the problem of synthesis of a mechanism by use of the method of point interpolation are given.

### The Equation of a Trajectory of a Spatial Five-Link Mechanism

Consider spatial five-link hinged mechanism of general form *ABCDE* (Fig. 1) with two input links *AB* and *DE*, the laws of motion of which with respect to time *t* can be represented as follows

$$\varphi_2 = \varphi_2(t) \quad \text{and} \quad \varphi_5 = \varphi_5(t), \tag{1}$$

where

$$\varphi_2 = \alpha_0 + \alpha \quad \text{and} \quad \varphi_5 = \beta_0 + \beta.$$

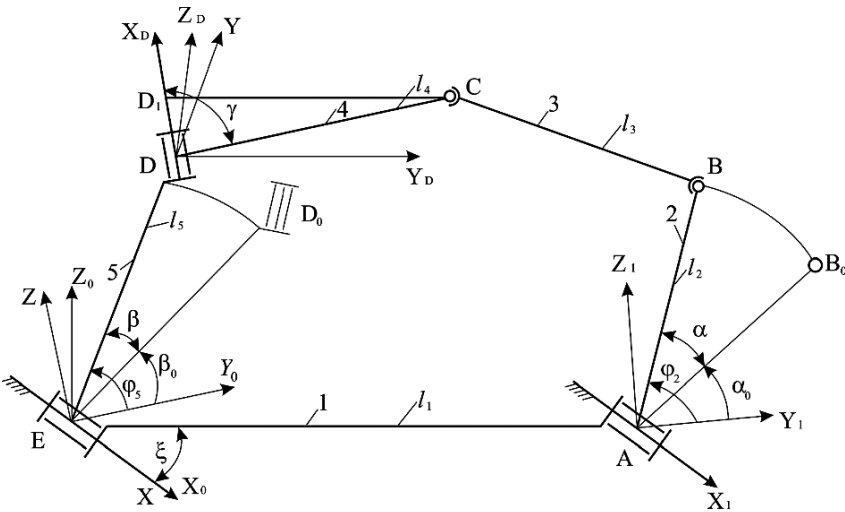


Fig. 1 A spatial five-link hinged mechanism of general form



Here  $\alpha_0$  and  $\beta_0$  are the angles determining initial positions of input links  $AB$  and  $DE$ ;  $\alpha$  and  $\beta$  – the variable angles, characterizing the motion of input links.

The kinematic dependence between input links is determined by gear ratio from link 5 to link 2, or vice versa. We have

$$u_{52} = \frac{\dot{\varphi}_5}{\dot{\varphi}_2} = \frac{\omega_5}{\omega_2} = \frac{\beta}{\alpha} = \pm \frac{p}{q}. \tag{2}$$

Not restricting the generality of the kinematic scheme assume that the longitudinal axes of cranks  $AB$  and  $DE$  are perpendicular to their axes of rotation.

The trajectory of the central connecting hinge  $C$  of connecting rods  $BC$  and  $DC$  lies on a circular surface of revolution with axes  $X_0$ . For setting a second equation of the trajectory of  $C$ , first it is necessary to establish functional dependence between input and output parameters of the mechanism. For this purpose we introduce notation:  $l_1, l_2, l_3, l_4, l_5$  – the lengths of links;  $\xi$  and  $\gamma$  – constructive angles;  $EX_0Y_0Z_0$  and  $AX_1Y_1Z_1$  – two right fixed coordinate systems connected to the supporting column;  $x_A = l_1 \cos \xi$ ;  $y_A = l_1 \sin \xi$ ;  $z_A = 0$  – the coordinates of point  $A$  in system  $EX_0Y_0Z_0$ ;  $EXYZ$  and  $DX_DY_DZ_D$  – moving coordinate systems.

The matrices of transformations of system  $DX_DY_DZ_D$  into system  $EXYZ$ ,  $EXYZ \rightarrow EX_0Y_0Z_0$ ,  $AX_1Y_1Z_1 \rightarrow EX_0Y_0Z_0$ , have the following form

$$\begin{pmatrix} 1 & 0 & 0 \\ 0 & \cos(\beta_0 + \beta) & \sin(\beta_0 + \beta) \\ 0 & -\sin(\beta_0 + \beta) & \cos(\beta_0 + \beta) \end{pmatrix}; \begin{pmatrix} a_{11} & a_{21} & a_{31} \\ a_{12} & a_{22} & a_{32} = 0 \\ a_{13} & a_{23} & a_{33} \end{pmatrix}; \begin{pmatrix} b_{11} & b_{21} & b_{31} \\ b_{12} & b_{22} & b_{32} = 0 \\ b_{13} & b_{23} & b_{33} \end{pmatrix}. \tag{3}$$

Point  $C$  lies on a sphere with center  $B$  and radius  $l_3$  and a circle with center  $D$  and radius  $l_4$ , besides, the circle is received by intersection of the sphere and a plane. Therefore the position of point  $C$  must be defined by three equations.

The equations of a sphere and a circle in initial system of coordinates  $EX_0Y_0Z_0$  after some transformations will have the form

$$x_C^2 + y_C^2 + z_C^2 + A_1x_C + A_2y_C + A_3z_C + A_4 = 0; \tag{4}$$

$$x_C^2 + y_C^2 + z_C^2 + B_1x_C + B_2y_C + B_3z_C + B_4 = 0, \tag{5}$$

where

$$A_1 = -2x_D = 0; A_2 = -2l_5 \cos(\beta_0 + \beta); A_3 = -2l_5 \sin(\beta_0 + \beta);$$

$$A_4 = l_5^2 - l_4^2; B_1 = -2[l_2(b_{12} \cos(\alpha_0 + \alpha) + b_{13} \sin(\alpha_0 + \alpha)) + l_1 \cos \xi];$$

$$B_2 = -2[l_2(b_{22} \cos(\alpha_0 + \alpha) + b_{23} \sin(\alpha_0 + \alpha)) + l_1 \sin \xi];$$

$$B_3 = -2b_{33}l_2 \sin(\alpha_0 + \alpha);$$

$$B_4 = l_1^2 + l_2^2 - l_3^2 + 2l_1l_2[\cos(\alpha_0 + \alpha)(b_{12} \cos \xi + b_{22} \sin \xi) + \sin(\alpha_0 + \alpha)(b_{13} \cos \xi + b_{23} \sin \xi)].$$

For setting third equation it is necessary that the coordinates of point  $C(x_C, y_C, z_C)$  satisfy the equation of a plane passing through point  $D_1$  parallel to plane  $Z_D D Y_D$ . By transformation of the equation of this plane  $x_C = l_4 \cos \gamma$  in system  $E X_0 Y_0 Z_0$  we have

$$c_1 x_C + c_2 y_C + c_3 z_C + c_4 = 0, \quad (6)$$

where

$$\begin{aligned} C_1 &= a_{11}; C_2 = a_{21} \cos(\beta_0 + \beta) - a_{31} \sin(\beta_0 + \beta); \\ C_3 &= a_{21} \sin(\beta_0 + \beta) + a_{31} \cos(\beta_0 + \beta); C_4 = -a_{21} l_5 - l_4 \cos \gamma. \end{aligned}$$

Let us eliminate angles  $\alpha$  and  $\beta$  from Eqs. (4), (5) and (6). By subtracting term-wise Eq. (6) from Eq. (5) we have

$$x_C^2 + y_C^2 + z_C^2 + (B_1 - C_1)x_C + (B_2 - C_2)y_C + (B_3 - C_3)z_C + (B_4 - C_4) = 0. \quad (6^*)$$

We introduce auxiliary angle  $\psi$ .

$$\psi = \frac{\alpha}{q} = \pm \frac{\beta}{p} \text{ and } \alpha = q\psi; \beta = \pm p\psi \quad (7)$$

Due to (7) from Eqs. (4) and (6\*) we receive

$$\begin{aligned} D_1 + D_2 \cos q\psi + D_3 \sin q\psi &= 0; \\ D_4 + D_5 \cos p\psi \pm D_6 \sin p\psi &= 0, \end{aligned} \quad (8)$$

where

$$\begin{aligned} D_1 &= x_C^2 + y_C^2 + z_C^2 - 2l_1(x_C \cos \xi + y_C \sin \xi) + l_1^2 + l_2^2 - l_3^2; \\ D_2 &= -2l_2[x_C(b_{12} \cos \alpha_0 + b_{13} \sin \alpha_0) + y_C(b_{22} \cos \alpha_0 + b_{23} \sin \alpha_0) + b_{33} z_C \sin \alpha_0] \\ &\quad + 2l_1 l_2 [\cos \alpha_0(b_{12} \cos \xi + b_{22} \sin \xi) + \sin \alpha_0(b_{13} \cos \xi + b_{23} \sin \xi)]; \\ D_3 &= 2l_2[x_C(b_{12} \sin \alpha_0 - b_{13} \cos \alpha_0) + y_C(b_{22} \sin \alpha_0 - b_{23} \cos \alpha_0) \\ &\quad - b_{33} z_C \cos \alpha_0] - 2l_1 l_2 [\sin \alpha_0(b_{12} \cos \xi + b_{22} \sin \xi) - \cos \alpha_0(b_{13} \cos \xi + b_{23} \sin \xi)]; \\ D_4 &= x_C^2 + y_C^2 + z_C^2 - a_{11} x_C + a_{21} l_5 + l_5^2 - l_4^2 + l_4 \cos \gamma; \\ D_5 &= y_C(-2l_5 \cos \beta_0 - a_{21} \cos \beta_0 + a_{21} \sin \beta_0) - z_C(2l_5 \sin \beta_0 + a_{31} \sin \beta_0 + a_{31} \cos \beta_0); \\ D_6 &= y_C[(2l_5 + a_{21}) \sin \beta_0 + a_{31} \cos \beta_0] - z_C[(2l_5 + a_{21}) \cos \beta_0 - a_{31} \sin \beta_0]. \end{aligned}$$

Let us eliminate  $\psi$  from system (8). Using well-known formulas of sine and cosine for multiple arcs and transforming the received equations, due to notations  $Z = \cos \psi$ ,  $\sin \psi = \sqrt{1 - Z^2}$ , we obtain

$$\begin{aligned}
 & B_{p+q-1}Z^{p+q-1} + B_{p+q-3}Z^{p+q-3} + B_{p+q-5}Z^{p+q-5} + \dots + B_{p-1}Z^{p-1} \\
 & + B_{p-3}Z^{p-3} + B_{p-5}Z^{p-5} + \dots + B_{q-1}Z^{q-1} + B_{q-3}Z^{q-3} \\
 & + B_{q-5}Z^{q-5} + \dots = 0,
 \end{aligned} \tag{9}$$

where

$$\begin{aligned}
 & B_{p+q-1} = D_2D_6S_1^pS_0^q \mp D_3D_5S_o^pS_1^q; \\
 & B_{p+q-3} = -D_2D_6(S_1^pS_2^q + S_3^pS_o^q) \pm D_3D_5(S_1^qS_2^p + S_3^qS_o^p); \\
 & B_{p+q-5} = D_2D_6(S_1^pS_4^q + S_3^pS_2^q + S_5^pS_o^q) \mp D_3D_5(S_1^qS_5^p + S_3^qS_2^p + S_5^qS_o^p); \\
 & \dots\dots\dots \\
 & B_{p-1} = D_1D_6S_1^p; \quad B_{p-3} = -D_1D_6S_3^p; \quad B_{p-5} = D_1D_6S_5^p; \\
 & B_{q-1} = \mp D_3D_4S_1^q; \quad B_{q-3} = \pm D_3D_4S_3^q; \quad B_{q-5} = \mp D_3D_4S_5^q; \\
 & \dots\dots\dots
 \end{aligned}$$

In turn, parameters  $S_0^q, S_0^p, S_1^q, S_1^p, \dots$  are determined by binomial coefficients.

The second equation can be obtained from one of the equations of system (8) by use of the formulas of sine and cosine for multiple arcs. The power of  $Z$  of this equation equals  $p, p < q$ , and  $\sin \psi = \sqrt{1 - Z^2}$ . For elimination of the radical let us square the last equation. We will receive an equation of power  $2p$  with respect to  $Z$ :

$$\begin{aligned}
 & C_0 + C_{2p}Z^{2p} + C_{2p-2}Z^{2p-2} + C_{2p-4}Z^{2p-4} + C_{2p-6}Z^{2p-6} + \dots \\
 & + C_pZ^p + C_{p-2}Z^{p-2} + C_{p-4}Z^{p-4} + \dots = 0,
 \end{aligned} \tag{10}$$

where

$$\begin{aligned}
 & C_0 = D_4^2; \quad C_{2p} = D_5^2S_0^{2p} + D_6^2S_1^{2p}; \\
 & C_{2p-2} = -\left[2D_5^2S_0^pS_2^p + D_6^2(S_1^{2p} + 2S_1^pS_3^p)\right]; \\
 & C_{2p-4} = D_5^2(S_2^{2p} + 2S_o^pS_4^p) + D_6^2(2S_1^pS_3^p + S_3^{2p} + 2S_1^pS_5^p)^2; \\
 & C_{2p-6} = -\left[2D_5^2(S_o^pS_6^p + S_2^pS_4^p) + D_6^2(S_3^{2p} + 2S_1^pS_5^p + 2S_3^pS_5^p)\right]; \\
 & C_p = 2D_4D_5S_o^p; \quad C_{p-2} = -2D_4D_5S_2^p; \quad C_{p-4} = 2D_4D_5S_4^p; \\
 & \dots\dots\dots
 \end{aligned}$$

The analysis of the coefficients of Eqs. (9) and (10) shows that they depend on Cartesian coordinates  $x_C, y_C$  and  $z_C$ , for which generalized polynomials have the form

$$\begin{aligned}
 B_{p+q-1} &= P_2(x_C, y_C, z_C); \dots B_{p-1} = P_3(x_C, y_C, z_C); \dots \\
 B_{q-1} &= P_3(x_C, y_C, z_C); \dots \\
 C_0 &= P_4(x_C, y_C, z_C); \dots C_{2p} = P_2(x_C, y_C, z_C); \dots \\
 C_p &= P_3(x_C, y_C, z_C); \dots
 \end{aligned}$$

The highest order of the polynomials with respect to Cartesian coordinates equals 4.

For different values of  $p$  and  $q$  the coefficients of (9) and (10) are being transformed, therefore for general case we have:

$$\begin{aligned}
 B_0 + B_1Z + B_2Z^2 + \dots + B_{p+q-1}Z^{p+q-1} &= 0; \\
 C_0 + C_1Z + C_2Z^2 + \dots + C_{2p}Z^{2p} &= 0.
 \end{aligned} \tag{11}$$

From system (11) by use of the Sylvester method let us eliminate  $Z$ . According to this method the number of rows in the determinant containing coefficients  $B$  equals  $2p$ , while the number of rows containing coefficients  $C$  equals  $p + q - 1$ . This means that after the last column containing  $B_0$  follows the column containing  $C_{2p}$ , and after the last column with  $C_0$  follows the column with  $B_{p+q-1}$ . We have:

$$F(x_C, y_C, z_C) = \begin{vmatrix}
 B_0 & B_1 & B_2 & \dots & \dots & B_{p+q-1} & \cdot & \cdot & 0 & \dots & 0 \\
 0 & B_0 & B_1 & B_2 & \dots & \cdot & B_{p+q-1} & \cdot & 0 & \dots & 0 \\
 0 & 0 & B_0 & B_1 & B_2 & \dots & \cdot & B_{p+q-1} & \cdot & \dots & 0 \\
 \cdot & \cdot & \cdot & \cdot & \dots & \cdot & \cdot & \cdot & \cdot & \dots & \cdot \\
 \cdot & \cdot & \cdot & \cdot & \dots & \cdot & \cdot & \cdot & \cdot & \dots & \cdot \\
 0 & 0 & 0 & \cdot & \dots & B_0 & B_1 & B_2 & \cdot & \dots & B_{p+q-1} \\
 C_0 & C_1 & C_2 & \cdot & \dots & \cdot & C_{2p} & 0 & 0 & 0 & \dots & 0 \\
 0 & C_0 & C_1 & C_2 & \dots & \cdot & \cdot & C_{2p} & 0 & 0 & \dots & 0 \\
 0 & 0 & C_0 & C_1 & C_2 & \dots & \cdot & \cdot & C_{2p} & 0 & \dots & 0 \\
 \cdot & \cdot & \cdot & \cdot & \dots & \cdot & \cdot & \cdot & \cdot & \dots & \cdot \\
 \cdot & \cdot & \cdot & \cdot & \dots & \cdot & \cdot & \cdot & \cdot & \dots & \cdot \\
 0 & 0 & 0 & \cdot & \dots & \cdot & \cdot & C_0 & C_1 & \dots & C_{2p}
 \end{vmatrix} = 0. \tag{12}$$

The received expression (12) and an algebraic equation of degree four for the circular surface of revolution mentioned earlier represent the trajectory of point  $C$  of the spatial five-link mechanism with two degrees of freedom. The diagonal elements of determinant (12) have the form

$$B_0^{2p} C_{2p}^{p+q-1} \quad \text{and} \quad C_0^{p+q-1} B_{p+q-1}^{2p} \tag{13}$$

The analysis of mentioned diagonal elements shows that the highest order of Eq. (12) relative to Cartesian coordinates  $x_C, y_C$  and  $z_C$  equals  $8p + 4q - 4$ .

Assuming that  $\alpha_0 = \beta_0; u_{52} = +1$ , i.e.  $p = 1$  and  $q = 1$ , the equation of the trajectory of point  $C$  of a spatial five-link mechanism will be simplified and

the degree will be equaled to eight with respect to Cartesian coordinates  $x_C, y_C, z_C$  ( $8p + 4q - 4 = 8 \cdot 1 + 4 \cdot 1 - 4 = 8$ ).

### The Synthesis of a Spatial Five-Link Mechanism

In the synthesis of spatial five-link mechanisms with two degrees of freedom it is necessary to determine input parameters such that they reproduce given laws of motion with sufficient precision.

As it was said above the equation of the trajectory of point  $C$  depends on coefficients  $D_i$ , which contain 17 parameters of the mechanism: the lengths of links  $l_1, \dots, l_5$ , angles  $\alpha_0, \beta_0, \xi, \gamma$  and the directional cosines of chosen systems of coordinates. The rest of directional cosines are determined from the expression defining interdependence between these cosines.

Consider the general case when required law of motion is known and according to the given laws of motion we have

$$f(x_C, y_C, z_C) = 0. \tag{14}$$

For determination of searched parameters of five-link mechanism, for which the equation of the trajectory (12) is being transformed into given, we can write

$$F(x_C, y_C, z_C) - f(x_C, y_C, z_C) = 0. \tag{15}$$

For general case Eq. (15), taking into account (12), has the form

$$(L_0 - L'_0) f_0(x_C, y_C, z_C) + (L_1 - L'_1) f_1(x_C, y_C, z_C) + \dots + (L_K - L'_K) f_K(x_C, y_C, z_C) = 0, \tag{16}$$

where  $L_0, L_1, \dots, L_k$  are constant coefficients in searched parameters;  $L'_0, L'_1, \dots, L'_k$  - given constant coefficients;  $f_0(x_C, y_C, z_C), f_1(x_C, y_C, z_C), \dots, f_k(x_C, y_C, z_C)$  - continuous functions of arguments  $x_C, y_C, z_C$ .

According to Eq. (16) the coefficients with the same names must be equal. We have:

$$L_0 - L'_0 = 0; L_1 - L'_1 = 0; L_K - L'_K = 0. \tag{17}$$

The quantity of equations of system (17) depends on the values of coefficients in Eq. (12).

The solution of system (17) gives the values of searched parameters of the mechanism.

If system (17) does not have a solution then it is necessary to change given parameters beforehand, first of all the values of angles  $\alpha_0, \beta_0, \xi, \gamma$ , afterwards the length of  $l_5$  and the values of directional cosines.

By described method can be solved the problems of synthesis of a spatial five-link mechanism with two degrees of freedom by given laws of motion of the output point of cranks.

## Conclusion

The investigation of a spatial five-link hinged mechanism with two degrees of freedom made possible to set the equation of the trajectory of a center of connective hinge of cranks. It is shown that the order of a trajectory equation, besides the dimensions of links, depends on the value of gear ratio between the input links taking into account their direction of motion and on the phase angle between the input links. The general statement of the problem of synthesis of a RSSRR type spatial five-link mechanism is considered and the ways of its solution are given.

## References

1. Ovakimov A.G. The problem on positions of spatial mechanisms with several degrees of freedom and its solution by the method of closed vectorial contour. *Machines Mechanics*. Moscow: Nauka, 1971, Issue 29–30, pp. 61–75.
2. Duffy J. Habib-Olahi H.Y. A displacement analysis of spatial five-link 3R-2C mechanisms. 1. On the closures of the RCRCR mechanism. *Journal of Mechanisms*. Vol. 5, N 3, 1971, pp. 289–301.
3. Duffy J. A derivation of dual displacement equations for five-six- and seven-link spatial mechanisms using spherical trigonometry. 3. Derivation of dual equations for seven-link spatial mechanisms. *Rev. Roum. Sci. Techn. Ser. Mech. Appl.* 1972. Vol. 17, pp. 291–317.
4. Kemal Ider S. Inverse dynamic of parallel manipulators in the presence of drive singularities. *Mechanism and Machine Theory*. Vol. 40, N 1, 2005, pp. 33–44.
5. Zhou H., Kwun-Lon Ting. Path generation with singularity avoidance for five-bar slider-crank parallel manipulators. *Mechanism and Machine Theory*. Vol. 40, N 3, 2005, pp. 371–384.
6. Davitashvili N. S. The influence of the parameters of a five-link hinged mechanism on the trajectory of points of connecting rods. *Communications of the Academy of Sciences of GSSR*. Vol. 86, N 2, 1977, pp. 412–420.
7. Davitashvili N. S. The equation of a trajectory of a spherical five-link hinged mechanism. *Communications of the Academy of Sciences of GSSR*. 1978, Vol. 89, N 2, pp. 429–432.
8. Davitashvili N. S., Tsotadze M. A. L., Abaishvili V. V. Questions on the kinematik investigation of spatial five-link mechanisms with two degrees of freedom. *Transactions of Tbilisi State University, Questions of Applied Mechanics*. Tbilisi, Vol. 2, 1984, pp. 99–111.
9. Davitashvili N. S. *Fundamentals of the theory of error and precision of linkage-lever mechanisms*. Tbilisi: Technical University, 1999.
10. Davitashvili N. S. *Theoretical fundamentals of synthesis, analysis and precision of hinged mechanisms with two degrees of freedom*. Tbilisi: Metsniereba, 2000.
11. Davitashvili N. S. *Dynamic investigation of plane five-link hinged mechanisms with two degrees of freedom*. Tbilisi: Georgian Committee of IFToMM, 2006.

# Synthesis of Mechanisms with Evolutionary Techniques

J.A. Cabrera, J.J. Castillo, F. Nadal, A. Ortiz and A. Simón

**Abstract** The paper deals with optimal synthesis solution methods to planar mechanisms. Several searching procedures are defined in this work, which apply algorithms based on evolutionary techniques. These algorithms are used to solve different synthesis problems of planar mechanisms. Concretely, a path, a multiobjective optimization and a structural synthesis of mechanism are used to test the method, showing that solutions are accurate and valid for all cases. This work is a summary of the research that our group has carried out over several years and we continue investigating due to the great interest shown by the mechanism synthesis community who use these kinds of techniques.

**Keywords** Mechanism synthesis · Evolutionary techniques

## Introduction

We can distinguish several kinds of mechanism syntheses: dimensional synthesis of linkages is the proportion determination of the links to generate the desired motion, path or function. In this kind of synthesis a known mechanism is used, but a more difficult problem can be proposed when we do not have any knowledge of the mechanism type. Then we talk about structural synthesis. Structural synthesis is the connection between type and dimensional synthesis. Dimensional synthesis is an amply studied problem, but it is obvious that type synthesis is currently an open problem as well as a more difficult one to solve. Basically, one of the principal problems is to determine an efficient way of representing the vast number of mechanisms used.

Different techniques have been used for mechanism synthesis over time. The great increase in computer power has permitted the recent development of routines that apply numerical methods to the minimization of a goal function.

On the other hand, many researchers have tried to obtain a rational strategy to structural synthesis. In [1], authors have built around 43 mechanical building blocks

---

J.A. Cabrera (✉)

Department of Mechanical Engineering, University of Málaga, Campus El Ejido,  
29013 Málaga, Spain

based on an investigation of hundreds of machines. Another approach [2] uses a matrix representation and a genetic algorithm to evolve the mechanisms, but in this approach the topology of the mechanisms is fixed a priori, i.e., the number of links is fixed and the genetic algorithm only changes the joint configuration. A graph theory is used in [3], where a truss ground structure of possible nodes and connections is designed and an optimization method is used to maximize a specific node displacement. Finally, in [4] a tree representation is developed and used as a genetic programming algorithm to evolve different 2D compound mechanisms. In this effort, the topology of the mechanisms is not fixed beforehand. Instead, only one type of joint, the hinge joint, is used. Thus, the mechanisms created are limited.

As observed in the previous paragraphs, all existing approaches have restrictions, due to the difficulty of the problem at hand.

The approach presented in this paper deals with three different syntheses of mechanism problems using Differential Evolution Algorithms [5] to solve the dimensional and multiobjective synthesis problems and genetic programming [6] to solve the structural synthesis problem. The main advantages of these methods are their simplicity in implementing the algorithms and their low computational cost.

## Dimensional Synthesis of Planar Mechanisms

In this first example a dimensional mechanism synthesis is shown [7]. This is clearly an optimization problem and as we saw in the introduction section, we can solve it in different ways. One of them is by means of genetic algorithms, [8]. The strategy of evolutionary methods for optimization problems begins with the generation of a starting population. For mechanisms synthesis the starting population is a set of design variables, whose values are randomly generated within the searching space. Each individual (chromosome) of the population is a possible solution to the problem and it is formed by parameters (genes) that set the design variables of the problem. Genes can be schematized by several forms. A way to express the genes, as follows in this paper, is directly as real values. All genes are grouped in a vector that represents a chromosome:

Next the starting population has to evolve to populations where individuals are a better solution. This task can be reached by natural selection, reproduction, mutation or other genetic operators. In this work, selection and reproduction are carried out sequentially and mutation is used as an independent process.

The goal function is the sum of two terms. The first part computes the position error as the sum of the square of the euclidean distances between each  $C_d^i$  and the corresponding  $C^i$  where, Fig. 1:

- $\{C_d^i\}$  is a set of target points indicated by the designer that should be met by the coupler of the mechanism.
- $\{C^i\}$  is the set of positions of the coupler of the designed mechanism for a set of values of the input angle  $\{\theta_2^i\}$  that is another design variable to be optimized.



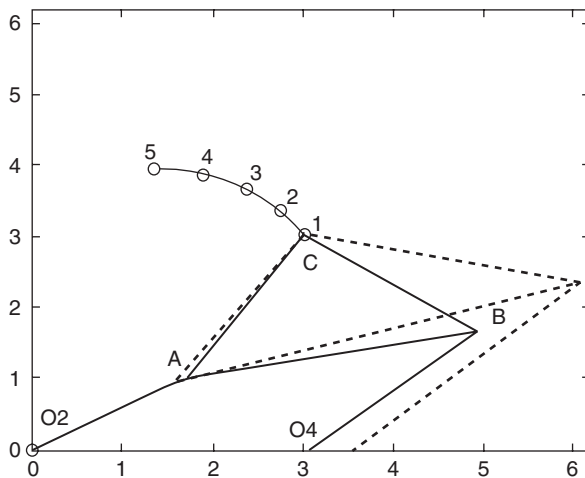


Fig. 1 Solution to the different optimization methods. (- -) KK algorithm; (-) proposed method

### Multiobjective Synthesis of Planar Mechanisms

In this case the optimization problem is given by:

$$\begin{aligned}
 &\min F(X) = (f_1(X), f_2(X), \dots, f_n(X)) \\
 &\text{subject to:} \\
 &\quad g_j(X) \leq 0 \quad j = 1, 2, \dots, m \\
 &\quad \Omega : \{x_i \in [l_i, l_s_i] \quad \forall x_i \in X\}
 \end{aligned} \tag{1}$$

Where  $f_i$  are the goal functions, i.e. a set of functions where each one expresses a feature or objective to be optimized, and where each individual  $X$  obtains a value, its fitness. Furthermore  $g_j(\cdot)$  are the constraints defining the searching space.

The evolutionary algorithms that we propose [9] are also based on the Differential Evolution Algorithm proposed by Storn and Price [5], but we introduce a set of new features:

- The original Differential Evolution Algorithm was used in optimization problems with one goal function. We use it with multiobjective problems.
- We use a Pareto-based approach to sort the population and this one is divided into non-dominated and dominated population. The “best” individuals are chosen to run the Differential Evolution strategy from the non-dominated sub-population.
- We use a genetic operator called mutation, which is not used in the original algorithm. This operator is of great significance in certain problems to prevent stagnation.
- We use a function to control the number of non-dominated individuals in the population.
- We introduce a procedure for handling the constraints.

The proposed algorithm, which is defined as Pareto Optimum Evolutionary Multiobjective Algorithm (POEMA), has the following steps:

1. The algorithm starts with the random generation of a starting population with  $NP$  individuals.
2. Next, the algorithm calculates the Pareto-optimal set of the total population and obtains its size,  $N_{pr}$ . To preserve diversity, the number of non-dominated individuals is maintained along iterations according to the following function:  $\forall k \in \{1, \dots, \text{itermax}\} : N_{pr} \leq N_0 + k \cdot \Delta N$ . Where  $\text{itermax}$  is the number of iterations in the algorithm,  $N_0$  is the number of allowed initial individuals in the Pareto-optimal set and  $\Delta N$  is a parameter to increase the allowed initial algorithms with the iterations. So a maximum number of non-dominated individuals are allowed. If this maximum is exceeded, the nearest neighbor distance function is adopted.
3. To create the new population, the selection of a couple, reproduction and a mutation operator are used according to the definitions described above.
4. If the algorithm reaches the maximum number of iterations, it finishes; otherwise return to step 2.

Once we have described the POEMA algorithm, we will develop the goal functions for the problem of a robot hand mechanism (Fig. 2). The advantage of using a multiobjective evolutionary algorithm is that we can include either kind of goal function that other works have resolved individually. When a mechanism is designed, several kinds of features are kept in mind:

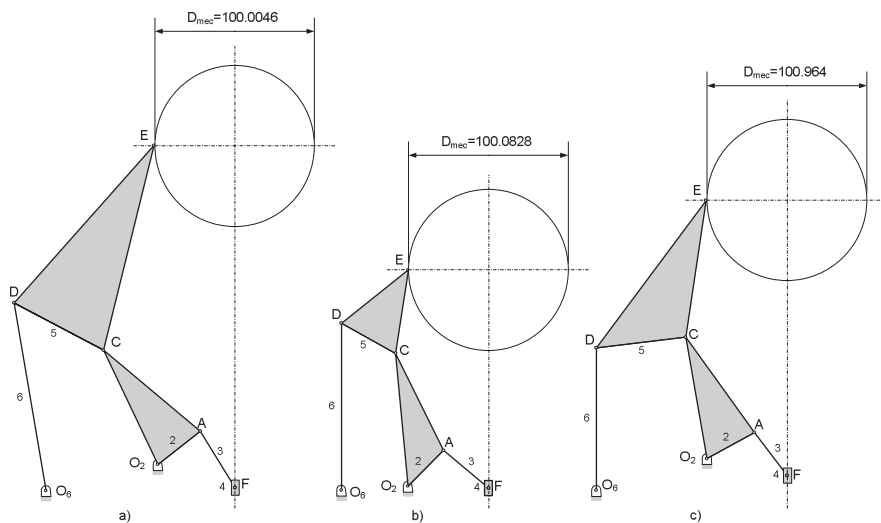


Fig. 2 Three mechanisms of the final population

- Geometric features: a link has to measure a specific length, etc.
- Kinematical features: a point in the mechanism has to follow a specific trajectory, velocity or acceleration law during its movements.
- Mechanical advantage: amount of power that can be transmitted by the mechanism for one complete cycle.

## Structural Synthesis of Planar Mechanisms

In this section we develop a genetic algorithm (GP) to solve a structural synthesis problem. One of the most important parts in an automated mechanism design cycle is the mechanism representation. There are different ways to represent a mechanism, graph representation and matrix representation, but these kinds of representations are less suitable when an evolutionary strategy is used because they over-constrain the motion and create deadlocked mechanisms. Using these representations, the likelihood of generating a mechanism with exactly one degree of freedom is vanishingly small. In order to allow an evolutionary algorithm to explore the space of one-DoF mechanisms more efficiently, a more suitable representation is required. This representation must have a tree-like architecture to be used by a GP.

We will use a bottom-up tree to represent the mechanisms and two atomic building elements called *-hinge-* and *-slider-*. With these two basic elements we can create a huge range of mechanisms. Each block has one-DoF when it is grounded. Thus, when we compound two atomic elements to build a more complex mechanism, the formed mechanism has exactly one-DoF, so that the compound operators do not modify the mechanism's degree of freedom. We can observe the three different basic compound operators *HH*, *HS* and *SS* in Fig. 3a.

The created mechanism maintains one-DoF when one of the operators is applied as we can see in Fig. 3a. Obviously we can compound not only the atomic building element but also more complex structures. Again, higher-level operators obtain one-DoF mechanisms when one of their links is grounded. As we have seen, the basic and higher-level operators are able to create complicated mechanism topologies which allow us to explore a huge search space. Once the operators are defined, a bottom-up tree representation is used to define the genotype in the evolutionary strategy.

An example of bottom-up tree representation is shown in Fig. 3b. In this kind of representation, the leaves of the tree (genes) are the atomic building elements and we hierarchically assemble them into components. The atomic building blocks are the hinge-dyad *H* and the slider-dyad *S*, and they have exactly one DoF when grounded. The ground link of the entire structure is specified at the root of the tree.

In order to create mechanisms, an evolutionary algorithm is used, using the genetic programming algorithms and bottom-up tree representation explained above. We mainly use two operators: mutation and reproduction. The mutations operators are:

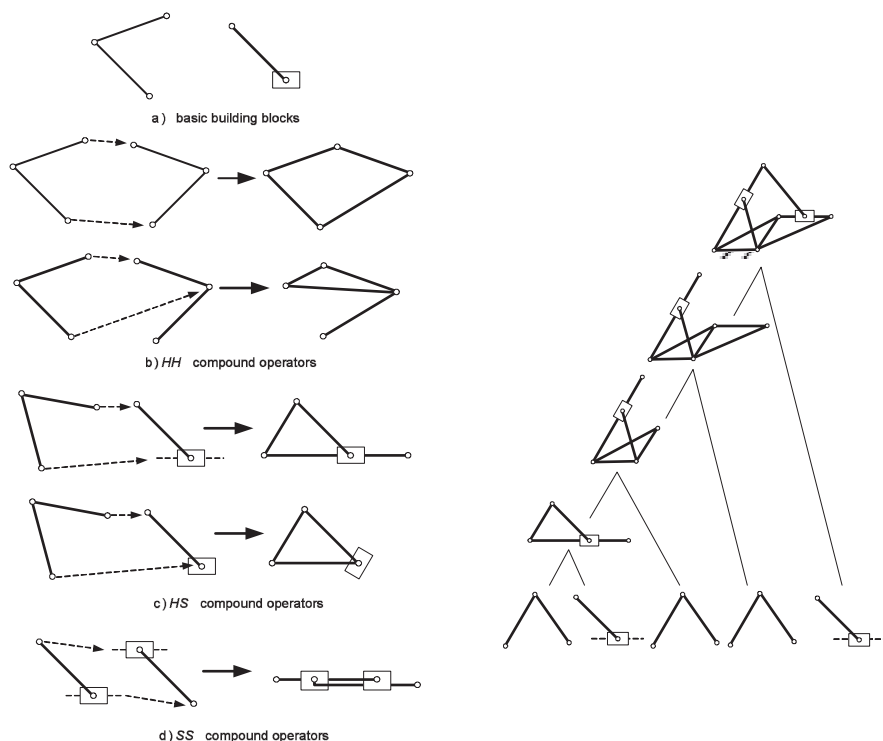


**Fig. 3** (a) Basic operators and building blocks. (b) Bottom-up tree representation

- Adding a new atomic building element to a mechanism represented by its tree.
- Erasing an atomic building element from a mechanism represented by its tree.
- Changing joint position.
- Changing the grounded joint.
- Changing the atomic building element.

To prove our methodology, we define a function synthesis problem. In this case, we seek a specific mathematical function between two links, the input and output link, and a relationship between the link angles. The mechanisms are actuated along its single DoF by applying some small force to one of its ungrounded nodes, arbitrarily selected. Then, we measure the formed angles between each link and evaluate the fitness function.

The fitness function was defined for this problem as:

$$f(X) = \min \left[ \sum_m \left( \theta_{ij}^m - 2\theta_{\text{input}}^m \right) \right] \quad (2)$$

$$\forall i, j \setminus i, j \in \{\text{links}\} - \{\text{input link}\}$$

where  $i$  and  $j$  are numbers of the mechanism links without the input link (link that belongs to the joint where the force is applied to move the mechanism) and  $m$  is the

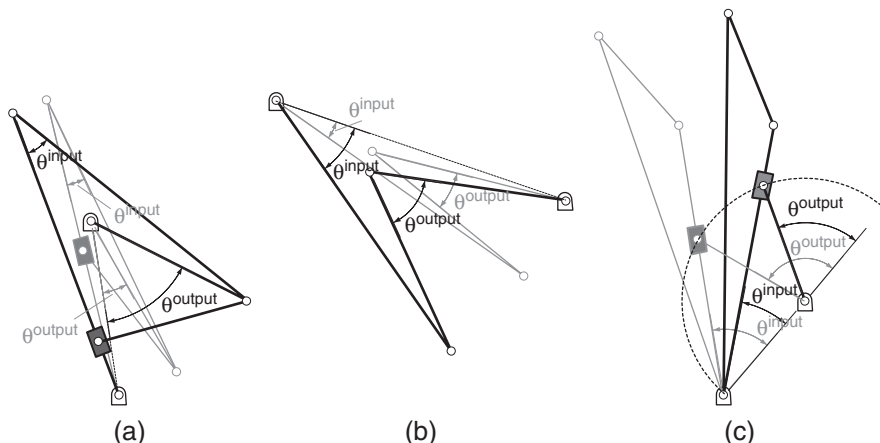


Fig. 4 Different mechanism topologies for the problem

number of times that the mechanism stored its new positions when it was moved. Hence, the fitness function seeks a mechanism in which the output angle doubles the input angle in all its movements.

We obtained several different mechanism topologies with different program runs. Some of these topologies are shown in Fig. 4.

## Conclusions

In this paper we have presented three algorithms based on evolutionary strategies to solve synthesis mechanisms problems. In the first place a path synthesis of planar mechanism problems. We have developed an algorithm to optimize the position error between the target points selected by the designer for the coupler point and the points reached by the resulting mechanism. Next, we showed a new algorithm (POEMA) based on the Differential Evolution strategy, but it has been extended to tackle multiobjective optimization problems. For this purpose, new features have been developed. The algorithm is used to optimize several goal functions in a hand robot mechanism, subject to different constraints. The same method can be applied to optimize any other goal functions in other different problems. Finally, we have presented the application of genetic programming for the synthesis of compound 2D kinematic mechanisms. A tree-based representation was proposed: a bottom-up representation that hierarchically composes atomic components.

In all cases, the results shown have been acceptable. We can improve our results in many aspects. We could enhance some features of the evolutionary process. Future work will further examine these issues and their application to other kinematic syntheses.

## References

1. Chiou, S.J., Kota, S., 1999, "Automated Conceptual Design of Mechanisms". *Mechanism and Machine Theory*, Vo. 34, pp. 467–495.
2. Liu, Y., McPhee, J., 2005, "Automated Type Synthesis of Planar Mechanisms Using Numeric Optimization with Genetic Algorithms". *Journal of Mechanical Design*. Vo. 127, pp. 910–916.
3. Kawamoto, A., Bendsøe, M.P., Sigmund, O., 2004, "Planar Articulate Mechanism Design by Graph Theoretical Enumeration". *Structural and Multidisciplinary Optimization*. Vo. 27, pp. 295–299.
4. Lipson, H., 2004, "How to Draw a Straight Line Using a GP: Benchmarking Evolutionary Design Against 19th Century Kinematic Synthesis". *Proceedings of Genetic and Evolutionary Computation Conference, Late Breaking Paper, GECCO, AAAI Press*.
5. Storn, R., Price, K., 1997. "Differential Evolution. A Simple and Efficient Heuristic Scheme for Global Optimization Over Continuous Spaces". *Journal of Global Optimization*. Vo. 11, pp. 341–359.
6. Koza, J., 1992, "Genetic Programming: On the Programming of Computers by Means of Natural Selection". MIT Press.
7. Cabrera, J.A., Simon, A., Prado, M., 2002, "Optimal Synthesis of Mechanisms with Algorithm Genetics". *Mechanism and Machine Theory*, Vo. 37, pp. 1165–1177.
8. Kunjur, A., Krishnamurty, S., 1997, "Genetic Algorithms in Mechanical Synthesis", *Journal of Applied Mechanisms and Robotics*, Vo. 4, (2) (1997) pp. 18–24.
9. Cabrera, J.A., Nadal, F., Muñoz, J.P., Simon, A., 2007, "Multiobjective Constrained Optimal Synthesis of Planar Mechanisms Using a New Evolutionary Algorithm". *Mechanism and Machine Theory*, Vo. 42, pp. 791–806.

# Optimal Synthesis of Steering Mechanisms Including Transmission Angles

Ana de-Juan, Ramon Sancibrian and Fernando Viadero

**Abstract** The application of a dimensional synthesis method to the design of steering mechanisms in road vehicles is presented in this work. Both kinematic requirements and transmission angles are considered, and also the limitation of space within the vehicle. Three different mechanisms have been considered to validate the method.

**Keywords** Steering linkages · Transmission angle · Ackermann condition · Function generator synthesis

## Introduction

The main aim of the steering mechanism in road vehicles is to provide the required change of direction. Different mechanisms can be used within the steering system [1]. Left column of Fig. 1 shows three of them in the straight-ahead position, which are studied in this paper: rack and pinion (a), four bar (b) and six bar (c). The first one is the most popular linkage used in road vehicles with independent front suspension. The other two are mostly used in buses and trucks.

The vehicle turns accurately when there is only one turn centre for the four wheels [2]. This condition is known as the Ackermann's law, which expresses the correlation between the two steering wheels. It can be formulated mathematically in terms of this expression

$$\delta_{od} = \arctan \left( \frac{1}{\cot(\delta_{in}) + z_1/L} \right) \quad (1)$$

were  $z_1$  is the distance between joints of the steerable axis and  $L$  is the wheel-base. Parameters  $\delta_{in}$  and  $\delta_{od}$  are the angles turned by the inner and the outer wheel,

---

A. de-Juan (✉)

Department of Structural and Mechanical Engineering, University of Cantabria, ETSIIT, Avda. De los Castros s/n. Santander (Spain)

e-mail: dejuanam@unican.es

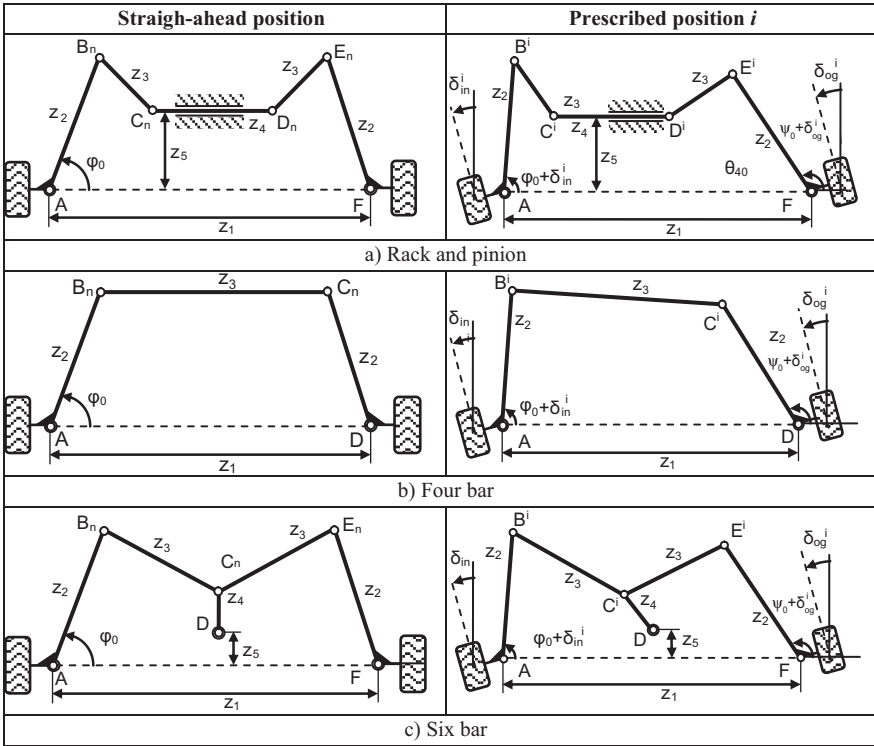


Fig. 1 Steering mechanisms

respectively. This means that if we consider the turn of one wheel as the input parameter, the desired turn of the other wheel is given by this Eq. (1). According to this, the design of a steering mechanism can be formulated as a function generation synthesis problem.

However, another aspect should be taken into account in the design of steering mechanism: the transmission angle. This parameter gives an idea of the efficiency of transmission forces in the mechanisms [3, 4]. Values of transmission angle close to the optimum during the motion are desirable. It reduces vibrations and noise and guarantee an effective forces transmission. Although power steering systems are now used in road vehicles, the optimization of the transmission angle can reduce the power required by these electrical or hydraulic systems.

Synthesis of steering mechanisms has been widely studied in literature [5–8]. In these works, parametric charts have been developed for helping the designer in the early stages of design [6, 7]. Searching for the global optimum has been performed too in the literature [9]. In this case, the most accurate solution is achieved, although some lengths of links are too big with respect to others and it is not possible to place the mechanism inside the space within the vehicle. To overcome this problem, Yao and Angeles [9] proposes to replace it with its focal six-bar equivalent.



The aim of this work is the application of a local optimization method for synthesizing steering mechanisms. The optimization method is based on exact gradient determination. Both kinematic and transmission angles requirements are imposed. The optimization method has been developed by the authors [10]. Moreover, space limitations are imposed to place the mechanism within the vehicle. These requirements are satisfactorily fulfilled by means of the optimization method.

### Definition of Transmission Angle in Steering Mechanisms

Transmission angle was originally defined for the four-bar linkage [3]. Although it has been widely used in optimal synthesis, as the number of links increases there can be actually more than one transmission angle.

In this paper, two transmission angles are defined for each linkage, as they must turn both left and right. The angles are measured between steering arms ( $z_2$ ) and connecting rods ( $z_3$ ), see Fig. 1. Figure 2 shows the angles for a generic mechanism. Mathematically, they are defined by means of scalar product between steering arms and tie rods.

$$\mu_B^i = \arccos \left( \frac{\overline{\mathbf{B}^i \mathbf{A}} \cdot \overline{\mathbf{B}^i \mathbf{C}^i}}{z_2 z_3} \right) \tag{2}$$

$$\mu_V^i = \arccos \left( \frac{\overline{\mathbf{V}^i \mathbf{W}} \cdot \overline{\mathbf{V}^i \mathbf{U}^i}}{z_2 z_3} \right) \tag{3}$$

Where  $\mu_B$  and  $\mu_V$  are transmission angles in revolute joints  $V$  and  $B$ , respectively.

Optimum value of transmission angle is the one which transmits the maximum force. Therefore the optimum,  $\mu_d$ , is the same for both  $\mu_B$  and  $\mu_V$  angles, i.e.  $90^\circ$ .

### The Synthesis Problem

The aim of optimal dimensional synthesis is to find the design variables vector,  $\mathbf{w}$ , which minimizes the objective function. Design variables are the lengths of the

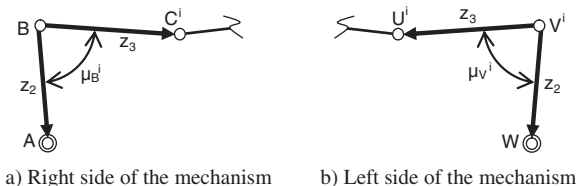


Fig. 2 Transmission angle in steering mechanisms

links and the reference coordinates for each mechanism. Thus, the objective function should be defined.

The resulting mechanism should achieve two conditions at the end of the optimization process. The first one, and the most important too, is the fulfilment of the Ackermann condition. The second one, to achieve values of transmission angles close to their optimum. Structural error shows the discrepancy between optimum and real behaviour of the mechanism. In this case, for a prescribed position  $i$ , structural error is formulated as follow

$$\boldsymbol{\varepsilon}(\mathbf{w})^i = \begin{bmatrix} \nu_1 & 0 & 0 \\ 0 & \nu_2 & 0 \\ 0 & 0 & \nu_2 \end{bmatrix} \begin{bmatrix} \delta(\mathbf{w})_{og}^i - \delta_{od}^i \\ \boldsymbol{\mu}(\mathbf{w})_B^i - \boldsymbol{\mu}_d \\ \boldsymbol{\mu}(\mathbf{w})_V^i - \boldsymbol{\mu}_d \end{bmatrix} \quad (4)$$

Where  $\nu_1$  and  $\nu_2$  are the weightings, considering the importance of each term.

First term of the vector in Eq. (4) is the Ackermann's error,  $\varepsilon_A^i$ . Parameter  $\delta_{og}$  is the real angle turned by the output wheel and  $\delta_{od}$  is given by Eq. (1). The second and third terms are the errors of the transmission angles  $\varepsilon_\mu^i$ .

Considering the straight-ahead position as the reference, the wheels orientation is defined within the range of motion. For one wheel, it goes from the maximum turning when it is the inner wheel to the maximum turning when it is the outer wheel. Right column of Fig. 1 shows the three mechanisms in a prescribed position  $i$ . Structural error is evaluated in a finite number of prescribed positions,  $p$ , within the range of motion.

$$\boldsymbol{\varepsilon}(\mathbf{w})^T = [\varepsilon_1(\mathbf{w}) \ \varepsilon_2(\mathbf{w}) \ \dots \ \varepsilon_p(\mathbf{w})] \quad (5)$$

The objective function has been formulated in terms of structural error

$$F = \frac{1}{2} \boldsymbol{\varepsilon}(\mathbf{w})^T \boldsymbol{\varepsilon}(\mathbf{w}) \quad (6)$$

This objective function is subject to both equality and inequality constraints.

Equality constraints come from the kinematic requirements of each mechanism. They relate design variables and input parameter with dependent coordinates,  $\mathbf{q}$ . These dependent coordinates, which include output parameters, are necessary for evaluating structural error. The number of equality constraints will be equal to the number of dependent coordinates.

Inequality constraints limit the lengths of the links and avoid the collision with wheels. They can be converted into equality constraints by means of slack variables [11].

Therefore, both equality and (converted) inequality constraints are grouped in vector  $\Phi^i$  in every prescribed position. They must be fulfilled for the whole range of motion

$$\Phi(\mathbf{q}(\mathbf{w}), \mathbf{w})^T = [\Phi^1(\mathbf{q}(\mathbf{w}), \mathbf{w}) \ \Phi^2(\mathbf{q}(\mathbf{w}), \mathbf{w}) \ \dots \ \Phi^p(\mathbf{q}(\mathbf{w}), \mathbf{w})] \quad (7)$$

Objective function is differentiated with respect to design variables in order to obtain the minimum value

$$\frac{dF}{d\mathbf{w}} = \frac{\partial \boldsymbol{\varepsilon}(\mathbf{w})^T}{\partial \mathbf{w}} \boldsymbol{\varepsilon}(\mathbf{w}) = \mathbf{J}(\mathbf{w})^T \boldsymbol{\varepsilon}(\mathbf{w}) = 0 \quad (8)$$

Where the Jacobian matrix,  $\mathbf{J}(\mathbf{w})$ , can be calculated differentiating vector  $\Phi$  with respect to design variables. Now, vector  $\boldsymbol{\varepsilon}(\mathbf{w})$  is expanded in Taylor series and curtailed after the first order derivative

$$\mathbf{J}(\mathbf{w})^T \boldsymbol{\varepsilon}(\mathbf{w})_k + \mathbf{J}(\mathbf{w})^T \frac{\partial \boldsymbol{\varepsilon}(\mathbf{w})_k}{\partial \mathbf{w}} \Delta \mathbf{w} = 0 \quad (9)$$

Reordering Eq. (9), the increment necessary of design variables to minimize objective function in the  $k$ th iteration is obtained

$$\Delta \mathbf{w} = \mathbf{w}_{k+1} - \mathbf{w}_k = -\alpha_K [\mathbf{J}(\mathbf{w})_k^T \mathbf{J}(\mathbf{w})_k]^{-1} \mathbf{J}(\mathbf{w})_k^T \boldsymbol{\varepsilon}(\mathbf{w})_k \quad (10)$$

Thus, the value of vector  $\mathbf{w}$  in the next iteration is  $\mathbf{w}_{k+1}$ . However, the increment  $\Delta \mathbf{w}$  is only a direction of descend, due to the approximation introduced by Taylor series. For this reason, the step size,  $\alpha_k$ , is introduced in Eq. (10)

## Results

The three mechanisms shown in Fig. 1 have been simulated under the same conditions: thirty nine prescribed positions ( $p = 39$ ) have been defined; the range of motion of the input wheel goes from  $+40^\circ$  to  $-27^\circ$ ; the relation between  $z_1$  and  $L$  is 0.75 for solving Eq. (1); inequality constraints have been introduced to limit the lengths of the links when it is necessary.

Two sets of approaches, Optimization 1 (Opt. 1) and Optimization 2 (Opt. 2), have been developed under the conditions mentioned in the previous paragraph. Opt. 1 has been carried out with  $\nu_1 = 1$  and  $\nu_2 = 0.01$ . In Opt. 2  $\nu_1 = 1$  and  $\nu_2 = 0.1$ . Tables 1 and 2 show numeric results of these simulations. Initial guesses and optimal solutions are shown for the design variables ( $\mathbf{z}$ ), maximum value of Ackermann's error ( $\varepsilon_A^{\max}$ ) and transmission angles in the straight-ahead ( $\mu_0$ ) position. Note that  $\mu_0$  is the value for both transmission angles because of the symmetry of the mechanism.

Figure 3 shows Ackermann error and values of transmission angle in the whole range of motion for the three optimized mechanisms. Note that error Ackermann for Opt. 1 is quite lower than for Opt. 2.

Inequality constraints have been used in the three mechanisms. For the four bar linkage, maximum value of steering arm,  $z_2$ , has been limited to 0.3 m, and collision with wheels is avoided. For the rack and pinion linkage, maximum value of  $z_2$  has been limited to 0.3 m. For the six bar linkage, maximum value of  $z_2$  and  $z_4$  has been

**Table 1** Initial guesses and optimal solutions for  $\nu_1 = 1$  and  $\nu_2 = 0.01$  (Opt. 1)

		Design variables					$\epsilon_A^{\max} (^\circ)$	$\mu_0 (^\circ)$
		$z_2$ (m)	$z_3$ (m)	$z_4$ (m)	$z_5$ (m)	$\varphi_0 (^\circ)$		
R&P	Initial guess	0.2	0.55	0.4	0.2	90	14.4	90
	Optimal solution	0.3	0.41	0.83	0.1	95.7	0.43	56
4 bar	Initial guess	0.2	1.5	–	–	90	12.75	90
	Optimal solution	0.1	1.61	–	–	121	1.15	59
6 bar	Initial guess	0.15	0.75	0.15	90	0.05	12.75	9.8
	Optimal solution	0.14	0.87	0.2	131.4	0.01	1.03	61

**Table 2** Initial guesses and optimal solutions for  $\nu_1 = 1$  and  $\nu_2 = 0.1$  (Opt. 2)

		Design variables					$\epsilon_A^{\max} (^\circ)$	$\mu_0 (^\circ)$
		$z_2$ (m)	$z_3$ (m)	$z_4$ (m)	$z_5$ (m)	$\varphi_0 (^\circ)$		
R&P	Initial guess	0.2	0.55	0.4	0.2	90	14.4	90
	Optimal solution	0.3	0.27	1.04	0.22	94	7	78
4 bar	Initial guess	0.2	1.5	–	–	90	12.75	90
	Optimal solution	0.1	1.56	–	–	107.1	6.92	73
6 bar	Initial guess	0.15	0.75	0.15	90	0.05	12.75	93.8
	Optimal solution	0.16	0.8	0.2	102	0.1	10.2	89

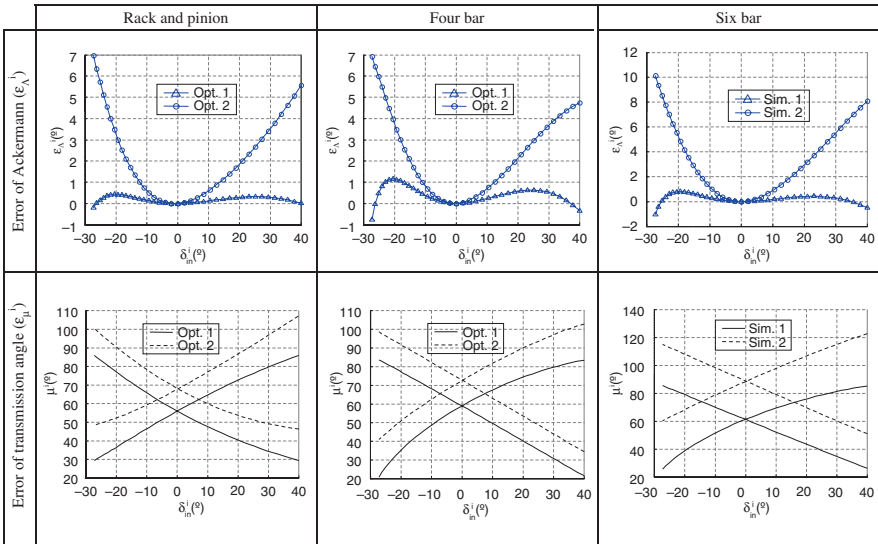


**Fig. 3** Error of Ackermann and transmission angle

limited to 0.2 m, maximum height of central joint  $z_5$  has been limited to 0.1, and collision with wheels has been avoided.

## Concluding Remarks

The local optimization method developed by the authors has been applied to the design of steering mechanisms in road vehicles. Three different mechanisms have been studied: four bar linkage, rack and pinion and six bar linkage. Both fulfilment of Ackermann's condition and acceptable values of transmission angles were the optimization requirements. The examples presented in this work show a good precision in the results obtained.

**Acknowledgments** This paper has been developed in the framework of the Project DPI2006-13945 funded by the Spanish Ministry of Education and Science.

## References

1. J. Reimpell, H. Stoll. *The automotive chassis: engineering principles*. Arnold 1996
2. R. Rao. Steering linkage design. A method of determining the configuration of the steering linkage so that the geometry conforms to Ackermann principle. *Aut. Engineer.* 58 (1968) 31–33
3. H. Alt. Der Übertragungswinkel und seine Bedeutung für das Konstruieren periodischer Getriebe. *Werkstattstechnik* 26 (1932) 61–64
4. S. S. Balli, S. Chand. Transmission angle in mechanisms (Triangle in mech). *Mech. Mach. T.* 37 (2002) 175–195
5. C. E. Zarak, M. A. Townsend. Optimal design of rack-and-pinion steering linkages. *ASME J. Mech. Trans. Auto. Des.* 105 (2001) 220–226
6. P. A. Simionescu, M. R. Smith. Initial estimates in the design of central-lever steering linkages. *J. Mechanical Des.* 124(4) (2002) 646–651
7. P. A. Simionescu, D. Beale. Optimum synthesis of the four-bar function generator in its symmetric embodiment: the Ackermann steering linkage. *Mech. Mach. T.* 37 (2002) 1487–1504
8. P. A. Simionescu, M. R. Smith, I. Tempea. Synthesis and analysis of the two loop translational input steering mechanism. *Mech. Mach. T.* 35 (2000) 927–943
9. J. Yao, J. Angeles. Kinematic synthesis of steering mechanisms. *Trans. Can. Soc. Mech. Eng.* 24(3–4) 453–476
10. R. Sancibrián, P. García, F. Viadero, A. Fernández. A general procedure based on exact gradient determination in dimensional synthesis of planar mechanisms, *Mech. Mach. T.* 41 (2006) 212–229
11. S. S. Rao. *Engineering optimization. Theory and practice*, 3rd edition. Wiley-Interscience. 1996

# Workspace Fitting and Control for a Serial-Robot Motion Simulator

Andrés Kecskeméthy, Ismar Masic and Martin Tändl

**Abstract** Described in this paper is a setup for a motion simulator based on the serial robot RoboCoaster of type Kuka KR500 TÜV. The paper addresses the issue of axis limit design such that both safety prescriptions as well as performance requirements are fulfilled. To this end, a surrogate mechanism for collision avoidance and a trade-off between manipulability and maximally achievable acceleration at the passenger's head to optimize fidelity of sensed motion are proposed. Experimental results are presented based on a control algorithm for matching target accelerations also presented in the paper.

**Keywords** Physical motion simulation · Workspace design · Serial robot

## Introduction

Robot design is a well-established topic with several now standard approaches available for optimizing motion and kinestatics, e.g., [1, 7, 8]. A field of arising interest is the use of serial robots for “flight-simulator” applications. In this case, the robot is used to simulate physical motion for a passenger seated at the end-effector (Fig. 1), producing target accelerations which mimic the sensing of the passenger in a real maneuver. This operation is different to normal robot applications in the sense that positions and constant linear velocity components have no effect on motion sensing and are arbitrary, hence posing new problems of design and control.

Currently, there is only one available robot fulfilling the safety regulations for passenger motion, namely, the Kuka RoboCoaster system [4]. While this system has been designed and is being used commercially for entertaining purposes, the basic mechanical system, termed Kuka KR500 TÜV, is being recently applied for simulating gross motion situations such as roll-over of cars, difficult steering maneuvers of heavy-duty vehicles or helicopter flights, or simulation of extreme motion

---

A. Kecskeméthy (✉)

Chair of Mechanics, University Duisburg-Essen, Lotharstraße 1, 47057 Duisburg, Germany  
e-mail: andres.kecskemethy@uni-due.de

such as in roller coasters. Currently, there are three generic-motion Kuka KR500 TÜV simulators available: one at the DLR [3], one at the Max Planck Institute for Biological Cybernetics in Tübingen [10], and one in the Chair for Mechanics and Robotics of the University Duisburg-Essen [9].

The basic task of such simulators is to generate user-prescribed acceleration profiles, both in offline and in on-line modus, which may be the result of a programmed track (such as in roller-coaster or roll-over playback) or of a hardware-in-the-loop model for some type of vehicle control (e.g. helicopter simulator) reacting under the influence of environmental parameters and pilot's inputs. In this setting, the position of the robot is not important, but its ability to produce acceleration peaks of some duration. Moreover, due to safety regulations, it must be guaranteed that even with a control failure no part of the passenger touches the ground or a robot part. This leads to two particular problems that need to be regarded in this setting, namely, axis limit design, and design of a suitable controller. The present paper mainly addresses the topic of axis limit design under the premises of collision avoidance and optimization of performance for acceleration purposes. The control issue has been addressed in [9] and is subsumed here for better reference.

Axis limit design for a Kuka flight simulator serial robot has been addressed in [6] and [10]. In [6], the eccentricity, i.e., the inverse of the condition number, is regarded. On the other hand, in [10] emphasis was put on the longest achievable straight-line trajectory. In this paper, we propose to use maximally achievable acceleration in conjunction with manipulability for the design of joint limits, which have some advantages over existing methods when regarding accelerations. The results are illustrated with experimental data gathered from our operating system.

## Design of a suitable workspace

The simulator setup used for the current work is shown in Fig 1. The motion of the robot is generated via six analog input signals  $u_j$ , which are produced by an external PC in feed-forward control mode. For safety reasons, a TÜV-approved roller-coaster seat is employed for passenger motion such that there is no risk of passenger dethrow. This seat can be replaced with other, more application-oriented seat environments such as quarter cars or operation cockpits upon demand.

The end-effector frame Frame  $\mathcal{K}_{EE}$  typically is placed on the head of the passenger, which is the main location where motion is physiologically sensed. Position vector  $r_{EE}$  and rotation matrix  ${}^0\mathbf{R}_{EE}$  are generated as functions of the axis angles  $q = [\varphi_1, \dots, \varphi_6]^T$ . The z-axis of  $\mathcal{K}_{EE}$  points in cranial, the x-axis points in view direction and the y-axis points to the left. Note that due to safety regulations accelerations in cranial direction are restricted to below 6 g, accelerations in caudal direction are restricted by 1,7 g, and accelerations in transversal direction are limited to 2–3 g [2]. Safety regulations also require that the clearance envelope determined as the set of points that any point of human extremity (tips of fingers of stretched arms or tips of toes of stretched legs) can reach when seated does not collide with

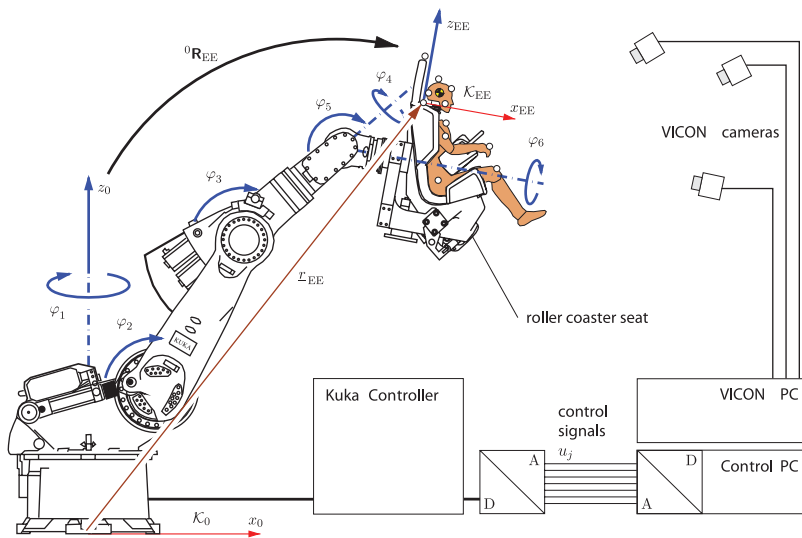


Fig. 1 Schematic representation of Kuka KR 500 flight simulator robot

the robot or the floor. For the minimal joint angles, collision between the clearance envelope and the robot is significant. This leads to a unique set of minimal axis limits at the closest contact posture (Fig. 2).

For maximally allowed joint limits, collision between the clearance envelope and the ground is relevant (Fig. 3). Here, rotation of the clearance envelope generates a sphere of radius  $R$  which should not intersect with the ground. In the limit, this

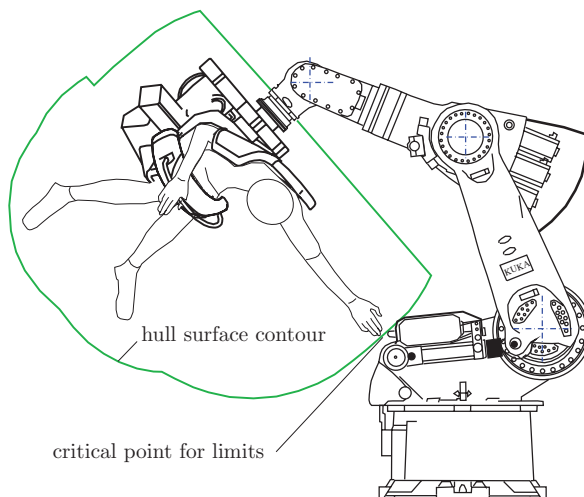
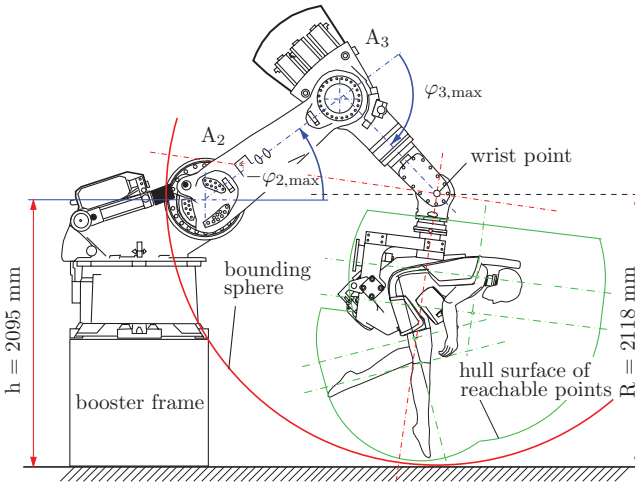


Fig. 2 Determination of lower axis angle limits for axes 2, 3, and 5





**Fig. 3** Determination of upper axis angle limits for axes 2 and 3

can be modeled by a surrogate crank-slider mechanism describing the sliding of the sphere on the ground (Fig. 4a). Thus, one obtains as relationship between maximal angles  $\varphi_{2,\max}$  and  $\varphi_{3,\max}$

$$\varphi_{3,\max} = \arcsin \frac{-\ell_2 \sin \varphi_{2,\max} + h - R}{\sqrt{\ell_3 + d}} - \varphi_{2,\max} + \arctan \frac{d}{\ell_3}, \quad (1)$$

where  $\ell_i$  is the length of link  $i$ ,  $d$  is the offset between axes 3 and 4,  $h$  is the height of axis 2 above the ground and  $R$  is the radius of the bounding sphere. Hereby, due to technical reasons the axis 4 is slightly oblique with respect to the axial direction of link 3, leading to a small angle correction for robot joint angle  $\varphi_3$  (Fig. 4a). From the solution plot shown in (Fig. 4b), it becomes clear that only the lower branch is relevant, as angles  $\varphi_{3,\max} > 90^\circ$  are unfeasible.

For the choice of the optimal limit for  $\varphi_{2,\max}$ , two criteria were regarded. One is the translational manipulability index [11] computed as the determinant of the sub-Jacobian  $\mathbf{J}_{s,1,2,3}(\varphi_{2,\max}, \varphi_{3,\max})$  consisting of the rows corresponding to translational motion and the columns corresponding to the first three axes. The second criterion is the maximal acceleration that can be achieved both in tangential ( $a_t$ ) and in centripetal ( $a_n$ ) direction when only axis 1 is actuated and the robot arm is horizontally extended to its maximum. This decomposition embodies the two alternatives for acceleration generation at the end effector, namely, by joint acceleration  $\ddot{q}_1(a_t)$  and by square of joint rate  $\dot{q}_1^2(a_n)$ . From Fig. 5 one can recognize that the two criteria have opposed improvement directions. Moreover, one recognizes that both criteria vary with the change of the reference point, where the values at the head of the passenger are higher than those at the wrist. Thus, as is clearly seen, (1) no unique optimum exists, and (2) performance criteria depend significantly on the operation point. Hence, no closed-form solution exists for optimal design and

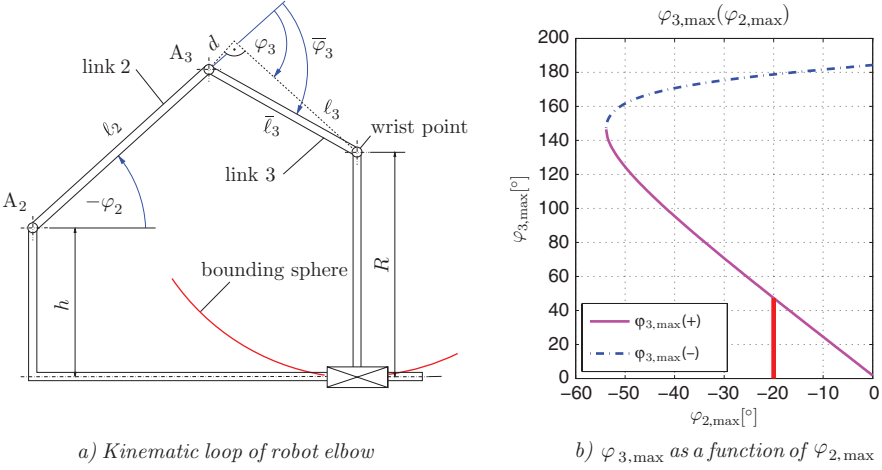


**Fig. 4** Solution of closed kinematic loop of robot elbow

the solution must be performed based on an engineering trade-off. In the present case, we chose  $\varphi_{2,\max} = 20^\circ$ , which is a point in which one can achieve high accelerations while remaining in the vicinity of the optimum manipulability point (Fig. 5). As shown in Fig. 6, both eccentricity (inverse of condition number) and maximal linear trajectory segment do not display a clear optimum point, and their minimization resp. maximization leads to a loss of acceleration potential. Hence, the above-mentioned pairing of acceleration and manipulability seems to be a good choice when a robot is pursued which should produce high accelerations.

### Control

For control, standard inverse kinematics fails to generate reasonable robot joint accelerations for given end-effector accelerations, since the Jacobian is badly conditioned due to the small regular domain. To avoid these problems, the input signal time histories at discrete time points are collected in a design vector  $\overset{x}{r}u$  and are determined by the optimization

$$\begin{aligned}
 &\text{minimize} \quad F(\overset{x}{u}) = \frac{1}{2} \sum_{i=1} [\widehat{a}_{EE,i} - \underline{a}_{EE}(\overset{x}{u}, t_i)]^2 \\
 &\text{subject to} \quad \underline{u}_{\min} \leq \overset{x}{u} \leq \overset{x}{u}_{\max}, \quad \underline{q}_{\min} \leq \underline{q}_i \leq \underline{q}_{\max}, \\
 &\quad \underline{\dot{q}}_{\min} \leq \underline{\dot{q}}_i \leq \underline{\dot{q}}_{\max}, \quad \underline{\ddot{q}}_{\min} \leq \underline{\ddot{q}}_i \leq \underline{\ddot{q}}_{\max} \quad \forall i \in [1, \dots, r]
 \end{aligned} \tag{2}$$

where  $\widehat{a}_{EE,i}$  is the target acceleration at time step  $t_i$ , and for every evaluation of  $F$ , the dynamic equations of the controller model are integrated using the input functions  $\underline{u}(t) = [u_1(t), \dots, u_6(t)]$ , leading to axis angle trajectories  $\underline{q}(t)$ , angle rates  $\underline{\dot{q}}(t)$  and

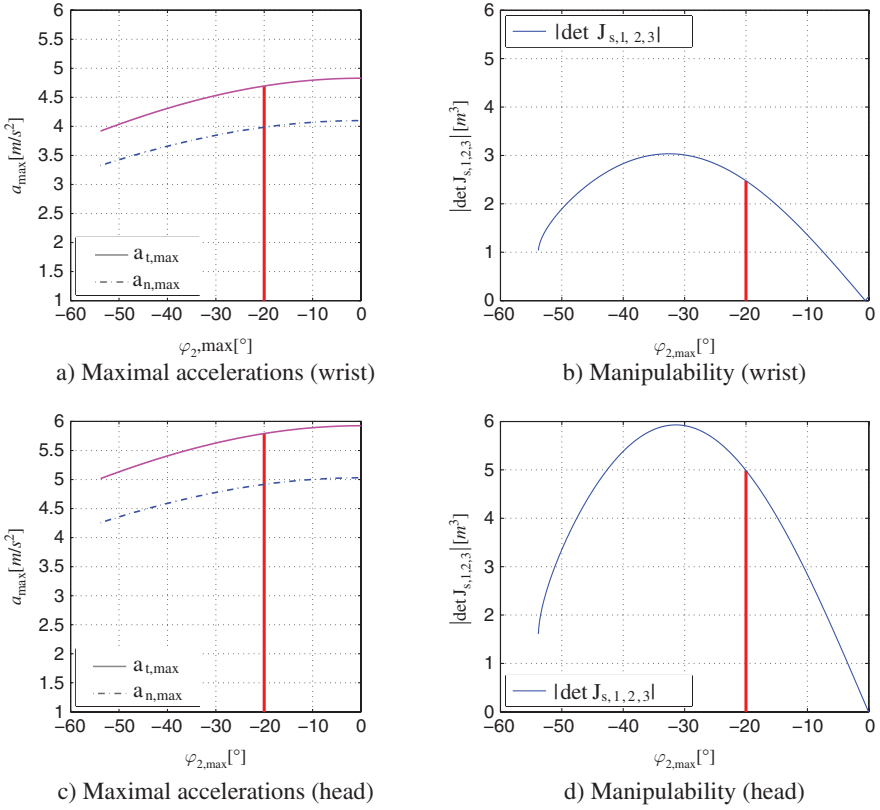
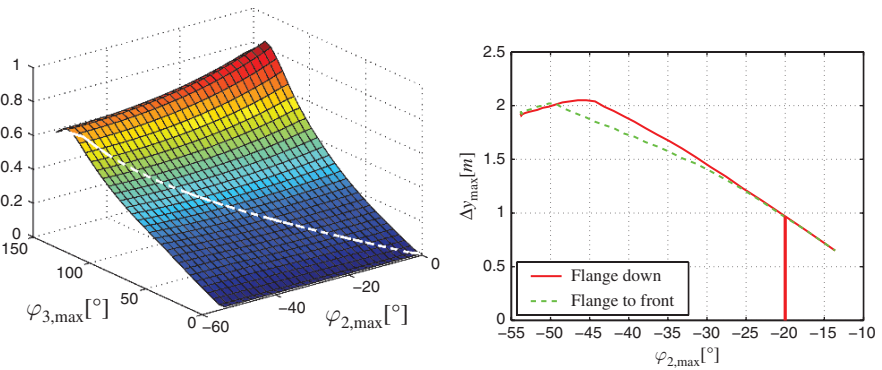


Fig. 5 Maximal accelerations and manipulability at wrist and head



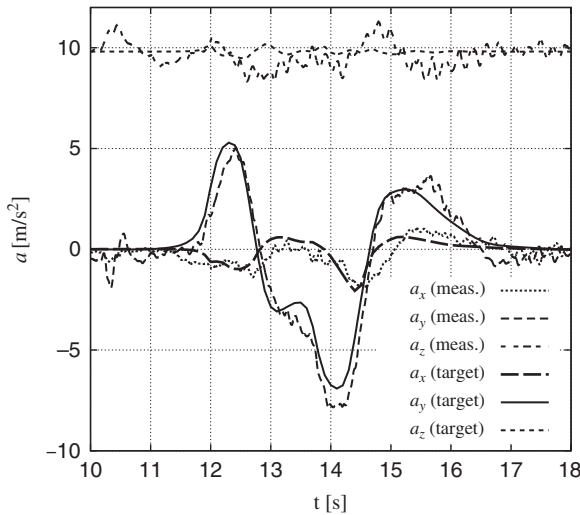


Fig. 7 Measured accelerations at end-effector for an elk test maneuver

joint accelerations  $\ddot{q}(t)$ , from which the linear end-effector acceleration  $\underline{a}_{EE}(\underline{x}, t_i)$  is computed. Solving the optimization problem, with the damped least squares solution of [5] as initial guess proved to warrant good convergence [9]. In Fig. 7, the result of an experiment in which a robot tracks real measured acceleration profiles for a so-called elk test (used as test maneuver in automotive engineering) is presented, showing a good agreement between target and generated accelerations.

## Conclusions

The paper presents a working setup for a serial-robot Kuka KR 500 TÜV motion simulator. Joint stop design is based on collision avoidance as well as peak acceleration and manipulability for performance optimization. The implementation of the concept shows a good dynamic behaviour, as illustrated by an example from vehicle dynamics.

**Acknowledgments** Financial support of the present project by Stiftung Maurer Söhne is gratefully acknowledged.

## References

1. D. Chablat and J. Angeles. On the kinetostatic optimization of revolute-coupled planar manipulators *Mechanism and Machine Theory*, 37(4):351–374, 2002.
2. Deutsches Institut für Normung e.V. DIN EN 13814 – Fliegende Bauten und Anlagen für Veranstaltungsplätze und Vergnügungsparks, 2004.

3. J. Heindl, M. Otter, H. Hirschmüller, M. Frommberger, N. Sporer, F. Siegert, and H. Heinrich. The robocoaster as simulation platform – experiences from the first authentic mars flight simulation. In *Proceedings of the Motion Simulator Conference*, Braunschweig, Germany, September 21 2005.
4. KUKA Roboter GmbH. Specification Robocoaster, 2002.
5. Y. Nakamura and H. Hanafusa. Inverse kinematics solutions with singularity robustness for robot manipulator control. *Journal of Dynamic Systems, Measurement and Control*, 108(3):163–171, 1986.
6. L. Pollini, M. Innocenti, and A. Petrone. Study of a novel motion platform for flight simulators using an anthropomorphic robot. In *AIAA Modeling and Simulation Technologies Conference and Exhibit*, pages 1–23, American Institute of Aeronautics and Astronautics, Keystone, Colorado, USA, August 2006.
7. A. Pott, A. Kecskeméthy, and M. Hiller. A simplified force-based method for the linearization and sensitivity analysis of complex manipulation systems. *Mechanism and Machine Theory*, 42(11):1445–1461, 2007.
8. F. Ranjbaran, J. Angeles, and A. Kecskeméthy. On the kinematic conditioning of robotic manipulators. In *IEEE International Conference on Robotics and Automation*, volume 4, pages 3167–3172, Minneapolis, April 22–28 1996.
9. M. Tändl, M. Conconi, and A. Kecskeméthy. Determining user-prescribed accelerations for a serial robot motion simulator. In *Proceedings of the 17th CISM-IFTOMM Symposium on Robot Design, Dynamics, and Control*, Tokyo, Japan, July 5–9 2008.
10. H. J. Teufel, H.-G. Nusseck, K. A. Beykirch, J. S. Butler, M. Kerger, and H. H. Bühlhoff. MPI motion simulator: development and analysis of a novel motion Simulator. In *AIAA Modeling and Simulation Technologies Conference and Exhibit*, pages 1–11, American Institute of Aeronautics and Astronautics, Reston, VA, USA, August 2007.
11. T. Yoshikawa. Manipulability of robotic mechanisms. *International Journal of Robotics Research*, 4(2):3–9, 1985.

# Operation Features of Milli-CaTraSys

Eusebio Hernandez-Martinez, Giuseppe Carbone and Carlos Lopez-Cajun

**Abstract** In this paper, the operation features of Milli-CaTraSys (Milli-Cassino Tracking System) are outlined. Models and formulations both for kinematics and statics are proposed. Results of experimental tests for calibration and operation are reported to show the feasibility and efficiency of a Milli-CaTraSys prototype.

**Keywords** Robotics · Measuring systems · Parallel architecture

## Introduction

Calibration of robotic systems requires measurement of the pose (position and orientation) of its end-effector for the purpose of compensating parameter errors and improving accuracy. Several measuring systems have been used to determine the pose of movable rigid bodies often by means of expensive measurement devices such as laser tracking systems [1], vision based measure devices [2, 3], or redundant systems [4]. Nevertheless, often measuring systems cannot measure position and orientation simultaneously or have limited accuracy, [5].

The option of cable based measuring systems is a feasible and cheap alternative for the identification of kinematic parameters on robotic systems. In fact, these systems can be a good compromise between expected accuracy and low cost. Some works have been focused on this type of architecture. For example, in [6] a parallel wire mechanism has been presented for pose measuring purposes. At LARM (Laboratory of Robotics and Mechatronics) in Cassino, a cable based measuring system has been studied and designed since late 1990s. It is named as CaTraSys (Catrasys Tracking System) and has been used to evaluate the serial robot workspace, [7]. In addition, a characterization of singularities and error analysis have been presented in [8, 9, 12], respectively. Recently, based on the design of CaTraSys, a new measuring system has been developed at LARM, [7, 10, 11]. This system, shown in Fig. 1, has been named as Milli-CaTraSys. In this work, models and formulations both

---

E. Hernandez-Martinez (✉)  
Facultad de Ingeniería, Universidad Autónoma de Querétaro, Qro, México  
e-mail: e.hernandez@unicas.it

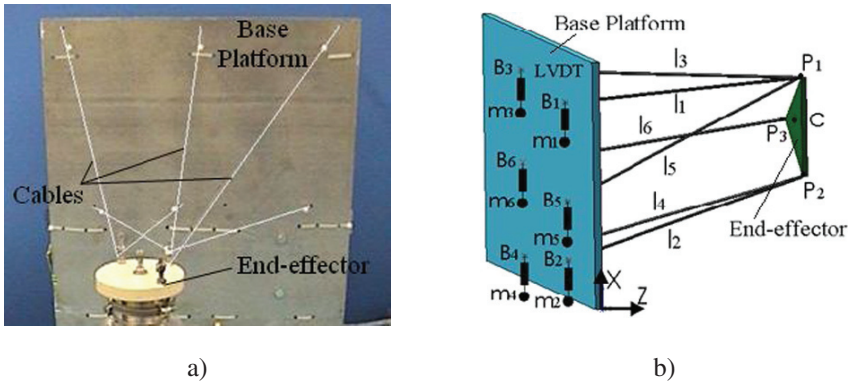


**Fig. 1** Milli-CaTraSys, (a) A prototype built at LARM in Cassino; (b) A 3D scheme with reference frame

for kinematics and statics are proposed for Milli-Catrasys. Experimental tests for calibration and operation have been carried out to show the feasibility and efficiency of a Milli-Catrasys prototype.

## Milli-CaTraSys Design

Milli-CaTraSys can be considered as a Gough-Stewart parallel manipulator with 3-2-1 configuration. It consists of two rigid bodies that are linked through six cables of variable lengths. Namely, the two rigid bodies are a base platform, and a moving platform that can be considered as end-effector, as shown Fig. 1a and 1b. By using the Milli-CaTraSys it is possible to evaluate the linear and angular compliant displacements occurring to a reference frame that is attached to the end-effector by measuring only linear distances. These linear distances are the lengths of cables that are measured by means of six LVDT transducers. Figure 1b shows the location of LVDT transducers on the fixed Milli-CaTraSys platform and the masses  $m_i$  ( $i = 1, \dots, 6$ ) that are applied on the free ends of the six cables. The data acquisition and the signal conditioning for the six transducers are implemented utilizing a NI DAQ Acquisition board PCI 6024, six LVDT transducers (with proper power supply and amplifiers) and a virtual instrument in LabVIEW environment. This virtual instrument has been developed to measure the data from the amplifiers of the LVDT transducers. In general, it consists of six channels to make the acquisition of the analogical inputs and a filter stage for the six signals. Then, data are stored in a suitable data file. For a detailed description of the virtual instrument see [7]. Applications of this measurement device include evaluation workspace and parameters identification of multibody robotic systems, Fig. 2. Milli-CaTraSys has been already successfully used for evaluation of workspace as show for example in [13]. Moreover, Milli-CaTraSys can be used to apply a known wrench on the end-effector of a robotic system. Since known masses can be applied to the free ends of its cables.

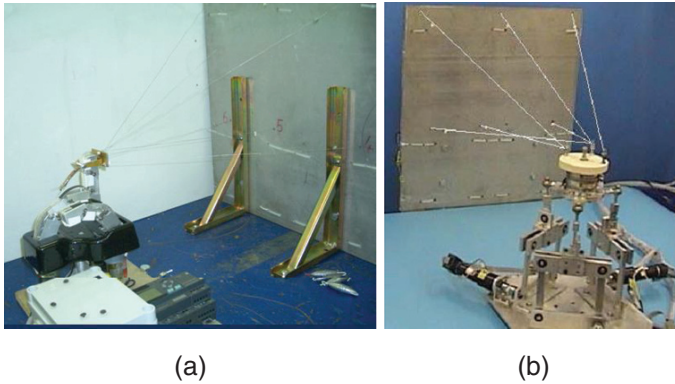


**Fig. 2** Milli-CaTraSys applications, **(a)** Workspace evaluation of LARM hand, [13]; **(b)** Measurement of stiffness performance for Cassino parallel manipulator version 2 bis, [14]

As a result, one can use Milli-CaTraSys for analyzing stiffness features of robotic systems as described in [14].

### Kinematic Operation

Considering the scheme that is shown in Fig. 1b  $\mathbf{B}_i(B_{ix}, B_{iy}, 0)$  (with  $i = 1, \dots, 6$ ) represent the vectors joining the origin with the points  $B_i$ , which are the sources of the cable lengths on the fixed base platform. Similarly,  $\mathbf{P}_i(P_{ix}, P_{iy}, P_{iz})$  (with  $i = 1, 2, 3$ ) represent the vectors joining the origin with  $P_i$  points, which are the attaching points of the cables on the end-effector. The centroid point on the Milli-CaTraSys end-effector is defined by  $\mathbf{C}(C_x, C_y, C_z)$ .

By construction the coordinates of  $B_i$  are known with respect to the fixed reference frame XYZ. The direct kinematic model expresses the relationship between the cable lengths and the pose of the end-effector. The position of  $P_1$  on the robot end-effector can be defined as the position of the point at which three arcs intersect. These arcs are defined by three spheres equations

$$l_i^2 = \|\mathbf{B}_i\mathbf{P}_i\|^2 \text{ with } i = 1, 2, 3 \tag{1}$$

Using Eq. (1) the coordinates of  $P_1$  can be obtained by referring to a tetrahedron with known edge lengths  $l_1, l_3$ , and  $l_5$ . Thus, the solution of Eq. (1) provides two mirror coordinates of  $P_j$ . However, the suitable solution can be chosen as the one having positive value. Then, the coordinates of  $P_2$  can be obtained by referring to a second tetrahedron that is defined by referring the cable lengths  $l_4, l_2$  and the known distance  $\overline{P_1P_2}$ . Finally, a third tetrahedron is defined by referring the cable length  $l_6$  and the known distances  $\overline{P_1P_3}$  and  $\overline{P_2P_3}$ .



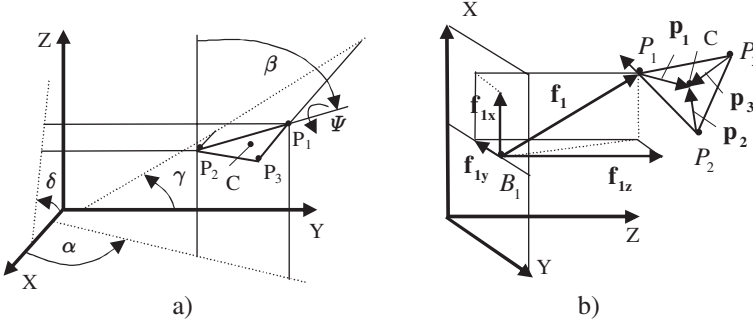


**Fig. 3** Schemes of Milli-CaTraSys, **(a)** Description of the orientation of the end-effector through the set angles ( $\alpha$  and  $\beta$ ) or ( $\gamma$  and  $\delta$ ) and  $\psi$ ; **(b)** Forces acting on one cable of Milli-CaTraSys

The coordinates of  $P_1$ ,  $P_2$ , and  $P_3$  can be used to compute the pose of the end-effector of Milli-CaTraSys as given by the coordinates of  $C$  and the orientation angles  $\alpha$ ,  $\beta$ , and  $\varphi$  or  $\gamma$ ,  $\delta$  and  $\varphi$  as it is shown in Fig. 3a in the form

$$C(C_X, C_Y, C_Z) = \left( \frac{P_{1x} + P_{2x} + P_{3x}}{3}, \frac{P_{1Y} + P_{2Y} + P_{3Y}}{3}, \frac{P_{1Z} + P_{2Z} + P_{3Z}}{3} \right) \quad (2)$$

$$\alpha = \tan^{-1} \left( \frac{P_{1y} - P_{2y}}{P_{1x} - P_{2x}} \right) \quad (3)$$

$$\beta = \tan^{-1} \left( \frac{P_{1z} - P_{2z}}{\left( (P_{1y} - P_{2y})^2 + (P_{1x} - P_{2x})^2 \right)^{1/2}} \right) \quad (4)$$

$$\psi = \tan^{-1} \left( \frac{P_{3z} - C_z}{\left( (P_{3y} - C_y)^2 + (P_{3x} - C_x)^2 \right)^{1/2}} \right) \quad (5)$$

The above-mentioned procedure has been implemented in Matlab environment so that the measures of cable lengths  $l_i$  ( $i = 1, \dots, 6$ ) provide automatically the end-effector pose of Milli-CaTraSys.

## Static Operation

Milli-CaTraSys uses known masses  $m_i$  (with  $i = 1, \dots, 6$ ) on the free ends of its cables in order to guarantee that all cables are always pulling (in tension). Thus,

one can compute the forces on the six cables of the system that are given by these masses. Please note that a fixed reference frame can be chosen as shown in Fig. 3b. Then, the forces acting on the end-effector by means of each cable can be written as

$$\mathbf{f}_i = f_i \frac{\mathbf{l}_i}{l_i} \quad \text{with } i = 1, \dots, 6 \quad (6)$$

where the subscript  $i$  denotes the  $i$ -th cable,  $f_i$  denotes the magnitude of  $\mathbf{f}_i$  and  $\frac{\mathbf{l}_i}{l_i}$  denotes a unit vector in the  $i$ -th cable direction.

Summing all the forces acting on the end-effector, the components of  $\mathbf{F}$  ( $F_x$ ,  $F_y$ ,  $F_z$ ) can be computed as

$$\mathbf{F} = \sum_{i=1}^6 f_i \frac{\mathbf{l}_i}{l_i} \quad (7)$$

Additionally, summing the moments given by all the forces about the centroid  $C$  of the end-effector, the components of  $\mathbf{N}$  ( $N_x$ ,  $N_y$ ,  $N_z$ ) can be computed as

$$\mathbf{N} = \mathbf{p}_1 \times (\mathbf{f}_1 + \mathbf{f}_2 + \mathbf{f}_3) + \mathbf{p}_2 \times (\mathbf{f}_4 + \mathbf{f}_5) + \mathbf{p}_3 \times \mathbf{f}_6 \quad (8)$$

where  $\mathbf{P}_1$ ,  $\mathbf{P}_2$  and  $\mathbf{P}_3$  are the vectors joining the  $P_1$ ,  $P_2$  and  $P_3$  points with the end-effector centroid  $C$ , as shown in Fig. 3b.

A suitable algorithm in Matlab environment can automatically provide the applied wrench as function of the pose and applied masses  $m_i$  ( $i = 1, \dots, 6$ ).

## Experimental Tests

### *Experimental Setup and Calibration*

A calibration process has been carried out in order to determine a suitable initial configuration for the measuring system and to verify its accuracy. The calibration procedure can be simplified as in the flowchart of Fig. 4, where  $\vartheta_i$  and  $\delta_i$  are considered as acceptable calibration errors in the process. The experimental measure of pose for the end-effector of Milli-CaTraSys has required to perform accurate measurements of distances from the reference frame origin to  $B_i$  points. X, Y-axis coordinates of points  $B_i$  are reported in Table 1; Z-axis coordinate is always equal to zero since points  $B_i$  are all on the X–Y plane of the fixed reference frame.

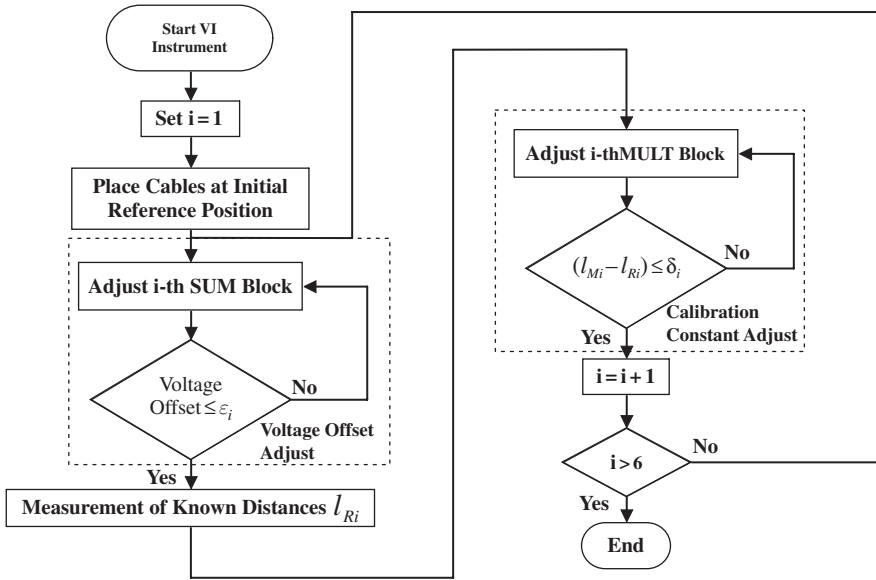


Fig. 4 A flowchart for the calibration procedure of Milli-CaTraSys

Table 1 Measured distances from the origin of the fixed reference frame to  $B_i$  points in [mm] units

Point	$B_1$	$B_2$	$B_3$	$B_4$	$B_5$	$B_6$
x-Axis Coordinate	411	224	35	387	187	68
y-Axis Coordinate	469	469	466	207	205	204

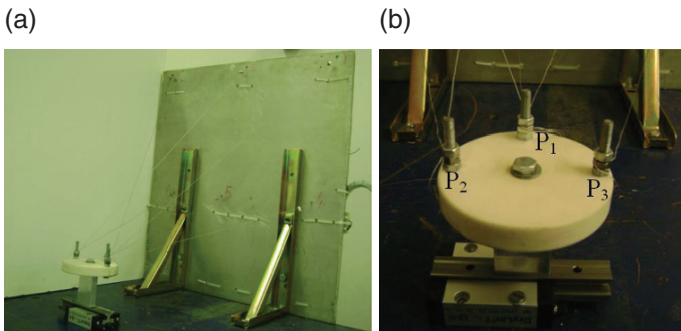
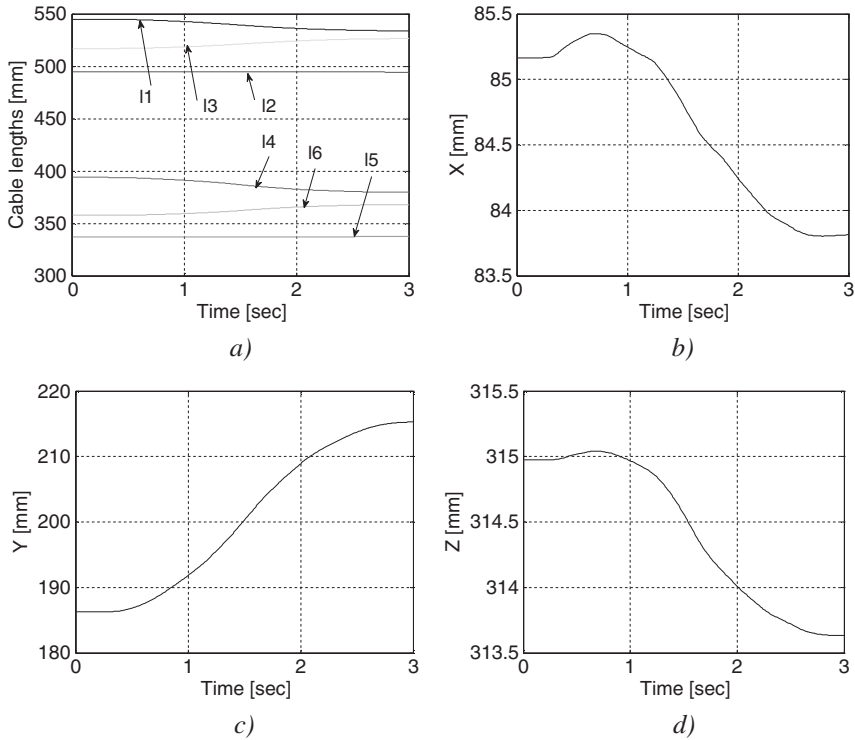


Fig. 5 End-effector of Milli-CaTraSys, (a) A general view; (b) A frontal view with the 3-2-1 configuration



**Fig. 6** Milli-CaTraSys end-effector moving along Y-axis, (a) Measured lengths of the six cables; (b) Displacements along X-coordinate; (c) Displacements along Y-coordinate; (d) Displacements along Z-coordinate

### Experimental Results

Experimental tests have been carried out by measuring with Milli-CaTraSys a known displacement along Y, and Z-axis with a slider guide. The setup for these experiments includes a slider guide to achieve known displacements as shown in Fig. 5a. The Milli-CaTraSys end-effector has been attached on the slider guide with a 3-2-1 configuration as shown Fig. 5b. Thus, Fig. 6a shows the plots of the measured lengths of the cables during an experimental test along Y-direction. Then, measured lengths of cables are used to give the position of the end-effector of Milli-CaTraSys through Eqs. (1), (2), (3), (4) and (5). The  $P_1$ ,  $P_2$ ,  $P_3$  coordinates of Milli-CaTraSys end-effector for the above-mentioned experimental test are reported in Fig. 6b, 6c and 6d, respectively. Similarly, Fig. 7a shows the plots of the measured lengths along Z-direction. Figure 7b, 7c, and 7d show the plots of the Milli-CaTraSys end-effector coordinates for this case. It is worth noting that the plot of Fig. 6b shows a maximum displacement of 1.5 mm, then the accuracy of Milli-CaTraSys system can be estimated. Two types of LVDT sensors have been tested to be implemented on Milli-Catrasys prototype. First type of LVDT sensors has a full

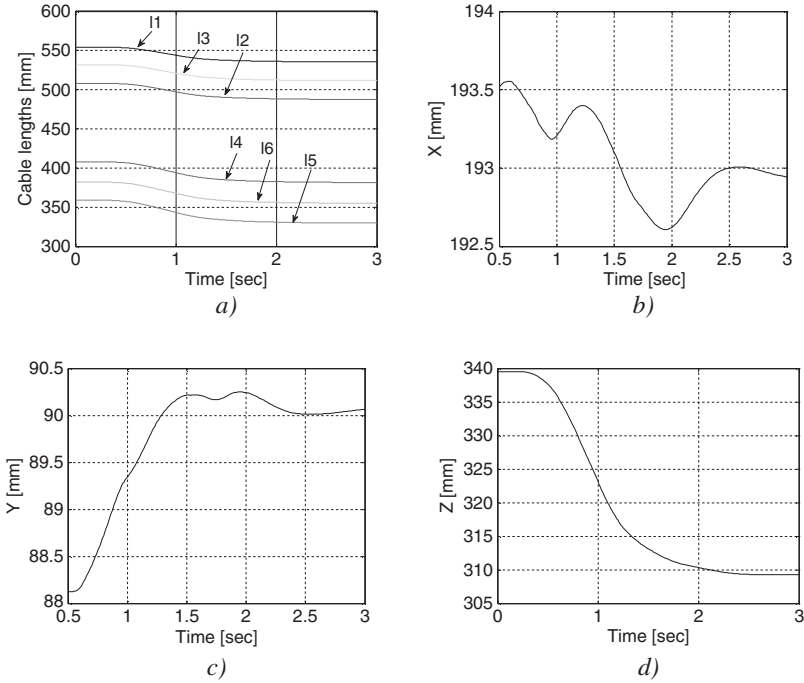


**Fig. 7** Milli-CaTraSys end-effector moving along Z-axis, (a) Measured lengths of the six cables; (b) Displacements along X-coordinate; (c) Displacements along Y-coordinate; (d) Displacements along Z-coordinate

scale measuring range of 200 mm and an accuracy of 0.25% of the full scale. The Milli-CaTraSys prototype can have an overall accuracy of 0.5 mm when equipped with this type of sensors. Second type of LVDT sensors has a full scale measuring range of 5 mm and an accuracy of 0.25% of the full scale. The Milli-CaTraSys prototype can have an overall accuracy of 0.01 mm when equipped with this type of sensors. Orientation plots have not been reported since the selected motions along Y and Z-axis do not measure any change on the orientation.

## Conclusion

In this paper, operation features for Milli-CaTraSys measuring system have been presented. Kinematic and static behaviour of Milli-CaTraSys has been described by means of suitable analytical models. Experimental results for calibration and operation are reported. Results of operation performance for Milli-CaTraSys show satisfactory accuracy, suitable low-cost, and easy-operation features.

**Acknowledgments** This work has been developed in a period of study of first author at LARM during the year 2008 within a cooperation program between University of Cassino and University of Queretaro, that has been supported by CONACyT through a scholarship program.

## References

1. Chai K. S., Young K. and Tuerley I., A Practical Calibration Process Using Partial Information for a Commercial Stewart Platform, *Robotica*, Vol. 20, No. 3, 2002, pp. 315–322.
2. Rauf A., Pervez A. and Ryu J., Experimental Results for Kinematic Calibration of Parallel Manipulators Using a Partial Pose Measurements Device, *IEEE Transactions on Robotics*, Vol. 22, No. 2, 2006, pp. 379–384.
3. Renaud P., Andreff N., Lavest J. M. and Dhome M., Simplifying the Kinematic Calibration of Parallel Mechanisms Using Vision-based Metrology, *IEEE Transactions on Robotics*, Vol. 22, No. 1, 2006, pp. 12–22.
4. Chiu Y. and Perng M., Self-calibration of a General Hexapod Manipulator with Enhanced Precision in 5 dof Motions, *Mechanism and Machine Theory*, Vol. 39, 2004, pp. 1–23.
5. Ceccarelli M., *Fundamentals of Mechanics of Robotic Manipulation*, Kluwer Academic Publishers, 2004.
6. Won Jeong J., Hyun Kim S., Keun Kwak Y., Smith C., Development of a Parallel Wire Mechanism for Measuring Position and Orientation of a Robot End-effector, *Mechatronics*, Vol. 8, 1998, pp. 845–861.
7. Ottaviano E., Ceccarelli M., Toti M., Avila-Carrasco C., Catrasys a Wire System for Experimental Evaluation of Workspace, *Journal of Robotics and Mechatronics*, Vol. 14, No. 1, 2002, pp. 78–87.
8. Ottaviano E. and Ceccarelli M., Numerical and Experimental Characterization of Singularities of a Six-Wire Parallel Architecture, *Robotica*, Vol. 25, No. 3, 2006, pp. 315–324.
9. Ceccarelli M., Avila Carrasco C., Ottaviano E., Error Analysis and Experimental Test of Catrasys (Cassino Tracking System), *IEEE International Conference on Industrial Electronics, Control and Instrumentation*, Nagoya, 2000, Paper SPC11-SP-4.
10. LARM homepage. Available at <http://webuser.unicas.it/weblarm/>, 2008.
11. Hong D., Mueller K. J., Velisky S. A., A Cable Extension Transducer Based Two-dimensional Position Sensor for Industrial Applications, *Transactions ASME Journal of Manufacturing Science Engineering*, Vol. 124, No. 1, 2002, pp. 105–108.
12. Thomas F., Ottaviano E., Ros Li., Cecarelli M., Performance Analysis of a 3-2-1 Pose Estimation Device, *IEEE Transactions on Robotics*, Vol. 21, No. 3, 2005, pp. 288–297.
13. Carbone G. and Ceccarelli M., Experimental Tests on Feasible Operation of a Finger Mechanism in the LARM Hand, *Mechanism Based Design of Structures and Machines*, Vol. 36, 2008, pp. 1–13.
14. Carbone G. and Ceccarelli M., A Procedure for Experimental Evaluation of Cartesian Stiffness Matrix of Multibody Robotic Systems, *15th CISM-IFTOMM Symposium on Robot Design, Dynamics and Control*, Romansy, Montreal, 2004, CD Proceedings, Paper Rom04–24.

# Design of an Actuation System for a Fatigue Test RIG

Luca Pugi, Andrea Rindi, Benedetto Allotta and Giuseppe Gori

**Abstract** Hydraulic servo systems are the product of a mature, reliable technology whose main advancements have been produced after the second world war in the so called “cold war” period. However even considering the recent development of electric linear actuator, and the general cost reduction of power electronics, this technology is still fashionable for many motion control applications in which heavy force/encumbrances ratio are required. Modern CAE techniques can be used to overcome traditional design troubles related to the modeling of components, often dominated by non linear effects due to complex physical phenomena like pressure drops, bulk modulus, etc.

In this work authors show a case study concerning a real application: the design of the actuation system for an advanced fatigue test rig that have to be used to verify structural and modal properties of compound panels used for the construction of railway vehicles.

**Keywords** Hydraulic · Servo system · Motion control

## Introduction: A Typical Case Study

In this paper authors present a study concerning the design of a rig for fatigue and modal testing of compound panels used for railway vehicle construction. The rig is composed by a rectangular frame of about 2.5 of length and 1 m of width on which the tested component is placed as in the simplified scheme visible in Fig. 1a. A linear actuator placed on a mobile portal is used to excite the panel with known force or position profiles for both static and dynamical tests that are often described in literature [1–3]. However the frame can be predisposed for wide variety of panels with different sizes, constrained in different ways according performed tests. In

---

L. Pugi (✉)  
Sez. Meccanica Applicata Dip. Energetica Sergio Stecco, Università di Firenze,  
Via Santa Marta 3, 50100 Firenze (FI), Italy  
e-mail: luca@mapp1.de.unfi.it

order to properly chose and size actuators and motion control system, authors produce a simplified finite element model of a typical tested panel in different load and constraint conditions using commercial software like MSC Nastran<sup>TM</sup> and Comsol Femlab<sup>TM</sup>. Using this tools it was possible to calculate typical panel receptance as visible in Fig. 1b. Specifications assign maximum amplitude of desired excitation forces, and their frequency range from 0 to 20 Hz. A run of 100 mm was prescribed with dynamic oscillations not exceeding  $\pm 10$  mm of amplitude. Maximum required force was about  $\pm 10$  kN. Mechanical frame of the rig have optimized both from static and modal point of view in order to assure negligible structural deflections during tests.

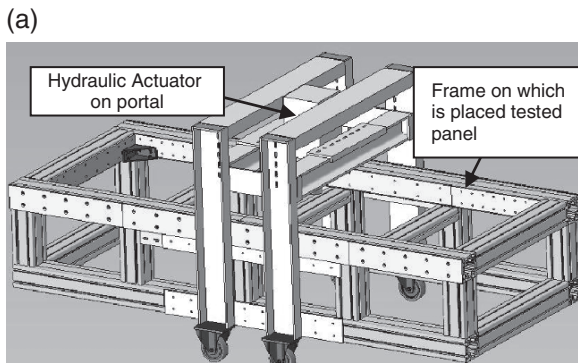


**Fig. 1a** Simplified scheme of the rig for fatigue test on panels

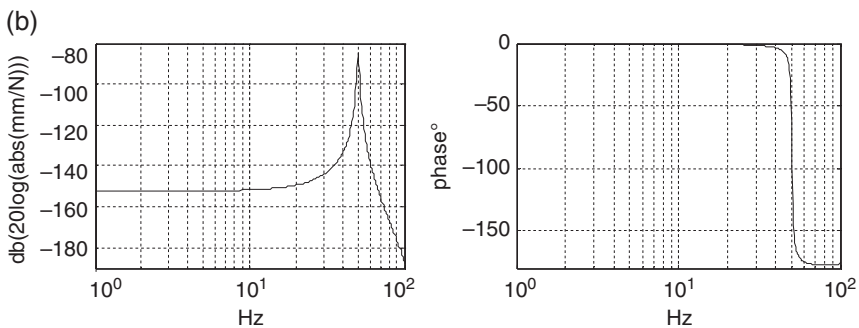


**Fig. 1b** Typical receptance curve calculated by MSC Nastran FEM model in the range of a compound panel tested on the rig (constraints modelled as ideal)



## Initial Plant Sizing and Layout

Hydraulic technology was chosen for the actuation system in order to privilege reliability and durability, standard plant pressure of 280 bar have been chosen. Actuator area was calculated supposing that maximum required force can be statically exerted with a plant pressure of 210 Bar. Servo-Valves nominal flow is typically [4–5] calculated considering a pressure drop of about 70 bar (1,000 psi). As consequence the chosen cylinder is able to exert the required force until a maximum speed corresponding to the nominal flow of the chosen Servo-Valve is reached. Servo-valve control instead of Pump Flow control [6] is mandatory in this kind of application where a good frequency response is required. A double rod cylinder with an area of about 5.5 cm<sup>2</sup> was chosen since customer specifications explicitly require an actuator with symmetrical force and speed performances. A no-friction seal cylinder with hydrostatic lubrication was chosen in order to prevent negative consequences of spurious lateral forces applied to actuator in case of asymmetrical loading or constraint conditions. Maximum Flow “ $Q_{max}$ ” required in order to properly size the valve can be easily calculated from (1):

$$Q_{max} = A \cdot V_{max} \approx 41\text{--}42 \text{ litres/min} \tag{1}$$

$A = \text{actuator area}; V_{max} = \text{max actuator speed}$

First actuator resonant frequency due to oil equivalent stiffness has to be much higher than operating frequencies. This first frequency can be calculated as the minimum eigen-frequency of an equivalent S.D.O.F. system that can be obtained approximating oil and tested panel stiffness with a lumped spring and equivalent inertia corresponding to the sum of load and piston reduced masses (2).

$$\omega_n(x) = \min_{x \in [0, r]} = \sqrt{\frac{1}{M} \left( \frac{E_b \cdot A \cdot r}{(r-x)x} + K \right)} = \omega_n \left( \frac{r}{2} \right) = \sqrt{\frac{E_b \cdot 4A}{M \cdot r} + \frac{K}{M}}$$

$E_b = \text{oil bulk modulus}; r = \text{total actuator run}; x = \text{actual run};$   
 $M = \text{load and piston inertia}; K = \text{panel stiffness}; \frac{E_b \cdot A \cdot r}{(r-x)x} = \text{oil stiffness}$   
*neglecting dead volumes*

$$\tag{2}$$

Considering the smoothing effect of an hydraulic accumulator placed near the valve the minimal size of the pump in terms of continuous fluid flow “ $Q_{mpr}$ ” can be calculated according (3) in the hypothesis of pure sinusoidal motion:

$$Q_{mpr} = \text{rms}(Q(t)) \gg 29\text{--}30 \text{ litres/min.} \tag{3}$$

“ $Q_{mpr}$ ” calculated according have to be increased by a safety factor that have to be calculated according further considerations:

- (1) Additional flow due Hydrostatic lubrication, valve and cylinder leakages, un-modeled pipes and oil capacitive effects.
- (2) Control implementation: in order to properly control the actuator the servo-valve continuously modulates the flow. A sub-optimal control implementation may also involve reduced system efficiency in terms of demanded flow.
- (3) At the end an over-sized pumping plant may also be the consequence of a rough optimization from a thermal point of view (more oil, more cooling surfaces etc.).

Also frequency response of valve has to be verified according desired system performances. In order to properly control both imposed force and position sensors are integrated in cylinder body and rod. Closed loop control will be implemented with a minimum sampling frequency of about 1 kHz according real time hardware performances. A simplified scheme of the resulting plant is shown in Fig. 2.

Modal response of the panel is approximated by an equivalent 1 D.O.F system that approximate panel receptance curves range among the first eigen-frequency of the system. Also modal shapes or receptances curves calculated from finite element model can be implemented. However the chosen approach is preferable since computational load is much lower. Also from calculated receptance function visible in Fig. 1b it can be easily noticed that typically only the first mode is interested by the frequency range exerted by the rig. Also this receptance curve has to be modified in order to take count of piston inertia (stiffness of rod is neglected). At the end higher frequencies modes are more sensitive to un-modeled phenomena like real constraint receptance or structural damping that can be hardly predicted.

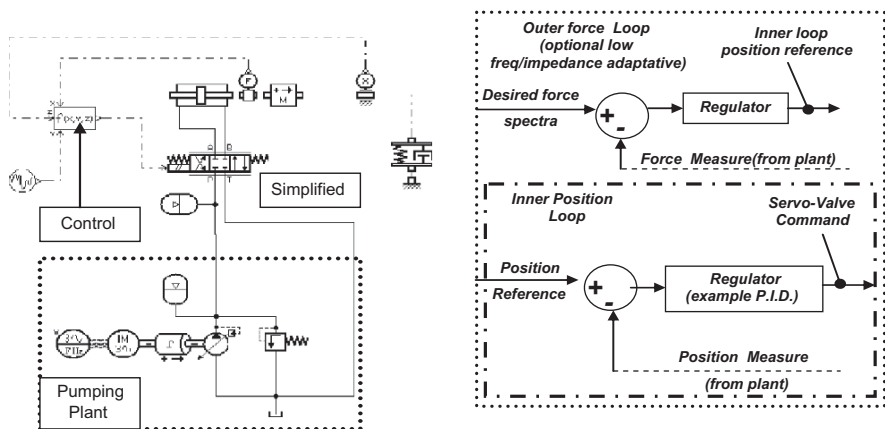
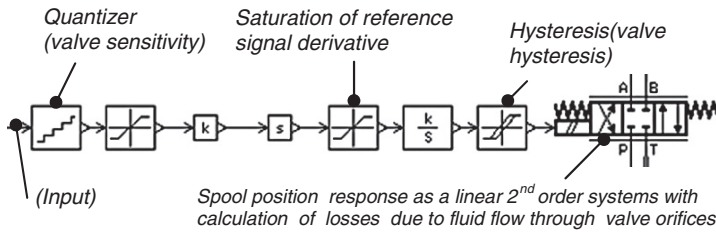


Fig. 2 View of equivalent LMS Amesim™ model with an example of the control on right

### Identification of Servovalve and Actuator Performances

The chosen servovalve, Moog G761-3005 [4], is a flow-control flapper valve with mechanical feedback whose nominal flow is about 63 l/min.

From valve response data, published by the supplier, supplier assures an optimal response of the valve for spool oscillations corresponding to the 40% of the nominal flow. If the valve works in this reduced amplitude range, frequency response is well approximated by a second order system whose coefficients have been easily identified by authors following classical to unconventional methodologies described in literature [4–11]. According rig specification spool velocity amplitude can be higher than this prescribed interval. Non linear behaviour negatively affects valve performances for full amplitude oscillations. Using a modern CAE system, LMS AMESIM™, authors have then tried to understand how non linear behaviour of components may negatively affect system performances. Iterative fitting procedures (example gradient based procedures, neural networks etc.) available in many simulation tools from LMS Amesim™ to Mathworks System Identification Toolbox™ need to identify such a non linear system of a sufficient amount of data, in order to



**Fig. 3** Simplified Plant Scheme (view of equivalent LMS Amesim™ model) with an example of the control on right

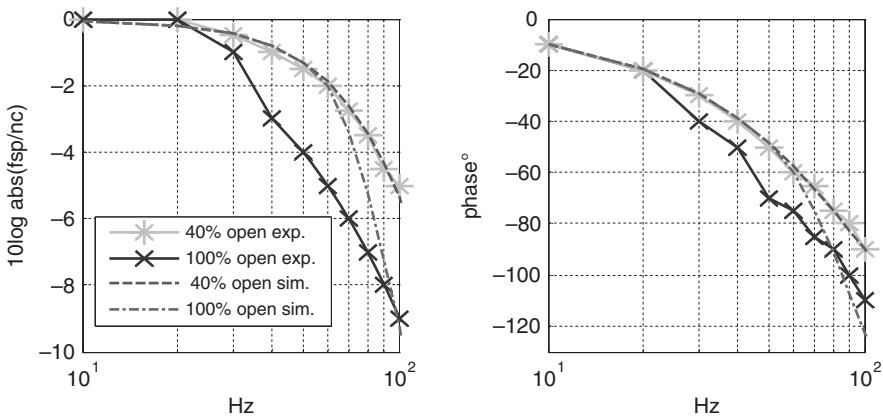
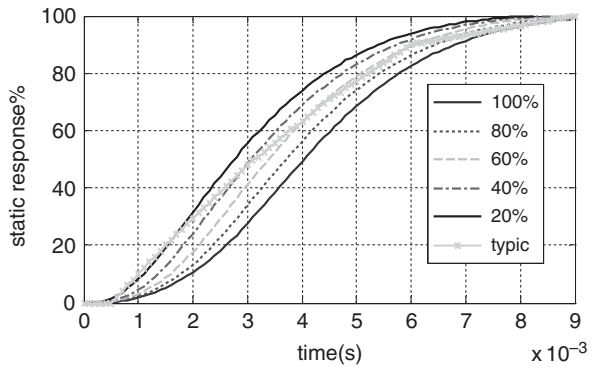


**Fig. 4** Comparison between experimental value from technical documentation and simulation results

**Fig. 5** Different step response according step amplitude



avoid typical problem of robustness and over-fitting. From technical documentation is available only a graph representing “typical time response of spool to a step input” [4]. So authors tries to model valve behaviour by introducing simple non linear blocks as visible in the scheme of Fig. 3

Limited speed of response is clearly visible from experimental data and is reproduced by adding saturations on value and first derivative of the reference signal. Also discretization and Hysteresis blocks are added in order to reproduce in a cautious way, sensibility and linearity limitation of the valve. Using supplier technical documentation, authors have tried to model a condition almost equivalent to worst values assured by production tolerances.

Then authors perform some simulations with known amplitude-frequency sinusoidal input in order to obtain, from spectral analysis of computed response, amplitude dependent transfer functions that can be compared with experimental results of valve supplier. Looking at results, the simple artifice proposed in this work seems to have a poor ability to fit experimental frequency response for 100% opening of the valve as visible in Figs. 4 and 5. However maximum required valve opening according system specification will be around 60% so a good fitting of the 40% curve is most important. Also a comparison of time responses to step excitation shows that this simplified approach lead to degradation of valve that increase gradually with step amplitude but that is quite similar to the typical response described by supplier technical documentation.

## Full Plant Simulation with LMS Amesim<sup>TM</sup>

Using simplified plant model described in Fig. 2 is possible to properly size components like accumulators or to verify sensitivity of the chosen solution to various uncertainties as, for example, variable receptances of tested panels. In Table 1 an example of difference tests population is shown.

**Table 1** Examples of different testing conditions

Case No.	Statical stiffness (N/m)	Inertia (Kg)	Damping (N/ms)	Imposed motion(m)	Max force range
1	2,000,000	30	100	0.002+0.002*Chirp (0-20 Hz, 2 Hz/s)	0-8,000 N
2	400,000	50	200	0.01*Chirp (0-20Hz, 2 Hz/s)	±8,000 N
3	8,000,000	10	10	0.0012*Chirp (0-20 Hz, 2 Hz/s)	±10,000 N

Imposed motion control is implemented as a simple proportional control working with 1 KHz sampling frequency, in order to reduce negative effects of modelled non linearities such as hysteresis and quantization, a zero mean dithering signal is summed to valve reference command. Chirp excitation is chosen to test in a rapid way response to different frequencies ranging from 0 to 20 Hz.

A constant oil bulk modulus of 17,000 bar and absolute viscosity of 51 cP is supposed. Deformation of pipes is evaluated supposing standard steel walls. Closed loop transfer functions from desired to measured displacement for the proposed are shown in Fig. 6. The system seems to be quite robust against this kind of parametric uncertainties since transfer function magnitude is quite close to the value of 0 db. However, as panels equivalent stiffness increases, unfavourable combination of high loads and little displacements (case 3) may involve performance degradation especially for higher frequencies. Also in this condition the system is more sensitive to noise on measured displacements or to structural deformations of the test rig frame which is considered rigid in this study.

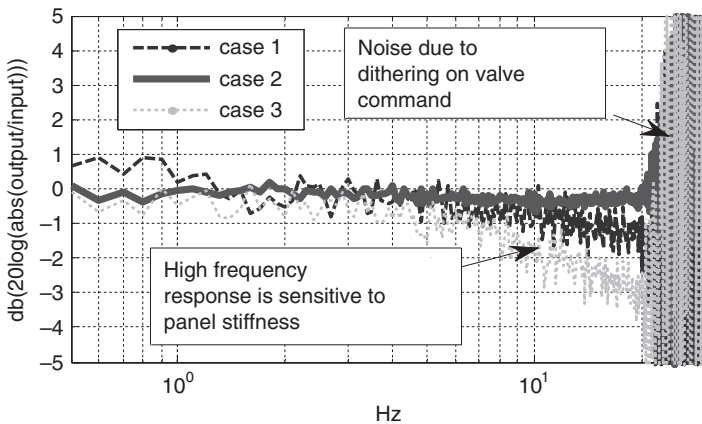


**Fig. 6** Comparison of closed loop transfer functions

## Conclusion and Future Hints

This case study is an example of how CAE tools may be used to complete traditional design methods in order to understand how interaction between different non linear phenomena may affect the complex dynamical behaviour of a hydraulic plant. This aspect is important especially on high performance proportional systems where rapid transients and great accuracy are often required. General lack of experimental data from components suppliers and the complexity of simulated phenomena often introduce heavy uncertainties if predictive results are required. However these tools are quite useful in order to verify robustness and sensitivity of the chosen design to parametric uncertainties and generally to disturbances and un-modeled dynamics. At the end existing CAE tools like LMS Amesim<sup>TM</sup> are quite mature reliable technologies. Further collaboration between software developer and major hydraulic components suppliers is needed to produce wide libraries of shared pre-calibrated models continuously updated and improved by an open community of users.

**Acknowledgments** Authors wish to thanks all the people that have cooperated to this study:

- (1) Specification arrangement and financing: Giuseppe Gori (Servindustria SRL)
- (2) Hydraulic components supplier: Ing. Fausto Argeri (Moog Italiana SRL)
- (3) Real time hardware and sensors consultants: Ing. Luigi Giorgi (National Instruments)

## References

1. K.A. Feichtinger, *Test Methods and Performance of Structural Core Materials* – 1. Static Properties Journal of Reinforced Plastics and Composites, Vol. 8, No. 4, 334–357, 1989
2. J.M. Di, Hodgkinson, *Mechanical Testing of Advanced Fibre Composites*, Woodhead Publishing 2003
3. R.B. Deo, C.R. Saff, *Composite Materials: Testing and Design*, ASTM International 1996
4. Moog Inc., *G761 Series Servovalves ISO 10372 Size 04*, Technical documentation 2008
5. W.J. Thayer, *Transfer Functions for MOOG Servovalves*, Moog Technical Bulletin 103 1965
6. N.D. Marning, *Hydraulic Control Systems*, John Wiley and Sons 2005
7. R.S. Cataldo, *Analysis of Electrohydraulic Valves and Systems* ISA-11-60, presented at JACC, Boston, USA September 1960
8. G.G. Lisini, *Servomeccanismi*, Editrice Tecnico Universitaria, PISA 1973
9. H.E. Merritt, *Hydraulic Control Systems*, New York John Wiley and Sons, Inc. 1967
10. Hydraulic Servo-systems: Modelling, Identification and Control, *Di Mohieddine Jelali, Andreas Kroll*, Pubblicato 2003 Springer ISBN: 1852336927
11. D.J. Martin, C.R. Burrows, Mathe, *Dynamic Characteristics of an Electro-Hydraulic Servo-valve*(American Society of Mechanical Engineers, 1976.) ASME, Transactions, Series G – Journal of Dynamic Systems, Measurement, and Control, Vol. 98, 395–406, December 1976

# The Influence of Motion Mode and Friction on the Dynamics of a Parallel Robot Used for Orientation Applications

Doina Pisla and Tiberiu Itul

**Abstract** This paper presents a method for the dynamical modeling of a 3-DOF parallel mechanism without and with friction used for orientation applications (TV satellite antenna or sun tracker). Parallel robots have some advantages over serial ones such as higher stiffness, very good accuracy, high speeds and accelerations, a better weight over payload rate. Using a numerical and graphical simulation, the diagrams for the dynamics representation are computed. In the paper the influence of the task duration and friction on the joint torques is studied.

**Keywords** Parallel robot · Dynamics · Kinematics · Simulation

## Introduction

Dynamics effects and analysis are the basis of design specification and advanced control of parallel mechanical systems. To establish the equations of motion, there exist essentially four methods: Newton-Euler equations; Lagrange equations of first kinds with so-called LAGRANGE multipliers; Lagrange equations of second kind with a minimum number of system coordinates; Virtual work formulation.

Until now, in the most existing papers, the experimental identification of dynamics for the parallel robots is restricted to simple models in combination with adaptive control algorithms [1–5]. The most important force source which is not included is the friction.

A new approach was presented in [6], where Grotjahn et al. develop a complex dynamic model including friction, which uses Jourdain's principle of virtual power and is suited for the parallel robot control of the innovative hexapod PaLiDA. The friction model includes friction in both active joints as well in passive joints. Poignet et al. [7] deal with the application of the interval analysis to estimate the 4-degrees

---

D. Pisla (✉)

Technical University of Cluj-Napoca, Constantin Daicovicu 15,  
RO-400020 Cluj-Napoca, Romania  
e-mail: Doina.Pisla@mep.utcluj.ro

of freedom parallel robot dynamic parameters. Yiu et al. [8] developed the dynamics with friction for a planar redundant parallel robot.

Riebe et al. [9] present a dynamic model for a Stewart platform with 6 DOF, based on Newton-Euler equations including the frictional behaviour. The parameters describing the friction model are identified and optimized. Chen et al. [10] present a dynamic model of a Cartesian guided tripod including the nonlinear compliance and mechanical friction. Quantitative analysis and comparison of the variation friction sources from the actuated joints and passive joints have been conducted. In [11, 12] different solutions for solving the dynamical model with friction for the guided in three points parallel robots are presented.

It is estimated that the forces due to the friction could represent a certain part from the forces/torques which are necessary for the manipulator movement in typical situations. Thus it is necessary to model these friction forces in order to reflect in the dynamic equations the physical reality.

In the paper a method for the additional forces evaluation from the drive joints due to the friction from the drive and passive joints is proposed.

The paper is organized as follows: *Kinematic Study and Dynamic Model Without Friction* is dedicated to the kinematic study and the dynamic modeling without friction of the 3-DOF parallel structure; *Dynamic Model with Computation of Additional Drive Generalized Forces Due to the Friction* deals with the dynamic modeling considering friction effects. *Some Numerical Results* presents some numerical results and their interpretation. The conclusions are detailed at the end of the paper.

## Kinematic Study and Dynamic Model Without Friction

The kinematic scheme of the 3-RRS mechanism is presented in the Fig. 1 [13]. As the mechanism has only 3 degrees of freedom, the mobile plate pose is given by three geometrical parameters: the Z coordinate of the platform center and two Euler angles  $\alpha = \varphi$  (azimuth angle),  $\beta = \theta$  (elevation angle) (Fig. 2).

The input–output equations for the geometric model have been already presented in [13]:

$$F_i \equiv \left( \frac{X_i}{c\delta_i} - R + Lcq_i \right)^2 + (Z_i - Lsq_i)^2 - l^2 = 0; i = 1, 2, 3 \quad (1)$$

where:  $X_i, Y_i, Z_i$  the coordinates of  $A_i$  point;  $q_i$  the generalized coordinates;  $R, L, l, \delta_i$  – geometric parameters of the mechanism (Fig. 1).

The kinematic model will be:

$$[A]\dot{\vec{X}} = [B]\dot{\vec{q}} \quad (2)$$

where



**Fig. 1** The 3-RRS parallel mechanism

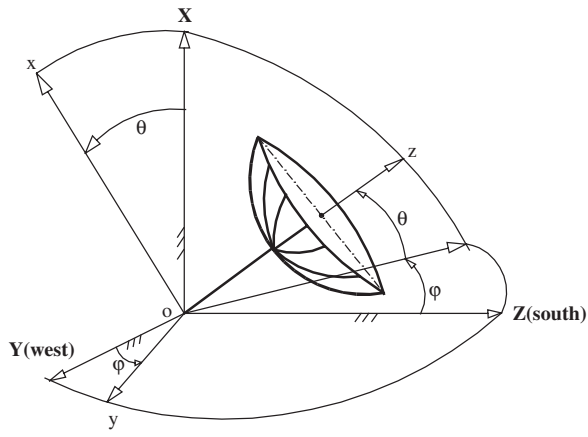
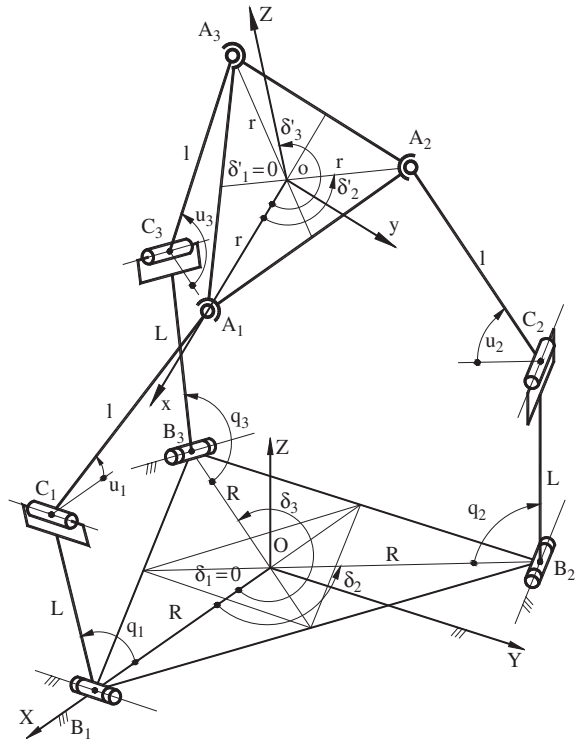


**Fig. 2** Antenna orientation

$$[A] = \begin{bmatrix} (\bar{P}_1 - \bar{P}_{C1}) \cdot \frac{\partial \bar{P}_1}{\partial \varphi} & (\bar{P}_1 - \bar{P}_{C1}) \cdot \frac{\partial \bar{P}_1}{\partial \theta} & (\bar{P}_1 - \bar{P}_{C1}) \cdot \frac{\partial \bar{P}_1}{\partial Z} \\ (\bar{P}_2 - \bar{P}_{C2}) \cdot \frac{\partial \bar{P}_2}{\partial \varphi} & (\bar{P}_2 - \bar{P}_{C2}) \cdot \frac{\partial \bar{P}_2}{\partial \theta} & (\bar{P}_2 - \bar{P}_{C2}) \cdot \frac{\partial \bar{P}_2}{\partial Z} \\ (\bar{P}_3 - \bar{P}_{C3}) \cdot \frac{\partial \bar{P}_3}{\partial \varphi} & (\bar{P}_3 - \bar{P}_{C3}) \cdot \frac{\partial \bar{P}_3}{\partial \theta} & (\bar{P}_3 - \bar{P}_{C3}) \cdot \frac{\partial \bar{P}_3}{\partial Z} \end{bmatrix} \quad (3)$$

$$[B] = L \cdot l \begin{bmatrix} s(u_1 - q_1) & 0 & 0 \\ 0 & s(u_2 - q_2) & 0 \\ 0 & 0 & s(u_3 - q_3) \end{bmatrix} \quad (4)$$

$$\dot{X} = [\dot{\varphi}, \dot{\theta}, \dot{Z}]; \dot{\vec{q}} = [\dot{q}_1, \dot{q}_2, \dot{q}_3]; P_i = \overline{OA_i}; P_{C_i} = \overline{OC_i} \quad (5)$$

$u_i$  – dependent joint coordinates,  $i = 1, 2, 3$ .

The dynamics consists of finding the relationships between the actuating joint torques  $Q_i(i = 1, 2, 3)$  and the laws of motion of the satellite antenna.

To study the dynamics without friction, several simplifying hypothesis were adopted: all joints frictionless; the inertia of guiding arms  $A_i C_i$  is neglected.

The mechanism dynamics using the Newton-Euler laws is done into two steps: In the first step the upper part of the structure containing the working platform and dish is separated from the rest of the mechanism (Fig. 3). The Newton-Euler equations, which are modeling the motion of the mobile working platform and dish, allow the determination of the spherical joints reaction components  $\vec{H}(H_1, H_2, H_3)$  and  $\vec{V}(V_1, V_2, V_3)$ . In the second step, the  $B_i C_i A_i$  kinematic chain is separated and all forces are introduced (Fig. 4). The moment equation relative to the  $B_i$  joint axis allows finding the active torque  $Q_i$ :

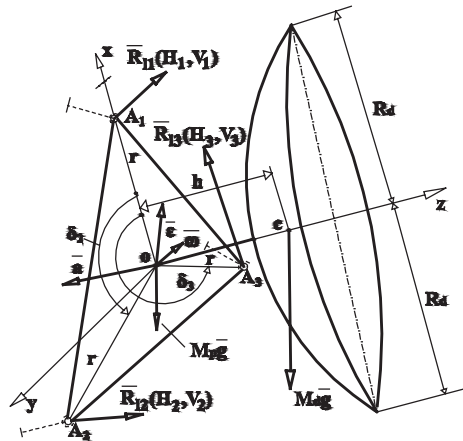
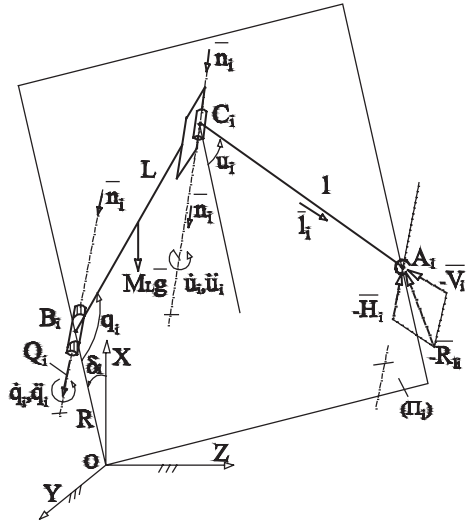


Fig. 3 Step 1

Fig. 4 Step 2



$$Q_i = -V_i L s(q_i - u_i) + \frac{M_L L^2}{3} \ddot{q}_i + M_L g \frac{L}{2} s q_i c \delta_i; \quad i = 1, 2, 3 \quad (6)$$

where  $M_L$  is the mass of  $B_i C_i$  link.

### Dynamic Model with Computation of Additional Drive Generalized Forces Due to the Friction

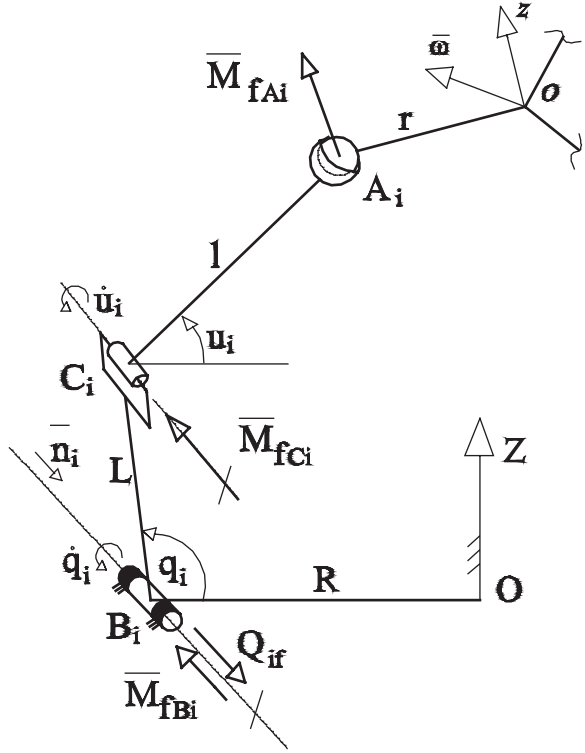
For the friction forces approximation the model of the viscous friction together with the model of Coulomb friction is chosen [14].

A friction torque in a passive joint is a vector situated along the relative rotational speed of the considered link with respect to the previous link (belonging to the same kinematic chain) (Fig. 5):

$$\bar{M}_{f_{C_i}} = - \left( c_r + \mu_r \frac{d_r}{2} \frac{|V_i|}{|\dot{u}_i - \dot{q}_i|} \right) (\dot{u}_i - \dot{q}_i) = -k_{r_i} (\dot{u}_i - \dot{q}_i) \quad (7)$$

$$\bar{M}_{f_{A_i}} = - \left( c_s + \mu_s \frac{d_s}{2} \frac{\sqrt{H_i^2 + V_i^2}}{|\bar{\omega} - \dot{u}_i \bar{n}_i|} \right) (\bar{\omega} - \dot{u}_i) = -k_{S_i} (\bar{\omega} - \dot{u}_i) \quad (8)$$

Fig. 5 The friction torques



In the  $B_i$  active point the friction torque is:

$$\bar{M}_{f_{B_i}} = - \left( c_R + \mu_R \frac{d_R}{2} \sqrt{\frac{V_i^2 + (M_L g c \delta_i)^2 + 2V_i M_L g c \delta_i c u_i}{|\dot{q}_i|}} \right) \dot{q}_i = -k_{R_i} \dot{q}_i \quad (9)$$

$H_i, V_i$  – the reaction force component from the spherical joint  $A_i$ ;  $c_s, c_r, c_R$  – the viscous coefficient from spherical joint, passive joint and active joint;  $\mu_s, \mu_r, \mu_R$  – the Coulomb friction coefficients from the same joints;  $d_r, d_R$  – diameters of the rotational joint spindler;  $d_s$  – diameter of the spherical joint ball;  $\bar{n}_i$  – the unit vector of  $B_i$  and  $C_i$  axes;  $\bar{\omega}$  – the absolute angular speed of the mobile plate;  $\bar{q}_i = \dot{q}_i \bar{n}_i$  and  $\bar{u}_i = \dot{u}_i \bar{n}_i$  – the absolute angular speed of  $B_i C_i$  and respectively  $C_i A_i$  link.

In order to get the drive torques which are necessary to overcome the frictions from the joints **the principle of virtual power** is applied.

$$\bar{Q}_f \cdot \bar{q} + \sum_{i=1}^3 \bar{M}_{f_{B_i}} \cdot \bar{q}_i + \sum_{i=1}^3 \bar{M}_{f_{C_i}} \cdot (\bar{u}_i - \bar{q}_i) + \sum_{i=1}^3 \bar{M}_{f_{A_i}} \cdot (\bar{\omega} - \bar{u}_i) = 0$$

Finally it yields:

$$\begin{aligned} \begin{bmatrix} Q_{1f} \\ Q_{2f} \\ Q_{3f} \end{bmatrix} &= \begin{bmatrix} k_{R1}\dot{q}_1 + k_{r1}(\dot{q}_1 - \dot{u}_1) \\ k_{R2}\dot{q}_2 + k_{r2}(\dot{q}_2 - \dot{u}_2) \\ k_{R3}\dot{q}_3 + k_{r3}(\dot{q}_3 - \dot{u}_3) \end{bmatrix} + [J_u]^T \begin{bmatrix} k_{r1}(\dot{u}_1 - \dot{q}_1) + k_{s1}(\dot{u}_1 - 2\bar{\omega} \cdot \bar{n}_1) \\ k_{r2}(\dot{u}_2 - \dot{q}_2) + k_{s2}(\dot{u}_2 - 2\bar{\omega} \cdot \bar{n}_2) \\ k_{r3}(\dot{u}_3 - \dot{q}_3) + k_{s3}(\dot{u}_3 - 2\bar{\omega} \cdot \bar{n}_3) \end{bmatrix} \\ &+ (k_{s1} + k_{s2} + k_{s3}) [J_\omega]^T \begin{bmatrix} \omega_X \\ \omega_Y \\ \omega_Z \end{bmatrix} \end{aligned} \quad (10)$$

where  $[J_u]$  and  $[J_\omega]$  are the Jacobi matrices that connect the passive joints velocities vector  $\dot{u}$  and the angular velocity  $\bar{\omega}$  of the mobile platform to the active joints velocities vector:

$$\dot{u} = [J_u] \cdot \dot{\bar{q}}; \quad \bar{\omega} = [J_\omega] \cdot \dot{\bar{q}} \quad (11)$$

The  $[J_u]$  matrix is obtained by deriving the closure equations for the direct geometric model. The  $[J_\omega]$  matrix is obtained from:

$$\frac{d}{dt} (\bar{P}_j - \bar{P}_i) = \bar{\omega} \times (\bar{P}_j - \bar{P}_i); \quad (i, j) = \{(1, 2), (2, 3), (3, 1)\} \quad (12)$$

and implies the necessity of obtaining of the pseudo-inverse of a  $6 \times 3$  matrix.

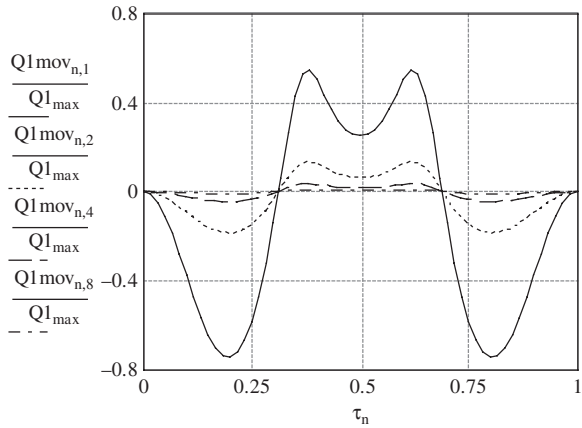
## Some Numerical Results

The kinematic and dynamic algorithms were implemented in a developed simulation program. The chosen geometrical and inertia data for the parallel mechanism are:  $R = 0.45$  m;  $r = 0.15$  m;  $l = 0.60$  m;  $L = 0.40$  m;  $\rho = 0.136$  m;  $\delta_1 = \delta'_1 = 0^\circ$ ;  $\delta_2 = \delta'_2 = 120^\circ$ ;  $\delta_3 = \delta'_3 = 240^\circ$ ;  $M = 8.8$  kg;  $M_L = 0.5$  kg;  $I_x = I_y = 0.57$  kg  $\cdot$  m<sup>2</sup>;  $I_z = 0.5$  kg  $\cdot$  m<sup>2</sup>. The selected displacement of the working platform has the equations:

$$\begin{cases} Z = 0.85 \text{ m} \\ \varphi_k = \frac{\pi}{6} \sin \lambda_k, \theta_k = \frac{\pi}{6} \cos \lambda_k, k = 1, 2, \dots, 8 \end{cases}$$

$$\begin{cases} \lambda_k = -\frac{2^{11}}{27\pi^2} \left(\frac{t_k}{k}\right)^3 + \frac{2^7}{3\pi} \left(\frac{t_k}{k}\right)^2; \quad t_k = \left[0, k \frac{3\pi}{8}\right] s \\ t_k = \left[0, k \frac{3\pi}{8}\right] \text{ sec}; \quad \tau_k = \frac{t_k}{t_{k\max}} = \frac{t_k}{k \frac{3\pi}{8}}; \quad \tau_k \in [0, 1] \text{ normalized time} \end{cases}$$

**Fig. 6** Fraction of the  $Q_{1mov}$  torque



The center of mobile plate for all  $k = 1, 2, \dots, 8$  laws describes in the plane  $Z = 0.85$  m a pseudo-ellipse with the semi-axes  $9.97 \cdot 10^{-3}$  m and  $9.78 \cdot 10^{-3}$  m. The generalized torques  $Q_i$  and the torques due to the motion  $Q_{imov}$  have been evaluated for all  $k$  motion laws. In the Figs. 6 and 7 are presented the fraction of the torques due to the motion with respect to the maximal generalized torques. It can be noticed the maximal fraction is obtained for  $k = 1$  (duration of motion =  $1.177$  s,  $a_{max} \approx 2.4$  m/s<sup>2</sup>,  $\varepsilon_{max} \approx 30$  rad/s<sup>2</sup>).

For  $k \geq 2$  ( $a_{max} < 0.65$  m/s<sup>2</sup> and  $\varepsilon_{max} < 8$  rad/s<sup>2</sup>) the fraction of the torques due to the motion decreases (under 20%), meaning it vanishes.

The same motion laws have been also used in the case of dynamic model with friction. The input data are:  $c_r = c_s = 0.02$ ;  $c_R = 0.04$ ;

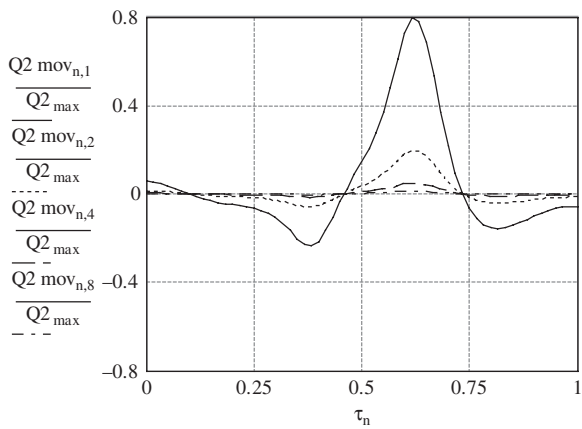


**Fig. 7** Fraction of the  $Q_{2mov}$  torque

$$\mu_{r,R} = \left( \mu + \frac{2s}{d_{r,R}} \right) / \left( \sqrt{1 + \mu^2} \right); \mu = 0.1(0.2); s = 0.00005(0.0005).$$

It can be noticed that the fraction of torques due to the friction in the case  $s = 0.00005$  and  $\mu = 0.1$  is under 3.5% (Figs. 8 and 9). An increase of rolling coefficient leads to an insignificant increase of the torques. The coefficient of the sliding friction has on the other hand a greater influence: for  $\mu = 0.2$  and  $s = 0.0005$  m it leads to a maximal fraction of 6%.

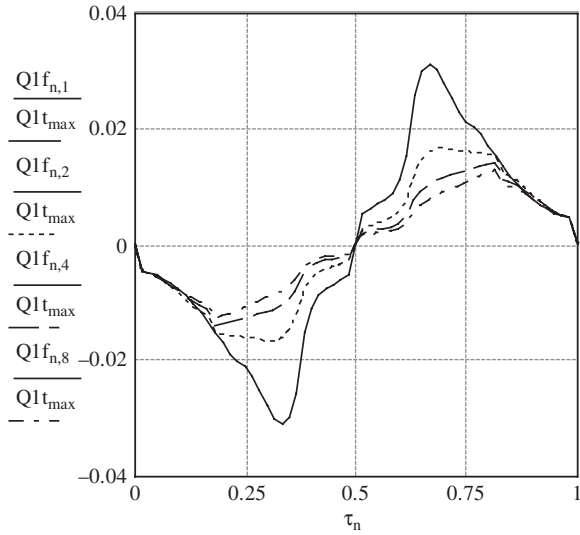


**Fig. 8** Fraction of the  $Q_{1f}$  torque

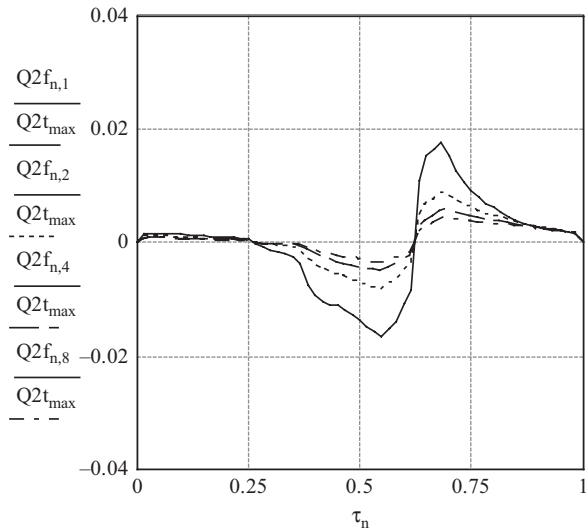


**Fig. 9** Fraction of the  $Q_{2f}$  torque

## Conclusion

This paper presents the dynamical modeling of a 3-DOF parallel mechanism for orientation applications. The dynamic models without and with friction are obtained. Using a numerical and graphical simulation, the diagrams for the dynamics representation are computed. The obtained dynamical algorithms offer the possibility of a more complex dynamic study in comparison with existing simple dynamic models.

**Acknowledgments** The authors gratefully acknowledge the financial support provided by the research grants awarded by the Romanian Ministry of Education and Research.

## References

1. Merlet, J.-P., *Parallel robots*, Kluwer Academic Publisher, 2000.
2. Honneger, M., Codourey, A., and Burdet, E., Adaptive control of the Hexaglide, a six d.o.f. parallel manipulator, In *IEEE Int. Conf. on Robotics and Automation*, Albuquerque, 1997, pp. 543–548.
3. Tsai, L.-W., *Robot analysis, the mechanics of serial and parallel manipulators*, Wiley, 1996.
4. Guégan, S., Khalil, W., *Dynamic modeling of the orthoglide*. *Advances in robot kinematics* (J. Lenarcic and F. Thomas, Ed.), Kluwer Academic Publication, Netherlands, 2002, pp. 387–396.
5. Plitea, N., Pisla, A., Pisla, D., Prodan, B., *Dynamic modeling of a 6-dof parallel structure destined to helicopter flight simulation*, ICINCO 2008, Madeira, 2008.
6. Grotjahn, M., Heimann, B., Abdellatif, H., *Identification of friction and rigid-body dynamics of parallel kinematic structures for model-based control*, *Multibody System Dynamics*, vol. 11(3), 2004, pp. 273–294.
7. Poignet, Ph., Ramdani, N., Vivas, O.A., *Robust estimation of parallel robot dynamic parameters with interval analysis*, In. *42nd IEEE Conference on Decision and Control*, Hawaii USA, 2003, pp. 6503–6508.
8. Yiu, Y.K., Li, Z.X., *Dynamics of a planar 2-dof redundant parallel robot*, In. *International Conference on Mechatronics Technology*, Singapore, 2001, pp. 339–343.
9. Riebe, S. Ulbrich, H., *Modeling and online computation of the dynamics of a parallel kinematic with six degrees-of-freedom*, *Archive of Applied Mechanics*, vol. 72: 2003, pp. 817–829.
10. Chen, J.-S., Yao-Hung, Kuo, Hsu, W-Y., *The influence of friction on contouring accuracy of a Cartesian guide tripod machine tool*, *Int. J. Adv. Manuf. Technol*, 30, 2006, pp. 470–478.
11. Itul, T., Pisla, D., Pisla, A., *Dynamic model of a 6-DOF parallel robot by considering friction effects*, in *12th IFToMM World Congress*, Besançon (France), June 18–21, CD-ROM edition, 2007.
12. Itul, T., Pisla, D., *The influence of friction on the dynamic model for a 6-DOF parallel robot with triangular platform*, *Journal of Vibroengineering*, October/December, vol. 9(4), ISSN 1392-8716, 2007, pp. 24–29.
13. Itul, T., Pisla, D., *Kinematics of a three degrees of freedom parallel structure with applications for the satellite antenna orientation*, RAAD2005, Bucharest, 2005, pp. 197–202.
14. Craig, J.J., *Introduction to robotics. Mechanics and Control*, Addison-Wesley, 1989.



# Elastohydrodynamic Models for Predicting Friction in Point Contacts Lubricated with Polyalphaolefins

J. Echávarri Otero, P. Lafont Morgado, J.B. Sánchez-Peñuela, J.L. Muñoz Sanz, J.M. Muñoz-Guijosa, A. Díaz Lantada and H. Lorenzo Yustos

**Abstract** This paper shows the results of a comparison between theoretical models for predicting friction in point contacts under elastohydrodynamic lubrication and the experimental results obtained in a Mini Traction Machine (MTM). The types of models used are two variations of the Newtonian Theory, applicable to polyalphaolefins (PAO): the Limiting Shear Stress Model and the Carreau's model. The experimental stage includes a wide variation of the operating conditions, by using different control parameters, such as temperature, contact materials, slide-roll ratio, sliding velocity and load.

**Keywords** Friction · Elastohydrodynamic · Point contact · MTM · PAO

## Introduction

The Newtonian fluid model is insufficient for predicting friction in elastohydrodynamic contacts when high contact pressures are reached. In these cases it is necessary to use new rheological behaviour models for the lubricant. In this way, two different variations of the Newtonian Theory are applied: the general Limiting Shear Stress Model for lubricants and the particular Carreau's Model for polyalphaolefins (PAO). The tests carried out with the MTM are used to observe the correlation between the theoretical models and the experimental behaviour.

## MTM-Test Equipment

Figure 1 shows the MTM, a test machine designed to obtain the friction (or traction) coefficient in lubricated point-type contacts. The equipment comprises a ball and a disc in contact, moved by independent axes, submerged in a reservoir full of

---

J.E. Otero (✉)

División de Ingeniería de Máquinas, Universidad Politécnica de Madrid, José Gutiérrez Abascal 2, 28006 Madrid, Spain

e-mail: jechavarri@etsii.upm.es

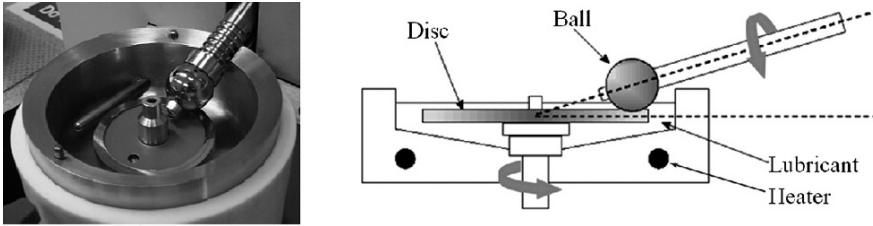


**Fig. 1** Photograph and diagram of the test zone in the MTM

lubricant at a controlled temperature. Therefore, both ball and disc can rotate independently at different speeds, that is different values can be chosen for the slide-roll ratio.

The MTM enables the average velocity ( $U$ ) to be regulated within a wide range (between 10 and 5,000 mm/s), which means the three main lubricating regimes can be distinguished: boundary, mixed and elastohydrodynamic. In this last lubrication regime the chart of Hamrock and Dowson [10] has been used in order to select the correlation applicable for calculating central film thickness ( $h_c$ ). Therefore, the following equation is used [9]:

$$\frac{h_c}{R} = 1.39 \left( \frac{\eta_0 U}{2E^* R} \right)^{0.67} (\alpha E^*)^{0.53} \left( \frac{E^* R^2}{W} \right)^{0.067} \quad (1)$$

where  $\eta_0$  is the viscosity at atmospheric pressure,  $W$  is the load,  $\alpha$  is the pressure-viscosity coefficient,  $U$  is the average velocity between surfaces,  $E^*$  is the Young's reduced modulus and  $R$  the reduced radius of curvature.

Once the film thickness ( $h_c$ ) and the surface roughness ( $\sigma_1$  y  $\sigma_2$ ) are known, the film thickness parameter ( $\lambda$ ) can be calculated [7].

$$\lambda = \frac{h_c}{\sqrt{\sigma_1^2 + \sigma_2^2}} \quad (2)$$

This film parameter allows the limit for elastohydrodynamic lubrication regime to be considered ( $\lambda > 3$ ) in accordance with the references [10]. The MTM measures the traction coefficient by sliding and not by rolling [6, 14]. Therefore, the theoretical developments in this paper will be aimed at measuring the sliding component.

## Limiting Shear Stress Model

The classic behaviour model of a viscous fluid is given by Newton's Model for viscous fluids. For the theoretical calculation of the shear stress the following hypotheses are made:

- The sliding component measured by the MTM is taken into account.
- The velocity gradient is taken as linear [6].
- Film thickness is approached as constant in the whole of the contact and equal to the central film thickness, [8].
- The increase in lubricant viscosity is given by Barus' Law [4].
- Circular point contact [6].
- Hertzian parabolic pressure distribution that depends on the maximum ( $p_0$ ) and the contact radius [11].

Therefore, for Newtonian model, shear stress ( $\tau$ ) is expressed as:

$$\tau = \eta_0 e^{\alpha p} \frac{\Delta U}{h_c} \quad (3)$$

where  $p$  is the pressure and  $\Delta U$  is the sliding velocity between surfaces.

However, studies on the rheology of lubricants reveal the existence of a shear stress at which point Newton's formulation is no longer valid [7]. This limiting shear stress ( $\tau_L$ ) is dependant on the pressure and temperature:

$$\tau_L = \tau_0 + \zeta p \quad (4)$$

The limiting shear stress at atmospheric pressure ( $\tau_0$ ) and the limiting shear stress-pressure parameter ( $\zeta$ ) are constants specific to each lubricant and incorporate the influence of temperature.

The Limiting Shear Stress Model constitutes an approach, [8], which consists in taking account of the Newtonian model until limiting shear stress is reached. From then on, shear stress is considered to take on its boundary value. That is:

$$\text{Newtonian: } \tau = \eta_0 e^{\alpha p} \frac{\Delta U}{h_c} \quad \text{Non Newtonian: } \tau = \tau_L = \tau_0 + \zeta p \quad (5)$$

Therefore, the contact area can be divided into two domains. The transition-points fulfil Eqs. (5). By carrying out an iteration, the value of the pressure reached at the limiting shear stress ( $p^*$ ) is found, where the transition between the Newtonian and non-Newtonian behaviour of the lubricant is produced. The aim is to calculate the radius ( $b$ ) in which a change in oil behaviour is produced.

$$b = a \sqrt{1 - \left(\frac{p^*}{p_0}\right)^2} \quad (6)$$

By calling  $r$  the radius of the contact zone, the Newtonian domain corresponds to the outermost zone ( $a > r > b$ ), while in the innermost zone ( $b < r < 0$ ) the concept of limiting shear stress is applied. Therefore, the friction force ( $F_\mu$ ) is:

$$F_\mu = \int_b^a \eta_0 e^{\alpha p} \frac{\Delta U}{h_c} 2\pi r dr + \int_0^b (\tau_0 + \zeta p) 2\pi r dr \tag{7}$$

By substituting pressure for the Hertzian distribution and dividing by the load ( $W$ ), the expression for the friction coefficient ( $\mu$ ) is obtained:

$$\mu = 3\eta_0 \frac{\Delta U}{h_c} \cdot \frac{\exp(m\alpha p_0)(m\alpha p_0 - 1) + 1}{\alpha^2 p_0^3} + \zeta(1 - m^3) \tag{8}$$

where  $p_0$  is the maximum pressure or Hertz pressure and  $m$  a parameter. They are calculated using the following (Eqs. 9):

$$p_0 = \frac{3W}{2\pi a^2}; \quad a = \sqrt[3]{\frac{3WR}{4E^*}}; \quad m = \sqrt{1 - \left(\frac{b}{a}\right)^2} \tag{9}$$

This model considers a simple transition between Newtonian and non-Newtonian behaviour (straight lines  $E-F$ , Fig. 2a), which produces an overestimation in shear stress. A transition zone is taken into account in more mathematically complex rheological models also shown in Fig. 2a.

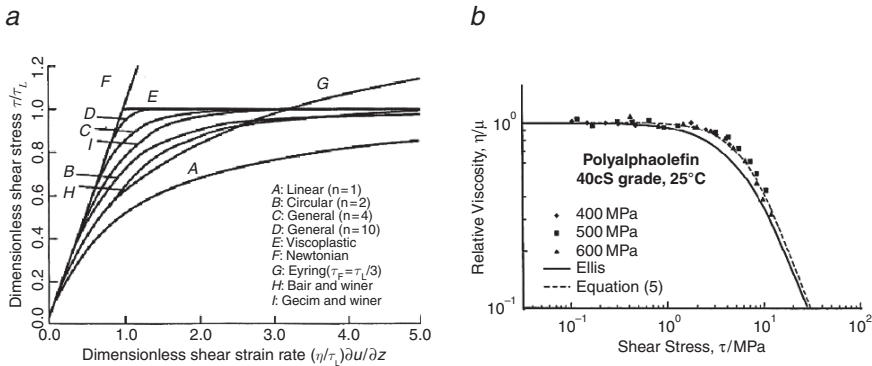


**Fig. 2** (a) Different transition zones in the Limiting Shear Stress Model; (b) Relationship between relative-viscosity and shear stress

### Carreau’s Model

Another way to analyse lubricant rheology [3] is by assuming that actual viscosity in the contact is less than that indicated by Barus’ Law. Thus, generalised viscosity ( $\eta$ ) is given by Carreau’s Equation [5] which, for this case, can be obtained from the relative-viscosity defined as:

$$\frac{\eta}{\eta_0 e^{\alpha p}} = \left[ 1 + \left( \frac{\eta_0 e^{\alpha p} \frac{\Delta U}{h_c}}{G} \right)^2 \right]^{\frac{n-1}{2}} \quad (10)$$

Figure 2b shows the relationship between relative-viscosity and shear stress for a polyalphaolefin [1]. As shear stress rises the relative-viscosity fall and therefore the Newtonian Model becomes inadequate.

Exponent  $n$  is specific to the lubricant and  $G$  is its shear modulus. Both parameters need to be fitted in line with the experimental results [2].

The calculating process consists in inserting the generalised viscosity into Newton's equation, integrating the shear stress in the contact area and dividing by the load. Thus, the friction coefficient equation is found:

$$\mu = 3 \left( \eta_0 \frac{\Delta U}{h_c} \right)^n G^{1-n} \frac{\exp(n\alpha p_0) [n\alpha p_0 - 1] + 1}{(n\alpha)^2 p_0^3} \quad (11)$$

## Experimentation

Different test profiles are performed with the purpose of detecting the response of the model to variations in velocity, temperature, load, materials and SRR. The range for each test parameters is as follows:

- Velocity: 10–3,000 mm/s.
- Temperature: 30, 40, 60, 80, 100°C.
- Load: 14, 20, 28 N.
- Materials: Steel-Steel, Steel-Copper.
- SRR =  $100 \cdot \Delta U/U$ : 5%, 25%.

Table 1 shows the properties of the materials used ( $E$ -Young's modulus and  $\nu$ -Poisson's ratio) and the physical properties of the polyalphaolefin [15, 12].

## Results and Discussion

For the test conditions indicated, the central film thickness was calculated using Eq. (1) and taking the surface roughness measured for the specimens ( $\sigma = 2.24 \times 10^{-8}$ m), the elastohydrodynamic limit was set ( $\lambda = 3$ ), which approximately corresponds to  $U = 2,000$  mm/s. Thus, the lubrication regime can be taken as elastohydrodynamic for velocities above approximately 2,000 mm/s.

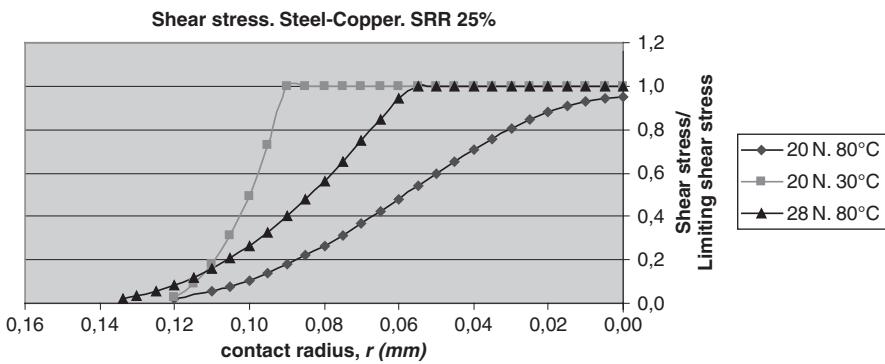
As to the suitability of the models, Fig. 3 shows that for a steel-copper contact, with load  $W = 20$  N, temperature  $T = 80^\circ\text{C}$ , SRR = 25% and average velocity  $U = 3,000$  mm/s, the polyalphaolefin (PAO) does not reach limiting shear stress

**Table 1** Properties of materials and PAO used in the laboratory

Material	E(GPa)	$\nu$
SteelE-52100	210	0.30
Copper	117	0.34

T(°C)	$H_0(\text{mPa}\cdot\text{s})$	$\alpha(\text{GPa}^{-1})$	$T_0(\text{MPa})$	$\zeta$
30	37.95	12.3	4	0.0403
40	25.00	11.5	4	0.0395
60	12.57	10.1	4	0.0389
80	7.36	9.0	4	0.0384
100	4.78	8.2	4	0.0380



**Fig. 3** Theoretical  $\tau/\tau_L$  ratio depending on the contact radius

and the Limiting Shear Stress Model is reduced to the Newtonian one. However, when the load is increased ( $W = 28 \text{ N}$ ) or the temperature reduced ( $T = 30^\circ\text{C}$ ), it can be seen in Fig. 3 that limiting shear stress is reached. The results for the full test plan show that for high loads or low temperatures there are broad zones of non-Newtonian behaviour.

Figure 4 shows the results for the friction coefficient in steel-copper contact at  $80^\circ\text{C}$ ,  $28 \text{ N}$  and  $\text{SRR} = 25\%$ . The predictions obtained for friction by using the Limiting Shear Stress Model show values higher than the experimental ones due to the shear stress overestimation commented previously, which increases the friction coefficient when Eqs. (5) are integrated in the contact area according to Eq. (7).

As for Carreau’s model, the  $n$  and  $G$  parameters, which vary with temperature, and less importantly, with pressure [13], have been fitted through previous tests in the MTM, using two different conditions for each temperature, in order to obtain two Eqs. (11) which allow the deduction of the parameters  $n$  and  $G$ . The values obtained at  $80^\circ\text{C}$ ,  $n = 0.79$  and  $G = 9 \cdot 10^4 \text{ Pa}$ , are similar to those consulted in references for polyalphaolefins [2].

Figure 5 shows a comparison between the theoretical results obtained by applying Carreau’s model and those obtained experimentally with the MTM for steel-copper

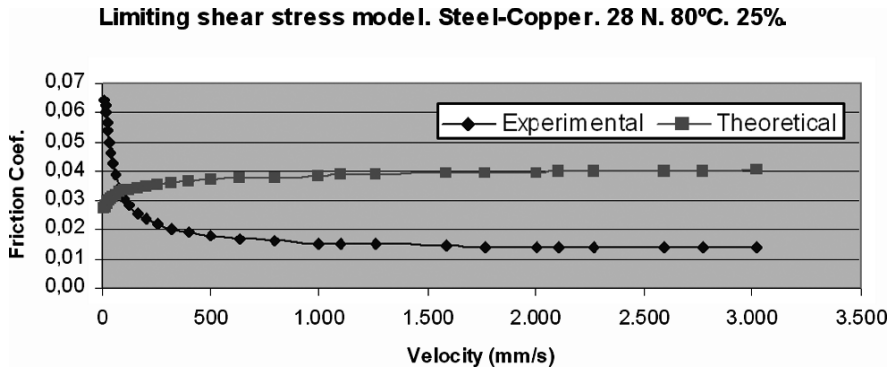


Fig. 4 Comparison between Limiting shear stress model and experimental results obtained in the MTM

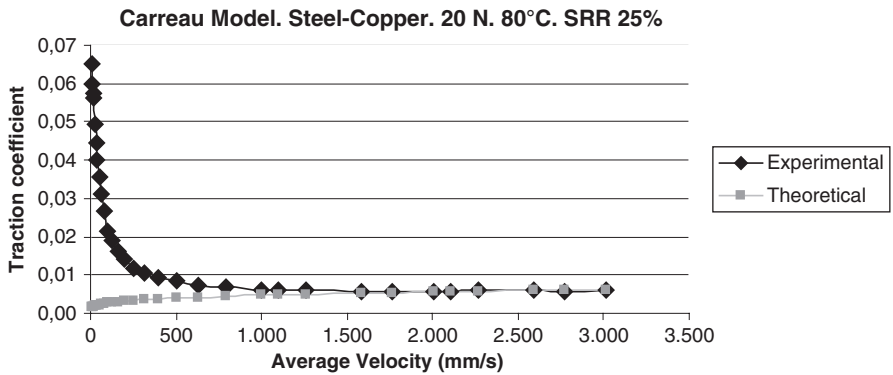


Fig. 5 Comparison between Carreau’s model and experimental results

contact at 80°C under a load of 20 N. It should be remembered that the lubrication regime can be taken as elastohydrodynamic for velocities above approximately 2,000 mm/s.

Carreau’s Model provides precise predictions for friction because generalised viscosity of Eq. (10) leads to an accurate shear stress result and therefore avoids the overestimation of the other model.

A broader theoretical-experimentation comparison has been developed under the elastohydrodynamic regime ( $2,000 < U < 3,000$  mm/s). In this way it can be seen how Carreau’s model responds to variations in parameters like velocity, SRR, load, materials or temperature, showing always deviations below 5% between predicted and experimental data.

For example, Fig. 6 shows the results when the contact materials are changed, the Carreau model perfectly describes the friction behaviour of the lubricant in the elastohydrodynamic region. The same occurs when other control parameters, no

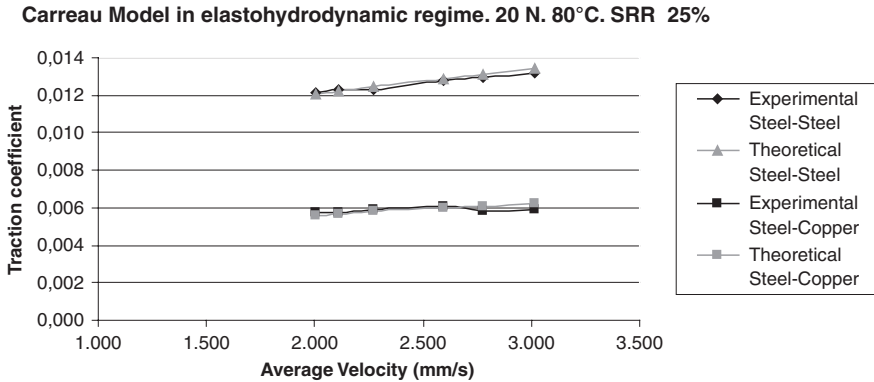


**Fig. 6** Comparison between Carreau's model and the experimental results in the elastohydrodynamic region ( $U > 2,000$  mm/s)

matter which, are varied, once the two constants  $n$  and  $G$  have been fitted to each temperature.

## Conclusions

The paper shows analytical methods for predicting shear stress and friction coefficient in point contacts under elastohydrodynamic lubrication. The test plan performed with the MTM enables these models to be verified.

On the one hand, the Limiting Shear Stress Model overestimates friction unless a detailed transition of non-Newtonian to Newtonian behaviour is taken into account. On the other hand, the more complex Carreau's Model is specifically designed for polyalphaolefins and is fitted to each particular lubricant and working temperature through the parameters  $n$  and  $G$ . As a consequence, Carreau's model fits perfectly to the experimental results in all the tests performed with different materials and working conditions.

**Acknowledgments** This work has been financed by the Repsol Foundation. The authors would like to thank Jorge Insa and Luis Fernández of the Lubricants Laboratory of Repsol-YPF's Technology Department for their valuable collaboration.

## References

1. Bair S., 2006. Reynolds-Ellis equation for line contacts with shear-thinning. *Tribology International* 39 310–316.
2. Bair S., Vergne P., Querry M., 2004. A unified shear-thinning treatment of both film thickness and traction in EHD. *Tribology Letters* 18 145–152.
3. Bair S., Winer W.O., 1982. Some observations in high pressure rheology of lubricants. *Trans. ASME, Journal of Lubrication Technology* 104 357.



4. Barus C., 1893. Isotherms, isopiestic and isometrics relative to viscosity. *American Journal of Science* 45 87–96.
5. Carreau P.J., 1972. Rheological equations from molecular network theories. *Trans Soc Rheol.* 16(1) 99–127.
6. De Vicente J., Stokes J.R., Spikes H.A., 2005. The frictional properties of Newtonian fluids in rolling-sliding soft-EHL contact. *Tribology Letters* 20.
7. Dowson D., 1995. Elastohydrodynamic and micro-elastohydrodynamic lubrication. *Wear* 190 125–138.
8. Ge P., Liu Z., 2002. Experimental and computational investigation of the traction coefficient of a ball traction drive device. *Tribology International* 35 219–224.
9. Hamrock B.J., 1994. *Fundamentals of fluid film lubrication*. McGraw-Hill, New York.
10. Hamrock B.J., Dowson D., 1981. *Ball bearing lubrication-the elastohydrodynamics of elliptical contacts*. Wiley-Interscience, New York.
11. Hertz H., 1896. *Miscellaneous papers by H. Hertz*. Jones & Schort (eds), Macmillan, London.
12. Höglund E., 1999. Influence of lubricant properties on elastohydrodynamic lubrication. *Wear* 232 176–184.
13. Johnson K.L., Tevaarwerk J.L., 1977. Shear behaviour of elastohydrodynamic oil films. *Proceedings of the Royal Society of London, Series A* 356 215–236.
14. PCS Instruments, 2007: [www.pcs-instruments.com](http://www.pcs-instruments.com).
15. Schmidt A., Gold P.W., Abmann C., Dicke H., Loos J., 2006. Viscosity-pressure-temperature behaviour of mineral and synthetic oils. *Journal of Synthetic Lubrication* 18 51–79.

# An Integrated Differentiation-Projection Approach for the Kinematic Data Consistency of Biomechanical Systems

F.J. Alonso, J. Cuadrado and P. Pintado

**Abstract** Several sources of error corrupt the results obtained in the kinematic and dynamic analysis of biomechanical systems and reduce its usefulness. The main source of error is the inaccuracy of velocities and accelerations derived from experimentally measured displacements of markers placed on the skin of joints. This error is mainly due to the amplification of high-frequency low-amplitude noise introduced by the motion capture system when the raw displacement signals are differentiated. Another source of error is the skin motion artifact, that produces violations of the kinematic constraint equations of the multibody system. An integrated differentiation-projection approach to ensure the kinematic data consistency in the context of the analysis of biomechanical systems is presented. The raw data differentiation problem is solved by applying a smoothing-differentiation technique based on the Newmark integration scheme. Several benchmark kinematic signals that include computer generated data of a four-bar mechanism were processed using the differentiation-projection method to study its performance.

**Keywords** Biomechanics · Skin motion · Kinematic consistency · Orthogonal projection methods · Raw data problem

## Introduction

The inverse dynamic analysis (IDA) of biomechanical systems uses kinematic and anthropometric data to calculate net joint reaction forces and net driver moments during a physical activity or motion.

The estimation of the skeletal motion obtained from marker-based motion capture systems is known to be affected by significant errors caused by skin motion artifact [1], i.e. the motion of the skin with respect to the underlying bone, and due

---

F.J. Alonso (✉)

Departamento de Ingeniería Mecánica, Energética y de los Materiales,  
Universidad de Extremadura, Avda. de Elvas s/n, 06071 Badajoz, Spain  
e-mail: fjas@unex.es

to the amplification of high-frequency low-amplitude noise introduced by the motion capture system when the raw displacement signals are differentiated to obtain velocities and accelerations [2].

To avoid raw data amplification during differentiation, the acquired displacement signals are smoothed prior to differentiation. The problem of filtering displacement time series to obtain noiseless velocities and accelerations with minimum loss of information has been widely studied. Digital Butterworth filters, splines, and filters based on spectral analysis among traditional smoothing methods [2, 3] and advanced smoothing techniques like discrete wavelet transform or SSA [4] have been applied and tested. Nevertheless, the smoothing procedure does not ensure the kinematic data consistency with the biomechanical model because the kinematic constraint equations are not necessarily satisfied.

In this work we propose the application of an integrated differentiation-projection approach to ensure the kinematic data consistency of biomechanical systems. The new procedure smooths and differentiates the kinematic signals in a single step using the Newmark integration scheme and then projects the positions and the obtained velocities and accelerations to the constraint manifold.

## The Newmark Method

The Newmark method is a single-step integration formula. The method constitutes a special category of finite difference methods that have been widely used in solving the multi-DOF second-order differential equations that appear in structural dynamics.

The state vector of the system at a time  $t_{n+1} = t_n + h$  is deduced from the already-known state vector at time  $t_n$ , through a Taylor expansion of the displacements and velocities [5]. The following are the two basic equations proposed by Newmark [5] for determining displacements and velocities of the structure at time  $t_{n+1}$ :

$$\dot{\mathbf{q}}_{n+1} = \dot{\mathbf{q}}_n + h[(1 - \gamma)\ddot{\mathbf{q}}_n + \gamma\ddot{\mathbf{q}}_{n+1}] \quad (1)$$

$$\mathbf{q}_{n+1} = \mathbf{q}_n + h\dot{\mathbf{q}}_n + h^2 \left[ \left( \frac{1}{2} - \beta \right) \ddot{\mathbf{q}}_n + \beta\ddot{\mathbf{q}}_{n+1} \right] \quad (2)$$

The constants  $\gamma$  and  $\beta$  are parameters associated with the quadrature scheme. The parameter  $\beta$  denotes the variation of the acceleration during the incremental time step  $h = t_{n+1} - t_n$ . The choice of  $\beta$  implies different schemes of interpolation for the acceleration over a time step. The value  $\beta = 0$  indicates a scheme equivalent to the central difference method,  $\beta = 1/4$  is a constant average acceleration method, and the value  $\beta = 1/6$  is a linear acceleration method. The parameter  $\gamma$  relates to the numerical damping introduced by discretization in the time domain. For the case with  $\gamma < 1/2$ , there exists some negative numerical damping while, for  $\gamma > 1/2$ , positive numerical damping will occur [5]. The method has been demonstrated to be unconditionally stable when:

$$\gamma \geq \frac{1}{2} \quad (3)$$

$$\beta \geq \frac{1}{4}(0.5 + \gamma)^2 \quad (4)$$

From Eqs. (2) and (3), the accelerations and velocities of the structure at time step  $t_{n+1}$  can be solved as

$$\ddot{\mathbf{q}}_{n+1} = \frac{1}{\beta h^2} (\mathbf{q}_{n+1} - \mathbf{q}_n) - \frac{1}{\beta h} \dot{\mathbf{q}}_n - \left( \frac{1}{2\beta} - 1 \right) \ddot{\mathbf{q}}_n \quad (5)$$

$$\dot{\mathbf{q}}_{n+1} = \dot{\mathbf{q}}_n + h(1 - \gamma) \ddot{\mathbf{q}}_n + h\gamma \ddot{\mathbf{q}}_{n+1} \quad (6)$$

## Kinematic Data Consistency

The skin motion artifact affects the kinematics of the multibody system, producing violations of the kinematic constraint equations. This violation is called kinematic data inconsistency and is regarded as one of the most critical sources of error in human movement analysis [6, 7]. This inconsistency produces spurious reaction forces and driver moments when the inverse dynamic analysis is performed.

A mechanical system is consistent with the acquired kinematic data when the constraint equations and their time derivatives are satisfied [6]. Silva and Ambròsio [6] applied a systematic procedure using a multibody formalism to ensure kinematic data consistency. They use the non-consistent  $\mathbf{q}^*$  positions as an initial guess to the Newton-Raphson procedure to obtain consistent positions:

$$\Phi_{\mathbf{q}}(\mathbf{q}_i) \Delta \mathbf{q}_i = -\Phi(\mathbf{q}_i) \quad (7)$$

Where  $\Delta \mathbf{q}_i = \mathbf{q} - \mathbf{q}_i$  is the generalized coordinates correction at iteration  $i$ . Consistent velocities  $\dot{\mathbf{q}}$  and accelerations  $\ddot{\mathbf{q}}$  are obtained by solving velocity and acceleration equations of the multibody system:

$$\begin{aligned} \Phi_{\mathbf{q}}(\mathbf{q}) \dot{\mathbf{q}} &= \mathbf{0} \\ \Phi_{\mathbf{q}}(\mathbf{q}) \ddot{\mathbf{q}} &= -\dot{\Phi}_{\mathbf{q}} \dot{\mathbf{q}} \end{aligned} \quad (8)$$

This procedure produces reasonable good results [6]. Nevertheless, the biomechanical model is driven by the angular histories calculated from the inconsistent input data, which are not the true angular histories. To overcome the calculation of the intersegmental angles from inconsistent data, this work proposes the simultaneous correction of the natural coordinates and intersegmental angles performing an orthogonal projection of the position solution to the constraint manifold, in order to obtain a new set of positions  $\mathbf{q}$  that satisfies  $\Phi = \mathbf{0}$ . This scheme projects the subset of natural coordinates measured with the motion capture system and calculates the angular histories from the consistent positions. The projection can be obtained by

the solution of the following constrained minimization problem [6]:

$$\min_{\mathbf{q}} V = \frac{1}{2} (\mathbf{q} - \mathbf{q}^*)^T \mathbf{W} (\mathbf{q} - \mathbf{q}^*) \quad s.t. \quad \Phi = \mathbf{0} \quad (9)$$

Where  $\mathbf{W}$  is a weighting matrix. Different weighting factors can be assigned to each natural coordinate to reflect the average degree of skin movement artifact associated to each coordinate. An identity weighting matrix has been used in this work. Using an augmented Lagrangian method to minimize the above function [8], the following iterative scheme to calculate the consistent data positions  $q$  is obtained:

$$[\mathbf{W} + \Phi_{\mathbf{q}}^T \alpha \Phi_{\mathbf{q}}] \Delta \mathbf{q}_{i+1} = -\mathbf{W} \Delta \mathbf{q}_i - \Phi_{\mathbf{q}}^T \alpha \Phi \quad (10)$$

Where  $\Delta \mathbf{q}_{i+1}$  and  $\Delta \mathbf{q}_i$  are the position data corrections and the subscripts indicate the iteration number. Equation (10) can be solved iteratively until  $\|\Delta \mathbf{q}_i\| < \varepsilon$  where  $\varepsilon$  is a user specified tolerance. The value of the penalty factor  $\alpha$  only affects the convergence rate. Bayo et al. [8] recommend penalty factors ranging from  $10^5$  to  $10^7$  to obtain a good convergence rate. The execution times to solve Eqs. (6) and (10) were similar. In order to obtain consistent velocities  $\dot{\mathbf{q}}$  again we perform an orthogonal projection of the velocities  $\dot{\mathbf{q}}^*$  calculated using the Newmark scheme to the velocity constraint manifold. This can be achieved by the solution of the linear equation:

$$[\mathbf{W} + \Phi_{\mathbf{q}}^T \alpha \Phi_{\mathbf{q}}] \dot{\mathbf{q}} = \mathbf{W} \dot{\mathbf{q}}^* \quad (11)$$

To obtain consistent accelerations, the projection of the accelerations  $\ddot{\mathbf{q}}^*$  calculated using the Newmark scheme onto the constraint manifold can be obtained through the solution of the following equation:

$$[\mathbf{W} + \Phi_{\mathbf{q}}^T \alpha \Phi_{\mathbf{q}}] \ddot{\mathbf{q}} = \mathbf{W} \ddot{\mathbf{q}}^* - \Phi_{\mathbf{q}}^T \alpha \dot{\Phi}_{\mathbf{q}} \dot{\mathbf{q}} \quad (12)$$

## Results

To test the performance of the proposed procedure several benchmark raw displacement signals (observed signals) were processed using the smoothing-differentiation procedure and the projection methods described in the previous sections. The computer-generated data include the simulation of a four-bar crank-rocker mechanism during two crank revolutions (Fig. 1a) The input angular velocity and

the lengths of the links were fixed to  $\dot{\theta} = 2\pi \text{ rad/s}$ ,  $L_1 = 2 \text{ m}$ ,  $L_2 = 8 \text{ m}$  and  $L_3 = 5 \text{ m}$ . The time step  $h = 0.01 \text{ s}$  and the total time of simulation is  $2 \text{ s}$ . The original data  $q = (x_1, y_1, x_2, y_2)^T$  were corrupted to simulate skin motion artifact and noise introduced by the motion capture system using three different patterns: Gaussian noise, Sinusoidal stationary noise and Non-stationary noise. The non-stationary noise is simulated by adding lumped point masses connected to the system by viscoelastic unions. Figure 1a, 1b, 1c, 1d, 1e and 1f show the original data and the corrupted data.

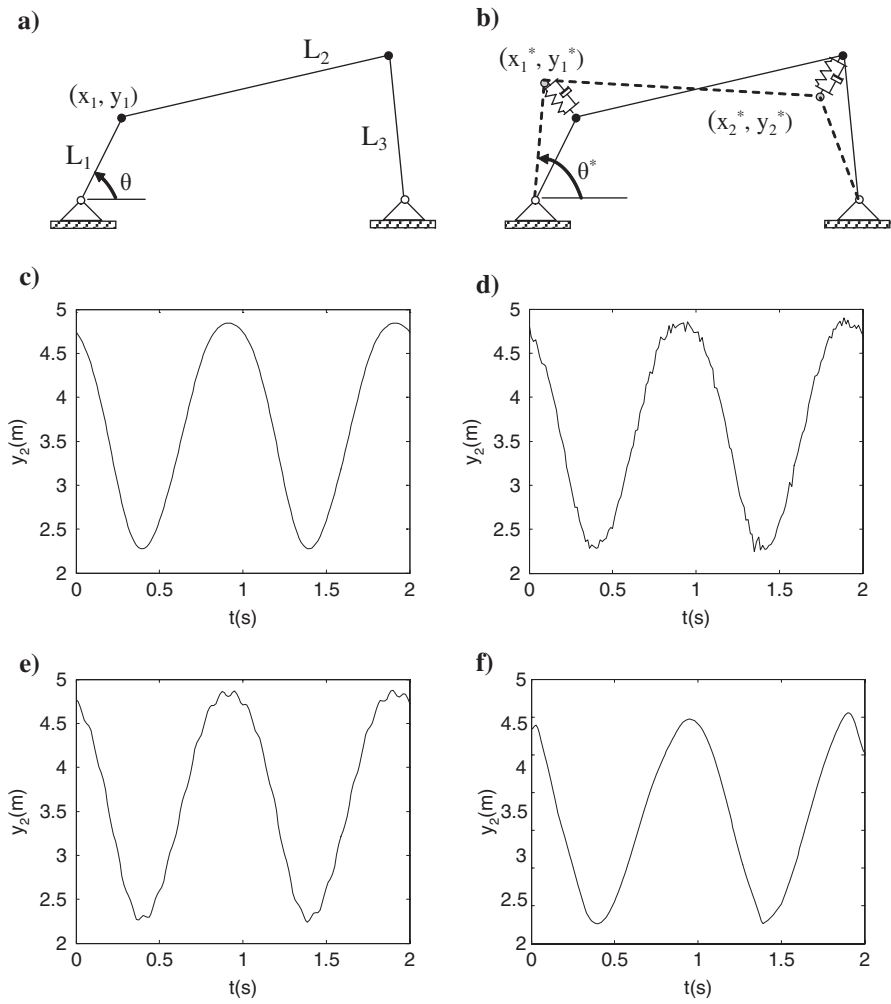


**Fig. 1** The four-bar example: (a) original coordinates; (b) model for the simulation of non-stationary noise; (c) the original  $y_2$ ; (d) the corrupted  $y_2^*$  using Gaussian noise; (e) the corrupted  $y_2^*$  using sinusoidal stationary noise; (f) the corrupted  $y_2^*$  using non-stationary noise

To perform the double differentiation using the Newmark scheme, several  $\gamma$  and  $\beta$  parameters in the stability region Eqs. (4) and (4) were chosen, and it was found that for  $\gamma = 3.5$  and  $\beta = 10/4(0.5 + \gamma)^2 = 40$  good results were obtained. Moreover, the results obtained by using the projection methods are compared with those obtained following the procedure proposed by Silva and Ambròsio [6]. In order to compare the results obtained by different procedures we use the normalized root mean square (rms) of the residuals produced corresponding to the original coordinate  $q_i$ :

$$\begin{aligned}\eta_i &= \sqrt{\frac{\sum_{i=1}^N [q_i - q_i^*]^2}{\sum_{i=1}^N q_i^2}} \\ \dot{\eta}_i &= \sqrt{\frac{\sum_{i=1}^N [\dot{q}_i - \dot{q}_i^*]^2}{\sum_{i=1}^N \dot{q}_i^2}} \\ \ddot{\eta}_i &= \sqrt{\frac{\sum_{i=1}^N [\ddot{q}_i - \ddot{q}_i^*]^2}{\sum_{i=1}^N \ddot{q}_i^2}}\end{aligned}\quad (13)$$

Figure 2a shows the results obtained for the Gaussian noise (amplitude  $p = 5L_1/100$ ) using the following procedures:

- Ensuring the kinematic consistency using the method proposed by Silva and Ambròsio [6] (KC).
- Using the projection methods for  $q = (x_1, y_1, x_2, y_2)^T$  and its higher derivatives (KCP).

Figure 2a shows that the proposed projection process improves the results obtained by conventionally imposing kinematic consistency using Eqs. (7) and (8). Moreover, the application of the Newmark scheme to calculate the higher derivatives prior to projection dramatically improves the results, as shown in Fig. 2b. This fact illustrates the importance of the raw displacement smoothing and differentiation method in this problem. Table 1 summarizes results for the sinusoidal stationary noise and non-stationary noise using KC (regular face) and KCP methods (boldface) and using the Newmark integration scheme with  $\gamma = 3.5$  and  $\beta = 10/4(0.5 + \gamma)^2 = 40$  to calculate the higher derivatives.

## Conclusion

A systematic multibody procedure based on differentiation-smoothing using the Newmark scheme and orthogonal projection of the position, velocity and acceleration to the constraint manifold to ensure the kinematic data consistency in the context of the analysis of biomechanical systems is presented. The results show

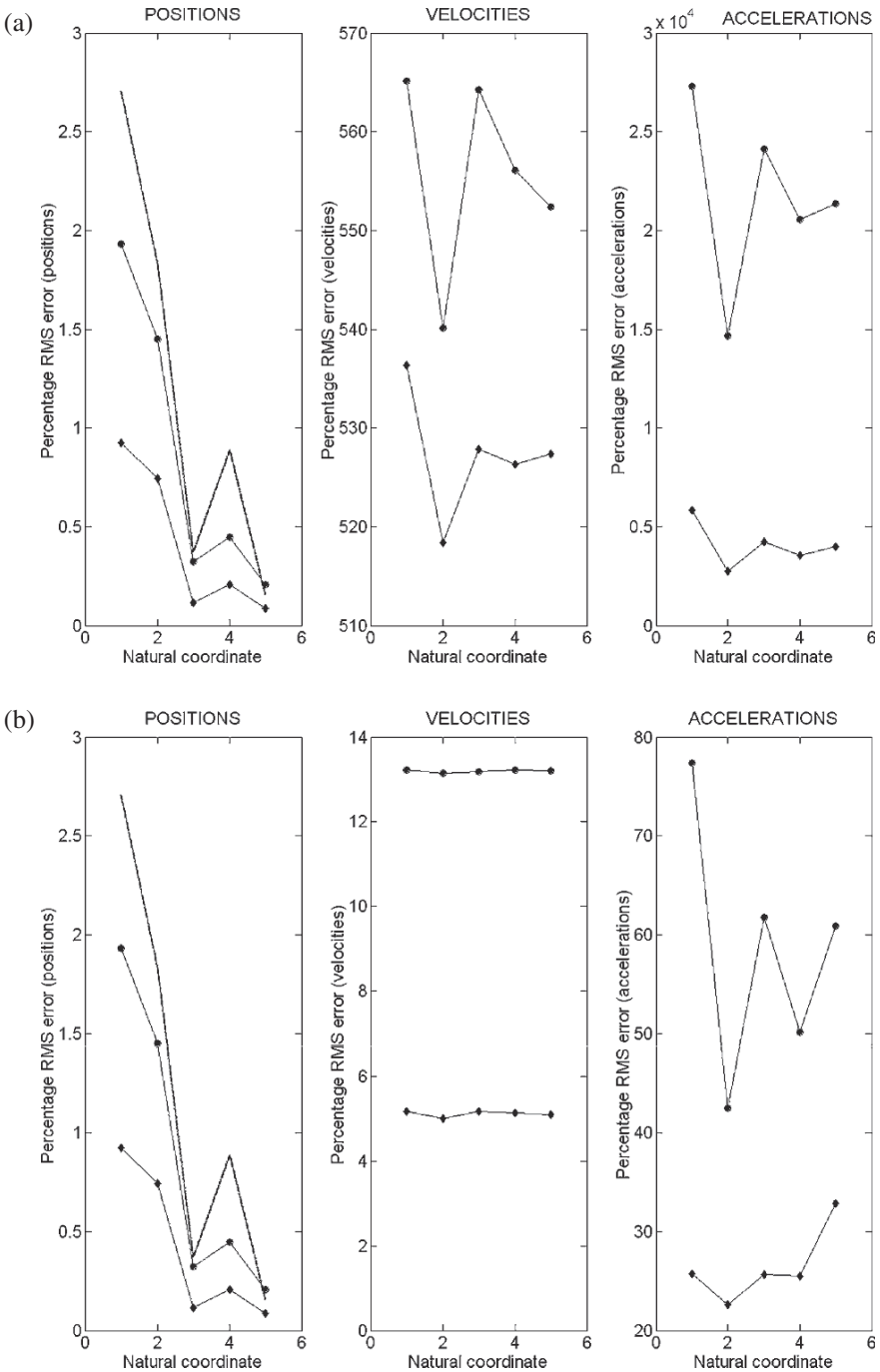


**Fig. 2** Residuals: (a) No smoothing technique applied; (b) Newmark-smoothed signals. (●) KC, (◆) KCP. The dashed line in the positions plots correspond to the corrupted position data



**Table 1** Summary of the results for the sinusoidal and non-stationary cases. KC in regular face, KCP in bold face

Coordinate	$\mathbf{q}$	$\dot{\mathbf{q}}$	$\ddot{\mathbf{q}}$
Sinusoidal	KC (KCP)	KC (KCP)	KC (KCP)
1	7.41 ( <b>3.59</b> )	11.23 ( <b>7.66</b> )	70.54 ( <b>30.19</b> )
2	5.53 ( <b>3.26</b> )	10.72 ( <b>6.23</b> )	59.12 ( <b>29.08</b> )
3	1.15 ( <b>0.68</b> )	9.01 ( <b>7.14</b> )	60.94 ( <b>27.29</b> )
4	1.20 ( <b>0.74</b> )	11.84 ( <b>9.58</b> )	54.19 ( <b>17.21</b> )
5	0.50 ( <b>0.32</b> )	10.45 ( <b>6.95</b> )	47.83 ( <b>23.16</b> )
Non-Stationary	KC (KCP)	KC (KCP)	KC (KCP)
1	1.46 ( <b>1.35</b> )	40.17 ( <b>38.12</b> )	52.14 ( <b>29.75</b> )
2	1.33 ( <b>1.32</b> )	39.15 ( <b>31.82</b> )	45.85 ( <b>23.57</b> )
3	0.23 ( <b>0.22</b> )	41.52 ( <b>29.14</b> )	46.05 ( <b>29.73</b> )
4	0.31 ( <b>0.27</b> )	46.73 ( <b>34.59</b> )	52.66 ( <b>22.18</b> )
5	0.17 ( <b>0.16</b> )	42.68 ( <b>35.29</b> )	33.75 ( <b>27.22</b> )

the superiority of these methods over other multibody procedures. Future works will need to focus on the possibilities of producing an automatic algorithm, and on the embedding the algorithm in commercial biomechanical analysis packages. Namely, techniques will be devised to automatically choose the  $\gamma$  and  $\beta$  parameters for smoothing and differentiation of the given signal. The next step is to ensure the kinematic data consistency using a detailed body model that accounts for the flexibility of the real biomechanical system bodies and joints.

## References

1. Hatze, H., The fundamental problem of myoskeletal inverse dynamics and its implications, *Journal of Biomechanics*, Vol. 35, 2002, pp. 109–115.
2. Vaughan, C. L., Smoothing and differentiation of displacement-time data: an application of splines and digital filtering, *International Journal of Bio-Medical Computing*, Vol. 13, 1982, pp. 375–386.
3. Dowling, J., A modelling strategy for the smoothing of biomechanical data, In: B. Johnsson, (Ed.), *Biomechanics*, Vol. XB. Human Kinetics, Champaign, IL, pp. 1163–1167, 1985.
4. Alonso, F. J., Del Castillo, J. M., Pintado, P., Application of singular spectrum analysis to the smoothing of raw kinematic signals, *Journal of Biomechanics*, Vol. 38, 2005, pp. 1085–1092.
5. Newmark, N. M., A method of computation for structural dynamics, *Journal of Engineering Mechanics Division, Proceedings of ASCE*, Vol. 85 (EM3), 1959, pp. 67–94.
6. Silva, M. P. T., Ambrósio, J. A. C., Kinematic data consistency in the inverse dynamic analysis of biomechanical systems, *Multibody System Dynamics*, Vol. 8, 2002, pp. 219–239.
7. Alonso, F. J., Del Castillo, J. M., Pintado, P., Motion data processing and wobbling mass modelling in the inverse dynamics of skeletal models, *Mechanism and Machine Theory*, Vol. 42, 2007, pp. 1153–1169.
8. Bayo, E., Ledesma, R., Augmented lagrangian and mass-orthogonal projection methods for constrained multibody dynamics, *Nonlinear Dynamics*, Vol. 9, 1996, pp. 113–130.

# Design of Simple Humanoid Dedicated to the Research on the Gait Synthesis

Teresa Zielinska, Krzysztof Mianowski and Przemyslaw Kryczka

**Abstract** The design of small biped is introduced. The robot is meant to serve as a research platform for human referred motion synthesis. The robot consist of the lower extremities and the torso. The paper summarizes the design process focusing on the dynamic analysis. The mechanical design method as well the approach to motion synthesis are presented.

**Keywords** Bipedes · Robot design · CAD/CAE · Dynamic analysis

## Introduction

Over the last two decades, a number of advanced humanoidal bipeds were developed, among the others Asimo, HRP-3, H7, Qrio, Robian, Wabian (i.e. [1]). A progress, worth mentioning, towards the more human like structure made the scientists from The University of Tokyo building a Kotaro robot Kotaro web. To obtain the robot movement similar to human is still a problem due to the mechanical construction limits or due to the weaknesses of motion generation methods [2]. The research being conducted at Warsaw University of Technology aims at developing biologically inspired motion patterns [3–5] for legged robots. As a first step of the work, a set of the human gait data was recorded. Based on the recorded data the robots design and motion synthesis was performed. Very fast development of the personal computers and their computational power, in past two decades, drastically improved the design process. The design summarized in this paper was also performed with use of the CAD/CAE software.

---

T. Zielinska (✉)

Faculty of Power and Aeronautical Engineering, ul.Nowowiejska 24, Warsaw University of Technology, 00-665 Warsaw, Poland  
e-mail: teresaz@meil.pw.edu.pl

## Design Study

The designed robot is meant to serve as a research platform for human referred motion synthesis. The robot comprises only of the lower extremities and the torso. Unlike in the professional design sequence we first had the servos and then had to suit the biped's structure to their dynamical capabilities. In order to do that the dynamic analysis had to be performed in the initial and the final stage of the design process. The main purpose of the analysis was the choice of the length of the links, so that the used servos will be able to actuate the structure. The link proportions were kept to match the proportion of the human body where the leg length is close to the length of the upper body. The aim of primary analysis was to find the biped size allowing the use of specified actuators. The DX-113 and DX-116 Robotics actuators are capable of generating  $1 Nm$  and  $2.8 Nm$  torque, respectively. By solving a set of inverse dynamic problems for different links lengths and the gait parameters the joints actuating torque with respect to the links lengths were found. The inverse dynamic problem was solved only for the single support phase, considering robot as a serial kinematic chain and using the Newton-Euler formulation. The analysis comprised of the following: (1) choosing the kinematic model – the kinematic model was limited to five links with the assumption that the pelvis is perpendicular to the sagittal plane and that only hip pitch, knee pitch and ankle pitch joints take part in the motion. The five values of the links lengths were tested  $l = \{100, 120, 130, 140, 150\}[mm]$ , where  $l$  – length of the thigh and shin links (further referred to as the links length). The length of the pelvis link was constant in all tests and was equal to  $l_p = 100 mm$ , (2) choosing the gait parameters – the parameters, such as the gait speed, step length and duration of the swing phase were those of human being, but appropriately scaled to suit the size of the robot. In the first design stage the overall size of the robot was assumed to be  $500 mm$ , the walking speed was  $v = 0.076 m/s$ , the step length  $d = 172 mm$  and the swing phase

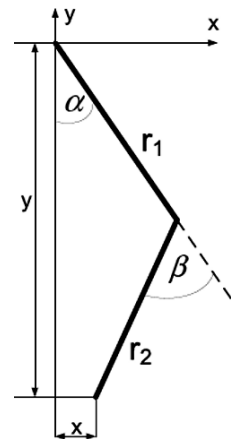


**Fig. 1** Schematic view of the leg

duration  $t = 1.4$  s. (3) solving the inverse kinematic problem—the two equations describing the simple geometric relationships were used (Fig. 1):

$$\begin{cases} x = r_1 \cos \alpha + r_2 \cos(\alpha + \beta) \\ y = -r_1 \sin \alpha - r_2 \sin(\alpha + \beta) \end{cases} \quad (1)$$

For the assumed hip and foot trajectories the non-linear equations (1) were solved numerically with respect to  $\alpha$  &  $\beta$  using the Newton-Raphson method implemented in Matlab environment. The obtained results were the time courses of hip pitch ( $\alpha$ ) and knee pitch ( $\beta$ ) angles. Finally the angular velocities and angular accelerations were calculated. The next stage was the development of mechanical model and the evaluation of robot masses — the simplified mechanical model was created in CAD environment. Because of the biped's sagittal symmetry only one leg and a pelvis were modeled. From the build model the mass properties (links' masses, their center location and moments of inertia) required for the dynamic analysis were extracted. With solving the inverse dynamic problem the torques in the particular joints were obtained basis on the two (forward and backward) steps according to the Newton-Euler formulation. In the forward step (progressing from the foot in the support phase to the foot in the swing phase), the linear and angular accelerations of the mass center were evaluated. Then the forces and moments acting on the mass center of each link were calculated using known formula:

$$\begin{aligned} {}^{i+1}F_{i+1} &= m_{i+1} {}^{i+1}v_{C_{i+1}} \\ {}^{i+1}N_{i+1} &= C_{i+1} I_{i+1} {}^{i+1}\dot{\omega}_{i+1} + {}^{i+1}\omega_{i+1} \times C_{i+1} I_{i+1} {}^{i+1}\omega_{i+1} \end{aligned}$$

In the backward step starting from the end of the kinematic chain (the foot in the swing phase) – forces, moments and torques in each joint were evaluated using:

$$\begin{aligned} {}^i f_i &= {}^i R^{i+1} f_{i+1} + {}^i F_i \\ {}^i n_i &= {}^i N_i + {}^i R^{i+1} n_{i+1} + {}^i P_{C_1} \times {}^i F_i + {}^i P_{i+1} \times {}^i R^{i+1} f_{i+1} \\ \tau_i &= {}^i n_i^T {}^i \hat{Z}_i \end{aligned}$$

This analysis was performed considering the simplified shape of leg-end trajectory being in transfer. In this preliminary study it was assumed to be semicircular. The trajectory of the human's foot differs from it, but the simplification is good enough to evaluate the motion general properties. After completing the preliminary robot design the dynamic properties of the structure were verified using the *Adams* environment. This led to the adjustment of the design details, and to the reduction of the masses considering the assembly components. *Adams* is the motion simulation software dedicated for detailed analysis of the complex mechanical structures performing the motion. The study was conducted in the following steps: (1) exporting the 3D model of the robot from CAD environment and importing it into *Adams* – from the CAD assembly model, created during the design process, the individual links were exported as *parasolids* (a geometrical model in form of the mathematical

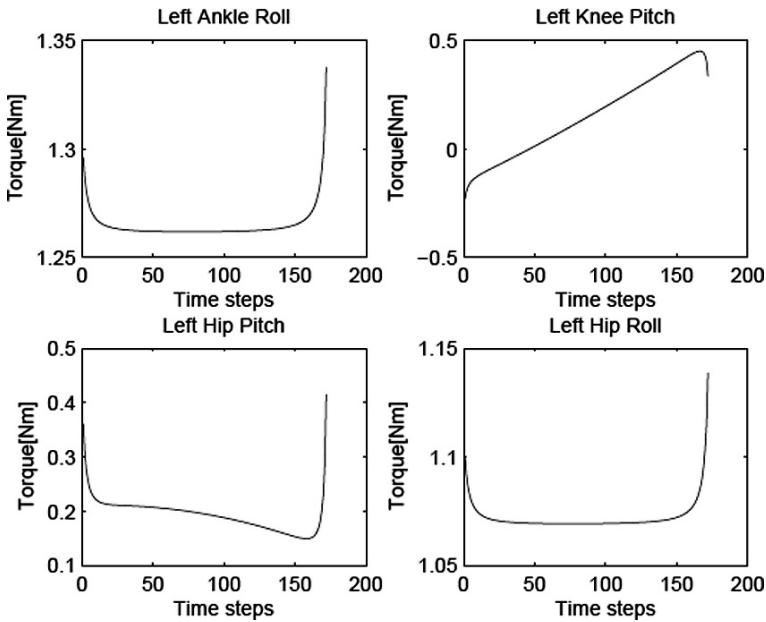


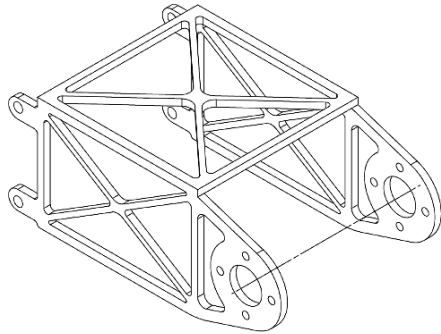
**Fig. 2** Torque in Ankle Roll, Knee Pitch, Hip Pitch, Hip Roll joints obtained for leg being in the support phase

definitions), (2) assigning the mass properties to the imported model – with the *parasolids* only the geometrical properties of the model were imported, for the dynamic analysis the mass properties had to be assigned to each link. In this case, it was enough to assign only the density to the particular solids considering the construction material. The resultant mass, mass centre location and the moments of inertia of each link were calculated automatically by *Adams*, (3) defining the motion parameters of the model – one of the last steps of this analysis was to assign the motion trajectory to each of the joints. In order to compare the results of the two methods, the motion assigned to the joints was the same as the one considered in the theoretical analysis conducted in the initial stage of the design, (4) obtaining torques in the joints. The magnitudes of torques, except the ankle roll, were similar to that obtained before designing the full structure (Fig. 2) what confirmed the results obtained in preliminary study.

## Mechanical Structure

Robot has 12 active DOFs. The final design fulfilling the limited torques supply and allowing the human like gait generation is given in Figs. 3 and 5. In the picture are given the final link dimensions resulting from the dynamic analysis with the aim to follow the human motion. To reduce the masses and to obtain the good prototyping

Fig. 3 Leg component



accuracy the elements were cut by laser in aluminium rectangular segments (Fig. 3). The crucial elements such as hip-knee and knee-ankle links form a semi-3D truss that which is known from its high weight to strength and rigidity ratio. Final design structure was elaborated using *Modelling* module of *Unigraphics NX4* – the integrated CAD/CAM/CAE software Fig. 4. The *Advanced Simulation* module (utilizing the Finite Elements Method – FEM dedicated for the structural analysis) was used in consecutive design iterations to tailor properly the mechanical structure and its mechanical strength.

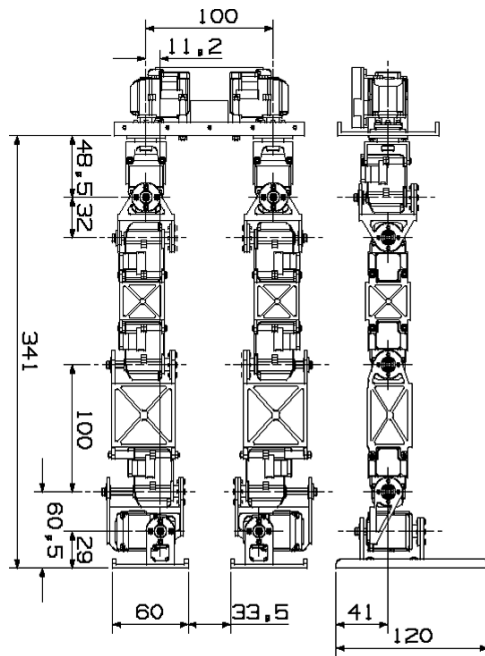
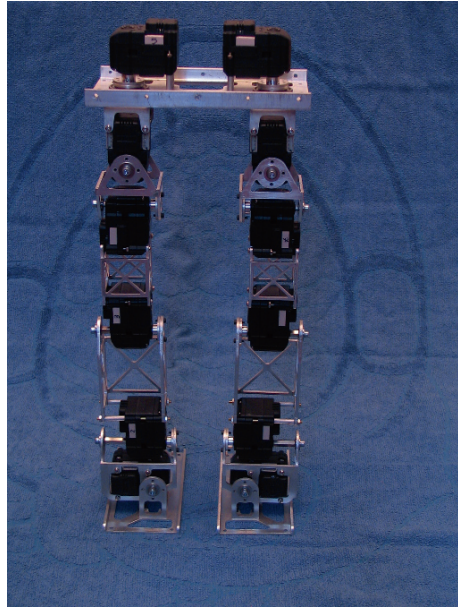


Fig. 4 Front and side view of the final assembly with given dimensions (the torso is not included)

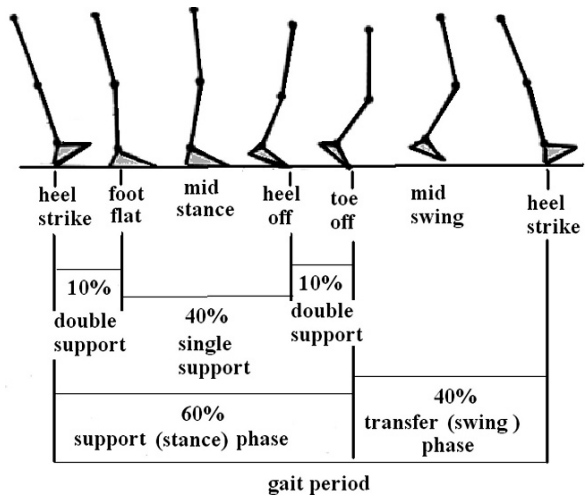
**Fig. 5** View of robot prototype



## Motion Synthesis

The normal human gait follows a common pattern (Fig. 6). In our research on biped motion synthesis we were interested to keep the similarity of human and robot gait. The trajectories recorded during human walk were considered as the reference. The recorded data were processed and evaluated using the specialized software combined with the VICON motion recording system. It was confirmed that the person (healthy young man) walks with statistically verified, representative gait. The motion was sampled every  $0.021\text{ s}$ , the gait period was  $1.04\text{ s}$ , walking speed was  $1.53\text{ m/s}$ , the support phase was about 60% of the gait period, in this the double support phase took 10% of the gait period. Those values matches the norm – [6, 7]. Our final prototype is  $0.3295\text{ m}$  tall, with length of thigh equal to  $0.10\text{ m}$  and shank with foot  $0.145\text{ m}$ . The mass of the robot is  $1.61\text{ kg}$ , mass of thigh is  $0.16\text{ kg}$ , mass of shank with foot –  $0.34\text{ kg}$ . The distance between the ground projection of the robot ankle and back of the foot is  $0.041\text{ m}$ . The point mass of thigh is below the hip joint at a distance of 50% of thigh length. Point mass of the shank was at a distance equal to 83.7% of the shank length from the knee. Here legs were about 3.7 times shorter than in the human. In experiments the step length was equal to  $0.26\text{ m}$ . To follow the robot–human size and speed proportion the change of the gait period was not required. The robot walking speed was expected to be  $0.41\text{ m/s}$  – 3.7 times smaller than in human walk. The length of thigh and shank matched also the proportion, however the size and mass of the upper part of the body was reduced. The lower part of leg (shank with foot) is heavier than thigh and that is another difference. Applied control hardware and servomotors required the increase of control

Fig. 6 Phases of human gait



step from 0.021 *s* (that was the time constant in human motion recording) to 0.05 *s*, gait period was 2.5 *s* and walking speed 0.172 *m/s*. First walking experiments were not successful. The robot was falling back, what was expected considering the position of ZMP (obtained by calculations using robot model). At the end of the single support phase the ZMP was outside the back of the footprint – the posture was not equilibrated. The gait was modified using experiments. It was found that not all servo motors exert the same speed and the control step must be again increased to 0.08 what resulted in gait period equal to 4 *s*. The ranges of hip joint trajectories were shifted towards positive direction reducing the leg-end backward shift at the end of the support phase and increasing the forward shift at the beginning of the support phase. In the knee a small bend during the support phase was added. Using reference to human motion the robot roll (trunk inclination in the frontal plane) was introduced. That referred to the feature of human gait however did not exactly imitated it. The resultant time course of ZMP was similar to that observed in human walk – compare Figs. 7 and 8.

### Summary

This paper presents the result of the mechanical model analysis and design of the robot. The method of prototype robot gait synthesis considering the 3D space is summarized. The novelty of presented work lies in the concept of the design where the motors power is limited and the target is to obtain the kinematic structure matching the human body proportions and being able to move as a human. Analyzing the design of popular world humanoids it is not the approach commonly used. First Honda robots had the mass equal to 210 kg [8], and first ASIMO robots walked on the bend legs which is not typical for human gait. Applied iterative and very detailed design procedure profited in the robot mass reduction, the masses proportion and



**Fig. 7** ZMP trajectory for human gait evaluated using human body model with consideration of trunk inclination (double support phase is included, the foot frame is shown)

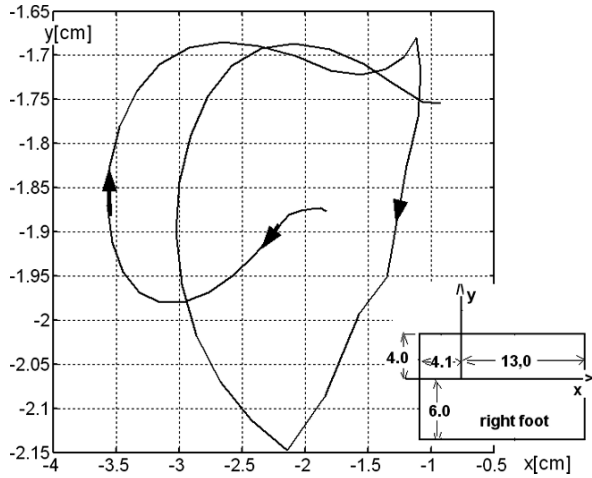
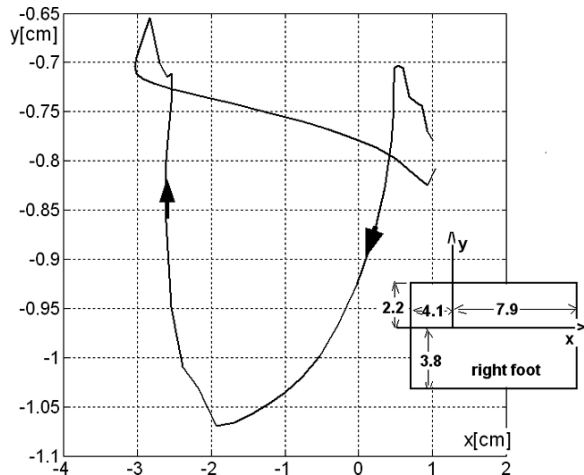


**Fig. 8** ZMP trajectory for modified robot gait with trunk inclination (double support phase is included, the foot frame is shown)



kinematic structure matches the human body, robot is able to follow the focused motion pattern. Presented results were validated by experiments. Other our publications describe the method of motion pattern storing and generating using coupled oscillators [9]. Our future target is to focus on the adaptable robot motion.

**Acknowledgments** The authors gratefully acknowledge the support. This work has been supported by Warsaw University of Technology (WUT) Research Program and Statutory Funds.

## References

1. Ouezdou F.B., Konno A. et al., *ROBIAN Biped Project – a Tool for the Analysis of the Human-being Locomotion System*, Proc. 5th Int. Conf. on Climbing and Walking Robots, 2002
2. Nakanishi J., Morimoto J., Endo G., Cheng G., Schaal S., Kawato M., *Learning from Demonstration and Adaptation of Biped Locomotion*. *Robotics and Autonomous Systems*, no. 47, hboxpp. 79–91, 2004.
3. Zielinska T., Chew C.M., *Biologically Inspired Motion Planning in Robotics*. Robot Motion and Control, Lecture Notes in Control and Information Sciences no. 335, Ed. K. Kozłowski. Springer, Chapter 13, pp. 201–219, 2006.
4. Zielinska T., *Biological Aspects of Locomotion*. Walking: Biological and Technological Aspects, CISM Courses and Lectures no.467. Ed. F. Pfeiffer, T. Zielinska. Springer, pp. 1–30, 2004.
5. Zielinska T. *Coupled Oscillators Utilised as Gait Rhythm Generators of a Two-Legged Walking Machine*. *Biological Cybernetics* 74, pp. 263–273, 1996.
6. Vaughan Ch.L., Davis B.L., O'Connor J.C., *Dynamics of Human Gait*, Human Kinetics Publishers, 1992.
7. Winter D.A., *Biomechanics and Motor Control of Human Gait: Normal, Elderly and Pathological*, University of Waterloo, 1991.
8. Hirai K., Hirose M., Haikawa Y., Takenaka T., *The Development of Honda Humanoid Robot*. Proc. ICRA: International Conference on Robotic and Automation, pp. 1321–1326, 1998.
9. Zielinska T., Kryczka P., Jargilo T., *Constructing the Biped Robot Motion Using the Reference to Human Locomotory System*. RoManSy 2008, Japan 2008, Tokyo 2008.

# A Comparison of Algorithms for Path Planning of Industrial Robots

Francisco Rubio, Francisco Valero, Josep Lluís Suñer and Vicente Mata

**Abstract** In this paper, the path planning problem for industrial robots in environments with obstacles has been solved using four algorithms that implement different methodologies. Our objective is to analyze the characteristics of these algorithms. Consequently, the results (solutions) obtained with each of them are compared through the analysis of three operational parameters that are relevant to determine the qualities of the solutions. These parameters are: the computational time, the distance travelled by the robot and the number of generated configurations. One of the algorithms can be catalogued as indirect and the other three are variations of a direct method. The four algorithms have been applied to a robot type PUMA 560.

**Keywords** Robotics · Path planning · Collision avoidance · Operational parameters

## Introduction

Path planning applied to industrial robots operating in environments with obstacles has been addressed extensively in the field of robotics (some of the many algorithms can be found in [1–6]), with a comprehensive overview of the state of the art in [4] and [7]. The aim is to achieve optimal solutions with reduced computational times. In this paper we introduce four different methodologies to solve the path planning problem. The aim is to study the characteristics of the solutions generated and to compare among them.

The first one is an indirect method that gives rise to what we have called sequential algorithm because it works in two stages: in the first, a discrete configuration space of the robot is generated and in the second the search for an optimal path in that discrete configuration space is made (see [8]). The other three methodologies are variants of a direct method which we have called simultaneous algorithm because the space state of the robotic system is analyzed and they have the particularity

---

F. Rubio (✉)

Dpt. of Mechanical Engineering, Politechnic University of Valencia, Camino de Vera s/n Valencia 46023, Spain  
e-mail: frubio@mcm.upv.es

that they find a solution (the path) at the same time when the robot reaches the goal, and therefore a path is provided without resorting to subsequent searches (see [7]).

The four algorithms work on a wired model of the robot in Cartesian coordinates (see [9]), and they generate collision-free configurations  $C^i$ . The obstacles are modelled on the basis of obstacles pattern: spheres  $S_i$ , cylinders  $C_i$  and planes  $P_i$ . In the following sections we discuss some of the features of the algorithms mentioned.

### Generation of Configurations

The algorithms work on a rectangular prism in which two of the opposed vertices correspond with the position of the end-effector of the robot in the initial and final configurations, and its sides are parallel to the global Cartesian reference system. The set of positions that the end-effector of the robot can adopt within the prism is restricted to a finite number of points resulting from the discretization of the prism according to the following increases:

$$\Delta x = \frac{|\alpha_{nx}^f - \alpha_{nx}^i|}{N_x} \quad \Delta y = \frac{|\alpha_{ny}^f - \alpha_{ny}^i|}{N_y} \quad \Delta z = \frac{|\alpha_{nz}^f - \alpha_{nz}^i|}{N_z} \quad (1)$$

Where the values of  $\Delta x$ ,  $\Delta y$  and  $\Delta z$  are calculated from the values of the number of intervals  $N_x$ ,  $N_y$  and  $N_z$  in which the prism is discretized, with the condition that those increments are smaller than the smallest dimension of the obstacle modelled in the workspace. Points  $(\alpha_{nx}^f, \alpha_{ny}^f, \alpha_{nz}^f)$  and  $(\alpha_{nx}^i, \alpha_{ny}^i, \alpha_{nz}^i)$  correspond to the coordinates of the end-effector of the robot for the initial and final configurations. In Fig. 1 it can be observed the way in which the prism is discretized that gives rise to the set of nodes that the end-effector of the robot PUMA 560 can adopt.

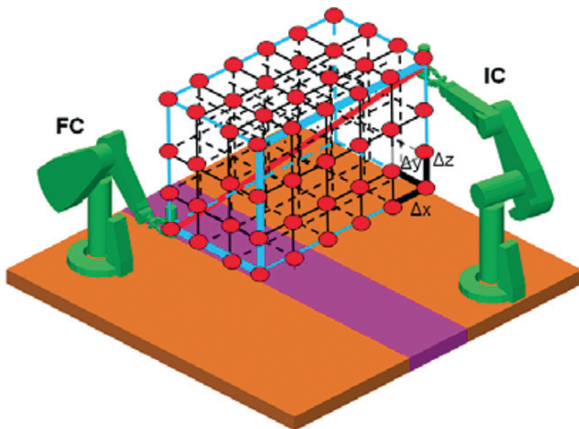


Fig. 1 Rectangular prism

To calculate the configuration space of the robot, adjacent configurations to a given one are generated (see [8] and [9]), according to the characteristics of each of the algorithms involved. Both the size of the prism and the size of the discretization can be modified to achieve covering the entire workspace using a size of discretization as small as necessary to reach a solution.

Given a feasible configuration  $C^k$ , it is said that a new configuration  $C^p$  is adjacent to the first one if it is also feasible (i.e. it fulfils the characteristics associated to the robot modelling and avoids collisions with the obstacles) and in addition the following four properties are fulfilled:

1. The position of the end-effector that corresponds with a node of the discrete workspace is at a distance of one unit with respect to the position of the end-effector of configuration  $C^k$ . That means that at least one of the following conditions has to be fulfilled:

$$|\alpha_{nx}^k - \alpha_{nx}^p| = \Delta x \quad |\alpha_{ny}^k - \alpha_{ny}^p| = \Delta y \quad |\alpha_{nz}^k - \alpha_{nz}^p| = \Delta z \quad (2)$$

Being  $n$  the subscript corresponding to the significant point associated to the end-effector of the robot. For the robot PUMA 560,  $n = 7$ .

2.  $C^p$  should be a collision-free configuration.
3. Verification of absence of obstacles between adjacent configurations  $C^k$  and  $C^p$ . It is necessary to verify that there are no obstacles between adjacent configurations for which the following condition is set out:

$$\left| \overrightarrow{\alpha_i^k \alpha_i^p} \right| \leq 2 \cdot \min(r_j) \quad (3)$$

where  $r_j$  is the characteristic dimension of the smallest pattern obstacle.

4. Configuration  $C^p$  must be such that it minimizes the following objective function:

$$\|C^p - C^f\| = \sum_{i=1}^n \left( (\alpha_{xi}^p - \alpha_{xi}^f)^2 + (\alpha_{yi}^p - \alpha_{yi}^f)^2 + (\alpha_{zi}^p - \alpha_{zi}^f)^2 \right) \quad (4)$$

## Algorithms to Calculate the Path

Four algorithms have been created and tested. The following lines are a brief description of them:

- 1st algorithm: also called sequential algorithm. This is an indirect and global method. The generation of configurations is always from the most old one that has not yet been used to branch out and continues until the positions of the end-effector of the robot that are adjacent to the final are reached.

With the configuration space obtained, a graph is created where the nodes correspond to the configurations and the arcs between nodes to the distance travelled by the robot between every two adjacent configurations  $C^k$  and  $C^p$ , i.e.,  $c(k, p) = \sqrt{\sum_{i=1}^n \left( (\alpha_{xi}^p - \alpha_{xi}^k)^2 + (\alpha_{yi}^p - \alpha_{yi}^k)^2 + (\alpha_{zi}^p - \alpha_{zi}^k)^2 \right)}$  (where  $n$  is the number of significant points of the robot).

In the second stage, the Dijkstra's algorithm is applied to the previous graph to determine the sequence of configurations of minimum distance. The result is the path of minimum distance.

- 2nd algorithm: also called simultaneous algorithm A\* (see [6]). This is a direct and global approach. It is direct because path is obtained simultaneously as the configuration space is being generated, so that a solution is obtained at the same time as the final configuration is reached, without splitting the process into sequential stages. The procedure creates the configuration space as a tree, following this strategy: a weight  $f(p)$  is assigned to each configuration  $C^p$  according to the function,

$$f(p) = f(k) + c(k, p) + h(p, f) \quad (5)$$

being  $f(k)$  the weight or cost to go from the initial configuration to the configuration from which  $C^p$  has been generated and

$c(k, p) = \sum_{i=1}^n \sqrt{(|\alpha_i^p - \alpha_i^k|^2)}$  is the weight between adjacent configurations and

$h(p, f) = \sum_{i=1}^n \sqrt{(|\alpha_i^p - \alpha_i^f|^2)}$  is the cost estimated to go from configuration  $C^p$  to the final configuration  $C^f$ .

Some new adjacent configurations from the configuration of minimum weight must be generated and so on until the final configuration is reached, moment in which the algorithm gives a solution. In order to ensure optimality of the solution the process should keep generating adjacent configurations to complete the configuration space to see if there is any solution that offers a smaller distance travelled.

- 3rd algorithm: also called simultaneous algorithm with uniform cost. Like the previous one, this is a direct and global approach. This algorithm works similarly to the 2nd algorithm, the main difference lays on the value of the weight  $f(p)$  which is assigned to each configuration  $C^p$ . This algorithm only takes into account the distance travelled by the robot from the initial configuration to the current  $C^k$  from which the branching process tries to reach new adjacent configurations as  $C^p$ . Therefore, the weight or cost to go to  $C^p$  is

$$f(p) = f(k) + c(k, p) \quad (6)$$

Similarly, the end-effector of the robot is travelling to the nodes until the final configuration is reached, and at the same time you obtain a solution. The first solution is the optimal one, namely that of minimum distance.

- 4th algorithm: called greedy and simultaneous algorithm is also a direct method and global method as the previous two. In this case weight assigned to each configuration only takes into account an estimation of the distance the robot should travel to go from the current configuration (from which the algorithm is branching for new adjacent configurations) to the final one.

$$f(p) = h(p, f) \tag{7}$$

Representing  $h(p, f)$  the cost estimated to go from  $C^p$  configuration to the final configuration  $C^f$  as it has been seen in the 2nd algorithm. At the same time the final configuration is reached, the algorithm provides a solution.

### Comparing Path Properties

The four algorithms proposed in this article have been applied to the robot type PUMA 560. A computer Pentium 4 with 2.4 GHz and 496 MB of RAM has been used. Three important operational parameters have been studied: the computational time used in generating a solution (in seconds), the distance travelled (in meters) and the number of configurations generated. Next, we show the results over 5 examples, Tables 1, 2, and 3.

Example 1: Configurations to be joined are given by joint values:

Initial Configuration:  $(59.09^\circ, -145.38^\circ, 13.03^\circ, 1.13^\circ, 31.68^\circ, 0^\circ, 0 \text{ mm})$

Final Configuration:  $(-34.65^\circ, -169.14^\circ, 58.56^\circ, 0^\circ, 15.78^\circ, 0^\circ, 0 \text{ mm})$

Location of Obstacles (in m.)			
1 <sup>st</sup> C Obs.: $c_{11}^{CO} = (-0.85, -0.5, 0)$	$c_{21}^{CO} = (-0.85, -0.5, 2)$	$r_1^{CO} = 0.15$	
2 <sup>nd</sup> C Obs.: $c_{12}^{CO} = (-0.75, 0, 0)$	$c_{22}^{CO} = (-0.75, 0, 2)$	$r_2^{CO} = 0.15$	
3 <sup>rd</sup> C Obs.: $c_{13}^{CO} = (-0.7, 0.2, 0)$	$c_{23}^{CO} = (-0.7, 0.2, 2)$	$r_3^{CO} = 0.15$	
1 <sup>st</sup> S Obs.: $c_1^{SO} = (-0.85, -0.4, 0.5)$		$r_1^{SO} = 0.15$	
2 <sup>nd</sup> S Obs.: $c_2^{SO} = (-0.75, 0, 0.5)$		$r_2^{SO} = 0.15$	
3 <sup>rd</sup> S Obs.: $c_3^{SO} = (-0.75, 0, 0.5)$		$r_3^{SO} = 0.15$	
1 <sup>st</sup> P Obs.: $a_1^{PO} = (-0.7, -0.35, 0)$	$q_{11}^{PO} = (-0.7, -0.35, 2)$	$q_{21}^{PO} = (-1.5, -0.35, 0)$	$q_{31}^{PO} = (-0.7, -0.45, 0)$
2 <sup>nd</sup> P Obs.: $a_2^{PO} = (-0.5, 0, 0)$	$q_{12}^{PO} = (-0.5, 0, 2)$	$q_{22}^{PO} = (-1.3, 0, 0)$	$q_{32}^{PO} = (-0.5, -0.15, 0)$
3 <sup>rd</sup> P Obs.: $a_3^{PO} = (-0.5, 0.3, 0)$	$q_{13}^{PO} = (-0.5, 0.3, 2)$	$q_{22}^{PO} = (-1.3, 0.3, 0)$	$q_{32}^{PO} = (-0.5, -0.45, 0)$

**Table 1**

Example 1 Fixed-based robot	Computational time (in s.)			
	Indirect algorithm: seq	Simultaneous algorithm: A*	Simultaneous alg.: uniform cost	Simultaneous algorithm: greedy
With 0 Obstacles	66.31	112.14	651.25	4.94
With 1 Cylinder Ob.	122.97	149.02	744.30	28.78
With 2 Cylinder Ob	260.63	270.52	987.85	15.03
With 3 Cylinder Ob	230.48	869.02	1457.44	23.80
With 1 Sphere Ob.	201.11	257.99	1267.76	10.48
With 2 Sphere Ob.	211.85	484.03	1685.76	44.86
With 3 Sphere Ob.	193.44	485.36	1682.36	44.98
With 1 Plane Ob.	76.17	110.36	529.52	16.14
With 2 Plane Ob.	198.45	346.43	869.47	67.80
With 3 Plane Ob.	1676.13	602.91	1406.94	82.27

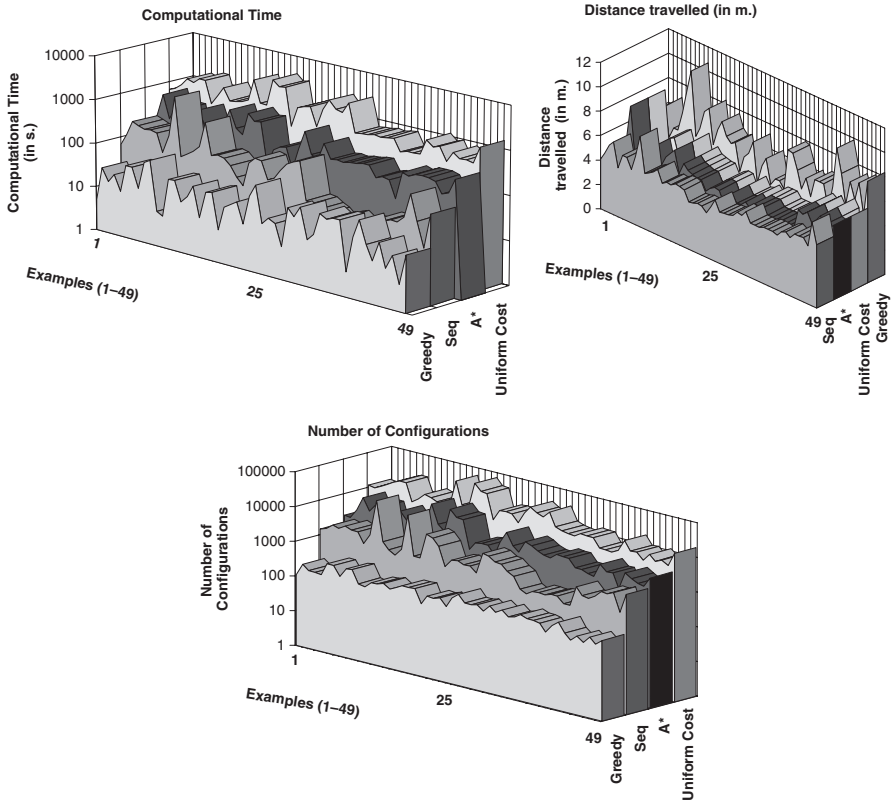
**Table 2**

Example 1 Fixed-based robot	Distance travelled (in m.)			
	Indirect algorithm: seq	Simultaneous algorithm: A*	Simultaneous alg.: uniform cost	Simultaneous algorithm: greedy
With 0 Obstacles	4.07	3.83	3.83	3.73
With 1 Cylinder Ob.	4.68	5.05	5.05	6.21
With 2 Cylinder Ob	5.56	5.23	5.23	5.99
With 3 Cylinder Ob	5.95	8.20	8.20	6.84
With 1 Sphere Ob.	4.01	4.03	4.03	4.46
With 2 Sphere Ob.	5.18	4.63	4.63	5.38
With 3 Sphere Ob.	5.19	4.63	4.63	5.38
With 1 Plane Ob.	4.37	4.13	4.13	6.93
With 2 Plane Ob.	5.60	5.70	5.70	8.98
With 3 Plane Ob.	7.42	5.94	5.94	10.71

**Table 3**

Example 1 Fixed-based robot	Number of configurations generated			
	Indirect algorithm: seq	Simultaneous algorithm: A*	Simultaneous alg.: uniform cost	Simultaneous algorithm: greedy
With 0 Obstacles	1483	2428	11431	108
With 1 Cylinder Ob.	1685	2284	10684	234
With 2 Cylinder Ob	2312	4165	12990	173
With 3 Cylinder Ob	2068	10145	15993	168
With 1 Sphere Ob.	2708	4759	21043	161
With 2 Sphere Ob.	2247	7711	24763	369
With 3 Sphere Ob.	2249	7711	24763	369
With 1 Plane Ob.	1167	2066	7855	194
With 2 Plane Ob.	2275	4811	10271	357
With 3 Plane Ob.	23821	7806	15691	383





Next, the graphs for all the cases are shown, computing the computational time required, distance travelled and number of configurations generated. They all correspond to a fixed-based robot

## Conclusions

In this paper the characteristics of the solutions to the path planning problem of industrial robots in environments with obstacles have been compared from four different algorithms. Three operational parameters have been analyzed: computational time (in s.), distance travelled by the robot (in m.) and number of configurations generated.

Conclusions of the conducted analysis are pointed out in the four following remarks:

- (a) The algorithms proposed allow solving the path planning problem and it is possible to be applied to any industrial robot (ABB).

- (b) The best results from the point of view of computational time are provided by the greedy algorithm followed by the simultaneous algorithm with uniform cost.
- (c) The analysis of the distance travelled gives very similar results for the simultaneous algorithms A\* and with uniform cost. The worse results are offered by the greedy algorithm.
- (d) The best results from the point of view of the smallest number of configurations generated are provided by the greedy algorithm followed by simultaneous algorithm with uniform cost.

**Acknowledgments** We would like to thank the Foreign Language Coordination Office at the Polytechnic University of Valencia for their help in revising this paper.

Also this paper has been possible thanks to the funding of Spanish Education and Science Ministry by means of the Researching and Technologic Development Project DPI2005-08732-C02-01 which is also supported by FEDER funds.

## References

1. Latombe, J-C., Robot motion planning: a distributed representation approach, *International Journal of Robotics Research*, vol. 10(6), 1991, 628–649.
2. Kavraki L. E., Probabilistic roadmaps for path planning in high dimensional configuration spaces, *IEEE Transactions on Robotics and Automation*, vol. 12, 1996, 566–580.
3. Ito P., A Slicing Connection Strategy for Constructing PRMs in High-Dimensional Cspaces, *IEEE International Conference on Robotics and Automation*, IEEE Press, 2006, 1249-1254.
4. LaValle S. M., *Planning Algorithms*. Cambridge University Press, Cambridge, U.K., Chapter 13: 2006.
5. Hsu D., On the probabilistic foundations of probabilistic roadmap planning, *International Journal of Robotics Research*, vol. 25(7), 2006, 627–643.
6. Fares A.D., Path planning optimization of industrial robots using genetic algorithm, *Proceedings of 16th International Workshop on Robotics in Alpe-Adria-Danube Region*, 2007, 424–429.
7. Rubio F., *Planificación de trayectorias de robots industriales. Análisis en entornos con obstáculos*, Tesis Doctoral, Universidad Politécnica de Valencia, España, 2006.
8. Valero. F. J., A formulation for path planning of manipulators in complex environments by using adjacent configurations, *Advanced Robotics*, vol. 11, 1997, 33–56.
9. Valero F. J., Trajectory planning in workspaces with obstacles taking into account the dynamic robot behaviour, *Mechanism and Machine Theory*, vol. 41(5), 2006, 525–536.

# Stiffness Analysis of Parallel Manipulator Using Matrix Structural Analysis

Rogério Sales Gonçalves and João Carlos Mendes Carvalho

**Abstract** This paper describes a stiffness analysis of a 6-RSS parallel architecture by using matrix structural analysis. The stiffness analysis is based on standard concepts of static elastic deformations. The formulation has been implemented in order to obtain the stiffness matrix that can be numerically computed by defining a suitable model of the manipulator, which takes into account the stiffness properties of each element such as links, actuators and joints. In order to simplify the model, joints and actuators stiffness have been neglected. The obtained stiffness matrix was used to map the end-effector compliant displacements when external forces and torques are applied on it.

**Keywords** Parallel manipulators · Stiffness analysis · Matrix structural analysis

## Introduction

Stiffness can be defined as the capacity of a mechanical system to sustain loads without excessive changes of its geometry [1]. These produced changes on geometry, due to the applied forces, are known as deformations or compliant displacements.

Compliant displacements in a parallel robotic system produces negative effects on static and fatigue strength, wear resistance, efficiency (friction losses), accuracy, and dynamic stability (vibration). The growing importance of high accuracy and dynamic performance for parallel robotic systems has increased the use of high strength materials and lightweight designs improving significant reduction of cross-sections and weight. Nevertheless, these solutions also increase structural deformations and may result in intense resonance and self-excited vibrations at high speed [1]. Therefore, the study of the stiffness becomes of primary importance to the design of multibody robotic systems in order to properly choose materials, component

---

R.S. Gonçalves (✉)

School of Mechanical Engineering, Federal University of Uberlândia, Campus Santa Mônica,  
CEP 38400-902, Uberlândia, MG, Brasil  
e-mail: ufursgoncalves@yahoo.com.br

geometry, shape and size, and interaction of each component with others. Some examples of design procedures based on stiffness analysis can be found in [2–4].

The overall stiffness of a manipulator depends on several factors including the size and material used for links, the mechanical transmission mechanisms, actuators and the controller [5]. In general, to realize a high stiffness mechanism, many parts should be large and heavy. However, to achieve high speed motion, these should be small and light. Moreover, one should point out that the stiffness is greatly affected by both the position and the values of the mechanical parameters of the structure parts [6].

There are three main methods have been used to derive the stiffness model of parallel manipulators [7]. These methods are based on the calculation of the *Jacobian matrix* [8–10]; the *Finite Element Analysis* (FEA) [11, 12] and the *Matrix Structural Analysis* (MSA) [7, 13, 14].

The methods based on calculation of the Jacobian matrix are simple and they supply one initial estimate of the stiffness matrix. The uses of Finite Element Analysis models are reliable, but these models have to be remeshed over again, involving very tedious and time-consuming routines. However these models are well adapted to validate analytical models, or some experimental results. Methods based on matrix structural analysis are simple and easy for computational implementation.

In this paper is presented a methodology to obtain the global stiffness matrix of a parallel manipulator, using the matrix structural analysis, and known the stiffness matrix of each structure element. The methodology is applied to a 6-RSS parallel architecture and the results are compared with those obtained from commercial software for finite element analysis.

## The 6-RSS Parallel Architecture

The 6-RSS parallel architecture is a 6 degree of freedom manipulator, which is characterized by a base and a mobile platform, connected by six *RS-SS* segments, where the R-joint is on the Cartesian axes, two joints by axis, as shown in Fig. 1. The Cartesian system is the base of the structure where the actuators are mounted, reducing dead loads. The links can be constructed by light and resistant materials that make them rigid, with low inertia and in a modular construction. One extremity of *SS*-segments is connected to the platform, consisting of a virtual cube, where the *S*-joints are tied on the center of its faces. Kinematics variables are the input angles  $\alpha_i$  ( $i = 1-6$ ) of the *R*-joints. The studied structure has the *RS*-segments and the *SS*-segments the same length and  $|b_1b_2| = |b_3b_4| = |b_5b_6| = |p_1p_2| = |p_3p_4| = |p_5p_6|$ , Fig. 1.

The prototype has six equal legs. Each leg subsystem is composed by a dc brushed gear-motor and encoder, joints and links. Segments are constructed with steel and commercial joints; the mobile platform is built in aluminum; the control system uses a motion control card installed in a PC. Virtual instruments have been used to program the motion.

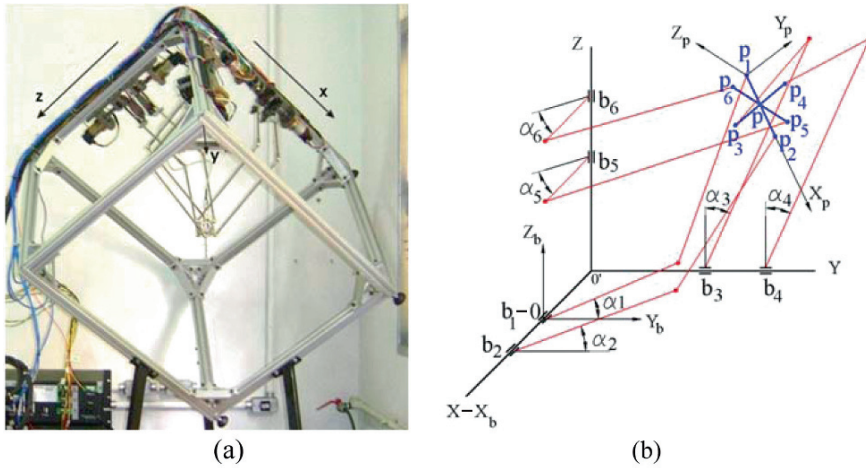


Fig. 1 (a) The built prototype of a 6-RSS parallel manipulator. (b) Generic configuration

### Stiffness Analysis

From the stiffness matrix,  $K$ , under the action of external force and torque,  $\{W\}$ , it is possible to calculate the compliant displacement,  $\{U\}$ , Eq. (1).

$$\{W\} = K\{U\} \tag{1}$$

In this paper, the stiffness matrix is obtained from the method *Matrix Structural Analysis* (MSA), also known as the *displacement method* or *direct stiffness method* (DSM). The methods of structural analysis is based on the idea of breaking up a complicated system into component parts, discrete structural elements, with simple elastic and dynamic properties that can be readily expressed in a matrix form. The discrete structure is composed by elements which are joined by connecting nodes. When the structure is loaded each node suffers translations and/or rotations, which depend on the configuration of the structure and the boundary conditions. For example, in a fixed linkage no displacement occurs. The nodal displacement can be found from a complete analysis of the structure. The matrices representing the beam and the joint are considered as building blocks which, when fitted together in accordance with a set of rules derived from the theory of elasticity, provide the static and dynamic properties of the whole structure [13].

### Stiffness of Beam and Joint

The stiffness matrix of the three-dimensional straight bar with uniform cross-sectional area is [15]:

$$k_j = \begin{bmatrix} k_{bj} & -k_{bj} \\ -k_{bj} & k_{bj} \end{bmatrix} \tag{2}$$

where  $k_{bj}$  is given by:

$$k_{bj} = \begin{bmatrix} \frac{A_j E_j}{L_j} & 0 & 0 & 0 & 0 & 0 \\ 0 & \frac{12E_j I_{zj}}{L_j^3} & 0 & 0 & 0 & \frac{6E_j I_{zj}}{L_j^2} \\ 0 & 0 & \frac{12E_j I_{yj}}{L_j^3} & 0 & -\frac{6E_j I_{yj}}{L_j^2} & 0 \\ 0 & 0 & 0 & \frac{G_j J_j}{L_j} & 0 & 0 \\ 0 & 0 & -\frac{6E_j I_{yj}}{L_j^2} & 0 & \frac{4E_j I_{yj}}{L_j} & 0 \\ 0 & \frac{6E_j I_{zj}}{L_j^2} & 0 & 0 & 0 & \frac{4E_j I_{zj}}{L_j} \end{bmatrix} \tag{3}$$

On Eq. (3)  $E_j$  and  $G_j$  are, respectively, the modulus of elasticity and the shear modulus of element  $j$ ;  $I_{yj}$ ,  $I_{zj}$  are the moment of areas about the  $Y$  and  $Z$  axes, respectively.  $J$  is the Saint-Venant torsion constant and  $A_j$  is the cross-sectional area.

The stiffness of a joint is given by [7]:

$$k_{j0 \text{ int}} = \begin{bmatrix} k_c & -k_c \\ -k_c & k_c \end{bmatrix} \tag{4}$$

Where  $k_c = \text{diag}(k_{tx}, k_{ty}, k_{tz}, k_{rx}, k_{ry}, k_{rz})$ ;  $k_{tx}, k_{ty}, k_{tz}$  are the translation stiffness and  $k_{rx}, k_{ry}, k_{rz}$  the rotational stiffness along the axes.

For application of MSA is necessary to write the stiffness matrices of all elements in the same reference frame. This transformation, element by element, must be held before the assembly of the stiffness matrix of the structure. This transformation matrix,  $T_j$ , can be obtained from [15].

Thus, the stiffness matrix of the elements in a common reference frame (elementary stiffness matrix), for segments,  $k_j^e$ , and for joints,  $k_{j0 \text{ int}}^e$ , are

$$[k_j^e] = [T_j][k_j][T_j]^T \tag{5}$$

$$[k_{j0 \text{ int}}^e] = [T_j][k_{j0 \text{ int}}][T_j]^T \tag{6}$$

After obtaining the stiffness matrix of each beam and joint in a common reference frame, the stiffness matrix of whole structure can be obtained using the MSA. Based on how the structure elements are connected, from their nodes, is possible to define a connectivity matrix. As each segment and joint stiffness are known, the global stiffness matrix is obtained by a superposition procedure. This global stiffness matrix is singular because the system is free. After application of the boundary conditions, for example, where the displacements are known, the new matrix is invertible and the compliant displacements can be done by:

$$\{U\} = K^{-1}\{W\} \tag{7}$$

This procedure is described in detail in [16].

Although the FEA and MSA have the same basic equations, Eqs. (1), (2), (3), (4), (5), (6) and (7), one can point out some advantages of the MSA method: (a) A robotic structure is composed by segments and joints. Then, each segment and each joint can be modeled by only two nodes for the MSA analysis. Otherwise on the FEA each beam is divided in several nodes and the joints stiffness, in general, are not considered. (b) Using a commercial FEA software (the usual procedure) one do not have the control of the solver. The MSA method one can follow step-by-step the stiffness matrix assembling. (c) In the FEA method at each variation of the structural configuration a remeshed must be made, increasing the computational cost. In the MSA method is only necessary improve the inverse kinematic model to obtain the stiffness mapping for all structure configuration.

### Stiffness Model of a 6-RSS Parallel Architecture

In this paper are presented results of the stiffness analysis considering only the compliance of segments. The arms and forearms are modeled as beam and the stiffness of whole structure is carried out according to the elements are arranged in the structure, Fig. 2.

The following parameters were used in the model: length of the arms and forearms equal to 0.3 m;  $|b_1b_2| = |b_3b_4| = |b_5b_6| = |p_1p_2| = |p_3p_4| = |p_5p_6| = 0.076$  m; the segments are built with steel ( $E = 2 \times 10^{11}$  N/m<sup>2</sup> and  $G = 0.8 \times 10^{11}$  N/m<sup>2</sup>); the cross-sectional area is circular with 0.005 m diameter. The boundary conditions

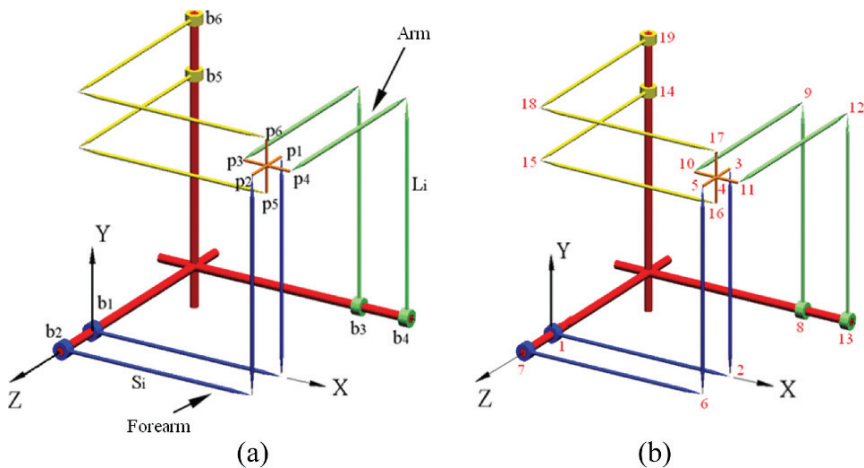


**Fig. 2** Stiffness model of a 6-RSS parallel architecture. (a) General arrangement; (b) Nodal points at joints

are given by actuators considered as blocked and, therefore, the forearms can be considered as fixed in the rotational joints (nodes 1, 7, 8, 13, 14 and 19). The external force and torque are applied on node 4, which is the center of the end-effector.

From nodes defined on Fig. 2b, the structure has 19 nodes with 6 d.o.f. at each node. Then the system has 114 d.o.f. with a  $18 \times 12$  connectivity matrix. The stiffness matrix of the structure after considering the boundary conditions (six fixed rotational joints) becomes a  $78 \times 78$  matrix.

In order to verify the presented analysis using the MSA method, a model was built in FEA using commercial software. The used system is a PC Pentium Dual Core<sup>®</sup>, 2 Gb of memory, and the Ansys<sup>®</sup> software. The used element is a beam type divided in 10 parts.

Table 1 provides results obtained from the FEA and MSA models. In Tables 1 and 2  $F_e$  is the external force ( $F_e = [Fx, Fy, Fz]$ ) and  $T_e$  the external torque ( $T_e = [Mx, My, Mz]$ ).

Results of Numerical simulations presented in Table 1 were made in order to show the soundness of the model due to symmetry of the structure. One can note that the compliant displacements are the same in the direction of the applied forces when other forces and torques are zero and, if the same effort values are applied, the compliant displacements are equals. In Table 2 are presented results for a generic configuration of the 6-RSS structure.

**Table 1** Compliant displacements of node 4 for  $\alpha_1 = \alpha_2 = \alpha_3 = \alpha_4 = \alpha_5 = \alpha_6 = 0^\circ$ . Forces are given in [N] and torques in [Nm]

$U$		$\delta_x[m]$	$\delta_y[m]$	$\delta_z[m]$	$\phi_x$ [rad]	$\phi_y$ [rad]	$\phi_z$ [rad]
$F_e = (10, 0, 0)$	MSA	0.002168	-0.000532	-0.000532	0.000857	0.001701	-0.005384
$T_e = (0, 0, 0)$	FEA	0.002173	-0.000534	-0.000534	0.000854	0.001727	-0.005378
$F_e = (0, 10, 0)$	MSA	-0.000532	0.002168	-0.000532	-0.005384	0.000857	0.001701
$T_e = (0, 0, 0)$	FEA	-0.000534	0.002173	-0.000534	-0.005378	0.000854	0.001727
$F_e = (0, 0, 10)$	MSA	-0.000532	-0.000532	0.002168	0.001701	-0.005384	0.000857
$T_e = (0, 0, 0)$	FEA	-0.000534	-0.000534	0.002173	0.001727	-0.005378	0.000854
$F_e = (10, 10, 10)$	MSA	0.001103	0.001103	0.001103	-0.002826	-0.002826	-0.002826
$T_e = (0, 0, 0)$	FEA	0.001105	0.001105	0.001105	-0.002796	-0.002796	-0.002796

**Table 2** Compliant displacements of node 4 for  $\alpha_1 = 1.5^\circ$ ;  $\alpha_2 = 5^\circ$ ;  $\alpha_3 = 1.5^\circ$ ;  $\alpha_4 = 3.5^\circ$ ;  $\alpha_5 = 3^\circ$ ;  $\alpha_6 = 1^\circ$ . Forces are given in [N] and torques in [Nm]

$U$		$\delta_x[m]$	$\delta_y[m]$	$\delta_z[m]$	$\phi_x$ [rad]	$\phi_y$ [rad]	$\phi_z$ [rad]
$F_e = (10, 0, 0)$		0.002366	-	-	0.008324	0.002119	-
$T_e = (1, 0, 0)$	MSA		0.001190	0.000391			0.005466
$F_e = (0, 10, 0)$		-	0.002302	-	-	0.008197	0.002205
$T_e = (0, 1, 0)$	MSA	0.000456		0.001196	0.005218		
$F_e = (0, 0, 10)$		-	-	0.002283	0.002089	-	0.007933
$T_e = (0, 0, 1)$	MSA	0.001146	0.000462	-	-	0.005136	
$F_e = (10, 10, 10)$		0.000763	0.000650	0.000696	0.005195	0.005179	0.004672
$T_e = (1, 1, 1)$	MSA						



Numerical simulations had been carried out considering both stiffness for beams and joints, using hypothetical translational and rotational stiffness for joints, Eqs. (4), (5) and (6). Experimental analyses have been carried out in order to verify the stiffness values for the used joints.

## Conclusion

In this paper was presented a methodology to obtain the stiffness matrix for robotic structures by using the matrix structural analysis.

For application of the presented methodology the kinematic model of the structure and the stiffness matrices of its elements (segments, joints and actuators) must be known.

The great advantage of the matrix structural analysis method to obtain the stiffness matrix of a whole structure is not to require calculating the Jacobian of the structure and, therefore, does not need to work with differential equations. Another advantage is that the method enables to perform the mapping of compliant displacements for nodes related to different configurations of the structure.

The methodology was applied in a complex parallel structure and, in order to simplify the model, it was considered only the segments stiffness. The blocked actuators are used as boundary conditions and then, the rotational joints can be considered as fixed. To evaluate the method, results were compared with a model built and solve by a commercial finite element program.

In future work the complete model of the presented structure considering the stiffness of the joints and actuators will be done and compared with experimental test.

## References

1. Rivin, E.I., 1999, "Stiffness and Damping in Mechanical Design", Marcel Dekker Inc., New York.
2. Liu, X.-J., Jin, Z.-L. and Gao, F., 2000, "Optimum Design of 3-Dof Spherical Parallel Manipulators with Respect to the Conditioning and Stiffness Indices", *Mechanism and Machine Theory*, Vol. 35, No. 9, pp. 1257–1267.
3. Simaan, N. and Shoham, M., 2002, "Stiffness Synthesis of a Variable Geometry Planar Robot", 8th International Symposium on Advances in Robot Kinematics ARK 2002, Lenarcic J. and Thomas F. (Editors), Kluwer Academic Publishers, Caldes de Malavella, pp. 463–472.
4. Carbone, G., Lim, H.O., Takanishi, A. and Ceccarelli, M., 2003, "Optimum Design of a New Humanoid Leg by Using Stiffness Analysis", 12th International Workshop on Robotics in Alpe-Andria-Danube Region RAAD 2003, Cassino, paper 045RAAD03.
5. Tsai, L.W., 1999, "Robot Analysis: The Mechanics of Serial and Parallel Manipulators", John Wiley & Sons, New York, pp. 260–297.
6. Yoon, W.K., Suehiro, T., Tsumaki, Y. and Uchiyama, M., 2004, "Stiffness Analysis and Design of a Compact Modified Delta Parallel Mechanism", *Robotica*, Vol. 22, pp. 463–475.
7. Deblaise, D., Hernot, X. and Maurine, P., 2006, "A Systematic Analytical Method for PKM Stiffness Matrix Calculation".

8. Zhang, D., Xi, F., Mechefske, C.M. and Lang, S.Y.T., 2004, "Analysis of Parallel Kinematic Machine with Kinetostatic Modeling Method", *Robotics and Computer-Integrated Manufacturing*, Vol. 20, No. 2, pp. 151–165.
9. Majou, F., Gosselin, C.M., Wenger, P. and Chablat, D., 2004, "Parametric Stiffness Analysis of the Orthoglide", *Proc. Of the 35th International Symposium on Robotics*, Paris, France.
10. Company, O., Pierrot, F. and Fauroux, J.C., 2005, "A Method for Modeling Analytical Stiffness of a Lower Mobility Parallel Manipulator", *Proceedings of IEEE ICRA: International Conference on Robotic and Automation*, Barcelona, Spain.
11. Bouzgarrou, B.C., Fauroux, J.C., Gogu, G. and Heerah, Y., 2004, "Rigidity Analysis of T3R1 Parallel Robot with Uncoupled Kinematic", *Proceedings of the 35th International Symposium on Robotics*, Paris, France.
12. Corradini, C., Fauroux, J.C., Krut, S. and Company, O., 2004, "Evaluation of a 4 Degree of Freedom Parallel Manipulator Stiffness", *Proceedings of the 11th World Congress. In Mechanism & Machine Science, IFTOMM'2004*, Tianjin, China.
13. Przemieniecki, J.S., 1985, "Theory of Matrix Structural Analysis", *Dover Publications, Inc.*, New York.
14. Dong, W., Du, Z. and Sun, L., 2005, "Stiffness Influence Atlases of a Novel Flexure Hinge-Based Parallel Mechanism with Large Workspace", *Proceedings of IEEE ICRA: International Conference on Robotic and Automation*, Barcelona, Spain.
15. Shabana, A.A., 1989, "Dynamics of Multibody Systems", *John Wiley & Sons*.
16. Alves, A.F., 2006, "Elementos Finitos A Base da Tecnologia CAE", *Editora Érica*. (in Portuguese).

# Modelling of Robot's Motion by Use of Vibration of Internal Masses

Jatsun Sergey, Dyshenko Vyacheslav, Yatsun Andrey  
and Malchikov Andrey

**Abstract** In this article dynamics of original mobile micro-robots are developed. Vibration-driven robots use ideas of moving as periodical motion by vibration of internal masses or shape changing. Such kind of robots is especially useful for medical applications designed for the motion through rather narrow channels and realization stop-start regimes of the robot body with small length of step.

**Keywords** Mobile robot · Vibration · Motion · Internal mass · Control system

## Introduction

Vibration-driven mobile robots can move in various environments without wheels, caterpillars or legs. The propulsion of the robot is provided due to vibration of internal masses inside the robot and the interaction of the robot's body with the environment [1–7]. The robot can move without separation from the supporting surface or hop (Fig. 1). On this figure we use following indication: 1 – robot body; 2 – environment of robot; 3 – supporting surface; 4 – trajectory;  $F_z$ ,  $F_x$  – forces appearing as a result of motion of internal masses;  $R_z$ ,  $R_x$  – interaction forces between robot body and supporting surface;  $V$  – velocity of robot body.

Describing robots consist of a body with movable internal masses inside. The forces of interaction of the internal masses with the body and friction forces applied to the body by the environment enable the robot to move. Some aspects of the dynamics of motion of a body with an internal mass in a resisting medium and control of such a motion have been studied in different scientific papers. It has been indicated in that an asymmetry in the friction forces acting in the forward and backward directions is necessary for mobile vibration-driven robots. The most interesting idea for realization of high speed motion is idea of hopping robots.

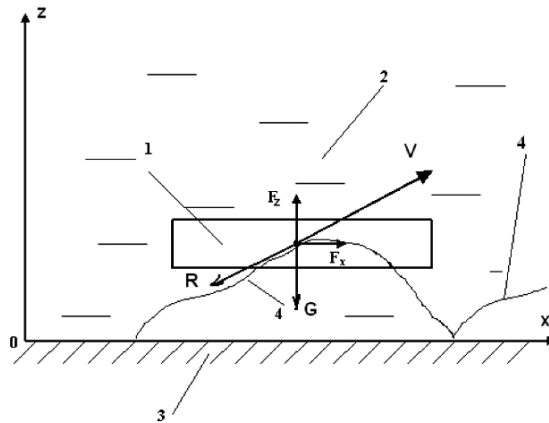
Describing robot consists of a body with movable internal masses inside. The forces of interaction of the internal masses with the body and friction forces applied

---

J. Sergey (✉)

Mechatrical Department, Kursk State Technical University, Kursk, Russia  
e-mail: jatsun@kursknet.ru

**Fig. 1** Hopping motion of the vibration-driven robot.  
 1 – internal movable masses,  
 2 – robot body, 3 – supporting surface, trajectory



to the body by the environment enable the robot to move. Some aspects of dynamics of motion of a body with an internal mass in a resisting medium and control of such a motion have been studied in different scientific papers [8, 9]. It has been indicated that an asymmetry in the friction forces acting in the forward and backward directions is necessary for mobile vibration-driven robots. The most interesting idea for realization of high speed motion is idea of hopping robots [10]. In considering case robot will jump if force appearing as a result of motion of internal masse  $\Phi_y$  periodically more than weight of the robot body  $G$ . For control of direction of locomotion of robot  $\Phi_x$  force may be used.

Control of direction and speed of motion is provided by the regulation of the amplitude and the phase shift of the horizontal and vertical vibration excitation forces  $\Phi_y, \Phi_x$ . In this case of the motion of robot is considered in two – dimensional space (2-D).

### Dynamic Model of Sliding Robot

The dynamical model of the vibration-driven robot with two internal masses, one of which moves in the horizontal direction and the other in the vertical direction, is schematically shown on Fig. 2 [8, 9].

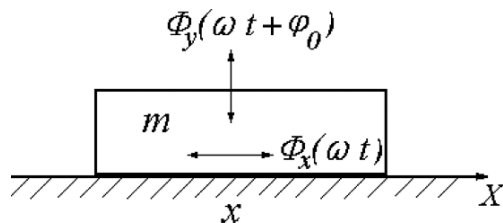


**Fig. 2** Dynamic model of the robot moving along a horizontal surface

This model is represented by a body of mass  $m$  moving along a horizontal line  $OX$  under the action of the forces  $\Phi_x$  and  $\Phi_y$  caused by the motion of the internal masses relative to the robot's body and the environment resistance force (not shown in the figure). Mass  $m$  is equal to the total mass of the robot's body and the internal masses,  $\Phi_x = -m_1\ddot{\xi}$ , where  $m_1$  and  $\ddot{\xi}$  are the magnitude of the horizontally moving mass and the acceleration of this mass relative to the body, and  $\Phi_y = m_2\ddot{\eta}$ , where  $m_2$  and  $\ddot{\eta}$  are the magnitude and acceleration of the vertically moving mass.

We assume the excitation horizontal force  $\Phi_x$  and  $\Phi_y$  to be harmonic and shifted in phase by the angle  $\varphi_0$  relative to one another,

$$\Phi_x = F_x \cdot \sin \omega t, \Phi_y = F_y \cdot \sin (\omega t + \varphi_0)$$

The purpose of this paper is to establish basic qualitative features of the dynamic behavior of vibration-driven robots and to investigate the possibilities for the control of such robots. To reach this goal, it could be helpful to have analytical relations, even for simplified cases. To do this end, we assume the friction forces to be small value, which is reflected in the small parameter  $\varepsilon$  occurring in the expressions for these forces.

### Numerical Simulations

The results of the numerical simulation of the motion of the robot are shown in Fig. 3. The simulation involved the solution of the differential Eqs. (1) and (3) subjected to the initial conditions  $x(0) = 0, \dot{x}(0) = 0,$  and  $u(0) = 0$ . The calculations were performed for  $m = 0.1, g = 9.81, F_x = 2, F_y = 0.9, \omega = 20$  and various values of the friction coefficients  $\varepsilon f$  and  $\varepsilon \mu$ . Here and in what follows, all quantities are measured in SI units.

Figure 4 plots the average velocity of the robot  $\langle V \rangle$  versus the phase shift angle  $\varphi_0$  for various  $\varepsilon f$  and  $\varepsilon \mu$ . Curves 1, 2, and 3 are correspond to  $(\varepsilon f = 0.05, \varepsilon \mu = 0.02), (\varepsilon f = 0.05, \varepsilon \mu = 0.2),$  and  $(\varepsilon f = 0.05, \varepsilon \mu = 0.02),$  respectively.

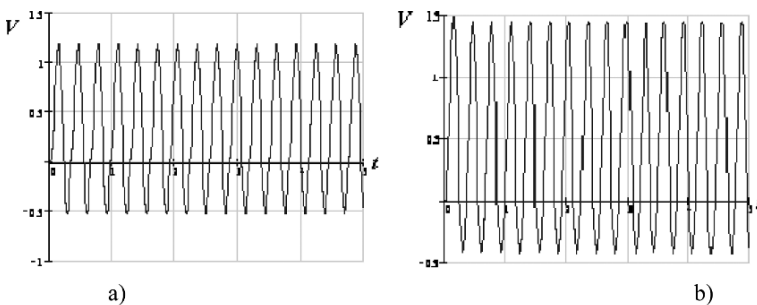
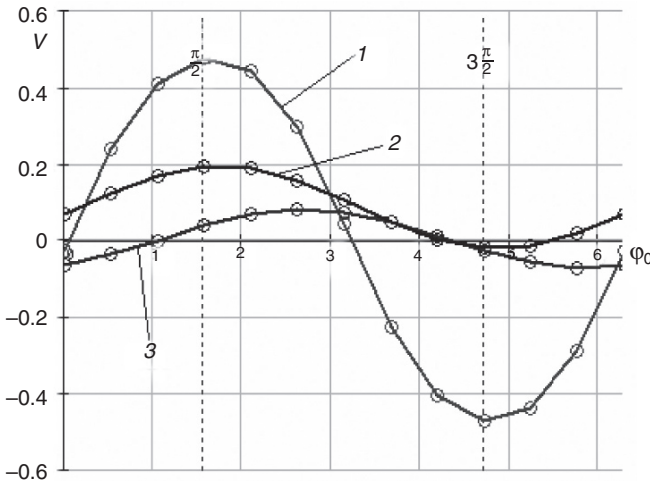


Fig. 3 Time history of the total velocity  $V$  at  $\varepsilon f = 0.5$  and  $\varepsilon \mu = 0.2$



**Fig. 4** Average velocity of the robot versus the phase shift angle  $\varphi_0$

Robots equipped with two-coordinate vibration exciters can move even in the absence of an asymmetry in the friction or vibration characteristics. The reverse in the direction of motion is provided by changing the phase difference between the vertical and horizontal excitation vibrations.

### Mathematical Model of Hopping Robot

On this stage we assume how the robot can separate from the supporting surface. If shows previous analysis robot body has maximum velocity for angle  $\varphi_0$  equal  $90^0$ . Therefore we will consider hopping robot for this case. It means that internal mass is rotating around central point of robot body. Calculating scheme of the hopping robot on the Fig. 5 is shown.

The motion of vibrating driven hopping robot can be described by system of differential equations. In a case when  $y > 0$ , pressure force of supporting surface equal zero ( $N = 0$ ) and motion can be described by following equations:

$$\begin{cases} m\ddot{x} = \Phi_x, \\ m\ddot{y} = \Phi_y - mg, \end{cases} \tag{1}$$

- where  $m$  – full mass of vibration – driven robot;
- $m = m_1 + m_k$ ,
- $m_1$  – mass of rotating body;
- $m_k$  – mass of robot body.

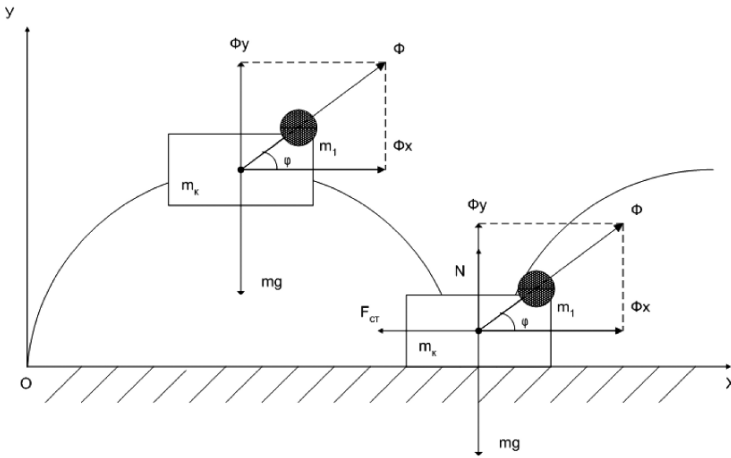


**Fig. 5** Calculating scheme of the hopping robot

Force  $\Phi$ , acting on the robot body, is determined as

$$\Phi = m_1 \omega^2 r, \tag{2}$$

where  $\omega$  – frequency of rotation of internal mass;  
 $r$  – distance between centers of masses.

Projections of force  $\Phi$  can be defined in a next form:

$$\begin{cases} \Phi_x = \Phi \cdot \cos \varphi, \\ \Phi_y = \Phi \cdot \sin \varphi, \end{cases} \tag{3}$$

$\varphi$  – angle between vector  $\Phi$  and axis  $Ox$ .

Angle  $\varphi$  is function of the time.

$$\varphi = \omega t + \psi, \tag{4}$$

$\psi$  – shift phase angle, defining by initial position of internal rotating mass.

When  $y = 0$ , the motion of considering system describing by differential equations:

$$\begin{cases} m\ddot{x} = \Phi_x + F_{TP}, \\ N = mg - \Phi_y, \end{cases}$$

Where  $F_{TP}$  – dry friction force:

$$F_{TP} = \begin{cases} -fN\text{sign}(x_2), & \text{if } \dot{x} \neq 0, \\ -F_0, & \text{if } \dot{x} = 0 \quad \text{and } |F_0| \leq fN, \\ -fN\text{sign}(F_0), & \text{if } \dot{x} = 0 \quad \text{and } |F_0| > fN \end{cases} \quad (5)$$

$f$  – friction coefficient;  $N$  – normal pressure force,  $F_0$  – is a sum of projections of external forces on axe OX, acting on the robot body.

Landing of the robot body depends on trajectory of flight and properties of supporting surface. We will consider simplest case, when each flight (separate motion from supporting surface) of robot body begins with such conditions:  $\dot{x} = 0, \dot{y} = 0$  and supporting surface if rigid body. Interaction of robot body and surface is described by friction force, see formula (5).

Separation of robot body from supporting surface is beginning when  $N = 0$ .

The results of numerical solution of Eqs. (1) and (5) are introduced on the figures in a form of time history of coordinates  $x$  and  $y$  and trajectories of central point of robot body. For solution of these equations special calculating algorithm was developed. Analysis of the results shows the shape of the trajectory of hopping motion depended on frequency and relation  $m1/r/m$ . Figures 6 and 7 illustrate completely different trajectories of robot body. Figure 8 introduce diagram of regimes of hopping motion of robot body. It is defined at least three zones providing the hopping motion. Zone 1 corresponds to trajectory introduced on the diagram on Fig. 7. Zone 2 accordingly – trajectory introduced on diagram Fig. 7.

Diagram on Fig. 8 shows dependence on maximal height of hopping robot dependence on frequency. We defined that height of hopping robot increase when frequency goes up. It is interesting that maximum average velocity corresponds to frequency equal about 260 1/s .

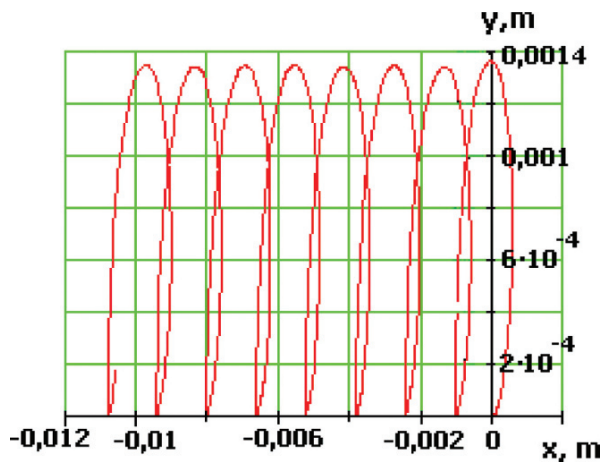


**Fig. 6** Trajectory of central point of robot body for one revolution of internal mass while one hop



**Fig. 7** Trajectory of central point of robot body for fore revolutions of internal mass while one hop

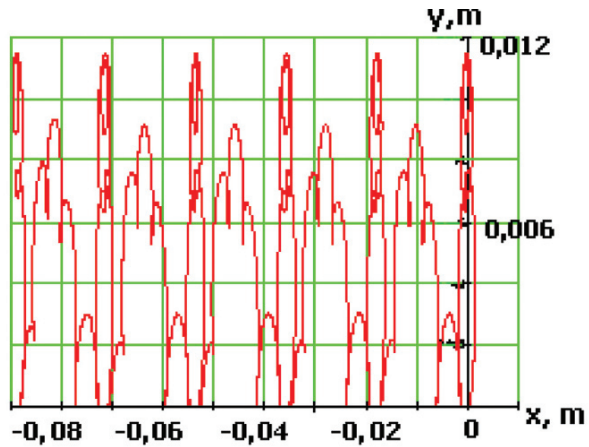
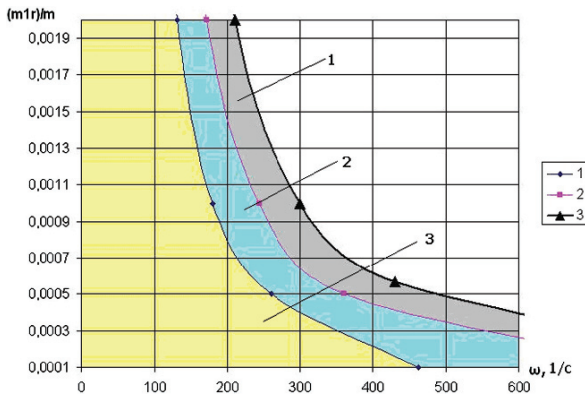


**Fig. 8** Diagram of different regimes of hopping of robot body dependence on frequency and relation  $m1/r/m$



## Conclusion

In this paper original schemes of mobile robots for sliding and hoping motion with rotating internal masses, were developed. Mathematical models of 1-D and 2-D vibration-driven robots were presented. By analytical method average velocity of robot body in different motion regimes were calculated. Numerical algorithm for calculation of dynamical parameters of motion allowed investigating periodical regimes of motion.

**Acknowledgments** This investigation is supported by RBRF Project No. 04-01-04002, No. 05-08-33382.

## References

1. Aoshima, S.; Tsujimura, T.; Yabuta, T.: A miniature mobile robot using piezo vibration for mobility in a thin tube. *Journal of Dynamic Systems, Measurement, and Control*, Vol. 115, 1993, pp. 270–278.
2. Yeh, R.; Hollar, S.; Pister, K.S.J.: Design of low-power silicon articulated microrobots. *Journal of Micromechatronics*, Vol. 1, Num. 3, 2001, pp. 191–203.
3. Gradetsky, V.G.; Knyazkov, M.M.; Kravchuk, L.N.; Solovtsov, V.N.: Microsensor control of motion of compact robots inside tubes (in Russian), *Mikrosistemnaya Tekhnika [Microsystem Engineering]*, No. 8, 2002, pp. 11–19.
4. Ma, J.; Lo, M.; Bao, Z.; Wang, A.: Micro peristaltic robot simulating earthworm and its control system. *Journal of Shanghai Jiaotong University*, Vol. 33, No. 7, 1999.
5. Bolotnik, N.N.; Chernousko, F.L.; Kostin, G.V.; Pfeiffer, F.: Regular motion of a tube-crawling robot in a curved tube. *Mechanics of Structures and Machines*, Vol. 30, No. 4, 2002, pp. 431–462.
6. Vartholomeos, P.; Papadopolos, E.: Dynamics, design and simulation of novel micro robotic platform employing vibration microactuators. *Journal of Dynamics System, Measurement and Control*, Vol. 128, March 2006, pp. 122–133.
7. Bolotnik, N.N.; Zeidis, I.M.; Zimmermann, K.; Yatsun, S.F.: Dynamics of controlled motion of vibration-driven systems. *Journal of Computer and Systems Science International*, Vol. 45, No. 5, 2006, pp. 834–840.
8. Bolotnik, N.N.; Zeidis, I.M.; Zimmermann, K.; Yatsun, S.F.: Mobile vibrating robots. *Proceedings of the 9th International Conference on climbing and welkin robots (CLAWAR2006)*. Brussels, Belgium. 2006. pp. 558–563.
9. Bolotnik, N.N.; Yatsun, S.F.; Chrepanov, A.A.: Automatically controlled vibration-driven. *Proceedings of International Conference on Mechatronics ICM2006*. Budapest, 2006. pp. 438–441
10. Kesner, S.; Plante, J.-S.; Dubovsky, S.: A hopping mobility concept for a rough terrain search and rescue robot. *Advances in Climbing and Walking Robots*.

# Mechanical Design of a 3-dof Parallel Robot Actuated by Smart Wires

Terenziano Raparelli, Pierluigi Beomonte Zobel and Francesco Durante

**Abstract** In this paper the design of the kinematics, the device elements and the drivers of a 3-dof (degrees of freedom) robot driven by smart wires is presented. The wires are made by a shape memory alloy (SMA) and have a diameter of 0.15 mm. This robot has a parallel structure including a fixed plate and a moving plate. The plates are linked together by 3 SMA wires and a mechanical spring is located in the central part. Possible applications are the control devices to orient a mirror, a sample under a microscope or to orient the head of a micro snake like robot.

**Keywords** Mechanical design · Kinematic design · Parallel robot · SMA actuators

## Introduction

Many technical applications, especially in the small dimensions, i.e. microtechnologies, ask for “non traditional” actuators that can be used successfully: micro grippers, tools for mini-invasive surgery, assembly of microsystems, micro-telemanipulation of biological samples, positioning and orienting of small pieces, etc. The Shape Memory Alloy (SMA) actuators have one basic characteristic that suggests their use in some of these devices: the high power/weight ratio [1] together with the possibility to manufacture the SMA in pieces of small dimensions. On the contrary the response rate is low, because of the natural cooling, but forced cooling can increase it. NITINOL (NICKel TITanium Naval Ordnance Laboratory) is a family of SMA, which contain a nearly equal mixture of nickel and titanium.

In this paper the mechanical design of a 3-dof (degrees of freedom) robot driven by SMA Nitinol actuators is presented. This robot has a parallel structure including a fixed plate and a moving plate. The plates are linked together by 3 SMA wires and a mechanical spring, that is located in the centre of the plates. Applications of this device include the positioning of a sample under a microscope, the orientation of a mirror or of the head of a micro snake like robot. The direct kinematics problem

---

T. Raparelli (✉)

Dipartimento di Meccanica, Politecnico di Torino, Corso Duca degli Abruzzi 24, Torino, Italy

can be found in [2], so in this paper the focus is on other aspects of the kinematics: graphical solutions, the inverse kinematics model and the working volume. Finally the design of the robot elements and of the SMA drives are included.

This paper is part of a research project that has the goal to design and manufacture a prototype of a 3-dof parallel robot driven by SMA wires [3]. The parallel structure was chosen for its rigidity, i.e. high position accuracy. Actually a position control system has been designed and manufactured, and the first experimental tests were carried out on a first prototype of the robot. The robot takes up a cylinder with a diameter of 100 mm and a height of 180 mm.

## The Mechanical Design: Kinematics

In the Fig. 1 the kinematic structure of the robot is shown. It has some difference from the 6-dof Stewart platform. In fact in the Stewart platform the six actuators are linked to the superior plate by six joints, while only three joints are used in this one. All the joints of the structure, of the upper plate, R, S and T, and of the lower plate, A, B, C, D, E and F, are spherical ones. Three SMA wires are used for the actuation: the wires ARB, CSD and ETF. A constraint stops the position of the middle point of the wires on the points R, S and T of the upper plate; therefore the three triangles ARB, CSD and ETF keep the shape of isosceles ones in any position of the robot. A complete solution of the direct kinematics problem for this mechanism can be found in [2], so in the following just some results are rewritten. The inverse kinematic model and the working volume is also defined and shown. From the kinematic point of view this scheme is equivalent to that shown in the Fig. 2a, where each actuator is replaced by a simple linear actuator linked to the upper plate by the real joint, and to the midpoint of the side of the lower plate by a virtual joint. In the middle of the upper plate, i.e. point O, a rod is fixed and the extremity of this one, i.e. point E, represents the end-effector for the following. The structure has 3 dof, i.e. the three coordinates of the point E. Each joint R, S and T can follow a circular trajectory, shown in dash line in the Fig. 2a, where the centre and radius are respectively the point  $O_r$  and the length  $l_r$ ,  $O_s$  and  $l_s$ ,  $O_t$  and  $l_t$ . These circular trajectories lie respectively in the planes orthogonal to the sides of the lower plate AB, CD and EF. The three points R, S and T belong to the plane of the upper plate. This architecture, as previously described, permits the positioning

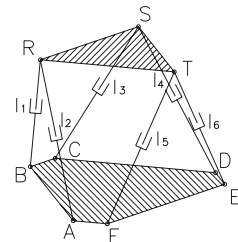


**Fig. 1** Kinematic structure of the robot

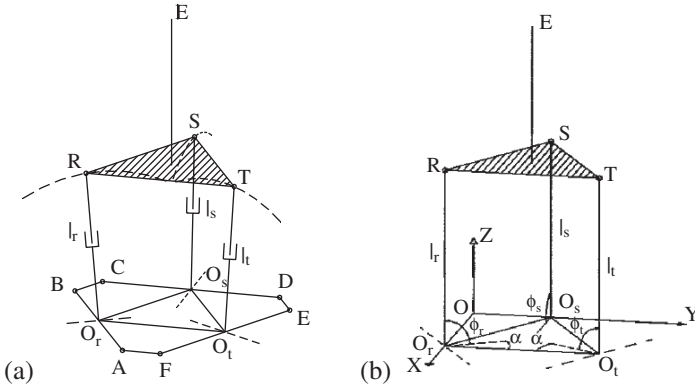


**Fig. 2** Equivalent kinematic mechanism

of the end-effector in the working volume. The direct kinematic model allows the calculation of the absolute coordinate of the end-effector, if the displacement of the SMA drivers is known. This model was used to calculate the working volume. In the following the two steps that describe this model are reported. The first step regards the definition of the absolute coordinates of the points of the upper plate R, S and T as a function of the length of the SMA drivers ( $l_r, l_s, l_t$ ). The second one involves the definition of the absolute coordinates of the end-effector ( $x_E, y_E, z_E$ ) versus the absolute coordinates of the points R, S and T. In the Fig. 2b the location of the absolute frame is shown.

The geometrical conditions of the points R, S and T are described as follows:

$$\begin{aligned}
 [x_r - x_s]^2 + [y_r - y_s]^2 + [z_r - z_s]^2 &= b_1^2 \\
 [x_s - x_t]^2 + [y_s - y_t]^2 + [z_s - z_t]^2 &= b_2^2 \\
 [x_t - x_r]^2 + [y_t - y_r]^2 + [z_t - z_r]^2 &= b_3^2
 \end{aligned}
 \tag{1}$$

that states that the sides of the upper plate ( $RS = b_1, ST = b_2, TR = b_3$ ) are set for a given geometry. The absolute coordinates of the three points R, S and T can be also explained as a function of the angles  $\Phi_r, \Phi_s, \Phi_t$  and  $\alpha$ , in Fig. 2b, as is shown in the following:

$$\begin{cases} x_r = x_{O_r} - l_r \cdot \cos(\phi_r) \cdot \sin(30^\circ) \\ y_r = l_r \cdot \cos(\phi_r) \cdot \cos(30^\circ) \\ z_r = l_r \cdot \sin(\phi_r) \end{cases}
 \begin{cases} x_s = l_s \cdot \cos(\phi_s) \\ y_s = y_{O_s} \\ z_s = l_s \cdot \sin(\phi_s) \end{cases}
 \tag{2}$$

$$\begin{cases} x_t = x_{O_t} - l_t \cdot \cos(\phi_t) \cdot \sin(30^\circ) \\ y_t = y_{O_t} - l_t \cdot \cos(\phi_t) \cdot \cos(30^\circ) \\ z_t = l_t \cdot \sin(\phi_t) \end{cases}
 \text{ where}$$

$$\begin{cases} x_{O_r} = x_{O_t} = a \frac{\sqrt{3}}{2} \\ y_{O_s} = \frac{a}{2} \\ y_{O_t} = a \end{cases}$$

In our case  $\alpha$  is  $30^\circ$  because the triangle  $O_r O_s O_t$  is equilateral.

After some mathematical steps [2] it is possible to arrive at the equation in the unknown  $x_r$ :

$$c_1 \cdot x_r^{16} + c_3 \cdot x_r^{14} + c_5 \cdot x_r^{12} + c_7 \cdot x_r^{10} + c_9 \cdot x_r^8 + c_{11} \cdot x_r^6 + c_{13} \cdot x_r^4 + c_{15} \cdot x_r^2 + c_{17} = 0 \quad (3)$$

where the expressions of the other coefficients  $c_i$  are omitted because of their length.

This equation is in the 16th order of  $x_r$  and lead to 16 solutions. Because of the power is always an even number, the solution is attained by solving an 8th degree equation. After knowing the quantities  $x_r$ , it is convenient to calculate the angle  $\Phi_r$  by means of the  $x_r = \tan \Phi_r/2$ . Then it is possible to obtain [2] similar equations for  $x_s$  and  $x_t$ . The absolute coordinates of the points R, S and T are obtained using the equations' system (2).

Finally a criterion has to be used to choose the right solution among these 16 ones. The criterion is based on the following geometrical considerations. The total solutions are 16, 8 of these are symmetrical with respect to the XY plane. Some of these solutions could be an imaginary number; in this case they cannot be reached. In the case of real solutions 7 of these ones are not practically possible because of the constraints of the structure. In the Fig. 3 the 8 solutions are shown in the case of all real solutions. This figure reveals the right solution, named as A. In fact in the other positions the upper plate should be positioned upside down partially or completely, and it is not possible to reach these positions without dismantling the upper plate. It should be clear that all the 8 positions are obtained for the same length of the three actuators. The criterion to select the right solution A is based on the maximum value of the summation of the z coordinate of the three points R, S and T ( $z_r, z_s, z_t$ ).

The second step of the direct kinematic model involves the definition of the absolute coordinates of the end-effector ( $x_E, y_E, z_E$ ) versus the absolute coordinates of the points R, S and T. The position of the end-effector, point E in the Fig. 2, can be calculated considering a 3 equations' system represented by three spheres for the points E and respectively R, S and T, having as radius respectively  $l_{e1}, l_{e2}$  and  $l_{e3}$ :

$$\begin{aligned} [x_r - x_e]^2 + [y_r - y_e]^2 + [z_r - z_e]^2 &= l_{e1}^2 \\ [x_s - x_e]^2 + [y_s - y_e]^2 + [z_s - z_e]^2 &= l_{e2}^2 \\ [x_t - x_e]^2 + [y_t - y_e]^2 + [z_t - z_e]^2 &= l_{e3}^2 \end{aligned} \quad (4)$$

where  $l_{e1}, l_{e2}$  and  $l_{e3}$  are equal because the point O, Fig. 2a, is the centroid of the equilateral triangle RST. In this case the 3 spheres have 2 intersection's points, one above and the other one under the triangle RST. The criterion to select the right position is that of the maximum value of  $z_e$ , i.e. above the triangle RST.

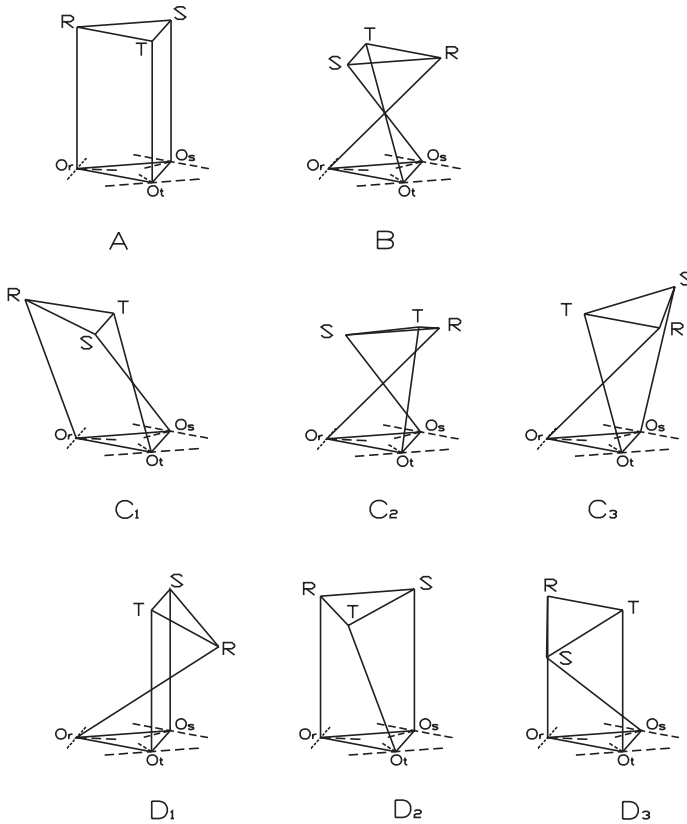


Fig. 3 Solutions of the direct kinematic model

In the following the inverse kinematic model is described. This model is necessary to know the displacement of the SMA drivers to reach a given position of the end-effector. Considering the upper plate RST as the end-effector, the solution is quite simple. In fact this 3 equations' system in the 3 unknown  $l_r$ ,  $l_s$  and  $l_t$  gives us the solution:

$$\begin{aligned}
 [x_r - x_{Or}]^2 + [y_r - y_{Or}]^2 + [z_r - z_{Or}]^2 &= l_r^2 \\
 [x_s - x_{Os}]^2 + [y_s - y_{Os}]^2 + [z_s - z_{Os}]^2 &= l_s^2 \\
 [x_t - x_{Ot}]^2 + [y_t - y_{Ot}]^2 + [z_t - z_{Ot}]^2 &= l_t^2
 \end{aligned}
 \tag{5}$$

In the 6-dof Stewart platform the calculation of the coordinates of the joints of the upper plate is quite simple because one can decide by itself the position and the orientation of the upper plate, by fixing, for example, the three coordinates of one point and three angles. On the contrary in this structure to state the three coordinates of one point, means to fix, at the same time, the three angles too, that are unknown.

So the calculation of the coordinates of the points R, S and T is possible, for a given position of E, by solving a 9 equations' mathematical system with 9 unknowns. The equations' system is formed by the Eqs.( 1) together with the (4)s and the three following ones, which states that the points R, S, T belong to the vertical planes orthogonal respectively to the directions AB, CD and EF, through  $O_r$ ,  $O_s$  and  $O_t$ :

$$\frac{O O_r - x_r}{y_r} = \tan \alpha; \frac{O O_r - x_t}{O_r O_t - y_t} = \tan \alpha; y_s = \frac{O_r O_t}{2}$$

The unknowns of this equations' system are the coordinates of the points R, S and T and it can be solved numerically.

By using the direct kinematic model the working volume of this robot has been numerically defined. The input of this model is the length of the 3 actuators, while the output is the end-effector position. By changing the length of the 3 actuators opportunely, to cover all the displacement field, the external surface of the working volume has been obtained. The Fig. 4 shows the top and lateral view of the working volume. It has a shape of a convex lens. Its thickness, Fig. 4b, decreases from the centre, 2 mm, to the border, 0 mm, and the lateral perimeter, Fig. 4a, has the shape of an hexagon. The side of the hexagon is about 7 mm.

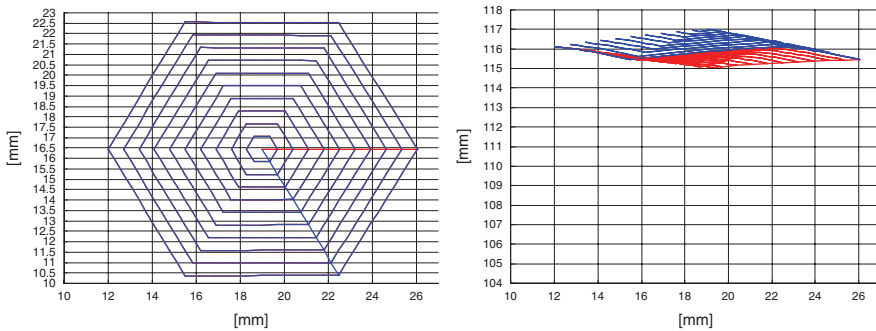


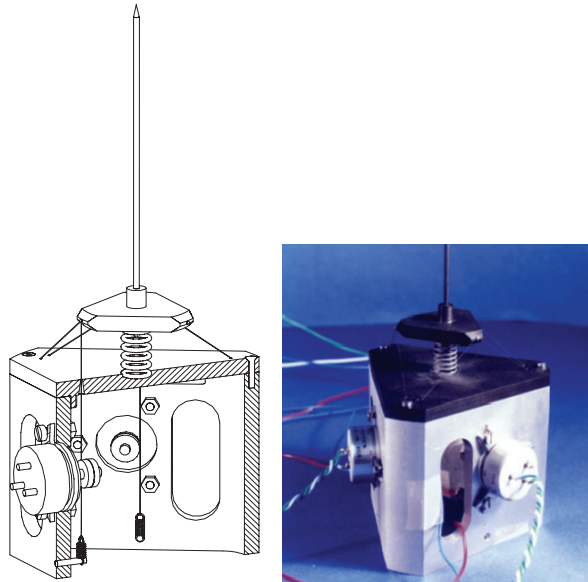
Fig. 4 Top (left) and lateral (right) view of the working volume of the robot

### The Mechanical Design: Robot Elements and SMA Drivers

The Fig. 5 shows a section view and a photo of the prototype. The kinematic structure previously described was carried out positioning the SMA wires in the triangle disposition of the Fig. 1. The wires are fed by 3 independent electrical circuits at 6 Vdc, managed by the control system. When the SMA's temperature goes up the wire has a phase transformation from martensite to austenite, reducing its length of about 4%. The lower plate was fixed at a base frame, Fig. 5. It is used as base of the robot and case to host the displacement transducers and the springs for the



**Fig. 5** Section view (*left*) and photo (*right*) of the prototype



tensioning of the SMA wires. The displacement transducers are rotational conductive plastic potentiometers.

In Fig. 1  $l_1$  and  $l_2$  represent two pieces of a continuous SMA wire and the same for, respectively,  $l_3$  and  $l_4$ ,  $l_5$  and  $l_6$ , so that 3 wires drive the robot. The SMA drivers used in this robot are commercial nickel-titanium alloy, named Nitinol, in wire form, manufactured by Mondo-tronic inc.: Flexinol 150 HT. The main technical properties of the SMA wire [5], are the following: *wire diameter* is 150  $\mu\text{m}$ ; *maximum recovery force*, the largest force that the wire exerts when heated, is 10.4 N; *recommended recovery force*, suggested value of force to preserve the wire, is 3.2 N; *recommended deformation force*, force value to be applied to extend the cooled wire, is 0.61 N; *maximum and recommended deformation ratio*, respectively the largest strain to expect from the wire and the recommended one for millions of cycles life, are 8% and 3-5%. Finally the *activation start and finish temperature*, from one side, and the *relaxation start and finish temperature*, from the other side, represent the start and finish temperature of the transformation from martensite to austenite phase and of the reverse transformation, respectively: 371-361 K for activation and 335-345 K for relaxation.

For the design of the prototype it was considered a displacement of the end-effector of a few millimeters, 2 mm as maximum z displacement, and a force between 10 and 30 mN. The upper and lower triangles were made in PVC in the form of thin plates. The lower plate was fixed at a base frame in aluminium. It is used as base of the robot and case to host the displacement transducers and the spring for the tensioning of the SMA wires. The mechanical spring has a rest length of 25 mm and a stiffness value of 1.25 N/mm. A design procedure has been implemented to calculate the main geometrical dimensions of the robot including the SMA wires

(length and orientation). The main target was to maximise the working volume (having  $z_{\max} = 2$  mm) and to minimise the global dimension of the robot. As a result of this step it was obtained a side of the lower plate of 66 mm, a rest distance between the two plates of 17 mm and a side of the upper plate of 33 mm. The 3 wires transmit a global force on the upper plate of about 10 N. To fix the end part of the SMA wire at the base plate a spherical plumb fastener is used. To link the upper plate at the displacement transducers three nylon cables are used. The cable turns over a small pulley, fixed to the shaft of the transducer and with a diameter of 9 mm, and finally it is linked to a mechanical spring, fixed to the base frame, to tension the cable. A position control system, PC based, was defined to reach and hold a specified position of the end-effector. During the motion it is necessary to measure the length of each actuator, to calculate the end-effector position by the kinematic model for the feedback loop, and send the heating current to the SMA wires.

## Conclusion

This paper presents the mechanical design of a 3-dof robot with a parallel structure driven by three SMA wires. The kinematic models, the working volume and the design of the robot elements and the SMA drives are described. Some preliminary experimental tests were conducted on the prototype to validate the design. The results states the feasibility of this robot. Some notes arise. The assembly of the robot is critical and needs much attention. Further work involves the use of a measurement system for the position of the end-effector to complete the experimental validation of the prototype.

## References

1. Funakubo H., Shape memory alloys, Gordon and Breach Science Publisher, London, 1984.
2. Nanua P., Waldron K. J., Murthy V., Direct kinematic solution of a Stewart platform, IEEE Trans. Robot. Automat., vol. 6, pp. 438–444, 1990.
3. Raparelli T., Beomonte Zobel P., Durante F., A 3-dof robot driven by shape memory alloy actuators, Proc. of the 2001 IEEE Int. Conf. on Intelligent Engineering Systems, Helsinki, Finland, pp. 301–306, Sept 16–18, 2001.
4. Gilbertson R. G., Muscle wires project book, Mondo-tronics, Inc., San Anselmo, CA, pp. 2.1–2.8, 1994.
5. Brailovski V., Trochu F., Leboeuf A., Design of a shape memory linear actuators, Proc. 2st Int. Conf. On Shape Memory and Superelastic Technologies, California, USA, 2–6 March 1997.

# A Multicriteria Approach for Optimal Trajectories in Dynamic Parameter Identification of Parallel Robots

Xabier Iriarte, Miguel Díaz-Rodríguez and Vicente Mata

**Abstract** When dealing with the development of accurate robot dynamic models, the estimation and validation of the dynamic parameters through experiments becomes necessary. One of the most important objectives to achieve in the design of the experiment, aimed at identification, is to properly excite the system so that the unknown parameters can be accurately estimated. It is customary to find proper excitations optimizing the observation matrix of the model w.r.t. a certain criterion. In this paper the suitability of some trajectory optimization criteria are evaluated for parallel robots. Moreover, a multicriteria algorithm is proposed in order to reduce the deficiencies derived from the single criterion optimization.

**Keywords** Robot · Dynamics · Identification · Dynamic parameters · Multicriteria optimization

## Introduction

The need for increasing the speed of robotic systems, without loss of accuracy at the end effector robot positioning, requires the implementation of model-based control algorithms, see for instance [1]. The accuracy of the models depends on the values assigned to the parameters of the model. Geometrical parameters are usually well known through CAD models or direct measuring. However, the dynamic parameters (inertial and frictional) are not likely to be estimated through direct measuring or CAD models. Disassembling the robot is not practical and frictional behaviour depends on the operational conditions. These drawbacks make the experimental dynamic parameter estimation necessary in order to obtain accurate predictions of the system behaviour.

A customary method for performing this task is through a linear model that relates the instantaneous movement of the robot with the forces exerted by the

---

X. Iriarte (✉)

Departamento de Ingeniería Mecánica, Energética y de Materiales,  
Universidad Pública de Navarra, 31006, Pamplona, España  
e-mail: xabier.iriarte@unavarra.es

actuators. The model is linear w.r.t. the dynamic parameter, an observation matrix is related to the external forces by means of the dynamic parameters. The error transmissibility from the forces measurements to the parameters calculation depends on this matrix. Hence, in order to improve the estimation, the trajectories can be designed by a certain optimality criterion regarding the observation matrix.

Armstrong [2] introduced the concept of “exciting trajectories”. In his paper such trajectories were found by a nonlinear optimization problem in which the smallest singular value of the observation matrix was used as a criterion for designing the robot motion. After that, several papers have focused on the design of exciting trajectories [2–11]. The most extended method considers trajectory points guided by a certain analytical function. Hence, finding the optimal trajectory consist of determining the parameters, of this analytical function, that satisfy any criterion.

The objective of this paper is to evaluate the optimality criteria that have been proposed in the literature, search the influence that optimizing with a certain criterion has on the solution obtained in the parameter identification of parallel robots. In addition it is proposed and evaluated an algorithm based on multicriteria optimization.

In the following section the development of the dynamic model of the robot is briefly outlined; next the main procedures and different optimization criteria are shown for obtaining optimal exciting trajectories. Single criterion results are also shown here. *Multicriteria Trajectory Optimization* deals with the development and analysis of the optimal trajectories obtained by multicriteria optimization. The experimental procedures are explained in *Experiments* while the main results are shown in *Identification and Validation Results*. The main conclusions are drawn in *Conclusions*.

## Robot Modeling

Assuming a linear friction model and starting from the Gibbs-Appell equations, the dynamic model for a constrained robotic system can be written in its linear form w.r.t. the dynamic parameters, as follows [12–13],

$$K \left( \vec{q}, \dot{\vec{q}}, \ddot{\vec{q}} \right) \times \vec{\Phi} = \vec{\tau} \quad (1)$$

where  $\vec{\tau}$  is the vector of generalized forces and  $\vec{\Phi}$  is a vector of the regrouped inertia parameters.  $K$  can be denoted as a single configuration observation matrix. This matrix depends on the generalized kinematic variables (the Denavit-Hartenberg modified convention has been considered in order to model the system). The vector of dynamic parameters  $\vec{\Phi}$  contains the mass  $m_i$  of each body, and first mass moments  $[m x_i \ m y_i \ m z_i]^T$  and elements of the inertia tensor of body ( $i$ )  $[I_{xx_i} \ I_{xy_i} \ I_{xz_i} \ I_{yy_i} \ I_{yz_i} \ I_{zz_i}]^T$ , both w.r.t. the body joint coordinated system.

Evaluating the Eq. (1) for different configurations and putting them all together, the system model for parameter identification can be written in compact form as:

$$W \left( \bar{q}, \dot{\bar{q}}, \ddot{\bar{q}} \right) \cdot \vec{\Phi} = \vec{\tau} \tag{2}$$

where  $W$  is called the observation matrix.

The model expressed by Eq. (2) does not describe independently the dynamic behaviour of the mechanical system. In fact, some inertial parameters do not affect the dynamics of the robot and others have a relative effect on the external generalized forces. Therefore, the identifiable parameter space has to be found (the so-called base parameters). This can be performed by singular value decomposition of the observation matrix as propose in [14]. By doing so, the overdetermined linear system can be easily solved using the Least Squares Method (LSM) or Weight Least Squares (WLS).

In this paper, a 3-RPS parallel robot was used for experiments. The robot was built in the Polytechnic University of Valencia. After geometry and symmetry simplifications, an 18 parameter model, listed in Table 1, was obtained involving the following inertial and frictional parameters.

**Table 1** Dynamic parameters of the 3-RPS parallel robots

No.	Physical meaning	No.	Physical meaning
1	$M_y(1)$	10	$F_c(1)$
2	$I_{zz}(1)+I_{yy}(2)$	11	$F_v(1)$
3	$mz(2)$	12	$F_c(2)$
4	$I_{xx}(3)-0.3952my(3)$	13	$F_v(2)$
5	$I_{yy}(3)+0.3952my(3)-0.2082(m(3)+m(2))$	14	$F_c(3)$
6	$I_{zz}(3)-0.2082(m(3)+m(2))$	15	$F_v(3)$
7	$mx(3)+0.5774my(3)-0.4563(m(3)+m(2))$	16	$J_s(1)+J_f(1)$
8	$m(5)-2.531my(3)+m(3)+m(2)$	17	$J_s(2)+J_f(2)$
9	$m(7)+2.531my(3)$	18	$J_s(3)+J_f(3)$

## Optimal Trajectories

The problem of designing optimal trajectories can be established as,

$$\begin{aligned} \text{minimize} \quad & f \left( W(\bar{q}, \dot{\bar{q}}, \ddot{\bar{q}}) \right) \quad \text{subject to} \\ & g \left( \bar{q}, \dot{\bar{q}}, \ddot{\bar{q}} \right) \leq 0 \end{aligned} \tag{3}$$

where  $g \left( \bar{q}, \dot{\bar{q}}, \ddot{\bar{q}} \right)$  are constrain functions related to the limitations of the actuators and the set of all achievable poses in the workspace of the robot.

The information matrix ( $W'GW$ ) plays an important role in the resolution of (2) with the LSM. Based on this matrix, Amstrong [2] proposed the design of the so-called “exciting trajectories” by maximizing the minimum singular value of the information matrix. On the other hand, the condition number of the  $W$  matrix is another trajectory optimization criterion that tries to estimate all the parameters with the same absolute accuracy. This is one of the most extended approaches and differences among authors are due to different trajectory parameterization methods.

Nonetheless, condition number is not the only criterion for optimizing the trajectory for the robot. The *D-optimality* criterion used in statistical frameworks makes use of the following maximum likelihood function:

$$f(\ddot{q}, \dot{q}, \dot{q}) = -\log(\det(W^T G^{-1} W)) \quad (4)$$

In order to obtain optimal exciting trajectories for a 3-RPS parallel robot, several optimizations were run from random seeds for each criteria. The parameterization of the trajectories was based on a finite Fourier series method, as mentioned in [8]. Table 2 shows the results obtained for 4 trajectories optimized with each criterion. The evaluation of the criterion not used for optimization is shown in brackets. Limitations to the movement of the parallel robot were introduced in the optimization algorithm as: upper and lower bound limitations to the stroke and velocities of the linear actuators; and upper bound limitations on the aperture of the spherical joints that also served to avoid singularity regions of the manipulator. The optimization process was carried out in MatLab using the nonlinear constrained optimization routine (“fmincon”).

Analysing the table, it was found that it was not possible to have proper values of both criteria if the optimization procedure was based on only one of them. Therefore, in order to overcome this inconvenient, a combined method is presented in this paper. This time, rather than using a weighted objective function as in [2], a multicriteria procedure based on goal programming [15] was proposed.

**Table 2** Values of the objective functions of the exciting trajectories

Cond( $W$ )	$-\log(\det(W^T G^{-1} W))$
595 (−93)	(1285) −110
555 (−98)	(1553) −108
577 (−94)	(1504) −107
806 (−86)	(1802) −104

## Multicriteria Trajectory Optimization

Instead of using any of the weighted objective function methods available for multicriteria programming, the goal attainment method has been used in this application because in the formers the weights do not necessarily correspond to the relative importance of the objectives. The goal attainment problem can be expressed as:

$$\begin{aligned} \text{minimize } \gamma \quad \text{such that } & F_i \left( W(\bar{q}, \dot{\bar{q}}, \ddot{\bar{q}}) \right) - \omega_i \gamma \leq F_i^* \quad i = 1 \dots n \\ & g(\bar{q}, \dot{\bar{q}}, \ddot{\bar{q}}) \leq 0 \end{aligned} \tag{5}$$

where  $F_i$  are the objectives to be fulfilled in the optimization problem. The objectives are fulfilled when their values are lower than certain goal  $F_i^*$ . The terms  $\omega_i$  introduce an element of slackness into the problem, which enforces the goals to be rigidly met. The algorithm used in this application was the “fgoalattain” provided by MatLab.

The goal values are set by performing an optimization for each of the criteria available, and taking the resultant optimization function value. This way, the goals consist of the best achievable values for each criterion. If the algorithm could not find a solution, the goals should be relaxed.

Table 3 shows the results for 4 different trajectories obtained by goal attainment method. It can be seen that for the goal values  $\text{cond}(W) < 650$  and  $-\log(\det(W^T G^{-1} W)) < -105$ , the results achieve function values comparable with the ones obtained by single criterion optimizations.

Having found some optimal trajectories, the following section shows the results for a parameter identification applied to an actual 7 3-RPS robot.

**Table 3** Objective function values for the multicriteria optimization

Trajectory	Cond(W)	$-\log(\det(W^T G^{-1} W))$
1	561	-107
2	613	-105
3	605	-106
4	590	-110

## Experiments

The experiments were carried out as follows:

- Experiment design: several optimizations were performed for each of the two criteria and the multicriteria approach.
- Data collection: a digital PID controller was used to impose the trajectories at the frequency also used for measuring. The position of the actuators was measured with incremental encoders while its time derivatives were calculated through Fourier series analytical differentiation. Trajectories were repeated several times and passed through a Butterworth second order low pass filter.
- Identification: parameters values were calculated by means of the WLS, with weights as the variances of the measured forces.
- Validation: 12 trajectories that had not been used for identification were employed for validation. The accuracy in prediction was verified in terms of the relative absolute error ( $\epsilon_{RA}$ ) of the estimated forces.

## Identification and Validation Results

If the forces estimation error is supposed to be normally distributed, WLS provides the possibility to calculate the standard deviations of the parameter estimates. According to the high standard deviation of some of the parameters, the model was reduced to only have the 12 parameters (7–18) that are provided in Table 1. The identified values of these parameters and their standard deviations are listed in Table 4.

This table shows that the *D-optimality* provides the lowest relative standard deviations, while the multicriteria method captures half of the properties of each criterion leading to results, in terms of relative standard deviation, between the obtained through both criteria.

The validation of the parameters required trajectories not used for the identification. The selected trajectories were obtained from the first steps of the optimizations and are representative of a real working trajectory that the robot could accomplish.

Validation of the identified parameters were the average and standard deviation of the  $\epsilon_{RA}$ , which were listed in Table 5. The 3 optimization procedures gave similar results while the lowest  $\epsilon_{RA}$  were achieved for the condition number procedure. On the other hand the multicriteria procedure shows a lower deviation for the  $\epsilon_{RA}$ .

**Table 4** Identified parameter of the 3-RPS parallel robots

Parameter	Cond(W)		$-\log(\det(W^T G^{-1} W))$		Multicriteria	
1	-2.31	6.475	-2.70	4.73	-3.06	4.801
2	11.18	4.086	11.97	3.188	12.77	3.413
3	6.102	2.517	6.05	2.185	6.68	2.288
4	3483.28	3.406	3898.41	2.195	4272.38	2.191
5	152.33	6.332	129.27	4.04	96.84	7.072
6	2099.86	5.083	2315.87	3.637	2184.92	4.9
7	119.94	7.001	114.26	4.355	125.86	6.297
8	3057.99	1.872	2250.87	2.382	3096.19	2.066
9	202.21	1.849	258.21	1.477	197.29	2.015
10	493.6	2.037	502.03	1.508	492.52	1.225
11	453.14	3.028	463.12	2.213	439.64	3.313
12	540.68	0.758	540.34	1.179	562.30	0.827
mean		3.70		2.76		3.36

**Table 5** Average and deviation of  $\epsilon_{RA}$  for the 12 validation trajectories

	Cond(W)	Multicriteria	$-\log(\det(W^T G^{-1} W))$
Average ( $\epsilon_{RA}$ )	12.23	12.25	12.40
Deviation ( $\epsilon_{RA}$ )	1.09	0.99	1.16



## Conclusions

Finding optimal trajectories according to a single criterion has shown to worsen the objective values of other criteria. Therefore, a multicriteria optimization procedure has been proposed based on the goal attainment method to overcome this inconvenience. The results in terms of the  $\varepsilon_{RA}$  were similar for the three criteria; however, in terms of the deviation of  $\varepsilon_{RA}$ , the multicriteria approach gave the lowest errors, showing that this approach can improve the results obtained for the dynamic parameter identification of parallel robots.

## References

1. J. Swevers, W. Verdonck, and J. D. Schutter, Dynamic Model Identification for Industrial Robots, *IEEE Control Systems Magazine*, 27, 58–71 (2007).
2. B. Armstrong, On Finding Exciting Trajectories for Identification Experiments Involving Systems with Nonlinear Dynamics, *International Journal of Robotics Research*, 8, 28–48 (1989).
3. M. Gautier, Optimal motion planning for robot's inertial parameters identification, in 31st IEEE Conference on Decision and Control, Tucson, AZ, USA, pp.70–73 (1992).
4. M. Gautier and W. Khalil, Exciting Trajectories for the Identification of Base Inertial Parameters of Robots, *The International Journal of Robotics Research*, 11, 362–375 (1992).
5. R. Lucyshyn and J. Angeles, A symbolic approach to determining exciting trajectories for identification of manipulator dynamic models, in IECON 1993, International Conference on Industrial Electronics, Control, and Instrumentation., Maui, HI, USA, pp. 1684–1689 (1993).
6. J. Schaeffers, S. J. Xu, and M. Darouach, A Parameter Identification Approach Using Optimal Exciting Trajectories for a Class of Industrial Robots, *Journal of Intelligent and Robotic Systems*, 15, 25–32 (1996).
7. E. Lizama and D. Surdilovic, Designing G-optimal experiments for robot dynamics identification, in IEEE International Conference on Robotics and Automation, Minneapolis, MN, USA, pp. 311–316 (1996).
8. J. Swevers, C. Ganseman, J. DeSchutter, and H. VanBrussel, Experimental Robot Identification Using Optimised Periodic Trajectories, *Mechanical Systems and Signal Processing*, 10, 561–577 (1996).
9. J. Swevers, C. Ganseman, D. B. Tukul, J. DeSchutter, and H. VanBrussel, Optimal Robot Excitation and Identification, *IEEE Transactions on Robotics and Automation*, 13, 730–740 (1997).
10. J. Swevers, C. Ganseman, J. DeSchutter, and H. VanBrussel, Generation of Periodic Trajectories for Optimal Robot Excitation, *Journal of Manufacturing Science and Engineering-Transactions of the Asme*, 119, 611–615 (1997).
11. G. Calafiore and M. Indri, Experiment design for robot dynamic calibration, in IEEE International Conference on Robotics and Automation, Leuven, Belgium, pp. 3303–3309 (1998).
12. V. Mata, F. Benimeli, N. Farhat, and A. Valera, Dynamic Parameter Identification in Industrial Robots Considering Physical Feasibility, *Journal of Advanced Robotics*, 19, 101–120 (2005).
13. N. Farhat, V. Mata, A. Page, and F. Valero, Identification of Dynamic Parameters of a 3-DOF RPS Parallel Manipulator, *Mechanism and Machine Theory*, 43, 1 (2008).
14. M. Gautier, Numerical Calculation of the Base Inertial Parameters of Robots, *Journal of Robotic Systems*, 8, 485–506 (1991).
15. F. Gembicki, and Y. Haimes, Approach to Performance and Sensitivity Multiobjective Optimization: The Goal Attainment Method, *IEEE Transactions on Automatic Control*, 20, 769 (1975).

# Reinforcement Neural Network for the Stabilization of a Furuta Pendulum

Benedetto Allotta, Luca Pugi and Fabio Bartolini

**Abstract** The Furuta pendulum is a well known mechatronic system in which the goal of the control system is to stabilize the pendulum in the upright position. The control strategy is split into two different stages: the “swing-up,” aimed at rising the pendulum near the upright position and the “stabilization” that stabilises the upright equilibrium point by actuating the horizontal arm. The researchers of the University of Florence have realized two prototypes of the Furuta pendulum in order to enlarge the didactical offer of the Mechatronics Laboratory and the Complex Dynamics and Control Systems laboratory and to supply a test bed for control techniques. The features of the prototype are described in this paper as well as the application of a Reinforcement Neural Network to the stabilization phase.

**Keywords** Furuta pendulum · Control system · Reinforcement neural networks

## Introduction: The Furuta Pendulum

The Furuta Pendulum (FP in the following), whose name derives from its inventor - Professor Katsuhisa Furuta [1] -, is a direct evolution of the inverse pendulum. The FP overcomes the inverse pendulum problems related to the limited stroke of the trolley. The kinematics of a FP consists of three links (a fixed frame plus two moving rigid bodies) connected by two rotational joints. The first moving link is a horizontal arm rotating around an actuated vertical joint. The second moving link is a pendulum connected to the horizontal link by an unactuated rotational joint, as visible in Fig. 1.

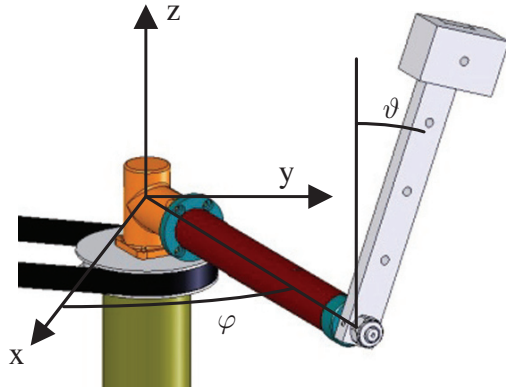
The FP has 2 DOF, so the configuration is described by  $\varphi$  for the first (vertical) joint and by  $\vartheta$  for the second (horizontal) joint.

---

B. Allotta (✉)

Sezione di Meccanica Applicata alle Macchine, Dipartimento di Energetica “Sergio Stecco”,  
Università di Firenze, Via Santa Marta 3, 50100 Firenze (FI), Italy  
e-mail: ben@mapp1.de.unifi.it

**Fig. 1** Kinematic scheme of a Furuta pendulum



## The University of Florence's Furuta Pendulum

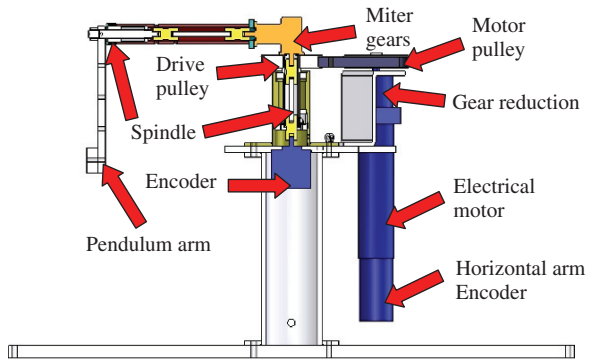
The authors have designed the mechatronic systems and two prototypes have been built (see Fig. 2). One is available in the Mechatronics Lab and the other in the Complex Dynamics and Control Systems laboratory [2].

The University of Florence FP shows some differences with respect to existing FP [3, 4]. The main difference, visible in Fig. 3, is that, whether the  $\phi$  angle is measured by an encoder placed on the motor axis, the  $\vartheta$  angle is calculated as a linear combination of  $\phi$  and the measurement of an encoder connected to the



**Fig. 2** Furuta pendulum prototype of the University of Florence

**Fig. 3** Section view of the pendulum prototype



pendulum by means of a pair of miter gears, allowing an infinite travel of the horizontal arm.

In fact, should the  $\vartheta$  angle be measured by a sensor placed on the horizontal arm, as in most of the existing solutions, the wire connection would reduce the rotational freedom of the horizontal arm.

The use of the timing belt to connect the electric motor to the vertical pillar may introduces undesired dynamics in the system due to the elasticity of the transmission but, after some experiments on the real prototype, the authors have verified that this problem does not affect the control design since it introduces high frequency plant disturbancy with large separation from the system's rigid body eigenfrequencies (in the range of a few hertz).

## Mathematical Models

In order to speed up the control design and to verify the mechanical design choices, parametric mathematical models of the pendulum have been developed. The dynamic models have been used to design first attempt versions of the control algorithms to be tuned on the real system. An experimental campaign has been then performed in order to identify the exact value of inertia, friction and electrical motor parameters. The experiments carried out consist on fixing one of the two degrees of freedom of the pendulum in order to evaluate the mass, inertia and viscous and Coulomb friction reflected on the other joint. As expected, the geometrical and physical properties of the pendulum, in particular masses and inertia tensors, are approximately the same obtained from a 3D CAD model of the prototype, but only experimental results and the identification process give useful information about the friction coefficients.

Two different models have been developed:

1. A symbolic model based on Lagrange's equations;
2. A multibody Simulink model using the application SimMechanics.

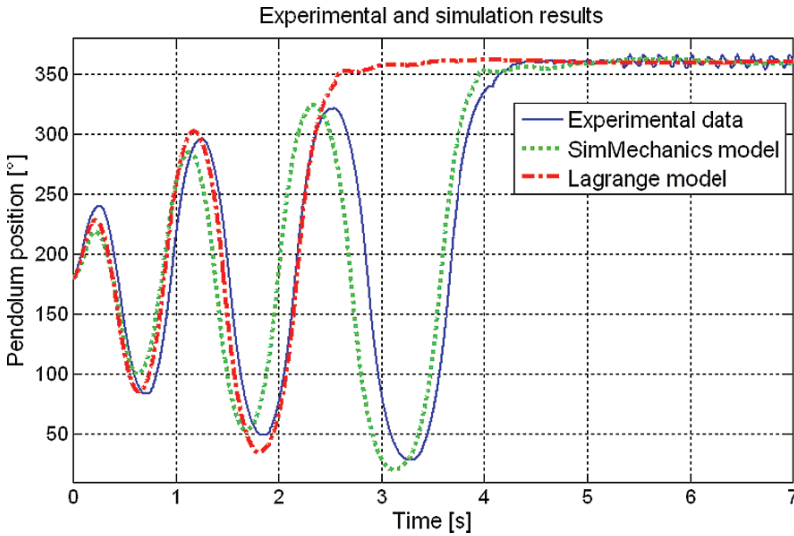


Fig. 4 Comparison between the prototype and the mathematical models

Figure 4 shows a comparison among the time histories of the pendulum angle  $\vartheta$  during a swing-up phase followed by a stabilization phase. The same experiment has been repeated on the real prototype, on the Lagrange model, and on the SimMechanics model. As visible in Fig. 4, the FP dynamics is sufficiently well described by both models. Comparing the results obtained with different models some little differences can be recognized. This behaviour can be explained since the tuning of the two models has been done using different identification procedures. Hence either the “Lagrange” model or the multibody model can be used to test and speed up the design of new control strategies.

## Control Strategy

As described in the previous paragraph, the goal of the control, as visible in Fig. 4, is to stabilize the position of the pendulum in the upright position, after swing-up, by actuating the horizontal arm.

In order to achieve this result, a sort of scheduling is performed, and the control strategy is split into two different stages. In the first one, defined “swing-up”, the control actuates the horizontal arm in order to rise the pendulum from the downward position to a configuration around the upright position. In the second stage, named “stabilization”, the control system has to transform the unstable equilibrium of the upright position in a stable one. In the following we will illustrate a simple method for the swing-up and an application of the Reinforcement Neural Network (RNN in the following) [5] for the stabilization phase.

## Swing-Up Phase

In order to swing-up the pendulum in a repetitive way, the authors have implemented a swing-up strategy based on the “Energy control” [6]. This swing-up method, similar to what all of us do in the seesaw swing, consists of accelerating the pivot ( $a$ ) of the pendulum in order to increase the energy of the oscillation. To impose a defined acceleration of the pivot the control system is designed in order to regulate the motor torque.

In order to achieve a positive increment of energy it is necessary to evaluate the equation of the uncontrolled ( $a = 0$ ) pendulum energy (1) and its derivative with respect to time (2).

$$E = \frac{1}{2} \int_{\rho} \vartheta^2 + mgl (\cos(\vartheta) - 1) \quad (1)$$

$$\frac{dE}{dt} = \int_{\rho} \vartheta \vartheta - mgl \vartheta \sin(\vartheta) \quad (2)$$

Where:

- $E$  = pendulum energy
- $l_p$  = pendulum moment of inertia
- $m$  = pendulum mass
- $g$  = gravity acceleration
- $l$  = position of the centre of mass with respect to the pivot point

By merging Eqs. (2) and (3) we obtain the relationship between energy increment and acceleration of the pendulum pivot ( $a$ ) as shown in Eq. (4).

$$\int_{\rho} \vartheta - mgl \sin(\vartheta) + mal \cos(\vartheta) = 0 \quad (3)$$

$$\frac{dE}{dt} = -mal \vartheta \cos(\vartheta) \quad (4)$$

As visible in Eq. (4), the maximum increment of energy is obtained for  $\vartheta = \pi$  and  $\vartheta = \max$  (downward position of the oscillation) and, in order to obtain a positive increment of energy, is necessary that the value of  $a$  is opposite to  $\text{sign}(\vartheta \cos(\vartheta))$ . With this principle is possible to realize many different control laws. In particular the authors have decided to design the swing-up strategy by applying torque impulses, with defined amplitude and width, when the pendulum reaches the downward position as visible in Fig. 5.

As visible in Fig. 5 using a swing-up behaviour of this type is possible to have a perfect control of the oscillation phase and, in addition, the pendulum reaches the upright position with small value of  $\frac{d\vartheta}{dt}$  which turns out very useful in order to start the stabilization phase.

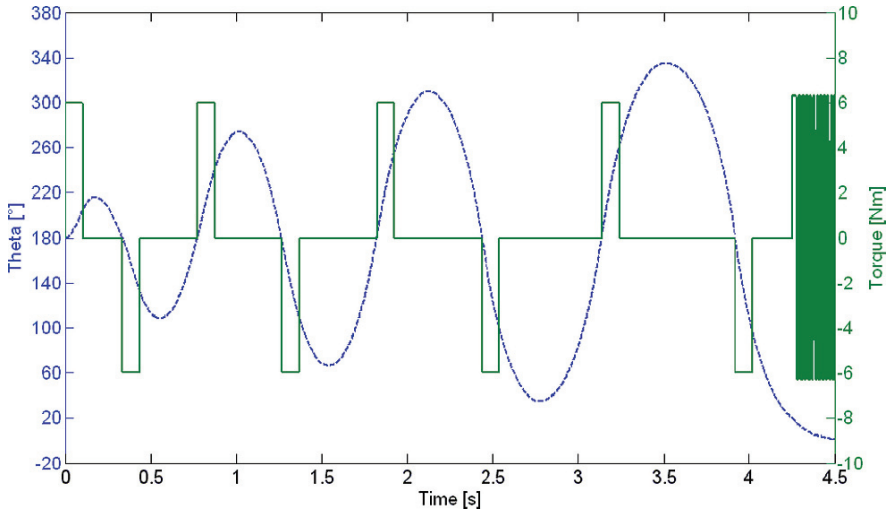


Fig. 5 Swing-up phase (Theta dotted and Torque continuous)

### ***Stabilization Phase and Experimental Results***

In this phase the control system has to transform the instable equilibrium of the upright position into a stable one. In order to achieve this result, several control strategies are being studied based on both linear approaches (such as LQ) and non-linear ones. In this work the authors want to illustrate the behaviour of a strategy based on a RNN. The RNN is capable of learning without knowing exact results given by previous tests. It is necessary only to know when the control system fails and the network tries to minimize these failures. In order to compare the RNN behaviour with a well known control strategy the authors have realized an LQ controller based on the mathematical model described in *Mathematical Models*. LQ controller is a control strategy that is able to calculate an optimal gain vector  $f$  that minimize a cost function defined on the linearized discrete-time state-space mode  $x(t)$  [7]. In this way the torque, that the electrical motor have to apply, is calculate by the following relation (5)

$$u(t) = -f \cdot x(t) \quad (5)$$

The RNN could learn from experiments on the real prototype but, in order to reduce the learning time and to avoid dangerous situations, the dynamic models described in *Mathematical Models* have been used for training. The RNN has been trained in simulations with a limit of 10,000 trials. In order to evaluate the quality of the resulting control system the static attraction basin, which is the maximum angle that the control can stabilize starting from a steady condition, has been then evaluated by means of real experiments. This test, done on the real prototype shows that the static attraction basin of the trained RNN is about  $\pm 45^\circ$ . This value is the same of the LQ

control, designed for the linearised model obtained from the Lagrange equations, that the authors have used to compare the results.

In Figs. 6 and 7 we show a comparison between the LQ controller and the trained RNN.

As visible in Figs. 6 and 7, the current version of the RNN achieves better results on the behaviour of the vertical arm ( $\vartheta$ ) but the horizontal arm position ( $\varphi$ ). This can be explained by different weight, for the horizontal and vertical arm, in the performance evaluation of the RNN training process.

### Conclusion

The FP is a good test bed for control techniques of unstable systems, useful both for research and teaching purposes. In this paper the FP prototype of the University of Florence has been described. Dynamic models of the system have been developed

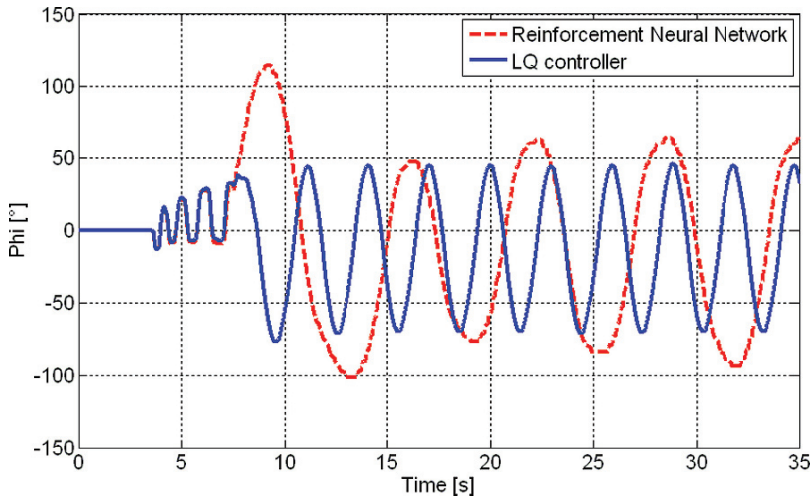


Fig. 6 Behaviour of  $\varphi$  on a swing-up and stabilization phase

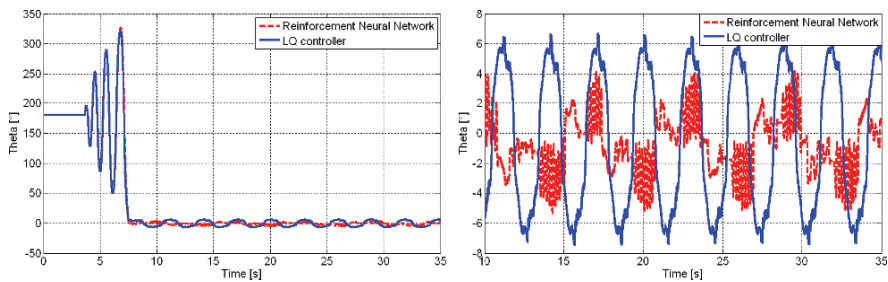


Fig. 7 Behaviour of  $\vartheta$  on a swing-up and stabilization phase



and experimental identification of the dynamic parameters of the real prototype has been performed with good accordance between experimental and simulation results. Using the models different control systems can be tested. The comparison between the LQ linear approach and the RNN is reported in the paper. Future work will concern the design and test of other control techniques like friction compensation and different approach to the RNN in order to achieve smoother behaviour of the vertical arm position.

## References

1. Furuta K., Yamakita M., Kobayashi S., Nishimura M., A new inverted pendulum apparatus for education - IFAC 11th World Congress, Boston, 1994, pp. 191–196
2. <http://control.dsi.unifi.it/>
3. [http://www.tfe.umu.se/forskning/Control\\_Systems/Set\\_Ups/Furuta\\_Pendulum/Furuta\\_Pendulum\\_info.html](http://www.tfe.umu.se/forskning/Control_Systems/Set_Ups/Furuta_Pendulum/Furuta_Pendulum_info.html)
4. <http://www.control.lth.se/~kja/pendulum/doublep.html>
5. Sutton R. S., Barto A. G., Reinforcement learning: an introduction. MIT Press. refSutton 1998. ISBN 0-262-19398-1, 1998
6. Åström K. J., Furuta K., Swinging up a pendulum by energy control – IFAC 13th World Congress, San Francisco, California, 1996
7. Gäfvert M., Modelling the furuta pendulum-ISSN0280.5316-ISRNLUTFD2/TFRT-7574-SE

# A Technique for Vibration Suppression of a 2 DOF Compliant Manipulator

Giovanni Incerti

**Abstract** The paper describes a motion planning method that is able to reduce the vibrations of robots having non-rigid transmissions. The proposed approach is based on the use of parametric motion laws (for each axis of the machine) derived from standard polynomial functions. The parameters that define the shape of the motion profiles are selected in such a way as to reduce the so called “overshooting effect”, that is the mechanical vibration arising at the end of the motion time. The calculation procedure employs a mathematical model of the manipulator and an optimization algorithm, that acts as a motion planner and automatically selects the acceleration profiles of the robot actuators.

**Keywords** Motion planning · Robot · Optimization · Vibration

## Introduction

Vibration of the end-effector is a problem that frequently occurs during the operation of an industrial robot, in particular during the execution of high-speed movements. In many cases the gripper oscillations persist even after the end of the motion time (residual vibrations) and therefore they need overtime to be damped.

It is clear that these vibratory effects are due, for the most part, to the compliance of the mechanical transmissions, since the robot arms can be considered substantially rigid. A great number of industrial processes can not be carried out if the manipulators exhibit a vibratory behaviour: so it is very important to develop motion strategies, that allow these machines to execute fast movements with good dynamic performances and high positioning precision.

Many authors have studied this problem over several years using theoretical and experimental approaches [1–6]. The motion planning procedure described in this paper has been developed in order to eliminate or to reduce the residual

---

G. Incerti (✉)  
Dipartimento di Ingegneria Meccanica e Industriale,  
Università di Brescia, Via Branze 38, 25123 Brescia, Italy  
e-mail: giovanni.incerti@ing.unibs.it

vibrations of a manipulator, without augmenting the motion time, nor introducing overtime for vibration damping; clearly both solutions reduce the rhythm of production of the industrial plant where the robot operates, with obvious economical consequences. The proposed technique is based on a suitable choice of the motion profiles assigned to the robot actuators [7, 8]. As it will be clarified in the following paragraphs, the motion of each axis is defined through some coefficients that determine the shape of the displacement, velocity and acceleration diagrams; these coefficients can be modified without changing the motion time (usually imposed by production requirements), nor altering the continuity conditions imposed on the displacement and on its time derivatives at the initial and final time instants. This calculation procedure can be used if the end-effector should not follow a pre-defined trajectory inside the workspace and therefore it is well-suited for “pick and place” operations, where only the initial and final position of the robot gripper are assigned. It is important to underline that this technique can be implemented on an actual machine with very low costs; namely it is not necessary to modify the mechanical structure of the machine, neither to use complex control algorithms for the servomotors or additional feedback sensors to measure the vibration amplitude: it is only sufficient to modify the reference motion profiles memorized in the robot controller to improve the dynamic performances of the manipulator.

In the following paragraphs this approach is used to optimize the dynamic performances of a polar manipulator working in an horizontal plane: in particular, Section *Model of a Polar Robot with Elastic Transmissions* shows a mathematical model of the robot, taking into account the joint compliance; a class of parametric motion suitable for driving the axes of the machine is defined in Section *Pseudo-polynomial Motion Profiles*; Section *Elimination of the Overshooting Effects* illustrates a criterion for the elimination of the overshooting effects; finally Section *A Numerical Example* shows an example of application of this technique and some numerical results.

## Model of a Polar Robot with Elastic Transmissions

The polar robot schematically represented in Fig. 1 has two degrees of freedom and moves in an horizontal plane: the position of the end effector is defined by two coordinates: the rotation angle of the arm  $\alpha$  and the translational displacement of the gripper along the arm  $\varrho$ . The mechanical transmissions of the manipulator are modeled by means of non rigid elements (springs and dampers in parallel). The motion laws of the actuators are assigned through two time functions  $\alpha_0(t)$  and  $\varrho_0(t)$ , that will be defined in detail in Section *Pseudo-polynomial Motion Profiles*.

The motion equations of the robot can be easily derived through the Lagrangian approach. For a two DOF mechanical system the Lagrange’s equations have the following general form:

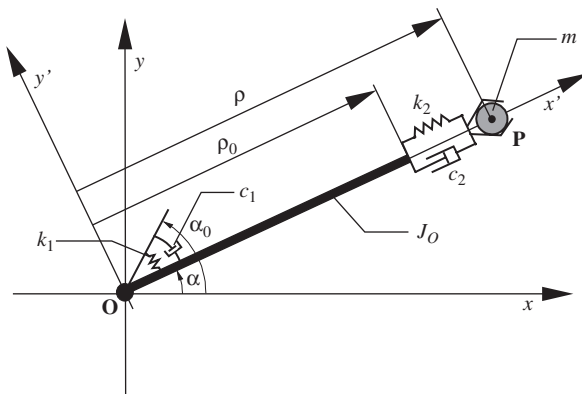


Fig. 1 Model of a polar robot with elastic transmissions

$$\frac{d}{dt} \left( \frac{\partial T}{\partial \dot{q}_k} \right) - \frac{\partial T}{\partial q_k} + \frac{\partial D}{\partial \dot{q}_k} + \frac{\partial V}{\partial q_k} = Q_k \quad k = 1, 2 \tag{1}$$

where  $q_k$  and  $\dot{q}_k$  are the generalized coordinates and velocities respectively;  $Q_k$  is the  $k$ th generalized force or torque applied to the mechanism.

In the case under study the generalized coordinates are the angular displacement  $\alpha$  and the linear displacement  $\varrho$ . So we have  $\alpha \equiv q_1$  and  $\varrho \equiv q_2$ . The generalized force  $Q_k$  is null, because the driving actions are given through the motion of the actuators and therefore there are no forces or torques directly applied to the masses.

The symbols  $T$ ,  $D$  and  $V$  indicate respectively the kinetic energy of the system, the Rayleigh dissipative function and the potential energy due to the elastic deformation of the mechanical transmissions. Using the symbols given in Table 1, the kinetic energy of the robot can be written as:

$$T = \frac{1}{2} [J_O \dot{\alpha}^2 + m(\dot{\varrho}^2 + \varrho^2 \dot{\alpha}^2)] \tag{2}$$

whereas the Rayleigh's function and the potential energy can be expressed in the following form:

Table 1 Parameters of the robot

Symbol	Description	Value
$m$	End-effector mass (gripper and payload)	4 kg
$J_O$	Moment of inertia of the robot arm (about O)	5.76 kg m <sup>2</sup>
$k_1$	Torsional stiffness of joint "1"	18 kNm/rad
$c_1$	Torsional damping constant of joint "1"	80 Nms/rad
$k_2$	Stiffness of joint "2"	12 kN/m
$c_2$	Damping constant of joint "2"	35 Ns/m

$$D = \frac{1}{2} [c_1(\dot{\alpha} - \dot{\alpha}_0)^2 + c_2(\dot{\varrho} - \dot{\varrho}_0)^2] \quad (3)$$

$$V = \frac{1}{2} [k_1(\alpha - \alpha_0)^2 + k_2(\varrho - \varrho_0)^2] \quad (4)$$

Substituting the expressions of  $T$ ,  $D$  and  $V$  into (1) and carrying out the required mathematical operations, we obtain the motion equations of the polar manipulator:

$$\begin{cases} \ddot{\alpha} = -\frac{1}{J_O + m\varrho^2} [2m\varrho \dot{\alpha}\dot{\varrho} + k_1(\alpha - \alpha_0) + c_1(\dot{\alpha} - \dot{\alpha}_0)] \\ \ddot{\varrho} = \varrho \dot{\alpha}^2 - \frac{1}{m} [k_2(\varrho - \varrho_0) + c_2(\dot{\varrho} - \dot{\varrho}_0)] \end{cases} \quad (5)$$

If we assign the functions  $\alpha_0(t)$  and  $\varrho_0(t)$ , it is possible to integrate the differential equations and to determine in this way the dynamic behaviour of the manipulator; the solution of system (5) must be obtained by numerical procedure, since the equations are non linear. By extending the integration interval beyond the motion time  $t_m$ , it is possible to calculate the time history of the residual vibration.

## Pseudo-polynomial Motion Profiles

After deducing the equations that describe the dynamics of the polar robot with elastic transmission, it is now necessary to define the motion laws for each axis of the machine.

These profiles are defined in parametric form, so that it is possible to modify their shape by changing the numerical values of some coefficients.

In the technical literature some classes of motion profiles can be found, which are dependent on a series of user definable coefficients. These functions can be defined by a single analytic expression, valid for the total motion interval or by different expressions inside this interval.

In this paragraph we will introduce a particular class of parametric motion laws, whose profiles are dependent by a set of numerical coefficients, named *shape coefficients*; the values assigned to these coefficients determine the shape of the displacement, velocity and acceleration diagrams and they can be modified without altering the boundary conditions (that is the conditions at the time instants  $t = 0$  and  $t = t_m$ ).

A particularly simple analytical expression used to define these motion profiles is the following:

$$y(t) = h [1 - \sum_{i=1}^3 C_i (1 - t/t_m)^{\lambda_i}] \quad (6)$$

where  $y$  is the displacement and  $t$  the time. The symbols  $h$  and  $t_m$  indicate the total displacement and the motion time respectively, whereas the exponents  $\lambda_i$  are the

shape coefficients. The constants  $C_i$  can be easily determined by imposing suitable boundary conditions, as it will be explained subsequently.

To simplify the analytical developments it is convenient to define two new variables: the *non-dimensional displacement*  $\eta = y/h$  and the *non-dimensional time*  $\tau = t/t_m$ . Using these new definitions, we can rewrite (6) in the form:

$$\eta(\tau) = 1 - \sum_{i=1}^3 C_i(1 - \tau)^{\lambda_i} \tag{7}$$

The first and second derivatives of this function are respectively:

$$\eta'(\tau) = \sum_{i=1}^3 \lambda_i C_i(1 - \tau)^{\lambda_i-1} \tag{8}$$

$$\eta''(\tau) = - \sum_{i=1}^3 \lambda_i(\lambda_i - 1)C_i(1 - \tau)^{\lambda_i-2} \tag{9}$$

We observe that Eqs. (7), (8) and (9) satisfy the following conditions:

$$\eta(1) = 1 \quad \eta'(1) = 0 \quad \eta''(1) = 0 \tag{10}$$

In order to calculate the coefficients  $C_i$  ( $i = 1, 2, 3$ ), we impose that the displacement, the velocity and the acceleration are null for  $t = 0$ ; therefore we can write:

$$\eta(0) = 0 \quad \eta'(0) = 0 \quad \eta''(0) = 0 \tag{11}$$

By imposing the conditions (11) we obtain the following linear system of equations:

$$\begin{cases} \sum_{i=1}^3 C_i = 1 \\ \sum_{i=1}^3 \lambda_i C_i = 0 \\ \sum_{i=1}^3 \lambda_i(\lambda_i - 1)C_i = 0 \end{cases} \tag{12}$$

The symbolic solution of the system (12) gives the values of the constants  $C_1$ ,  $C_2$  and  $C_3$  as function of the exponents  $\lambda_1$ ,  $\lambda_2$  and  $\lambda_3$ :

$$C_1 = \frac{\lambda_2\lambda_3}{(\lambda_3 - \lambda_1)(\lambda_2 - \lambda_1)} \quad C_2 = \frac{\lambda_1\lambda_3}{(\lambda_2 - \lambda_1)(\lambda_2 - \lambda_3)} \quad C_3 = \frac{\lambda_1\lambda_2}{(\lambda_1 - \lambda_3)(\lambda_2 - \lambda_3)} \tag{13}$$

It is important to observe that the displacement, velocity and acceleration diagrams can be easily manipulated by changing the values of the exponents  $\lambda_1$ ,  $\lambda_2$  and  $\lambda_3$ . If these exponents assume integer positive values, we obtain the classical polynomial functions, widely cited in the technical literature and frequently employed to design cam mechanisms [9, 10].

On the contrary, if these parameters assume non integer (but always positive) values, the corresponding functions are no more polynomial, even if, from the analytical point of view, they can be still calculated with the previous described

procedure. In this case we can introduce the concept of *pseudo-polynomial* function, to put in evidence, at the same time, the analogies and the differences with a standard polynomial function.

New motion profiles can be generated, if the shape parameters are suitably changed; these parameters can be automatically selected by a numerical optimization procedure, that determines the maximum or minimum value of a particular target function, which will be defined in Section *Elimination of the Overshooting Effects*. Using this approach, it is also possible to introduce some algebraic constraints, in order to reduce the computational time and to drive the optimization process towards a satisfactory solution.

## Elimination of the Overshooting Effects

As previously stated, the overshooting effect, from the analytical point of view, is a free vibration that appears at the end of the motion interval, that is for  $t > t_m$ . In this situation the motors of the manipulator are kept locked in the final positions defined by the reference motion laws, whereas the masses connected to the elastic transmissions are subjected to vibrations. This is possible because some mechanical energy is stored in the system at the time instant  $t = t_m$ . This energy will be subsequently dissipated by friction and other by damping effects, which are always present inside an actual system.

Starting from these considerations, it is now clear that the overshooting effect can be eliminated if we impose that the total mechanical energy  $E_{\text{tot}}$  of the system is null at the time instant  $t = t_m$ ; if this is not possible, we can impose that the value of  $E_{\text{tot}}$  is reduced to a minimum. In this case the residual oscillations will be in any case strongly reduced, even if they will not be completely eliminated.

From the practical point of view, the total mechanical energy stored in the system at the end of the motion time represents our target function; it can be calculated by adding the kinetic energy  $T$  to the potential elastic energy  $V$  due to the transmission elasticity (see Eqs. (2) and (4) in Section *Model of a polar Robot with Elastic Transmissions*). All position and velocity variables must be calculated at the time instant  $t_m$ .

The value of the target function changes when the reference motion profiles of the actuators are modified; having at our disposal two profiles  $\alpha_0(t)$  and  $\varrho_0(t)$ , defined in parametric form through the shape coefficients, this function will depend also on these parameters, which will be opportunely selected, to obtain a minimum.

It may be observed that this is a typical problem of non linear mathematical programming; for the solution of these problems some efficient algorithms are available, which are used to determine a local minimum of the selected target function.

## A Numerical Example

This paragraph presents some numerical results, obtained by means of the motion planning technique described in the previous sections. The calculation are

performed for a polar robot, working in an horizontal plane (no gravity effects are considered) and having the physical and geometrical parameters listed in Table 1.

To define the motion strategy it is firstly necessary to assign the motion time  $t_m$  (equal for both robot axes) and the coordinates of the end-effector inside the working space of the manipulator at the time instants  $t = 0$  (starting point  $P_1$ ) and  $t = t_m$  (ending point  $P_2$ ).

Table 2 shows the values used for this numerical example, expressed in both Cartesian and polar coordinates. The use of polar coordinates allows us to calculate immediately the arm rotation  $\Delta\alpha = \alpha_2 - \alpha_1$  and the gripper translation along the robot arm  $\Delta\varrho = \varrho_2 - \varrho_1$ , that are needed to execute the movement from point  $P_1$  to point  $P_2$ .

To drive the axes of the machine, we use two motion profiles  $\alpha_0(t)$  and  $\varrho_0(t)$ , defined by Eq. (6). The coefficients  $C_1$ ,  $C_2$  and  $C_3$  can be calculated through Eqs. (13).

We denote with the symbols  $\Lambda_1 = \{\lambda_1^{(1)} \lambda_2^{(1)} \lambda_3^{(1)}\}^T$  and  $\Lambda_2 = \{\lambda_1^{(2)} \lambda_2^{(2)} \lambda_3^{(2)}\}^T$  two vectors containing the shape parameters of the motion laws; the superscripts between the round brackets indicate the corresponding actuators: (1) for the rotation  $\alpha_0(t)$  and (2) for the translation  $\varrho_0(t)$ .

According to the criterion suggested in Section *Elimination of the Overshooting Effects*, the performance index  $\Psi$  is defined as the total mechanical energy at the time instant  $t = t_m$ ; since the value of this index depends on the shape coefficients, we can write with mathematical formalism:

$$E_{tot}(t_m) = T(t_m) + V(t_m) = \Psi(\Lambda_1, \Lambda_2) \tag{14}$$

In order to minimize the target function an optimization procedure has been implemented using the conjugate gradient method [11], available inside a software package addressed to the solution of non linear optimization problems. The initial values of the shape parameters are  $\Lambda_1 = \Lambda_2 = \{3 \ 4 \ 5\}^T$ , corresponding to a standard fifth degree polynomial function. At the end of the optimization process the following final values have been found:

$$\Lambda_1 = \{8.610 \ 6.171 \ 5.167\}^T \quad \Lambda_2 = \{5.740 \ 5.803 \ 5.780\}^T \tag{15}$$

**Table 2** Motion parameters used for simulation

Symbol	Description	Value
$(x_1; y_1)$	Initial position (cartesian coordinates)	(0.2 m; 0.1 m)
$(\varrho_1; \alpha_1)$	Initial position (polar coordinates)	(0.224 m; 26.6°)
$(x_2; y_2)$	Final position (cartesian coordinates)	(-0.3 m; 1 m)
$(\varrho_2; \alpha_2)$	Final position (polar coordinates)	(1.044 m; 106.7°)
$\Delta\alpha$	Arm rotation	80.1°
$\Delta\varrho$	End-effector translation	0.82 m
$t_m$	Motion time	1 s



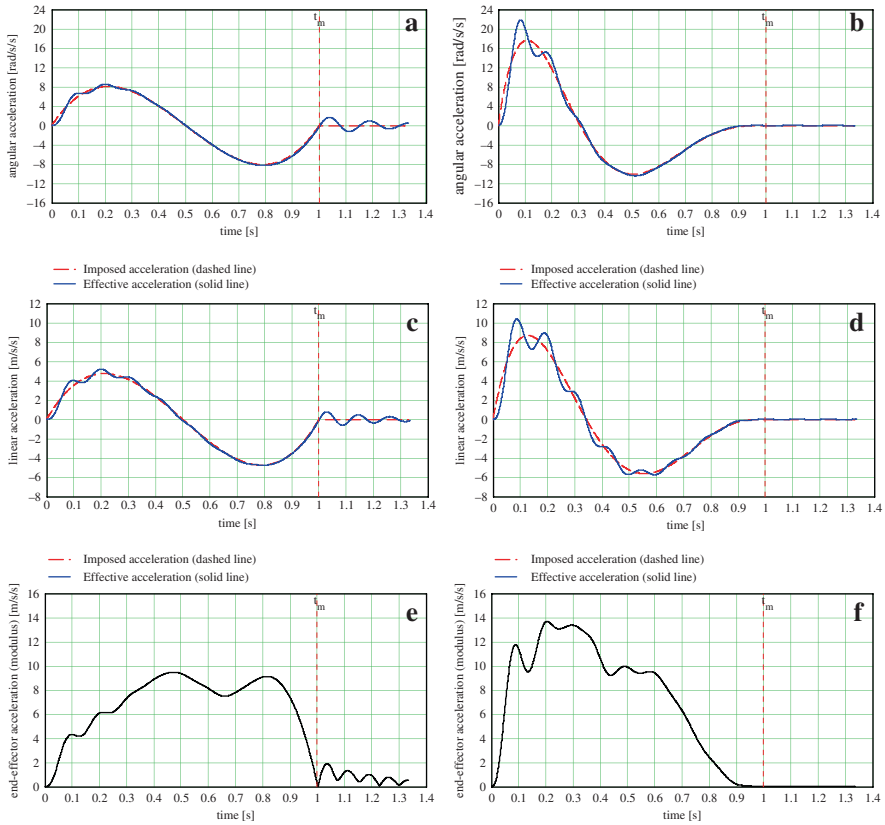


**Fig. 2** Comparison between the non-optimized case (*left column diagrams*) and, the optimized case (*right column diagrams*): **(a, b)** angular acceleration of the robot arm; **(c, d)** linear acceleration of the end effector along the radial direction; **(e, f)** modulus of the end-effector acceleration

The diagrams in Fig. 2a, b, c and d show the time histories of the accelerations  $\ddot{\alpha}(t)$  and  $\ddot{\rho}(t)$ , obtained with the numerical values listed in Tables 1 and 2. The modulus of the end-effector acceleration as function of the time is plotted in Fig. 2e, f.

The comparison between the diagrams in the left and right columns clearly shows that the overshooting effect disappears, when optimized motion profiles are used to drive the robot actuators.

## Conclusions

A method for vibration damping of compliant robots was presented in the paper. The proposed approach employs a class of motion laws derived from the standard polynomial functions and a numerical algorithm, which minimizes the total energy of the

system, in order to eliminate or reduce the overshooting effects. The method here described can be applied to assembly robots, which should not follow a particular trajectory, but only perform a point to point movement in a prefixed time, compatible with the requirements of the production cycle and with the working speed of the machine. The optimization procedure is performed off line, using a mathematical model that reproduces the vibratory phenomena that occurs during the operation of a real robot. The absence of constraints on the end effector trajectory allows the use of parametric motion laws, whose acceleration profile is modified by varying the numerical values of some coefficients. The optimized motion laws can be easily transferred into the memory of the motion controller of the robot: so it is possible to improve the dynamic behaviour of a machine in a simple and inexpensive way.

## References

1. Pham C.M., Khalil W., Chevallereau C., A nonlinear model-based control of flexible robots, *Robotica*, 11, pp. 72–82, 1992.
2. Singhose W.E., Crain E.A., Seering W.P., Convolved and simultaneous two-mode input shapers, *IEEE Proceedings Control Theory and Applications*, 144(6), pp. 515–520, 1997.
3. Boyer F., Khalil W., An efficient calculation of flexible manipulator inverse dynamics, *International Journal of Robotics Research*, 17(3), pp. 282–293, 1998.
4. Aoustin Y., Formal'sky A.M., On the feed-forward torques and reference trajectory for flexible two-link arm, *Multibody System Dynamics*, 3(3), Kluwer Academic Publishers, pp. 241–265, 1999.
5. Kapucu S., Gürsel A., Bayseç S., Residual swing/vibration reduction using a hybrid input shaping method, *Mechanism and Machine Theory*, 36, pp. 311–326, 2001.
6. Mimmi G., Rottenbacher C., Bonadrini C., One-Mode extra insensitive input shapers to reduce residual vibration in flexible arms: Experimental verification, 12th IFToMM Conf., Besançon (France), 2007.
7. Incerti G., Elastodynamic synthesis of motion profiles for SCARA robots with non rigid transmission, *Vibration, Noise and Structural Dynamics '99*, Venice (Italy), pp. 260–267, 1999.
8. Incerti G., An optimization method for reducing residual vibrations of compliant manipulators, *The Thirteenth International Congress on Sound and Vibration (ICSV 13)*, Vienna, Austria, July 2–6, 2006.
9. Magnani P.L., Ruggieri G., *Meccanismi per macchine automatiche*, UTET, Torino, 1986 (in Italian).
10. Norton R.L., *Cam design and manufacturing handbook*, Industrial Press, New York, 2002.
11. Rao S.S., *Engineering optimization – theory and practice*, Wiley, New York, 1996.

# Investigation on the Baumgarte Stabilization Method for Dynamic Analysis of Constrained Multibody Systems

Paulo Flores, Rui Pereira, Margarida Machado and Eurico Seabra

**Abstract** This paper presents an investigation on the Baumgarte stabilization method for dynamic analysis of constrained multibody systems. The purpose of this work is to study the influence of the main variables that affect the constraints violation, namely, the values of the Baumgarte parameters. In the process, the formulation of the dynamic equations of motion of constrained multibody systems and the main issues of the Baumgarte stabilization method are revised. Attention is given to the techniques to help in the Baumgarte parameters selection. A demonstrative example is presented and the results of some simulations are discussed.

**Keywords** Multibody dynamics · Constrained systems · Baumgarte method · Baumgarte parameters

## Introduction

Over the last decades the importance of the dynamic simulation of constrained multibody systems (MBS) has been recognized as playing a crucial role in a broad variety of engineering fields, such as robots, biomechanics, automobile systems and railway vehicles [1]. The equations of motion of constrained MBS are composed by a set of differential and algebraic equations (DAE) of index three. The numerical solution of the set of DAE is not straightforward problem. One of the most popular and used methods to solve this problem consists of converting the system of DAE into a set of ordinary differential equations (ODE) by appending the second derivative with respect to time of the constraint equations. However, with this approach, the state of variables, i.e., the generalized position and velocity constraint equations do not satisfy due to numerical error, being the global results not acceptable in practical applications.

---

P. Flores (✉)  
Departamento de Engenharia Mecânica, Universidade do Minho,  
Campus de Azurém, 4800-058 Guimarães, Portugal  
e-mail: pflores@dem.uminho.pt

In recent years, a lot of attempts have been made dealing with the constrained multibody systems. Due to its simplicity and easiness for computational implementation, the Baumgarte stabilization method (BSM) is the most attractive technique to overcome the drawbacks of the standard integration of the equations of motion. Baumgarte's method can be looked upon as an extension of feedback control theory [2]. The principle of this method is to damp out the acceleration constraint violations by feeding back the violations of the position and velocity constraints. The choice of the feedback parameters depends on several factors, namely, the integrator used and the model of the MBS. This method does not solve all possible numerical instabilities as, for instance, those that arise near kinematic singularities. The major drawback of Baumgarte's method is the ambiguity in choosing feedback parameters. The coordinate partitioning method and the augmented Lagrangian formulation are alternative methods to deal with the constraints violation. In addition to these approaches, many research papers have been published on the stabilization methods for the numerical integration the equations of motion of multibody systems [3–5].

In this paper, an investigation on the Baumgarte's method for dynamic simulation of constrained MBS is presented. The formulation of the equations of motion of general MBS is also reviewed. The equations of motion are solved by using the Baumgarte stabilization technique with the intent of keeping the constraint violations under control. Finally, an eccentric slider crank mechanism is used as an application example.

## Equations of Motion for Constrained MBS

When the configuration of a constrained MBS, with  $f$  degrees of freedom, is modeled through a set of  $n$  dependent coordinates, then a set of  $m$  algebraic constraints can be written as [1],

$$\Phi(\mathbf{q}, t) = \mathbf{0} \quad (1)$$

where  $\mathbf{q}$  is the vector of generalized coordinates and  $t$  is the time variable. The equations of motion for a constrained MBS can be represented by [1],

$$\mathbf{M}\ddot{\mathbf{q}} + \Phi_{\mathbf{q}}^T \boldsymbol{\lambda} = \mathbf{g} \quad (2)$$

where  $\mathbf{M}$  is the generalized mass matrix,  $\ddot{\mathbf{q}}$  is the system accelerations,  $\Phi_{\mathbf{q}}$  is the Jacobian matrix,  $\boldsymbol{\lambda}$  is the Lagrange multipliers vector and  $\mathbf{g}$  is the generalized force vector that includes the gravitational, centrifugal and Coriolis force terms. In order to progress with solution, the constraint velocity and acceleration equations are required. Thus, differentiating Eq. (1) with respect to time yields the velocity constraint equations,

$$\Phi_{\mathbf{q}}\dot{\mathbf{q}} = -\Phi_t \equiv \mathbf{v} \quad (3)$$

in which  $\dot{\mathbf{q}}$  is the vector of generalized velocities and  $\mathbf{v}$  is the right hand side of velocity equations, which contains the partial derivatives of  $\Phi$  with respect to time. A second differentiation of Eq. (1) with respect to time leads to the acceleration constraint equations,

$$\Phi_q \ddot{\mathbf{q}} = -(\Phi_q \dot{\mathbf{q}})_q \dot{\mathbf{q}} - 2\Phi_{qt} \dot{\mathbf{q}} - \Phi_{tt} \equiv \boldsymbol{\gamma} \quad (4)$$

where  $\ddot{\mathbf{q}}$  is the acceleration vector and  $\boldsymbol{\gamma}$  is the right hand side of acceleration equations. Equations (1), (3) and (4) must be satisfied during the simulation. Equation (4) can be appended to Eq. (2) and rewritten in matrix form as,

$$\begin{bmatrix} \mathbf{M} & \Phi_q^T \\ \Phi_q & \mathbf{0} \end{bmatrix} \begin{Bmatrix} \ddot{\mathbf{q}} \\ \boldsymbol{\lambda} \end{Bmatrix} = \begin{Bmatrix} \mathbf{g} \\ \boldsymbol{\gamma} \end{Bmatrix} \quad (5)$$

This system of equations is solved for  $\ddot{\mathbf{q}}$  and  $\boldsymbol{\lambda}$ . Then, in each integration time step, the accelerations vector,  $\ddot{\mathbf{q}}$ , together with velocities vector,  $\dot{\mathbf{q}}$ , are integrated in order to obtain the system velocities and positions for the next time step. This procedure is repeated up to final time analysis is reached.

In order to keep the constraint violations under control, the Baumgarte stabilization method is used [2]. The BSM allows constraints to be slightly violated before corrective actions can take place, in order to force the violation to vanish. The goal of Baumgarte's method is to replace the differential Eq. (4) by the following equation,

$$\ddot{\Phi} + 2\alpha\dot{\Phi} + \beta^2\Phi = \mathbf{0} \quad (6)$$

Equation (6) is the differential equation for a closed loop system in terms of kinematic constraint equations. The terms  $2\alpha\dot{\Phi}$  and  $\beta^2\Phi$  in Equation (6) play the role of a control terms. Thus, utilizing the Baumgarte's approach, the equations of motion for a system subjected to constraints are stated in the form,

$$\begin{bmatrix} \mathbf{M} & \Phi_q^T \\ \Phi_q & \mathbf{0} \end{bmatrix} \begin{Bmatrix} \ddot{\mathbf{q}} \\ \boldsymbol{\lambda} \end{Bmatrix} = \begin{Bmatrix} \mathbf{g} \\ \boldsymbol{\gamma} - 2\alpha\dot{\Phi} - \beta^2\Phi \end{Bmatrix} \quad (7)$$

In general, if  $\alpha$  and  $\beta$  are chosen as positive constants, the stability of the general solution of Eq. (7) is guaranteed. When  $\alpha$  is equal to  $\beta$ , critical damping is achieved, which usually stabilizes the system response more quickly. Baumgarte [2] highlighted that the suitable choice of the parameters  $\alpha$  and  $\beta$  is performed by numerical experiments. It should be highlighted that the improper choice of these coefficients can lead to unacceptable results in the dynamic simulation of multibody systems.

## Techniques to Select the Baumgarte Parameters

The first and simplest way to evaluate the Baumgarte parameters consists of expanding in Taylor's series the constraint equation and neglecting the terms of order higher than two. Thus, it is possible to write,

$$\Phi(t+h) = \Phi(t) + \dot{\Phi}(t)h + \ddot{\Phi}(t)\frac{h^2}{2} \quad (8)$$

where  $h$  represents the time step. Considering that function  $\Phi$  is null at instant  $t+h$ , then Eq. (8) can be written as,

$$\ddot{\Phi}(t) + \frac{2}{h}\dot{\Phi}(t) + \frac{2}{h^2}\Phi(t) = 0 \quad (9)$$

By comparing and analyzing Eqs. (6) and (9) the mathematical relation for Baumgarte parameters and time step can be expressed by,

$$\alpha = \frac{1}{h} \quad (10)$$

$$\beta = \frac{\sqrt{2}}{h} \quad (11)$$

From Eqs. (10) and (11) it can be observed that with this technique the Baumgarte parameters are inversely proportional to the time step. This approach is quite simple, very easy to implement in any general code and works reasonably well from the computational view point. However, this procedure can lead to some numerical instability which ultimately produces incorrect results when the time step is too small, because the damping terms dominate the numerical value of Eq. (6) and make the system to become stiff. Thus, a more sophisticated methodology should be considered, being the Euler's integration method used to show how to select an appropriate set of  $\alpha$  and  $\beta$  parameters. Herein, the proposed methodology is based on the stability analysis procedure in digital control theory. Applying the Laplace transform technique to a first order differential yields,

$$sY(s) = F(s) \quad (12)$$

where  $s$  is the operator of Laplace domain. Moreover, when Euler's integration method is used, the numerical solution of a first order differential yields,

$$y_{n+1} = y_n + hf_n \quad (13)$$

in which the subscript represents the numerical solution at the corresponding time step and  $h$  is the integration time step.

Since Eq. (13) is a difference equation, that is, a discrete data function, the Z transform technique must be used to study it. Thereby, the Z transform of Eq. (13) results in

$$zY(z) = Y(z) + hF(z) \quad (14)$$

where  $z$  is the Z transform variable. Re-arranging Eq. (14) yields,

$$\frac{F(z)}{Y(z)} = \frac{z - 1}{h} \quad (15)$$

Analyzing Eqs. (12) and (15), striking resemblances between Laplace and Z transform techniques results in,

$$s = \frac{z - 1}{h} \quad (16)$$

This means that the substitution of Eq. (16) in any  $F(s)/Y(s)$  yields a  $F(z)/Y(z)$  based on the Euler's integration method.

Considering now Eq. (6), the corresponding characteristic equation is,

$$s^2 + 2\alpha s + \beta^2 = 0 \quad (17)$$

Equation (17) suggests that if  $\alpha$  and  $\beta$  are greater than zero, the system will be stable. However, Eq. (17) is not adequate to select  $\alpha$  and  $\beta$  parameters. In order to select the appropriate values of the parameters  $\alpha$  and  $\beta$ , the response of the second order characteristic equation (17) for different locations of its roots in the  $z$ -plane must be known first. Letting  $s = \sigma + j\omega$ , it is possible to write,

$$z = e^{t(\sigma + j\omega)} = e^{\sigma t} \angle \omega t \quad (18)$$

since  $1 \angle \omega t = \cos \omega t + j \sin \omega t$ .

A system is stable if all roots of the characteristic equation are inside the unit circle on the  $z$ -plane, that is,  $|z| < 1$ . Conversely, a system is said to be unstable when the roots are outside the unit circle, that is,  $|z| > 1$ . When a system has its roots on the unit circle,  $|z| = 1$ , is called as marginally stable. In order to study the stability of characteristic Eq. (17), let substitute Eq. (16) yielding the characteristic equation in terms of  $z$ -plane as,

$$z^2 + (2\alpha h - 2)z + (\beta^2 h^2 - 2\alpha h + 1) = 0 \quad (19)$$

Equation (19) shows that  $\alpha$ ,  $\beta$  and  $h$  influences the location of the roots and, consequently, the dynamic system response. In order to have a criterion to help in the selection of the  $\alpha$  and  $\beta$  parameters independently of the time step  $h$ , let

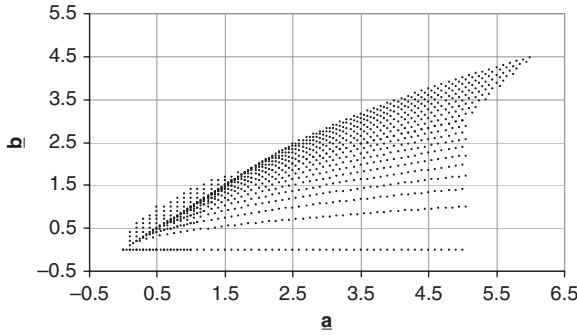


Fig. 1 Stability region in the  $\underline{\alpha}$ - $\underline{\beta}$  plane for the Euler integration method

consider two additional coefficients  $\underline{\alpha}$  and  $\underline{\beta}$  defined by,  $\underline{\alpha} = \alpha h$  and  $\underline{\beta} = \beta^2 h^2$ . The relationship between the  $\underline{\alpha}$  and  $\underline{\beta}$  coefficients for the Euler integration method is illustrated in Fig. 1, being easier to identify the stability region as function of the Baumgarte parameters.

### Demonstrative Example

The purpose of this section is to demonstrate the computational effectiveness of the presented techniques to an eccentric slider crank mechanism, which is illustrated in Fig. 2. The system is driven by the crank which rotates with a constant angular velocity. Several representative simulations are performed in order to study and compare the efficiency of different values for  $\alpha$  and  $\beta$  parameters on the stabilization of the constraint violations. A measure of their efficiency can be drawn from the error of the third constraint equation  $\Phi_3$ , that are representative of the rest of the constraint equations and their derivatives, which present similar results. Eight sets of

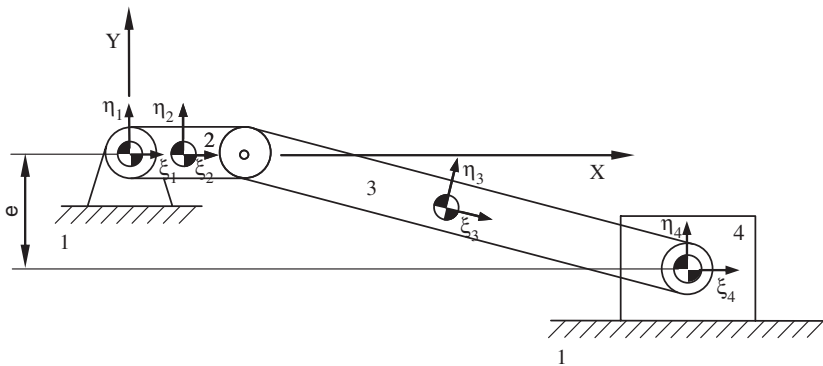


Fig. 2 Initial configuration of the eccentric slider crank mechanism



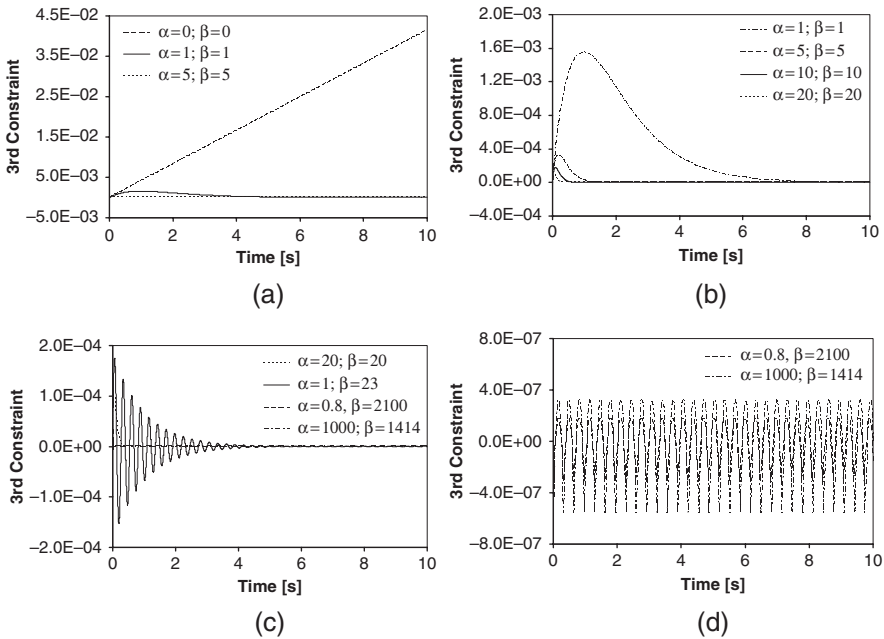


Fig. 3 Error of the 3rd constraint equation  $\Phi_3$

Baumgarte parameters were used, which were selected based on the methodologies presented in the previous section. Other variables were studied, chiefly, the values of the integration method, the size of the time step and the quality of the initial system guess for positions, being the results not presented due to lack of space.

Figure 3(a) shows that when  $\alpha = \beta = 0$  is used the violation of the constraints grows indefinitely with the time. For nonzero values for parameters  $\alpha$  and  $\beta$ , the behaviour of the system is slightly different, as it is illustrated in Fig. 3(b–d). Moreover, when the parameters  $\alpha$  and  $\beta$  are equal, the critical damping is reached, which stabilizes the system response more quickly, that is, after a transient phase the first and second derivatives converge to zero. Thus, the constraint equations, and not only their second derivatives, are satisfied at any give time. Figure 3 (d) illustrates a stiff system, which occurs when the values of  $\alpha$  and  $\beta$  are high.

### Concluding Comments

An investigation on the Baumgarte stabilization method for dynamic analysis of constrained multibody systems was discussed in this work. A demonstrative example is presented and the results of some simulations were discussed. Several numerical simulations were performed in order to study the influence of the main variables that affect the constraints violation. In the process, the formulation of the dynamic equations of motion of constrained multibody systems and the Baumgarte

stabilization method are revised. Special attention is also given to the techniques to help in the selection of the Baumgarte parameters. From the main results obtained, it can be concluded that the selection of the Baumgarte parameters play a key role on the dynamic systems' response.

## References

1. Nikravesh PE, *Computer-Aided Analysis of Mechanical Systems*, Prentice Hall, Englewood Cliffs, New Jersey, 1988.
2. Baumgarte J, *Stabilization of Constraints and Integrals of Motion in Dynamical Systems*, *Computer Methods in Applied Mechanics and Engineering*, Vol. 1, pp. 1–16, 1972.
3. Wehage RA, Haug EJ, *Generalized Coordinate Partitioning for Dimension Reduction in Analysis of Constrained Systems*, *Journal of Mechanical Design*, Vol. 104, pp. 247–255, 1982.
4. Bayo E, García de Jálón J, Serna AA, *Modified Lagrangian Formulation for the Dynamic Analysis of Constrained Mechanical Systems*, *Computer Methods in Applied Mechanics and Engineering*, Vol. 71, pp. 183–195, 1988.
5. Yoon S, Howe RM, Greenwood DT, *Geometric Elimination of Constraint Violations in Numerical Simulation of Lagrangian Equations*, *Journal of Mechanical Design*, Vol. 116, pp. 1058–1064, 1994.

# Cornering Stability and Dynamic Analysis of a Four Steering Wheels Vehicle Driven by “In Wheel” Engines

Massimo Callegari, Andrea Gabrielli and Matteo-Claudio Palpacelli

**Abstract** The paper describes the dynamic analysis of an innovative vehicle driven by two “in wheel” brushless motors and provided with four steering wheels. Such electric car has been designed for an academic competition where different trials have to be passed: for this purpose a deep investigation on the dynamic behaviour of both the suspended and the heavy unsuspended masses has been performed. A multi-body analysis allowed to evaluate the vehicle’s cornering stability and the vibration level induced on motors’ parts, in order to prevent the detachment of the permanent magnets glued onto the spinning rotor. A particular attention has been paid to the design of car’s suspensions.

**Keywords** Electric vehicle · Mechanism design · Dynamics of multi-body systems

## Introduction

In the automotive industry a new sensibility towards some aspects of eco-design is currently increasing and issues like energy efficiency and environmental impact represent nowadays a primary objective of the design.

A relevant example is given by the recent interest in the development of electric vehicles driven by “in-wheel” engines, technology that shows several benefits: the functions conventionally assigned to mechanical devices like gearbox, clutch and transmission elements are in this case managed by control systems which directly drive the electric motors integrated inside the wheels. As a result a more flexible arrangement of vehicle architecture is also obtained.

The object of the present study is a light car designed and prototyped by the Polytechnic University of Marche in collaboration with an Italian manufacturer, which is provided with four steering wheels and two electric radial flux brushless motors placed on the rear axle [1]. The vehicle is addressed to a competitive demonstration

---

M. Callegari (✉)

Dipartimento di Meccanica, Università Politecnica delle Marche,  
Via Brezze Bianche s/n, 60131 Ancona, Italy  
e-mail: m.callegari@univpm.it

where the main evaluation criterions promote the use of new technologies in support of sustainable and efficient mobility.

The vehicle's design and dynamic characterisation have been carried out by means of multibody simulations in a virtual prototyping environment [2]. First attempt simulations have been performed by simple mathematical models in order to define overall suspension characteristics; then springs stiffness has been increased so as to improve the vehicle's performances notwithstanding passengers comfort; a more detailed dynamic analysis has been undertaken to study the cornering stability and on road handling. A study of the tire loadings has led towards an optimization of the spring stiffness of the front and rear axle and of the damping ratio of the shock absorbers.

Moreover the results of such simulations have also provided important information about the dynamic loads transmitted to the electric motors: in fact the vertical forces generated by both car's frame and (heavy) wheels dynamics cause a variable gap in the motors and consequently a cyclic stress on the polar expansions and on the permanent magnets glued to the spinning rotor.

## Description of the Vehicle

The vehicle has a simple architecture based on a light chassis with four independent suspensions; different kinds of linkages have been used for the front and rear axles: the former has been inherited together with the chassis from an already available city car provided by the industrial manufacturer, with swing longitudinal arms, while the latter has been designed with a conventional MacPherson scheme, as shown in Fig. 1. Each suspension arm is connected to wheel's hub by means of a knuckle that allows wheel's steering; for the sake of safety the front steering is mechanically operated by means of a steering gear, while the rear steering is electrically managed by means of drive-by-wire technology. Two radial flux brushless motors are positioned inside the rear wheels, with their external rotor, holding the permanent magnets,

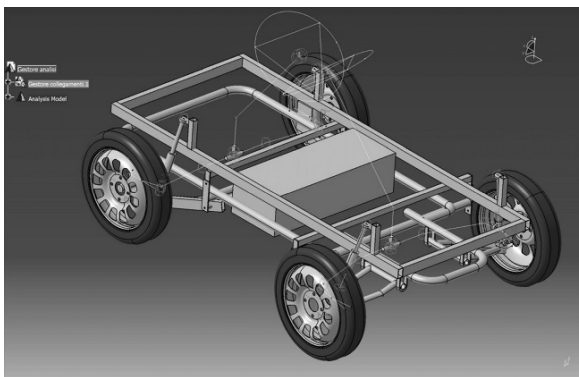


**Fig. 1** Mock-up of the vehicle developed in LMS VirtualLab Motion

**Table 1** Vehicle specifications

Technical Chart	
Chassis	Welded steel
Drive	2 brushless motors (rear)
Power	3.5 + 3.5 kW
Weight	500 kg
Max load	80 kg
Max velocity	60 km/h

rigidly connected to the wheel rim. On the contrary the stator, fixed on the hub, is characterised by several radial expansions with copper wire windings.

The chassis has been slightly modified to gain more space for the arrangement of the suspensions and of the wheels and to accommodate the battery packages under the driver seat. Certainly a tailored design of the chassis and of the front suspension system would bring substantial benefits to vehicle dynamic behaviour and cornering stability. The vehicle’s main technical characteristics are listed in Table 1.

### Multibody Model of the Vehicle

The development of a multibody model of the vehicle has been worked out in order to define suspensions type and size necessary to ensure a fine handling during competition tests: first attempt values for springs and dampers have been initially considered then they have been optimised after several analysis on roll and pitch dynamics of the vehicle.

Once the tires have been selected, with the technical characteristics listed in Table 2, it has been possible to evaluate the stiffness of both the front and rear suspensions: supposing that the tires stiffness and the sprung mass are significantly higher respectively than the springs stiffness and the unsprung mass, a mathematical quarter car model can be developed.

The assumption of a desirable body vibration rate  $f$  equal to 1 Hz, generally desirable for reasons of comfort [3], imposes that the springs stiffness  $k$  is:

$$k = \frac{m_s \cdot (2\pi f)^2 \cdot p}{p - m_s \cdot (2\pi f)^2} \tag{1}$$

**Table 2** Technical data of the tyre

Technical Chart	
Radius	275 mm
Damping constant	2 000 kg/s
Rolling resistance	0.02
Friction coefficient	0.9
Vertical stiffness	200 kN/m
Cornering stiffness	35 kN/rad

where  $m_s$  is the rate of the sprung mass and  $p$  is the global stiffness of the suspension.

The obtained values are  $k_{\text{front}} = 5250 \text{ N/m}$  and  $k_{\text{rear}} = 4500 \text{ N/m}$ , which satisfy the following desirable relations on indexes  $\eta$  and  $\rho$  [4]:

$$\eta = \frac{k_{\text{front}} \cdot a_{\text{front}}}{k_{\text{rear}} \cdot a_{\text{rear}}} < 1$$

$$\rho = \frac{J_{yy}}{m_{s\text{-tot}} \cdot a_{\text{front}} \cdot a_{\text{rear}}} < 1 \quad (2)$$

with  $a_{\text{front}} = 610 \text{ mm}$  and  $a_{\text{rear}} = 730 \text{ mm}$ , that indicates the position of the centre of mass with respect to the front and rear axles and  $J_{yy} = 200 \text{ kg} \cdot \text{m}^2$  being the moment of inertia around the pitch axis. The stiffness of the suspension can be increased according to relations (2) to the detriment of the vibration rate transferred to the car passenger; first attempt damping coefficients of the suspensions have been estimated from the optimal values of the tire's road vertical loading versus the frequency curve for a mathematical quarter car model, namely  $d_{\text{front}} = 1800 \text{ Ns/m}$  and  $d_{\text{rear}} = 1400 \text{ Ns/m}$ .

An augmented model has been built by the introduction of the radial compliance on the bearings between the hub and wheel rim, with the aim of estimating the electro-magnetic forces, affected by the magnetic gap between stator and rotor, which cause loading cycles on polar expansions and on the magnets. Their radial stiffness has been indirectly calculated from the weight of the sprung mass acting at the same time on the internal and external bearings of each wheel, assuming the same radial deformation for a pure vertical motion of the chassis:  $c_e = 72.93 \text{ N}/\mu\text{m}$  and  $c_i = 81.95 \text{ N}/\mu\text{m}$ . To assign the bearings an ordinary under-damped behaviour, the following damping characteristics have been imposed, making use of the expression of the critical damping for a typical mass-spring-damper system:  $C_e = 250000 \text{ kg/s}$  and  $C_i = 300000 \text{ kg/s}$ .

A non linear model of the tire, for instance with an empirical Magic Formula, should be considered between the slip angle and the tire's lateral force in order to improve the correctness of the model.

The front suspension is made up of independent longitudinal swing arms, namely forced to rotate around a transversal axis connected to the vehicle frame. The extension of the arms is limited because of the wide related change that they involve on the camber angles. At the lower extreme of the arms a revolute joint allows the wheel to rotate about an axis that moves on a plane designed to be tilted of 2 degrees with respect to a vertical plane; the swing arm is then supported by a spring-damper.

On the other hand, the rear suspension is made by two independent MacPherson struts with a swing arm rotating around a longitudinal axis and connected to the wheel hub by a spherical joint; therefore the wheel is supposed to rotate around the spring axis with small changes of the camber angle. In order to guarantee a good handling and preserve a good comfort during cruise, springs and dampers values of both the suspensions have been tuned up by analysing several simulation runs featuring different dynamic conditions.

## Finite Element Model of the Motors

The integration of electric motors inside the wheels entails an increase of the wheel's weight and on the contrary they undergo the dynamic loads due to the vehicle's motion. The complex state of stress perceived by motors is given by the sum of dynamic and magnetic loads.

Therefore a multiphysics analysis has been requested to investigate the magnetic torques and forces developed between the stator's polar expansions and the rotor's permanent magnets in order to evaluate the risk of their detachment. It is noted that magnetic forces depend on the magnetic gap and its continuous variation produces load cycles on mechanical parts. The weight of the vehicle and its vibratory dynamic behaviour tend to modify the clearance in the ball bearings and accordingly the magnetic forces.

In addition a Ansys modal analysis has allowed to identify the natural frequencies and modes of the stator, as a matter of fact, when the vehicle operates at working conditions the eigenfrequencies of motor's parts should not be excited.

Moreover a tailored 2D model of the motor, relative to the maximum magnetic gap configuration obtained by the multibody simulations, has allowed to quantify the magnetic torque and forces acting inside the motor: they represent the most severe operating conditions.

## Simulation Results

A virtual mock-up developed in the Virtual.Lab environment has allowed to modify the dynamic parameters set in the quarter car model with the aim of improving the cornering stability of the vehicle; it should be noted that the initially imposed values resulted from a vertical dynamic analysis of a single suspension, while a more complex dynamics is obtained by considering the coupling caused by car's chassis and the related pitch and roll movements.

Steady-state response to control inputs has been investigated; moreover understeer and oversteer behaviour of the vehicle with a wheelbase  $L$  at constant speed  $V$  has been assessed by measuring the understeer gradient  $K$ , the yaw rate  $r$  and the lateral acceleration  $a_y$  of the sprung mass for several steering angles, which are linked together by the following approximated formula [5]:

$$\delta = 57.3 \frac{L \cdot r}{V} + K \cdot a_y \quad (3)$$

with the first term on the right called *Ackerman steer angle gradient*. Steer angle has been incrementally increased until a new steady-state condition characterised by an increase of 0.05 g of lateral acceleration [6]. Figure 2 plots the resulting

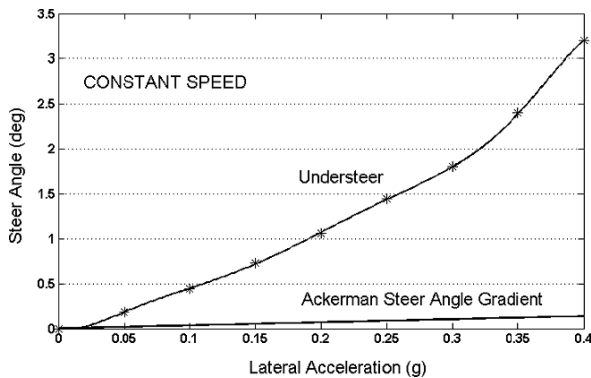


Fig. 2 Steer angle versus lateral acceleration curve

steer angle versus the lateral acceleration, demonstrating a tendency of the vehicle to understeer rather than oversteer justified by the higher value of the steer angle gradient with respect to that of the Ackerman steer. The initial understeer gradient for European cars should be between 1 and 3 deg/g, therefore springs stiffness and damping ratios of the shock absorbers have been increased to fit this requirement, favouring understeer rather than oversteer [7].

The optimal springs stiffness calculated from the multibody simulations,  $k_{\text{front}} = 12\,000$  N/m and  $k_{\text{rear}} = 11\,000$  N/m, causes an increase of the natural frequencies perceived by the chassis in relation to the previous lower values and of the corresponding optimal damping coefficients, yielding  $d_{\text{front}} = 2\,000$  Ns/m and  $d_{\text{rear}} = 1\,600$  Ns/m.

To evaluate vehicle's cornering behaviour, several sinusoidal paths cornering around differently spaced skittles have been simulated, always maintaining a constant linear velocity: it resulted that the chosen stiffness and damping coefficients yield a good road holding by limiting the variation of the tire vertical force in a range of few hundreds of Newtons. Moreover, by reducing the step of the sinusoid from 12 m down to 7 m the lateral acceleration increased but the vehicle demonstrated reasonable roll angles.

In parallel to the mentioned dynamic analyses of the whole vehicle, the natural modes of the motor's components have been investigated by means of an Ansys modal analysis: the lowest natural mode of 1 953 Hz results high enough to be filtered by tires [8]; moreover it refers to a bending mode as shown in Fig. 3, not directly excited by the radial dynamic loads.

Finally a torque of 40.1 Nm with a flux density of 2.1 T has been evaluated performing a Ansys magnetic analysis in relation to the most severe conditions [9], Fig.3: the radial forces of 580 N and 557 N corresponding respectively to maximum and minimum air gap of 5.05 mm and 4.95 mm between stator and rotor show no appreciable dependency on the measured magnetic gap changes.



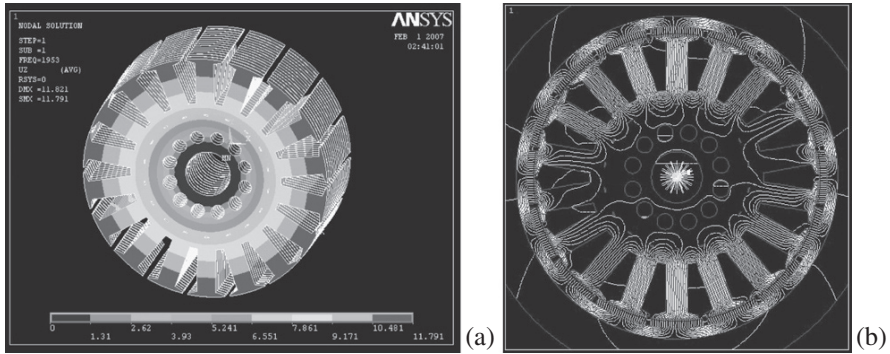


Fig. 3 First natural mode of the stator and magnetic flux streamlines

### Conclusion

A combined analysis of mathematical and multibody models of a road vehicle driven with two “in wheel” brushless motors and provided with four steering wheels has allowed to design the suspension system in such a way that a good handling for different steer inputs could be achieved. The increased weight of the unsprung masses of the rear suspensions did not represent a significant drawback within car operative conditions.

The performed analyses have also allowed to find out the dynamic stresses on the motors, providing information about the clearance between stator and motor. Furthermore a FE analysis has been executed in order to assess on the one hand the natural frequencies of the stator and on the other hand the magnetic stresses suffered by motor parts, showing a coherent design with the requested project specifics.

**Acknowledgments** A sincere thank to Eng. Luca Carbonari for his expertise and enthusiasm in performing the simulations.

### References

1. M. Callegari, M. Palpacelli, M. Principi. Dynamic Analysis of a Utility Car Driven By “In Wheel” Engines. Proc. of ECCOMAS Thematic Conference Multibody dynamics 2007, Milano, Italy, June 25–28, 2007.
2. A. A. Shabana. Dynamics of Multibody Systems. Cambridge University Press, 2nd Ed., 1998.
3. J. Reimpell, H. Stoll, J. Betzler. The Automotive Chassis: Engineering Principles. Butterworth-Heinemann, 2nd Ed., 2001.
4. M. Guiggiani. Dinamica del veicolo. Città Studi, 2007.
5. T. D. Gillespie. Fundamentals of Vehicle Dynamics. Society of Automorive Engineers (SAE), 1992.
6. D. A. Fittanto, A. Senalik. Passenger Vehicle Steady-State Directional Stability Analysis Utilizing EDVSM and SIMON. Engineering Dynamics Corporation and Daniel A. Fittanto, P.E., 2004.

7. J. K. Dixon. *Tires, Suspension and Handling*. SAE International, 2nd Ed., 1996.
8. N. D. Smith. *Understanding Parameters Influencing Tire Modeling*. Department of Mechanical Engineering, Colorado State University, 2004.
9. U. Kim, D. K. Lieu. Effects of Magnetically Induced Vibration Force in Brushless Permanent-Magnet Motors. *IEEE Transactions on Magnetics*, 41(6), 2164–2172, 2005.

# Dynamic Modelling of a Single – Link Flexible Arm to be Used as a Sensing Antenna

Javier Guerra Fernández, Vicente Feliu Batlle  
and Miguel Ángel Caminero Torija

**Abstract** The objective of this research is to design a sensing antenna, a robot based on a single – link flexible arm which will enable us to locate a contact position with an object in order to detect the precise shape of that object. In the first approach, this paper focuses on the dynamics of a single-link flexible arm. It was designed under the assumption that its mass was concentrated at the tip. A comprehensive dynamic model for the arm is derived with the Lagrangian Formulation in which the elastic characteristics of the arm are modeled using the Euler-Bernoulli beam theory and simulated using Matlab/Simulink®. The governing equations of the model are nonlinear. A finite element model of the single-link flexible arm was developed and the deflection of the tip was determined in order to be compared with the theoretical solution and simulation.

**Keywords** Flexible arm · Dynamic modelling · Nonlinear system

## Introduction

Antennas are important mechanic – sensory organs. An antenna will rotate or bend as forces act upon it, and its sensory capabilities will therefore be influenced by its mechanical properties (such as stiffness). A deflection torque, applied to the base, can be measured with sensors and the tip point can be determined. From a mechanical point of view, insect antennae are cantilever beams [1].

There are many papers discussing antenna type sensor. Kaneko et al. [2] use the measured compliance of an active antenna consisting of an insensitive beam, actuators, position sensors, and a two-axis moment sensor to determine the contact length. Ueno et al. [3] design a dynamic antenna that measures the whisker vibration via a torque sensor to determine contact length. In Ref. [4], Scholz and Rahn used

---

J.G. Fernández (✉)

Departamento de Ingeniería Eléctrica, Electrónica y Automática, ETS Ing. Industriales,  
Universidad de Castilla – La Mancha, Avda. Camilo José Cela,  
s/n 13071 Ciudad Real, Spain  
e-mail: Javier.Guerra@uclm.es

an actuated whisker sensor to determine the contacted object profiles for underwater vehicles. This whisker sensor predicted contact point based on the measured hub forces and torques with a planar elastic model. Wijaya et al. has developed a sensor array [5] by mounting whisker sensors on a mobile robot, and in the same way, Fend et al. [6] have developed an active multi-whisker array modelled on the rat whisker system. Recently, Bebek et al. [7] presented a whisker sensor design to measure the heart motion in three dimensions.

This sensing antenna can find many applications but its main problem is to control their vibration. In order to account for the flexibility of the robot arm, many modelling methodologies have been proposed. The most common techniques used to model such systems are the Newtonian, Lagrangian, Hamiltonian methods and most recently, a finite element analysis of a rotating flexible cantilever beam with commercial FEM software [8].

In the present study, a Lagrangian formulation is employed to derive the motion equations [9] and elastic characteristics are modeled using Euler – Bernoulli beam theory [10]. In this paper, the vibration analysis of several very flexible beams with deflections using the finite element approach is implemented to compare with the theoretical solution.

## Basic Structure

The structure of the flexible arm considered in this study is presented in Fig. 1. It consists of a single link flexible arm and two motors. Hence, this arm has two degrees of freedom in rotation. The first motion produces an azimuthal movement and the second motion produces an elevation movement. A local three – dimensional

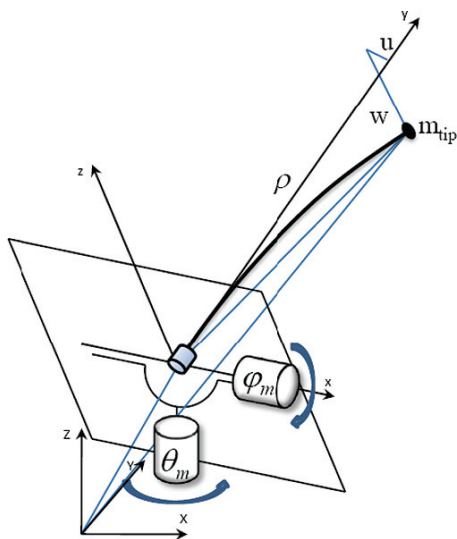


**Fig. 1** Single flexible – link flexible arm

**Table 1** Mechanical features and dimensions of the structure

Parameter	Notation	Value
Length	$l$ (mm)	300
Sectional area	$A$ (mm × mm)	3.1416
Young module	$E$ (N/m <sup>2</sup> )	$6.6847 \times 10^{10}$
Inertia moment	$I$ (m <sup>4</sup> )	$3.63 \times 10^{-9}$
Density	$\rho$ (kg/m <sup>3</sup> )	2698
Tip mass load	$m_{tip}$ (kg)	$\sim 2m_{link}$

coordinate is assigned to the flexible arm, and the coordinate’s origin is located at the arm’s joint.

The arm was designed of aluminum bar whose most important mechanical features are presented in Table 1. Aluminum was considered for its low flexibility and lightweight. Hence, as the deflections become small, we can use the next method. Its tip mass is substantially greater than the arm mass, and hence a one – lumped – mass model is accurate enough. Experimental results have validated this assumption. Next, the model of the single – link flexible arm is developed.

### Dynamic Modelling of the Single – Link Flexible Arm

Dynamics robot models describe the relations between the motions of the robot and the forces that cause the motions. The flexible arm is assumed as an Euler–Bernoulli beam. The length of the flexible arm is assumed to be constant, and deformation due to shear, rotary inertia and the effects of axial force are neglected. It was designed under the assumption that its mass was concentrated at the tip. Since, Lagrange’s equation of motion is used in obtaining the equations of motion and where energy terms have to be evaluated.

Let us define a tip point as  $P_{tip} = (\rho\theta_1, \varphi_1)^T$  where  $\theta_1$  is the azimuthal angle,  $\varphi_1$  is the elevation angle and  $\rho$  denotes the tip radius.  $(XYZ)$  is the global reference frame, while  $(xyz)$  is the local frame. These spherical coordinates can be expressed in a Cartesian frame as:

$$\begin{aligned}
 x &= \rho \cos\varphi_1 \cos\theta_1 \\
 y &= \rho \cos\varphi_1 \sin\theta_1 \\
 z &= \rho \sin\varphi_1
 \end{aligned}
 \tag{1}$$

Differentiating (1) with respect to time we obtain the tip speed expresses in spherical coordinates:

$$v_{tip} = \begin{pmatrix} v_\rho \\ v_\theta \\ v_\varphi \end{pmatrix} = R \cdot \begin{pmatrix} v_x \\ v_y \\ v_z \end{pmatrix} = \begin{pmatrix} \dot{\rho} \\ \rho \cos\varphi_1 \cdot \dot{\theta}_1 \\ \rho \dot{\varphi}_1 \end{pmatrix} = \begin{pmatrix} 0 \\ \rho \cos\varphi_1 \cdot \dot{\theta}_1 \\ \rho \dot{\varphi}_1 \end{pmatrix}
 \tag{2}$$

Radial speed is considered neglected because the length of the flexible arm was assumed to be constant and where that transformation matrix  $R$  is defined as:

$$R = R(y, -\varphi_1) \cdot R(z, \theta_1) = \begin{pmatrix} \cos \varphi \cos \theta & \cos \varphi \sin \theta & \sin \varphi \\ -\sin \theta & \cos \theta & 0 \\ -\sin \varphi \cos \theta & -\sin \varphi \sin \theta & \cos \varphi \end{pmatrix} \quad (3)$$

By using obtained velocity terms, kinetic energy of the flexible flexible arm can be evaluated, where the kinetic energy of the tip payload is

$$T_m = \frac{1}{2} m v_{\text{tip}}^T v_{\text{tip}} \quad (4)$$

Potential energy due to flexible deformations is written as sum of the elastic potential energy of the flexible link due to bending

$$V_d = V_{d1} + V_{d2} = \int_0^l \frac{1}{2} E I u'' dx + \int_0^l \frac{1}{2} E I w'' dx \quad (5)$$

where the arm's bending deflections with respect to their local co – ordinates are denoted by  $u$  and  $w$ . These deflections are detailed in Appendix A.

And the gravitational potential energy

$$V_g = \frac{3}{2} m g l \sin \varphi_1 \quad (6)$$

Where the Lagrangian is defined as

$$\zeta = (T_m + T_{\text{mot}}) - (V_{d1} + V_{d2} + V_g) \quad (7)$$

Therefore, the Euler-Lagrange equations can be applied to  $\zeta$  to find the equations of motion given by

$$\frac{d}{dt} \frac{\partial \zeta}{\partial \dot{q}_i} - \frac{\partial \zeta}{\partial q_i} = \frac{\partial w^{nc}}{\partial q_i} = \Gamma_i \quad (8)$$

With the generalized coordinate vector  $q_i = [\theta_1 \ \varphi_1]^T$  and the input vector  $\Gamma_i = [\theta_m \ \varphi_m]^T$ .  $\theta_m$  and  $\varphi_m$  are the motor angles. The dynamics equations of the flexible arm are derived substituting equation (7) into (8) and given as follows:

$$m l^2 \cos^2 \varphi_1 \cdot \ddot{\theta}_1 = -\frac{3 E I}{l} (\theta_1 - \theta_m) \quad (9)$$

$$\left( \frac{1}{2} \sin(2\varphi_1) \cdot \dot{\theta}_1^2 + \ddot{\varphi}_1 \right) = -\frac{3 E I}{m l^3} (\varphi_1 - \varphi_m) + \frac{3 g}{2 l} \cos \varphi_1$$

### Simulating

In this section, the development of an interactive environment for simulation systems has been used. Sinoidal track is used as system input for both movements. Instability of the tip position is observed in Fig. 2 with regard to the wished position given by the engine angles, state that it is possible to see also for the vertical movement in the same figure.

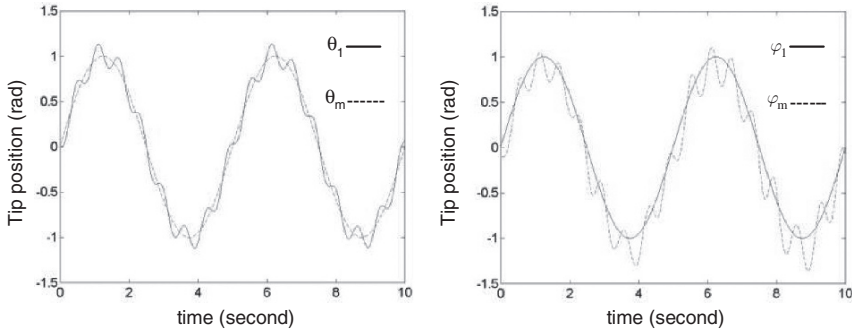


Fig. 2 Tip position. Simulation results

### Validation by a Finite Element Method

The dynamics of flexible bodies can be simulated by using the finite element method (FEM), which is the most common of the numerical approaches available for solving geometric nonlinearities.

The object is to investigate the nonlinear vibration problem of a uniform cantilever beam undergoing very large deflection. The motion of flexible beam is simulated by using the ADINA Finite Element program, which solves the problem by direct integration of the nonlinear equations of motion, Fig. 3. This analysis can

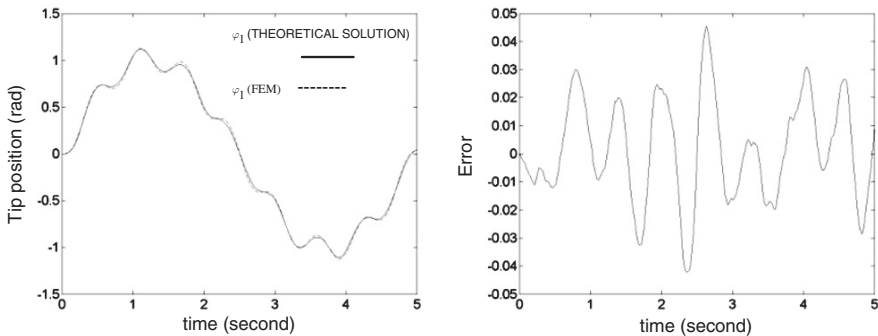


Fig. 3 Simulation results of a single flexible – link flexible arm with commercial FEM software

be used to determine the time-varying displacements. A three-dimensional elastic beam element was used to model the flexible structure.

### Appendix A

Our considered arm, see Fig. 4, is composed of two motors at the base, a flexible beam, length  $l = \rho$  and a payload of mass  $m_{tip}$ . The motor angles are denoted  $\varphi_m$  and  $\theta_m$ . A non-inertial frame  $(xyz)$  rotates with the motor and the overall structure rotates in an inertial frame  $(XYZ)$ .

For system modelling, the following assumptions are made: (1) the Euler-Bernoulli beam theory can be used to model the elastic behaviour of the flexible arm, and the axial deformation due to the centrifugal force can be omitted; (2) the gravitational effects cannot be ignored in the vertical direction. The mechanical part of the dynamics of the distributed mass single-link flexible manipulator can be approximated by a one lumped mass model [11].

This method is based on the assumption that the mass of the beam is concentrated in the tip. The link between motor and the tip is considered to be of negligible mass.

The deflection,  $w$ , is represented by the Euler-Bernoulli relation:

$$\frac{d^{IV}w(x)}{dx^{IV}} = 0 \tag{10}$$

$EI$  being the stiffness of the beam. The deflection is given by the third-order polynomial

$$w(x) = a_0 + a_1x + a_2x^2 + a_3x^3 \tag{11}$$

where  $a_i$  are the polynomial coefficients. To obtain these coefficients, we impose the continuity conditions. In addition, this set of equations is completed by expressing deflections at the point where the lumped mass is located in terms of these coefficients.

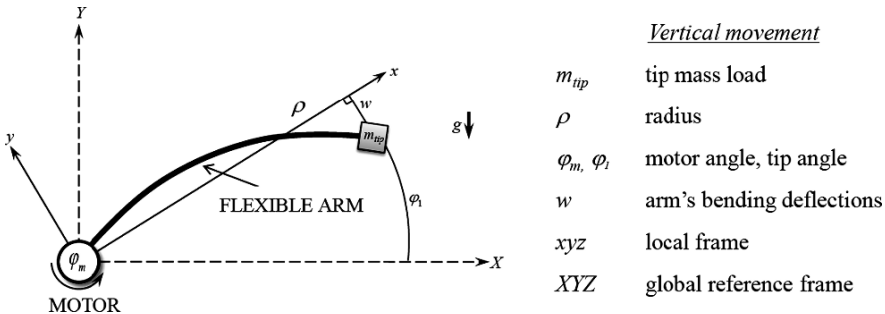


Fig. 4 One lumped mass flexible beam



$$\begin{aligned}
w(0) &= 0 \\
w'(0) &= 0 \\
EIw''(x) &= 0 \\
EIw'''(x) &= m\ddot{w}(L)
\end{aligned} \tag{12}$$

Where we use  $(\cdot)$  and  $(\prime)$  to denote  $\partial/\partial t$  and  $\partial/\partial y$ , respectively. Considering (11) and, after some algebraic manipulations, the following equation is obtained:

$$w(x) = \frac{3}{2l^2}w(L)x^2 - \frac{1}{2l^3}w(L)x^3 \tag{13}$$

And the elastic potential energy in the vertical movement is

$$V_{d1} = \frac{3EI}{2l}(\varphi_1 - \varphi_m)^2 + \frac{3}{2}T_1 \tag{14}$$

Where  $T_1$  is the torque produced at the base of the flexible arm by the tip mass and  $w$  is defined as:

$$w = (\varphi_1 - \varphi_m)l \tag{15}$$

This result is similar to horizontal deflection. However, the gravitational effects can be ignored. Therefore, the elastic potential energy in the horizontal movement is given as:

$$V_{d2} = \frac{3EI}{2l^3}u^2(l) = \frac{3EI}{2l}(\theta_1 - \theta_m)^2 \tag{16}$$

## Conclusions and Future Works

In this work, the single-link flexible arm has two degrees of freedom for rotations. That flexible arm can bend freely in the horizontal and vertical plane. The governing equations of the system, which have been derived rigorously, are nonlinear. A finite element model of the single-link flexible arm was developed and the deflection of the tip was determined in order to be compared with the theoretical solution and simulation.

In future research, the vibration analysis of highly flexible antenna with larges deflections will be studied. The objective of this future study is the application of metal matrix composites to our sensing antenna. Finally, our project will be to build it. It is hoped that this design will demonstrate that sensor antenna can be used as a practical robot sensor in environments that will not allow the use of conventional visual or ultrasonic sensors.

## References

1. Loudon, C. Flexural stiffness of insect antennae. *American Entomologist*, 2005, 51(1):49–51.
2. Kaneko, M., Kanayama, N. and Tsuji, T. Active antenna for contact sensing. *IEEE Transactions on robotics and automation*, 1998, 14(2):278–291.
3. Ueno, N., Svinin, M. and Kaneko, M. Dynamic contact sensing by flexible beam. *IEEE/ASME Transactions on Mechatronics*, 1998, 3(4).
4. Sholz G. R. and Rahn, C. D. Profile sensing with an actuated whisker. *IEEE Transactions on Robotics and Automation*, 2004, 20:124–127.
5. Wijaya, J. and Russell, R. A. Object exploration using whisker sensor. *Australasian Conference on Robotics and Automation*, 2002.
6. Fend, F., Yokoi, H. and Pfeifer R. Optimal morphology of a biologically-inspired whisker array on an obstacle-avoiding robot. No. 1, February 2004, pp. 124–127.
7. Bebek, O. and Cenk M. Whisker sensor design for three dimensional position measurement in robotic assisted beating heart surgery. *IEEE International Conference on Robotics and Automation*, 2007.
8. Fotouhi, R. Dynamic analysis of very flexible beams. *Journal of Sound and Vibration*, 2007, 305:521–533.
9. Low, K. L., Vidyasagar, M. A Lagrangian formulation of the dynamic model for flexible manipulator systems, *ASME Journal of Dynamic System Measurement, and Control*, 1988, 110:175–181.
10. Feliu, V., Rattan, K. S. and Brown, H. B. A new approach to control single-link flexible arm. Part I: modelling and identification in the presence of joint friction. *The Robotic Institute, Carnegie Mellon University, Pittsburgh, Pennsylvania 15213*, 1989.
11. Feliu, V., Rattan, K. S. and Brown, H. B. Modelling and control of single-link flexible arms with lumped masses, *ASME Journal of Dynamic Systems, Measurement, and Control*, 1992, 114:59–69.

# Method of Dynamic Analysis of Mechanisms of Variable Structure

Assylbek Jomartov and Z.G. Ualiyev

**Abstract** In work dynamics of MVS (mechanisms of variable structure) with geometrical constraints which form wide enough class most frequently used mechanisms in mechanical engineering is investigated. In this connection research of MVS with geometrical constraints represents the big interest from the point of view of the theory and their practical application.

Reorganization of structure of MVS occurs to geometrical constraints at achievement by some functions of the generalized coordinates of the certain values.

For drawing up of the equation of movement of MVS with elastic parts we use a method of stiff penalty function in the dynamic analysis of mechanisms with elastic parts.

**Keywords** Dynamic analysis · Mechanisms of variable structure · Elastic parts · Stiff penalty function

## Introduction

Mechanisms of variable structures (MVS) that during the operation change their structure are widespread in the machine industry, i.e. rapid change of links number, kinematic pairs or their mobility, geometrical sizes, inertial and elastic parameters, kinematic transfer functions, etc. occurs at operation of MVS. Classification [1], of the MVS is developed based on features of constraints, kinematic and dynamic properties of mechanisms and functional characteristics.

In this classification features of mechanisms are shown as features of dynamic objects built on the basis of mathematical models of their dynamic systems. From this points of view the MVS form an extensive class included in mechanisms with nonlinear properties, i.e. dynamic models of such mechanisms can be described by piecewise-linear or piecewise-nonlinear differential equations. In the work [1]

---

A.A. Jomartov (✉)

Institute of Mechanics and Machine Sciences, Valikhanov st. 106,  
050010 Almaty, Republic Kazakhstan  
e-mail: legsert@mail.ru

it is shown a classification scheme of basic varieties of MVS made on the basis of properties generality of their dynamic systems. In this classification features of links and reduced parameters of mechanisms, their functionalities, etc are taken into account within certain limits.

From this classification we shall examine basically mechanisms of MVS with geometric constraints. MVS with geometric constraints form enough wide class of most frequently used mechanisms in the machine industry. Therefore research of MVS with geometric constraints has the big interest from the point of view of the theory and their practical application.

Structure reconstruction of MVS with geometric constraints occurs at reaching defined values by some functions of generalized coordinates.

## A Classical Methods at the Dynamic Analysis of MVS

To form motion equations of MVS with geometric constraints on section of constant structure it is possible to use the known equations of Lagrange [1] [2]

$$\frac{d}{dt} \left( \frac{\partial T}{\partial \dot{q}_j} \right) + \frac{\partial V}{\partial q_j} + \frac{\partial V}{\partial q_j} = Q_j + \sum_{i=1}^n \lambda_i h_{ij} \quad (j = 1, 2, \dots, m+n), \quad (1)$$

$$\sum_{j=1}^{m+n} h_{ij} \dot{q}_j + h_i = 0, \quad (i = 1, 2, \dots, n) \quad (2)$$

where  $m$  – generalized coordinates  $q_1, q_2, \dots, q_m$ ,  $n$  – redundant coordinates,  $\lambda_i$  – Lagrangian coefficients,  $h_{ij}$  – some functions.

In the formula (1)  $T$  – kinetic energy of the holonomic system,  $V$  – potential energy of system,  $Q_j$  – generalized forces.

Principal feature at formulation of the motion equations of MVS is that at change of MVS structure there is a rupture of some functions at the reconstruction moment.

These functions can be transfer functions of the mechanism, reduced moments of inertia, forces, the moments of forces, etc.

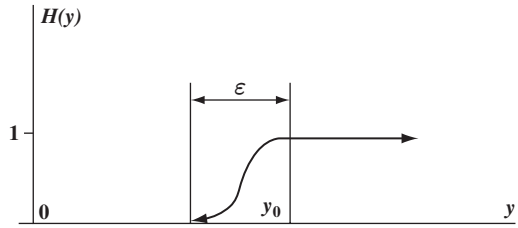
Rupture of the above-stated functions is presented by the following ratio:

$$\Delta f_i(q_k) = f_i(q_k - 0) - f_i(q_k + 0) \quad (3)$$

where  $q_k$  – value of the generalized coordinate at which the MVS structure is changed.

Motion of MVS is presented by the differential equations with discontinuous coefficients. For dynamic research of MVS we shall model ruptures in the motion equations with the help of symmetric Hevisaid step function of  $H(y)$  which is determined as follow

**Fig. 1** The transition width



$$H(y) = \begin{cases} 0, & y < 0, \\ \frac{1}{2}, & y = 0, \\ 1, & y > 0. \end{cases} \tag{4}$$

For approximation of Hevisaid step function it is used the following representation of the step-function offered in the work [3], where

$$H(y) = \frac{1}{2} \frac{|y|^{2n+1} + y^{2n+1}}{|y|^{2n+1} + \frac{1}{2} [|y - \varepsilon|^{2n+1} - (y - \varepsilon)^{2n+1}]} = \begin{cases} 0, & y \leq 0, \\ 1/2, & y = \varepsilon/2 \\ 1, & y \geq \varepsilon \end{cases} \tag{5}$$

where  $\varepsilon > 0$  is the transition width (Fig. 1),  $n$  – is selected from a continuity condition of a derivative of  $d$  according to inequality  $2n + 1 > d$ .

The basic advantage of this function is that the width of the transition region is defined and does not influence a value outside of the transition region; moreover there is an opportunity of derivation. Width of a transition zone  $\varepsilon$  is selected basically from physical reasons and by holding an experiment, besides the smaller zone of transition demands more calculating time, and the larger zone can define a physical process.

Then using the formula (5), any rupture function (Fig. 2) can be presented as follow:

$$f(x) = (1 - H(x - x_0)) \cdot f_1(x) + H(x - x_0) f_2(x) \tag{6}$$

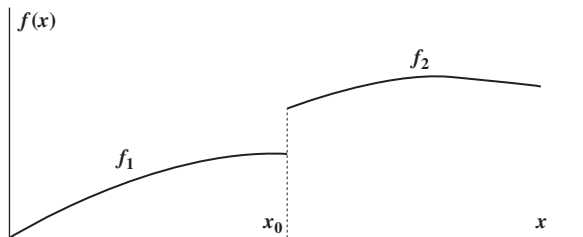


**Fig. 2** The rupture function

## A Method of Stiff Penalty Function at the Dynamic Analysis of MVS [3]

To form the motion equation of MVS with elastic constraints we use a method of stiff penalty function at the dynamic analysis of mechanisms with elastic links [4]. We can find the following functional

$$A = \int_{t_1}^{t_2} L dt + \int_{t_1}^{t_2} W dt + \int_{t_1}^{t_2} \sum_{k=1}^{m-n} \lambda_k S_k dt \quad (7)$$

where  $L = T - V$ -function of Lagrange,  $T, V$  – kinetic and potential energy of system accordingly;  $W = W(q_j, t)$  – operation of nonconservative forces;  $Q_j$  – generalized forces;  $q_j (j = 1, 2, \dots, m)$  – full set of generalized coordinates;  $n$  – degrees number of system freedom,  $\lambda_k$  – Lagrangian coefficients;

$$S_k(q_j, t) = 0, \quad (k = 1, \overline{m-n}) \quad (8)$$

– equations of holonomic constraints of mechanical system.

Applying the Hamilton's principle [4] and equating the first variation of the functional  $A$  we can find the following:

$$\frac{d}{dt} \left( \frac{\partial L}{\partial \dot{q}_j} \right) - \frac{\partial L}{\partial q_j} - \sum_{k=1}^{m-n} \lambda_k \frac{\partial S_k}{\partial q_j} = Q_j \quad (9)$$

Method of stiff penalty function will consist in adding of following fictitious potential to expression of the Hamilton's principle

$$V^* = \sum_{k=1}^{m-n} \frac{1}{2} \alpha_k S_k^2 \quad (10)$$

where  $\alpha_k$  – penalty coefficient.

Expressions for the functional have the following form:

$$A^* = \int_{t_1}^{t_2} L dt + \int_{t_1}^{t_2} W dt - \int_{t_1}^{t_2} \sum_{k=1}^{m-n} \frac{1}{2} \alpha_k S_k^2 dt \quad (11)$$

In the work [5] it is shown the solution of the equation  $\delta A^* = 0$  coincides with solution of the initial task  $\delta A = 0$  at  $\alpha_k \rightarrow \infty$ .

The first variation of the functional (11) results in the following ordinary differential equations  $m$

$$\frac{d}{dt} \left( \frac{\partial L}{\partial \dot{q}_j} \right) - \frac{\partial L}{\partial q_j} + \sum_{k=1}^{m-n} \alpha_k S_{\hat{e}} \frac{\partial S_k}{\partial q_j} = Q_j \tag{12}$$

At the big values  $\alpha_k \rightarrow \infty$  the dynamic equilibrium of the system (12) is possible only, if  $S_{\hat{e}} = 0$ .

MVS are of special interest that contains the constraints described by the following equations

$$S_{\hat{e}} = P_{\hat{e}}(q_j) - q_i = 0$$

where  $P_{\hat{e}}(q_j)$  – functions of mechanisms positions.

The equation (12) is convenient for investigation of MVS with geometric constraints as it do not contain second derivatives from position function, which are not defined in the change point of the kinematic structure.

Disadvantage of this method is that there are problems at solution of the equations (12) connected to the numerical stiffness as penalty factors effect on force members instead of on accelerations that are initial variables of the equation (12).

To overcome these problems it is possible to apply at calculation a fine pitch of integration or to use special numerical solution methods of differential equations with numerical stiffness such as Gear method and others.

### An Example

Let's consider as an example the cam-lever mechanism of variable structure Fig. 3. We shall make for the given mechanism dynamic model Fig. 4.

Let's accept besides the independent generalized coordinates

$$q_1 = \varphi_1, q_2 = \varphi_2 - \varphi_1, q_3 = \varphi_4 - \varphi_3$$

and one superfluous coordinate  $q_4 = \varphi_3$ .

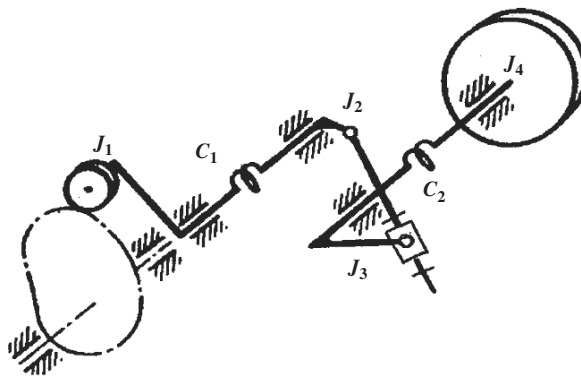


Fig. 3 The cam-lever mechanism of variable structure

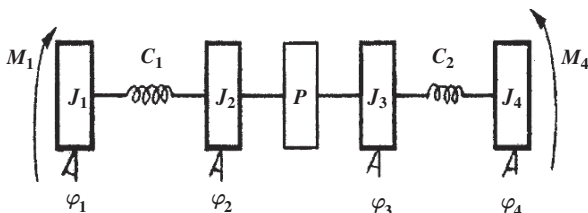


Fig. 4 Dynamic model

The equations of connection for the mechanism

$$S_1 = P(q_1 + q_2) - q_4 = 0$$

Kinetic and potential energy of system

$$T = \frac{1}{2} [J_1 \dot{q}_1^2 + J_2 (\dot{q}_1 + \dot{q}_2)^2 + J_3 \dot{q}_4^2 + J_4 (\dot{q}_3 + \dot{q}_4)^2]$$

$$V = \frac{1}{2} (c_1 q_2^2 + c_2 q_3^2)$$

Let's define functions  $\frac{\partial S_1}{\partial q_j}$ ,  $j = \overline{1, 4}$

$$\frac{\partial S_1}{\partial q_1} = P'(\varphi_2); \quad \frac{\partial S_1}{\partial q_2} = P'(\varphi_2); \quad \frac{\partial S_1}{\partial q_3} = 0; \quad \frac{\partial S_1}{\partial q_4} = -1$$

Let's substitute in the equation (6) we shall receive the equations of dynamics of the cam-lever mechanism of variable structure

$$(J_1 + J_2)\ddot{q}_1 + J_2\ddot{q}_2 = Q_1 - \alpha S_1 P'$$

$$J_2\ddot{q}_2 + J_2\ddot{q}_2 + \tilde{n}_1 q_2 = Q_2 - \alpha S_1 P'$$

$$J_4\ddot{q}_3 + J_4\ddot{q}_4 + \tilde{n}_2 q_3 = Q_3$$

$$J_4\ddot{q}_3 + (J_3 + J_4)\ddot{q}_4 = Q_4 + \alpha S_1$$

Here  $\alpha$  penalty coefficient,  $P$  – function of position,  $P'$  – the transfer function  $P''$  – the second transfer function Fig. 5.

Let's define the generalized forces, for this purpose we shall make the equations of works on possible movings

$$\delta W = M_1 \delta \varphi_1 + M_4 \delta \varphi_4 = M_1 \delta q_1 + M_4 \delta q_3 + M_4 \delta q_4$$

$$Q_1 = M_1, \quad Q_2 = 0, \quad Q_3 = M_4, \quad Q_4 = M_4$$



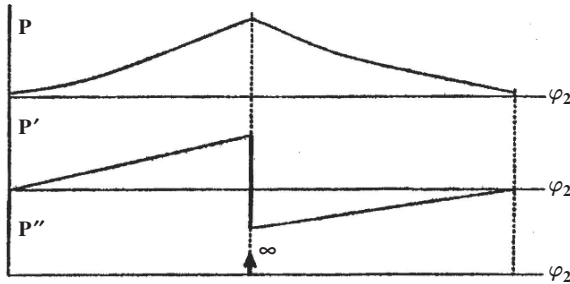


Fig. 5 Transfer functions

## Conclusion

The methods of the dynamic analysis of MVS with geometric constraints considered in the paper can be divided into two:

- the first method is classical and lies in application of different approximations of Hevisaid's step-function for discontinuous parameters of MVS with following application of standard numerical integration methods of differential equations. Disadvantage of this method is insufficiently exact reflecting of MVS dynamic at the moment of sudden change of parameters;
- the second method lies in use of stiff penalty function. Disadvantage of this method is problems with numerical stiffness at integration of the differential equations.

A method of stiff penalty function at the dynamic analysis of MVS is to be preferred than classical method because it's do not contain second derivatives from position function, which are not defined in the change point of the kinematic structure.

## References

1. Kozhevnikov S.N. Classification of mechanisms with variable structure. Analysis and systematization of models. Report No.01811013750. Institute of mechanics AS Ukrainian SSR, Kiev, 1982.
2. Woolfson I.I. Dynamic calculations of cyclic mechanisms. L.: Machine industry, Leningrad, 1976.
3. Dzhomartov A., Ualiyev G. Mechanisms dynamic of variable structure with geometric constraints. 12th IFToMM World Congress, Besançon (France), June 18–21, 2007.
4. Beyo E. Serna M.A. Methods of penalty functions in the dynamic analysis of mechanisms with elastic links. In Z. Current machine industry, Series B No. 4. M.: Publishing house "Mir", 1990, pp. 79–86.
5. Eel R.E. and Hog E.Zh. Method of logical functions for the dynamic analysis and analysis of constructions responsively of mechanical systems with discontinuous motion. In Z. Design and manufacturing engineering, No. 1.-M.: Publishing house "Mir", 1982, pp. 11–20.

# A Contribution to the Synthesis of a Trihedral Conjugate Cam

Miroslav Václavík and Zdeněk Koloc

**Abstract** A trihedral conjugate cam is a triple mechanism with forced constraint between the driving link and the driven link, whose cam active surface is formed from circular arcs connected to each other and the active surface of the driven link is created from two parallel planes. This mechanism is simple as to its design and it is often used for generating a motion with two rest positions, however, its disadvantage is unsuitability for higher working velocities caused by the discontinuous curvature of the cam active surface. Those discontinuities can be eliminated by changing law of motion when preserving the forced contact of the single active cam profile with the driven link. In the paper there are given the conditions for functions meeting the mentioned requirements. The properties of this solution are illustrated by comparing with the original cam with circular arcs.

**Keywords** Kinematics · Mechanism design · Cam Mechanism

## Introduction

The trihedral conjugate cam is a triple mechanism with forced constraint between the driving link and the driven link [1–3]. The active cam surface is formed from circular arcs connecting to each other and two parallel planes are the active surfaces of the driven link. Larger use of this mechanism with simple design is limited by its unsuitable properties at higher working velocities caused by the discontinuities of cam active surface curvature. To eliminate this disadvantage, a new form of active surface of the driving link has been proposed.

---

M. Václavík (✉)

Research Institute of Textile Machines Liberec, Plc., U Jezu 525/4, 461 19 Liberec, Czech Republic  
e-mail: miroslav.vaclavik@vuts.cz

### Law of Motion Properties

As a law of motion we will indicate function  $n(\tau)$  where  $n$  means the normal distance of the planar active surface of the driven link from cam axis of rotation  $O$  and  $\tau$  determines the angle between that normal and the origin on the cam.

As to Fig. 1, active surfaces of the driven link are designated as  $a$  or  $b$ , corresponding feet of perpendiculars as  $A$  or  $B$  and quantity  $l$  indicates groove width.

As the angular pitch of points  $A, B$  equals to straight angle, the sum of the normal lines of those points equals to the groove width.

When designing the cam it is possible to choose the form of function  $n(\tau)$  in interval  $(\tau \in < 0, \pi)$  then and function values in the next interval  $\tau \in < \pi, 2\pi)$  will emerge from the relation

$$n(\tau + \pi) = 1 - n(\tau). \tag{1}$$

Continuity of function  $n(\tau)$  in interval  $(\tau \in < 0, 2\pi)$  requires continuity  $n(\tau)$  for  $\tau \in < 0, \pi)$  and condition  $n(\pi) = 1 - n(0)$ . Similar requirements must be also met by higher derivations of function  $n(\tau)$  in interval  $(\tau \in < 0, \pi)$  and conditions for arguments  $0$  or  $\pi$ .

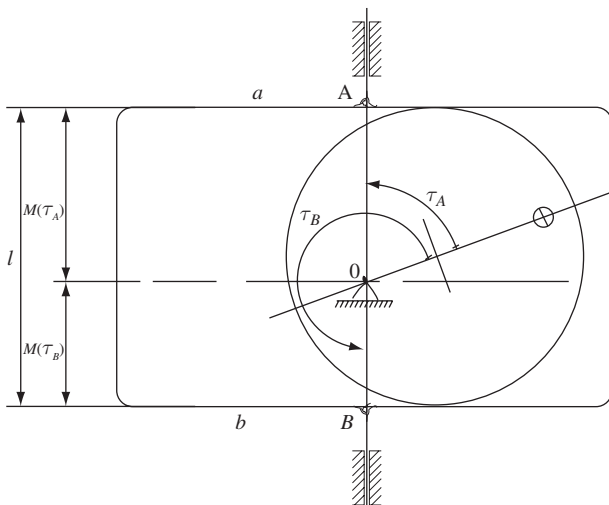


Fig. 1 Mechanism scheme

### Cam with Circular Arcs

As an example we will use a cam with an active surface formed from six cylinder segments as to Fig. 2.

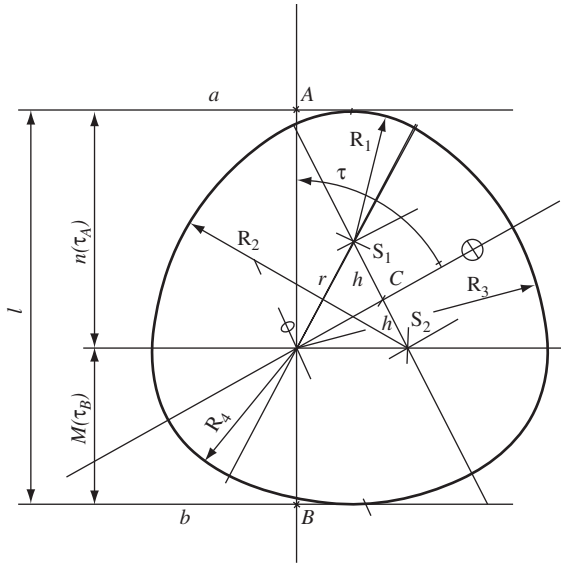


Fig. 2 Cam with circular arcs outline

The cam is symmetrical along the axis containing axis of rotation  $O$  and point  $C$  which halves the distance between arc centres  $S_1, S_2$ . The distance of active surfaces  $a, b$  of the driven link is  $l = 24$  mm, circle radii  $R_1 = 8$  mm,  $R_2 = 16$  mm. Other dimensions are  $p = 7.5$  mm and  $h = 4$  mm. The corresponding law of motion  $n(\tau)$ , Fig. 3 has normal angle  $\tau$  measured from the cam symmetrical axis in positive sense.

Normal line size  $n(\tau)$  is in limits  $R_4 = 8.5$  mm up to  $R_3 = 15.5$  mm, the shape of the law of motion is regarding angle  $\tau = \pi$  symmetrical, courses of the first and the second derivation of this function are given in Figs. 5 and 6.

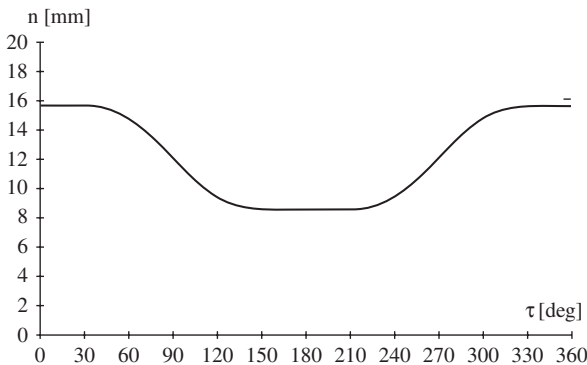


Fig. 3 Law of motion of the cam with circular arcs

### A Cam with Polynomial Law of Motion

To approximate the original cam with circular arcs we will use six polynomial segments of identical angular interval  $\pi/3$ . When choosing the seventh degree of particular polynomials we can achieve the continuity of law of motion up to the third derivation inclusive.

When preserving the limit values of law of motion  $n_{\min} = 8.5$  mm and  $n_{\max} = 15.5$  mm as well as length  $l = 24$  mm, we will choose boundary values in the first half of the revolution as follows:

$$\begin{aligned}
 n(0) &= 15.5 & n(\pi/3) &= n_1 & n(2\pi/3) &= l - n_1 \\
 n'(0) &= 0 & n'(\pi/3) &= n'_1 & n'(2\pi/3) &= n'_1 \\
 n''(0) &= 0 & n''(\pi/3) &= n''_1 & n''(2\pi/3) &= -n''_1 \\
 n'''(0) &= 0 & n'''(\pi/3) &= 0 & n'''(2\pi/3) &= 0
 \end{aligned}
 \tag{2}$$

In the second half of the revolution, those boundary values will emerge from the geometric constraint:

$$\begin{aligned}
 n(\pi) &= 8.5 & n(4\pi/3) &= l - n_1 & n(5\pi/3) &= n_1 \\
 n'(\pi) &= 0 & n'(4\pi/3) &= -n'_1 & n'(5\pi/3) &= -n'_1 \\
 n''(\pi) &= 0 & n''(4\pi/3) &= -n''_1 & n''(5\pi/3) &= -n''_1 \\
 n'''(\pi) &= 0 & n'''(4\pi/3) &= 0 & n'''(5\pi/3) &= 0
 \end{aligned}
 \tag{3}$$

Quantities  $n_1 = 14.65$  mm,  $n'_1 = -3.25$  mm.rad<sup>-1</sup>,  $n''_1 = -8$  mm.rad<sup>-2</sup> were determined so that they minimize the deviation of this law of motion from the original one. The difference between the laws of motion for polynomials  $n_p$  and for circular arcs  $n_k$  is given in Fig. 4. The maximum absolute value of this difference is 0.0873 mm.

A comparison of the first or second derivations of both laws of motion is given in Fig. 5 or 6. The first derivation for circular arcs is a continuous broken function

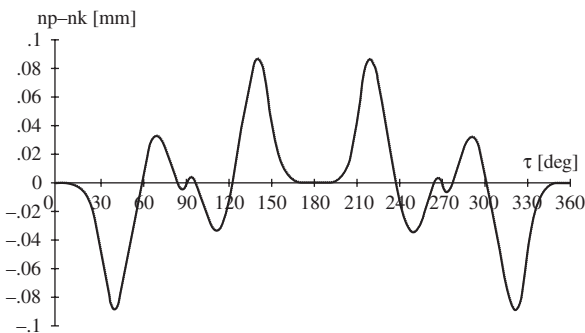


**Fig. 4** Difference of laws of motion

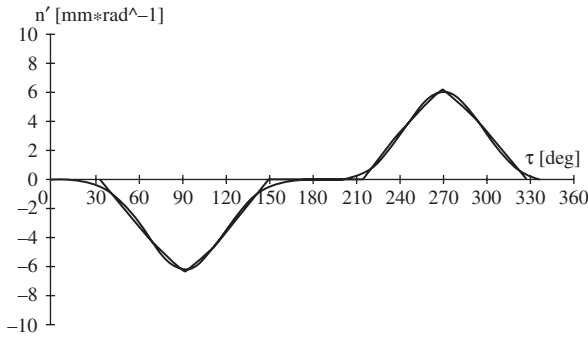


Fig. 5 Comparison of the first derivations of laws of motion

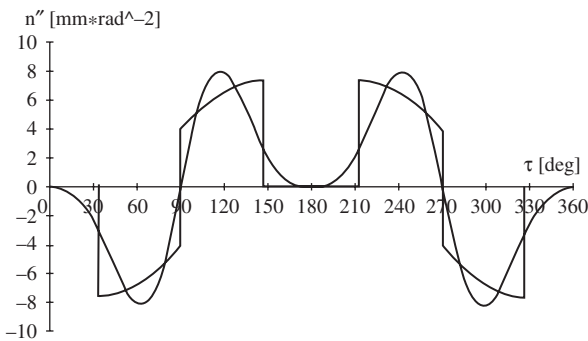


Fig. 6 Comparison of the second derivations of laws of motion

in limits  $\pm 6.344285 \text{ mm}\cdot\text{rad}^{-1}$ , the polynomial function has the smooth first derivation, it is in limits  $\pm 6.164643 \text{ mm}\cdot\text{rad}^{-1}$ .

The courses of the second derivations of laws of motion differ markedly. The function for circular arcs is discontinuous with jumps  $\pm 7.5 \text{ mm}\cdot\text{rad}^{-2}$  and  $\pm 8 \text{ mm}\cdot\text{rad}^{-2}$ , the polynomial function has the smooth second derivation in limits  $\pm 8 \text{ mm}\cdot\text{rad}^{-2}$ .

Curvature discontinuities of the cam active surface composed from circular arcs is the cause of the discontinuity of the second derivation of the corresponding law of motion. The cam consisting from polynomial segments has its second derivation of the law of motion smooth, therefore, considerably more favourable dynamic properties can be expected with it.

### Measuring of the Mechanism

Both observed cams were manufactured by the same technological process and installed in the mechanism of lateral motion of the industrial sewing machine needle. At various working velocities, noise and acceleration shape of working link were

namely measured. Noise measurement at working revolutions 2000, 2500, 3000, 3500, 4000, 4400 RPM determined those values of the difference between the cam with polynomials and that with circles  $-1.8, -2.9, -3.0, -1.1, +0.1, -0.4$  dB.

The acceleration course of the working link of the observed mechanism was considerably influenced by the compliance of the mechanism; therefore, it is not evaluated.

## Summary

The condition of cam contact with two parallel active surfaces was set and at a cam with circular arcs, kinematic quantities were determined. Moreover, a cam with polynomial segments was designed and the properties of laws of motion of the observed cams were compared. This comparison is also extended on the noise of the mechanism with both cams.

The result is a constation of remarkably more suitable dynamic properties of the cam with polynomial segments. The mentioned solution is subject of patent proceedings.

## References

1. Hoschek J., Paare kongruenter Kurvenscheiben, MMT, 13, 1978, pp. 281–292.
2. Koloc Z., Václavík M., Cam Mechanisms, Elsevier, 1993.
3. Carbone G., Incerti G., Lanni Ch., Ceccareli M., A Characterization of Cam Transmissions Through Identification of Lumped Parameters, Journal of Mechanical Design (prepared for press).

# Experimental and Theoretical Research of Cams Wearing of Cams Mechanism

Alexander Golovin, Alexey Lafitsky and Alexey Simuskhin

**Abstract** Experimental method of cam mechanisms with roller follower sizes measuring with digital photograph treatment results interpretation is studied. These results define displacement of cam mechanisms of bending automatic press. We have defined transfer functions of velocity and acceleration, which indicate the wear of cams. Method of recover of original cam profile by transfer function of velocity of follower of worn cam mechanism has been studied. Having compared original and worn profiles, the picture of cam wearing has been obtained. Based on functional analog of contact stress, obtained from the Hertz formula, the simulation model of cams wearing was constructed. Comparison of actual wear value and wear value was calculated by simulation model demonstrated its quality concurrence. Recommendations have been given on choosing the law of motion of follower framed by given cyclogram at cam recover.

**Keywords** Cam · Follower · Roller · Wear · Simulation model

## Introduction

Cam mechanisms are widely used in nonpower elements of machines. In case of their applications in power elements, for example, in gas – distributing engines, where the changing of sizes of cam mechanism elements may be considerable, various compensators of clearance or in forming machine are used. There are at least two reasons why designers avoid using cam mechanisms in highly loaded elements. Firstly, there is possibility of great wear of cam mechanism elements compared to link connection, for example. This reason can not be eliminated. The second reason is unsuccessful design of mechanism, connected with the choice of follower motion law. However, the problems of cam mechanisms wear are paid not enough attention to [1–4]. The questions associated with loading of cam mechanisms with roller

---

A. Golovin (✉)

Department of Theory Mechanisms and Machines, Bauman Moscow State Technical University, 2nd Baumanskaya Str., 5, 105005 Moscow, Russia  
e-mail: aalgol@rambler.ru



follower and attendant wear are considered rarely [5]. Inherently of discussable in [5] methods built sequence “construction of cam profile and set the roller follower – calculation of contact stress and comparison it with permissible – changing of cam dimensions and etc”. At [6] suggested another method. This method includes transition to dimensionless (analog) form of contact stress, loading and cam geometry calculations. It allows determining unsafe point of profile, where determine profile radius of curvature by maximal assumed contact stress. The presented work is continuation of [6], in which the research of cam mechanisms wear has been carried out and its simulation model is being offered. The investigation results are demonstrated on the most worn cam mechanism.

## Defining the Size of the Cam Mechanism According to Digital Photos

Sizes measurement of cam mechanism was done according to results of digital photograph results treatment. We have defined possible errors of measurements and because of lack of parallelism and coaxialness of front plane of cam and focal plane of camera. The digital photo was processed with the program AutoDesk AutoCAD by five times going over the contour of the cam. The sequence of coming from photo picture to drawing of cam mechanism is shown in Fig. 1. The measurements of follower movement and profile angle of cam were done after every  $5^\circ$  of cam turning. Maximal absolute error value of measurement (in case of hand-made measures by display) was obtained about 0.04 mm. The image resolution obtained by digital camera is 180 dpi. To get the maximal measurement precision it is recommended to use digital camera with image resolution about 300 dpi or higher. It is strongly recommended to write the image file from camera in RAW format, because the JPEG compression algorithm brings inaccuracy into measurement process by blurring the contrast bounds. After studying the measurements with the methods mathematical statistics cam profile was constructed and cam mechanism was reconstructed. The homogeneity of variance and half-width of confidence interval was used as the statistical treatment criterions. Homogeneity of variance was checked up by  $G_\alpha(n \cdot (m - 1)) = G_{0,05}(72 \cdot 4)$  criteria. The half-width of confidence interval was calculated by Student's Test ( $\Delta = t_p [n \cdot (m - 1)] \cdot S_b$ ), where

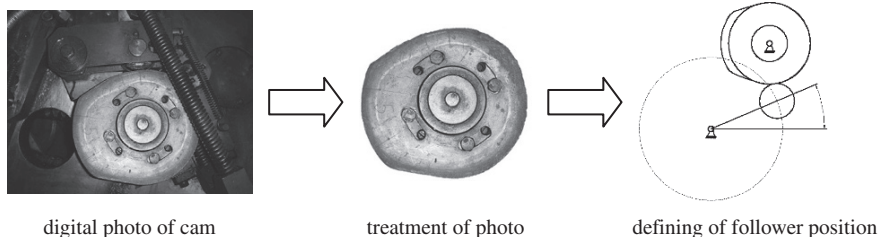


**Fig. 1** The sequence of defining of sizes of cam and cam mechanism

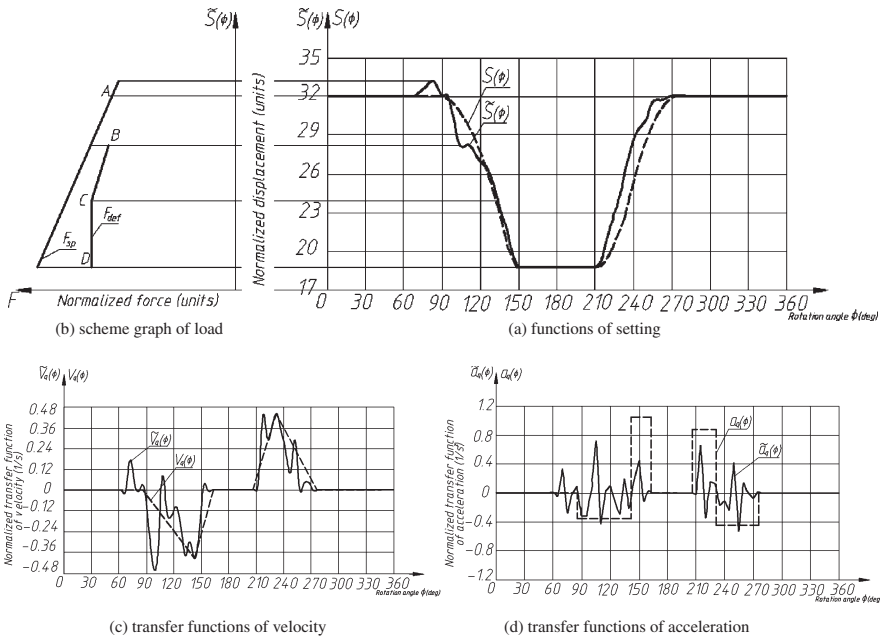


**Fig. 2** Experimental and recovered dependences of function of setting and transfer functions of velocity and acceleration

$t_p(n \cdot (m - 1)) = t_{0,95}(72 \cdot 4)$  is tabbed value of the Student’s test criteria;  $S_b$  – the mean-square deviation of homogeneity of repeatability, [7, 8].

After that using the method of reversed motion, the function of setting of cam mechanism was made (Fig. 2a). To consider the loads on bearing surfaces Fig. 2b contains:

1. load from spring  $F_{sp}$ , making force – closure of kinematic pair;
2. scheme graph of strength  $F_{def}$ , affecting the follower.

Correlation between these loads will be given in Section “Making the Simulation Model of Cam Contour Wearing”.

### Constructing Graph Plot of Metric Characteristics of Cam Mechanism Using Experimental Data. Recover of Original Metric Characteristic by Graph Plot

In Fig. 2 (curves 1) you can see dependences made according to experimental data: function of setting  $\tilde{S}(\varphi)$  (Fig. 2a); transfer function of velocity  $\tilde{V}_q(\varphi)$ (Fig. 2c); transfer function of acceleration  $\tilde{a}_q(\varphi)$  (Fig. 2d). Comparing function of setting  $\tilde{S}(\varphi)$  and original cycle sequence, as well as the graph of mechanism itself shows the considerable wearing of cam. Recover of original form of function of setting is based

on analyses of possible scheme dependences of transfer function of velocity, which were taken for designing of cam mechanisms at that time. The recover of original dependences was based on the following items: given motion of follower  $h$ ; defining the starting point of lift motion of follower according to cyclogram; choosing the most appropriate law of changing of transfer function of velocity  $V_q$  [3], based on given motion of follower:

$$\int_0^{360} \tilde{V}_q d\varphi = \int_0^{360} V_q d\varphi = h \quad (1)$$

In Fig. 2 the experimentally obtained curves are indicated with continuous lines, recovered dependences – with dotted lines.

### Constructing the Picture of Wearing of Cam Contour on the Results of Experiments

According to the recovered function of setting the original cam profile was constructed, which was later matched with the profile of worn cam (Fig. 3). The contour has some points characterizing the beginning of the following working phases of mechanism: A – the starting point of lift motion of follower; B – the starting point of contact of backer with workpiece; C – deformation force becomes constant; D – the finishing point of deformation force; D' – maximal wearing; E – the starting point of reverse stroke; F – the stopping of follower.

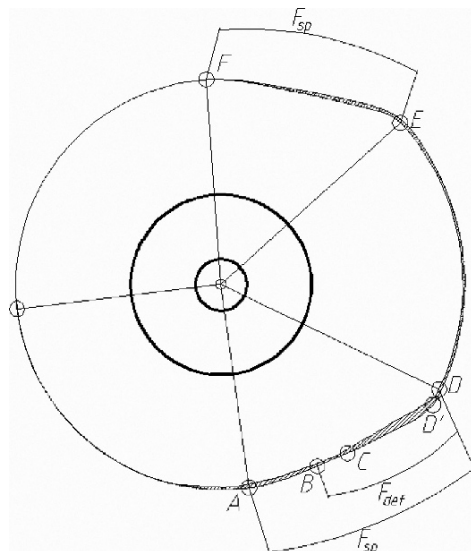


**Fig. 3** Comparing original and worn contours of cam

The greatest wear of profile is observed in the area of combined loads from deformation force and spring C-D. The maximum wear is observed around point D, which corresponds with the least radius of curvature of profile and sudden change of acceleration. Comparing loaded (A-D) and unloaded (F-E) branches of profile allows to define correlation between load of spring and resistance force:

$$1 + \frac{F_{\text{def}}}{F_{\text{sp}}} = \frac{\Delta_{\text{fs}}}{\Delta_{\text{rs}}} \tag{2}$$

where

$F_{\text{def}}$  – deformation force;  $F_{\text{sp}}$  – force of spring;  
 $\Delta_{\text{fs}}$  – cam wear of working stroke;  $\Delta_{\text{rs}}$  – cam wear of reverse stroke.

### Making the Simulation Model of Cam Contour Wearing

The simulation model of primary phase of cam wearing is made according to the Hertz formula for determination of maximum contact stress under compression of two cylinders wit parallel axis, same modulus of elasticity and with Poisson ratio equal 0,3, [6, 9, 10]. All dimensions are referred to the quantity of complete stroke of follower  $h$ .

$$\sigma_c = 0.418 \cdot \sqrt{Q^n \cdot E l b} \cdot \sqrt{(1/\rho_1 \pm 1/\rho_2)} = A \sqrt{Q^n} \cdot \sqrt{1/R_r + 1/R_{dp}} \tag{3}$$

where

$b$  – height of the cylinders;  
 $A = 0.418 \cdot \sqrt{F_{\text{MAX}} \cdot E / b \cdot h} = \text{const}$   
 $\bar{Q}^n = f(\varphi) / \cos \nu = F / (F_{\text{MAX}} \cdot \cos \nu)$  – reaction force in contact point;  
 $F$  – follower load, which is imposed to its axis;  
 $\nu$  – pressure angle in the higher pair;  
 $R_r = \bar{R}_r / h$  – relative radius of the follower;  
 $R_{dp} = \bar{R}_{dp} / h$  – cam design profile’s relative radius of curvature;  
 $E$  – modulus of elasticity.

It is based on dividing the origin of wear into two components. The first component indicates the influence of cam geometry (Fig. 4a) and is calculated by the following formula

$$\sigma_\rho = \sqrt{1/R_r \pm 1/R_{dp}} \tag{4}$$

$\sigma_\rho$  – the geometrical analog of contact stress component is concerned with radius of curvature of profile at the contact point and the radius of follower. The second component indicates the influence of load (Fig. 4b) and is calculated by the following formula

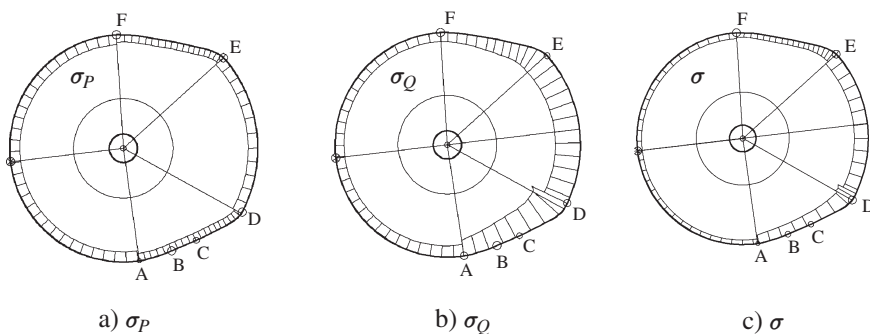


Fig. 4 Simulation model of cam wearing

$$\sigma_Q = \sqrt{f(\varphi) / \cos v} \tag{5}$$

$\sigma_Q$  – the geometrical analog of contact stress component is determined by reaction force at the contact point.

Distribution diagram of wear refers to the formula

$$(\sigma = \sigma_\rho \cdot \sigma_Q) \tag{6}$$

and is given in Fig. 4c.

### Comparing Actual Wear with Wear in Simulation Model

Figure 5a gives qualitative comparing of a actual cam wearing (curve  $w$ ) and primary phase of wearing in simulation model (curve  $\sigma$ ). The curve lines of wearing are made on cam contour. For comparative analysis of results the dependence of load (Fig. 5b) and repaired transfer function of acceleration are given (Fig. 5c).

The comparative analysis of actual and theoretical wearing is given in the following table.

Thus, the qualitative concurrence of actual and theoretical wearing can be pointed out. The differences in results obtained by simulation model and actual wear process

Characteristic sections of contour	Actual wear	Wear in simulation model
A	displacement of starting point	displacement of starting point
AB	wear increase	wear increase
B	max 1	decrease of grad $w$
BC	wear decrease	wear increase
C	min	discontinuity
CD	max 2	high gradient of wear increase
D	min	max
DE	const	const
E	const	const
EF	max 3	wear decrease
F	const	const

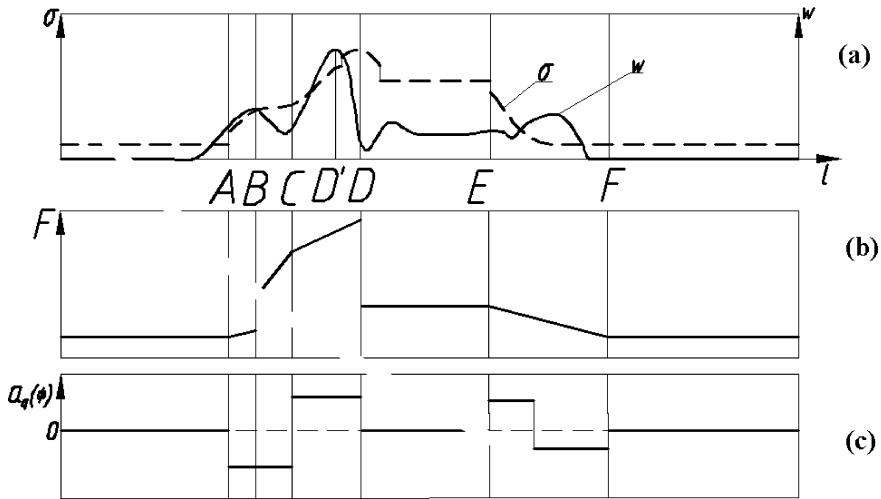


Fig. 5 Qualitative comparing of actual wearing (curve  $w$ ) and its simulation model (curve  $\sigma$ )

are possible to explain in fact of the simulation model accords with the conceptual stage of the wearing process only.

### Conclusion

1. In conclusion of work the function of follower position was obtained by results of digital photography. It was statistically treated. The functions of velocity and acceleration analogs were obtained by results of the treatment.
2. Using the experimentally obtained function of velocity analog, the original function of velocity was recovered; the original dependences of position and acceleration function were reconstructed and the original cam profile figure was retrieved by results.
3. Based on the Hertz formula the simulation model of cam profile wearing was made.
4. Comparing reconstructed and worn cam profiles allows us to obtain the picture of cam wearing. Comparing the actual picture of wearing and the same one obtained by the simulation model demonstrated high acceptability of the presented model.

### References

1. K.V. Frolov, S.A. Popov: Theory of Mechanisms and Mechanics of Machines, Textbook, edited by K.V. Frolov, 2d edition, revised, M.: Higher School, 1998, p. 496 (in Russian)
2. D.N. Reshetov: Parts of Machines. Textbook for machinebuilding and Mechanical Universities 4th edition, revised, M.: Machinebuilding, 1989, p. 496 (in Russian)
3. V.A. Yudin, L.V. Petrokas: Theory of Mechanisms and Machines. Textbook for Universities, 2d edition, revised, M.: Higher School, 1977, p. 527 (in Russian)

4. L.N. Reshetov: Cam Mechanisms of Lathes. M.-L. ONTI, 1935, p. 43 (in Russian)
5. G. Druce: Unit Design – Cam Mechanism (SEED Publications), <http://www.co-design.co.uk/dpg/cam/camhome.html>
6. A. Golovin, A. Borisov, A. Oskin: Geometrical Analogues of Contact Stress for Cams Design//Proceedings of EuCoMeS, the first European Conference on Mechanism Science Obergurgl (Austria), February 21–26, 2006. Manfred Husty and Hans-Peter Schrocker, editors.
7. E.M. Chetirkin, I.L. Kalihman: Probability and Statistics, M.: Finances and Statistics, 1982, p. 319 (in Russian)
8. A.A. Golovin: Researching of Mechanical Efficiency with Methods of Active Planning of Experiment, Moscow, 1984, p. 9 (in Russian)
9. Strength, Rigidity, Oscillation. Reference book in 3 volumes, Volume 2, Edited by I.A. Birgera, J.G. Panovko, M.: Machinebuilding, 1968, p. 463 (in Russian)
10. A. Golovin, A. Borisov, I. Drozdova, B. Shuman: The Simulation Model of a Gearing Wear//Proceedings of CK2005, International Workshop on Computational Kinematics Cassino, May 4–6, 2005

# Dynamic Features of Speed Increaseers from Mechatronic Wind and Hydro Systems. Part I: Structure Kinematics

C. Jaliu, D.V. Diaconescu, M. Neagoe and R. Săulescu

**Abstract** The paper main objectives are to extend the library of planetary increaseers that can be used in wind and hydro systems and to establish the dynamic properties of a speed increaseer that are necessary in the controller design. The proposed increaseers are derived from some representative speed reduceers by flow power inversion. A comparative analysis of the structural, kinematical and dynamic specific features of the different types of planetary speed increaseers is presented in the first part of this paper.

**Keywords** Structure · Kinematics · Speed increaseer · Renewable energy systems

## Introduction

The wind and hydro turbines are designed for certain environmental parameters (wind power or water flow). Most wind turbines and hydro-power stations' drive trains (Fig. 1a,b) include a gearbox to increase the speed of the input shaft to the generator. An increase in speed is needed because the wind turbines rotors and the hydro turbines shafts turn at a much lower speed than is required by most electrical generators. The range in which the input angular speed must be increased is 3...30, as specified in [1–3], by Manwell, Harvey and von Schon. A sensor of the control system measures any changes in the wind power or water flow, and a control plate commands the speed increaseer coupling/decoupling from the system, in order to function at the efficient level. Taking into account these considerations, it can be derived that it is important for the wind/hydro system running, to establish the premises necessary in designing the control system, part of these requirements being given by the speed increaseer dynamics.

---

C. Jaliu (✉)

Department of Product Design and Robotics, Transilvania University of Brasov, Bdul Eroilor 29, 500036 Brasov, Romania  
e-mail: cjaliu@unitbv.ro



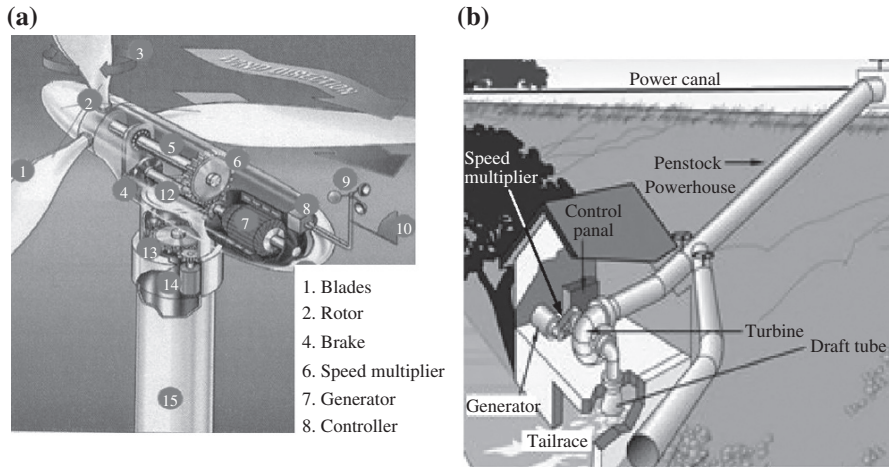


**Fig. 1** Wind turbine (a) and hydro system (b) drive trains

Therefore, the paper main objectives are the enlargement of the library of speed increasers for wind and hydro systems, and the establishment of the increaser dynamic model. The first objective is achieved in the first part of the paper, by proposing new solutions of speed increasers with high transmission ratios and efficiencies, which are derived from some representative speed reducers by flow power inversion. A comparative analysis of the structural, kinematical and dynamic specific features of the different types of planetary speed increasers is also presented in the first part of the paper. The dynamic model is developed in the second part of this paper, based on the example of a proposed speed increaser, and it is meant to give the initial data for the design of the system controller.

## New Solutions of Planetary Speed Increasers

In order to extend the library of planetary increasers that can be used in wind turbines' and hydro units' applications, the first step is to establish a list of requirements, taking into account the turbine and the generator prerequisites. Thus, a speed increaser for wind and hydro units must accomplish the following main requirements:

- (1) the increase of the multiplication ratio  $i = \omega_{\text{output}} / \omega_{\text{input}}$ ,  $|i| > 1$ ;
- (2) an acceptable efficiency  $\eta$ ,
- (3) the reduction of the radial/axial overall size,
- (4) the reduction of the complexity degree,
- (5) the reduction of the technological costs etc.

The development of new schemes of speed increasers means the minimization of some of the disadvantages, in the condition of an increased multiplication ratio. The

schemes proposed in this paper take into account the cost reduction, by reducing the transmission complexity degree, while an acceptable efficiency and the necessary multiplication ratio are obtained.

A source in the development of new schemes of increaseers with higher performances, which can be used in wind turbines and hydro stations is represented by the planetary reducers with a large technical use [4, 5]. The reducers with one sun gear, which were taken into account to generate speed increaseers, are relatively new developments of the planetary reducers with two sun gears. These developments have, as main objective, the *increase of the efficiency*; the development is reduced to the replacement of one of the 2 gear pairs by a *synchronic coupling with a superior efficiency*, like: the *Green coupling* (coupling of *Oldham* type, with rollers), the semi-coupling of *Schmidt* type in the *articulated* variant or in the variant with *pins* or *rollers* (used for small distances between the axes of the gear pair), the ball coupling of *Rzeppa* type (used in the *conical reducers*), the *claw* coupling, the *elastic tubular* coupling etc. Some representative solutions of 1 DOF simple planetary increaseers, developed from these planetary reducers, by inverting the energy flow, are illustrated in Table 1c,d,e. The increaseer derived from

**Table 1** A comparative analysis of some representative speed increaseer solutions

The increaseer type; the increaseer structural scheme; the multiplication ratio and the efficiency for the fixed axes mechanism ( $i_0, \eta_0$ ) and for the speed increaseer ( $i, \eta$ ), respectively; the increaseer transmission functions	
<b>a. Two-stage planetary increaseer used in wind turbines</b>	
$i_0^I = i_{1,3}^{h1} = \omega_{1,h1} / \omega_{3,h1} = -3.5; \quad i_0^{II} = i_{5,3'}^{h2} = \omega_{5,h2} / \omega_{3',h2} = -4;$ $\eta_{0I} = \eta_{0II} = 0.97; \quad i = \omega_{output} / \omega_{input} = \omega_5 / \omega_{h1} = +22.5; \quad \eta = 0.9529$ $\omega_5 = \omega_{5,3'} = 22.5 \cdot \omega_{h1}; \quad T_5 = -T_{h1} / 23.61133$	

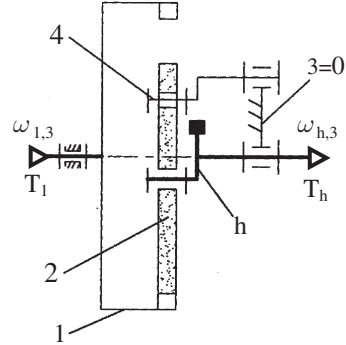
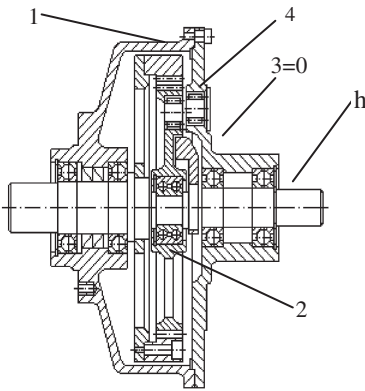
**Table 1** (continued)

<p><b>b. Increaser derived from an involute planetary reducer with two sun gears (1;3) and a double satellite (2=2')</b></p>	
<p> <math>i_0 = i_{1,3}^H = +0.98437</math>; <math>\eta_0 = \eta_{1,3}^H = 0.94</math>; <math>i = \omega_H / \omega_1 = +64</math>; <math>\omega_{H,3} = 64 \cdot \omega_{1,3}</math>;  <math>\eta_{1,H}^3 = -3.021 \Rightarrow</math> <i>Transmission is blocked!</i> It is running if: <math>1 - i_0 / \eta_0 &gt; 0 \Leftrightarrow \eta_0 &gt; i_0</math>                      (see the second part of the paper)                 </p>	
<p><b>c. Increaser derived from the a <i>Stratline</i> reducer: involute planetary increaser with one sun gear (3=0), a simple satellite (2) and a <i>Green</i> coupling (1-2)</b></p>	
<p> <math>i_0 = i_{1,3}^H = +1.0357</math>; <math>\eta_0 = \eta_{1,3}^H = 0.99</math>; <math>w = \text{sgn}(\omega_{1,H} T_1) = +1</math>  <math>i = \omega_H / \omega_1 = -28.01</math>; <math>\eta_{1,H}^3 = 0.71</math>; <math>\omega_{H,3} = 28.01 \cdot \omega_{1,3}</math>; <math>T_H = T_1 / 40</math> </p>	

the planetary reducer *Stratline*, illustrated in Table 1c, has an internal spur gear pair (2-3), with *involute* teeth and a *synchronic* radial coupling of *Green* type; the coupling transmits the revolute motion of the satellite-gear 2, *without any modification* (synchronic), to the output shaft 1. The increaser uses a counterweight 4 for the equilibration of the satellite 2. In the case of the increaser from Table 1d, a radial articulated synchronic semi-coupling of *Schmidt* type is used, with three cranks

Table 1 (continued)

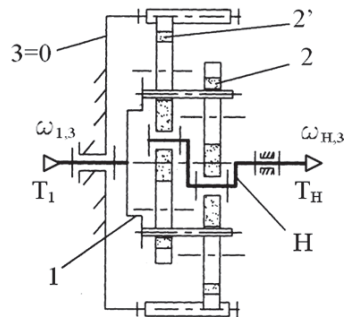
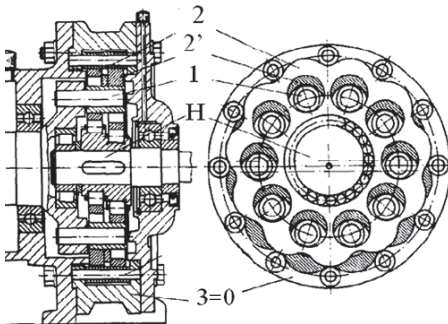
d. Inverter derived from an involute planetary reducer with one sun gear (1), a simple satellite (2) and 3 mechanisms of parallelogram type (4-2-h-3, at 120°)



$$i_0 = i_{1,3}^h = +0.9655; \quad \eta_0 = \eta_{1,3}^h = 0.99; \quad w = \text{sgn}(\omega_{1,h} T_1) = -1$$

$$i = \omega_h / \omega_1 = +29; \quad \eta_{1,h}^3 = 0.717; \quad \omega_{h,3} = 29 \cdot \omega_{1,3}; \quad T_h = -T_1 / 40$$

e. Inverter derived from a cycloidal reducer with one sun gear (3), 2 equiangular simple satellites (2, 2') and 10 equiangular bolt mechanisms of parallelogram type



$$i_0 = i_{1,3}^H = 12 / 11 = +1.0909; \quad \eta_0 = \eta_{1,3}^H = 0.99; \quad i = \omega_H / \omega_1 = -11;$$

$$\eta_{1,H}^3 = 0.88; \quad \omega_{H,3} = -11 \cdot \omega_{1,3}; \quad T_H = T_1 / 12.5$$

(4) that are disposed in parallel and equiangular (at  $120^\circ$ ). The equilibration of the satellite 2 is made by fitting a counterweight on the carrier  $h$ . The increaser from Table 1e contains 2 satellites in parallel connection and a *Schmidt* semi-coupling with *rollers* or *pins*, which allows the satellites parallel and equiangular assembling.

The other two solutions presented in Table 1, a and b have a more complex structure: the increaser from Table 1b is equipped with 2 sun gears, and is derived from the planetary reducers with 2 sun gears; the two-stage planetary solution, presented in Table 1a, is a speed increaser used in wind turbines [1]. The transmission has a complex structure: the increaser low-speed shaft  $h_1$  is rigidly connected to a planet carrier, which holds three identical small gears; these satellites mesh to a large ring gear and a small sun gear, forming a planetary unit; in order to increase the kinematical multiplication ratio, a second planetary unit of the same type, is serially connected to the first one (the sun gear 1 drives the high speed carrier  $h_2$ , to which it is connected by a teeth coupling).

The speed increaser presented in Table 1a is characterized through a good multiplication ratio ( $i = +22.5$ ), a good efficiency ( $\eta = 0.9529$ ), but high degree of complexity and overall dimensions, and, therefore, a high technological cost [6]. In order to reduce the disadvantages presented by this solution, new schemes of speed increasers are proposed and briefly analyzed in the paper. Their multiplication ratios, efficiencies and expressions for speeds and torques are systematized in Table 1, in the premise that the gears teeth numbers ( $i_0$ ) and the internal efficiency  $\eta_0$  are known (these sizes regard the gearbox with fixed axes derived from the planetary gear-set by motion inversion).

## Structural and Kinematical Features

The dynamic model of a speed increaser is presented in the second part of the paper, on the basis of the example from Table 1d. The dynamics of the other solutions from Table 1 can be obtained by analogy with this one.

The first step in the development of the dynamic model is to define the increaser structural and kinematical features. The considered speed increaser, consisting of one sun gear, one satellite gear and 3 mechanisms of parallelogram type (4-2-h-3, at  $120^\circ$ ), has two external links ( $L = 2$ ): an input 1 from the turbine and an output  $h$  to the generator. The *degree-of-freedom* is given by (1):

$$M = 6n - \left[ \sum c_i - c^* \right] = 6 \cdot 8 - [(9 \cdot 5 + 1 \cdot 2) - 0] = 1, \quad (1)$$

in which  $n = 8$  is the number of elements,  $c_i$  – joint “ $i$ ” degree of constraint (there are 9 joins with  $c_i = 5$ , and 1 joint with  $c_i = 2$ ) and  $c^* = 0$  – the number of redundant constraints. Thus, the gearbox is defined by:

$$\begin{aligned}
 M = 1 &\rightarrow \text{an external independent motion} : (\varphi_{1,3}, \omega_{1,3}, \varepsilon_{1,3}); \\
 &\rightarrow \text{a transmission function for forces} : T_1 = T_1(\varphi_{1,3}, T_h). \\
 L - M = 1 &\rightarrow \text{a transmission function for motions} : \\
 &\varphi_{h,3} = \varphi_{h,3}(\varphi_{1,3}), \omega_{h,3} = d\varphi_{h,3}/dt, \varepsilon_{h,3} = d\omega_{h,3}/dt; \\
 &\rightarrow \text{an external independent force} : T_h.
 \end{aligned}$$

The gearbox *transmission function for motions* can be obtained by using the planetary gearbox multiplication ratio. Therefore, according to Table 1d, and under the prerequisite that the associated fixed axes unit (obtained by reversing the motion relative to the carrier *h*) has the internal kinematical ratio:

$$i_0 = i_{1,3}^h = \omega_{1,h}/\omega_{3,h} = +0.9655, \tag{2}$$

for the analyzed speed increaseer the following multiplication ratio and speeds transmission function are obtained:

$$\begin{aligned}
 i = i_{h-1} &= \frac{\omega_{h3}}{\omega_{13}} = \frac{\omega_{hh} - \omega_{3h}}{\omega_{1h} - \omega_{3h}} = \frac{1}{1 - i_0} = +29 \\
 \omega_h = \omega_{h3} &= \omega_{1,3}, i = 29 \cdot \omega_{1,3}. \tag{3}
 \end{aligned}$$

Taking into account relation (3), the analyzed planetary gearbox multiplies the input speed  $\omega_{1,3}$  29 times and offers it, as output speed  $\omega_h$ ; therefore, the gearbox is, obviously, a torque reducer.

The dynamic model of the analyzed speed increaseer will be developed in the second part of the paper.

## Conclusions

The following conclusions are highlighted from the comparative analysis of the data included in Table 1:

- (A) There are two basic types of gearboxes used in wind turbines and hydro-plants applications: gearboxes with fixed axes and planetary gearboxes. In the first case, in order to obtain higher values of the transmission ratio, multiple stages are placed in series. This arrangement increases the multiplication ratio but, also, increases the gearbox overall dimension and reduces the global efficiency. Because in a planetary gearbox, the input and output shafts are coaxial, the overall dimension becomes smaller and the gearbox becomes lighter and more compact.
- (B) The reducers with one sun gear, used in the paper to generate speed increaseers, are relatively recent developments of the planetary reducers with two sun gears.

The solutions consist in keeping only one of the two gear pairs and replacing the rest of the gear pairs by a synchronic coupling with a superior efficiency. Some representative examples of speed increasers derived from 1 DOF planetary reducers by reversing the power flow are illustrated in Table 1b-e. The multiplication ratios of the speed increasers, the efficiencies and their expressions for speeds and torques are systematized in Table 1.

- (C) The proposed schemes of speed increasers (Table 1b–e) reduce some of the disadvantages offered by the increaser used in wind turbines (Table 1a). Thus, the speed increasers derived from planetary reducers with 1 or 2 sun gears have a good multiplication ratio, an acceptable efficiency, reduced complexity degree and overall size, and, therefore, a reduced technological cost. Their disadvantage consists in the very pretentious technology required to obtain a good efficiency.
- (D) A way to improve the transmission efficiency is referring to the use of *internal cycloidal gears with rollers or pins*, whose efficiencies are higher than of the involute gears. The speed increasers with cycloidal gears [7], (Table 1e) can obtain multiplication ratios that are comparable to the reduction ratios of the reducers from which they were derived; this type of increasers can obtain high multiplication ratios because the cycloidal gears can simply accomplish the condition  $\Delta z \geq 1$  (the difference between the numbers of teeth can be equal to 1, without the risk of interference). The results analysis highlight the fact that the planetary cycloidal reducers with one sun gear can be efficiently used as speed increasers by reversing the role of the input and output shafts; thus, a considerable enlargement of the library of speed increasers can be obtained.
- (E) The previous conclusion remains valid, in principle, also for the involute gears (Table 1a,b,c,d), with the following specification: the multiplication ratios are smaller due to the fact that the internal involute gears can, usually, accomplish only  $\Delta z \geq 4$ ;
- (F) Taking into account that the micro wind turbines and hydro units usually need multiplication ratios higher than 3, it outcomes that the previously presented schemes are directly usable; tacking into account their efficiency, the scheme from Table 1b can not function as speed increaser due to the negative efficiency ( $\eta_{1,H}^3 = -3.021\%$ ); the scheme can be used as speed increaser with an efficiency higher than 50% if its interior efficiency  $\eta_0$  becomes  $\eta_0 \geq 99.525\%$  (i.e. accuracy that needs high costs).
- (G) The efficiencies of the planetary gearboxes from Table 1 decrease as their multiplication ratios increase; the best efficiency is obtained by the increaser from Table 1a; but, in this case, the degree of complexity and overall size are maximum.
- (H) The complexity degree and overall dimensions are smaller at the planetary increasers derived from reducers, due to the use of synchronic couplings; the speed increasers from Table 1c, d and e have the simplest structure.
- (I) The technological costs of the increaser with cycloidal teeth (Table 1e) are smaller than of the increasers with involute teeth due to the superior accuracy needed in the last case (see Table 1b).

## References

1. Manwell, J.F., McGowan, J.G., Rogers, A.L. Wind energy explained, John Wiley & Sons, 2005.
2. Harvey, A. Micro-hydro design manual, TDG Publishing, 2005.
3. Von Schon, H.A.E.C. Hydro-Electric Practice – A practical manual of the development of water power, its conversion to electric energy, and its distant transmission, France Press, 2007.
4. Miloiu, G., Dudiță, FL., Diaconescu, D.V. Modern mechanical transmissions (in Romanian), Ed. Tehnică, București, 1980.
5. Jaliu, C., Diaconescu, D., Saulescu, R. Speed multipliers variants used in wind turbines and hydro-power stations. 11th International Research/expert Conference "Trends in the Development of Machinery and Associated Technology", TMT 2007 Hammamet, pp. 1115–1118, Tunisia, ISBN 978-9958-617-34-8.
6. Jaliu, C., Diaconescu, D.V., Săulescu, R. Kinematical and dynamic properties of a speed multiplier used in wind turbines. RECENT Journal, Vol. 8 (2007), no. 3a(21a), 2007, pp. 507–512, ISSN: 1582-0246.
7. Neagoe, M., Diaconescu, D., Jaliu, C. On a new cycloidal planetary gear used to fit mechatronic systems of RES. Proc. Of the 11th International Conference OPTIM 2008, Brasov, Vol. II(B), IEEE no. 08EX1996, pp. 439–448, ISBN 978-973-131-028-2.



# Dynamic Features of Speed Increaseers from Mechatronic Wind and Hydro Systems. Part II: Dynamic Aspects

C. Jaliu, D.V. Diaconescu, M. Neagoe and R. Săulescu

**Abstract** The paper main objectives are to extend the library of planetary increaseers that can be used in wind and hydro systems [1–3] and to establish the dynamic properties of a speed increaseer that are necessary in the controller design. The proposed increaseers are derived from some representative speed reducers by flow power inversion. A comparative analysis of the structural, kinematical and dynamic specific features of the different types of planetary speed increaseers was presented in the first part of the paper. The dynamic model of a speed increaseer used in wind turbines is further developed in the second part of the paper.

**Keywords** Dynamic model · Planetary speed increaseer · Renewable energy system

## Introduction

Most wind turbines and hydro-power stations' drive trains include a gearbox to increase the speed of the input shaft to the generator. There are two basic types of gearboxes used in wind and hydro applications: parallel-shaft speed increaseers and planetary speed increaseers. New solutions of speed increaseers with high transmission ratios and efficiencies, derived from some representative speed reducers by flow power inversion, are presented in the first part of the paper. In the second part of this paper it is developed the dynamic model of one of the generated increaseers, transmission that was analyzed in the first part of the paper, from the structural and kinematical point of view.

---

C. Jaliu (✉)

Department of Product Design and Robotics, Transilvania University of Brasov,  
Bdul Eroilor 29, 500036 Brasov, Romania  
e-mail: cjaliu@unitbv.ro

### Dynamic Aspects

The dynamic model of a speed increaser is presented on the basis of the example from Fig. 1a, a<sub>1</sub> and Table 1d (Part I: Structure Kinematics).

The first step in the development of the dynamic model (the establishment of the increaser structural and kinematical features) was presented in the first part of the paper. It was established that the analyzed planetary gearbox multiplies the input speed  $\omega_{1,3}$  29 times, being, obviously a torque reducer.

Under the prerequisite that the fixed axes unit associated to the planetary gear from Fig. 1a, a<sub>1</sub> is characterized by the multiplication ratio and internal efficiency [4, 5]:

$$i_0 = i_{1,3}^h = +0.9655; \eta_0 = \eta_{1,3}^h = 0.99, \tag{1}$$

and the following power flow exponent [4, 5]:

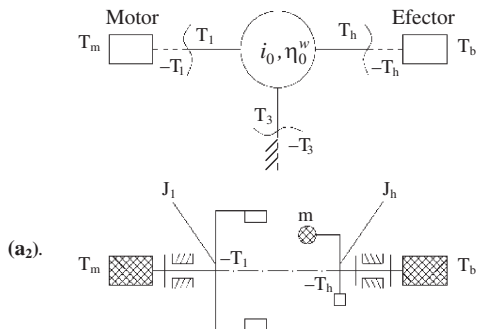
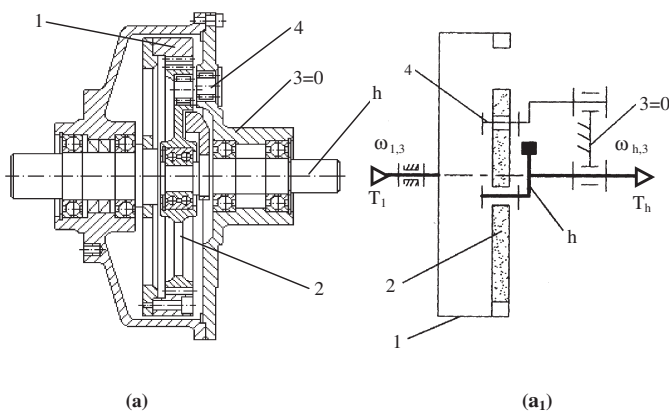


Fig. 1a, a<sub>1</sub> and a<sub>2</sub> Schemes used in the dynamic analysis based on the Newton-Euler method

$$\begin{aligned}
 w &= \operatorname{sgn}(\omega_{1,h} \cdot T_1) = \operatorname{sgn}[(\omega_{1,h} \cdot T_1 / \omega_{1,3} \cdot T_1)] \\
 &= \operatorname{sgn}[i_0 / (i_0 - 1)] = \operatorname{sgn}[+0.9655 / (0.9655 - 1)] = -1
 \end{aligned}
 \tag{2}$$

the gearbox has the *efficiency*:

$$\begin{aligned}
 \eta &= \eta_{h,1}^3 = -\frac{-\omega_{h,3} T_h}{\omega_{1,3} T_1} = \frac{-T_h}{T_i} i = \frac{-T_h}{T_1} \frac{1}{1 - i_0} = \frac{(1 - i_0 \eta_0^w)}{(1 - i_0)} = 0.717 \\
 \Rightarrow T_h &= -T_1 \eta / i = -T_1 \cdot 0.717 / 29 = -T_1 / 40.4463
 \end{aligned}
 \tag{3}$$

Thus, in ideal conditions ( $\eta = 1$ ), the speed increaser reduces the input moment 29 times ( $T_h = -T_1 / i = -T_1 / 29$ ), while, in real conditions, the planetary gearbox reduces the input moment 40.4463 times.

An aggregate composed from a DC motor, the analyzed planetary speed increaser and a brake is considered in the dynamic simulations (that means that the analyzed planetary speed increaser is mounted into an experimental testing stand – Fig. 1a<sub>1</sub>, a<sub>2</sub>); this modeling relies on the Newton-Euler's method and on the following premises:

- (a) the elements are rigid bodies and are made of steel;
- (b) the rotational inertial effects from the satellite (considered lonely – Fig. 1a, a<sub>1</sub>) are neglected;
- (c) the rubbing effect is considered by means of the efficiency  $\eta$ ;
- (d) the inertia moments are considered vs. the axes that passes their masspoints (Fig. 1a<sub>2</sub>): the aggregate rotor + shaft + ring gear:  $J_1 = 0.05 \text{ kgm}^2$ ; the aggregate satellite gear 2 + parallelograms + brake rotor:  $J_h = 0.03 \text{ kgm}^2$ .

In the dynamic modelling, the inertial effects due to the satellite gears rotation are neglected (their masses being considered in the axial inertial moment of the afferent carrier shaft), while the inertial effects of the mobile central elements are considered integrated into the shafts that materialize the external links of the planetary gears; under this premise, the static correlations between the external torques of each planetary gear are valid, while the dynamic correlations interfere only for the shafts that materialize the planetary gears external links.

- (e) the DC motor and the brake have known mechanical characteristics: the motor is characterized by equation:  $T_m = -0.1273 \cdot \omega_m + 25.6$  [Nm], the brake is characterized by a linear mechanical characteristic:  $T_b = -\omega_b$  [Nm].

The dynamic modeling is made in the following cases:

- I. The motion equation is modeled by neglecting rubbing, and
- II. The motion equation is modeled by considering rubbing effects.

Thus, the following correlations can be written, taking into account the previous relations and Fig. 1:

$$\begin{aligned} \omega_h = i \cdot \omega_1 = 29 \cdot \omega_1 \Rightarrow & T_1 + T_h + T_3 = 0; & J_1 \varepsilon_1 = T_m - T_1; \\ \varepsilon_h = i \cdot \varepsilon_1 = 29 \cdot \varepsilon_1 & T_1 + T_h + T_3 = 0; & J_h \varepsilon_h = T_b - T_h. \end{aligned} \quad (4)$$

After replacements, it outcomes the *motion equation*:

– for case I ( $\eta = 1$ ):

$$\epsilon_h + 33.2724 \cdot \omega_h - 29.3817 = 0 \quad (5)$$

– for case II ( $\eta < 1$ ):

$$\epsilon_h + 33.2896 \cdot \omega_h - 21.0900 = 0 \quad (6)$$

By making  $\epsilon_h = 0$  in (5) and (6), the angular speed  $\omega_h$  in steady-state regime, for both cases, is obtained (neglecting and considering rubbing effects): for case I ( $\eta = 1$ ) :  $\omega_h = +0.883065 \text{ s}^{-1}$ , for case II ( $\eta < 1$ ):  $\omega_h = +0.633531 \text{ s}^{-1}$ .

Obviously, in the cases in which  $\eta < 1$ , by reducing the motor speed, the motor torque becomes bigger and covers friction effects.

The change in time of the angular speed  $\omega_h$ , the angular acceleration  $\varepsilon_h$  and the input and output torques (see Fig. 3) are obtained for both cases by solving (5) and (6) with Matlab-Simulink software (see Fig. 2).

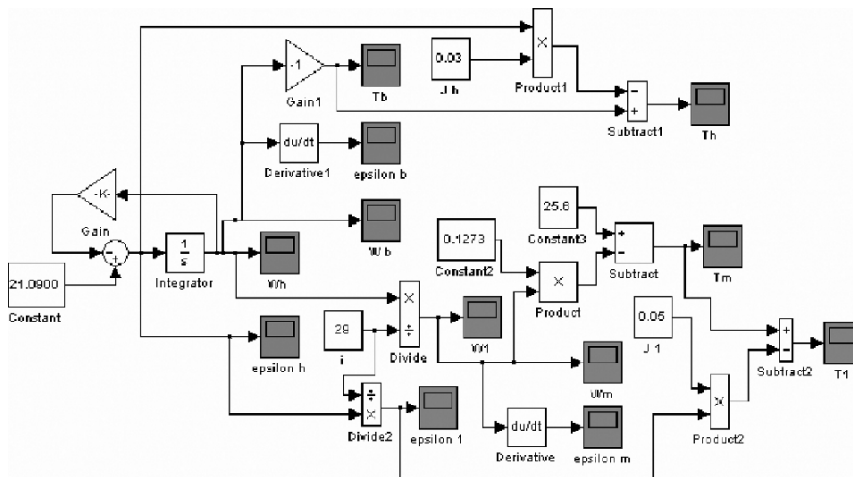


Fig. 2 The Simulink scheme that models the motion equation of the planetary speed increaser

### Comments and Conclusions

- (1) Representative examples of speed increasers derived from 1 DOF planetary reducers by reversing the power flow are illustrated in Table 1b–e (Part I: Structure Kinematics). The multiplication ratios of the speed increasers, the efficiencies

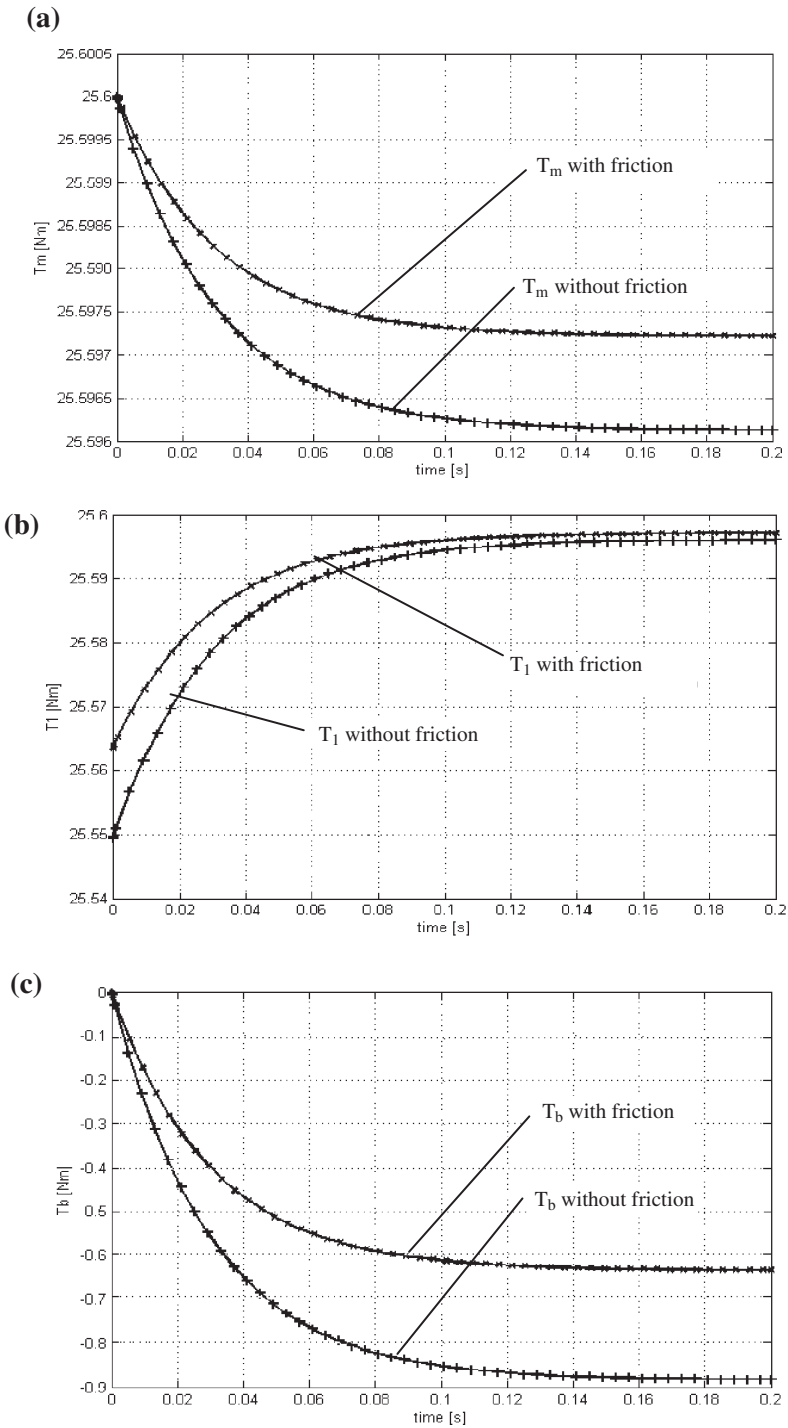


Fig. 3a,b,c Dynamic response of the aggregate: motor moment (a), input moment (b), output moment (c)

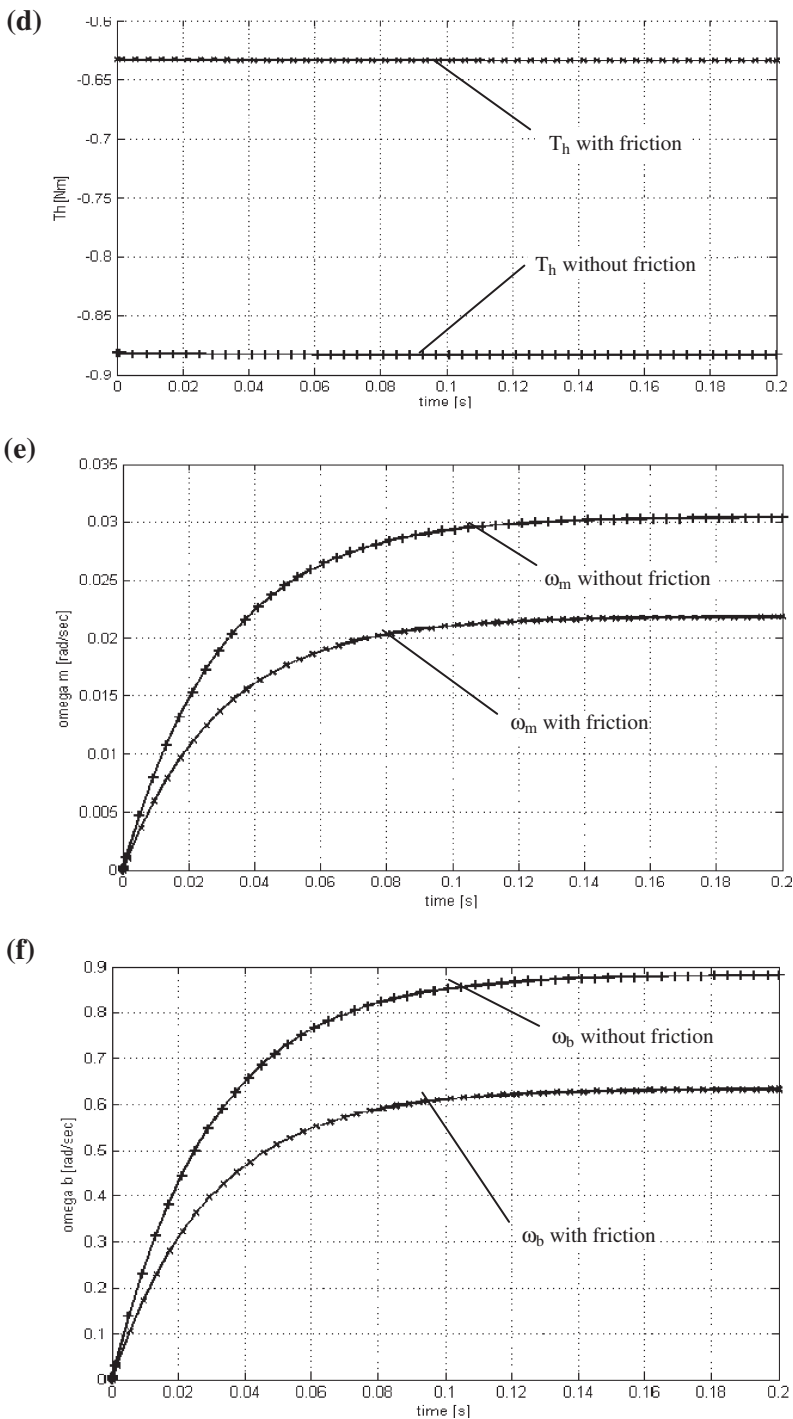
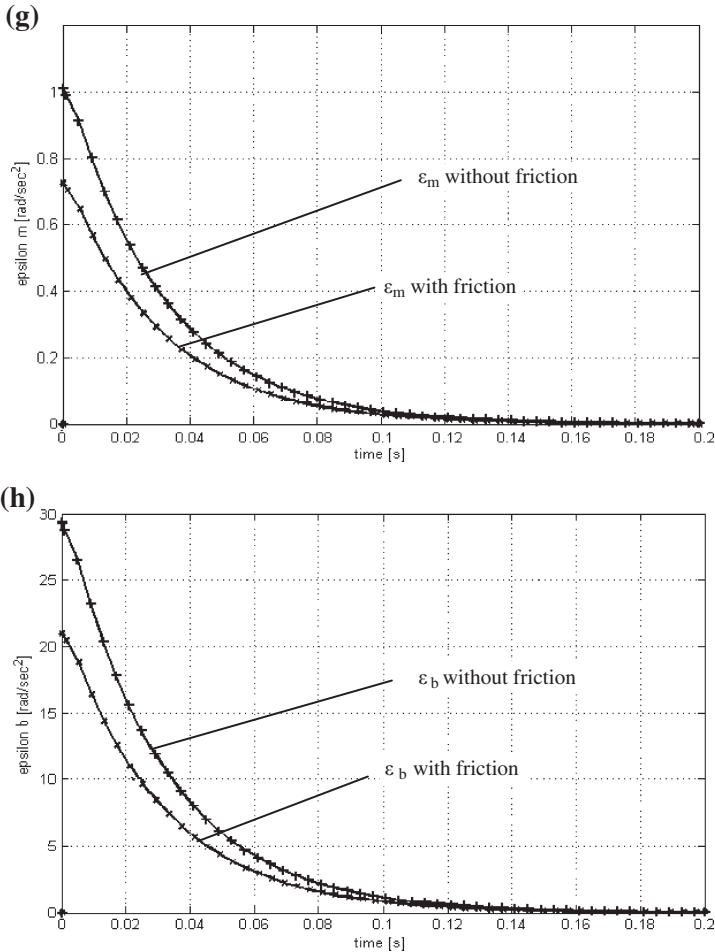


Fig. 3d, e, f Dynamic response of the aggregate: brake moment (d), input angular speed (e), output angular speed (f)



**Fig. 3g, h** Dynamic response of the aggregate (DC motor + increase + brake): input angular acceleration (g), out angular acceleration(h)

and their expressions for speeds and torques are also systematized in Table 1 (Part I: Structure Kinematics), in the premise of knowing the gears teeth numbers ( $i_0$ ) and the internal efficiency  $\eta_0$ ; the values are obtained using the same calculus procedure as for the speed increaser from Fig. 1a.

The speed increaser from Table 1b (Part I: Structure Kinematics) can become efficient if a good technological accuracy is used ( $\eta \geq 0.7 \iff \eta_0 \geq 0.99525$ ); obviously, this modification means an increasing of the transmission technological costs.

- (2) The dynamic modeling developed in the paper is made in the premise that the speed increaser is used in a testing system of type: motor + increaser + brake. In the case of neglecting the rubbing effects, the output angular speeds  $\omega_{h,3}$  are

bigger than in the case of considering friction (but with insignificant values, see Fig. 3e), while the external torques behavior ( $T_m$  and  $T_b$ , see Fig. 3a and c) is reversed.

The variations of the angular acceleration  $\varepsilon_h$ , with and without rubbing, are almost superposed (Fig. 3h).

The system consisting of motor, speed increaser and brake starts, practically, in about 0.13 s (in both cases), after which enters in the steady-state regime.

- (3) The results analysis highlight the fact that the selection of one particular planetary increaser to be applied in a practical case depends on the design requirements established in the pre-feasibility study.
- (4) The algorithm used to obtain the dynamic model can be applied for all speed increasers through analogy to the considered example.
- (5) The dynamic model is useful in the design of the control system for the wind turbines and hydro stations. The system control program can be established by considering certain environmental conditions/seasons and by replacing the motor and the brake from the dynamic modeling with a turbine and a generator.
- (6) Based on the dynamic modeling, the authors will accomplish the design, manufacturing and testing of a speed increaser for stand-alone hydropower stations in the framework of the research project “Innovative mechatronic systems for micro hydros, meant to the efficient exploitation of hydrological potential from off-grid sites”, ID\_140.

## References

1. Manwell, J.F., Mcgowan, J.G., Rogers, A.L. Wind energy explained, John Wiley & Sons, 2005.
2. Harvey, A. Micro-hydro design manual, TDG Publishing, 2005.
3. Von Schon, H.A.E.C. Hydro-Electric Practice – A practical manual of the development of water power, its conversion to electric energy, and its distant transmission, France Press, 2007.
4. Miloiu, G., Dudiță, FL., Diaconescu, D.V. Modern mechanical transmissions (in Romanian), Ed. Tehnică, București, 1980.
5. Jaliu, C., Diaconescu, D., Saulescu, R. Speed multipliers variants used in wind turbines and hydro-power stations. 11th International Research/expert Conference “Trends in the Development of Machinery and Associated Technology”, TMT 2007 Hammamet, pp. 1115–1118, Tunisia, ISBN 978-9958-617-34-8.



# A Computer Aided Method for Cam Profile Design

A. Petropoulou, S. Dimopoulos, D. Mourtzis and T.G. Chondros

**Abstract** A computer-aided numerical method for the design of a cam-follower mechanism and NC milling for a planar cam profile is presented. The method consists of an iteration method for the calculation of the follower motion properties (oscillation, velocity and acceleration, jerk) using the vector differences for three successive points on the cam profile. With the aid of a CAD program the results of the method are exported to the NC milling machine, thus facilitating the programming procedure and leading to a significant reduction of the NC code size. Numerical examples have been reported to compare differences of the proposed method versus the analytical design parameters of the cam-follower mechanism.

**Keywords** Cam-follower mechanism

## Introduction

Cam-follower mechanisms are commonly used in almost every mechanical system to transmit a desired motion to another mechanical element by direct surface contact. Cam and follower mechanisms are very cheap, and simple, they have few moving parts and can be built with very small size. Generally, a cam mechanism is composed of three different fundamental parts from a kinematic viewpoint [1]: a cam, the driving element; a follower, the driven element and a fixed frame. Cam mechanisms are usually implemented in most modern applications and in particular in automatic machines and instruments, internal combustion engines and control systems. Automation with cam mechanisms, although they offer a low degree of flexibility, are frequently used, due to their low cost and to the fact that they provide the simplest way of achieving almost any desired follower motion [2].

The cam mechanism design includes two stages. First, the selection of the appropriate transfer functions which fulfil prescribed kinematic specifications, and

---

A. Petropoulou (✉)

University of Patras, Department of Mechanical Engineering & Aeronautics, 265 00 Patras, Greece  
e-mail: chondros@mech.upatras.gr

secondly, the optimization of the mechanism geometry, regarding constructive restrictions. The evolution of the cam profile design techniques is generally based on the use of splines. The motion characteristics of the cam are usually synthesized through a combination of the standard motion, parabolic, simple harmonic and cycloidal functions according to the design requirements. In the past, design of the cam profile was a tedious job requiring application of graphical or analytical methods [2]. In most applications today, a cam profile is generated by a numerically controlled milling cutter that can be programmed to cut the cam profile, so that the desired follower motion will be generated without explicitly determining the cam profile first.

A significant characteristic for a mechanical design of a cam is the sudden change in the acceleration at the profile points where arcs of different radii are joined [3]. The profile of any cam depends on the required follower motion characteristics, normally stated in terms of displacement and velocity attributes. In the case of an automatic lathe, primitive curves forming the shape of planar cams such as dwell-rise-dwell are governed by the tool tip motion characteristics required for turning a component having the desired dimensions and geometric attributes such as a spherical profile. A variety of methods for the design of a cam profile are available in the literature today.

Ceccarelli et al. [3, 4] present an analytical formulation based on simple geometric relations for three circular-arc cams since this type of cams can be used in low-speed applications. In addition, circular-arc cams can be used for micro-mechanisms and nano-mechanisms given that very small manufacturing can be properly obtained by using elementary geometry.

Wang and Yang [5] presented a computer aided method to construct the motion program of the follower-cam mechanism based on piecewise polynomial splines. This approach allows the designer to directly specify and modify the design requirements such as lift, velocity, acceleration and the dwell period of the follower.

Chen [6] presents a method for the design of a cam profile based on simple geometric curves, such as: parabolic, harmonic, cycloidal and trapezoidal curves and their combinations.

Borg et al. [7] use cam profile blending models and edge vector based cam milling path approach for the design and manufacturing of automatic lathe cams.

Yan et al. [8] studied the effect of varying the cam input driving speed to improve the follower motion characteristics. They use a polynomial speed trajectory to reduce the peak values of the motion characteristics. The cam geometry optimization is handled in many publications [4–8], in which among others, the formulation of an objective function is presented.

Dixon et al. [9] presented a method for determining the design equations and an outline of integrated synthesis-optimization procedures for the cam-link mechanism.

Tsay and Lin [10] analyzed the geometric characteristics for the pressure angles and principal curvatures of the cylindrical cam surfaces to show the effect of the refined follower motion on the cam surfaces. Favourable results were obtained by

using the rational B-splines, and they are compared with those obtained by other traditional methods.

Lampinen [11] presents a genetic algorithm based computer aided approach for a preliminary design and shape optimization of cam profiles. A systematic approach is developed for a preliminary cam shape design including cam shape design optimization with respect to the simulated computer models of cam mechanisms. Bouzakis [12] presents an integrated CAD-CAM system for cam mechanisms with the aid of an optimization technique. The transfer functions that fulfil prescribed kinematic specifications are selected according to the VDI 2143 guideline. The optimization of the cam geometry is achieved through the formulation of an objective function that has to be minimized for optimum transfer functions and minimum cam dimensions.

In this paper the definition of the cam profile curvature for a desired follower motion is calculated through an analytical formulation of the vector difference for three successive points on the cam profile. Then, a similar algorithm is used for the definition of the follower motion properties. The velocity, acceleration and jerk are calculated by an iteration process through the elementary geometry of the same vector model for three successive points on the cam profile. The method provides results for the milling cutter position almost in real time. A computer algorithm was developed to export the results of the method to a CNC programming algorithm. The method is useful for low speed machinery or low precision applications or in case that the size of a mechanical design is reduced to the scale of millimetres (mini-mechanisms) and even micron (micro-mechanisms). In this case the manufacturing of polynomial cam profiles becomes difficult and even more complicated to verify it. A numerical example is used to show the engineering feasibility of the proposed method and compare differences from the analytical design parameters of the cam-follower mechanism.

## A Numerical Method for Cam-Follower Motion Analysis

The profile of any cam depends on the required follower motion characteristics [2] normally stated in terms of displacement and velocity attributes. For a cam with a rectilinear (translating) flat face follower, Fig. 1 the cam rotates about point  $O_A$  and a flat follower is always moving so that its geometric axis is always on the line  $O_A B$ .  $R_b$  is the base circle radius. A reference line fixed on the cam has an angle  $\theta$  to the follower axis  $O_A B$  at time  $t$ . The follower contacts the cam in this position at  $A$ . The milling cutter has centre at  $O_c$  and radius  $R_c$ . The distance  $s(\theta)$  is the displacement of the follower and is a function of the angle of rotation  $\theta$ . In a milling cutter, the cam stock can rotate about  $O_A$  by a prescribed angle at a time and for each angle, the centre of the milling cutter can be programmed to have such a position that the displacement of the follower will be prescribed by the function  $s(\theta)$ . Thus, given data is the radius of the milling cutter  $R_c$ , the location of the cam centre of

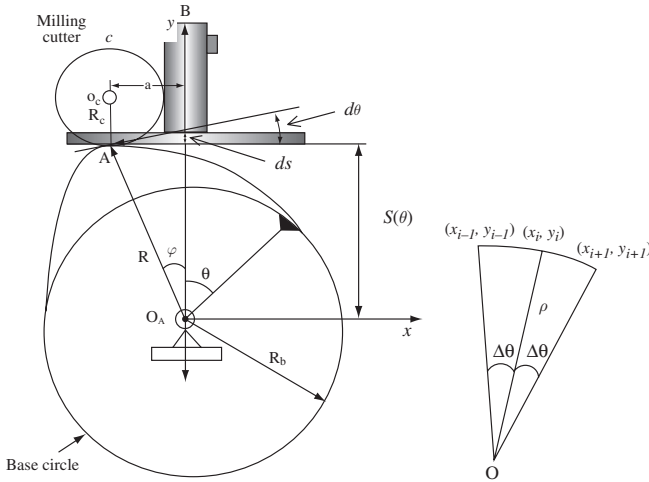


**Fig. 1** Cam with a translating flat-face follower and three successive points on the cam profile

rotation  $O_A$  and the required location of the centre of the milling cutter  $O_c$  (distance  $a$  and radii  $R$  and  $R_c$ ) for each angle  $\theta$ .

Assuming a small incremental rotation of the cam  $d\theta$  about  $O_A$  the centreline of the follower rotates counter-clockwise by  $d\theta$ . The dashed line shows the new position of the follower and the change of location  $ds = a d\theta$ . The position of the vector  $\mathbf{R}$  in regard with the centreline,  $\varphi$  is

$$\tan \varphi = a/s = ds/sd\theta \text{ or } \varphi = \arctan(ds/sd\theta) \tag{1}$$

and the coordinates of the centre  $O_c$  of the milling cutter are calculated as:

$$\begin{aligned} x_c &= -s(\theta) \tan \varphi = ds/sd\theta \\ y_c &= s(\theta) \cot \varphi + R_c = s^2(\theta)/(ds/d\theta) + R_c \end{aligned} \tag{2}$$

The polar coordinates of point  $A$ , the contact point of the cam and the cutting-tool are obtained in the form:

$$R(\theta) = \sqrt{s^2(\theta) + a^2} = \sqrt{s^2(\theta) + (ds/d\theta)^2} \tag{3}$$

The analytical equation for the calculation of the minimum cam profile curvature  $\rho$  is [13]:

$$\rho = \frac{\{(R_b + s(\theta))^2 + [s'(\theta)]^2\}^{3/2}}{(R_b + s(\theta))^2 + 2 \cdot (s'(\theta))^2 - (R_b + s(\theta)) \cdot s''(\theta)} \tag{4}$$

where  $R_b$  is the base circle radius and  $s(\theta)$  the displacement of the follower.

The calculation of  $s(\theta)$  and the derivatives  $s'(\theta)$  and  $s''(\theta)$  is a time tedious procedure usually resulting in a wide margin of error depending on the corresponding time increment  $\Delta t$ . The error in velocity, acceleration and jerk is proportional to  $1/\Delta t$ ,  $1/\Delta t^2$ , and  $1/\Delta t^3$  respectively. Alternatively, an approximate numerical method will be employed for the calculation of the cam profile curvature  $\rho$  based on an approximate graphical analysis for the determination of the milling-cutter and cam-surface contact point according to the desired follower displacement. Then the follower's velocity and acceleration yield based on the cam profile determined, and a graphical representation helps the user to accept or reject the cam-follower kinematic pair's characteristics.

Since the centre of curvature is stationary on the cam surface, the magnitudes of the cam-profile curvature and the vector defining the instantaneous centre of curvature do not change for small change in cam rotation [13], considering that three successive points on the cam profile located on the same arc of a circle of radius  $\rho$  with a centre located at  $O(x_\rho, y_\rho)$ , with Cartesian coordinates  $(x_{i-1}, y_{i-1})$ ,  $(x_i, y_i)$ ,  $(x_{i+1}, y_{i+1})$ . Those points belong on successive radii of equal angles  $\Delta\theta$  and the curvature of each arc is calculated from the Pythagorean Theorem as follows:

$$\begin{aligned} \rho &= \sqrt{(x_\rho - x_{i-1})^2 + (y_\rho - y_{i-1})^2} = \sqrt{(x_\rho - x_i)^2 + (y_\rho - y_i)^2} \\ \rho &= \sqrt{(x_\rho - x_i)^2 + (y_\rho - y_i)^2} = \sqrt{(x_\rho - x_{i+1})^2 + (y_\rho - y_{i+1})^2} \\ \rho &= \sqrt{(x_\rho - x_{i+1})^2 + (y_\rho - y_{i+1})^2} = \sqrt{(x_\rho - x_{i-1})^2 + (y_\rho - y_{i-1})^2} \end{aligned} \quad (5)$$

where  $x_\rho$  and  $y_\rho$  the coordinates of the arc centre.

Equations (5) yield:

$$\begin{aligned} x_{i-1}^2 - x_i^2 - 2x_\rho(x_{i-1} - x_i) + y_{i-1}^2 - y_i^2 - 2y_\rho(y_{i-1} - y_i) &= 0 \\ x_i^2 - x_{i+1}^2 - 2x_\rho(x_i - x_{i+1}) + y_i^2 - y_{i+1}^2 - 2y_\rho(y_i - y_{i+1}) &= 0 \\ x_{i+1}^2 - x_{i-1}^2 - 2x_\rho(x_{i+1} - x_{i-1}) + y_{i+1}^2 - y_{i-1}^2 - 2y_\rho(y_{i+1} - y_{i-1}) &= 0 \end{aligned} \quad (6)$$

The system of equations (6) yields the  $x_\rho$  and  $y_\rho$  coordinates. Then, the cam profile curvature  $\rho$  is calculated as

$$\rho = \sqrt{(x_\rho - x_{i-1})^2 + (y_\rho - y_{i-1})^2} = \sqrt{(x_\rho - x_i)^2 + (y_\rho - y_i)^2} = \sqrt{(x_\rho - x_{i+1})^2 + (y_\rho - y_{i+1})^2} \quad (7)$$

Equation (7) yields the cam profile curvature for the follower motion displacement  $s(\theta)$  based on the cam-follower configuration and the geometric relations for the follower displacement available in the data-base [2].

For three successive points on a cam profile (Fig. 1), the angle  $\Delta\theta$  equals  $360/N$ , where  $N$  is the number of the discrete points configuring the cam profile. For a large number of points  $N$ ,  $\Delta\theta$  is becoming very small and then the velocity, acceleration and jerk for the cam profile, considering infinitesimal increments of time, are calculated respectively as:

$$\begin{aligned} u_i &= (s_i - s_{i-1})/\Delta t & \text{or} & & u_i &= (s_{i+1} - s_i)/\Delta t \\ \alpha_i &= (u_i - u_{i-1})/\Delta t & \text{or} & & \alpha_i &= (u_{i+1} - u_i)/\Delta t \\ j_i &= (\alpha_i - \alpha_{i-1})/\Delta t & \text{or} & & j_i &= (\alpha_{i+1} - \alpha_i)/\Delta t \end{aligned} \quad (8)$$

For better precision the average of the above follower motion characteristics, Equations (8), will be considered as:

$$\begin{aligned} u_i &= (u_{i-1} + u_{i+1})/2 \\ \alpha_i &= (\alpha_{i-1} + \alpha_{i+1})/2 \\ j_i &= (j_{i-1} + j_{i+1})/2 \end{aligned} \quad (9)$$

From Equations (7), (8) and (9) the follower displacement, velocity, acceleration and jerk and the cam profile curvature are determined.

A design procedure was developed by using the above-mentioned formulation in order to compute the cam-follower design parameters. Various configurations of cam-follower kinematic pairs integrated in the algorithm and the corresponding geometric relations for the follower displacement specified at any cam rotation angle were incorporated. The time-step increment has to be defined first, usually as multiples of 360 degrees. Then, the user selects either the follower motion characteristics from the functions available or provides the required data for a specific follower motion. This procedure is required for the solution of Equation (3) and the definition of the discrete points corresponding to the selected time step. The coordinates of those points are stored in a specific array by the algorithm. For the determination of the cam profile and the velocity, acceleration and jerk configurations yield from the solution of Equations (7) and (9). Since the algorithm is intended for low speed kinematic pairs or low precision applications it was proved that a discretization of 1440 points provides results of good accuracy compared with the analytical ones. Of course the discretization depends on the specific cam-follower pair investigated, and the method provides the appropriate checks of the pressure angle and radius of curvature magnitude interrupting the process in case of failure or violating the limitation prescribed as will be shown below.

An algorithm in Visual Basic was developed for the generation of the cam geometry, and the follower motion characteristics. The algorithm provides an animation of the cam and follower mechanism motion and furthermore, a preview of the mechanism is possible for an initial verification of the selected design. The method requires starting the displacement function from a certain value which usually is the radius of the cam at the arc corresponding to the lowermost position of the follower at the dwell. A user-friendly graphics environment facilitates the aforementioned tasks.

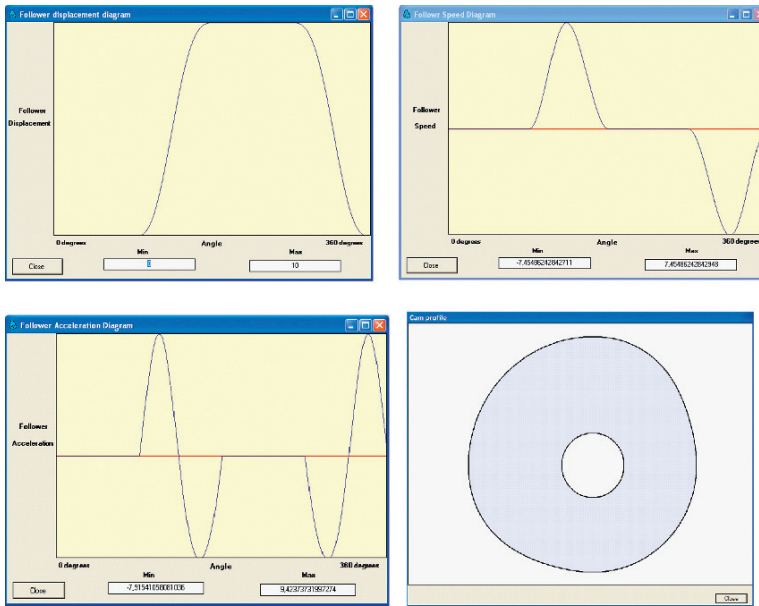


Fig. 2 The follower displacement, speed and acceleration diagrams and the cam profile

The proposed application is demonstrated with an example of a disk cam mechanism with a point follower. First, the cam-follower configuration and the corresponding follower displacement relationship is selected from the incorporated data-base. The cam-follower displacement, speed and acceleration diagrams are obtained from Eq. (8) as shown in Fig. 2. Then, the required follower motion characteristics normally stated in terms of displacement and velocity attributes are easily identified. In Fig. 2 the cam-follower motion characteristics are drawn over the corresponding points calculated by an analytical method for a cycloidal-type follower motion [2, 13].

The algorithm performs a check of the cam profile to assure that it will lead to a correct follower motion. Additionally, the minimum cam profile curvature is checked against the following limitations:

1. The profile curvature should be larger than the cutting tool radius.
2. If the follower is a roller follower, the profile curvature should be larger than the follower radius (to prevent undercut).
3. If the follower is not a radius follower, but a flat faced follower, the centre of the coefficient circle should be an internal point, otherwise there will be a loss of contact or two simultaneously located points of contact for the follower circle. Additionally, the size of the base circle radius  $R_b$  is checked by the algorithm to ensure that concave sections are avoided for that follower as well as sharp concave sections for roller followers [14]. The method is based on the determination of the milling cutter centre coordinates and the milling-cutter-cam contact point A in Fig. 1 rather than the cam profile itself, providing direct information

for the manufacturing process. With the aid of a CAD program the results are exported to the NC milling machine, thus facilitating the programming of the NC code.

## Conclusion

The algorithm developed here consists of a numerical procedure for the definition of the cam profile curvature for a desired follower motion through a vector difference algorithm for three successive points on the cam profile. Through a similar iteration process the follower motion properties (velocity acceleration, jerk) are defined and furthermore, the verification of the acceptance of the cam profile design is achieved. Numerical examples have been reported to prove the soundness of the analytical design procedure, minimization of the numerical errors, and show its engineering feasibility.

## References

1. Hartenberg R. and J. Denavit 1964 *Kinematic Synthesis of Linkages*, Mc Graw Hill, New York.
2. Dimarogonas A.D. 2000 *Machine Design, A CAD Approach*, John Wiley and Sons, Inc. New York.
3. Lanni C., Ceccarelli M. and G. Figliolini 2002 An analytical design for three circular-arc cams. *Mechanism and Machine Theory*, 37:915–924.
4. Lanni C., Ceccarelli M. and J.C.M. Carvalho, 1999 An analytical design for two circular-arc cams, in: *Proceedings of the Fourth Iberoamerican Congress on Mechanical Engineering*, Santiago de Chile, Vol. 2.
5. Wang L.C.T and Y.T. Yang 1996 Computer aided design of cam motion programs. *Computers in Industry*, 28:151–161.
6. Chen F.Y. 1977 A survey of the state of the art of cam system dynamics. *Mechanism and Machine Theory*, 12:201–204.
7. Borg J., Bonello P. and C. Ciantar 1997 A computer based tool for the design and manufacture of automatic lathe cams. *Computers in Industry*, 34:11–26.
8. Yan, H.S., Tsai M.C. and M.H. Hsu 1996 An experimental study of the effects of cam speeds on cam follower systems. *Mechanism and Machine Theory*, 31:397–412.
9. Huey C.O. and M.W. Dixon 1974 The cam-link mechanism for structural error-free path and function generation. *Mechanism and Machine Theory*, 9:367–384.
10. D.M. Tsay and B.J. Lin 1996 Improving the geometry design of cylindrical cams using non-parametric rational B-splines. *Computer-Aided Design*, 20(1):5–15.
11. Lampinen J. 2003 Cam shape optimisation by genetic algorithm. *Computer Aided Design*.
12. Tuma J.J. 1987 *Engineering Mathematics Handbook*, Mc Graw-Hill, New York.
13. Shigley E.S. and J.J. Uicker 1981 *Theory of Machines and Mechanisms*, Mc Graw Hill, New York.
14. Bouzakis K.D., Mitsi S. and J. Tsiafis 1997 Computer aided optimum design and NC milling of planar cam mechanisms. *International Journal of Mechanism Tools Manufacturing*, 37(8):1131–1142.



# On the Power Transmission and Running Quality of Micro-Mechanisms

Hanfried Kerle

**Abstract** Generally micro-mechanisms are mechanisms of smaller dimensions compared with their correspondingly similar and bigger original ones that are really or only virtually existing on a special design stage. It is the goal of this paper to find out the conditions under which downward scaled micro-mechanisms can match with their original ones on a mechanically correct level concerning the transmission of mechanical power and running quality.

**Keywords** Kinematics · Mechanism design · Similarity mechanics · Micro-mechanisms · Mechanical efficiency

## Introduction

Micro-mechanisms often form the mechanical part of a mechatronical system and serve in the same way as their corresponding similar (and bigger) original mechanisms to transmit motion and forces/torques from the input to the output link [1]. The mechatronical system shown in Fig. 1 is a Micro-SCARA-Robot used for micro-assembly tasks, say, for the assembly of miniature parts [2].

But, especially with micro-mechanisms *Coulomb friction forces/torques* may cause problems and may reduce the *running quality*. In the following the measure to assess the running quality is to be the (*mechanical*) *efficiency* of the two mechanisms under investigation, the micro-mechanism and the original one [3, 4]. It is assumed that the micro-mechanism is designed and/or built similar to the original one, according to the rules of similarity mechanics [5–7]. The idea is now to observe the mechanical power flow, generally from the input to the output. By calculating the loss of power caused by the Coulomb friction forces in the joints it is possible to

---

H. Kerle (✉)

Institut für Werkzeugmaschinen und Fertigungstechnik, Technische Universität Braunschweig, Langer Kamp 19b, D-38106 Braunschweig, Germany  
e-mail: h.kerle@t-online.de

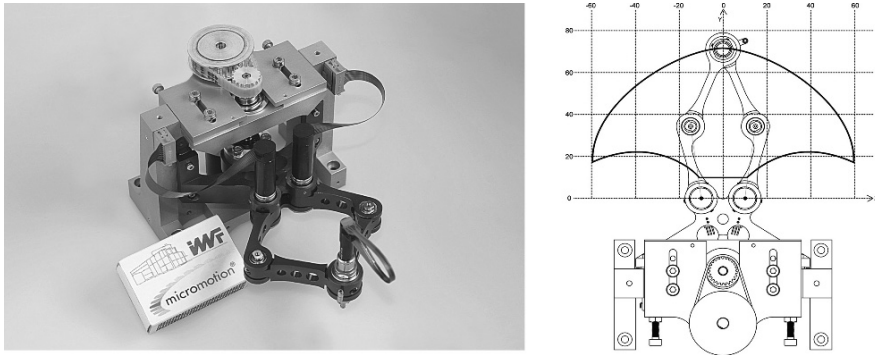


**Fig. 1** Micro-SCARA-Robot as a micro-mechanism

find out the efficiencies of the two mechanisms, dependent on the Coulomb friction coefficients and the joint forces.

### Design Series and Geometric Similarity

A *design series* of mechanisms is a group of mechanisms that appear on different dimensional levels, but consist of the same types of mechanisms, are made of the same materials and also were submitted to the same manufacturing processes as regards links and joints [6]. The original mechanism represents the basic dimensional level from which the subsequent mechanisms on smaller dimensional levels are derived. The mechanisms with smaller dimensions are also called *models* having the characteristics named above. The most important design law is that of *geometric similarity* represented by an angular ratio  $\Phi$  and length ratio  $\Lambda$  between model M and original O. We have

$$\Phi = \varphi_M / \varphi_O \equiv 1, \tag{1a}$$

$$\Lambda = L_M / L_O = \text{konst.} < 1. \tag{1b}$$

The angle  $\varphi$  [deg, rad] is arbitrary and the length L [m] is arbitrary as well and both are measured at the same corresponding places on the model and on the original. The ratio  $\Lambda$  is also called the *basic model scale (factor)*. We get for a design series of order k the *model scale (factor) of order k*, i.e.

$$\Lambda_k = (L_M / L_O)^k = \Lambda^k, k = 1, 2, 3, \dots \tag{2}$$

In Fig. 2 four slider-crank mechanisms are shown which all belong to a design series marked by  $\Lambda = 0.5$  and  $k = 0$  (Original), 1, 2, 3.

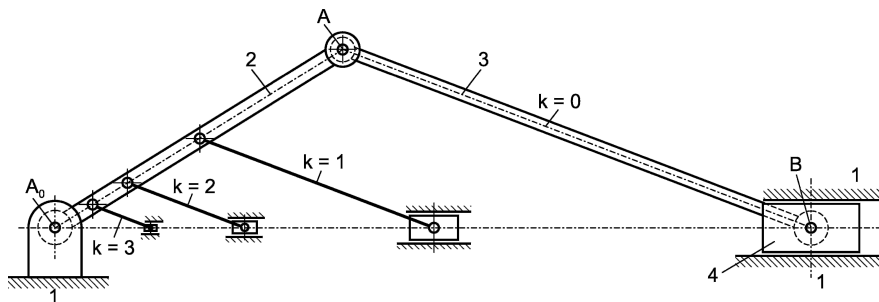


Fig. 2 Design series of a centric slider-crank

### Mechanical Power Balance and Efficiency

To start we assume a mechanism having one d.o.f. The mechanical power balance can be expressed by a sum of single power terms  $P$  of external input and output forces/torques (indices “Inp” and “Out”) as well as gravitational, frictional and inertial forces/torques (indices “G” and “F” and “I”), correlated to an acceptable state of velocity and dependent on the input coordinate, say, input angle  $\varphi$  as time function  $\varphi(t)$ . The sum must vanish according to the power theorem in mechanics, i.e.

$$P_I + P_{Inp} + P_{Out} + P_G + P_F = 0. \tag{3}$$

This power equation can be divided by the input angular velocity  $\omega \equiv d\varphi/dt$  and instead of power terms we now sum up torque terms  $M^*$  that are functions of  $\varphi(t)$ :

$$M_{Inp}^* - M_{Out}^* + M_G^* - M_F^* = M_I^*, \quad \text{where} \tag{4}$$

$$P_I/\omega = -M_I^* = -\sum_i \left( \vec{F}_{I,i} \cdot \vec{s}'_{I,i} \right) \tag{4a}$$

$$P_{Inp}/\omega = M_{Inp}^* = M_{Inp}, \tag{4b}$$

$$P_{Out}/\omega = M_{Out}^* = \sum_i \left( \vec{F}_{Out,i} \cdot \vec{s}'_{Out,i} \right) + \sum_i \left( \vec{M}_{Out,i} \cdot \vec{\varphi}'_{Out,i} \right), \tag{4c}$$

$$P_G/\omega = M_G^* = \sum_i \left( \vec{F}_{G,i} \cdot \vec{s}'_{G,i} \right) \quad \text{and} \tag{4d}$$

$$P_F/\omega = M_F^* = \sum_i \sum_j \left( \vec{F}_{F,ij} \cdot \vec{s}'_{F,ji} \right) + \sum_i \sum_j \left( \vec{M}_{F,ij} \cdot \vec{\varphi}'_{F,ji} \right). \tag{4e}$$

Here single vector forces are written  $\vec{F}$  and vector torques are designated by  $\vec{M}$ . A special term is given to the inertial force of link  $i$  assigned to and passing through the so-called *inertial pole* of this link and thus causing no additional torque [7]. Equations (4a), (4c) to (4e) sum up scalar products of forces (torques) and velocities (angular velocities) of the corresponding points and links where they act upon. As a result of the division of all the single power terms in Eq. (3) by  $\omega$ , we reduce the velocities to so-called *transmission functions of 1st order* dependent on  $\varphi$  alone, for example  $\vec{s}'_{G,i} \equiv d\vec{s}_{G,i}/d\varphi$ , etc.

The calculation of the (*coefficient of mechanical*) *efficiency* is usually performed by setting

$$\eta = 1 - \left| \frac{P_F}{P_{\text{Inp}}} \right| = 1 - \left| \frac{M_F^*}{M_{\text{Inp}}^*} \right|, \quad 0 \leq \eta \leq 1. \quad (5)$$

Generally the efficiency  $\eta$  is not constant, but a function of the input angle  $\varphi$ . Therefore, instead of  $\eta = \eta(\varphi)$  often the average value during one cycle motion of the mechanism is determined for practical reasons.

Looking at Eq. (5) and subsequently also at Eq. (4e) it becomes necessary to calculate the Coulomb friction forces  $F_{F,ij}$  and friction torques  $M_{F,ij}$  in all the joints “ij” between links  $i$  and  $j$  of the mechanism [8]. In sliding and cam joints the friction force  $F_{F,ij}$  is a tangential force in direction of the relative motion of the links  $i$  and  $j$  and – together with the normal force  $F_{N,ij}$  – part of the joint force  $G_{ij}$ , i.e.

$$G_{ij} = \sqrt{(F_{F,ij})^2 + (F_{N,ij})^2}, \quad (6a)$$

and for the friction torques in turning pairs “ij” with a pin radius  $r_{ij}$  we have

$$M_{F,ij} = r_{ij} \cdot F_{F,ij}. \quad (6b)$$

The Coulomb friction law introduces the friction coefficient  $\mu_{C,ij}$  between the two forces  $F_{F,ij}$  and  $F_{N,ij}$  and a friction angle  $\rho_{C,ij}$  can be defined, namely

$$\mu_{C,ij} = F_{F,ij}/F_{N,ij}, \quad (7a)$$

$$\rho_{C,ij} = \arctan(\mu_{C,ij}), \quad (7b)$$

so we have

$$F_{N,ij} = G_{ij} \cdot \cos(\rho_{C,ij}) = \frac{G_{ij}}{\sqrt{1 + \mu_{C,ij}^2}}. \quad (7c)$$

To proceed efficiently, we assume the following items [9]:

- Each pair (joint) of the mechanism has the same friction coefficient, i.e.  $\mu_{C,ij} = \mu_C$ ,
- each turning pair of the mechanism has the same pin radius, i.e.  $r_{ij} = r$ ,
- the value  $\mu_C^2$  is very much smaller than 1, which yields  $F_{N,ij} = G_{ij}$ .

The last assumption simplifies the calculation of  $M_F^*$  considerably, now it is possible to determine all the joint forces on a preliminary stage *without* paying respect to power losses because of Coulomb friction. Due to all these assumptions we can now insert

$$M_F^* = \mu_C \cdot \left[ \sum_i \sum_j \left( \left| \vec{G}_{ij} \right| \cdot \left| \vec{s}'_{ji} \right| \right) + r \cdot \sum_i \sum_j \left( \left| \vec{G}_{ij} \right| \cdot \left| \vec{\varphi}'_{ji} \right| \right) \right] \quad (8)$$

into Eq. (5) where the *relative* transmission functions of 1st order run

$$\left| \vec{s}'_{ji} \right| = s'_{ji} = \left| \vec{s}'_j - \vec{s}'_i \right|, \quad (9a)$$

$$\left| \vec{\varphi}'_{ji} \right| = \varphi'_{ji} = \left| \vec{\varphi}'_j - \vec{\varphi}'_i \right|. \quad (9b)$$

### Model Laws

There are only two model laws in similarity mechanics that can be assigned to mechanisms being mechanical systems, the FROUDE law and the CAUCHY law. For both laws we can *either* choose the model scale  $\Lambda = L_M/L_O$  according to Eq. (1b) or the time scale

$$T = t_M/t_O \quad (10)$$

freely. Additionally the mechanical quantities *linear velocity*  $V$  [m/s] =  $L/t$  and *linear acceleration*  $A$  [m/s<sup>2</sup>] =  $L/t^2$  as well as the three dimensional constants *mass density*  $\rho$  [kg/m<sup>3</sup>], *modulus of elasticity*  $E$  [N/m<sup>2</sup> = kgm<sup>-1</sup>s<sup>-2</sup>] and *gravitational coefficient*  $g = 9.81\text{m/s}^2 = g_M = g_O$  are introduced for the model  $M$  and the original mechanism  $O$ . Besides, we keep in mind that for design series the equations  $\rho_M = \rho_O = \rho$  and  $E_M = E_O = E$  hold.

The FROUDE law [10, 11] equates the ratio  $f_G = F_{G,M}/F_{G,O}$  of the gravitational forces  $F_G = \rho \cdot L^3 \cdot g$  with the ratio  $f_I = F_{I,M}/F_{I,O}$  of the inertial forces  $F_I = \rho \cdot L^3 \cdot A$  for  $M$  and  $O$ , which results in  $\Lambda = T^2$  and  $f_G = f_I = f_{Fr} = \Lambda^3 = T^6$ .

The CAUCHY law [10, 11] equates the ratio  $f_E = F_{E,M}/F_{E,O}$  of the elastic forces  $F_E = E \cdot L^2$  with the ratio  $f_I = F_{I,M}/F_{I,O}$  of the inertial forces  $F_I = \rho \cdot L^3 \cdot A$  for  $M$  and  $O$ , which results in  $\Lambda = T$  and  $f_E = f_I = f_{Ca} = \Lambda^2 = T^2$ .

Following the FROUDE law means to establish a balance of influence between the gravitational and inertial forces in  $M$  – model or micro-mechanism – and in  $O$

as well, whereas the CAUCHY law cares for a balance of influence of the elastic and inertial forces. So, when dealing with mechanisms running with low speed (no elastic vibrations of the links excited), it is recommended to make use of the FROUDE law, and when dealing with mechanisms running with high speed (elastic vibrations excited), one should apply the CAUCHY law in the process of designing micro-mechanisms that are similar to original mechanisms.

### Similar Mechanical Power Transmission

Mechanical power is generally defined by the scalar products  $P = \vec{F} \cdot \vec{V}$  or  $P = \vec{M} \cdot \vec{\omega}$ . We can derive two equations on the base of the two presented model laws, namely

$$\text{FROUDE} \quad \frac{P_M}{P_O} \equiv \frac{P_{Fr}}{P_O} = f_{Fr}(\Lambda) = \sqrt{\Lambda^7} = T^7, \tag{11a}$$

$$\text{CAUCHY} \quad \frac{P_M}{P_O} \equiv \frac{P_{Ca}}{P_O} = f_{Ca}(\Lambda) = \Lambda^2 = T^2. \tag{11b}$$

These equations are shown graphically in Fig. 3. The FROUDE model can transmit less power from the input to the output link than the CAUCHY model, especially in the lower  $\Lambda$  range which is undoubtedly the preferred range for micro-mechanisms (Fig. 3, left). If, for example, we want to limit the power transmission ratio  $P_M/P_O$  to a value of, say, 0.1 for practical or life cycle reasons, marked by the horizontal line on the right zoomed side of Fig. 3, we notice that this condition can be fulfilled for the FROUDE model with a model scale  $\Lambda = \Lambda_{min} = 0.52$ , in contrast to the lightweight CAUCHY model with a model scale  $\Lambda = \Lambda_{min} = 0.32$ , a difference of 62.5 %!

To calculate the difference of the loss of power caused by Coulomb friction between M and O we set

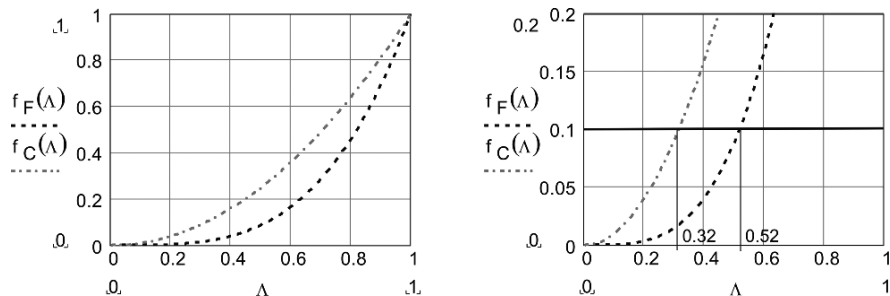


**Fig. 3** Similarity scales for the transmission of mechanical power with FROUDE and CAUCHY models: Unity square (left), zoom range  $0 < f_{Fr}, f_{Ca} \leq 0.2$  (right)

$$\mu_{Cr} = \mu_{C,M}/\mu_{C,O} \tag{12}$$

and thus introduce the ratio of the Coulomb friction coefficients of M and O. We then take from Eq. (5) the ratio of the efficiencies of M and O, i.e.

$$\eta_r = \frac{\eta_M}{\eta_O} = \frac{|P_{Inp,O} - \mu_{Cr} \cdot P_{F,O}|}{|P_{Inp,O} - P_{F,O}|} = \frac{|M_{Inp,O}^* - \mu_{Cr} \cdot M_{F,O}^*|}{|M_{Inp,O}^* - M_{F,O}^*|}, \tag{13}$$

and get two very interesting and at the same time simple results:

1. The ratio of efficiencies of M and O depends only on the ratio of their Coulomb friction coefficients, not on the model laws, and therefore neither on the actual model scale.
2. The running quality of a model in general and consequently also of a micro-mechanism having a model scale of  $\Lambda_k \ll 1$  is only inferior to the running quality of the original mechanism, i.e.  $\eta_r < 1$ , if the friction coefficient of the model is bigger than the friction coefficient of the original, i.e.  $\mu_{Cr} > 1$ . The case  $\mu_{Cr} = 1$  is equivalent with  $\eta_M = \eta_O$ .

### Example of Application

A centric Scotch-yoke mechanism being the “original mechanism” is shown in Fig. 4. The slider 4 with an output force  $F_{Out}$  is moved by the rectangular lever 2 with an input force  $F_{Inp}$  at point B with input angle  $\varphi$  and input angular velocity  $\omega \equiv d\varphi/dt$ . The dimensions of this slider can be neglected compared with the dimensions of the rest of the links. There is Coulomb friction ( $\mu_{C,O} = \text{const.}$ ) only

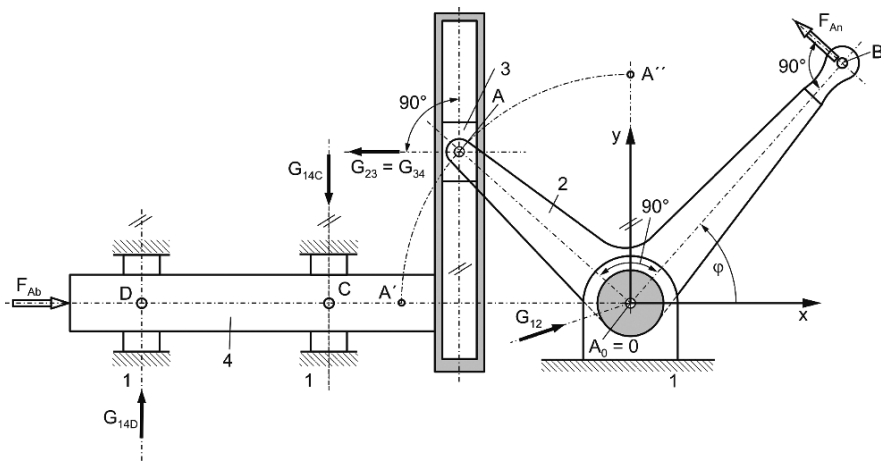


Fig. 4 Scotch-yoke mechanism and designations

between the sliding pairs 14 (C, D) and 34 (A). The question is for the efficiency  $\eta_O$  of the original mechanism and for the ratio  $\eta_r = \eta_M/\eta_O$  in case  $\mu_{C,M} \neq \mu_{C,O}$ .

Assuming that the mechanism is driven manually, we neglect inertial forces (and also gravitational forces) and apply Eqs. (4, 5, 8) with  $r = 0$  which after some detailed calculations finally yields

$$\eta_O = 1 - |\mu_{C,O} \cdot (2 \cdot \lambda_2 \cdot \cos \varphi + \tan \varphi)|, \quad 0 \leq \eta_O < 1, \tag{14}$$

where  $\lambda_2 = OA/CD$ . The efficiency includes a  $\varphi$ -function that is unique characterizing the mechanism.

Now let us assume that a micro-mechanism is to be derived from the original mechanism. After the process of machining the joints of the micro-mechanism a Coulomb friction coefficient of, say,  $\mu_{C,M} = 1.1 \cdot \mu_{C,O}$ , i.e.  $\mu_{Cr} = 1.1$ , is revealed which is approximately valid for all the joints. To find out what will be the consequences during operation we apply Eq. (13) and get

$$\eta_r = \frac{1 - |\mu_{Cr} \cdot \mu_{C,O} \cdot (2 \cdot \lambda_2 \cdot \cos \varphi + \tan \varphi)|}{1 - |\mu_{C,O} \cdot (2 \cdot \lambda_2 \cdot \cos \varphi + \tan \varphi)|}. \tag{15}$$

In Fig. 5 the functions  $\eta_O$  (left, continuous curve),  $\eta_M$  (left, dashed curve) and  $\eta_r$  (right) are drawn representing the following data:  $\mu_{C,O} = 0.1$ ,  $\mu_{Cr} = 1.1$ ,  $\lambda_2 = 2.0$ . The maximum efficiency of the original mechanism is 0.63 at the angle position of around  $\varphi = 60^\circ$ , the model or micro-mechanism still achieves 0.59, i.e. 94% of it. Around  $\varphi = 80^\circ$  the efficiency of the Scotch-yoke mechanism dramatically falls down to zero, the mechanism reaches its locking position.

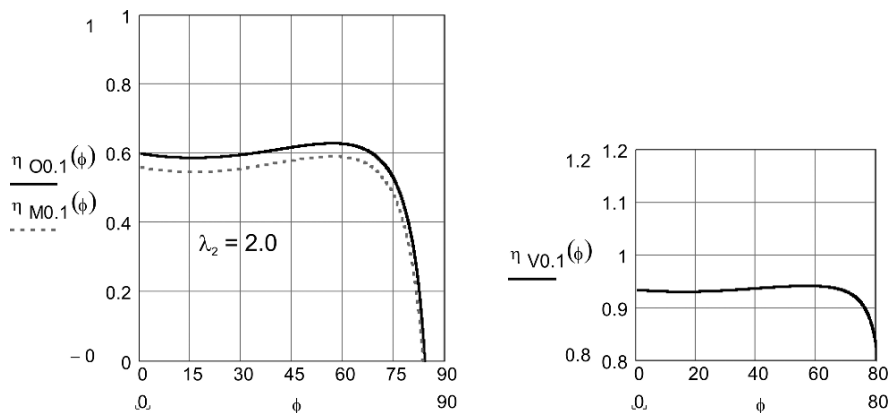


Fig. 5 Efficiencies versus input angle of the Scotch-yoke mechanism



## Conclusion

The planning, design and manufacturing of micro-mechanisms has to be performed on the basis of the model laws FROUDE or CAUCHY in similarity mechanics in order to avoid mechanical failures under operation. Micro-mechanisms can then be regarded as models smaller in dimensions, but nevertheless with the ability to bear loads similar to the originals, only on a lower, but predictable level. The model laws simplify for design series made of the same material(s) for links and joints. Based on the model laws the running quality of the micro-mechanism measured by means of the mechanical efficiency will remain unchanged compared with the original. Differences of the running quality between model and original only occur in cases where the Coulomb friction coefficients differ from each other. This is demonstrated with the example of a Scotch-yoke mechanism.

## References

1. Carbone G., Ceccarelli M., Kerle H., Raatz A., Design and Experimental Validation of a Microgripper, *Journal of Robotics and Mechatronics*, Vol. 13, 2001, No. 3, pp. 319–325.
2. Slatter R., Burisch A., Entwicklung eines Mikro-Scara-Roboters für hochpräzise Montageaufgaben, *Konstruktion*, Vol. 57, 2005, No. 5, pp. 42–45.
3. Kraus R., Zur graphisch-rechnerischen Bestimmung des Wirkungsgrades von Getrieben, *Reuleaux-Mitteilungen – Archiv für Getriebetechnik*, Vol. 2, 1934, No. 8, pp. 57–58 and plate No. 15.
4. Huhn E., Zur Optimierung der Laufgüte ungleichmäßig übersetzender Getriebe, *Wiss. Zeitschrift der TH Karl-Marx-Stadt*, Vol. 7, 1965, No. 3, pp. 73–82.
5. Kerle H., Zur Entwicklung von Baureihen für Getriebe und von belastbaren Getriebemodellen auf der Grundlage der Ähnlichkeitsmechanik, *VDI-Berichte No. 1966*, 2006, pp. 221–240.
6. Pahl G., Beitz W., Feldhusen J., Grote K.-H., *Konstruktionslehre*, 5th ed., Springer Verlag, Berlin, 2003.
7. Federhofer K., Die Trägheitspolkurve als Hilfsmittel der Dynamik ebener Getriebe, *VDI-Tagungsheft No. 1*, Düsseldorf, 1953, pp. 101–102.
8. Kerle H., Pittschellis R., Corves B., *Einführung in die Getriebelehre – Analyse und Synthese ungleichmäßig übersetzender Getriebe*, 3rd ed., B.G. Teubner Verlag, Wiesbaden, 2007.
9. Stündel D., Der Einfluß der Mechanismengeometrie auf die Reibungsverluste in den Gelenken, *Feingerätetechnik*, Vol. 23, 1974, No. 1, pp. 7–10.
10. Beitz W., Küttner, K.-H. (Eds.), *DUBBEL – Handbook of Mechanical Engineering*, Springer Verlag, London, 1994, pp. A69–A72.
11. Weber M., Das Allgemeine Ähnlichkeitsprinzip der Physik und sein Zusammenhang mit der Dimensionslehre und der Modellwissenschaft. In: *Jahrbuch der Schiffbautechnischen Gesellschaft*, Vol. 31, Chapt. XIV, pp. 274–354, Verlag Julius Springer, Berlin, 1930.

# Probable Simulating Models of Wear for Open<sup>1</sup> Gearing with High-Ratio Gear

Alexander Golovin and Tamara Milevskaya

**Abstract** Following properties of open<sup>1</sup> involute gearing with a high-ratio gear are analysed: analog of the contact stress and analog of the energy dissipation. It is shown that two wear types are characteristic of open power involute gearings with a high-ratio gear. These types are: wear due to the contact stress for a pinion, and wear due to the energy dissipation for a gear on the initial stage. Further wear is defined by the pitch point location. If it is inside the engagement area, then this pitch point is a singular point initiating the intense wear in this point's vicinity. Then the wear is developing due to the energy dissipation until the next singular point appears, etc. The case of recessing engagement is considered, when the pitch point is outside the engagement area. It is demonstrated that in this case the pinion wear can be decreased, and the intense development of the gear wear in the pitch point vicinity can be avoided. Theory is illustrated by the wear of gearing of sheet-stamping press "Toledo", and of gearing AEG of electric motor coach.

**Keywords** Gearing · Wear · High ratio · Geometrical analogs of wear · Teaching methods

## Introduction

It is usually recommended to apply involute gearings with gear ratios  $u = 2 \dots 3$  [1]. Though sometimes [2, 3, 4] the gearings with higher ratios (Fig. 1) are used. Figure 1a shows the "Toledo" press mechanical diagram. Figure 1b demonstrates the part of initial tooth profile for the intermediate power open involute gearing ( $u = 6, 33; z_1 = 15; z_2 = 95; m = 26\text{mm}$ ). Part of gearing for the AEG electric motor coach is shown on Fig. 1c ( $u = 3, 69; z_1 = 19; z_2 = 70; m = 9\text{mm}$ ). Examples

---

A. Golovin (✉)

Department of Theory Mechanisms and Machines, Bauman Moscow State Technical University,  
2nd Baumanskaya Str., 5, 105005 Moscow, Russia  
e-mail: aalgol@rambler.ru

<sup>1</sup> *Open gearing*—the gearing that has no protection from negative factors of the working environment (this definition may include the absence of grease). Syn.: *Unprotected gearing*.

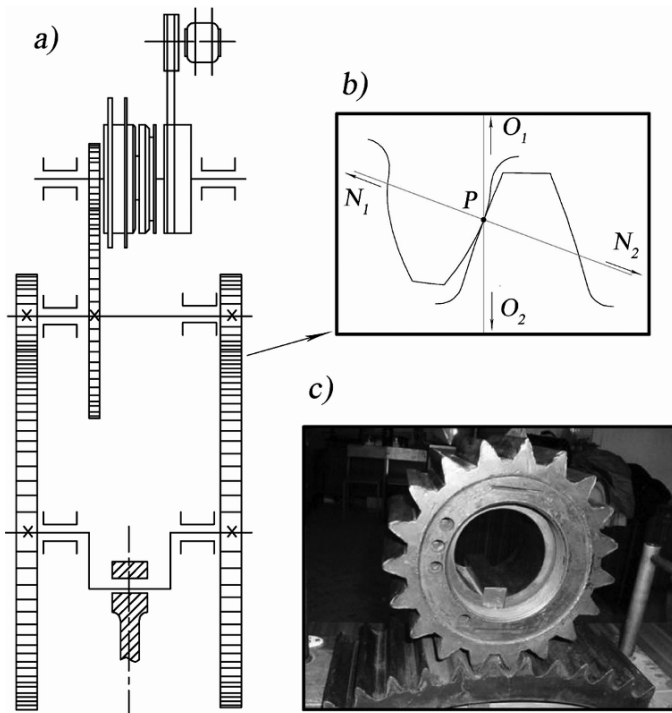


**Fig. 1** Examples of gearing with big gear ratios

of gears with essential wear are demonstrated deliberately. Both gears were operated under severe conditions: “Toledo” press gearing is an open one, and it was operated in blanking workshop; AEG gearing is a closed one, but with bad discharge of the wear debris. It must be noticed that mechanical properties of the pinion are better than those of the gear in both cases.

In the present paper the wear is analysed on macroscopic level. It allows to get rough, simple, and plausible model. Any engineer should simplify and apply basic regularities rather than search for them. According to the classification given in [4, 5], on the simple simulating model level the following wear types can be explained: continuous wear, pitting, and galling. It can be understood through insight that the wear phenomenon cannot be described by any single model. But on each stage one or several factors highly influencing the process, can be determined. Model is based on two criteria: geometrical analog of contact stress ( $\sigma$ ) and that of energy dissipation. The latter one takes into account the sliding path of mating profiles ( $\sigma \cdot v_{sl}/v^t$ ). Operating conditions of the gears are shown on Fig. 1 according to [2–7], and can be described as follows:

- pair friction is high; properties of material and the tooth surface of the pinion are better than those of the gear;

- expected wear of the pinion surface is a bearing-pitting one; that of the gear is galling.

In this case contact stress  $\sigma_c$  is a dominating factor of the pinion wear. This factor was calculated by the Herz formula [3, 9]:

$$\sigma_c = 0.418 \sqrt{\frac{Q^n E}{b} \left( \frac{1}{\rho_1} \pm \frac{1}{\rho_2} \right)} \tag{1}$$

where

$\rho_1, \rho_2$ —radii of curvature for mating involutes;  
 $\rho_1 + \rho_2 = N_1 N_2$ ;  $Q^n$  – reaction in the kinematic pair;  
 b—wheel width.

Contact stress corresponds to its geometrical analog  $\sigma$  [3–5]

$$\sigma = \sigma_Q \sigma_\rho = \sigma_k / B, \tag{2}$$

where

$\sigma_Q = (Q^n / Q^n_{max})^{1/2}$  – analog of normal reaction in higher pair;  
 $\sigma_\rho = \sigma(\rho_1, \rho_2) = \sqrt{\frac{1}{\rho_1} \pm \frac{1}{\rho_2}}$  – analog of contact stress in the contact point under unit load;  
 $\sigma = \sigma_Q \sigma_\rho$ —contact stress analog in the contact point.

On the initial phase of the gear wear the dominating galling factor is the energy (power) dissipation  $\sigma_c \cdot v_{sl}$ . Further phases depend on the wear in special points on the gear tooth surface [3–5]. Geometrical analog of the galling gear wear is  $(\sigma \cdot v_{sl} / v^t)$  considering the profile sliding path. Rolling friction loss is not sufficient and thus is not considered.

Here are:

$v_{sl}$ —analog of sliding velocity in higher pair;  
 $v^{\tau 1,2}$ —analog of tangential components of contacting points velocities;  
 $(\sigma \cdot v_{sl})$ —analog of the energy dissipation in the contact point.

Therefore, the pinion wear is

$$w_{pin} \sim \sigma,$$

and the gear wear

$$w_g \sim \sigma \cdot v_{sl} / v^t.$$

### Properties of Involute Gearing

Figure 2 shows curves of the pinion and gear wear for two gearings with different gear ratios: high one (Fig. 2b, “Toledo” press gearing,  $u = 6.33$ ), and moderate one (Fig. 2b, [8],  $u = 1.5$ ). Here  $N_1N_2$ —path of contact,  $P$ —pitch point,  $B_1; B_2$ —engagement and disengagement points for the pair,  $B_1^*; B_2^*$ —tooth remating points.

It can be seen from Fig. 2b that the engagement zone with low gear ratio corresponds to the  $\sigma_c$  maximum values and minimum values of  $(\sigma \cdot v_{sl}/v^f)$ . Hence the contact strength analysis is convenient to be done for stresses in the pitch point [8].

In the case of a high-ratio gearing the engagement zone moves toward the beginning of path of contact being point  $N_1$ . Therefore,  $\sigma_c$  and  $\sigma_v$  in points  $B_1$  and  $B_1^*$  grow sufficiently. Thus the contact strength analysis should be performed for

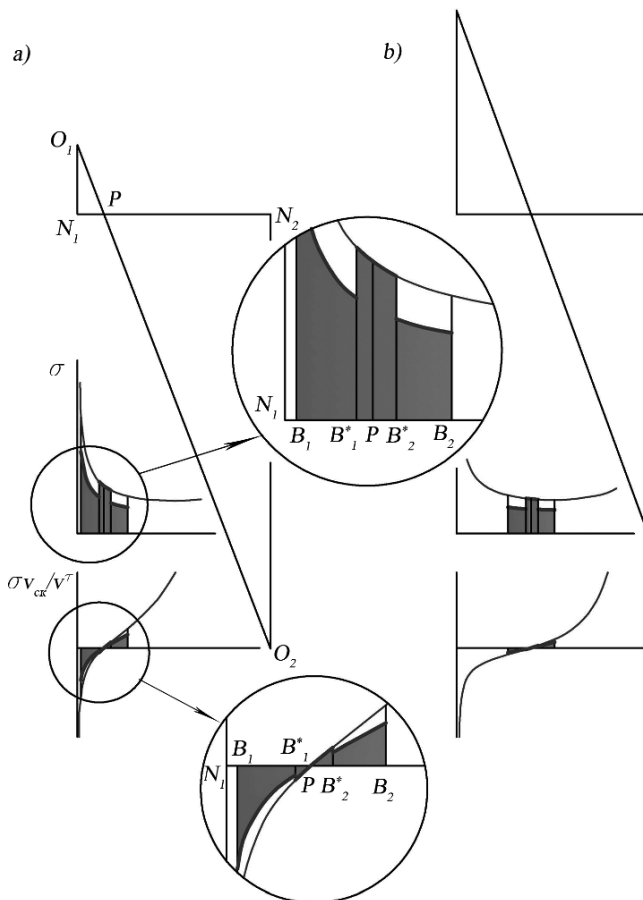


Fig. 2 Curves of wear for gearings with different gear ratios

stresses in points  $B_1$  and  $B_1^*$ . Though to all gearings of the  $B_1 - P - B_2$  types; It is peculiar that the  $(\sigma v)$  wear takes place in the vicinity of point  $P$ , while the  $\sigma$  wear is situated in the very point  $P$ . Therefore, the pitch point is a singular point.

Figure 3 shows the simulating model of wear for a pair of the  $B_1 - P - B_2$  type gears described in [3]. Initial wear stage and subsequent two-three stages can be simulated rather easily. First stage is made in the assumption that, for example, the gear is rigid while the pinion is worn.

Further it is supposed that the pinion is rigid, and the gear is subjected to wear, etc. (Fig. 3a-c). Analysis of this stage yields plausible results: pinion wear, growing number of singular points during the wear process, and path of contact distortion described in [3]. Further wear of a pair could be predicted: more rigid pinion keeps its convex profile while less rigid gear is being destroyed under alternate action of galling, singular points appearance, and destruction in the said points due to the contact stresses, etc. Natural continuation of this process is a sufficient change in the gear tooth profile. On figures above the worn teeth have concave profiles. Two peculiarities of the process are not amenable to the above simulating procedure.

The first one is a contact stress jump at the pair engagement and disengagement (Fig. 3b). This problem can be considered as an analog of Shtaerman's [9] problem on the contact of a punch with an elastic half-plane.

The second peculiarity is a plastic flow at the engagement pass through the pitch point (Fig. 3d).

Proposed description of the process is proved by the examples shown in Figs. 4 and 5.

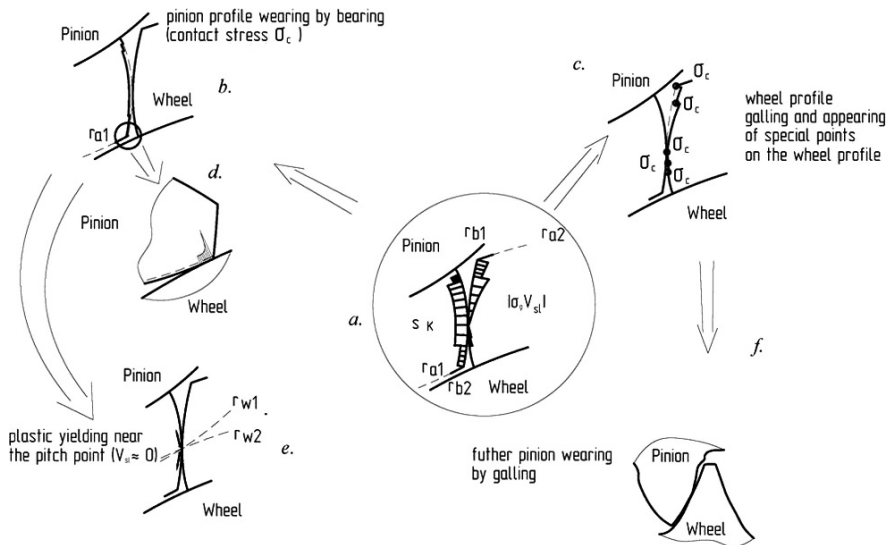


Fig. 3 Wear evolution for a pair of gears of the  $B_1 - P - B_2$  type

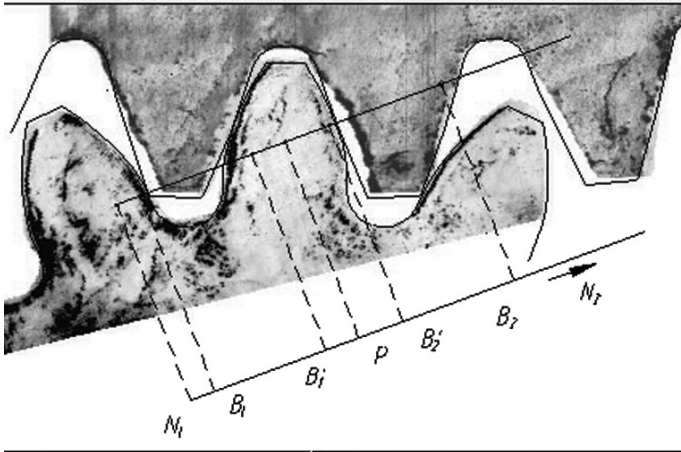
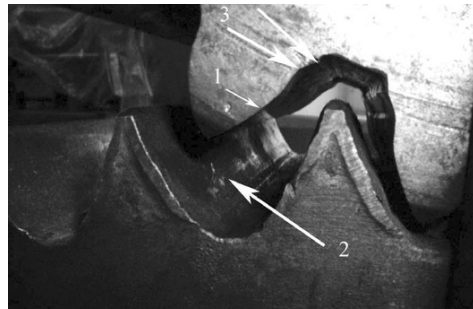


Fig. 4 Wear of the “Toledo” press gearing, and comparison of worn gearing with the initial one

Fig. 5 Wear of gearing shown on Fig. 1c



### Statement of Problem on the Wear of Recessing Gearing with High-Ratio Gear

It was shown in Part 1 that the appearance of a singular point in the pitch point at the initial wear stage is a source of the intense teeth destruction for a gearing with high-ratio gear. Besides, the pinion tooth points and the gear dedenda are subjected to high contact stress as compared with a low-ratio gear gearing (Fig. 2a,b). This stress can be lowered if active segment of path of contact is outside the pitch point, that is the engagement sequence  $B_1 - P - B_2$  is replaced with  $P - B_1 - B_2$ . In this case the teeth wear is increased but the destruction source in the pitch point disappears. Therefore the following problem can be stated:

1. Define the less intense wear zone;
2. Define the existence area of possible coefficient  $x_1 - x_2$  of displacement.

It is enough to find derivative  $d(\sigma \cdot v_{s1}/v^t)/d\rho$  (Fig. 6) and select the zone where this derivative is close to constant to solve the first problem. This segment has a

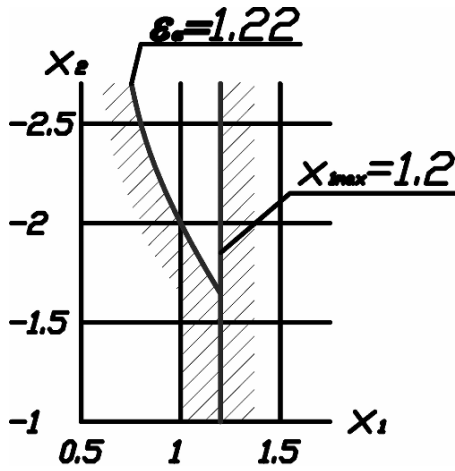


Fig. 6 Domain of existence of displacements  $x_1 - x_2$

sufficient extent. It can be easily seen that the inflection point for function  $(\sigma \cdot v_{sl}/v^t)$  depends on the gear ratio.

The second problem is to find an area of existence of  $x_1 - x_2$  displacement, and is solved by natural restrictions  $x_1 > 0.123$ ;  $x_2 > -4.5$ ;  $\epsilon_\alpha > [\epsilon_\alpha]$ ;  $s_{a1} > [s_a]$ . If the latter restriction can't be imposed, then the diameter of the pinion teeth point circle can be decreased.

Result is the displacement existence domain for gear and pinion (Fig. 7). Example to design the recessing gearing for  $x_1 = 1$ ,  $x_2 = -2$  and curves of initial stage of the pinion and gear wear are shown on Fig. 8a. For comparison, Fig. 8b shows the "Toledo" press gearing designed for  $x_1 = 0.2$ ,  $x_2 = 0$  displacements. The table contains results of comparison for these cases. Comparison objects are chosen to be ratios

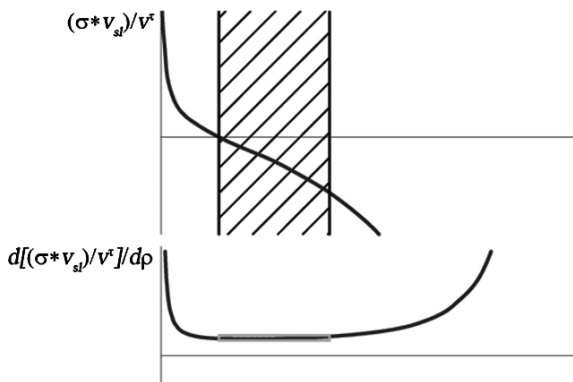
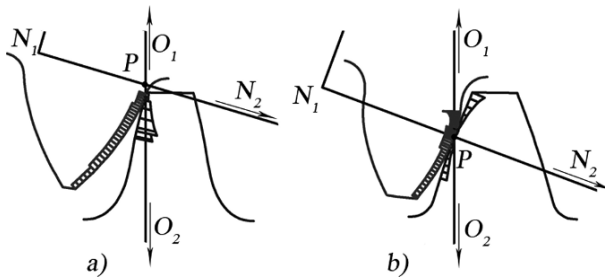


Fig. 7 Properties of recessing engagement





**Fig. 8** Comparison of wear curves for the recessing gearing and that analysed according to usual recommendations

$$\sigma_{1gr} : \sigma_{2gr} \text{ and } (\sigma \cdot v_{sl}/v^t)_{1gr} : (\sigma \cdot v_{sl}/v^t)_{2gr}$$

		$\sigma_{gr}$	$(\sigma \cdot v_{sl}/v^t)_{gr}$
gear	$P - B_1 - B_2$	4.495	9.98
	$B_1 - P - B_2$	7.892	6.797
ratio		0.57	1.468

### Conclusion

1. It is shown that the elevated pinion wear due to the contact stresses and the gear wear due to the energy dissipation at the pair engagement are peculiar to open gearings with a high-ratio gear and pitch point located inside active path of contact. Gear wear progress is defined by the singular point appearance in the pitch point.
2. It is proposed to design a gearing with a pitch point located outside the path of contact – that is, recessing gearing. Segment with a constant gradient of the energy dissipation analog function is taken as a criterion. Domain of existence of the gear and pinion displacements for such gearing is found.
3. Recessing gearing design is shown in the example. Advantages of this gearing as compared with the usual one are: essentially lowered contact stresses on the pinion profile, and minimum energy dissipation at the gear tooth engagement. Disadvantages are: elevated energy dissipation at the gear tooth disengagement, and decreased length of the active profile for the gear tooth.

### References

1. T. Bolotovsaya, I. Bolotovskiy, G. Goncharov et al.: Handbook on geometric analysis of involute and worm gearings. Edited by I. Bolotovskiy. M.: MashGiz, 1962 (in Russian).

2. Borisov, A. Golovin, A. Ermakova: Some examples from history of machinery in TMM teaching. Proceeding of International Symposium on History of Machines and Mechanisms, Kluwer Academic Publishers, 2004, pp. 107–118.
3. Golovin, A. Borisov, I. Drozdova, B. Shuman: The simulating models of a gearing wear. Proceeding of CK2005, International Workshop on Computational Kinematics, Cassino, May 4–6, 2005. Paper XX-CK2005.
4. Golovin, A.: An possible mechanisms of kinematic pair wear in the TMM course. Proceedings of Symposium “Gydrodynamics theory of oiling – 120 years”. Orel, May 18–20 2006, vol. 2, pp. 43–51 (in Russian).
5. D. Moor: Basics of tribology application. Translated from English by “Mir” Press, 1978, p. 487 (in Russian).
6. F. Barwell: Lubrication of bearing. Butterworths, London, 1956.
7. V. Starzhinsky, V. Antonyuk, M. Kane et al.: Dictionary – reference book on gearing: Russian – English-German-French / 4th edition corrected and enlarged. Edited by V. Starzhinsky. Minsk: BelGISS, 2007, p. 186.
8. L. Reshetov: Involute gearing correction. Moscow-Leningrad, 1935, p. 144 (in Russian).
9. N. Bezoukhov: Theory of elasticity and plasticity, Moscow, 1953, p. 420 (in Russian).

# Alternative in Harmonic Train Design

Valentin Tarabarin and Zinaida Tarabarina

**Abstract** The paper describes designs of drives with harmonic trains (HT) developed with the assistance of authors at the Bauman Moscow State Technical University, the “Theory of Machines and Mechanisms” Department. The paper deals with both existing and new drives as well as design solutions which have not been put into practice yet. Experimental results for manufactured drives are presented.

**Keywords** Harmonic train · Differential wave mechanism · Wave generator · Experimental research · Efficiency

## Introduction

Drives for gantries, scaled-down modelling test benches, hoisting machinery and manipulators were designed and tested at the Bauman MSTU, the “Theory of Machines and Mechanisms” Department in 1970–1990. New HTs were developed and recognized as inventions [1–4]. These works are little known in Russia and practically unknown abroad.

## Design of Gear Drives with Harmonic Trains

Let us consider a ring wave generator of external deformation [1]. The gearing design and a photograph of its model are shown in Fig. 1. Flexible spline 2 of this HT has internal teeth, and the wave generator consists of two rings (5 and 6) and deforms spline 2 from the outside. Circular spline 3 is positioned inside the flexible spline, and has external teeth. Generator rings are mounted on two (or more) crankshafts 7 and 8, and they form together a mechanism of parallel cranks. When one crank

---

V. Tarabarin (✉)

Department of the “Theory of Machines and Mechanisms”, the Bauman Moscow State Technical University, 2nd Baumanskaya Str., 5, 105005, Moscow, Russia  
e-mail: vtarabarin@gmail.com

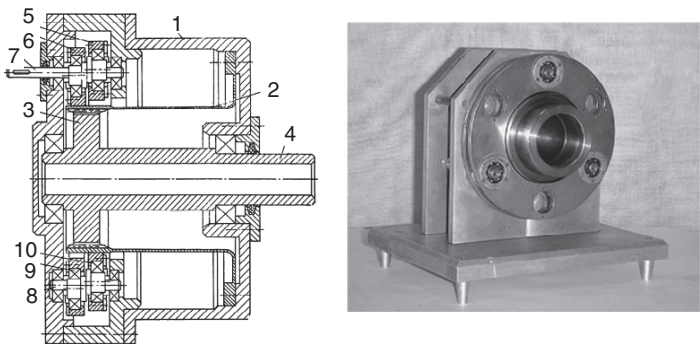


Fig. 1 Harmonic train with ring wave generator

rotates, an elliptic hole formed by internal surfaces of rings starts rotating and assigns movable deformation to the flexible spline toothing. Engagement of cog-wheels in the train of external deformation occurs on a minor axis of the deformed curve of flexible spline.

The advantages of the HT of external deformation are as follows: small moment of inertia; misalignment of the motors, which liberates the central part of the mechanism; convenient arrangement of several motors, etc.

A series of drives, both harmonic and combined – planetary-harmonic, were developed on the basis of this mechanism. The mechanism shown in Fig. 2 on the left makes use of the ring generator and two flexible splines: one with external teeth 3, the other with internal teeth 2 [2]. The generator (links 4, 5, 6) deforms synchronously both flexible splines. Deformation of each spline halves in such

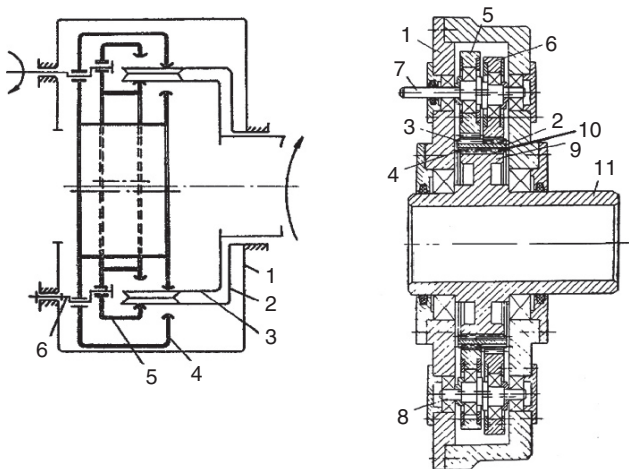
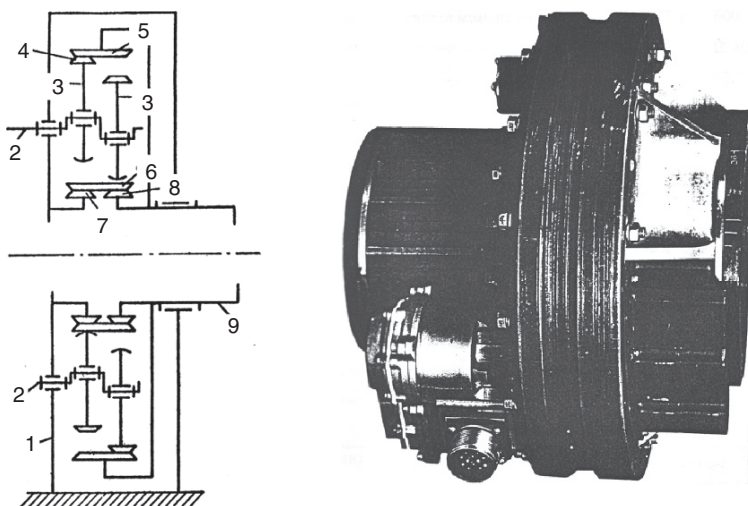


Fig. 2 Harmonic train with ring wave generators: on the left—with two flexspine; on the right—with toothed ring

mechanism. Minimum transmission ratio in gearings with a steel flexible spline is defined by the flexible spline fatigue limit  $u_{min} = 60-80$ . It can be approximately halved in this mechanism. A play-free engagement of two flexible splines can be provided, and it will preserve zero clearance for a long time. Besides, all other advantages of the ring generator remain.

One more HT design presented in Fig. 2 on the right uses toothed deforming rings 5 and 6 [3]. Flexible spline – ring 10 has the external and internal toothings. The external tothing interlocks with the internal toothings of rings and the internal tothing – with the external one of circular spline 9. The circular spline is fixed on the output shaft. Construction is of a small axial dimension. The mechanism reduction ratio is less than that of common HTs.

It is possible to enhance the drive accuracy and reliability by using a combined planetary-wave mechanism (CPWM) [4]. Two mechanisms: crank-planetary and harmonic (wave) ones are connected in parallel therein (Fig. 3). They have identical reduction ratios and common input and output shafts. Power stream division in four parts increases the drive accuracy, rigidity and load-carrying capacity. Crank input shafts 2 (two or more) transmit translational motion on circular trajectories to rings 3. Toothings of the planetary mechanism satellites are cut on the rings external surfaces, and their internal surfaces are the deforming surfaces of the ring wave generator. Flexible spline-ring has internal tothing, and the tothing interlocks with two circular splines. The right circular spline is related to the HT of external deformation, the left one – to the wave gearing. Spline 5 with internal teething of planetary mechanism and circular spline 8 of the HT are fixed on output shaft 9. The pilot CPWM models were manufactured and tested [5]. Results of experimental determination of the efficiency and torsional stiffness are presented in Fig. 4.



**Fig. 3** Diagram of combined planetary-wave mechanism and photo of the drive with such mechanism

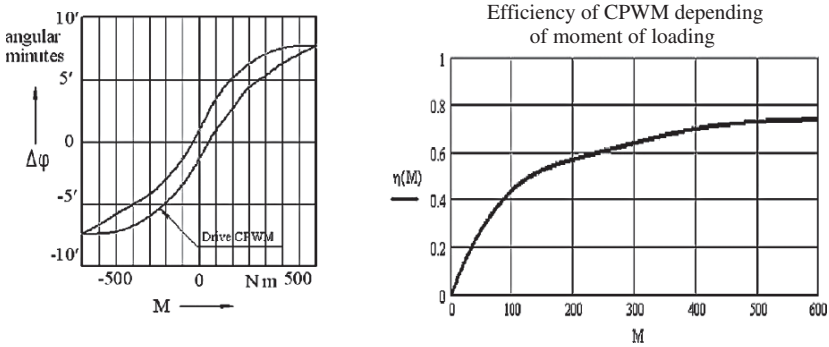


Fig. 4 Experimental graphs of the efficiency and torsional stiffness of planetary-wave mechanism

Electromechanical drives with two motion freedoms find their application in various engineering fields. Examples of their use in metallurgy, hoisting machines, and rolling mills, drilling rigs, electric locomotives and transport machinery as well as in automatic control systems are given in [6]. These drives have the following advantages: reduction of dynamic loads at start-up of the drive, extension of the range of velocity control, automatic redistribution of the load among the engines, absence of overloading in case of failure of one of the motors, opportunity to preserve the motor high rotation velocity at low output shaft velocity, possibility to start and reverse the mechanism due to the velocity control of only one motor.

Two drives with double-moving wave mechanism were designed and manufactured at the Bauman MSTU TMM Department [7, 8]. The diagram and photos of WM-1 drive are presented in Fig. 5. The drive consists of two DC motors, two tachogenerators, and differential wave mechanism. The HT reduction ratio  $u = 120$ , gear

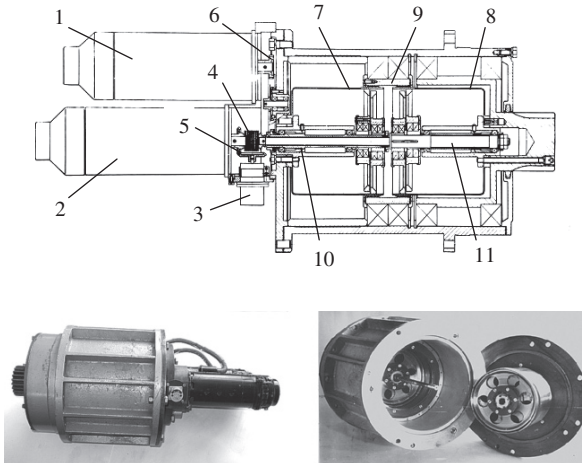


Fig. 5 Differential mechanism WM-1 with HT inner deformation

module  $m = 0.4 \text{ mm}$ , numbers of teeth: that of flexible spline  $z_{f1} = z_{f2} = 240$ , that of circular spline  $z_{s1} = z_{s2} = 240$ . Motors 1 and 2 have integrated friction brakes switched off at applying a voltage. Shaft 10 of motor 1 is connected with wave generator by bellows coupling 4, and with tachogenerator 3 shaft – by bevel gearing 5 with reduction ratio  $u = 1$ . Motor 2 shaft is connected with input shaft 11 and tachogenerator by bevel gears 6 with  $u = 1$ . Both wave generators are double-wedged. Flexible splines 7 and 8 are performed as thin-walled shells. Circular splines form ring 9 with two internal toothings. Coaxiality of the HT complicates the mechanism design and assembling. The mechanism’s moment of inertia has increased owing to additional gearings and long input shafts.

The destination of drive WM-2 (Fig. 6) is the same as that of WM-1; so, the same engines and tachogenerators, gear modules and reduction ratios are used. HTs applied in WM-2 have different designs: one of them is an internal deformation gearing, the other is an external one with a ring oscillator and a flexible wheel-ring. The shaft of central motor 10 is connected with a wave generator by bellows coupling, and with a tachogenerator – by a bevel gearing. Deforming splines 4 of the tachogenerator are mounted on three crankshafts 6. Bellows coupling connects one of these shafts with the second motor; the second shaft is connected with the tachogenerator. Flexible spline 3 with external teeth has double tootthing. One of them is a flexible tootthing of the HT of internal deformation; the second one operates as circular spline in the HT of external deformation. In order not to be deformed this tootthing is leaned on disk 12 mounted in the housing on bearing 13. Flexible spline 2 of the HT of external deformation has two internal tootthings. The right tootthing is related to the external deformation HT, the left tootthing – to the wave gear coupling. Circular spline 9 is fastened on output shaft 14. Mechanism WM-2 has the following advantages as compared to mechanism WM-1: smaller overall dimensions and weight, smaller moment of inertia on the input shaft, and misalignment of input shafts.

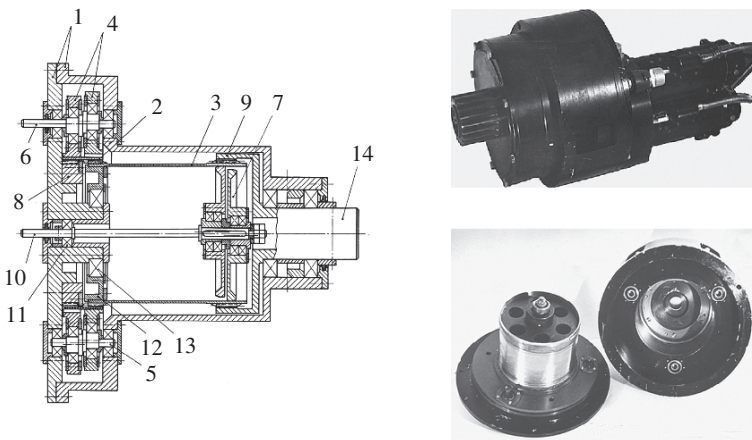


Fig. 6 The differential mechanism WM-2 with HT inner and external deformation

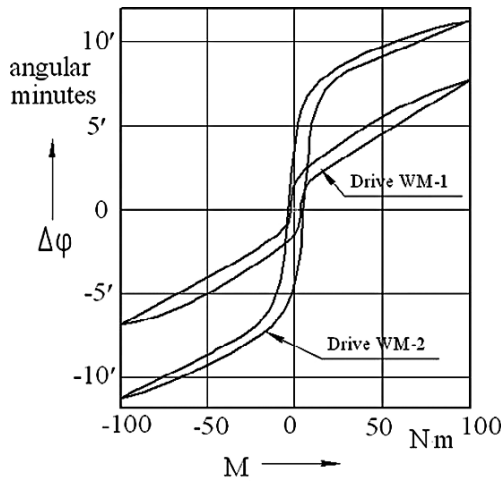


Fig. 7 Torsional stiffness of drives WM-1 and WM-2

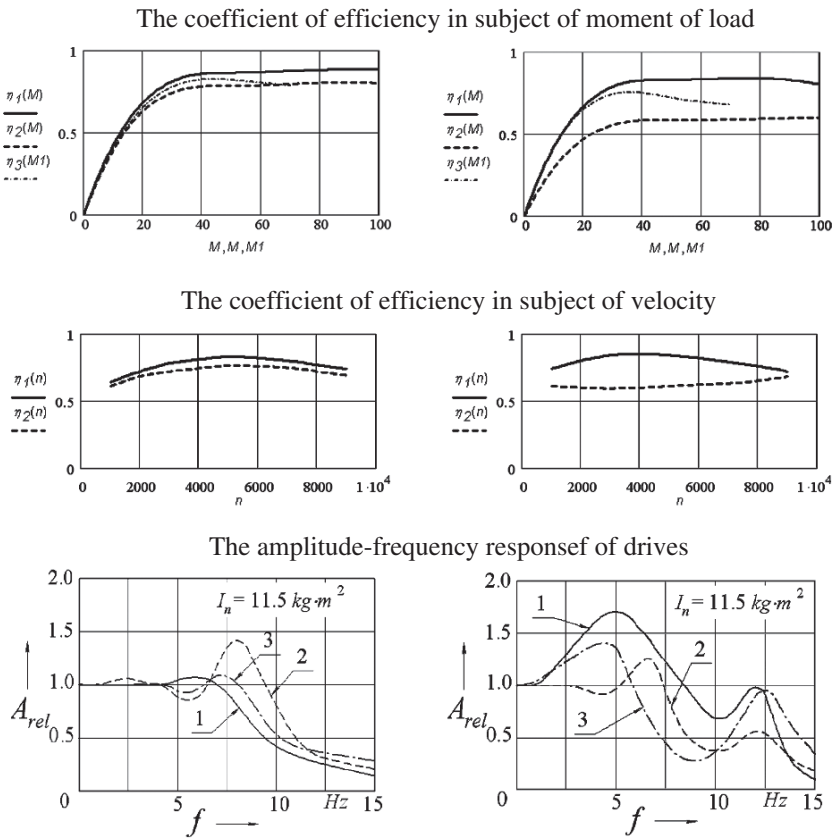


Fig. 8 Comparison of the experimental research results for drives WM-1 (on the left) and WM-2 (on the right)



Comparative testing of drives WM-1 and WM-2 [8] has shown that drive WM-1 has better features of efficiency, backlash, and dynamic error. The test results are presented in Figs. 7 and 8.

## Conclusions

The considered constructions of harmonic trains are a modest part of the HT developments performed at the Bauman MSTU, TMM Department. Many of developed drives have original designs. Their application in various mechanical systems will allow to improve their qualitative figures (efficiency, accuracy, moment of inertia, etc.), to reduce dimensions and weight.

**Acknowledgments** The authors would like to thank the HT group employees for their help in carrying out the theoretical and experimental research and Prof. A. Golovin for his advice, proposals and remarks regarding this paper.

## References

1. Tarabarin V., Timofeev G. Harmonic train. Inventor's certificate USSR No 541057 MKI 16H 1/00, declared 14.08.1973, publication 30.12.1976, bulletin No 48 (in Russian).
2. Ermakova I., Tarabarin V. Harmonic train. Inventor's certificate USSR No 2335716 MKI 16H 1/00, declared 14.03.1976, publication 23.04.1981, bulletin No 15 (in Russian).
3. Skvortcova N., Tarabarin V. Harmonic train. Inventor's certificate USSR No 549629 MKI 16H 1/00, declared 21.03.1974, publication 5.03.1977, bulletin No 9 (in Russian).
4. Tarabarin V., Tarabarina Z., Kostikov Ju. et al. The device for transfer and transformations of rotary movement. Inventor's certificate USSR No 1569467 MKI 16H 1/00, declared 8.03.1988, publication 7.06.1990, bulletin No 21 (in Russian).
5. Samoilova M. Research of combined planetary-wave mechanisms. The dissertation on competition of a scientific degree of Cand.Tech.Sci. – M.: BMSTU – 2000 (in Russian).
6. Margolin S. Differential the electric drive. M.: "Energy", 1975. pp.168, ill. (in Russian).
7. Artamonov P., Lyulyaev V, Tarabarin V. et al. Development and an experimental research of a drive with a differential harmonic trains. "Questions of radio electronics", 11, a general-technical series, Moscow, 1976 (in Russian).
8. Tarabarin V. Research of harmonic differential mechanisms for follow-up device. The dissertation on competition of a scientific degree of Cand. Tech. Sci. – M.: BMHTS – 1976 (in Russian).

# On the Position of the Single Pair Tooth Segment Relative to the Pitch Point, for Internal Gears, with Effect on Contact Stress Calculus

Radu Velicu, Gheorghe Moldovean and Cristina A. Bozan

**Abstract** In the case of internal gears, the contact stress along the gearing line has a specific variation. Since ISO standard is recommending the contact stress calculus in the pitch point  $C$  or in one of the inner points of single pair tooth contact  $B$  or  $D$ , without any details on how important are the differences, this paper is analysing the influence of addendum modification, pinion number of teeth and gear ratio on the position of the single pair tooth segment relative to the pitch point and on the maximum contact stress, for internal gears.

**Keywords** Internal gears · Contact stress · Pitch point

## Introduction

Contact stress for internal gears is less important in comparison with bending stress. Although, in the case of gears made of mild steel without case hardening, contact stress cannot be neglected and contact stress calculus has its importance.

The maximum contact stress shall appear where a single pair tooth is in contact. This is the case of the single pair tooth gearing segment  $BD$  and ISO standard [1, 2] is recommending the contact stress calculus in the pitch point  $C$  or in one of the inner points of single pair tooth contact  $B$  or  $D$ . As it has been demonstrated for exterior gears, the pitch point can be placed inside or outside the single pair tooth gearing segment  $BD$  [3–5].

## Theoretical Analysis

The calculus model for contact stress of an internal gear, presented in Fig. 1, is based on Hertz's model for contact along generator, between an exterior and an internal cylinder. The calculus relation, established by Hertz for the contact stress  $\sigma_H$ , at

---

R. Velicu (✉)

Department of Product Design and Robotics, Transilvania University of Braşov,  
Bdul Eroilor 27, 500036 Braşov, Romania  
e-mail: rvelicu@unitbv.ro

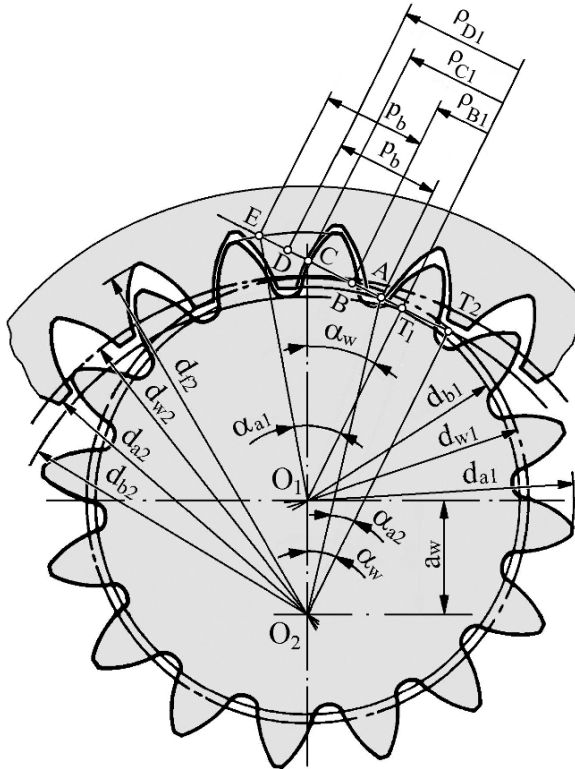


Fig. 1 Curvature radii for B, C and D points on gearing line

any  $Y$  point, based on presumptions presented in [6], with corrections applied for the real gear, is

$$\sigma_{HY} = Z_E \sqrt{\frac{F_{nc}}{l_k} \frac{1}{\rho_Y}}, \tag{1}$$

where:  $Z_E$  is the elasticity factor;  $F_{nc}$  – normal force between teeth, with corrections depending on dynamic inner or outer loads and distribution of load in frontal plane on tooth width and also between the simultaneous tooth pairs in gearing;  $1/\rho_Y = 1/\rho_{Y1} - 1/\rho_{Y2}$  – relative curvature,  $\rho_{Y1}, \rho_{Y2}$  – curvature radii of tooth profiles;  $l_k$  – contact length,  $l_k = b/Z_\epsilon^2$ , where  $Z_\epsilon$  is the contact ratio factor, depending on frontal contact ratio  $\epsilon_\alpha$ ; its value has small variation depending on the addendum modifications.

Relation (1) shows that, for an internal gear, the contact stress in any  $Y$  point is mainly depending on the term  $\sqrt{1/\rho_Y}$ , and so, on the curvature radii in the considered  $Y$  point.

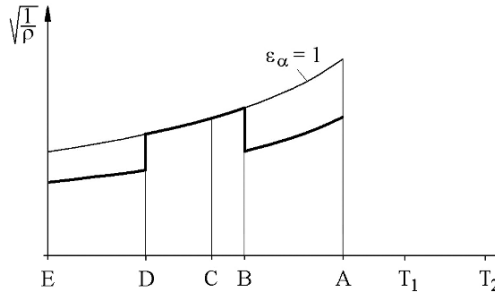


Fig. 2  $\sqrt{I/\rho}$  (contact stress) along the gearing line

The reduced curvature can be written as

$$\frac{1}{\rho_Y} = \frac{1}{\rho_{Y1}} - \frac{1}{\rho_{Y2}} = \frac{\rho_{Y2} - \rho_{Y1}}{\rho_{Y1}\rho_{Y2}} = \frac{T_1 T_2}{\rho_{Y1} (\rho_{Y1} + T_1 T_2)} \tag{2}$$

because the difference between the curvature radii is a constant, equal with the length of the  $T_1 T_2$  segment. The contact stress, for an internal gear, can be described by the term  $\sqrt{I/\rho_Y}$ , with values along the gearing line, presented in Fig. 2, for two case: first case, showed with the thin line refers to the theoretical frontal contact ratio equal to 1, corresponding to single tooth pair gearing; second case, showed with thick line, corresponds to the real internal cylindrical gear with frontal contact ratio  $\epsilon_\alpha > 1.0$ , considering a single tooth pair gearing on segment  $BD$  and double tooth pair gearing on segments  $AB$  and  $DE$ , the normal force  $F_n$  being uniformly distributed between the two pairs of teeth.

For an internal cylindrical gear the pitch point  $C$  keeps its position at the intersection between centre line and gearing line, while the real gearing segment  $AE$  and the single tooth pair gearing segment  $BD$  are modifying their position along the gearing line and towards the pitch point  $C$ . The bigger influence on the position of the two gearing segments  $AE$  and  $BD$  comes from total addendum modification coefficient of the gear  $x_d$ , from how it is divided between pinion and wheel  $x_1$  și  $x_2$ , addendum shortening for internal gear wheel in order to avoid interferences between teeth but also to maintain a normal addendum clearance  $c$ , pinion number of teeth  $z_1$  and gear ratio  $u$ .

ISO standard recommends calculus of contact stress in pitch point  $C$  (for usual calculus – method C) or in one of the three points  $C$ ,  $B$  or  $D$  (for more exact calculus – method B). The position of the pitch point  $C$  inside or outside the single tooth pair gearing segment  $BD$  is very important in order to establish the correct point of maximum contact stress. For example, if point  $C$  is outside segment  $BD$  and, from relation (1), is considered to be the point of maximum stress, it is actually a point with more than two tooth pair gearing. The position of the single tooth pair gearing segment  $BD$  is established depending on the relationship between curvature radii from pitch point  $C$  and, respectively points  $B$  and  $D$ , calculated for pinion tooth profile (see Fig. 1).

Based on Fig. 2, showing that always  $\rho_{D1} > \rho_{B1}$ , the following conclusions can be drawn:

- If  $\rho_{D1} > \rho_{C1} > \rho_{B1}$ , so  $\rho_{C1}/\rho_{B1}$  and  $\rho_{C1}/\rho_{D1} < 1$ , the pitch point  $C$  is placed between points  $B$  and  $D$ , and the maximum contact stress appears in point  $B$ ;
- If  $\rho_{C1} \leq \rho_{B1}$ , so  $\rho_{C1}/\rho_{B1} \leq 1$ , then the single tooth pair gearing segment  $BD$  is place between the pitch point  $C$  and point  $E$  of the gearing line, and the maximum contact stress appears in point  $C$ ;
- If  $\rho_{C1} \geq \rho_{D1}$ , so  $\rho_{C1}/\rho_{D1} \geq 1$ , then the single tooth pair gearing segment  $BD$  is place between the pitch point  $C$  and point  $A$  of the gearing line, and the maximum contact stress appears in point  $B$ .

The addendum of the pinion tooth (external gear) is modified in order to keep a normal clearance with the internal gear wheel, the tooth truncation coefficient [7] being calculated with relation

$$k_1 = (x_2 - x_1) - \frac{z_2 - z_1}{2} \left( \frac{\cos \alpha}{\cos \alpha_w} - 1 \right), \quad (3)$$

and the addendum of the wheel tooth (internal gear) is modified with coefficient  $k = \min(k_1, k_2)$ , where  $k_2$  is the tooth truncation in order to avoid interference between dedendum of pinion tooth and addendum of wheel tooth [8], determined with relation

$$k_2 = \frac{1}{2} \left[ z_2 - \sqrt{z_2^2 + (z_2 - z_1)^2 \tan^2 \alpha_w \cos \alpha} \right] - (h_a^* - x_2). \quad (4)$$

The curvature radius at pinion tooth profile in contact at point  $C$  is determined with relation (see Fig. 1)

$$\rho_{C1} = \frac{d_{b1}}{2} \tan \alpha_w = \frac{m z_d}{2(u-1)} \cos \alpha \tan \alpha_w, \quad (5)$$

where:  $z_d = z_2 - z_1$ , and  $x_d = x_2 - x_1$ .

The curvature radii at pinion tooth profile in contact at points  $B$  and  $D$  of the single tooth pair segment, results from Fig. 1:

– For point  $B$ , relation

$$\rho_{B1} = \frac{d_{b1}}{2} \tan \alpha_{a1} - p_b = \frac{m z_d}{2(u-1)} \cos \alpha \tan \alpha_{a1} - \pi m \cos \alpha \quad (6)$$

becomes

$$\rho_{B1} = \frac{m z_d}{2(u-1)} \cos \alpha \left[ \tan \alpha_{a1} - \frac{2\pi(u-1)}{z_d} \right]; \quad (7)$$

– For point  $D$ , relation

$$\rho_{D1} = \frac{d_{b2}}{2} \tan \alpha_{a2} + p_b = \frac{m z_d}{2} \frac{u}{u-1} \cos \alpha \tan \alpha_{a2} + \pi m \cos \alpha \quad (8)$$

becomes

$$\rho_{D1} = \frac{m z_d}{2} \frac{u}{u-1} \cos \alpha \left[ \tan \alpha_{a2} + \frac{2\pi u - 1}{z_d} \frac{u}{u} \right]. \quad (9)$$

By expressing  $z_d$  depending on  $z_1$  and gear ratio  $u$ , with relation  $z_d = z_1(u-1)$ , relations for curvature radii are

$$\frac{\rho_{C1}}{\rho_{B1}} = \frac{z_1 \tan \alpha_w}{z_1 \tan \alpha_{a1} - 2\pi}; \quad (10)$$

$$\frac{\rho_{C1}}{\rho_{D1}} = \frac{z_1 u \tan \alpha_w}{z_1 u \tan \alpha_{a2} + 2\pi}. \quad (11)$$

The real gearing angle  $\alpha_w$  is determined with relations

$$\operatorname{inv} \alpha_w = \operatorname{inv} \alpha + 2 \frac{x_d}{z_d} \operatorname{tg} \alpha; \quad (12)$$

$$\operatorname{inv} \alpha_w = \operatorname{tg} \alpha_w - \alpha_w [\operatorname{rad}]. \quad (13)$$

In order to determine the calculus relations for addendum pressure angles for pinion and wheel it must be started from the calculus relations of the addendum diameters considering both addendum modification and tooth truncation:

$$d_{a1} = m [z_1 + 2(h_a^* + x_1 - k_1)]; \quad (14)$$

$$d_{a2} = m [z_2 - 2(h_a^* - x_2 + k)], \quad (15)$$

the pressure angles being:

$$\alpha_{a1} = \arccos \left( \frac{d_1}{d_{a1}} \cos \alpha \right) = \arccos \left( \frac{z_1 \cos \alpha}{z_1 + 2(h_a^* + x_1 - k_1)} \right); \quad (16)$$

$$\alpha_{a2} = \arccos \left( \frac{d_2}{d_{a2}} \cos \alpha \right) = \arccos \left( \frac{z_2 \cos \alpha}{z_2 - 2(h_a^* - x_2 + k)} \right). \quad (17)$$

ISO standard [2] gives calculus relations for contact stress at point  $C$ ,  $\sigma_{HC}$ , and respectively at points  $B$  and  $D$ ,  $\sigma_{HB} = Z_B \sigma_{HC}$  and  $\sigma_{HD} = Z_D \sigma_{HC}$ , where contact factors are

$$Z_B = \sqrt{\frac{\rho_{C1}\rho_{C2}}{\rho_{B1}\rho_{B2}}} \quad \text{and} \quad Z_D = \sqrt{\frac{\rho_{C1}\rho_{C2}}{\rho_{D1}\rho_{D2}}}. \quad (18)$$

If one of the values of the contact factors  $Z_B$  or  $Z_D$  is smaller than 1 (contact stress at point  $C$  is bigger) it must be considered as equal to 1. ISO standard [2] states that “for internal gears,  $Z_D$  shall be taken as equal to 1”. This is showing that point  $D$  is not important in determining the point of maximum contact stress for internal gears, as also seen from Fig. 2.

## Implementation and Conclusions

Calculus relations presented above have been implemented in a software module. By running the software module, several values for ratio  $\rho_{C1}/\rho_{B1}$  and contact factors  $Z_B$  and  $Z_D$  have been computed depending on different values of the parameters: pinion number of teeth,  $z_1$ ; gear ratio,  $u$ ; total addendum modification of gear,  $x_d$ ; addendum modification of pinion,  $x_1$ . The helix angle of the gear has been considered equal to 0.

Figure 3 presents ratio  $\rho_{C1}/\rho_{B1}$  and contact factor  $Z_B$ , depending on addendum modification of pinion  $x_{n1}$  for internal gears characterised by: same gear ratio  $u = 3$ , same values for the total gear addendum modification ( $x_d = 0.5$ ) and different values of number of teeth at pinion  $z_1$ .

Figure 4 presents contact factors  $Z_B$  and  $Z_D$  depending on addendum modification of pinion  $x_1$  for internal gears characterised by: same gear ratio  $u = 3$ , same values for the total gear addendum modification ( $x_d = 0.5$ ) and different values of number of teeth at pinion  $z_1$ .

The following conclusions are drawn:

- The ratio  $\rho_{C1}/\rho_{B1}$  and the contact factor  $Z_B$  have the same variation, being similar (see Fig. 3). They are both giving an idea on the relative position of points  $C$  and  $B$ . Usual values, bigger than 1 for ratio  $\rho_{C1}/\rho_{B1}$  and contact factor  $Z_B$ , correspond to a position of point  $C$  at the left side of point  $B$  (see Fig. 2). Values smaller than 1 correspond to a position of point  $C$  at the right side of point  $B$  (see Fig. 2). Similar curves are intersected when reaching value of 1, corresponding to coincident points  $C$  and  $B$ ;
- The case of positioning point  $C$  at the right side of point  $B$  appears for relative high values of addendum modification of pinion  $x_1$  and relative high pinion number of teeth  $z_1$  (see Fig. 3);
- Bigger values of contact factor  $Z_B$ , showing big difference between contact stress at point  $B$  in comparison with point  $C$ , appear at small values of addendum modification of pinion  $x_1$  and relative small pinion number of teeth  $z_1$  (see Fig. 3);

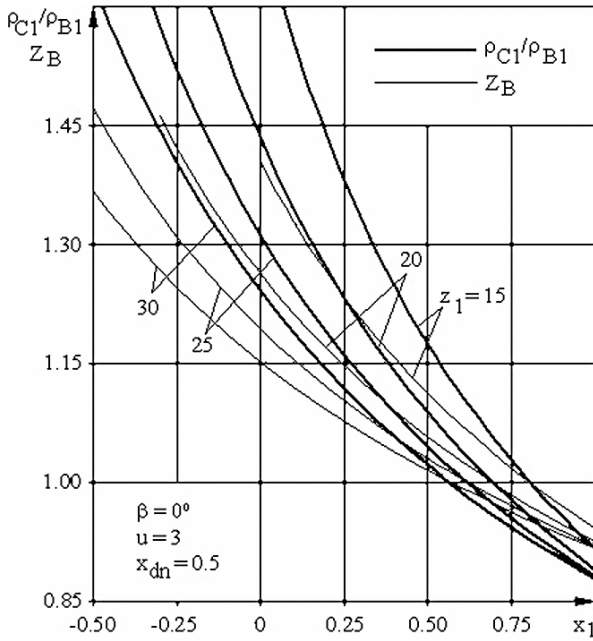


Fig. 3  $\rho_{C1}/\rho_{B1}$  and  $Z_B = f(x_1, z_1, u = 3)$

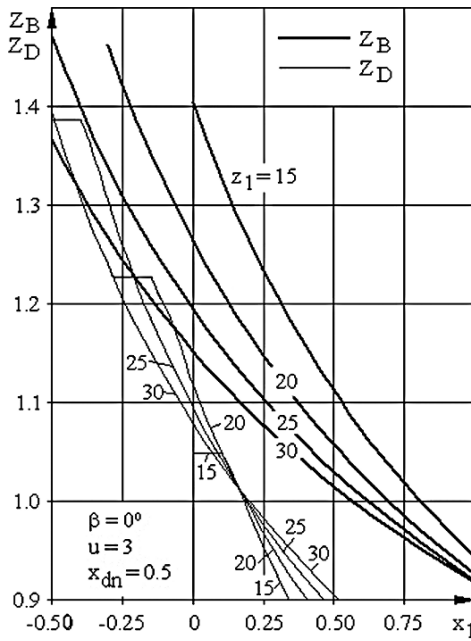


Fig. 4  $Z_B$  and  $Z_D = f(x_1, z_1, u = 3)$



- The value of contact factor  $Z_D$  is always smaller than the value of contact factor  $Z_B$  (see Fig. 4) as already has been shown;
- The variation of contact factor  $Z_D$  stabilises at small values of  $x_1$ , showing that point  $D$  is stabilized on gearing line, due to tooth truncation in order to avoid interference between dedendum of pinion tooth and addendum of wheel tooth;
- Values of  $Z_D$  bigger than 1, involving position of point  $C$  at the left side of point  $D$  (see Figs. 2 and 4), appear at  $x_1 < 0.2$ . Since  $x_d = x_2 - x_1 = 0.5$ , it results that this case appear at  $x_2 > 0.7$ .

Figures 5 and 6 presents ratio  $\rho_{C1}/\rho_{B1}$  and contact factor  $Z_B$ , depending on addendum modification of pinion  $x_1$  for internal gears characterised by same number of teeth at pinion  $z_1 = 20$ . The other variable parameter is gear ratio  $u$  (Fig. 5), respectively total addendum modification coefficient  $x_d$  (Fig. 6). Few other conclusions can be drawn:

- The case of positioning point  $C$  at the right side of point  $B$  also appears for relative high values of gear ratio  $u$  (see Fig. 5) and relative small (usual) total addendum modification coefficient  $x_d$  (see Fig. 6);
- Bigger values of contact factor  $Z_B$ , showing big difference between contact stress at point  $B$  in comparison with point  $C$ , appear at small values of gear ratio  $u$  (see Fig. 5) and relative high total addendum modification coefficient  $x_d$  corresponding to high value of  $x_2$  (see Fig. 6).

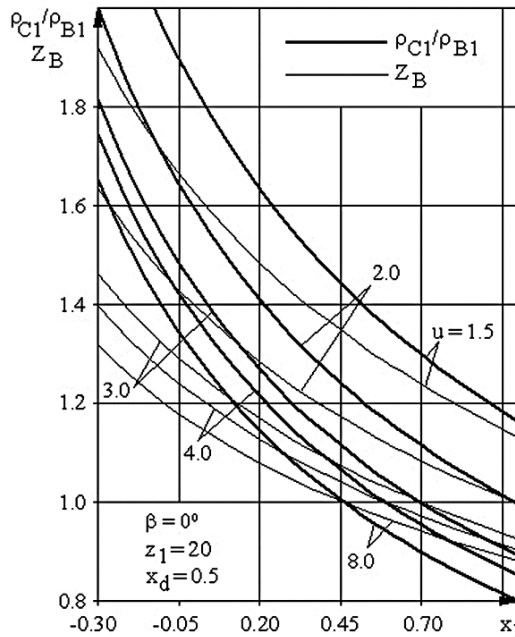


Fig. 5  $\rho_{C1}/\rho_{B1}$  and  $Z_B = f(x_1, u, z_1 = 20)$

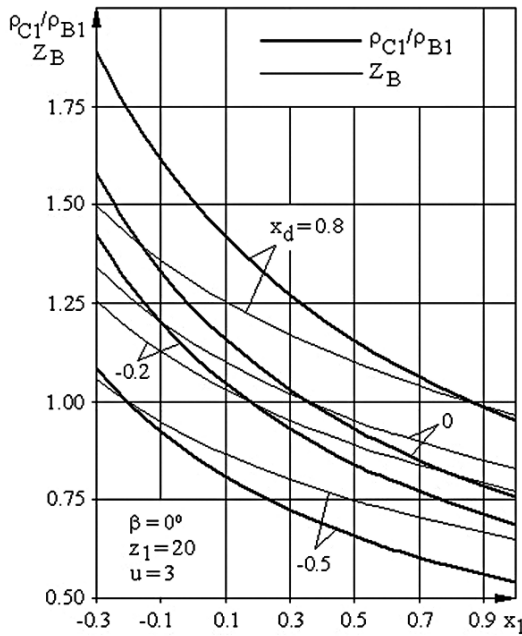


Fig. 6  $\rho_{C1}/\rho_{B1}$  and  $Z_B = f(x_1, x_d)$

As a general conclusion, it can be stated that, in the case of internal gears, maximum contact stress shall always be calculated in the inner single tooth pair point *B*, with important differences with the contact stress in pitch point *C* for high values of addendum modification of wheel  $x_2$ , relative small pinion number of teeth  $z_1$  and small values of gear ratio  $u$ , when point *D* moves at the right side of point *C*.

## References

1. ISO 6336-1: 1996 (E). Calculation of load capacity of spur and helical gears. Part 1: Basic principles, introduction and general influence factors.
2. ISO 6336-2: 1996 (E). Calculation of load capacity of spur and helical gears. Part 2: Calculation of surface durability (pitting).
3. Chişu, E., Moldovean, Gh. On the influence of gear ratios and addendum corrections over the contact stress. In Bulletin of the Transilvania University of Braşov, vol. 12(47) New Series, Series A, pages 25–28, 2005.
4. Velicu, R., Moldovean, Gh. Angrenaje cilindrice. Reductoare cilindrice. (Cylindrical gears. Cylindrical speed reducers.) Ed. Universităţii “Transilvania” din Braşov, 2002.
5. Moldovean, Gh., Velicu, R., Velicu, D. On the maximal contact stress point for cylindrical gears, 12th IFToMM World Congress, Besançon (France), June 18–21, 2007.
6. Moldovean, Gh., Velicu, D., Velicu, R. et al. Angrenaje cilindrice şi conice, Calcul şi construcţie. (Cylindrical and bevel gears. Calculus and constructions.) Lux Libris, Braşov, 2001.

7. Deaky, B. A., Gavrilă, C. C. Influența deplasărilor de profil asupra scurtării dinților angrenajelor cilindrice (Influence of addendum modifications on tooth truncation on cylindrical gears). Proc. of Conference Prasic 2006, Brașov, Romania.
8. Eiff, H., Hirschmann, K. H., Lechner, G. Influence of gear tooth geometry on tooth stress of external and internal gears. În *Journal of Mechanical Design. Transactions of the ASME*, Vol. 112, pages 575–583, 1990.

# Gears and Belt Drives for Non-Uniform Transmission

Hellmuth Stachel

**Abstract** Ordinarily, gears and belt drives are used for uniform transmission of rotations between parallel axes. Here we focus on the nonuniform case, i.e., with non-constant transmission ratio. We treat the geometry of tooth profiles and pulleys and their algorithmic computation. Concerning gears, we recall a method due to S. Finsterwalder. Concerning belt drives, we study their relation to tooth profiles and focus on ‘strict’ cases which work without tightener.

**Keywords** Nonuniform transmission · Planar gearing · Belt drives · Geometric kinematics

## Introduction

The problem of designing *noncircular gears* has often been addressed in publications (see [1–4] and in particular Litvin’s monograph [5], pp. 346–381). Such gears are used for nonuniform transmission between parallel axes. Similarly, certain cam-like mechanisms have rolling centrode contact surfaces. Here we recall an applicable, classical design method formulated by S. Finsterwalder (1862–1951, see [6], [7, p. 284] or [8, p. 205]) which is also useful for an algorithmic computation.

J. Hoschek [9] and F. Freudenstein [10] (see also [11]) created methods to design belt drives for given nonuniform transmission such that the length of the surrounding belt remains constant. Such belt drives with belt slack zero will briefly be called *strict*. After discussing geometric properties of belt drives we present a modification of Hoschek’s method for computing conjugate pulleys for strict belt drives that is not confined to discrete (i.e., polygonal) models, like those treated in [12] or [13], but nevertheless produces satisfactory results. However implementation of large transmission ratio variations results in pulley profiles with singularities analogous to

---

H. Stachel (✉)

Institute of Discrete Mathematics and Geometry, Vienna University of Technology,  
Wiedner Hauptstr. 8-10/104, A 1040 Wien, Austria  
e-mail: stachel@dmg.tuwien.ac.at

undercut gear teeth. Hoschek's method as well as ours fail in the case of global 1:1 transmissions where a full rotation of the input wheel corresponds to a full rotation of the output wheel.

## Gearing for Nonuniform Transmission

Let the driving wheel  $\Sigma_1$  rotate about the center  $O_1 = 01$  through the angle  $\varphi_1$  with respect to the frame of the fixed housing  $\Sigma_0$  while the output wheel  $\Sigma_2$  rotates about  $O_2 = 02$  through  $\varphi_2$ . Then the pole 12 of the relative motion  $\Sigma_2/\Sigma_1$  divides the segment  $O_1O_2$  in the ratio of instantaneous angular velocities, i.e.,  $O_112 : O_212 = \dot{\varphi}_2 : \dot{\varphi}_1 = \omega_2 : \omega_1$ .

In the sequel we seek gears and belt drives that transmit rotary motion according to some *transmission function*

$$\varphi_2 = f(\varphi_1) \quad \text{for } 0 \leq \varphi_1 \leq 2\pi.$$

Function  $f(\varphi_1)$  is assumed to be strictly monotonic, quite often differentiable, and obeys  $f(\varphi_1 + 2\pi) = f(\varphi_1) + 2\pi/n$  for  $n \in \mathbb{Z}$ ,  $n \neq 0$ . The integer  $n$  is called *global transmission ratio*. The transmission function  $f(\varphi_1)$  defines the associated *perturbation function*  $g(\varphi_1)$  by

$$g(\varphi_1) = n \cdot f(\varphi_1) - \varphi_1 \quad \text{or} \quad f(\varphi_1) = [\varphi_1 + g(\varphi_1)]/n.$$

Because of  $g(\varphi_1 + 2\pi) = g(\varphi_1)$  function  $g(\varphi_1)$  is periodic and can be set up as a Fourier series. In the gear box  $\Sigma_0$  we use a coordinate frame (see Fig. 3) with  $O_1 = (0, 0)$ ,  $O_2 = (e, 0)$ , and  $12 = (r_1(\varphi_1), 0)$ . Then the coordinate  $r_1(\varphi_1)$  of 12 obeys  $\omega_2 : \omega_1 = r_1 : (r_1 - e)$ , hence

$$r_1(\varphi_1) = \frac{e f'(\varphi_1)}{f'(\varphi_1) - 1} = \frac{e(1 + g'(\varphi_1))}{1 - n + g'(\varphi_1)}, \quad (1)$$

when the prime indicates differentiation by  $\varphi_1$ .  $c_1 \subset \Sigma_1$  and  $c_2 \subset \Sigma_2$  are conjugate tooth profiles if and only if they are an *enveloping pair* of the relative motion  $\Sigma_2/\Sigma_1$ . Due to the 'Law of Gearing' the common normal line at the meshing point  $C$  passes always through the relative pole 12 (Fig. 1). We express the position of  $C$  in polar coordinates  $(\rho, \psi)$  with respect to the relative pole 12 and choose the negative vector of the pole velocity as zero-axis for measuring the polar angle  $\psi$ . We may suppose  $0 \leq \psi \leq \pi$  for  $\rho \in \mathbb{R}$ . Angle  $\psi$  with the meshing normal is unique even for  $\rho = 0$ . As the two polodes  $p_1, p_2$  are in contact at 12, these coordinates of  $C$  are the same with respect to  $\Sigma_1$  and  $\Sigma_2$ .

Let  $(\mathbf{t}_i, \mathbf{n}_i)$  denote the Frenet frame of the polode  $p_i$ ,  $i = 1, 2$ , with position vector  $\mathbf{p}_i(t)$  and arc length  $s$ . The derivatives by time  $t$  are

$$\dot{\mathbf{t}}_i = v \kappa_i \mathbf{n}_i, \quad \dot{\mathbf{n}}_i = -v \kappa_i \dot{\mathbf{t}}_i \quad \text{and} \quad \dot{\mathbf{p}}_i = v \mathbf{t}_i$$

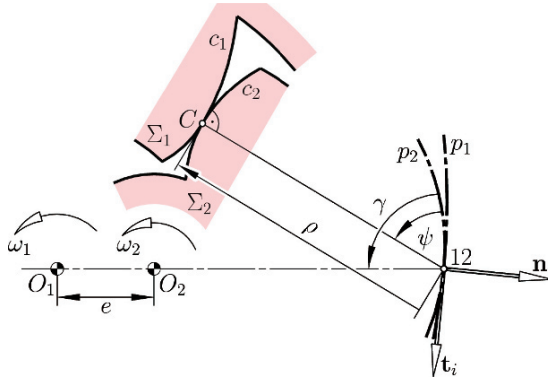


Fig. 1 Conjugate tooth profiles  $c_1, c_2$  for the relative poles  $p_1, p_2$

with pole velocity  $v = ds/dt$  and curvature  $\kappa_i$  of  $p_i$ . The position vector  $\mathbf{c}_i = \mathbf{p}_i + \rho(\cos\psi \mathbf{t}_i + \sin\psi \mathbf{n}_i)$  of the tooth profile has the velocity

$$\dot{\mathbf{c}}_i = v \mathbf{t}_i + \dot{\rho}(\cos\psi \mathbf{t}_i + \sin\psi \mathbf{n}_i) + \rho \dot{\psi}(-\sin\psi \mathbf{t}_i + \cos\psi \mathbf{n}_i) + \rho v \kappa_i(\cos\psi \mathbf{n}_i - \sin\psi \mathbf{t}_i)$$

orthogonal to  $\mathbf{c}_i - \mathbf{p}_i$ . This implies

$$\dot{\rho} = -v \cos\psi \tag{2}$$

This differential equation for  $\mathbf{c}_i(t)$  is independent of the curvature  $\kappa_i$  of the poles  $p_i$  and is therefore the basis for

**S. Finsterwalder’s principle of gearing** [6, p. 243]:<sup>1</sup> *We imagine  $p_1$  as a flexible metal band and replace  $c_1$  by a discrete set of line elements, each attached to the pole  $p_1$  by fixing the angle  $\psi$  and the distance  $\rho$  (Fig. 2). Then for any flex  $p_2$  of  $p_1$  the curve  $c_2$  formed by the attached line elements is conjugate to  $c_1$  if the relative motion  $\Sigma_2/\Sigma_1$  is defined by  $p_2$  rolling along  $p_1$ . This principle works not only for wheels rotating about fixed centers, but for any planar motion given by a pair of poles.*

In the sense of Differential Geometry the functions  $\rho(s)$  and  $\psi(s)$  obeying ( 2) can be called *natural functions of the specified gearing*.

If the metal band is stretched like  $p_0$  in Fig. 2 then  $c_0$  is the tooth profile of the conjugate broaching rack. A straight line segment  $c_0$  defines a constant angle  $\psi$  and therefore the nonuniform *involute gearing*.

<sup>1</sup> This is the discretized version of the general Reuleaux (or Camus) principle saying that conjugate profiles are envelopes of any curve  $c_0$  while an auxiliary curve attached to  $c_0$  is rolling on the poles.

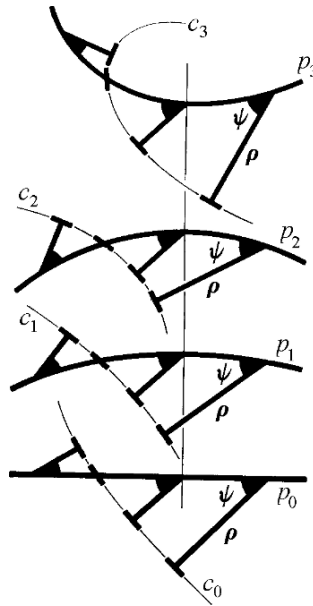


**Fig. 2** S. Finsterwalder's principle of gearing (extracted from [7], p. 284, Fig. 446, compare [8], Abb. 151)

**Theorem 1.** *The following conditions are necessary to avoid local undercuts of conjugate tooth profiles given by their natural functions:*

$$(1 + v \kappa_i) \rho - v \sin \psi \neq 0 \text{ for}$$

$$i = 1, 2 \text{ and } \dot{\psi} \neq \rho - v \sin \psi.$$

The proof is based on Frenet equations of the tooth profile  $c_i$ . The first condition excludes singularities, the second avoids intersections between  $c_1$  and  $c_2$  because of 3-point contact.

For computing conjugate tooth profiles  $c_1, c_2$  of a given transmission one has to take the following steps:

- (1) Compute the polode  $p_1$  in  $\Sigma_1$  with polar coordinates  $(r_1, -\varphi_1)$  and  $r_1$  by (1) as well as  $p_2$  in  $\Sigma_2$  with coordinates  $p_2 = (r_1 - e, -\varphi_2)$ .
- (2) Rectify  $p_1$ , i.e., bend it into the straight line  $p_0$ . Freely choose the rack tooth profile  $c_0$  as long as it is nowhere orthogonal to  $p_0$  and compute the polar coordinates  $(\rho(s), \psi(s))$  with respect to  $p_0$ .
- (3) Bend  $p_0$  back into  $p_1$  and  $p_2$  and use  $(\rho, \psi)$  with respect to the Frenet frames of  $p_1$  and  $p_2$  for obtaining  $c_1$  and  $c_2$ .
- (4) The applicable segments of  $c_1$  and  $c_2$  are arrived at by inspecting their relative movement in view of local and global undercuts.

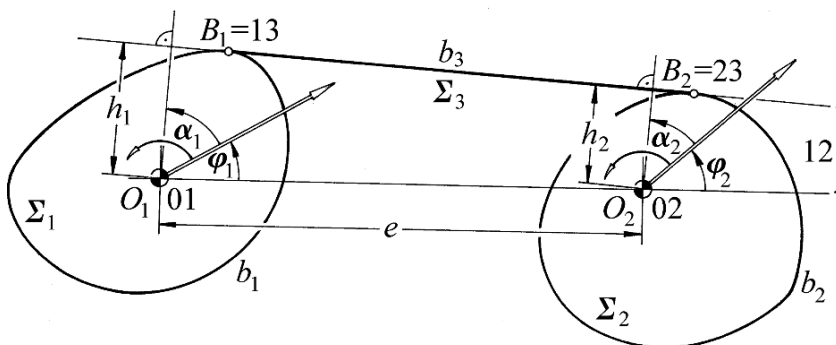


Fig. 3 The upper belt span connects the relative poles 13 and 23

### Geometry of Belt Drives

Let  $b_1, b_2$  be conjugate pulley profiles (Fig. 3). The upper belt span between the contact points  $B_1 \in b_1$  and  $B_2 \in b_2$  defines a new system  $\Sigma_3$ . As line  $b_3 = B_1B_2$  rolls on  $b_1$  and  $b_2$ , the points  $B_1, B_2$  are the relative poles 13 and 23, resp., and this implies the necessary condition [8–10, 14].

**Theorem 2.** *At each instant the upper belt span must be aligned with the relative pole 12.*

Under the relative motion  $\Sigma_3/\Sigma_1$  an arbitrary point  $C$  attached to the line  $B_1B_2$  traces an involute  $c_1$  of  $b_1$  (see Fig. 4). The path of  $C \in \Sigma_3$  under  $\Sigma_3/\Sigma_2$  is an involute  $c_2$  in  $\Sigma_2$ , which contacts  $c_1$  under  $\Sigma_2/\Sigma_1$  at  $C$ .

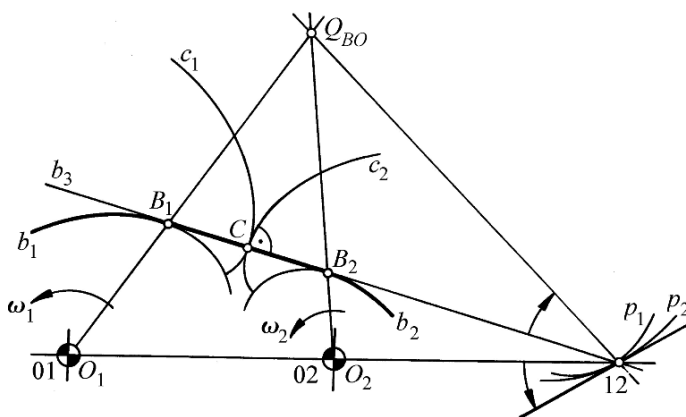


Fig. 4 Points  $B_2 \mapsto B_1$  and  $O_2 \mapsto O_1$  are corresponding under the curvature transformation of  $\Sigma_2/\Sigma_1$  (Bobillier’s construction, see [14], Abb. 152)



**Theorem 3.** *Conjugate pulley profiles  $b_1 \subset \Sigma_1$  and  $b_2 \subset \Sigma_2$  produce the given transmission from  $\Sigma_1$  to  $\Sigma_2$  if and only if  $b_2$  and  $b_1$  are evolutes of an enveloping pair  $(c_2, c_1)$  of the relative motion  $\Sigma_2/\Sigma_1$ . At each instant the endpoints  $B_2$  and  $B_1$  of the upper belt span are corresponding under the curvature transformation of the relative motion  $\Sigma_2/\Sigma_1$  (see Fig. 4).*

Of course,  $b_1$  and  $b_2$  must be closed curves – contrary to the locally acting tooth profiles  $c_1$  and  $c_2$ .

Now we recall Finsterwalder’s method with the polodes  $p_1, p_2$  as metal bands. This time we focus on the envelopes of the attached normal lines making the oriented angle  $\psi$  with the polodes. These envelopes  $b_1, b_2$  are conjugate pulley profiles. Hence we obtain

**Theorem 4.** *For any transmission function and any driving pulley  $b_1$  there is a unique conjugate profile  $b_2$ . However,  $b_2$  needs not be convex.*

We call  $\psi(s)$  the *natural angle function* of this design. The important case  $\psi = \text{const.}$  of involute gearing corresponds to *evolutoides*<sup>2</sup> of the polodes as conjugate pulley profiles  $b_1, b_2$ .

### Strict Belt Drives

When in each position the length of the surrounding belt with taut spans remains constant, then the lower belt span rolls on  $b_1$  and  $b_2$ , too.

**Theorem 5.** [9]: *Conjugate pulley profiles  $b_1$  and  $b_2$  operate without needing a tightener if and only if at each instant both the upper and the lower belt span are aligned with the relative pole 12 (Fig. 5).*

Wunderlich and Zenow [15] discovered 1975 the following nontrivial example of a nonuniformly transmitting strict belt drive for  $n = -1$ :  $\Sigma_2/\Sigma_1$  is a line-symmetric

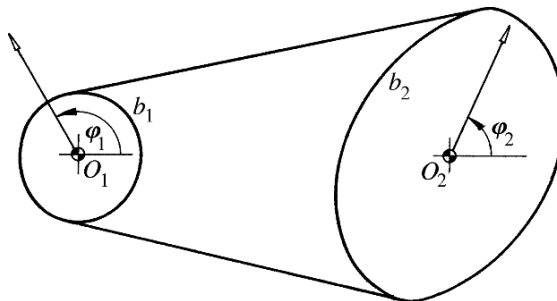


**Fig. 5** A strict belt drive for the transmission function  $\varphi_2 = 0.5 [\varphi_1 + 0.2 \sin \varphi_1 + 0.16 \sin 2\varphi_1 + 0.008 \cos 2\varphi_1]$ . The length of the surrounding belt varies within about 0.002 %

<sup>2</sup> An evolutoide of curve  $p$  is the envelope of lines meeting  $p$  at a constant angle  $\psi$ .

motion with ellipses as polodes  $p_1$  and  $p_2$ . The pulleys are ellipses  $b_1, b_2$  confocal with  $p_1, p_2$  (Theorem of Graves). It should be noted that in the uniform case with  $n = 1$  any convex disk together with a translated copy yield a strict belt drive.

Theorem 5 implies an algorithm for computing strict belt drives:

- (1) In an arbitrary initial position ( $\varphi_1 = \varphi_1^{(0)}$ ) we specify an upper belt span ( $\psi = \psi^{(0)}$ ) passing through  $I_2$ . We attach this line to  $\Sigma_1$ .
- (2) The next point of intersection of this line with the polode  $p_1$  defines a position ( $\varphi_1 = \varphi_1^{(1)}$ ) where this line becomes a lower belt span. This must be tangent to the conjugate profile  $b_2$ , and we attach it to  $\Sigma_2$ .
- (3) When its next point of intersection with  $p_2$  becomes the relative pole ( $\varphi_1 = \varphi_1^{(2)}$ ), the line again covers an upper belt span. In general, this gives a new tangent line of  $b_1$  ( $\psi = \psi^{(2)}$ ).

Iteration gives a finite set of lines tangent to  $b_1$ . In contrast to Hoschek’s method using Bézier curves we represent the tangent lines by their support function  $h_1(\alpha_1)$  (see Fig. 3). Then we use a least square method for finding the Fourier series of fixed order which approximates the computed tangent lines best. By Theorem 4 we obtain the conjugate  $c_2$ .

This algorithm works well (see Fig. 5) in all examples with global transmission ratio  $n \neq 1$ . The computed lines obviously envelope a unique curve  $c_1$ . This observation together with some arguments give rise to

**Conjecture 1.** *For a given nonuniform transmission function with global transmission ratio  $n \neq 1$  there is a one-parametric set of conjugate pairs  $(b_1, b_2)$  of profiles for a strict belt drive. However, these profiles are convex ( $h_i + h_i'' > 0$  by [16]) only if the given transmission lies sufficiently close to the uniform transmission with the same global ratio  $n$ .*

A rigorous mathematical proof is open but there is some supporting evidence: For convex relative polodes and an analytic transmission function the mapping  $(\varphi_1^{(0)}, \psi^{(0)}) \mapsto (\varphi_1^{(2)}, \psi^{(2)})$  of lines is analytic, too. Lines tangent to  $p_1$  ( $\psi = 0$ ) are fixed. Passing through  $O_1$  ( $\psi = \gamma$ , see Fig. 1) is preserved. And the support function obeys

$$h_1(\varphi_1^{(2)}) : h_1(\varphi_1^{(0)}) = \Omega(\varphi_1^{(2)}) : \Omega(\varphi_1^{(1)}) \quad \text{with} \\ \Omega = \omega_2 / \omega_1.$$

The excluded case  $n = 1$  shows a strange behavior that was observed –but not reported – by J. Hoschek: The lines obtained by the above algorithm do not envelope any curve. It is proved in [17] that in this case a starting line passing through  $O_1$  after iteration does not rotate fully about  $O_1$  but approaches a limiting position. By continuity, this seems to contradict the required convexity of  $b_1$  and leads to

**Conjecture 2.** *There is no pure belt drive for nonuniform transmission with global transmission ratio  $n = 1$ .*

## Conclusion

Tooth profiles for gears and pulleys of belt drives are closely related. However, the determination of strict belt drives for a given non-uniform transmission leads to deeper mathematical problems. It is to hope that in the near future the conjectures stated above can be proved rigorously.

## References

1. Biing-Wen B., Computer aided design of elliptical gears with circular-arc teeth, *Mechanism and Machine Theory*, Vol. 39, 2004, pp. 153–168.
2. Chang S.-L., Tsay C.-B., Wu L.-I., Mathematical model and undercutting-analysis of elliptical gears generated by rack cutters. *Mechanism and Machine Theory*, Vol. 31, 1996, pp. 879–890.
3. Peters R.M., Analysis and synthesis of eccentric chainwheel drives, *Mechanism and Machine Theory*, Vol. 7, 1972, pp. 111–119.
4. Spitas V., Costopoulos T., Spitas C., Fast modeling of conjugate gear tooth profiles using discrete presentation by involute segments, *Mechanism and Machine Theory*, Vol. 42, 2007, pp. 751–762.
5. Litvin F.L., *Gear Geometry and Applied Theory*. Prentice Hall, Englewood Cliffs, NJ, 1994.
6. Baier O., Über die Abstandsempfindlichkeit ebener Verzahnungen. *Konstruktion*, Jg. 5, Heft 8, 1953, pp. 242–245.
7. Hohenberg F., *Konstruktive Geometrie in der Technik*. 2. Aufl., Springer-Verlag, Wien, 1961.
8. Wunderlich W., *Ebene Kinematik*. Bibliographisches Institut, Mannheim 1970.
9. Hoschek J., Konstruktion von Kettengetrieben mit veränderlicher Übersetzung mit Hilfe von Bézier-Kurven. *Forsch. Ing.-Wes.*, Vol. 48, 1982, pp. 81–87.
10. Freudenstein F., Ch.-K. Chen., Variable-ratio chain drives with noncircular sprockets and minimum slack – theory and application, *Journal of Mechanical Design*, Vol. 113, 1991, pp. 253–262.
11. Fraulob S., Nagel T., Ungleichförmig übersetzende und hochübersetzende Zahnriemen-Getriebe. *VDI-Berichte 1845*, 2004, pp. 249–261.
12. Xin C.L., Jian L., Research on the mapping models and designing methods of variable-ratio chain/belt drives, *Mechanism and Machine Theory*, Vol. 37, 2002, pp. 955–970.
13. Wang H., Wang Sh., Wang Y., Design and machinery of non-circular sprocket's tooth, *Proceedings of the 9th World Congress on the Theory of Machines and Mechanisms*, Milano 1995, Vol. 1, pp. 556–559.
14. Tidwell P.H., Bandukwala N., Dhande C.F., Reinholtz C.F., Webb G., Synthesis of Wrapping Cams, *Transactions of the ASME*, Vol. 116, 1994, pp. 634–638.
15. Wunderlich W., Zenov P., Contribution to the geometry of elliptic gears, *Mechanism and Machine Theory*, Vol. 10, 1975, pp. 273–278.
16. Strubecker K., *Differentialgeometrie I*. Sammlung Götschen, Walter de Gruyter, Berlin, 1964.
17. Stachel H., Nonuniform chain-wheel drives, *Proceedings of the 8th World Congress on the Theory of Machines and Mechanisms*, Prague 1991, Vol. 5, pp. 1343–1346.

# Fulleroid-Like Linkages

Gökhan Kiper

**Abstract** The Fulleroid, discovered by K. Wohlhart, is a 48-link overconstrained spatial linkage which expands and contracts within a rhombic dodecahedral boundary. In this paper, some similar types of linkages are synthesized based on some observations on the Fulleroid. First an infinite class of 24-faced polyhedral linkages is described. Next the idea is generalized for polyhedra having rhombic faces. Then analyzing these linkages a basic closed chain is derived as a module and some dipyramidal and stellated polyhedral linkages are synthesized using this module.

**Keywords** Overconstrained Spatial Linkages · Polyhedral Linkages

## Introduction

Just as objects with planar boundaries, i.e. polyhedra, have been a center of attraction for people, linkages that stay in certain planar boundaries are attracting attention especially among kinematicians. Many *polyhedral linkages* were synthesized so far by Fuller [1], Verheyen [2], Hoberman [3], Wohlhart [4], Röschel [5], Agrawal et al. [6], Kovács et al. [7], Gosselin et al. [8] and Kiper et al. [9].

The Fulleroid was synthesized by K. Wohlhart together with several alike linkages [4, 10, 11]. In this study, the structure of the Fulleroid is analyzed and similar linkages are synthesized in the light of these analyses.

## The Fulleroid

The Fulleroid is a highly overconstrained single degree-of-freedom (dof) linkage. The linkage has 24 ternary and 24 binary links (the gussets) connected by a total number of 60 revolute joints (Fig. 1). There are 6 loops comprising 4 ternary links

---

G. Kiper (✉)

Mechanical Engineering Department, Middle East Technical University, İnönü Bulvarı, 06531 Ankara, Turkey  
e-mail: kiper@metu.edu.tr

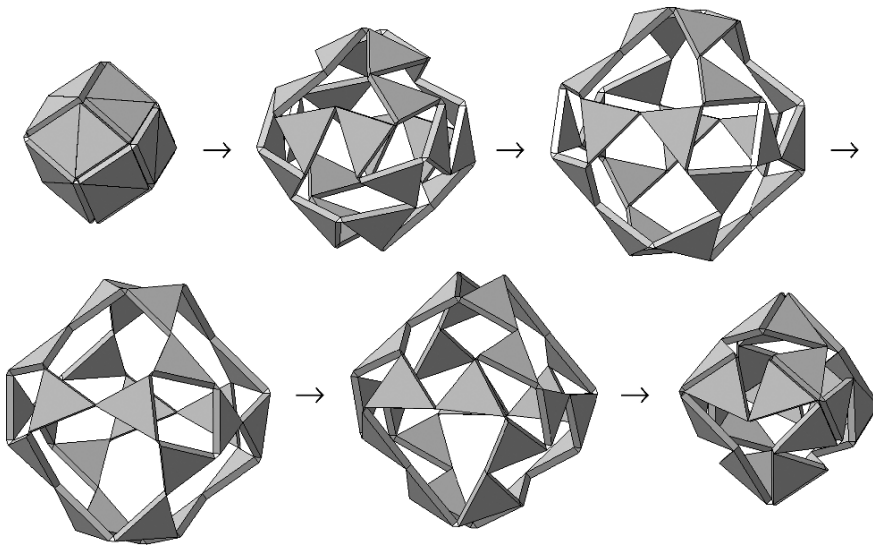


**Fig. 1** The Fulleroid in motion

with 4 gussets and 6 loops comprising 6 ternary links with 3 gussets and 3 revolute joints. In all configurations, the linkage is bounded by a rhombic dodecahedral shape of varying scale. Although this enclosing polyhedral shape has 12 faces, the geometry described will be considered to be a 24-faced polyhedron, 12 pairs of faces being coplanar. The reason for this novel way of thinking will be apparent in the following section.

## Icositetrahedral Linkages

As a first step we ask what if the revolute joints of the Fulleroid are replaced by gussets and ternary link dimensions are changed accordingly? That is to say, what if our 24-faced polyhedron, i.e. the icositetrahedron, had no coplanar faces while it had the same group of symmetries (the octahedral group)? The infinite family of polyhedra described by the cumulation series of the cube satisfy these conditions. *Cumulation* is the operation which replaces the faces of a polyhedron with pyramids of height  $h$  (where  $h$  may be positive, zero, or negative) having the face as the base [12]. The cumulation series of the cube is illustrated in Fig. 2.

If the faces of these cumulations are connected by dihedral angle preserving gussets, the resulting linkages are movable with single dof (Figs. 3, 4, 5, and 6). The mobility checks were performed as a kinematic simulation in Catia V5<sup>®</sup>. For a physical model of a concave linkage the thickness dimensioning should be done carefully, because overlapping occurs when simple prismatic links are used. Note that the concave linkage in Fig. 6 is fully closed in both closed configurations.

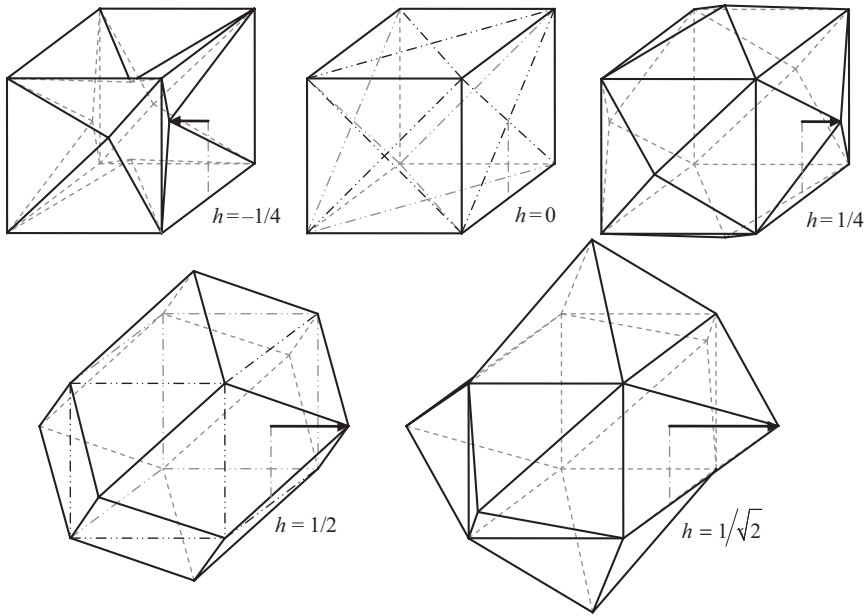


**Fig. 2** Some cumulations of a cube with unit edge length: A concave icositetrahedron, the cube, the tetrakis hexahedron, the rhombic dodecahedron and another concave icositetrahedron

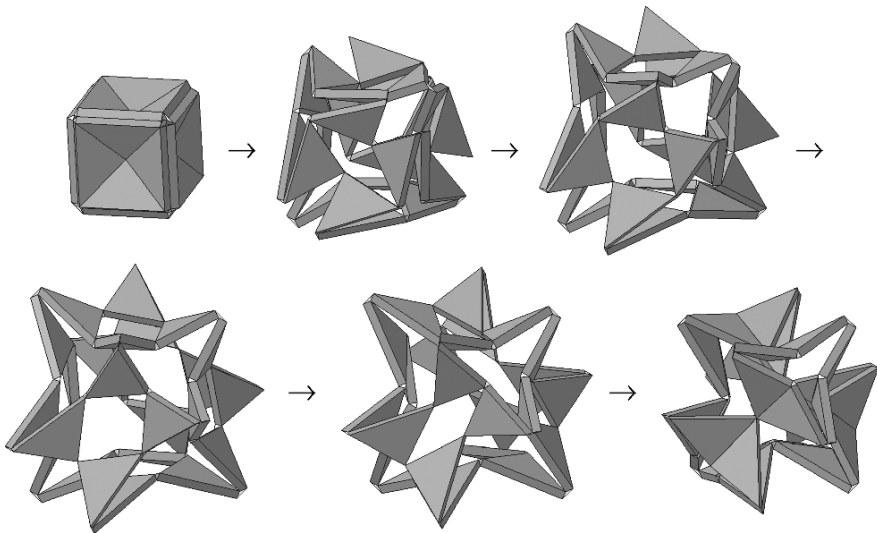


**Fig. 3** A concave icositetrahedral linkage (obtained by cumulating the cube inwards by 1/4th of the edge length)

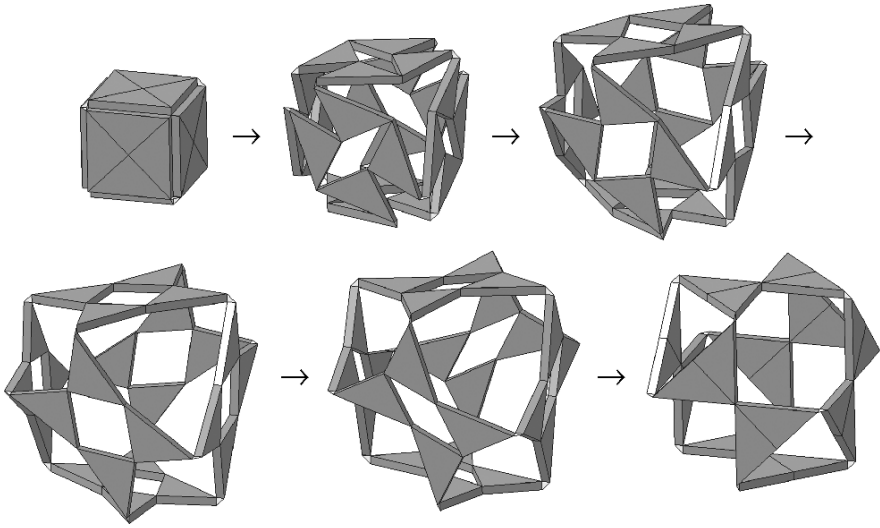


**Fig. 4** A cubic linkage

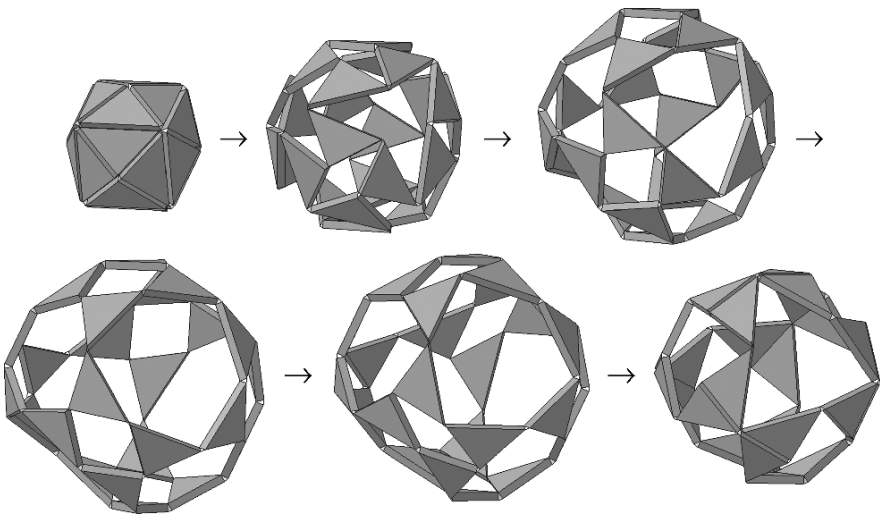


**Fig. 5** A tetrakis hexahedral linkage (obtained by cumulating the cube outwards by  $1/4$ th of the edge length)

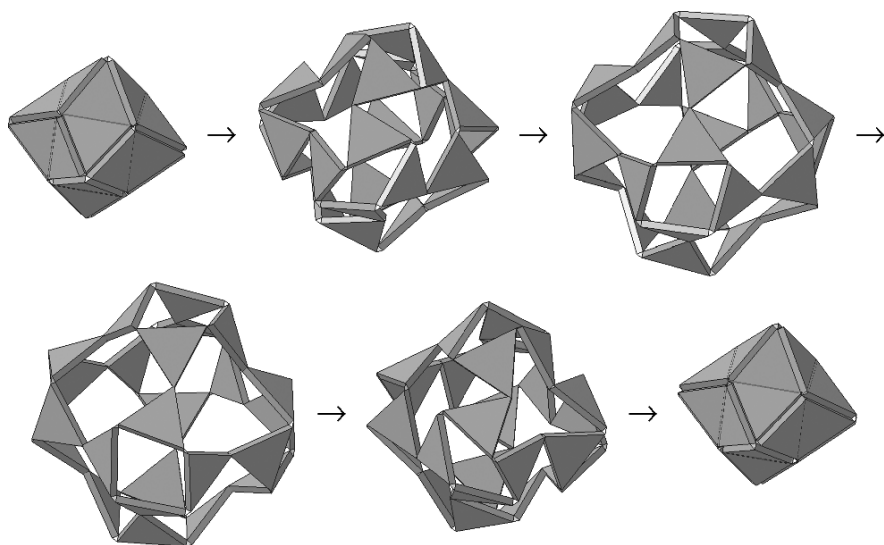


**Fig. 6** A concave icositrahedral linkage (obtained by cumulating the cube outwards by  $1/\sqrt{2}$  th of the edge length)

## Rhombohedral Linkages

Next, we ask what if we distort the cube such that we obtain a rhombohedron: a 6-faced polyhedron in which all faces are congruent equilateral parallelograms, i.e. rhombi. Again we obtain an icositrahedral linkage, but if three of the gussets

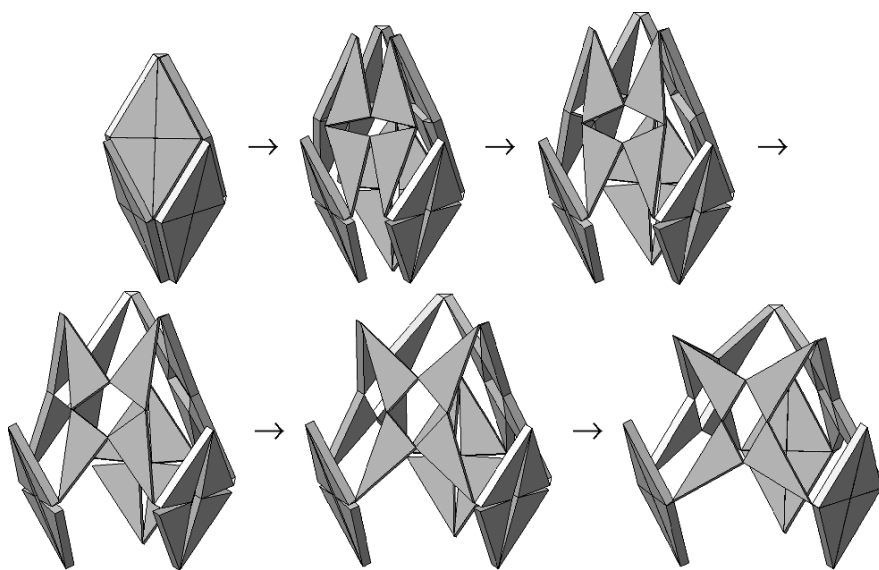


**Fig. 7** A rhombohedral linkage with faces that have diagonal ratio  $\sqrt{2} : 1$



(out of twelve gussets used for the cubic linkage) are removed (Fig. 7). Note that the expansion is not uniform in this linkage, i.e. not all the faces perform similar expansion. This is probably because of the non-uniformity of the vertices: at three of the vertices the plane angles are not all equal. This linkage, maybe, should not be considered in the same class with the previous ones, but it is a quite notable spatial linkage. Due to the spider-like appearance of the final phase of the linkage, we shall tag this linkage as the *spiderohedral linkage*.

## Dipyramidal and Stellated Linkages

In most of the linkages considered so far, we have the assembly of a certain module, a spatial 8R closed chain with the following properties: every joint axis is intersecting one of the neighboring axes and is parallel to the other, the four intersection points are separated by the closest distance between the four parallel axes, the distances being equal and two opposite intersecting joint axis pairs have the same angle in between (Fig. 8). If we call the intersecting joint pair as a V joint, the linkage can be described as a 4V equilateral closed chain. Note that in the degenerate case,  $\alpha$  and/or  $\beta$  may be zero, in which case a VRVR or a 4R chain is obtained. Indeed, the Fulleroid has the VRVR chains and the *spiderohedral linkage* has the 4R chains.

If one of the links of this linkage is fixed, the resulting mechanism has 2 dof. If four of these linkages are assembled using some more V and/or R joints, special design parameters are necessary to have mobility (A very general case is given by O. Röschel [5]). Note that the 4V linkage can only be employed at 4-valent vertices (vertices at which four faces meet). The detailed mobility analysis of these assemblies is kept out of scope this paper, but the observation is employed in synthesis of some other linkages.

Using these 4V chains as modules, dipyramids can be mobilized. For  $\alpha = \beta = 2 \tan^{-1}(1/\sqrt{2}) = 70.53^\circ$ , if the six of the 4V linkages are assembled such that neighboring three equilateral links form a triangle, the Jitterbug [1] is obtained.

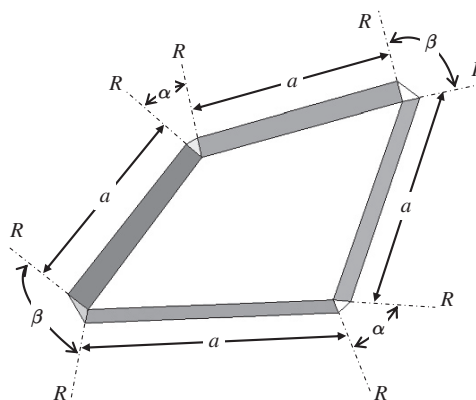
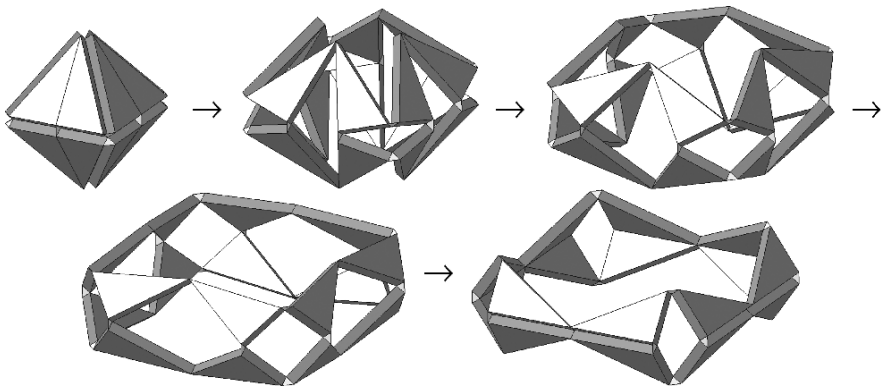


Fig. 8 A symmetrical spatial 8R closed chain



**Fig. 9** Octahedral linkage

Some other dipolygonids (Jitterbug-like linkages, classification of which is given by Verheyen [2]) may also be synthesized this way (ex: cuboctahedral linkage  $8\{3\} + 6\{4\}\{54^\circ 44' 08''\}$  [2]).

Another way of mobilizing the octahedron is to dissect each face into two, hence obtaining 16-faced linkages (Fig. 9). the triangular faces of the polyhedral shape need not be equilateral (Fig. 10). For these linkages, as the number of the sides of the base polygon increases, the openings about the apexes become larger and a ring-like form is obtained.

Also, the 4V chains can be used to mobilize stellated polyhedra (Fig. 11 – VRVR chains are used in this example).

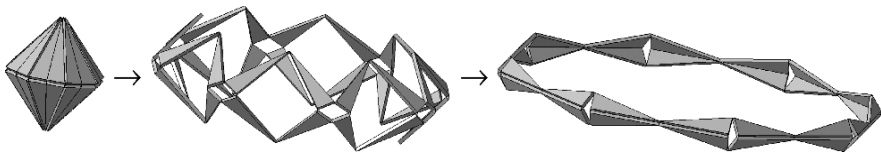


**Fig. 10** An octagonal dipyramidal linkage

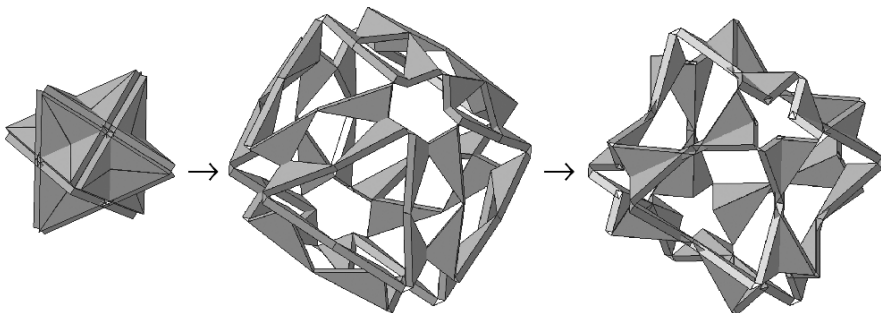


**Fig. 11** A stella octangula linkage

## Conclusion

New types of polyhedral linkages are synthesized starting with some observations on the Fulleroid. First, cumulations are used to obtain icositetrahedral linkages similar to the Fulleroid. Then, the cubic form is distorted by changing the plane angles to obtain rhombohedral linkages. Finally observing that these linkages are obtained by assembling symmetrical 8R/6R/4R linkages, dipyramidal and stellated polyhedral linkages are synthesized.

As a final note, the linkages synthesized here, except the spiderohedral linkage, are special cases of Röschel's *unilaterally closed mechanisms* [5], of which the author was not aware when this paper was written.

## References

1. Fuller, R. B., *Synergetics*, Macmillan, New York, Sections 460–465, 1979.
2. Verheyen, H. F., The Complete Set of Jitterbug Transformers and the Analysis of Their Motion, *International Journal of Computers and Mathematics with Applications*, Vol. 17, 1989, pp. 203–250.
3. Hoberman, C., Reversibly Expandable Doubly-Curved Truss Structure, Patent US4942700, 1990.
4. Wohlhart, K., New Overconstrained Spheroidal Linkage, *Proceedings of the 9th IFToMM World Congress*, Vol. 1, Milano, 1995, pp. 149–154.
5. Röschel, O., Zwangläufig Bewegliche Polyedermodelle III, *Math. Pannonica*, Vol. 12, 2001, pp. 55–68.
6. Agrawal, S. K., Kumar, S., Yim, M., Polyhedral Single Degree-of-Freedom Expanding Structures: Design and Prototypes, *Journal of Mechanical Design*, Vol. 124, 2002, pp. 473–478.
7. Kovács, F., Tarnai, T., Guest, S. D., Fowler, P. W., Double-link Expandedhedra: A Mechanical Model for Expansion of a Virus, *Proceedings of the Royal Society: Mathematical, Physical & Engineering Sciences*, Vol. 461(2051), 2004, pp. 3191–3202.
8. Gosselin, C. M., Gagnon-Lachance, D., Expandable Polyhedral Mechanisms Based on Polygonal One-Degree-Of-Freedom Faces, *Proc. IMechE Part C: Journal of Mechanical Engineering Science*, Vol. 220, 2006, pp. 1011–1018.
9. Kiper, G., Söylemez, E., Kişisel, A. U. Ö., A Family of Deployable Polygons and Polyhedra. *Mechanisms and Machine Theory*, Vol. 43(5), 2008, pp. 627–640.
10. Wohlhart, K., Kinematics and Dynamics of the Fulleroid, *Multibody System Dynamics*, Vol. 1, 1997, pp. 241–258.
11. Wohlhart, K., New Regular Polyhedral Linkages, *Proceedings of 8th IFTOMM Intern. Symposium on Theory of Machines and Mechanisms*, Bucharest, Rom., Vol. II, pp. 365–370, 2001.
12. Weisstein, E. W., “Cumulation” From MathWorld – A Wolfram Web Resource, <http://mathworld.wolfram.com/Cumulation.html>, accessed: 25.03.2008.

# On the Classification of Compliant Mechanisms

Lena Zentner and Valter Böhm

**Abstract** An intrinsic compliance of technical systems is often required in a lot of applications i.e. medical technology and man-machine interaction. This requirement can be realised constructively by utilisation of compliant mechanisms. This paper presents a classification of the deformation behaviour of compliant mechanisms to simplify their systematic construction. Especially focused on their enlarged functional properties, one objective is to minimize or replace the sensory effort by using “intelligent” mechanics, another one is to show future-oriented possibilities for their development.

**Keywords** Compliant · Structures · Mechanisms · Classification

## Introduction

Due to the development of novel materials and corresponding manufacturing technologies, in many tasks concerning motion- or force-transmission conventional rigid body systems are more and more replaced or retrofitted successfully by fully or partially compliant mechanisms.

Generally the advantages of compliant mechanisms are: less friction and accordingly grease, ease of miniaturisation, ease of manufacturing because of easier or no assembly and low maintenance. Therefore one important application field is microtechnology i.e. microrobot joints. However, the great complexity of the constructive design of such mechanisms and fatigue of the material among large deformation have to be considered.

A general nomenclature of compliant mechanisms as well as their classification based on their functional design is given in [1], [2] and [3].

In the following a classification of compliant mechanisms regarding their compliance and their deformation behaviour is presented.

---

L. Zentner (✉)

Fakultät für Maschinenbau, Technische Universität Ilmenau, PF 100565, 98684 Ilmenau, Germany  
e-mail: lena.zentner@tu-ilmenau.de

## Classification of Compliant Structures Regarding Their Compliance

The compliance of the mentioned structures can be distinguished into a fixed and variable one (Fig. 1).

Structures having a fixed compliance which is explicitly defined by the system’s geometric parameters and material properties can adopt one or more equilibrium shapes for a given fixed load. Structures with one equilibrium shape have a one-to-one dependency of the deformation on the load. In case structures have several stable and instable equilibrium positions for a given load (static stability) a particular equilibrium shape is defined by the user himself or by the environmental conditions.

In case of structures having a reversibly variable compliance the latter can be changed by manipulating the geometry or by varying the structure’s material properties. The compliance of these structures can be divided into those with self-determined compliance and those with user-defined compliance. In the first changes of the compliance are caused by environmental conditions (loads, temperature, etc.) and in the second by the user himself.

In many future-oriented applications compliant mechanisms with variable compliance will gain in importance because of their increased performance.

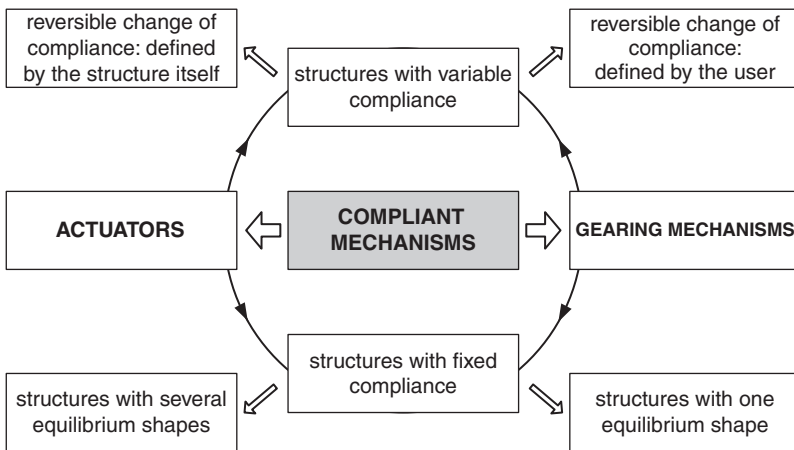


Fig. 1 Classification of compliant structures regarding their compliance

## Classification of Compliant Structures Regarding Their Deformation

In case the deformation-behaviour is chosen as a criterion for classifying compliant structures, two subgroups – dynamic and static deformation – can be distinguished. In the following the static deformation behaviour of compliant mechanisms which have a fixed compliance are regarded. Therefore inertia and damping are neglected.

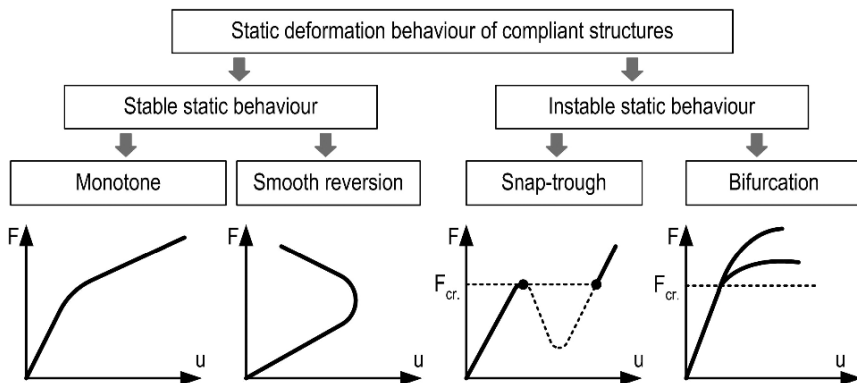


Fig. 2 Classification of the static deformation of compliant structures

The static deformation behaviour can be divided into stable and instable behaviour (Fig. 2). Stable deformation behaviour is characterised by a surjective mapping of a particular load  $F$  on the deformation  $u$ . Thereby one can differentiate between a monotonic behaviour and a behaviour with a singular smooth reversion. In case of instable behaviour of compliant structures snap-through (discontinuous deformation-behaviour) and bifurcation (local bifurcation) are possible.

### Stable Deformation Behaviour of Compliant Structures – Monotonic Deformation

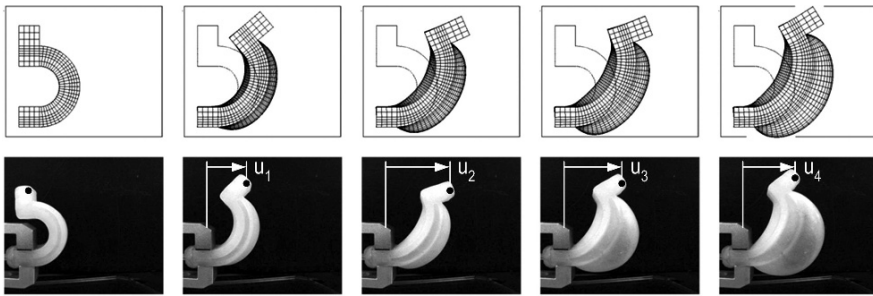
Figure 3 shows an example of the monotonic deformation behaviour of a pneumatically driven compliant structure. By increasing the load (here: internal pressure) the characteristic deformation parameters such as the angle between the longitudinal-axis of the rigid structural parts also increases [4]. Most of the known compliant structures show this behaviour. Recent research fields are focused primarily on different methods of shape optimisation and on increasing the motion range of structures which have such a deformation characteristic [5].



Fig. 3 Monotonic deformation behaviour of a pneumatically driven compliant mechanism made of silicone rubber

## Stable Deformation Behaviour of Compliant Structures – Deformation Behaviour with Direction Reversion

The deformation behaviour with direction reversion of a pneumatically driven compliant structure is shown in Fig. 4. The geometry of the structure is optimised specifically by means of FEM, to achieve a smooth reversion of the moving direction by increasing the internal pressure. The horizontal displacement of the working element was chosen as the characteristic parameter, whereat the vertical displacement and the distance of the working element to the fixed support might be also possible characteristic parameters. The horizontal displacement rises to a maximum and thereafter decreases, whereat the pressure is increased [6]. This effect, whereat the geometric parameters are designed by numerical optimisation, could be verified by experimental investigations.



**Fig. 4** Static deformation behaviour of a compliant structure with smooth direction reversion: at the *top* – FEM-calculations; at the *bottom* – experimental study with the characteristic parameter  $u_i, i = 1, \dots, 4$

Figure 5a graphically presents the change of the characteristic parameter mentioned above. Therein the horizontal displacement of the working element  $u_3$  equals the reversal point of the structure. Structures with such a specific path can be utilised e.g. as extremities in locomotion systems.

Due to model based optimisation a modified dependency of the load on the displacement can be achieved (Fig.5a, broken line). Therein the characteristic

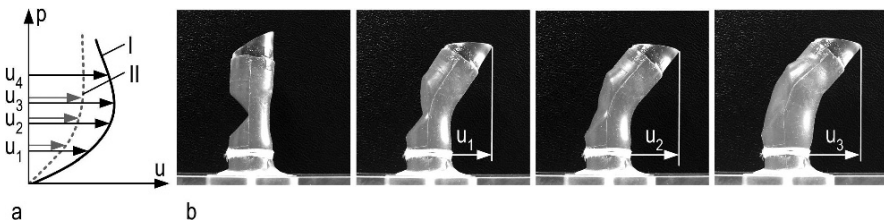


**Fig. 5 (a):** I – Dependency of displacement  $u$  on internal pressure  $p$  of structures introduced in Fig. 4, II –  $p(u)$  characteristic of a gripping-finger with bounded maximal gripping-force; **(b):** gripping-finger with bounded maximal gripping-force made of silicone rubber at increased pressure

displacement increases until the specific displacement  $u_3$  is reached. During the whole deformation process pressure is increased but the characteristic displacement stays constant for  $p > p(u_3)$ , (Fig. 5b). A preferred application of such a characteristic with respect to compliant structures is to use it as gripping fingers. Because of the specific characteristic, the maximal gripping force is bounded and therefore no sensor is needed to monitor the gripping force.

### Instable Deformation-Behaviour of Compliant Structures – Snap-Through

In contrast to the stable deformation behaviour of compliant structures the instable case has more than one equilibrium position for a particular load. The instable deformation behaviour shows snap-through or bifurcation.

In case of snap-through a sudden transition from one equilibrium position to another happens. Thereby a given load corresponds to several equilibrium positions. In most of the known solutions the mechanisms have 2 or 3 stable equilibrium positions [7]. In Fig. 6 a rotationally structure in the origin state is shown which have a double curved cross section. One characteristic feature of such a structure is the bistable deformation behaviour which can be defined by the specified geometric parameters (shape, wall thickness, etc.). Two different structures with different wall thicknesses are presented in Figs. 6 and 7. By increasing the load, the centre point of both structures moves outwards until the critical load  $p_{cr}$  is reached (Fig. 8a). Herein the value of the critical load depends on the wall thicknesses. An arbitrary small raise of load causes a huge displacement, as soon as the critical load is reached. During this process the centre curvature penetrates completely (state 2 in Figs. 6, 7). If the load

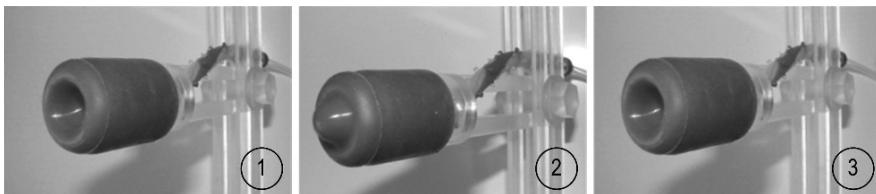


Fig. 6 Snap-through of a curved structure having a monostable deformation behaviour

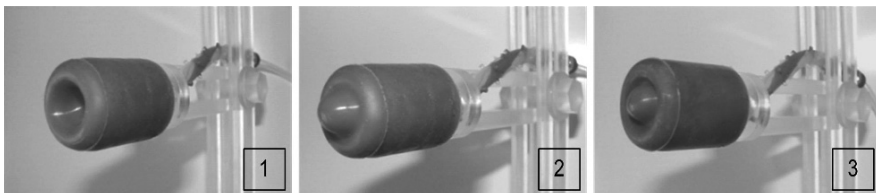
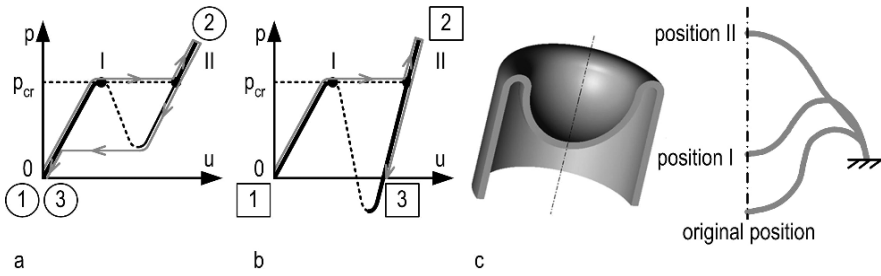


Fig. 7 Snap-through of a curved structure having a bistable deformation behaviour





**Fig. 8** Sketch of Snap-through behaviour of a curved structure: **a** – structure with monostable characteristic, **b** – structure with bistable characteristic; **c** – three calculated characteristic positions of these structures by means of FEM, origin:  $p = 0$ ,  $p = p_{cr}$  for positions I and II

is removed, the first structure reverses to the original position (monostable characteristic). This is demonstrated by state 3 in Fig. 6. The second structure switches to another equilibrium position (bistable characteristic) which is shown in Fig. 7. A sketch of both deformation characteristics and the calculated positions by means of FEM are shown in Fig. 8.

Figure 9 shows a possible application of these structures used as mechanical valve, whereat three several configurations are illustrated. A curved structure with bistable deformation behaviour with an opening in the centre is sketched in Fig. 9a. Because of the critical pressure the structure is deformed and the flow is interrupted. In this case the current position guarantees the closure of the pipe. To back up the origin state, low-pressure have to be applied on the left side of the structure. This restores the flow.

The next Fig. 9b shows a structure with monostable deformation behaviour. If the critical pressure is applied, the valve closes the pipe. If the pressure falls under the critical one, the original position is recaptured and the flow is reconstituted. The last example in Fig. 9 illustrates a valve installed in a pipe with two outputs. Output B is disabled, as soon as the critical pressure is reached. Decreasing the pressure enables this output again.

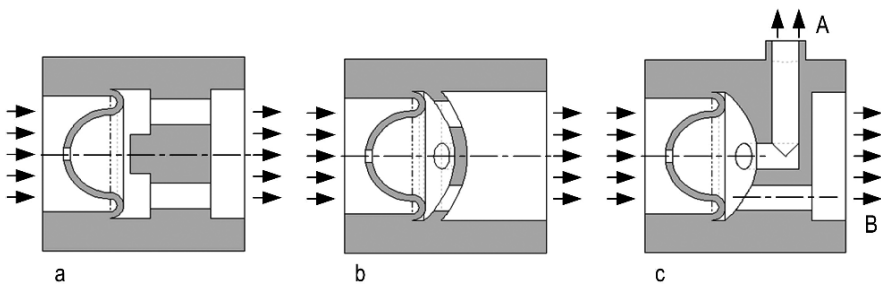


**Fig. 9** Applications of compliant structures as mechanical valves: **a, b** – pipe with one output is disabled for  $p \geq p_{cr}$ , **c** – pipe with two outputs A and B, output B is disabled for  $p \geq p_{cr}$

## Instable Deformation-Behaviour of Compliant Structures – Bifurcation

Situations in which load leads to bifurcation of structures are avoided generally in engineering.

As an example for this case, structures among the influence of an axial load are regarded. Figure 10 illustrates such structures whereat the load is generated by a tensile force of the filaments e.g. SMA-wires or by the low-pressure in cavities. If these wires are uniformly pulled or the same low-pressure exists in the cavities, the classical Euler stability problem (bifurcation) can be regarded. The response of a systematically designed system with bifurcation behaviour (deformation or displacement in several directions) on external (e.g. temperature change) or on user-defined conditions leads to one preferred direction. The deformation direction is selected “autonomously” whereas the drive regime for each process stays always the same. The sensory and control effort are minimised enormously. The control of the system is partly adopted by “intelligent” mechanics.

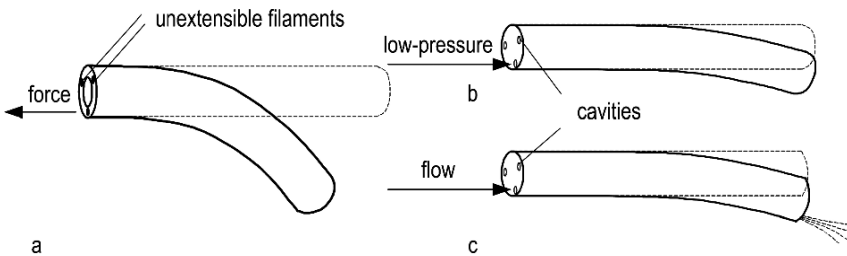


**Fig. 10** Structures among the influence of an axial load which is generated by a tensile force of the filaments or Shape-Memory-Alloy-wires (a) and by the low-pressure in cavities (b, c)

## Conclusion

The introduced classification which considers the deformation of compliant mechanisms should facilitate their development and their implementation in rigid body systems with respect to a functional expanded substitution of rigid body parts. The meaningful application of compliant mechanisms especially of such structures with instable static behaviour offers a great development potential. The role of the sensor system can be partly or completely adopted by “intelligent” mechanics. With the application of compliant structures and structural elements, which show an instable static behaviour and therefore segue from one state to another depending on external conditions, elementary characteristics of the system can change. Hence such systems will autonomously and directly adapt to the working conditions.

In relation with functional dominating compliant characteristics many application-oriented tasks like special valves, gripping-fingers with particular characteristics, medical structural elements and systems are conceivable.

## References

1. Midha, A., Norton, T.W., Howell, L.L.: On the Nomenclature, Classification and Abstractions of Compliant Mechanisms, *ASME Journal of Mechanical Design*, Vol. 116, No. 1, 1994, 270–279.
2. Howell, L.L.: *Compliant Mechanisms*, John Wiley & Sons, Inc., New York, 2001.
3. Lobontiu, N.: *Compliant Mechanisms: Design of Flexure Hinges*, CRC Press, 2003, ISBN: 0849313678.
4. Zentner, L., Böhm, V., Turkevi-Nagy, N.: Fluidisch Angetriebenes Stoffschlüssiges Gelenkelement, Offenlegungsschrift, Deutsches Patent- und Markenamt, DE 103 16 959 A1, 2004.
5. Trease, B.P., Moon, Y.M., Kota, S.: Design of Large-Displacement Compliant Joints, *Journal of Mechanical Design*, Vol. 127, No. 4, 2005, 788–798.
6. Zentner, L., Böhm, V., Minchenya, V.: On the New Reversal Effect in Monolithic Compliant Bending Mechanisms with Fluid Driven Actuators, *Journal of Mechanism and Machine Theory*, DOI information: 10.1016/j.mechmachtheory.2008.05.014.
7. Pendleton T., Jensen B.: Development of a Tristable Compliant Mechanism, Proc. of the 12th IFToMM World Congress, Besancon, June 18–21, 2007.

# Comparative Kinematics of Mobile Transversal Coupling, as Multibody System

Cornel Cătălin Gavrilă

**Abstract** Mechanical systems definition as multibody systems is a modern way of modeling aiming to the real time simulation of complex product's dynamic behavior. The paper presents aspects regarding the comparative kinematics of the transversal mobile coupling as multibody system. First there are presented the structural schemes of the analyzed mobile couplings. Then are defined: the parts of the multibody system associated to the mobile coupling; the body reference frames and also the general reference frame; the geometrical and kinematical constraints. Based on these, there are determined the kinematical equations, useful to found the optimal geometrical configuration of the coupling, depending by the initial requests of a mobile coupling. Finally, the conclusions are presented.

**Keywords** Mobile Coupling · Kinematics · Multibody System

## Introduction

The transversal couplings are used in torque transmission between two shafts with parallel axis [1]. The shafts 1 and 3 are connected by a planar kinematical linkage 2, which give the possibility to have translations in the transversal plane between the shaft axes. These translations are named transversal movements (Fig. 1).

A transversal coupling is homokinetic if the shafts angular speeds are identical. If the shafts angular speeds are almost identical, the mobile coupling is quasihomokinetic [1, 2].

The transversal coupling multibody model has, as bodies, the input and output shafts and also, some of the intermediary bodies which have, usually, more than two connections [2, 3]. If the semicouplings are connected to the basis, will result

---

C.C. Gavrilă (✉)  
Product Design and Robotics Department, Transilvania University  
of Brasov, Eroilor 29, 500036 Braşov, România  
e-mail: cgavrila@unitbv.ro

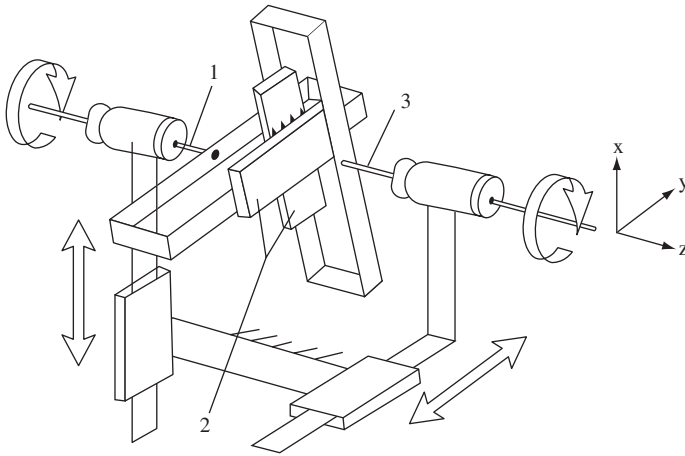


**Fig. 1** Example of a mobile transversal coupling, with transversal movements

the associated mechanism [1, 2]. The bodies of the multibody system are: input coupling, 1, intermediary body 2, output semicoupling 3 and the basis 0.

The most simple known linkages [1, 2] that may realise a translation between two elements are the parallelogram linkage contour and also the anti-parallelogram linkage contour (Fig. 2, where 1, 2, 3, 4 are the links of the linkages).

In practice, is preferable to use the parallelogram linkage contours, which led to homokinetic couplings [1, 2]. The anti-parallelogram linkage contours are quasi-homokinetic (in Fig. 3, for link 4 it appears the supplementary angle  $\Delta\beta$ ) and led to quasihomokinetic couplings [1, 2].

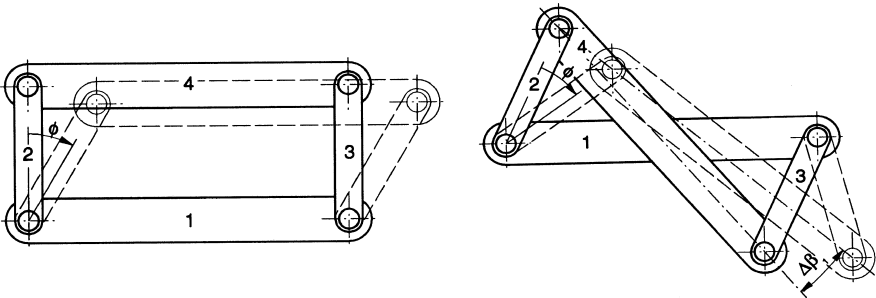


**Fig. 2** Parallelogram and antiparallelogram linkage contours

### Multibody Models: Kinematic Study

The coupling presented in Fig. 1, with the translation joints between semicouplings, is used in practice as Oldham. The Oldham mobile coupling is composed by two semicouplings 1 and 3, and between them there is the intermediary element 2 (Fig. 3) [1, 2].

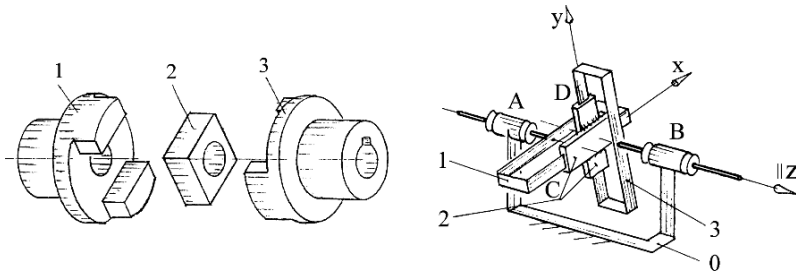


Fig. 3 Oldham coupling

Between the bodies there are the geometrical restrictions types rotation (R) and translation (T), detailed in Table 1. The geometrical and kinematical multibody model with the interest points coordinates is presented in Fig. 4.

The mobility of the associated mechanism multibody system is [1, 2, 4]

$$M = 3(n_b - 1) - \sum g_c = 3(4 - 1) - 8 = 1, \tag{1}$$

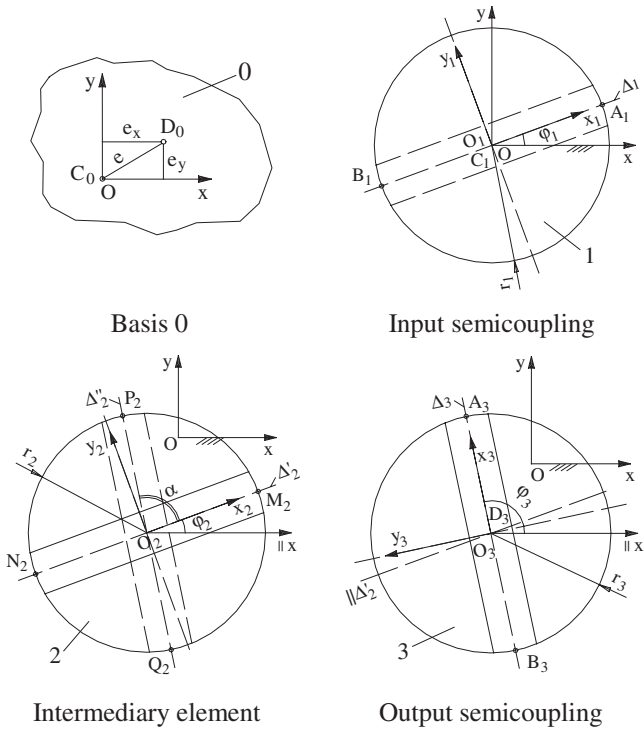


Fig. 4 Kinematical multibody model for Oldham coupling

**Table 1** Restrictions

Bodies	Geometrical constraints	Joints (Fig. 3)	Number of restrictions
0-1	R	A	2
0-3	R	B	2
1-2	T	C	2
2-3	T	D	2

where  $n_b = 4$  is the number of the associated mechanism bodies and  $\sum g_c = 8$  is the number of the geometrical constraints between the bodies.

For geometrical restrictions definition, it is necessary to know the points coordinates relative to the fixed coordinates system [3]. The general relation of these coordinates is:

$$\begin{bmatrix} x_{M_i} \\ y_{M_i} \end{bmatrix} = \begin{bmatrix} x_{0i} \\ y_{0i} \end{bmatrix} + \begin{bmatrix} \cos \varphi_i & -\sin \varphi_i \\ \sin \varphi_i & \cos \varphi_i \end{bmatrix} \begin{bmatrix} r_{ix} \\ r_{iy} \end{bmatrix}, \quad (2)$$

where  $i = 1, 2, 3$ .

Generally, for the rotation geometrical restriction (R) between two bodies, the equation is [3, 4]

$$P_i \equiv P_j. \quad (3)$$

Also, for the translation (T) geometrical restriction between two bodies, the equation is [3, 4]

$$\Delta_i \equiv \Delta_j. \quad (4)$$

The kinematical restriction equation is

$$\rho_1 - f(t) = 0. \quad (5)$$

Based on the relations (2) . . . (5), it is obtained an equation system with 9 equations and 9 unknowns :  $x_{01}, y_{01}, \varphi_1, x_{02}, y_{02}, \varphi_2, x_{03}, y_{03}, \varphi_3$ . To resolve the equation system, it is necessary to take account by the mobile transversal coupling constructive conditions [1, 2]. Taking account of previous conditions, and for  $r_1, r_2, r_3$  with arbitrary values, the equation system led to

$$\sin(\varphi_1 - \varphi_2) = 0. \quad (6)$$

The result is  $\varphi_1 = \varphi_2 + 2K\pi$ , for  $K \in \mathbb{Z}$  and  $\forall \varphi_1, \varphi_2 \in \mathbb{R}$ .

For the real coupling case,  $K = 0$ , will obtain the homokinetism condition between the input semicoupling 1 and intermediary element 2

$$\varphi_2 = \varphi_1. \quad (7)$$

Analogue, will obtain

$$\sin [(\varphi_2 + \alpha) - \varphi_3] = 0. \tag{8}$$

The result is  $\varphi_2 + \alpha = \varphi_3 + 2K\pi$  for  $K \in \mathbb{Z}$ , and  $\forall (\varphi_1 + \alpha), \varphi_3 \in \mathbb{R}$ . For the real coupling case,  $K = 0$ , will obtain the homokinetic condition between the intermediary element 2 and output semicoupling 3

$$\varphi_3 = \varphi_1 + \alpha. \tag{9}$$

For the real coupling,  $\alpha = \pi/2$ , result that the coupling is homokinetic.

If, for the coupling presented in Fig. 1, one of the translation joints is replaced with parallelogram linkage contour, it will be obtained the Oerlikon coupling, presented in Fig. 5, used in practice [1, 2].

The mobility of the associated mechanism multibody system is also given by the relation (1). For the Oerlikon coupling shown in Fig. 5, the geometrical and kinematical multibody model with the interest points coordinates is presented in Fig. 4, and, for the changed parts, in Fig. 6. Between the bodies there are the geometrical restrictions types rotation (R) and translation (T) and, for parallelogram linkage contour, double rotation – rotation (RR+RR), detailed in Tables 1 and 2.

**Table 2** Changed restriction, to obtain Oerlikon coupling

Bodies	Geometrical constraints	Joints (Fig. 3)	Number of restrictions
2-3	RR+RR	DE, FG	1+1

Generally, for the rotation-rotation (RR) geometrical restriction between two bodies, the equation is [2 – 4]

$$(x_{Pj} - x_{Pi})^2 + (y_{Pj} - y_{Pi})^2 = d^2. \tag{10}$$

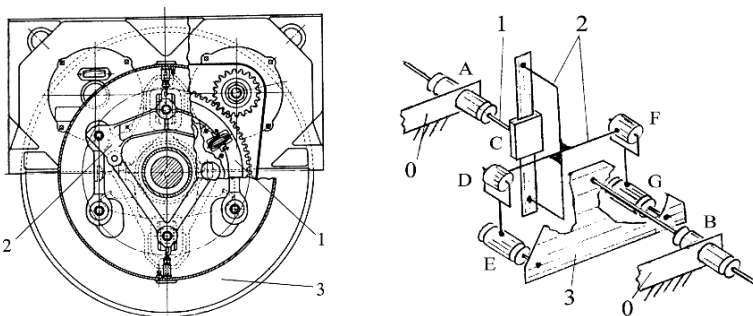


**Fig. 5** Oerlikon coupling



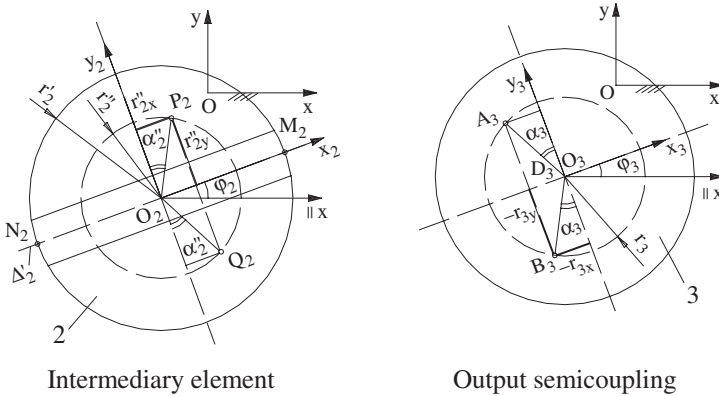


Fig. 6 Kinematical multibody model parts for Oerlikon coupling

Based on the relations (2, 3, 4, 5, 10), first will result the relations (6) and (7) for the homokinetism condition between the input semicoupling 1 and intermediary element 2. Then, will result the homokinetism condition between the intermediary element 2 and the output semicoupling 3

$$r_2'' \cos \alpha_2'' = r_3 \cos \alpha_3, \tag{11}$$

The result is  $\varphi_2 = \varphi_3 + 2K\pi$ , where  $K \in \mathbb{Z}$ , for  $\forall \varphi_2, \varphi_3 \in \mathbb{R}$ . For the real coupling case  $K = 0$ , it is obtained

$$\varphi_2 = \varphi_3. \tag{12}$$

Taking account the relations (7) and (12), it is obtained the homokinetism condition of the Oerlikon mobile coupling

$$\varphi_1 = \varphi_3. \tag{13}$$

Finally, if, for the coupling presented in Fig. 1, the translation joints are both replaced with parallelogram linkages contours, it will be obtained the Semiflex coupling, presented in Fig. 7, used in practice [1, 2].

The mobility of the associated mechanism multibody system is also given by the relation (1). For the Semiflex coupling shown in Fig. 7, the geometrical and kinematical multibody model with the interest points coordinates is presented in Fig. 4, and, for the changed parts, in Figs. 6 and 8. Between the bodies there are the geometrical restrictions types rotation (R) and, for parallelogram linkage contours, double rotation – rotation (RR+RR), detailed in Tables 1 and 3.

Based on the relations (2, 3, 5, 10), first will result the relation for the homokinetism condition between the input semicoupling 1 and the intermediary element 2

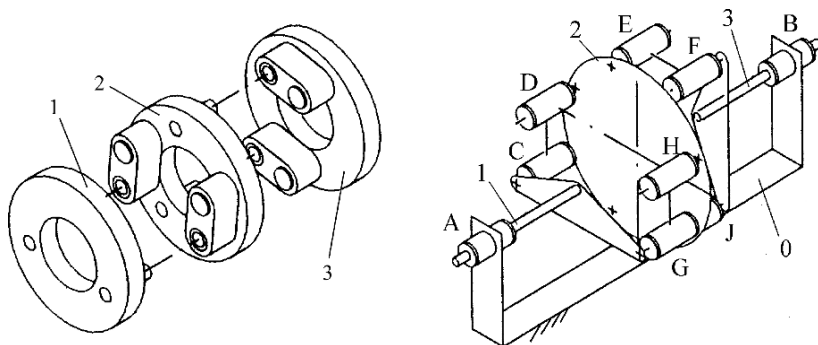


Fig. 7 Semiflex coupling

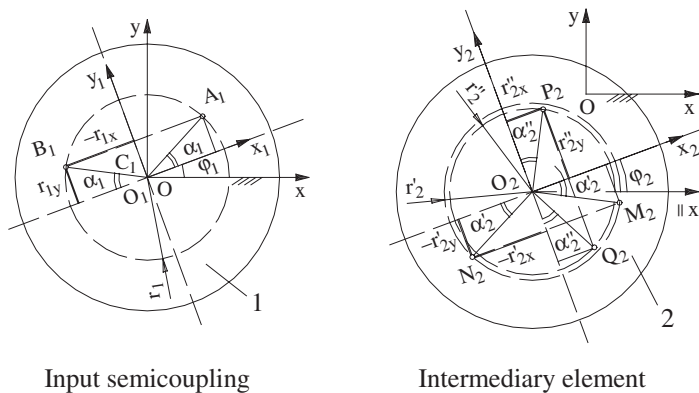


Fig. 8 Kinematical multibody model parts for Semiflex coupling

Table 3 Changed restrictions, to obtain Semiflex coupling

Bodies	Geometrical constraints	Joints (Fig. 3)	Number of restrictions
1-2	RR+RR	CD, GH	1+1
2-3	RR+RR	DE, FG	1+1

$$r'_2 \cos \alpha'_2 = r_1 \cos \alpha_1 \tag{14}$$

The result is  $\varphi_1 = \varphi_2 + 2K\pi$ , where  $K \in \mathbb{Z}$ , for  $\forall \varphi_1, \varphi_2 \in \mathbb{R}$ . For the real coupling case  $K = 0$ , it is obtained the condition (7).

Then, based on relation (11) will result the homokinetism condition between the intermediary element 2 and the output semicoupling 3. Taking account the relations (7) and (12), it is obtained the homokinetism condition of the Semiflex mobile coupling, given by the relation (13).

## Conclusions

In the case of the mobile couplings as multibody systems with three bodies, the homokinetism can be proved in two steps: first  $\varphi_1 = \varphi_2$ , and then  $\varphi_2 = \varphi_3$ . As a result, the Oerlikon mobile coupling can be considered a combination between Oldham and Semiflex, depending which translation couple is replaced with parallelogram linkage contour.

The method can be applied also for other known mobile couplings, as multibody systems with three, four or five mobile bodies and for other new solutions of mobile couplings.

The method is useful in the study of the kinematics of these couplings and dynamic behavior of them with performant software.

## References

1. Dudiță, Fl., Diaconescu, D., *Mobile Couplings Linkages*. Ed. Oriental Latin, Brașov, 2001 (in romanian).
2. Vișa, I., Gavrilă, C.C., *Structural Synthesis of Transversal Couplings by Multibody Systems Method*, 12th IFToMM World Congress, Besançon, France, June 18–21, 2007, CD-Rom edition.
3. Schiehlen, W., *Multibody System Handbook*. Springer-Verlag, Germany, 1990.
4. Shigley, J.E., *Kinematic Analysis of Mechanisms*. McGraw-Hill, New York, 1959.

# The Synthesis of a Linkage with Linear Actuator for Solar Tracking with Large Angular Stroke

Ion Visa, Dorin Diaconescu, Valentina Popa, Bogdan Burduhos  
and Radu Saulescu

**Abstract** In the bi-axial tracking of the PV modules (aiming to maximize the normal direct solar radiation on panels), one of the two axes, which has a large angular stroke ( $180^\circ \dots 360^\circ$ ), is usually driven by a gear speed reducer and the other axis, which has a smaller angular stroke ( $\leq 90^\circ$ ), is driven by a linear actuator. Because a linear actuator is more economical than a rotary one, the paper reports on the use of linear actuators for the large angular strokes; this aim is fulfilled by the synthesis of a linkage composed of two simple linkages, serially connected: a triangle linkage with a linear actuator and a four-bar linkage which amplifies the output angle of the first linkage up to about  $180^\circ$ .

**Keywords** Tracking linkage · Linkage synthesis · Pressure angle transmission angle · Angular stroke · Plane linkage · Spatial linkage

## Introduction

The PV tracking, single or bi-axial, is used for maximizing the normal incident direct solar radiation on the PV panels; thus a 20%...50% increase in the energetic efficiency can be achieved [1].

Bi-axial PV tracking systems of azimuthal- and equatorial type are mostly used [1]; one axis has a maximum  $90^\circ$  angular stroke (type I) and the other one has an angular stroke way beyond this limit (type II).

The PV panel tracking around an axis of type I implies driving a revolute joint by a triangle linkage with the deformable side consisting in a linear actuator. The tracking around an axis of type II supposes driving a revolute joint by a worm speed reducer or other gear reducer with a high speed ratio; unlike the tracking with linear actuator, the tracking by a gear reducer ensures larger angular strokes, but has

---

I. Visa (✉)

Department of Product Design and Robotics, Transilvania University of Brasov, Eroilor Boulevard 29, 500036 Brasov, Romania  
e-mail: visaion@unitbv.ro

significant disadvantages: higher technological cost, higher complexity, difficulties in reducing the backlashes, lower efficiency in the case of the worm speed reducer.

Consequently, there were developed systems that extend the use of the triangle linkage for the axis of type II; in this case, a reduction of the stroke (under  $120^\circ$ – $140^\circ$ ), due to the pressure angles [2], is expected.

The paper solves *the angular stroke increase, using a linear actuator*, by the synthesis of a linkage composed of two simple linkages, serially connected: a triangle linkage with a linear actuator and a four-bar linkage which amplifies the output angle of the first linkage up to about  $180^\circ$ .

## Synthesis Input Data

In the bi-axial tracking of the PV panels, there are usually used three *angular systems*, which interfere in modelling the current angular position of the sun-ray and in the structure of the bi-mobile open chains (BOC) of the tracking linkages (see Figs. 1, 2 and 3):

- (a) *The Equatorial System* (Fig. 2a): *hour angle*  $\omega$  and *declination*  $\delta$ ; the BOC, resulted by serial connection of the 2 rotations in the given order, is named *equatorial* or *polar* BOC (Fig. 1a) and is less applied;
- (b) *The Pseudo-Equatorial System* (Figs. 1b and 2b<sub>1</sub>): *seasonal angle*  $\gamma \approx \varphi - \delta$  and *daily angle*  $\beta \approx \omega$ ; the BOC, obtained by serial connection of the 2 rotations in the given order, is named *pseudo-equatorial* or *pseudo-polar* OC and is relatively wide applied; according to Figs. 1b and 2b<sub>1</sub>, the *pseudo-equatorial* BOC results from the *equatorial* BOC (Fig. 1a) by reversing the connection order of the 2 rotations.
- (c) *The Azimuthal System* (Figs. 1c and 2b<sub>2</sub>): *azimuth*  $\psi$  and *altitude*  $\alpha$ ; the BOC, resulted by serial connection of the 2 rotations in the given order is named *azimuthal* BOC and is the most applied.

The sun-ray angles (see Table 1) depend on the angles  $\omega$  and  $\delta$ , considered as primary input data [3, 4]. Unlike the sun-ray motions, the motions of the tracked panel are made stepwise; to distinguish them, in this paper the tracker's angles are noted:  $(\beta^*, \gamma^*)$  and  $(\psi^*, \alpha^*)$ .

For the existing trackers, the angular movements  $\alpha^*$  and  $\gamma^*$  (with strokes  $\leq 90^\circ$ ) are made with linear actuators; unlike this case, the angular movements  $\omega^*$ ,  $\beta^*$  and  $\psi^*$  (with strokes  $\geq 180^\circ$ ) is made usually with rotary actuators, *which are usually less economically efficient than linear actuators*. Extending the use of the linear actuators for the angular movements  $\omega^*$ ,  $\beta^*$  and  $\psi^*$  is exemplified in the Fig. 1a,b and c, where the linear actuators are represented by dot-dash lines segments.

The use of a triangle linkage with linear actuator (Fig. 1) reduces the orientation angular stroke due to the excessive increase of the pressure angle; this correlation follows from Fig. 3:

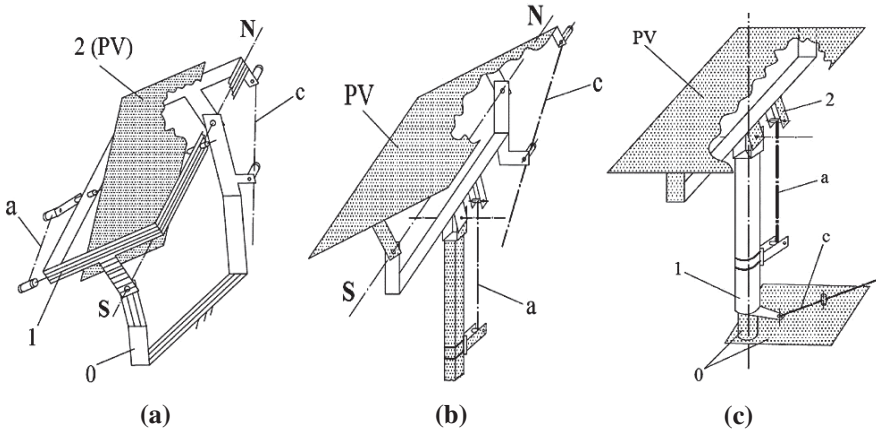


Fig. 1 Trackers: (a) equatorial; (b) pseudo-equatorial and (c) azimuthal

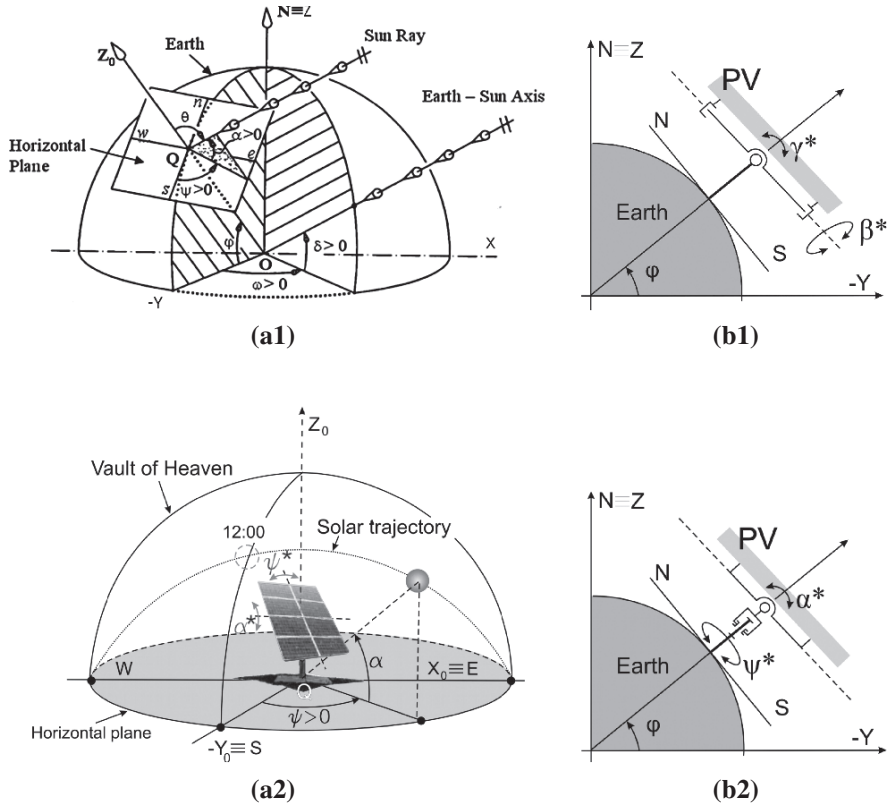
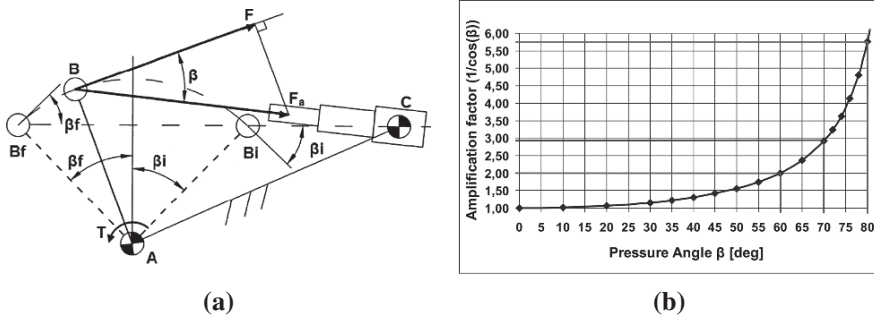


Fig. 2 (a1, a2) Sun-ray angles; (b1, b2) Earth-tracker relative positions



**Fig. 3** (a) Scheme of the triangle linkage with linear actuator; (b) The variation of the amplification factor depending on the pressure angle

**Table 1** Main correlations corresponding to the PV panels' tracking

$$\delta = 23.45^\circ \cdot s[360 \cdot (N - 80)/365] \quad (1)$$

$$\omega = 15^\circ \cdot (12 - T); \quad (2)$$

$$s\gamma = \frac{c\delta \cdot c\omega \cdot s\phi - s\delta \cdot c\phi}{c\beta} \quad (3)$$

$$s\beta = c\delta \cdot s\omega; \quad (4)$$

$$s\alpha = s\delta \cdot s\phi + c\delta \cdot c\phi \cdot c\omega \quad (5)$$

$$\psi = (sgn\omega) \cdot c^{-1} \frac{s\alpha \cdot s\phi - s\delta}{c\alpha \cdot c\phi}; \quad (6)$$

$$cv = c\beta \cdot c\beta^* \cdot c(\gamma - \gamma^*) + s\beta \cdot s\beta^*; \quad (7)$$

$$cv = c\alpha \cdot c\alpha^* \cdot c(\psi - \psi^*) + s\alpha \cdot s\alpha^* \quad (8)$$

$$R_d = 1367 \cdot [1 + 0.0334 \cdot c(0.9856^\circ \cdot N - 2.72^\circ)] \cdot e^{\left(-\frac{T_R}{0,9 + 9,4 \cdot s\alpha}\right)} \quad (9)$$

$$R_{dr} = R_d \cdot cv \quad (10)$$

$c = \cos$ ;  $s = \sin$ ;  $\phi$  – latitude;  $\delta$  – declination;  $\omega$  – hour angle;  $N$  – day number;  $T$  – solar time;  $\gamma$ ,  $\beta$  – pseudo-equatorial angles;  $\alpha$  – altitude;  $\psi$  – azimuth;  $v$  – incidence angle;  $\beta^*$ ,  $\gamma^*$ ;  $\psi^*$ ,  $\alpha^*$  – tracker's angles;  $R_d$  – and  $R_{dr}$  – direct solar radiation and direct radiation which falls normal on panel;  $T_R$  – lost factor.

- (a) Figure 3a shows that in a current position ABC (with the pressure angle  $\beta_B = \beta$ ), the balance of the resistant moment  $T=F^*AB$  compels the actuator to produce a force:  $F_a = F^*(1/\cos \beta)$ ; the variation of the *amplification factor*  $1/\cos \beta_B = F_a/F$ , (Fig. 3b) confirms that the limitation of the pressure angle maximum value to  $60^\circ$ ,  $70^\circ$  or  $80^\circ$  determines a 2, 3 and, respectively, 6 times force amplification.
- (b) Figure 3a also shows that the extreme values of  $\beta_i$  and  $\beta_f$  have equal modules if the points C,  $B_i$  and  $B_f$  are collinear; in this case, the angular stroke becomes  $B_iAB_f = 2^* \beta_{B,max. admitted} \approx 120^\circ \dots 140^\circ$ ; increasing the angular stroke beyond these values can have negative consequences.

Further, *the angular stroke increase, using a linear actuator; is solved* by synthesis of a linkage consisting in two simple linkages which are serially connected: a triangle linkage with linear actuator (Fig. 3a) and a four-bar linkage which amplifies the output angle of the first linkage up to  $180^\circ$ ; the priority belongs to the synthesis of the angular amplifier linkage.

### Tracking Linkage Synthesis

The synthesis of the conceptual solutions of the linkage with linear actuator for reaching an  $180^\circ$  angular stroke is presented in Fig. 4 and has the following formulation: the output angular stroke of a triangle linkage with linear actuator is amplified to  $180^\circ$  by a four-bar linkage; the requirement is to establish the reduced dimensions (related to the length of one of the elements) of the four-bar linkage elements, considering that the *maximum admissible pressure angle* is  $70^\circ$  (implicitly, the *minimum admissible transmission angle* is  $90^\circ - 70^\circ = 20^\circ$ ).

The synthesis is graphically presented in the Fig. 5a:

- (1) the little rocker AB (with angular stroke of  $180^\circ$ ) is traced in the extreme positions  $AB_i$  and  $AB_f$ ; its length is considered as unit (1);
- (2) for improved stability, the connecting rod extreme positions  $B_iC_i$  and  $B_fC_f$  are traced, so that the connecting rod and the little rocker form a  $40^\circ$  transmission angle (i.e.  $20^\circ + 0^\circ \dots 20^\circ$ ); the connecting rod length is chosen as little as possible, but considering that in the initial position, the rocker  $C_iD$  will not interfere with the revolute joint A;
- (3) the line  $\Delta$  through the points  $C_i$  and  $C_f$  and the median perpendicular of  $C_iC_f$  (which contains the joint centre D of the big rocker) are traced; the point D is chosen so that between the connecting rod ( $B_fC_f$ ) and the rocker  $C_fD$  a transmission angle of  $30^\circ$  is formed (i.e.  $20^\circ + 0^\circ \dots 20^\circ$ ); thus, the following reduced dimensions result (see Fig. 4a): the reduced connecting rod  $BC/AB = 2.1694$ , the reduced rocker  $CD/AB = 2.4742$  and the reduced base  $DA/AB = 1.0714$ ; so, the obtained linkage (Fig. 4a) achieves an amplification ratio of  $180^\circ/87^\circ = 2.07$ ;
- (4) then, a linear actuator is attached to the rocker CD, like Fig. 3a;
- (5) if the triangle  $C_iC_fD$  (Fig. 4a) is turned with  $180^\circ$  round to line  $\Delta$ , the second plane solution from Fig. 4b is obtained; this new solution (see Fig. 4b) is forced to use the minimum transmission angle (i.e.  $20^\circ + 0^\circ$ ) and achieves an amplification ratio of  $180^\circ/37^\circ = 4.86$  with the reduced dimensions:  $BC/AB = 1.8$ ,  $CD/AB = 3.6538$  and  $DA/AB = 4.5746$ .
- (5) if the triangle  $C_iC_fD$  (Fig. 4a) is turned with  $180^\circ$  round to line  $\Delta$ , the second plane solution is obtained (see Fig. 4b); this solution (see Fig. 4b) is forced to use the minimum transmission angle (i.e.  $20^\circ + 0^\circ$ ), achieves an amplification ratio of  $180^\circ/37^\circ = 4.86$  and has an overall size bigger than the first solution.
- (6) if the triangle  $C_iC_fD$  (Fig. 4a) is turned with  $90^\circ$  round to line  $\Delta$ , a spatial solution is obtained (see Fig. 4c<sub>1</sub> and 4c<sub>2</sub>); this spatial solution can use a trans-



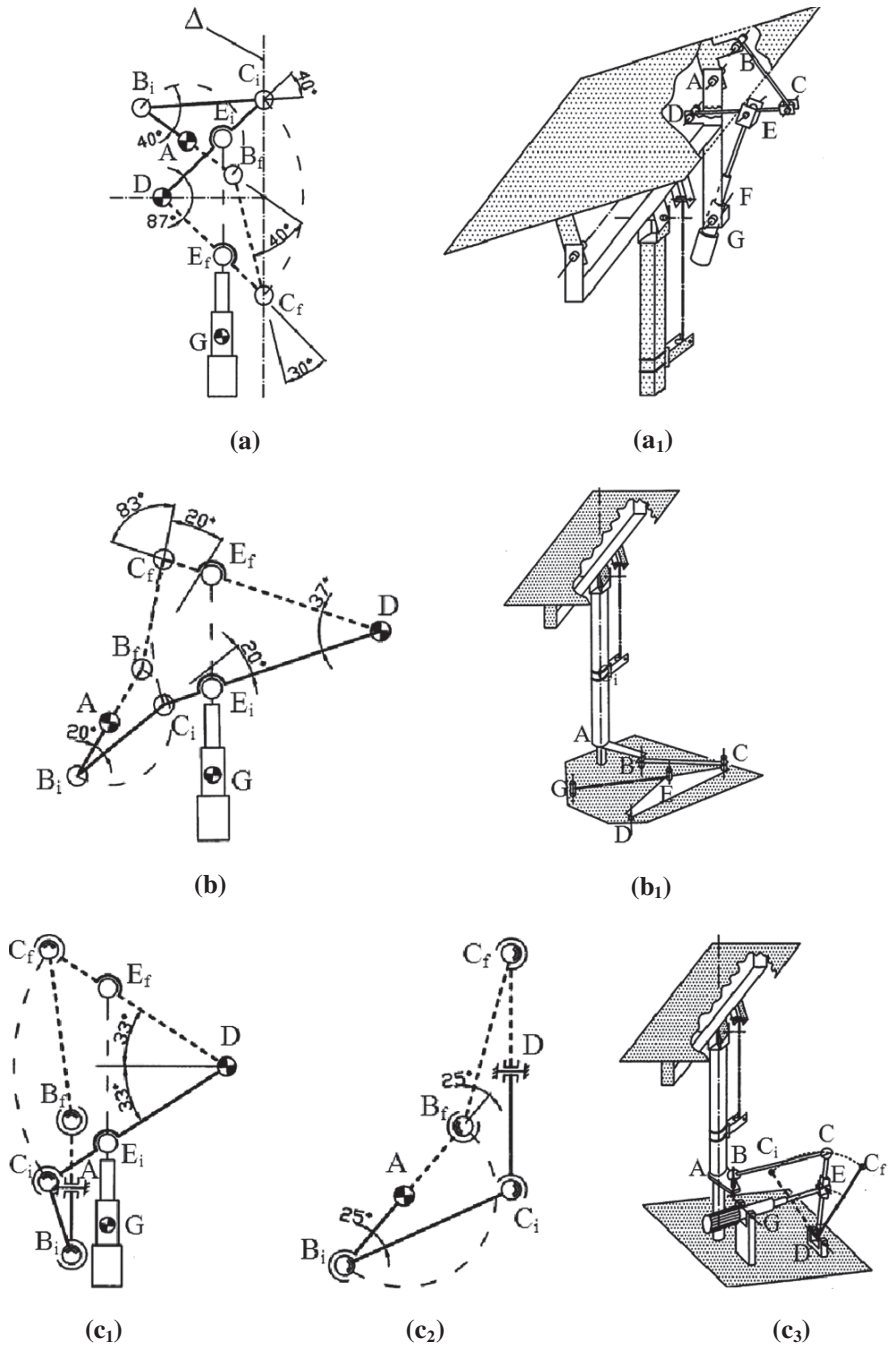


**Fig. 4** Three synthesis solutions: (a, a<sub>1</sub>) first plane solution used in pseudo-equatorial tracking; (b, b<sub>1</sub>) second plane solution used in azimuthal tracking; (c<sub>1</sub>, c<sub>2</sub>, c<sub>3</sub>) spatial solution used in azimuthal tracking

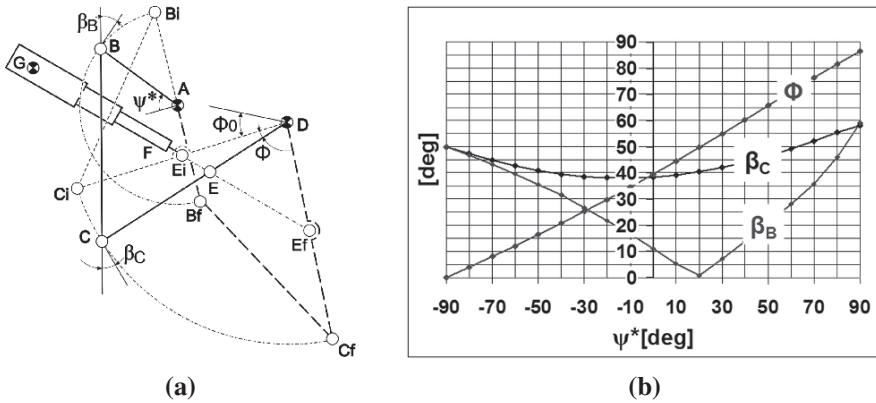


**Fig. 5** (a) The current and extreme positions of the linkage from Fig. 4a; (b) The variations of the pressure angle  $\beta_B$ ,  $\beta_C$ , and of the angle  $F$

mission angle only of  $25^\circ$  (instead of  $40^\circ$ ; see Fig. 4a), achieves an amplification ratio of  $180^\circ/66^\circ = 2.73$  with the reduced dimensions  $BC/AB = 2$ ,  $CD/AB = 2.4$  and the base configuration (AD) described by: the reduced distance between the axes A and D: 1.373; the reduced distance from the vertical articulation A to the vertical median plane of the rocker CD: 1.667; the reduced distance from the horizontal articulation D to the horizontal median plane of the rocker AB: 1.746.

In Fig. 4a<sub>1</sub>, b<sub>1</sub> and c<sub>3</sub> there are presented three applications of these solutions: Fig. 4a<sub>1</sub> exemplifies the use of the linkage from Fig. 4a, in a pseudo-equatorial tracker, for the movement  $\beta^*$  driving, while the Fig. 4b and Fig. 4c<sub>1</sub> and c<sub>2</sub> represent applications of the linkages from Fig. 4b and from Fig. 4c<sub>1</sub> and c<sub>2</sub>, in an azimuthal tracker, for the movement  $\psi^*$  driving.

For the first application (Fig. 4a and a<sub>1</sub>), Fig. 5 shows the relevant positions and the specific geometrical parameters, along with the variations of the pressure angles  $\beta_B$ ,  $\beta_C$  and of the angular displacement  $\Phi$ , depending on the angular displacement  $\psi^*$ ; these correlations were obtained using MBS (Multi-Body Systems) Method [5].

## Conclusions

- (a) A gear speed reducer ensures angular strokes no matter how large, but is usually less economical than a rotary linkage with a linear actuator; though economically more efficient, the use of a simple triangle linkage with linear actuator reduces the angular stroke of the tracking axis, due to the pressure angle limitation (the maximal angular strokes are usually limited at  $120^\circ$ – $140^\circ$ ).
- (b) The increase of the angular stroke, considering a linear actuator, is presented in the paper by synthesis of a linkage composed from two simple linkages which are serially connected: a triangle linkage with a linear actuator (Fig. 3a) and a four-bar linkage which *amplifies* the output angle of the first linkage up to  $180^\circ$ .

- (c) By the above synthesis, three solutions were generated for an *angular amplifier*, applicable in tracking the solar PV panels: two plane solutions (Fig. 4a,  $a_1$  and b,  $b_1$ ) and a spatial solution (Fig. 4c<sub>1</sub>, c<sub>2</sub> and c<sub>3</sub>). The first plane solution (Fig. 4a,  $a_1$ ) has the best transmission angles but achieves the least amplification ratio, while the second plane solution (Fig. 4b,  $b_1$ ) achieves the biggest amplification ratio and has the least transmission angles; the performances of the spatial solution (Fig. 4c<sub>1</sub>, c<sub>2</sub> and c<sub>3</sub>) are situated between the performances of the two plane solutions.
- (d) The analysis of the first solution (see Figs. 4a,  $a_1$  and 5a, b) shows that the angular displacement  $\Phi$  has a linear variation vs. angular displacement  $\psi^*$ , while the pressure angles  $\beta_B$  and  $\beta_C$  have nonlinear variations between  $0^\circ$  and  $60^\circ$ , respectively  $38^\circ$  and  $60^\circ$ .

## References

1. [www.wattsun.com](http://www.wattsun.com), [www.lorentz.com](http://www.lorentz.com), [www.deger.de](http://www.deger.de)
2. Norton, R.L., Design of Machinery, Mc Graw Hill, Boston, 1999.
3. Messenger, R., Ventre, J., Photovoltaic System Engineering, London, CRC Press, 2000.
4. Visa, I. et al., On the Dependence between the Step Orientation and the Received Direct Solar Radiation of a PV Panel, International Conference on Renewable Energy and Power Quality, Santander, 12–14 March, 2008.
5. Haug, J.E., Computer Aided Kinematics and Dynamics of mechanical Systems, Allyn and Bacon, USA, 1989.

# Dynamics of Heel Strike in Bipedal Systems with Circular Feet

Josep Maria Font and József Kövecses

**Abstract** Energetic efficiency is a fundamental subject of research in bipedal robot locomotion. In such systems, the collision of the foot with the ground at heel strike is the main cause of energy loss during the gait. In this work, a Lagrangian framework to study the impulsive dynamics of collisions is presented. Based on the inert constraints of this event, a decomposition of the dynamics to the spaces of constrained and admissible motions is introduced. It is used to analyze the energy redistribution at heel strike in circular-foot bipeds. We present results that show the effect of the foot radius and the impact configuration on the energetic cost of walking.

**Keywords** Bipedal locomotion · Dynamics · Robotic walking systems · Collisions · Mechanism design

## Introduction

In recent years, a large effort has been invested in the development of bipedal walking systems and in the control and analysis of gaits. In this field, energetic efficiency appears to be a major objective to increase the autonomy of those robotic systems [1]. Underactuated robots based on the idea of *passive dynamic walking* [2], appear to be energetically more efficient than anthropomorphic robots that use precise joint-angle control as in [3]. Passive dynamic walking refers to simple mechanical systems that are able to walk down a slightly inclined walkway with no external control or actuation, i.e., the gravity alone powers the motion [4–6].

The work on those walkers was primarily motivated by the drive for energy efficiency and showed that it was possible to obtain dynamically stable limit cycles, with remarkably human-like motion, without any kind of actuation. Although pure passive walking is in itself not very useful for many robotic applications, since the prototypes cannot walk on level ground, it has led to important insight regarding

---

J.M. Font (✉)

Department of Mechanical Engineering, Centre for Intelligent Machines, McGill University, 817 Sherbrooke Street West, H3A 2K6 Montréal, Québec, Canada  
e-mail: josep.font@mcgill.ca

the dynamics of walking and its energetic aspects. Recently, a type of powered *passive-based* robot has appeared in the literature. These robots use minimal actuation, sensing and control to walk like a purely passive-dynamic walker but on level ground [7–9]. According to [7], these walkers use less energy and are easier to control than other anthropomorphic robots. The mechanical energy consumption of such systems is due to the loss of kinetic energy when the swing leg impacts the ground at heel strike [8]. This loss has to be compensated by actuation forces applied during the gait cycle.

The aim of this work is to gain a better understanding on the energetic aspects of such impacts that represent a change of topology. For this purpose, a Lagrangian framework to analyze the impulsive dynamics involved is introduced. Based on the post-impact inert constraints, we interpret a concept that completely decouples the dynamic characteristics of the system (including the kinetic energy) to the spaces of *constrained* and *admissible* motions [10, 11]. It will be seen that the kinetic energy decomposition at the pre-impact time yields powerful insight regarding how the kinetic energy is redistributed at heel strike.

The article is structured as follows. In Section “Dynamic Model of the Walking System” the dynamic model of the circular-feet walker is presented. Next, in Section “Lagrangian Impulsive Dynamics of Collisions” the dynamic equations for impulsive motion are introduced. Section “Energetic Analysis of Periodic Walking Motion” analyzes the energetics of walking from a novel perspective based on the decomposition of the dynamics at impact. Finally, Section “Results and Discussion” presents results regarding the influence of different parameters on the energetic losses.

## Dynamic Model of the Walking System

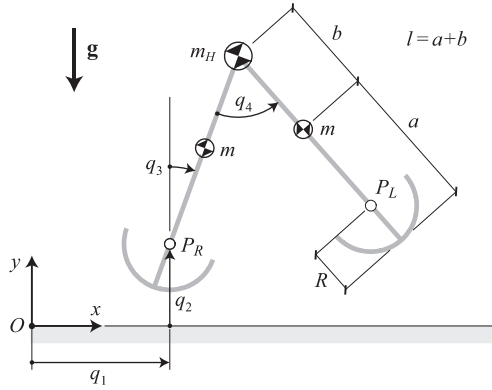
In this work, we study a compass-gait biped with circular feet, which consists of two identical straight legs of length  $l$  and mass  $m$ , Fig. 1. Their centres of mass are at a distance  $b(= l - a)$  from the hip. The radius of the feet is  $R$  and the hip is modelled as a point mass  $m_H$  located at the revolute joint between the two legs. Points  $P_R$  and  $P_L$  refer to the centres of the circumferences defining the *right* and *left* foot, respectively.

To study the general motion of the biped four generalized coordinates are required (Fig. 1). They define the vector of generalized coordinates,  $\mathbf{q} = [q_1, q_2, q_3, q_4]^T$ . Coordinates  $q_1$  and  $q_2$  give the  $(x, y)$ -position of  $P_R$  with respect to the inertial frame. Coordinate  $q_3$  indicates the absolute orientation of the right leg, and  $q_4$  denotes the relative angle between the two legs.

The kinetic energy of the walker can be expressed in the following form

$$T(\mathbf{q}, \dot{\mathbf{q}}) = \frac{1}{2} \dot{\mathbf{q}}^T \mathbf{M}(\mathbf{q}) \dot{\mathbf{q}}, \quad (1)$$

**Fig. 1** Dynamic model of the compass-gait biped with circular feet



where  $\dot{\mathbf{q}} = [\dot{q}_1, \dot{q}_2, \dot{q}_3, \dot{q}_4]^T$  is the vector of generalized velocities, and  $\mathbf{M}$  is the  $4 \times 4$  symmetric mass matrix of the walker.

### Lagrangian Impulsive Dynamics of Collisions

The single support phase of walking ends when the swing foot impacts the ground at heel strike. At this time, the system undergoes a sudden change of topology. The dynamics of this impulsive motion phase can be characterized by the following impulse-momentum level dynamic equations [12, 13]

$$\left[ \frac{\partial T}{\partial \dot{\mathbf{q}}} \right]_{-}^{+} = \mathbf{M} (\dot{\mathbf{q}}^{+} - \dot{\mathbf{q}}^{-}) = \bar{\mathbf{f}}, \tag{2}$$

where “-” and “+” denote the pre- and post-impact instants, and  $\bar{\mathbf{f}}$  are the generalized impulses. Assuming that only constraints provide forces at the impulse-momentum level, then  $\bar{\mathbf{f}} = \mathbf{A}_j^T \bar{\lambda}$ , where  $\bar{\lambda}$  is the vector of constraint impulses and  $\mathbf{A}_j$  is the Jacobian matrix. The subscript  $j$  is either  $R$  or  $L$  depending on which is the colliding foot. Since the colliding foot is required to stay in contact with the ground without slipping (i.e., the collision is inelastic), the impulsive motion can be characterized by the following *inert* constraints [12, 13]

$$\mathbf{A}_j \dot{\mathbf{q}}^{+} = 0, \tag{3}$$

where the Jacobian matrix takes one of the following expressions

$$\mathbf{A}_R = \begin{bmatrix} 1 & 0 & -R & 0 \\ 0 & 1 & 0 & 0 \end{bmatrix}, \tag{4}$$

$$A_L = \begin{bmatrix} 1 & 0 & -R & (l-R)\cos q_3 + R \\ 0 & 1 & -2(l-R)\sin q_3 & (l-R)\sin q_3 \end{bmatrix}, \quad (5)$$

depending on which foot collides the ground;  $\mathbf{A}_R$  if the *right* foot collides and vice versa. Note that when collision takes place,  $q_3$  completely defines the configuration of the system, since at this time  $q_4 = 2q_3$ .

Based on the inert constraints expressed in (3), the tangent space of the configuration manifold of the walking system can be decomposed to the spaces of *constrained* and *admissible* motions for the pre-impact instant. This will then also hold for the entire duration of the contact onset, since the configuration of the system is assumed to be unchanged during this short period of time. These two subspaces can be defined so that they are orthogonal to each other with respect to the natural, mass metric of the tangent space [10, 13]. The decomposition to the two subspaces can be accomplished via two projector operators [10, 11]. The projector associated with the space of constrained motion can be written as

$$\mathbf{P}_c = \mathbf{M}^{-1} \mathbf{A}_j^T (\mathbf{A}_j \mathbf{M}^{-1} \mathbf{A}_j^T)^{-1} \mathbf{A}_j, \quad (6)$$

and the projector for the space of admissible motion as

$$\mathbf{P}_a = \mathbf{I} - \mathbf{P}_c = \mathbf{I} - \mathbf{M}^{-1} \mathbf{A}_j^T (\mathbf{A}_j \mathbf{M}^{-1} \mathbf{A}_j^T)^{-1} \mathbf{A}_j, \quad (7)$$

where  $\mathbf{I}$  stands for the  $4 \times 4$  identity matrix. These projectors are not symmetric, which is a direct consequence of the nature of the metric of the tangent space. The use of them allows the decomposition of the generalized velocities  $\dot{\mathbf{q}}$  and impulsive forces  $\bar{\mathbf{f}}$  as [10, 11]

$$\dot{\mathbf{q}} = \mathbf{v}_c + \mathbf{v}_a = \mathbf{P}_c \dot{\mathbf{q}} + \mathbf{P}_a \dot{\mathbf{q}}, \quad (8)$$

$$\bar{\mathbf{f}} = \bar{\mathbf{f}}_c + \bar{\mathbf{f}}_a = \mathbf{P}_c^T \bar{\mathbf{f}} + \mathbf{P}_a^T \bar{\mathbf{f}}. \quad (9)$$

Based on (1) and (8), it can be shown that  $T$  can also be decoupled as

$$T = T_c + T_a = \frac{1}{2} \mathbf{v}_c^T \mathbf{M} \mathbf{v}_c + \frac{1}{2} \mathbf{v}_a^T \mathbf{M} \mathbf{v}_a. \quad (10)$$

To obtain this equation it was used that the projectors in (6) and (7) are orthogonal with respect to the system mass matrix, i.e.,  $\mathbf{P}_c^T \mathbf{M} \mathbf{P}_a = \mathbf{P}_a^T \mathbf{M} \mathbf{P}_c = \mathbf{0}$ , with  $\mathbf{0}$  denoting the  $4 \times 4$  zero matrix. Based on the decompositions above, the equations in (2) can also be decoupled as

$$\left[ \frac{\partial T_c}{\partial \mathbf{v}_c} \right]_{-}^{+} = \mathbf{M} (\mathbf{v}_c^{+} - \mathbf{v}_c^{-}) = \mathbf{A}_j^T \bar{\boldsymbol{\lambda}}, \quad (11)$$

which are the dynamic equations for the space of constrained motion, and

$$\left[ \frac{\partial T_a}{\partial \mathbf{v}_a} \right]_{-}^{+} = \mathbf{M} (\mathbf{v}_a^{+} - \mathbf{v}_a^{-}) = \mathbf{0}, \quad (12)$$

which gives the impulse-momentum level dynamics for the space of admissible motion. From (12) it comes immediately that  $\mathbf{v}_a^{+} = \mathbf{v}_a^{-}$ , and therefore  $T_a^{+} = T_a^{-}$ . Based on (3) and (8) it can also be concluded that  $\mathbf{v}_c^{+} = \mathbf{0}$ , which means that the kinetic energy of constrained motion is completely lost at heel strike, i.e.,  $T_c^{+} = 0$ . Therefore, the total post-impact kinetic energy equals the pre-impact kinetic energy of admissible motion,  $T^{+} = T_a^{+} = T_a^{-}$ . Finally, from the results above, the following expression can be used to determine the post-impact velocities  $\dot{\mathbf{q}}^{+}$

$$\dot{\mathbf{q}}^{+} = \mathbf{v}_a^{+} = \mathbf{v}_a^{-} = \mathbf{P}_a \dot{\mathbf{q}}^{-}, \quad (13)$$

where  $\dot{\mathbf{q}}^{-}$  can be determined from the previous finite motion analysis of the single support phase of the gait.

## Energetic Analysis of Periodic Walking Motion

Energetic aspects are very important for the optimal design and control of bipedal mechanisms [1]. In this section, the energetic balance of one complete *level-ground* and *periodic* gait is analyzed. The application of the energy theorem to the walking system between the instants after two successive collisions yields

$$\Delta T + \Delta U = W_{\text{act}} + W_{\text{col}} = 0, \quad (14)$$

where  $\Delta T$  and  $\Delta U$  represent the change of kinetic and potential energies respectively;  $W_{\text{act}}$  ( $> 0$ ) is the work done by actuators during the walking cycle; and  $W_{\text{col}}$  ( $< 0$ ) is the negative work done by the contact forces at heel strike. Note that in (14)  $\Delta T = \Delta U = 0$ , since the walking motion is periodic and on flat ground. The work  $W_{\text{col}}$  can be obtained from the energetic analysis of the impact. The application of the energy theorem between the pre- and post-impact instants yields

$$[\Delta T]_{-}^{+} = T^{+} - T^{-} = -T_c^{-} = W_{\text{col}} < 0, \quad (15)$$

which means that the magnitude of  $W_{\text{col}}$  equals the decrease in the kinetic energy at collision. Note that during the short impact period, the potential energy of the system does not change,  $U^{+} = U^{-}$ . From (10), (13) and (15), it can be concluded that the loss of energy at collision in absolute value, as expected, is the constrained pre-impact kinetic energy, i.e.,  $-W_{\text{col}} = T_c^{-}$ . We define the energetic loss per unit distance walked by the robot as



$$\eta = \frac{T_c^-}{L_S} = \frac{\frac{1}{2} (\dot{\mathbf{q}}^-)^T \mathbf{P}_c^T \mathbf{M} \mathbf{P}_c \dot{\mathbf{q}}^-}{2(l - R) \sin q_3 + 2Rq_3}, \tag{16}$$

where the denominator  $L_S$  accounts for the length of one step.

### Results and Discussion

The aim of this section is to study the effect of the impact configuration and the foot radius on the energy dissipation per unit distance walked by the robot. The fixed dynamic parameters of the robot are  $m_H = 2m = 10$  kg and  $a = b = 0.5$  m ( $l = 1$  m). We assume that the right foot is in contact with the ground at pre-impact time,  $q_2 = R$ , and that the left foot collides the ground. The impact configuration is completely defined by angle  $q_3$ . We also assume that the system controls, by means of actuation, the pre-impact angular velocities:  $\dot{q}_3^- = 1$  rad/s,  $\dot{q}_4^- = 0$ . This physically means that the pre-impact tangential component of the velocity of the colliding point is zero, which is often the case in walking motion to avoid slipping.

Figure 2 shows the pre-impact decoupling of the kinetic energy. Only the impacts that satisfy  $\dot{q}_2^+ > 0$  are analyzed, this is the reason why the curves do not cover the same range of impact configurations  $q_3$ . This inequality means that the non-colliding foot is lifting from the ground after impact. If this condition is not satisfied, other constraints become active and the gait does not evolve in a natural way.

From Fig. 2 it can be observed that for a given configuration, the kinetic energy of the constrained motion  $T_c^-$  decreases with the radius  $R$ . Consequently, the kinetic energy of the admissible motion  $T_a^-$  grows with  $R$  for a fixed  $q_3$ . Since  $T_c^-$  is completely lost at heel strike, a design with a radius  $R = l = 1$  m is the best because in that case no energy is lost at impact. This completely agrees with [2], in which McGeer showed that a circular-feet walker with  $R = l$ , which he called “synthetic wheel”, could walk on flat ground with no energy expenditure. From Fig. 2 it can

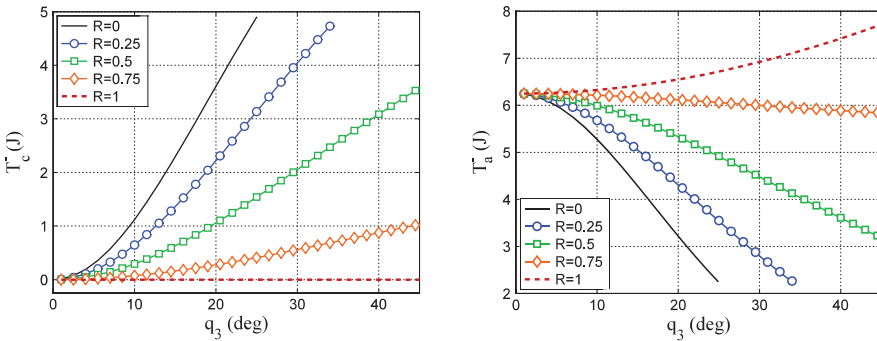


**Fig. 2** Decomposed parts of the kinetic energy  $T_c$  and  $T_a$  as functions of  $q_3$  for different values of  $R$

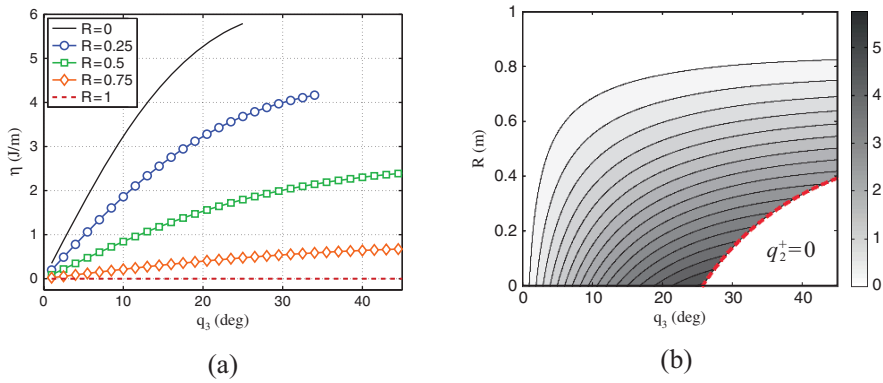


Fig. 3 Energy lost per unit distance  $\eta$  (J/m) as a function of  $q_3$  and  $R$

also be noticed that a low impact angle  $q_3$  also reduces the amount of kinetic energy lost for a given radius  $R$ .

Measure  $\eta$  can be used to evaluate the energetic expenditure per unit distance. Figure 3a represents its value as a function of the impact angle for five values of  $R$ . Figure 3b represents  $\eta$  as a function of  $q_3$  and  $R$ . From the results obtained, it can be concluded that a high value of  $R$  and low impact angles are better to reduce the energetic expenditure per unit distance. Then, in terms of energetic cost, it is better to walk a certain distance with more short steps than with less long steps.

Figure 3b is also interesting because the white area delimited by the dashed line ( $\dot{q}_2^+ = 0$ ), shows conditions for which the non-colliding foot does not lift up, and therefore natural walking does not materialize. As it can be seen, for values of  $R > 0.4$  m the non-colliding foot always lifts up at the post-impact instant for angles  $q_3 \in [0, 45^\circ]$ . The results obtained in this work are in accordance with the conclusions of previous studies of circular-feet walkers, purely passive [14] or actuated [15]. Both studies concluded that bipeds with circular feet are energetically more efficient than point-foot walkers, because the energetic losses at collision are lower.

## Conclusions

In this work, we presented a Lagrangian formulation applicable to the study of the impulsive dynamics of heel strike. Based on the inert constraints that characterize this event, we introduced a decomposition of the tangent space of the system to the spaces of constrained and admissible motions. This concept, which is novel in the field of bipedal locomotion, totally decouples the impulse-momentum level dynamic equations and the kinetic energy into two independent parts. It is useful in the analysis of velocity change and energy redistribution at heel strike.

The formulation was applied to the compass-gait biped with circular feet, and we analyzed the energetic losses at collision for different impact configurations and

values of the foot radius. From the obtained results, some important conclusions were drawn regarding the energetic aspects of walking in bipeds with circular foot.

We believe that the presented framework can be of considerable value to understand the dynamics and the energetics of bipedal locomotion machines. Furthermore, its generality makes it possible to analyze more complex systems like for example walkers with knees and torso. The presented work can also be of interest in the analysis, design and control of energetically efficient humanoid robots.

**Acknowledgments** This work has been supported by the Natural Sciences and Engineering Research Council of Canada, the Canada Foundation for Innovation, and a Postdoctoral Mobility Scholarship from the Technical University of Catalonia (UPC). The support is gratefully acknowledged.

## References

1. Schiehlen W., Energy-optimal design of walking machines, *Multibody Systems Dynamics*, Vol. 13, 2005, pp. 129–141.
2. McGeer T., Passive dynamic walking, *Int. J. Robotics Research*, Vol. 9(2), 1990, pp. 62–82.
3. Hirai K., Hirose M., Haikawa Y. and Takenake T., The development of Honda humanoid robot, in *Proc. IEEE Int. Conf. Robotics and Automation*, Leuven, Belgium, 1998, pp. 1321–1326.
4. Collins S.H., Wisse M., and Ruina A., A three-dimensional passive-dynamic walking robot with two legs and knees, *Int. J. Robotics Research*, Vol. 20(7), 2001, pp. 607–615.
5. Garcia M., Chatterjee A., Ruina A. and Coleman M., The simplest walking model: stability, complexity and scaling, *J. Biomechanical Engineering*, Vol. 120(2), 1998, pp. 281–288.
6. Goswami A., Thuilot B., and Espiau B., A study of the passive gait of a compass-like biped robot: symmetry and chaos, *Int. J. Robotics Research*, Vol. 17(12), 1998, pp. 1282–1301.
7. Collins S.H., Ruina A., Tadrake R., and Wisse M., Efficient bipedal robots based on passive-dynamic walkers, *Science*, Vol. 307, 2005, pp. 1082–1085.
8. Kuo A.D., Energetics of actively powered locomotion using the simplest walking model, *J. Biomechanical Engineering*, Vol. 124, 2002, pp. 113–120.
9. Wisse M. and van Frankenhuyzen J., Design and construction of MIKE; a 2-D autonomous biped based on passive dynamic walking, in *Proc. Conf. on Adaptive Motion of Animals and Machines*, Kyoto, Japan, 2003.
10. Kövecses J., Piedboeuf J.C., and Lange C., Dynamics modeling and simulation of constrained robotic systems, *Trans. Mechatronics*, Vol. 8(2), 2003, pp. 165–177.
11. Modarres Najafabadi S.A., Kövecses J., and Angeles J., Energy analysis and decoupling in three-dimensional impacts of multibody systems, *J. Appl. Mech.*, Vol. 74(5), 2007, pp. 845–851.
12. Pars L.A., *A treatise on analytical dynamics*, Heinemann, London, England, 1965.
13. Kövecses J. and Cleghorn W.L., Finite and impulsive motion of constrained mechanical systems via Jourdain's principle: discrete and hybrid parameter models, *Int. J. Non-Linear Mechanics*, Vol. 38(6), 2003, pp. 935–956.
14. Kwan M. and Hubbard M., Optimal foot shape for a passive dynamic biped, *J. Theoretical Biol.*, Vol. 248(2), 2007, pp. 331–339.
15. Asano F. and Luo Z.W., The effect of semicircular feet on energy dissipation by heel-strike in dynamic biped locomotion, in *Proc. IEEE Int. Conf. Robotics and Automation*, Rome, Italy, 2007, pp. 3976–3981.

# Parallel Manipulators with Simple Geometrical Structure

Adolf Karger

**Abstract** In this paper we describe many properties of Stewart – Gough type parallel manipulators which have simple geometrical structure concerning singularities and direct kinematics. It appears that they are characterized by a very simple condition, the rank of the matrix of coordinates of anchor points is equal to three. They have affinely equivalent platform and base, have no self-motions unless they are architecture singular. They are architecture singular iff the points of the platform and as well of the base lie on a conic. They have special singular set and if the platform and base are equiform, the direct kinematics has closed form solution.

**Keywords** Stewart-Gough platforms · Direct kinematics · Self-motions

## Introduction

To describe geometry of the motion of a parallel manipulator is a very complicated problem. We use the method developed in Husty [4] and explain it in short, referring to equations below. By using Euler and Study parameters  $x_i, y_i, i = 0, 1, 2, 3$  we obtain six quadratical equations (4) and together with the Study equation (1) and norming condition (2) we have eight equations for eight motion parameters  $x_i, y_i, i = 0, 1, 2, 3$ . This means that these parameters are determined.

As it is well known, the direct kinematics can have up to forty solutions, there exist cases with all of them real. In this paper we shall discuss a case, for which the problem of direct kinematics is much simpler, we shall describe a class of manipulators for which the direct kinematics has a closed form solution. This means that the motion parameters can be expressed from geometry of the platform and distances of points of the platform and base by roots of quadratic expressions.

After solving equations (1) and (4) for parameters  $y_i$  (in the general case), we obtain three equations for Euler parameters  $x_i$  of rather high degrees, two of them

---

A. Karger (✉)

Charles University Praha, Faculty of Mathematics and Physics, Czech Republic  
e-mail: Adolf.Karger@mff.cuni.cz

are of degree 4 and one is of degree 8. It was recently shown by author that for manipulators with planar platform and base there is always a linear combination of equations (4) which does not contain  $y_i$ . This simplifies the problem slightly, as in that case we have equations of degrees 2,4,8.

For this reason we shall treat only manipulators with planar platform and base, supposing automatically that the third coordinate of any point is equal to zero. The natural candidate for manipulators with closed form direct kinematics would be the case where we have more then one quadratic equation obtained as linear combination of equations (4).

## Geometry of the S.-G. Type Platform

To describe the geometry of a S.- G. type parallel manipulator, we shall use the Study representation of the displacement group of the Euclidean space in the projective space  $P_7$  with homogeneous coordinates  $x_0, \dots, x_3, y_0, \dots, y_3$  (see [2, 4]).

$x_i, i = 0, 1, 2, 3$  represent the orientation of the platform,  $y_i, i = 0, \dots, 3$  describe translations.

Let  $S$  be the set in  $P_7$  determined by

$$U = x_0y_0 + x_1y_1 + x_2y_2 + x_3y_3 = 0, \quad (1)$$

where  $x_0^2 + x_1^2 + x_2^2 + x_3^2 \neq 0$ , the so called Study quadric.

We can normalize coordinates in  $S$  by

$$\kappa \equiv x_0^2 + x_1^2 + x_2^2 + x_3^2 = 1. \quad (2)$$

In this way a space motion is represented by a curve on  $S$ .

*Remark 1.* Usually we treat the Study parameters of the motion as homogeneous coordinates in the projective space  $P_7$ , the norming condition (2) is used at the very end. In this way we are able to use properties of the projective space and methods of projective geometry.

The parallel manipulator consists of two parts – platform and base. To describe its motion, we have to describe the relative position of these two parts. The upper part of the platform lies in the moving space, the lower one lies in the fixed space. The upper part of the platform will be described by small letters, for the base we use capital letters.

The platform consists of six points  $m_i = [a_i, b_i], i = 1, \dots, 6$ , similarly the base is determined by points  $M_i = [A_i, B_i], i = 1, \dots, 6$ .

The connection between a point  $m = [a, b]$  of the platform and point  $M = [A, B]$  of the base is given by a homogeneous quadratic equation in Study parameters as follows,

$$\begin{aligned}
 h = R\kappa + 4(y_0^2 + y_1^2 + y_2^2 + y_3^2) + 2(x_3^2 - x_0^2)(Aa + Bb) + 2(x_2^2 - x_1^2)(Aa - Bb) \\
 + 4[x_0x_3(Ab - Ba) - x_1x_2(Ab + Ba) + (x_0y_1 - y_0x_1)(A - a) + \\
 (x_0y_2 - y_0x_2)(B - b) - (x_1y_3 - y_1x_3)(B + b) + (x_2y_3 - y_2x_3)(A + a)] = 0,
 \end{aligned}
 \tag{3}$$

where  $R = A^2 + B^2 + a^2 + b^2 - d(mM)^2$ , and  $d(mM)$  is the distance of points  $M$  and  $m$ .

Substitution of coordinates of points  $M_i$  and  $m_i$  for  $i = 1, \dots, 6$  yields six equations

$$h_1 = 0, \dots, h_6 = 0, \tag{4}$$

which together with (1) and (2) completely describe the mutual position of the two parts of the manipulator.

### Direct Kinematics of the Platform

To solve the direct problem for such a manipulator we have to solve equations (1), (2), (4) for unknown Study parameters of the motion under the assumption that the geometry of the platform is known (points  $m_i, M_i, i = 1, \dots, 6$  are given and parameters  $R_i$  are known). We obtain 8 quadratic equations for 8 unknown Study parameters  $x_j, y_j, j = 0, 1, 2, 3$ .

Equations (4) are “almost” linear in  $y_j, j = 0, \dots, 3$  and therefore there is a chance to find a linear combination of these equation in such a way that  $y_j$  will disappear.

Let  $q = k_1h_1 + k_2h_2 + \dots + k_6h_6$  be such a linear combination with coefficients  $k_i, i = 1, \dots, 6$ . We shall look for condition for  $k_i$  such that  $q$  does not contain  $y_j$ . First of all we must have  $k_1 + k_2 + \dots + k_6 = 0$ , because of quadratical terms. A simple look at the structure of the equation (3) shows that in total we obtain equations

$$\sum_{k=1}^6 k_i = 0, \sum_{i=1}^6 k_i A_i = 0, \sum_{i=1}^6 k_i B_i = 0, \sum_{i=1}^6 k_i a_i = 0, \sum_{i=1}^6 k_i b_i = 0. \tag{5}$$

We have obtained five homogeneous linear equations for coefficients  $k_i, i = 1, \dots, 6$  of the linear combination. The matrix  $M$  of this system is

$$M = \begin{pmatrix} 1 & 1 & 1 & 1 & 1 & 1 \\ A_1 & A_2 & A_3 & A_4 & A_5 & A_6 \\ B_1 & B_2 & B_3 & B_4 & B_5 & B_6 \\ a_1 & a_2 & a_3 & a_4 & a_5 & a_6 \\ b_1 & b_2 & b_3 & b_4 & b_5 & 6 \end{pmatrix} \tag{6}$$

From linear algebra we know that such a system always has a nontrivial solution. This means that there is always such a linear combination of equations  $h_i = 0$  which does not contain  $y_j$ .

The number of independent solutions of system (5) depends on the rank of the matrix  $M$ . If the rank of  $M$  is maximal, which means that it is equal to five, we obtain one quadratical equation in  $x_i$ . It was shown [11] that this equation disappears iff the manipulator is architecture singular. In this paper we shall be interested what happens if the rank of  $M$  is not maximal. The case of rank one or two is not interesting, for rank one all the points collapse to one point, for rank two all points are on a line, for rank four no special properties are known so far.

So let us suppose that the rank of  $M$  is equal to three. This follows that not all points of the base or platform lie on a line. We can choose the system of coordinates in such a way that

$$A_1 = B_1 = B_2 = a_1 = b_1 = b_2 = 0.$$

Then we can suppose  $A_2B_3 \neq 0$ . Computation of the rank of  $M$  shows that in that case

$$b_i = B_i b_3 / B_3, \quad a_i = [(A_2 a_3 - a_2 A_3) B_i + a_2 B_3 A_i] / (A_2 B_3). \quad (7)$$

This shows that there exists an affine correspondence between the base and platform described by equations

$$x = [B_3 a_2 X + (A_2 a_3 - A_3 a_2) Y] / (B_3 A_2), \quad y = b_3 Y / B_3, \quad (8)$$

where  $(x, y)$  and  $(X, Y)$  are Cartesian coordinates in the plane of the platform and base, respectively. This yields the first result:

**Theorem 1.** *The rank of  $M$  is equal to three iff the base and platform are affinely equivalent (see also [5], pages 512–513).*

*Remark 2.* It is known that parallel manipulator with affinely equivalent base and platform is architecture singular iff points of the platform lie on a conic [1, 3]. This fact can be easily proved by direct computation of the determinat of the Jacobi matrix (simply Jacobian), the condition for six points on a conic factors out of the equation of the Jacobian. In that case points of the base are also on a conic. To the concept of architectural singularity see Ma (Angeles) or Merlet [12, 13], Karger [8], Karger [10].

*Remark 3.* It was shown (Karger [11]) that for the case of rank of  $M$  equal to five the manipulator is architecture singular iff the quadratical equation obtained as a combination of (4) is identically zero. This can be reformulated as follows.

**Theorem 2.** *If the rank of  $M$  is equal to five, the manipulator is architecture singular iff there exist a linear combination of equations  $h_i = 0, i = 1, \dots, 6$  which is identically equal to zero. A similar result is:*

**Theorem 3.** *If no four points are on a line, the statement of the Theorem is true also for rank three.*

This can be easily proved by direct computation.

For manipulators with affinely equivalent platform and base we can also explicitly describe the singular set. The singular set  $\Sigma$  is by definition the set of all points in  $S$ , for which the Jacobian of corresponding position is equal to zero. The equivalent formulation is that lines  $m_i M_i, i = 1, \dots, 6$  belong to a linear complex or that the determinant of Plücker coordinates of these lines is equal to zero.

The Jacobian for such a manipulator factorizes into two factors, let us denote them  $Sing_1$  and  $Sing_2$ .  $Sing_1$  is independent of translations and has equation

$$(b_3 A_2 - B_3 A_2)(x_0^2 + x_3^2)x_1 x_2 + (a_2 A_3 - A_2 a_3)(x_0^2 x_1^2 + x_2^2 x_3^2) + (b_3 A_2 + B_3 A_2)x_0 x_3(x_1^2 + x_2^2) = 0. \tag{9}$$

Geometric properties of this surface were so far not systematically studied. The equation of  $Sing_2$  is not so interesting, it is of the form  $t_1 q_1 + t_2 q_2 + t_3 q_3 = 0$ , where  $q_i, i = 1, 2, 3$  are simple quadratical expressions in  $x_j, j = 0, 1, 2, 3$ . Details can be found in Karger [9].

S.-G. type platforms with rank of  $M$  equal to three have an another interesting feature. For large subclasses the direct kinematics of the platform has closed form solution given by square roots only. One of such subclasses consists of manipulators with equiform platform and base. To avoid presenting large equations, we shall demonstrate the situation by a simple example, Fig. 1.

*Example 1.* Let the upper and lower parts of the platform be similar (equiform) with similarity coefficient  $k = 1/2$ , the upper part be the smaller one. We choose points

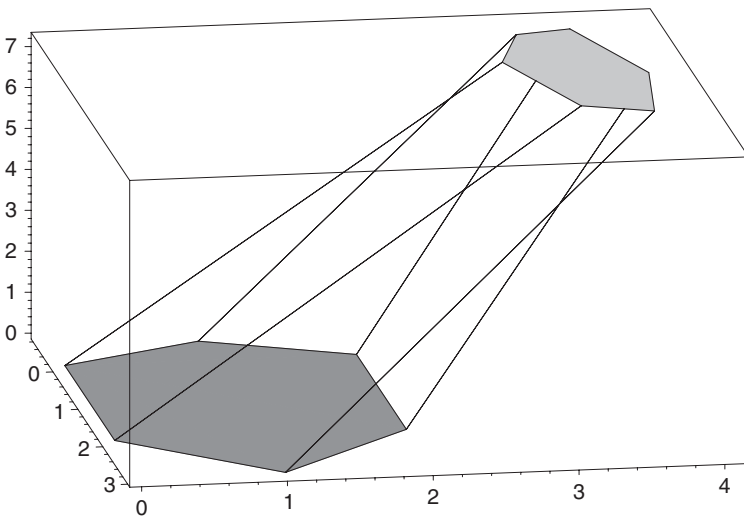


**Fig. 1** The platform from example



$$M_1 = [0, 0], M_2 = [2, 0], M_3 = [3, 1], \\ M_4 = [2, 2], M_5 = [0, 2], M_6 = [-1/2, 1].$$

Distances of points  $m_i M_i$ ,  $i = 1, \dots, 6$  be determined by

$$R_1 = R_3 = R_5 = -10, R_2 = -11, R_4 = -12, R_6 = -9.$$

Points  $M_i$  do not lie on a conic and matrix  $M$  has rank three. We denote  $u_i = h_1 - h_i$ ,  $i = 2, \dots, 6$ . We see that  $u_i$ ,  $i = 2, \dots, 6$  are linear in  $y_j$ ,  $j = 0, \dots, 3$ .

After solving  $u_2 = 0, u_3 = 0, u_4 = 0$  for  $y_1, y_2, y_3$  and substituting the result into remaining equations  $u_4 = 0, u_5 = 0, u_6 = 0$  we obtain three quadratical equations which read as

$$u_4 = -2x_3^2 + x_1^2 - 3x_2^2 + 2x_1x_2, \\ u_5 = x_0^2 - 7x_3^2 + 5x_1^2 - 11x_2^2 + 24x_1x_2, \\ u_6 = 2x_0^2 - 5x_3^2 + 2x_1^2 - 5x_2^2 + 28x_1x_2.$$

We see that  $y_0$  disappeared as expected, it is determined by quadratic equation  $h_1 = 0$ .

The decisive feature of equations  $u_4 = 0, u_5 = 0, u_6 = 0$  (also in general case) is that in  $x_0$  and  $x_3$  they contain only terms with  $x_0^2$  and  $x_3^2$ . This means that they can be solved linearly with respect to  $x_0^2, x_3^2$ . In our case we solve  $u_4 = 0, u_5 = 0$  and obtain

$$x_0^2 = (-3x_1^2 - 34x_1x_2 + x_2^2)/2, x_3^2 = (x_1 + 3x_2)(x_1 - x_2)/2.$$

Substitution into  $u_6$  yields

$$u_6 = 7x_1^2 + 22x_1x_2 - 7x_2^2 = 0.$$

As we are interested only in demonstration of the possibility of closed form solution, we present only one, the others are obtained by change of signs. Solution is (we denote  $\mu_{1,2} = 11 \pm \sqrt{170}$  with  $\mu_1$  for plus sign)

$$x_1 = -x_2\mu_1/7.$$

The norming condition (2) yields

$x_2 = \sqrt{(-7\mu_2)/28}$ . Values of  $x_0, x_3, y_1, y_2, y_3$  are obtained by substitution of values of  $x_1, x_2$  into previously found expressions for them, we do not present them as they are not interesting and give no new information. It remains to find the value of  $y_0$  from equation  $h_1 = 0$ . We obtain

$$526064y_0^2 + \sqrt{(-7\mu_2)}y_0(4860\sqrt{170} + 52368) + 5253\sqrt{170} - 12058 = 0.$$

This finishes the solution of the problem, numerical values show that the obtained Study parameters are real.

The equiformal case is not the only one, for which we obtained the solution of the direct problem in closed form. If the manipulator satisfies one of the following systems of equations  $q_4 = 0, q_5 = 0, q_6 = 0$ , where

$$q_4 = B_4(A_2a_3 - a_2A_3) + B_3(a_2A_4 - A_2a_3) + \epsilon A_2b_3(A_3 - A_4) \quad (10)$$

and  $q_5, q_6$  are obtained by index changes 4 to 5 or 4 to 6.  $\epsilon$  is  $\pm 1$ , one for each system. We see immediately that equations( 10) are satisfied if the platform and base are equiform, but there exist also other solutions. Unfortunately all this cases are not very interesting, as we see that in that case points  $M_3, M_4, M_5, M_6$  are on one line.

### Self-motions of Manipulators with Rank of $M$ Equal to Three

It was shown in Karger (2002) that parallel manipulators with affinely equivalent platform and base, which are not equiform, have self-motions only in the architecture singular case.

*Remark 4.* Self-motion of a parallel manipulator appears if the direct kinematics has continuous solution. Practically it means that the three algebraic equations for  $x_i, i = 0, \dots, 3$  mentioned above, have a curve in common (see for instance Karger [7], Karger [11], Karger [6]).

The equiform case with not congruent platform and base was discussed in Karger [6] with the same result. It remains to discuss the congruent case. Here we proceed in a similar way as in the equiform case. From equations  $u_4 = 0, u_5 = 0$  we express  $x_0^2, x_3^2$  and substitute the result into  $u_6 = 0$ , which yields the condition for points  $M_i$  to lie on a conic. Special case appears if points  $M_1, M_2, M_3, M_4$  are on a circle. Then we are not able to express  $x_0^2, x_3^2$  from  $u_4 = 0, u_5 = 0, u_6$ . By taking permutations of points  $M_i$ , we can suppose that all these points are on a circle, again a conic section.

### Conclusion

We have shown that parallel manipulators with rank of  $M$  equal to three have the following properties:

1. The manipulator has rank of  $M$  equal to three iff the platform and base are affinely equivalent.
2. The manipulator is architecture singular iff points  $M_i, i = 1, \dots, 6$  lie on a conic section.
3. The manipulator is architecture singular iff there is a linear combination of  $h_i, i = 1, \dots, 6$  which is identically equal to zero.

4. The singular set of such manipulators factors into two factors. One of them is independent of translations, the other one is linear in translations.
5. The manipulator has self-motion only in the case if it is architecture singular, in that case it has self-motion in every possible position.
6. There is a large subclass of such manipulators (including equiform ones) for which the direct kinematics has closed form solution.

**Acknowledgments** The research reported here was supported by Grant VZ 0021620839 of the Ministry of Sports and Education of the Czech Republic.

## References

1. Borel E. (1908): Mémoire sur les déplacements à trajectoires sphériques. *Mém. présentés par divers savants*, Paris, (2), 33, pp. 1–128.
2. Bottema, O., Roth, B (1990): Theoretical Kinematics, Dover Publishing, 1990.
3. Bricard R. (1906): Mémoire sur les déplacements à trajectoires sphériques. *J. École Polyt.* (2), 11, pp. 1–96.
4. Husty M.L. (1996): An algorithm for solving the direct kinematics of general Stewart-Gough platforms. *Mech. Mach. Theory*, 31, pp. 365–380.
5. Husty M., Karger A., Sachs H., Steinhilper W. (1997): Kinematik und Robotik. Springer, Berlin, Heidelberg, ISBN 3-540-63181-X.
6. Karger A. (2001): Singularities and self-motions of equiform platforms. *Mech Mach Theory*, 36, pp. 365–380.
7. Karger A. (2002): Singularities and self-motions of a special type of platforms. *Advances in Robot Kinematics*, eds. Lenarcič J., Thomas F., Kluwer Acad. Publ., pp. 155–164.
8. Karger A. (2003): Architecture singular planar parallel manipulators. *Mech Mach Theory*, 43(3), pp. 335–346.
9. Karger A. (2006): Stewart – Gough platforms with simple singularity surface. *Advances in Robot Kinematics*, eds. Lenarcič J., Roth B., Kluwer Acad. Publ., pp. 247–254.
10. Karger A. (2008a): Architecture singular non-planar parallel manipulators. *Mech Mach Theory*, 38, pp. 1149–1164.
11. Karger A. (2008b): New Self-Motions of Parallel Manipulators, *ARK* 2008.
12. Ma O., Angeles J. (1992): Architecture singularities of parallel manipulators. *Int. J Robotics Automation*, 7, pp. 23–29.
13. Merlet J.P. (1992): Singular configurations of parallel manipulators and Grassmann geometry. *Int. J. Robotics Res*, 8, pp. 45–56.

# Analysis of Wire Elasticity for Wire-driven Parallel Robots

Jean-Pierre Merlet

**Abstract** This paper presents an experimental study of the elasticity of wires that may be used for wire-driven parallel robot. Although wire behavior have been studied since a long time (e.g. in civil engineering) their use in parallel robots are quite different as they are submitted to large changes in length and tension while being usually much lighter than the one used in civil engineering. These experiments show that the tension in a wire submitted to a given change in length  $\Delta L$  is a function of  $\Delta L$  but also of time and we propose an empiric model to characterize this deformation. However we show that an appropriate elastic model may still be used for control purposes, provided that the zero-tension wire lengths are regularly updated through calibration.

**Keywords** Elasticity · Wire-driven parallel robot

## Introduction

### *Wire-driven Parallel Robots*

Among the category of parallel robot (i.e. robot in which the end-effector is connected to the ground through multiple independent kinematic chains) there is a special class of robot which uses wire as the connecting element between the end-effector and the ground. The pose of the end-effector is controlled by changing the lengths of the connecting wires. Numerous such robots have been proposed in the past [1, 2, 4–7, 9–12]. Most of them use the coiling of the wires on a drum to allow for wire lengths changes but we have proposed recently another approach, namely the use of a linear actuator combined with a pulley system [8].

Compared to their counterpart with rigid links, wire-driven parallel robots have the advantages of

---

J.-P. Merlet (✉)  
COPRIN Project-Team, INRIA Sophia Antipolis, France  
e-mail: Jean-Pierre.Merlet@sophia.inria.fr

- allowing large changes in link lengths and consequently a larger workspace
- high dynamics due to the reduced mobile mass

On the other hand their drawback is that the control must ensure that the tension in the wires is always positive as it is not possible to push a wire.

Another important point is the potential deformation of the wires under the tension to which they are submitted. Such deformation will indeed modify the wire length and consequently the location of the end-effector.

### *Wire Deformation and Forward Kinematics*

It is usually assumed that for a wire of initial length  $L_0$  submitted to a tension  $\tau$  there will a change in length that follows Hooke's law

$$\tau = k \frac{(L - L_0)}{L_0} \quad (1)$$

where  $L$  is the new wire length and  $k$  a constant. It is also mentioned in the literature that the wire may experiment a *creep* phenomenon, which consists in a permanent deformation of the wire even if it is used in its elastic domain [3]. It is usually assumed that the amount of permanent deformation  $\epsilon$  is given by

$$\epsilon = B\tau^U \quad (2)$$

where  $B, U$  are constants. But this law is established under the assumption that the amount of tension and the application time are sufficient for the permanent deformation to take place, an hypothesis that is not valid for our robot. Additionally the wires that are used in parallel robot have usually a low mass/unit length ratio and we may therefore assume that there is no deformation of the wire due to its own mass. Surprisingly the material literature is extremely sparse regarding the elasticity of "light" wires while Hooke's law (1) is usually used in the robotics literature [5, 6]. Our motivation is therefore to experimentally determine if Hooke's law is indeed appropriate for the type of wire usually used for parallel robots and, otherwise, to propose a better model.

As will be shown in the experimental results the amount of wire length changes due to the tension is significant even for relatively small tension values. Hence these deformations will play an important role for the positioning accuracy of our robot. We have recently shown<sup>1</sup> that if the wire deformation follows Hooke's law (1) or the variant (3) that will be proposed in this paper, then it is possible to take the wire deformations into account into the forward kinematics problem (finding the location of the end-effector being given the measured value of the joint variables), even under real-time constraint, by using an interval analysis-based solver. This was a major issue as solving this problem amounts to be able to solve the classical rigid links forward kinematics problem (an already difficult issue) to which are added the

---

<sup>1</sup> The corresponding paper will be presented at ICRA 2008

mechanical equilibrium equations. We have also shown that our solver is also able to manage the modified Hooke's law

$$\tau = k \frac{(L - L_0)}{L} \quad (3)$$

under the same real-time constraint. Still we have to validate that our wires follows a deformation law that is reasonably close to (1) or (3) and this paper addresses this issue.

## Experimental Set-up

We are currently using three different wires for our parallel robot: one Roc Line fishing lines with 2.2 kg max load, a nylon wire with 15 kg maximal load while the third one is a wire that is used for small kites. Our purpose was to examine the relation between the tension in the wire and its deformation. For that purpose we have rigidly connected one extremity of a wire sample to a fixed point while the other extremity was connected to a force sensor, that allows one to measure the tension in the wire. The force sensor was fixed on the moving part of a milling machine whose displacement was accurately measured. The initial position of the wire extremity was such that a small but significant tension in the wire was measured. Then the force sensor was incrementally moved by a step of 1 mm and in this position the measured tension in the wire was recorded every 30 seconds for a period of 2 minutes.

For the Roc Line, 2.2 kg the experiment was performed for two samples with an initial length of 1 m and 1.71 m. The experimental results are presented in Table 1.

For the Nylon line the experiment was performed using a sample of length 1.5 m and the results are presented in Table 2. For the kite line the experiment was performed using a sample of length 1.5 m and the results are presented in Table 3.

## Analysis

As may be seen in the measurements tables, the wire tensions significantly change in time for a given change in the length of the wire. The analysis of the experimental result has led us to propose a deformation model in which a wire of initial length  $L_0$  that is submitted to a tension  $\tau$  for a sufficient amount of time will have a change in length  $\epsilon$  given by:

$$\epsilon = B\tau^U \quad (4)$$

in which  $B$ ,  $U$  are constants that depends on  $L_0$  and on the wire material. The time law for this deformation is obtained as:

$$L_0(t) = L_0 + \epsilon(1 - e^{-k_2 t^N}) \quad (5)$$

**Table 1** Measurement for the Roc Line, 2.2 kg, initial length 1 m and 1.71 m

Displacement (mm)	$\tau$	$\tau$ (30 s)	$\tau$ (1 mn)	$\tau$ (1 mn30 s)	$\tau$ (2 mn)
1 ( $L_0 = 1$ m)	0.95	0.88	0.86	0.85	0.85
2	1.5	1.4	1.37	1.35	1.34
3	2	1.91	1.88	1.86	1.84
4	2.63	2.52	2.47	2.44	2.42
6	3.79	3.66	3.61	3.57	3.55
7	4.31	4.2	4.15	4.11	4.08
8	4.92	4.79	4.73	4.69	4.65
9	5.44	5.32	5.27	5.22	5.18
10	6.05	5.91	5.85	5.80	5.76
11	6.55	6.42	6.36	6.31	6.26
12	7.14	6.99	6.93	6.87	6.83
1 ( $L_0 = 1.71$ m)	0.63	0.62	0.61	0.61	0.61
2	1.04	1.01	0.98	0.97	0.96
3	1.37	1.33	1.30	1.28	1.27
4	1.73	1.67	1.64	1.62	.161
5	2.06	1.99	1.95	1.93	1.91
6	2.38	2.31	2.28	2.25	2.23
7	2.68	2.61	2.58	2.55	2.53
8	3.02	2.94	2.91	2.88	2.86
9	3.33	3.24	3.20	3.17	3.15
10	3.64	3.55	3.51	3.48	3.45
11	3.91	3.84	3.80	3.76	3.74

**Table 2** Measurement for the Nylon line, initial length 1.5 m

Displacement (mm)	$\tau$	$\tau$ (30 s)	$\tau$ (1 mn)	$\tau$ (1 mn30 s)	$\tau$ (2 mn)
1	2.12	1.91	1.82	1.76	1.71
2	2.50	2.30	2.23	2.18	2.14
3	3.01	2.83	2.76	2.71	2.67
4	3.53	3.34	3.27	3.22	3.18
5	4.10	3.91	3.84	3.77	3.72
6	4.61	4.43	4.35	4.29	4.23
7	5.21	5.00	4.92	4.86	4.81
8	5.74	5.54	5.46	5.38	5.32
9	6.33	6.11	6.02	5.95	5.89
10	6.86	6.63	6.55	6.48	6.42
11	7.46	7.21	7.12	7.06	7.00

**Table 3** Measurement for the kite line initial length 1.5 m

Displacement (mm)	$\tau$	$\tau$ (30 s)	$\tau$ (1 mn)	$\tau$ (1 mn30 s)	$\tau$ (2 mn)
1	2.21	1.66	1.43	1.30	1.21
2	3.84	3.04	2.77	2.62	2.50
3	5.43	4.29	3.98	3.76	3.64
5	8.55	7.02	6.62	6.38	6.15
6	10.09	8.63	8.25	7.95	7.72
7	11.88	10.36	9.87	9.56	9.34
8	14.04	12.32	11.87	11.48	11.23
9	15.92	14.35	13.81	13.43	13.15

**Table 4** Parameters identification results

Wire	$k_1$	$B$	$U$	$k_2$	$N$
Roc Line, 2.2 kg, $L_0 = 1$ m	699.152	0.2068	1/2.5	0.02138	1
Roc Line, 2.2 kg, $L_0 = 1.71$ m	689.136	0.271	1/2	0.016	1
Nylon line, 15 kg, $L_0 = 1.5$ m	1545.245	2.047	0.1355	0.0147	0.5
Kite line, $L_0 = 1.5$ m	7049.85	0.4681	0.5123	0.05855	0.41

where  $k_2, N$  are constants. The tension in the wire may be calculated as

$$\tau(t) = k_1((L_1 + \Delta L)/L_0(t) - 1) \tag{6}$$

where  $L_1 = L_0(0)$  is the length of the wire at time 0. In summary the parameters of this model are  $B, U, k_1, k_2, N$ . Intuitively it may be thought that the parameter  $k_1$  is dependent on the material but not on the  $L_0$ , while the other parameters should be length dependent.

To determine these parameters for each wire we have run a least square fitting algorithm with the first five measurements, the remaining measurements being used to test the model. The parameter identification results are presented in Table (4) and some examples of comparisons between the model and unused experiments are presented in Figs. 1, 2, 3, 4. It may be seen that there is a very good match between the model and the experimental results.

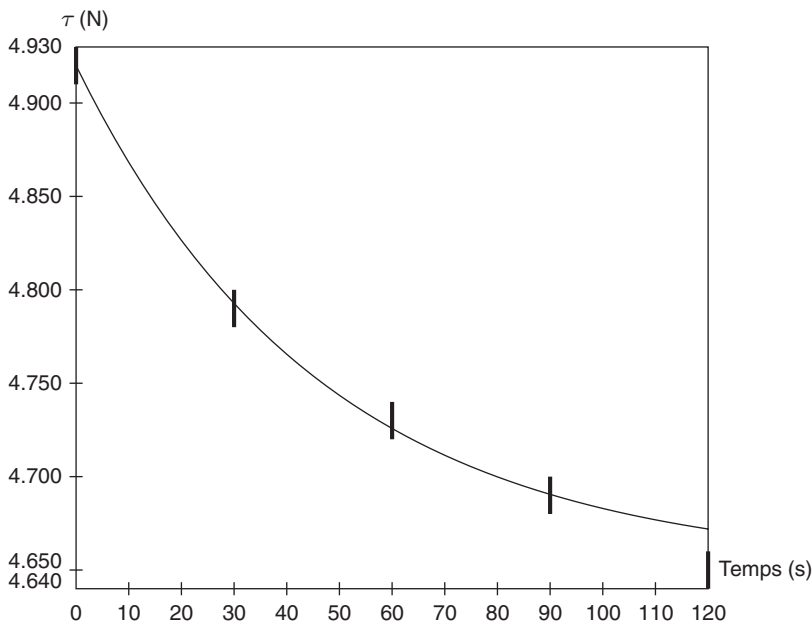


**Fig. 1** Model result for the last experiment for the Roc Line,  $L_0 = 1$  m. The experimental results are indicated with thick marks



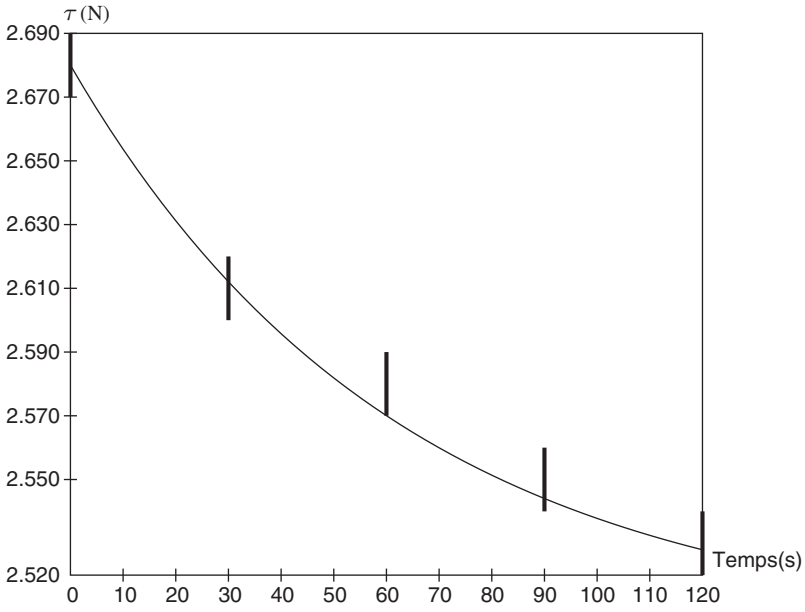


**Fig. 2** Model result for the last experiment for the Roc Line,  $L_0 = 1$  m. The experimental results are indicated with thick marks

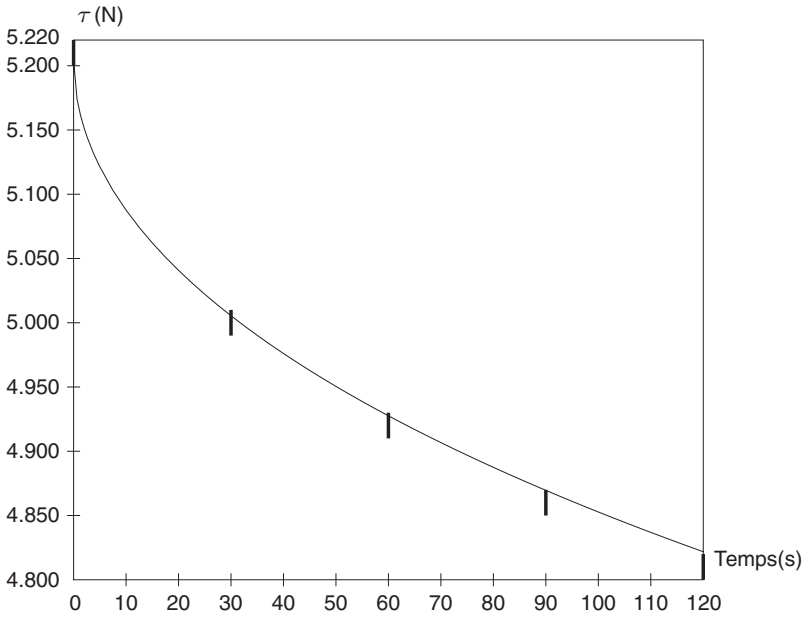


**Fig. 3** Model result for the last experiment for the Nylon line. The experimental results are indicated with thick marks

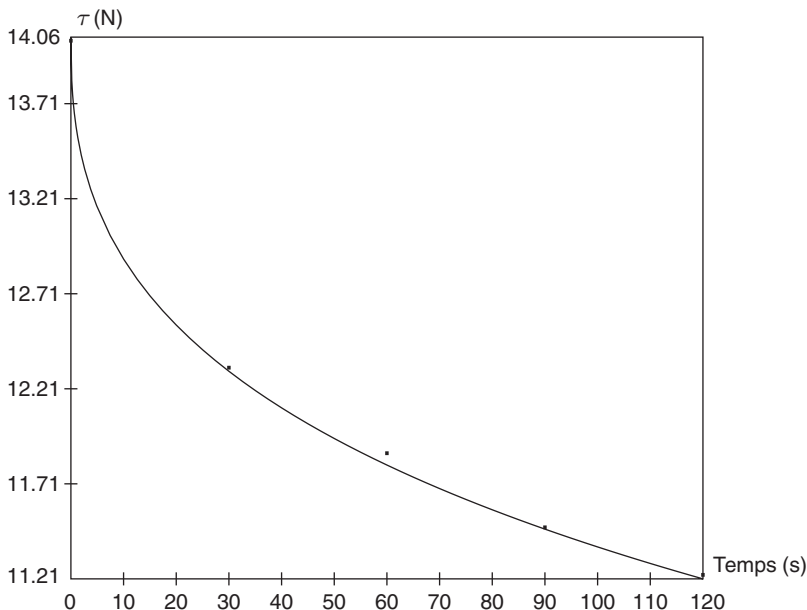


**Fig. 4** Model result for the last experiment for the kite line. The experimental results are indicated with thick marks

### Influence of the Deformations on the Control

We have introduced the model of wire deformation in the inverse kinematics, using equation (6) as a relation between the tension and the wire length and assuming that the total length of the wires with no tension  $L_0$  was known. Being given the mass of the end-effector this module will calculate the active joints values in such way that both the kinematics and mechanical equilibrium equations are satisfied.

For a desired pose where the end-effector normal should be vertical our simulation have shown that after 60 seconds the change in the location of the center of the end-effector will be small (typically less than 0.3 mm) while the angle between the normal and the vertical will be less than 0.055 degrees.

Such deviation in time is satisfactory but implies that we must calibrate the wire length  $L_0$  on a regular basis. Such calibration should be possible on-line without requiring external sensor to measure the pose of the end-effector as our robot is redundant. Introducing the wire deformation model in the calibration process is an open issue.

### Conclusion

We have presented a full wire deformation model that may be used for wire-driven parallel robots. Such experimentally determined deformation model was curiously

lacking in the robotics literature. Our simulation have shown that if the total wire lengths with zero tension is known, then the deviation of the end-effector pose as a function of time is low. We plan to confirm these simulations through measurements on our current platform.

**Acknowledgments** This research was supported in part by the ANR SIROPA project.

## References

1. Albus J., Bostelman R., and Dagalakis N. The NIST SPIDER, a robot crane. *Journal of research of the National Institute of Standards and Technology*, 97(3):373–385, 1992.
2. Fattah A. and Agrawal S.K. On the design of cable-suspended planar parallel robots. *ASME Journal of Mechanical Design*, 127(5):1021–1028, Septembre 2005.
3. Guimaraes G.B. and Burgoyne, C.J. Creep behaviour of a parallel-lay aramid rope *Journal of Materials Science*, 27(9):2473–2489, 1992.
4. Higuchi T., Ming A., and Jiang-Yu J. Application of multi-dimensional wire crane in construction. In *5th International Symposium on Robotics in Construction*, pages 661–668, Tokyo, June 6–8, 1988.
5. Hiller M., et al. Analysis, realization and application of the tendon-based parallel robot SEGESTA. In *2nd International Colloquium, Collaborative Research Centre 562*, 185–202, Braunschweig, 2005.
6. Kawamura S., et al. High-speed manipulation by using parallel wire-driven robots. *Robotica*, 18(1):13–21, January 2000.
7. Landsberger S.E. and Sheridan T.B. A new design for parallel link manipulator. In *Proceedings Systems, Man and Cybernetics Conference*, pages 812–814, Tucson, 1985.
8. Merlet J-P. and Daney D. A new design for wire-driven parallel robot. In *2nd Int. Congress, Design and Modelling of mechanical systems*, Monastir, March 19–21, 2007.
9. Ming A., Kajitani M., and Higuchi T. Study on wire parallel mechanism. In *2nd Japan-France Congress on Mechatronics*, pages 667–670, Takamatsu, November 1–3, 1994.
10. Ottaviano E. and Ceccarelli M. Numerical and experimental characterization of singularity of a six-wire parallel architecture. *Robotica*, 25(3):315–324, May 2007.
11. Pusey J., et al. Design and workspace analysis of a 6-6 cable-suspended parallel robot. *Mechanism and Machine Theory*, 139(7):761–778, July 2004.
12. Tadokoro S., et al. A motion base with 6-dof by parallel cable drive architecture. *IEEE/ASME Transaction on Mechatronics*, 7(2):115–123, June 2002.

# Kinematic Analysis of a Compliant, Parallel and Three-Dimensional Meso-Manipulator Generated from a Planar Structure

Cinzia Amici, Alberto Borboni, Pier Luigi Magnani and Diego Pomi

**Abstract** The study of a parallel meso-manipulator, characterized by flexure hinge joints and by an original planar structure, is addressed in this paper under small displacements. Once the manipulator structure has been briefly introduced, with a particular attention paid within the different possible actuators configurations, a kinematic analysis is performed, underlining different singularity configurations of the system. The analysis of the robot workspace is then addressed, by presenting the symbolical resolution of the problem and the extreme configurations of this architecture.

**Keywords** Kinematics · Parallel · Compliant · Meso-Manipulator

## Introduction

The architecture of industrial manipulators can be classified as serial, parallel or hybrid. The serial chains represent the most common kind of industrial robots, being characterized by a large workspace and reduced computational complexity of the inverse kinematic problem. On the other hand, the parallel architectures allow high accelerations and accurate positioning, as a consequence of their considerable stiffness and low inertias. In addition, these manipulators are usually characterised by a modular structure and by a strong symmetry, that lead the parallel robots to be interesting for applications with a reduced workspace [1].

The proposed architecture of the parallel, compliant meso-robot herein concerned is shown in Fig. 1.

This robot is characterized by a significant compliance as a consequence of the flexure hinges chosen as joints [2–4]. Furthermore, the three-dimensional structure can be physically generated starting from a planar configuration as the one

---

C. Amici (✉)

Dipartimento di Ingegneria Meccanica e Industriale (DIMI), Università degli Studi di Brescia,  
Via Branze 38, 25123 Brescia(BS), Italy  
e-mail: cinzia.amici@ing.unibs.it

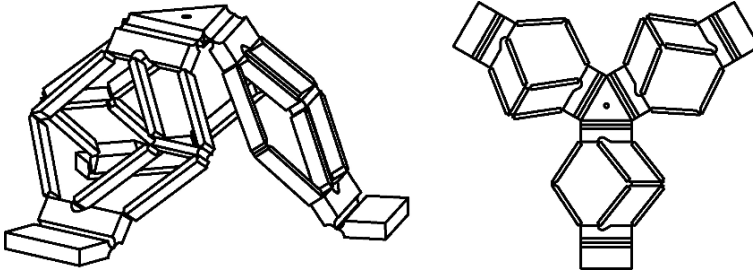


**Fig. 1** From the left: the parallel, flexible meso-manipulator and the top view of the planar configuration

illustrated in the same Fig. 1, with opportune plastic deformations in the proper flexure hinges.

The main peculiarity of this 3D architecture is therefore the easy feasibility of the manipulator: advantages on realization, accuracy and production cadence are associated to the planar configuration during the first phase of the production process.

Observing Fig. 1, an important symmetry is identifiable in the structure. The frame is composed by three fixed elements (called “feet” in the followings) at the periphery of the structure. Each foot is connected to the mobile central platform by a kinematic chain (called “leg” in the followings) composed by bars and flexure hinges.

The described structure appears as a hybrid architecture, while the behaviour of the manipulator is absolutely that of a parallel one: this fact can be cleared up through noting that every leg is composed by a four-bar mechanisms with an associated redundant isostatic structure. The presence of the redundant isostatic structure does not affect the kinematic functionality, thus it can be neglected in a functional analysis. Otherwise, the two four bar mechanisms in cascade for every leg allow the mobile platform only a pure translation, preventing it from every – finite or infinite – rotations.

With this kinematical property, any leg of the manipulator can be functionally substituted by a single kinematic chain composed of two simple elements [5–7].

## Manipulator Architecture

The manipulator has been modeled considering that the presence of two four bar mechanisms ( $B_i C_i F_i E_i$  and  $E_i F_i N_i M_i$  in Fig. 2) allows the platform just to move in a plane parallel to the one containing the feet. The lay-out of these three elements (the feet), at 120 degrees each other, avoids any rotation of the mobile base around the Z axis [5–8].

The robot presents three degrees of freedom (dof) obtained by removing the structural overconstraints of the architecture that ideally don’t modify the kinematic behaviour of the manipulator. Possible non idealities of the structure are however

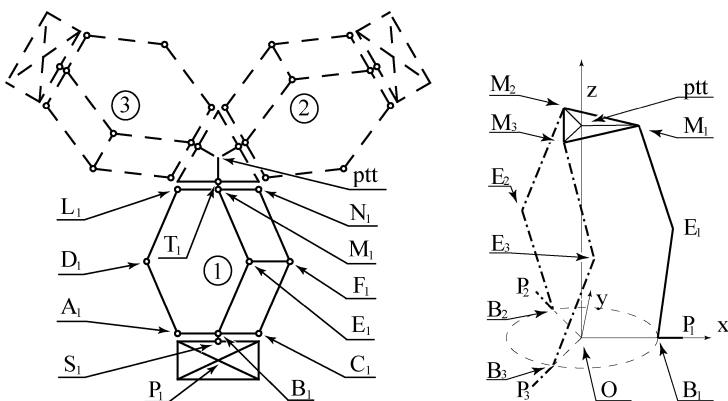


**Fig. 2** From the left: conventions adopted for the manipulator analysis and essential structure of the robot

re-absorbed by the material elasticity of the robot itself. These observations allow to simplify the structure by considering a fictitious equivalent system characterized by the same dof numbers, but free from overconstrains, as presented in Fig. 2. To underline is how unnecessary elements (for instance the isostatic triangle  $A_i D_i L_i$  in Fig. 2, on the right) can be neglected.

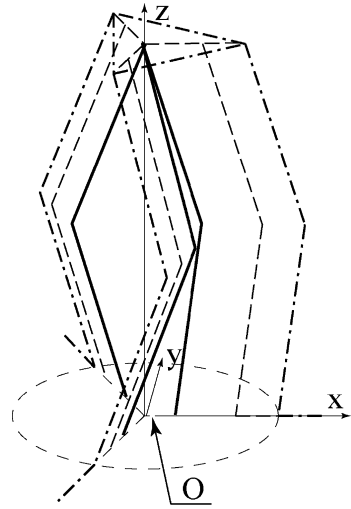
Four different possible configurations have been proposed for the positioning of the three required actuators: a linear actuator between the  $B_i$  and  $M_i$  joints (the basic configuration), a rotational actuator on the  $B_i$  joints, a linear actuator between the  $D_i$  and  $E_i$  joints, and a linear actuator between the  $A_i$  and  $M_i$  joints; all of these configurations can be referred to the first one through simple geometrical transformations.

### Kinematic Analysis

Once the position of the feet has been established, then the position of the platform centre results univocally defined by a tern of variable distances. Referring to Fig. 2, the distances  $P_i B_i$  and  $M_i ptt$ , with  $i = 1, 2, 3$  represent every leg and can be assumed as time-invariant on the geometry of the structure. The simplified equivalent basic configuration shown in Fig. 3 can be reached simply through consecutive pure geometrical translations, and the associated kinematic model is expressed as a function of the  $B_i M_i$  distances, (where  $i = 1, 2, 3$ , once again represents every leg) [7, 8].

The proposed configurations of the actuators can be led to this simplified version through easy geometrical considerations, thus the whole position kinematic problem is reduced to (1), in implicit and in explicit form, representing the intersection of three spheres, centred into the  $P_i^i$  points of the  $i$ -th legs, and with a  $q_i$  radiuses [9];  $S$  represents the column vector of the platform centre coordinates, while  $Q$  is the column vector of the joints coordinates.

**Fig. 3** The ideal process of simplification of the structure into the basic configuration



$$S = F(Q), (x - x_{p_i})^2 + (y - y_{p_i})^2 + (z - z_{p_i})^2 = q_i^2 \tag{1}$$

The associated speed and acceleration kinematic problems can be solved through consequential differentiations (2, 3), due to Jacobian matrix  $J$  and of its pseudo-inverse  $J^+$  [1, 10–13].

$$\frac{dS}{dt} = J(Q) \cdot \frac{dQ}{dt}, \quad \frac{d^2S}{dt^2} = \frac{d}{dt} J(Q) \cdot \frac{dQ}{dt} + J(Q) \cdot \frac{d^2Q}{dt^2} \tag{2}$$

$$\frac{dQ}{dt} = J^+ \cdot \frac{dS}{dt}, \quad \frac{d^2Q}{dt^2} = J^+ \left( \frac{d^2S}{dt^2} - \frac{d}{dt} J(Q) \cdot \frac{dQ}{dt} \right) \tag{3}$$

Once defined the relation (4) instead of the previously used form (1), typically adopted in the serial manipulator analysis approach, the relation (5) can be easily derived.

$$H(S, Q) = 0, \tag{4}$$

$$J_s \dot{S} = J_q \dot{Q}, \quad J_s \equiv \frac{\partial H}{\partial S}, \quad J_q \equiv \frac{\partial H}{\partial Q} \tag{5}$$

The matrixes shown in (5) allows to classify the workspace singularities [1, 8, 13]:

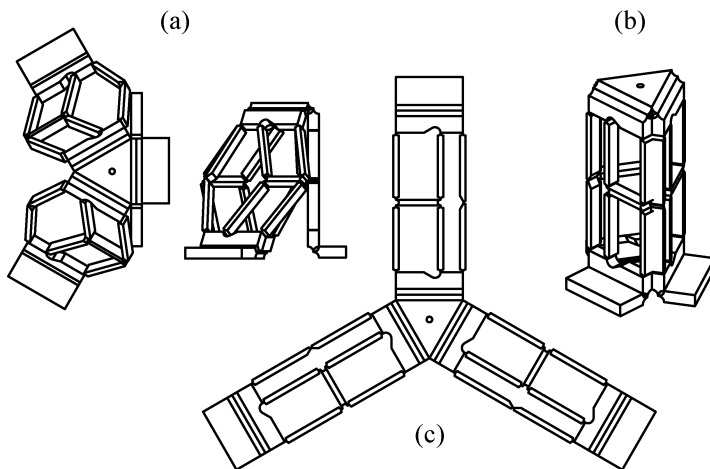


**Fig. 4** Singularity examples, physical visualization: (a) Direct kinematic case; (b) Inverse kinematic case; (c) Structural singularity case

- direct kinematic singularities, with  $|J_q| = 0$  and  $|J_s| \rightarrow \infty$ : in such a situation, the structure loses one or more dof and presents an infinite stiffness along defined directions;
- inverse kinematic singularities, with  $|J_s| = 0$  and  $|J_q| \rightarrow \infty$ : this case is the one considered by the class of the inverse kinematic singularities, where one or more dof are acquired by the manipulator, with a null stiffness along defined directions;
- structural singularities, when both of the previous cases happen.

Figure 4 shows examples of these.

The last two presented singularity configurations types are strictly related to the  $P_i O$  distances. These values can be set as structural hypotheses therefore such singularities can be easily avoided.

## Workspace

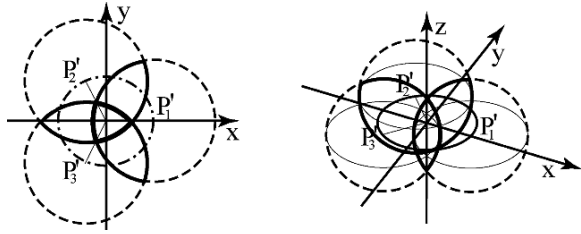
It has been already described how the structure of the manipulator can be simplified into its equivalent basic form, consisting of three serial robots, with two links each one, characterized by a common end effector.

For every serial structure treated as independent, a specific workspace can be identified. The shape of this volume is a spherical one, with the radius equal to the greatest distance that can be reached by the end effector, as presented in the system (6), where  $l_i \max$  with  $i = 1, 2, 3$  represents the addition of each link length.

$$Sphere_i := (x - x_{p_i})^2 + (y - y_{p_i})^2 + (z - z_{p_i})^2 - (l_i \max)^2 \quad (6)$$



**Fig. 5** From the left, visualization of the work-area and visualization of the workspace



In other words, the workspace will be composed by all those points resulting simultaneously reachable by the three serial structures [1, 8, 14, 15]. The intersection of the three identified spheres is shown in Fig. 5.

Once the robot symmetry has been considered, the coordinates of  $X_{max23}$  and  $X_{min23}$  can be easily calculated as (7), where  $r$  represents the radius of every circumference. In this way, the analytical form of the workspace becomes (8).

$$X_{max23} = \left( x_{P_2^i} - r; \frac{y_{P_2^i} + y_{P_3^i}}{2}; 0 \right), \quad X_{min23} = \left( x_{P_2^i} + r; \frac{y_{P_2^i} + y_{P_3^i}}{2}; 0 \right) \tag{7}$$

$$\begin{cases} Sphera1, & x \leq X_{min13}, & x \leq 0 \\ Sphera2, & X_{min12} \leq x \leq X_{min23}, & y \leq 0 \\ Sphera3, & X_{min13} \leq x \leq X_{min23}, & y > 0 \end{cases} \tag{8}$$

It can be guessed how the maximum ideal workspace is obtained when the  $P_i^i$  coincide: in this configuration, the workspace assumes the shape of a sphere, but cannot be physically realized. On the opposite side, the minimum workspace degenerates in a single point, obtained when the  $P_i^i$  are distributed at the  $r$  distance from the origin of the central fixed reference system. Every intermediate position of the translated feet generates a regular workspace, which shape can be easily derived by Fig. 5.

## Conclusions

The paper presents the kinematic analysis of a compliant, parallel and three-dimensional meso-manipulator; this architecture is characterized by a low-cost feasibility process, obtained with an interesting planar starting configuration. The symmetrical geometry of the robot drives to a simplified functional architecture to reduce the computational intensity of the kinematical analysis. Three different kind of singularities have then been identified, some of them avoidable through imposing careful assembly and design conditions. At last, the workspace analysis underlines once again the importance of correct assembly and design conditions, strictly related to the usable volume.

## References

1. Craig J. J., *Robotics. Mechanics and Control*, Addison Wesley, 1986.
2. El-Khasawneh B.S., and Ferreira P.M., Computation of stiffness bounds for parallel link manipulators, *International Journal of Machine Tools & Manufacture*, Vol. 39, 1999, pp. 321–342.
3. Howell L. L., *Compliant Mechanisms*, Wiley, New York, 2001.
4. Lobontiu N., and Raton B., *Compliant Mechanisms: Design of Flexure Hinges*, CRC Press, 2003.
5. Legnani G., and Riva R. “Kinematics of Modular Robots.” IFToMM, Siviglia, Spain.
6. Kong X., and Gosselin C. M., Type Synthesis of 3-DOF PPR-Equivalent Parallel Manipulators Based on Screw Theory and the Concept of Virtual Chain, *Journal of Mechanical Design*, Vol. 127(6), 2005, pp. 1113–1121.
7. Huynh P., and Hervé J. M., Equivalent Kinematic Chains of Three Degree-of-Freedom Tripod Mechanisms With Planar-Spherical Bonds, *Journal of Mechanical Design*, Vol. 127(1), 2005, pp. 95–102.
8. Li Y., and Xu Q., Kinematic Analysis and Design of a New 3-DOF Translational Parallel Manipulator, *Journal of Mechanical Design*, Vol. 128(4), 2006, pp. 729–737.
9. Wang S.-C., Hikita H., Kubo H., Zhao Y.-S., Huang Z., and Ifukube T., Kinematics and Dynamics of a 6 Degree-of-Freedom Fully Parallel Manipulator with Elastic Joints, *Journal of Mechanism and Machine Theory*, Vol. 38, 2003, pp. 439–461.
10. Erdman A. G., and Sandor G. N., *Mechanism Design: Analysis and Synthesis*, Prentice Hall, 1991.
11. Gallardo J., Rico J. M., Frisoli A., Checcacci D., and Bergamasco M., Dynamics of Parallel Manipulators by Means of Screw Theory, *Journal of Mechanism and Machine Theory*, Vol. 38, 2003, pp. 1113–1131.
12. Featherstone R., *Position and Velocity Transformations Between Robot End-Effector Coordinates and Joint Angles*, 1986.
13. Wu J., Wang J., Li T., and Wang L., Analysis and Application of a 2-DOF Planar Parallel Mechanism, *Journal of Mechanical Design*, Vol. 129(4), 2007, pp. 434–437.
14. Callegari M., Gabrielli A., and Ruggiu M., Kinetostatic Synthesis of a 3-CRU Spherical Wrist for Miniaturized Assembly Tasks, XVIII CONGRESSO AIMETA di Meccanica Teorica e Applicata, Brescia, Italia, 2007.
15. Zhao J.-S., Chen M., Zhou K., Dong J.-X., and Feng Z.-J., Workspace of parallel manipulators with symmetric identical kinematic chains, *Journal of Mechanism and Machine Theory*, Vol. 41, 2006, pp. 632–645.

# Dynamic Analysis of a Compliant, Parallel and Three-Dimensional Meso-Manipulator Generated from a Planar Structure

Cinzia Amici, Alberto Borboni, Pier Luigi Magnani and Diego Pomi

**Abstract** The dynamic study of a parallel meso-manipulator, characterized by flexure hinge joints and by an original planar structure, is addressed in this paper under small displacements. This work has to be considered as the continuation of a previous paper, developing the kinematic study and the workspace analysis of the same structure [1].

The present paper deals with the dynamic analysis of the meso-manipulator: as first outcome, a dynamic response strictly related to the implemented motion profile emerges from the simulations results. A noise contribute has been thereafter introduced into the symmetric trapezoidal profile to simulate a real-world behaviour, and also the compliance performances of the robot are evaluated with this noise force.

**Keywords** Dynamics · Workspace · Compliant · Parallel · Meso-Manipulator

## Introduction

The architecture of the meso-manipulator presented in Fig. 1 and its kinematic analysis have been already developed in a previous paper of the same authors [1]. The present work aims to develop the dynamic analysis of the parallel robot.

As presented in Fig. 1, a simple iterative nomenclature has been adopted, based on the symmetry and modularity of the structure. Once defined intuitively the procedure to name the most salient points of the first group of elements, the same algorithm can be easily repeated for the last two legs of the structure, obtained by rotation around the Z-axis [2, 3].

---

C. Amici (✉)

Dipartimento di Ingegneria Meccanica e Industriale (DIMI), Università degli Studi di Brescia,  
Via Branze 38, 25123 Brescia(BS), Italy  
e-mail: cinzia.amici@ing.unibs.it

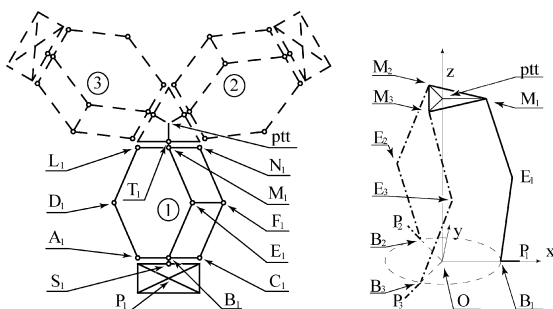


**Fig. 1** Conventions adopted for the manipulator analysis: from the left, the complete and the simplified structure

### Dynamic Analysis

The data for the dynamic analysis are identified with: the Cartesian coordinates  $S_0$  and  $S_f$  of the platform center, respectively, at the beginning and at the end of the movement; the actuators speed at the trajectory boundaries are set to zero; the joint coordinates  $Q_0$  and  $Q_f$ , respectively, at the beginning and at the end of the movement are computed with a previous kinematical analysis [1]. Furthermore, the architecture of the system is described in [1], while its diagonal mass matrix  $M$  is constructed with opportune lumped parameters in proper fictitious material points, as shown in the followings. Finally the external forces  $F_{se}$  are considered known and are applied in the fictitious material points associated with the elements of the matrix  $M$  [4–10].

The links have been approximated with a two concentrated masses model, while the platform geometry required the inertial moments  $I_x$  and  $I_y$  estimation around the  $x$  and  $y$  axes according to [11].

Different mathematical expressions has been used to describe the external forces  $F_{se}$ , as shown in the next section: a constant vector, a vector of random values into a fixed range, and a rational function of the time.

The motion profile along the trajectory has been implemented with: a constant acceleration/deceleration symmetric profile, a trapezoidal symmetric acceleration profile [12] or a trapezoidal symmetric acceleration profile with random noise [12]. Considering for instance the first presented profile, the actuators acceleration can be defined as in (1), while actuators velocity and position can be evaluated iteratively as (2), where  $t$  represents the time imposed to the motion,  $\Delta t$  is the time increment at every step, and  $i$  indicates the  $i$ -th step of the analysis.

$$\begin{cases} \ddot{Q}_i = \frac{9}{2} \cdot \frac{Q_f - Q_0}{t_i^2} & t_i \leq \frac{1}{3}t \\ \ddot{Q}_i = 0 & \frac{1}{3}t < t_i \leq \frac{2}{3}t \\ \ddot{Q}_i = -\frac{9}{2} \cdot \frac{Q_f - Q_0}{t_i^2} & t_i > \frac{2}{3}t \end{cases} \quad (1)$$

$$\dot{Q}_i = \dot{Q}_{i-1} + \ddot{Q}_i \Delta t, Q_i = Q_{i-1} + \dot{Q}_{i-1} \Delta t + \ddot{Q}_i \frac{\Delta t^2}{2} \tag{2}$$

Once these vectors have been defined, the direct kinematics allows to evaluate even the displacement, the velocity and the acceleration of the platform center, the Jacobian matrix and its time derivatives at the  $t_i$  instant. It is by considering these elements that the relations (3) and (4) can be written.

$$\bar{M}_i(Q_i) = J_i^T M J_i \tag{3}$$

$$\mathcal{V}_i(Q_i, \dot{Q}_i) = \overline{M}_i \dot{Q}_i = (J_i^T M J_i) \dot{Q}_i \tag{4}$$

The dynamics of the manipulator can be described, once the column vector of the generalized joints forces  $F_q$  is determined for every instant. Equations (5) and (6) allow to establish a relation between the unknown vector  $F_q$  and the quantities in (3) and (4).

$$\bar{M}_i(Q_i) \ddot{Q}_i + \mathcal{V}_i(Q_i, \dot{Q}_i) + \mathcal{G}_i(Q_i, F_i) = 0 \tag{5}$$

$$\mathcal{G}_i(Q_i, F_i) = -(J^T F_{sei} + F_{qi}) \tag{6}$$

The  $F_{se}$  vector of the external forces can be joined with the  $F_{elasticity}$  vector, that represents the reaction of the material elasticity at the  $i$ -th step (7).

$$F_{complete\_sei} = F_{se} + F_{elasticity} \tag{7}$$

This additional element has been identified by concentrated compliances in the joints (flexure hinges), that can be referred to the two different models shown in Fig. 2.

The compliance of the proposed flexure hinges can be approximated with (8), as shown in [13–15]. Thus, the elasticity action  $F_{elasticity}$  can be expressed as in (9), where  $\Delta dis$  represents the introduced displacement.

$$C_{type1} = \frac{9\pi \sqrt{R}}{2Eb\sqrt{t^5}}, C_{type2} = \frac{9\pi \sqrt{R}}{\sqrt{2}Eb\sqrt{t^5}} \tag{8}$$

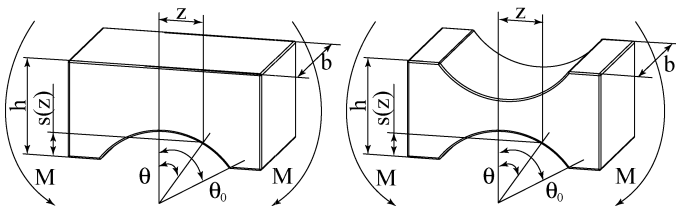


Fig. 2 From the left: type 1 and type 2 flexure hinge

$$F_{\text{elasticity}_i} \equiv C \cdot \Delta \text{dis} = C \cdot (Q_i - Q_0) \tag{9}$$

Any additional element is not required to estimate  $F_q$  at every step.

### Simulation Results

Manifold movement simulations have been developed with the geometrical parameters listed in Table 1 and with the force profiles listed in Table 2.

As previously mentioned, three different kinds of motion profile (Fig. 3) have been implemented with the parameter listed in Table 3.

Figure 4 presents the joints torques obtained through applying a constant external force with two different motion profiles: very similar maximum force values are reached, but a smoother profile is obtained with the second profile.

When the profile of external forces is associated to a random behaviour, the trapezoidal acceleration profile produces a quicker behaviour than the one realized with a constant acceleration profile, as shown in Fig. 5.

**Table 1** Default values of the main parameters implemented in the movement simulations

Geometry	Links length	0.05	m
	Links width	0.004	m
	Links thickness	0.002	m
	$\overline{AB}$ and $\overline{BC}$ distances for every leg element	0.03	m
	$\overline{PB}$ distance for every leg element	0.02	m
	$\overline{Mpit}$ distance for every leg element	0.04	m
	Distance between every foot and the origin of the central fixed reference system	0.07	M
Actuators configuration	B type		
Masses	Link mass	0.005	Kg

**Table 2** External forces profiles

Constant	$-100 \vec{i}$ [N]
Random	$0 \div 100$ [N]
Function of time	$3t \vec{i} + 2(t-3) \vec{j} + 6t \vec{k}$ [N]

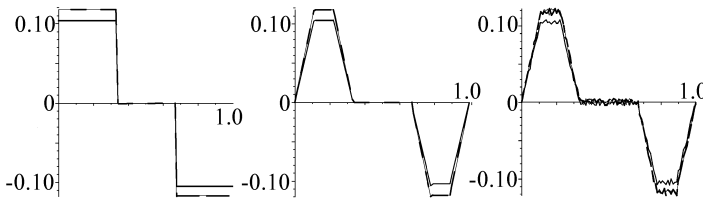


**Fig. 3** From the left: constant acc./dec. symmetric profile, trapezoidal symmetric acc. profile and trapezoidal symmetric acc. profile with random noise [mm/s<sup>2</sup>]; motion from (20, 10, 60) [mm] and (-20, -10, 60) [mm]; continuous line the first actuator (in the plane orthogonal to the trajectory), thin continuous the second actuator and dash the third one

**Table 3** Motion profiles

Movement time	1	s
Step length	0.01	s

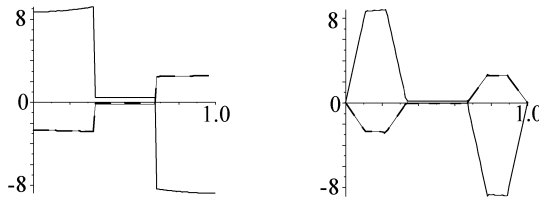


**Fig. 4** From the left, joints torques implementing constant and trapezoidal acceleration profiles [ $10^{-1}$ N]; motion from (20, 10, 60) [mm] and (-20, -10, 60) [mm]; continuous line the first actuator (in the plane orthogonal to the trajectory), thin continuous the second actuator and dash the third one

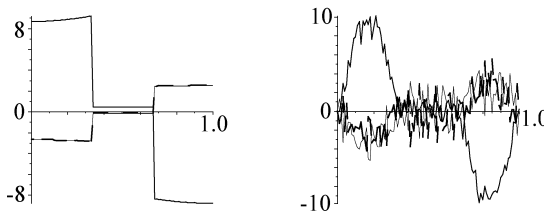


**Fig. 5** From the left, joints torques implementing constant and trapezoidal acceleration profiles [ $10^{-1}$ N]; motion from (20, 10, 60) [mm] and (-20, -10, 60) [mm]; continuous line the first actuator (in the plane orthogonal to the trajectory), thin continuous the second actuator and dash the third one

The peculiar characteristic for the proposed meso-manipulator is the compliance introduced by the flexure hinges. The limited inertial forces require the trapezoidal profile with random noise to appreciate a different behaviour of the joints torques as a consequence of applying a type 1 or a type 2 model for the hinges, as shown in Fig. 6.

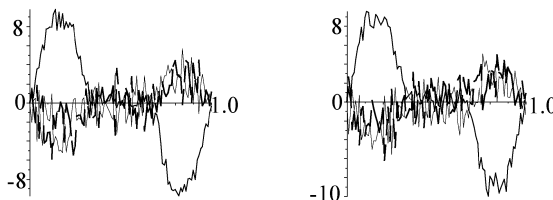


**Fig. 6** From the left, joints torques obtained by implementing type 1 and type 2 hinges models [ $10^{-1}$ N]; motion from (20, 10, 60) [mm] and (-20, -10, 60) [mm]; continuous line the first actuator (in the plane orthogonal to the trajectory), thin continuous the second actuator and dash the third one

## Conclusions

The main characteristic of the proposed parallel structure is the pure translation motion of the platform, due to the peculiarity of its legs architecture. A dynamic response strictly related to the implemented motion profile emerges from the simulations results. A noise contribute has been thereafter introduced into the symmetric trapezoidal profile to simulate a real-world behaviour, and also the compliance performances of the robot are evaluated with this noise force. The manipulator flexibility is to be considered as an advantage, as it can be completely determined, at least for small displacement; considering the robot as inserted in a major device, such a property can be used to compensate positioning errors in manipulation systems. From a manufacture viewpoint, an interesting characteristic is the original planar structure that is plastically deformed to obtain a 3d architecture, that allows low-cost feasibility process.

For all these reasons, the system presents a particular suitability for being employed as meso-manipulator.

## References

1. Amici C., Borboni A., Magnani P.L., Pomi D., Kinematic Analysis of a Compliant Parallel and Three-Dimensional Meso-Manipulator Generated from a Planar Structure, 2nd European Conference on Mechanism Science EUCOMES2008, Cassino, Italy, 2008.
2. Kong X., and Gosselin C.M., Type Synthesis of 3-DOF PPR-Equivalent Parallel Manipulators Based on Screw Theory and the Concept of Virtual Chain, *Journal of Mechanical Design*, Vol. 127(6), 2005, pp. 1113–1121.
3. Huynh P., and Hervé J.M., Equivalent Kinematic Chains of Three Degree-of-Freedom Tripod Mechanisms With Planar-Spherical Bonds, *Journal of Mechanical Design*, Vol. 127(1), 2005, pp. 95–102.
4. Craig J.J., *Robotics. Mechanics and Control*, Addison Wesley, 1986.
5. Xi F., Angelico O., and Sinatra R., Tripod Dynamics and its Inertia Effect, *Journal of Mechanical Design*, Vol. 127, 2005, pp. 144–149.
6. Wang S.-C., Hikita H., Kubo H., Zhao Y.-S., Huang Z., and Ifukube T., Kinematics and Dynamics of a 6 Degree-of-Freedom Fully Parallel Manipulator with Elastic Joints, *Journal of Mechanism and Machine Theory*, Vol. 38, 2003, pp. 439–461.
7. Gallardo J., Rico J.M., Frisoli A., Checcacci D., and Bergamasco M., Dynamics of Parallel Manipulators by Means of Screw Theory, *Journal of Mechanism and Machine Theory*, Vol. 38, 2003, pp. 1113–1131.
8. Featherstone R., *Position and Velocity Transformations Between Robot End-Effector Coordinates and Joint Angles*, 1986.
9. Callegari M., Gabrielli A., and Ruggiu M., Kinestatic Synthesis of a 3-CRU Spherical Wrist for Miniaturized Assembly Tasks, XVIII CONGRESSO AIMETA di Meccanica Teorica e Applicata, Brescia, Italia, 2007.
10. Cammarata A., Sinatra R., Callegari M., and Gabrielli A., Kinematics and Dynamics of a 3-CRU Spherical Wrist for Miniaturized Assembly Tasks, XVIII CONGRESSO AIMETA di Meccanica Teorica e Applicata, Brescia, Italy, 2007.
11. Longoria R. G., Modeling of Mechanical Systems for Mechatronics Applications, in Bishop R. H., *The Mechatronics Handbook*, CRC Press, 2002.



12. Borboni A., Antonini M., Bussola R., Faglia R., A Genetic Algorithm as Support in the Movement Optimisation of a Redundant Serial Robot, 8th Biennial ASME Conference on Engineering System Design and Analysis, Torino, Italy, 2006.
13. Howell L. L., *Compliant Mechanisms*, Wiley, New York, 2001.
14. Lobontiu N., and Raton B., *Compliant Mechanisms: Design of Flexure Hinges*, CRC Press, 2003.
15. El-Khasawneh B. S., and Ferreira P. M., Computation of stiffness bounds for parallel link manipulators, *International Journal of Machine Tools & Manufacture*, Vol. 39, 1999, pp. 321–342.

# Modelling of the Orientation Error of a 3-DOF Translational Parallel Manipulator

Zouhaier Affi and Lotfi Romdhane

**Abstract** This paper deals with the computation of the orientation error and the kinematic model of a 3-translational DOF parallel manipulator called the RAF robot. We derived a simple analytical model allowing the computation of the orientation, generated by the deformation of the PKLs, when an external load is applied to the platform. Due to its analytical nature, the developed model can also be used for the mapping of the orientation error on the workspace of the robot.

**Keywords** Parallel manipulator · Orientation error

## Introduction

One of the main advantages of parallel robots, and the translational ones in particular [1, 2], is a high rigidity and a high precision compared to serial robots. Therefore, several researches got interested in quantifying this rigidity [3, 4]. Ceccarelli and Carbone [5, 6], proposed an analytical model to calculate the stiffness of a hybrid parallel manipulator. They adopted the determinant of the stiffness matrix as a criterion to evaluate the global stiffness of the CaPaMan robot at a given configuration. Huang et al. [3] estimated the stiffness of a tripod based parallel kinematic machine through a finite element method. Simaan and Shoham [7] addressed the stiffness synthesis problem of variable geometry double planar parallel robots. They used the Grobner bases to solve a polynomial system corresponding to a desired stiffness. In Zhang [8] the global stiffness of the Tricept machine was proposed, allowing to compare two types of passive leg structures. Yoon et al. [4] evaluated the stiffness of a compact Delta parallel manipulator, in order to obtain a well balanced stiffness in each axial direction.

---

Z. Affi (✉)

Laboratoire de Génie Mécanique, \*Ecole Nationale d'Ingénieurs de Monastir,  
e-mail: zouhaier.affi@enim.rnu.tn

The significant contributions made in this paper are the closed form of the inverse kinematic model of the passive kinematic chains and the derived analytical model of the orientation error. These models will be used to find the distribution of the error within a given region of the workspace of the manipulator and can also be used in a sensitivity analysis.

This paper is organized as follows: Section *Architecture of the RAF Robot* presents a brief description of the architecture and the kinematic model of the RAF robot. In Section *Orientation Error Analyses of the RAF*, we present the static analysis of the RAF robot, and we derive the orientation error of the RAF robot, due to a couple applied to the platform. Finally, some concluding remarks are presented.

## Architecture of the RAF Robot

The RAF robot is a 3-translational-DOF in parallel manipulator. This robot is made of a mobile platform connected to the base by 3 extensible legs. The use of linear actuators has the advantage of supporting high loads compared to rotational actuators. These legs constitute the actuators of the manipulator, whereas two other passive kinematic legs (PKL) are used to eliminate the three rotations of the mobile platform with respect to the base [1] (Fig. 1).

The existence of the two PKLs, with the three extensible legs, leads to an over constrained RAF robot. In order to eliminate this over constraint, the body (4') is added to the first PKL (Fig. 2). This body has a vertical revolute joint with the platform (see Romdhane et al. [1] for more details).

The non over constrained version of the mechanism is the one chosen in this study, because, for the static model to be solved in the unknown joint reaction forces, the mechanism has to be a non over constrained one [1].

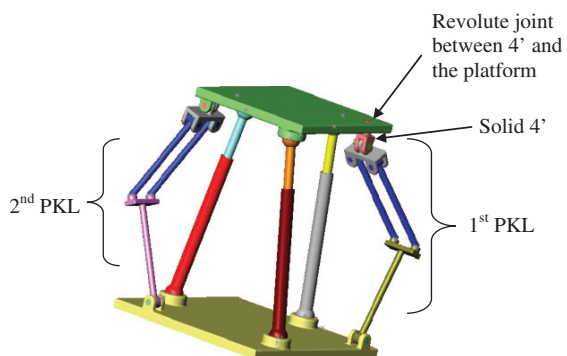


**Fig. 1** A solid model of the RAF robot

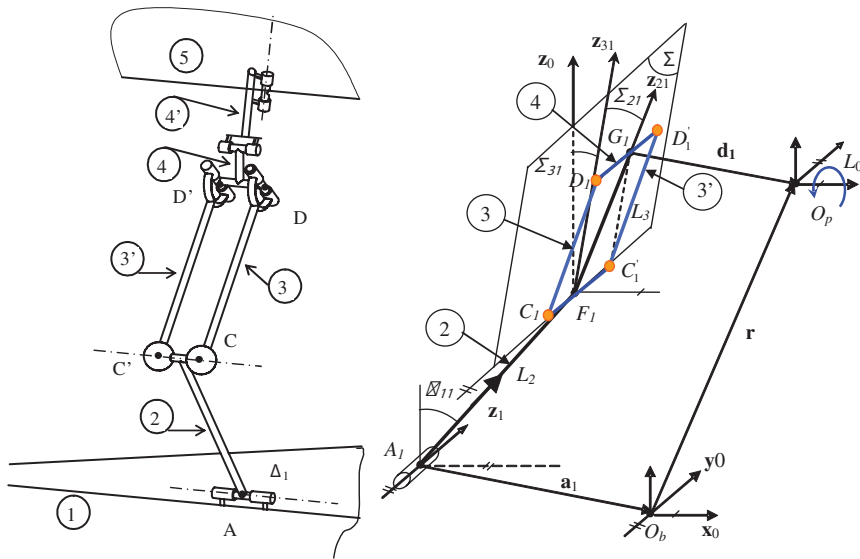


Fig. 2 A schematic of the first PKL

### Orientation Error Analyses of the RAF

The computation of the orientation error due to the deformation of the PKLs is based on beam theory and the superposition principal. Given a static or quasi-static couple applied to the platform, the deformation due to the elasticity of each body is computed. Then, based on the superposition principal, the orientation error of the platform is computed.

A general couple applied to the platform can be expressed as follows (Fig. 3):

$$c_{ext} = C\mathbf{u} = L_0\mathbf{x}_0 + M_0\mathbf{y}_0 + N_0\mathbf{z}_0 \tag{1}$$

where  $L_0 = C \sin \beta \cos \alpha$ ,  $M_0 = C \sin \beta \sin \alpha$  et  $N_0 = C \cos \beta$

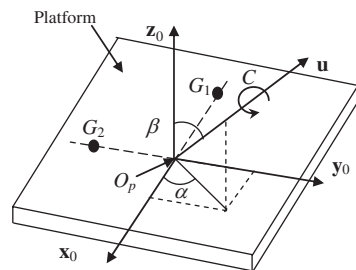


Fig. 3 General couple applied to the platform

In what follows, we assume that the first PKL is the one which has a revolute joint with the base along the  $y_0$  axis and the second PKL will have a revolute joint with the base along the  $x_0$  axis. In this configuration this PKL will support only the couple  $L_0$  around the  $x_0$  axis and the second PKL will support the couples  $M_0$  and  $N_0$  around the  $y_0$  and  $z_0$  axes, respectively. Figure 4 shows the free body diagram of the first PKL needed for the static analyses of the RAF robot.

Firstly, we will identify the deformation of each link of the PKLs as in Fig. 5, and then the orientation error angles of each PKLs are computed.

The arm is loaded by:

$$\Gamma_{F1/R11} = [L_0 \cos \varphi_{11} \ 0 \ L_0 \sin \varphi_{11}]^T \tag{2}$$

This couple produces a torsional loading around the local  $z_{21}$ -axis and a bending moment around the local  $x_{21}$ -axis.

The displacement of point  $C_1$ , due to the bending of the arm, expressed in  $R_{11}$ , is given by:

$$\Delta y_{11} = \frac{32L_2^2}{\pi E d_2^4} L_0 \cos \varphi_{11} \tag{3}$$

This displacement generates an error in the orientation of the arm. This error angle is around the  $x_{11}$  axis and is given by:

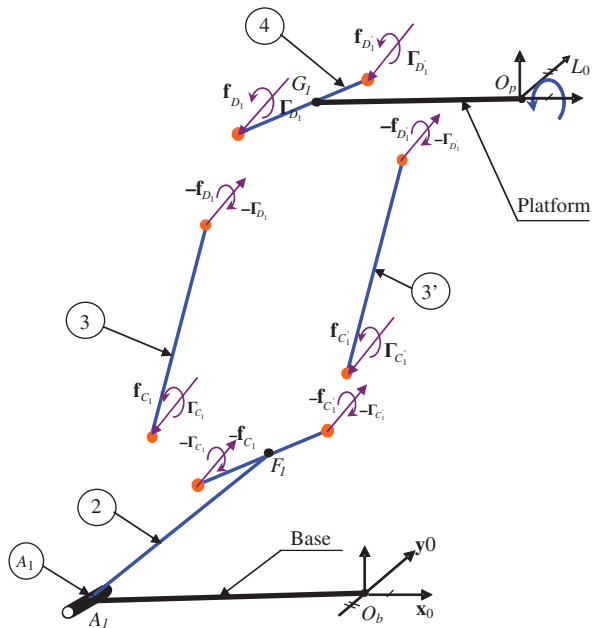


Fig. 4 Free body diagram of the 1st PKL

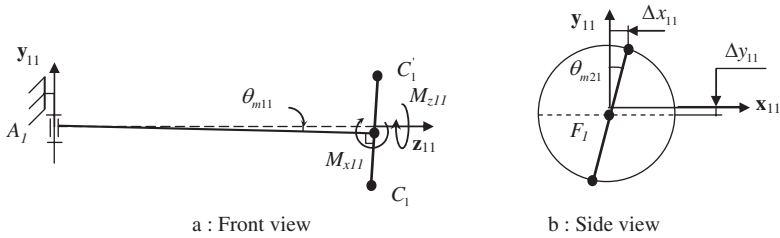


Fig. 5 Schematic of the arm sollicitation

$$\theta_{m11} = \frac{\Delta y_{11}}{L_2} = \frac{32L_2}{\pi E d_2^4} L_0 \cos \varphi_{11} \tag{4}$$

The torsional load gives an error of the orientation around the  $z_{11}$  axis. This error angle is given by:

$$\theta_{m21} = \frac{64(1 + \nu)}{\pi E d_2^4} \sin \varphi_{11} L_0 \tag{5}$$

The forearm of the first PKL is loaded by:

$$\mathbf{f}_{D1/R21} = \left[ \frac{L_0}{a} \sin \varphi_{31} \ 0 \ -\frac{L_0}{a \cos \varphi_{31}} \cos \varphi_{31} \right]^T \tag{6}$$

$$\mathbf{\Gamma}_{D1/R21} = \left[ 0 \ -\frac{L_0}{a} \sin \varphi_{31} L_3 \ 0 \right]^T \tag{7}$$

If we assume that all the rest of the manipulator remains rigid, the forearm loading can be presented as given in Fig. 6.

One can notice that the forearm has a bending moment around the  $y_{21}$ -axis, a shear force along the local  $x_{21}$ -axis, and a tensile force along the  $z_{21}$ -axis.

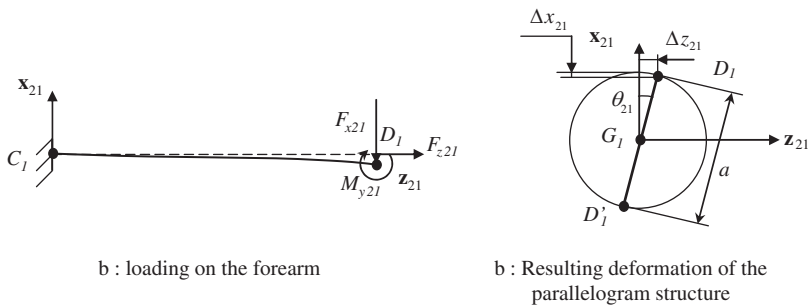


Fig. 6 Schematic of the forearm loading

The displacement of point  $D_1$  (Fig. 6), produced by the deformation of the forearm, expressed in the local frame  $R_{21}$ , is given by:

$$\Delta z_{21} = \frac{4L_3}{\pi E d_3^2} \left( \frac{-L_0 \cos \varphi_{31}}{a \cos \varphi_{21}} \right) \quad \Delta x_{21} = \frac{32L_3^3}{\pi a E d_3^4} \left( \frac{4L_0 \sin \varphi_{31}}{3} \right) \quad (8)$$

Due to the opposite loads acting on each forearm, the displacement of point  $D_1$  and  $D'_1$  are symmetric. This deformation leads to an error angle around the  $\mathbf{y}_{21}$  which can be approximated by:

$$\theta_{21} = \frac{2\sqrt{\Delta x_{21}^2 + \Delta z_{21}^2}}{a} \quad (9)$$

One can notice that the first PKL is attached to the platform by two revolute joints with axes  $\mathbf{y}_0$  and  $\mathbf{z}_0$  (by solid 4' (Fig. 1)). Hence, the only orientation error transmitted to the platform is  $\theta_{x1}$  given by:

$$\theta_{x1} = \theta_{m11} \cos \varphi_{11} + \theta_{m21} \sin \varphi_{11} - \theta_{21} \sin \varphi_{31} \sin \varphi_{21} \quad (10)$$

The same approach is adopted to evaluate the orientation error generated by the compliance of the second PKL.

The error angles due to the deformation of the arm are given by:

$$\theta_{m12} = \frac{\Delta x_{12}}{L_2} = \frac{32L_2}{\pi E d_2^4} (M_0 \cos \varphi_{12} - N_0 \sin \varphi_{12}) \quad (11)$$

$$\theta_{m22} = \frac{64(1 + \nu)}{\pi E d_2^4} (M_0 \sin \varphi_{12} + N_0 \cos \varphi_{12}) \quad (12)$$

The error angles  $\theta_{m12}$  and  $\theta_{m22}$  are around the axes  $\mathbf{y}_{12}$  and  $\mathbf{z}_{12}$ , respectively. Then the deformation of the forearm is given by:

$$\Delta z_{22} = \frac{4L_3}{\pi E d^2} \left( \frac{N_0 \sin \varphi_{32} - M_0 \cos \varphi_{32}}{a \cos \varphi_{22}} \right) \quad (13)$$

$$\Delta y_{22} = \frac{32L_3^3}{\pi a E d_3^4} \left( \frac{4(M_0 \sin \varphi_{32} + N_0 \cos \varphi_{32})}{3} \right) \quad (14)$$

The deformation of the forearms leads to an orientation error around the  $\mathbf{x}_{22}$  axis given by:

$$\theta_{22} = \frac{2\sqrt{\Delta y_{22}^2 + \Delta z_{22}^2}}{a} \tag{15}$$

Therefore, the orientation errors caused by the deformation of the second PKL are  $\theta_{y2}$  and  $\theta_{z2}$ . These error angles are given by:

$$\theta_{y2} = \theta_{m12} \cos \varphi_{12} + \theta_{m22} \sin \varphi_{12} - \theta_{22} \sin \varphi_{32} \sin \varphi_{22} \tag{16}$$

$$\theta_{z2} = -\theta_{m12} \sin \varphi_{12} + \theta_{m22} \cos \varphi_{12} - \theta_{22} \cos \varphi_{32} \sin \varphi_{22} \tag{17}$$

The total orientation error of the platform is given by:

$$[\theta_x \ \theta_y \ \theta_z] = [\theta_{x1} \ \theta_{y2} \ \theta_{z2}] \tag{18}$$

## Results

The following dimensions of the RAF robot are adopted (Table 1).

The presented results are the distribution of the error within a portion of the workspace (Fig. 7). For the presented design of the RAF robot, the first PKL will support only the couple  $L_0$  around the  $x_0$  axis and the second PKL will support the couples  $M_0$  and  $N_0$  around the  $y_0$  and  $z_0$  axes, respectively.

The minimum orientation error can be obtained around  $x = 0, y = 0$ . Moreover,  $\theta_x$  is sensitive to a displacement along the  $y$  direction, whereas  $\theta_y, \theta_z$  are sensitive to the  $x$  and  $z$  displacements. This behavior can be explained by the architecture of the platform which is made by two parallelogram based PKLs. For the first PKL, the case where  $y = 0$  yields the minimum value of  $\theta_x$  for all values of the  $x$  and  $z$  displacements. This behavior could be explained by the configuration of the parallelogram in its plane. Indeed, the configuration for  $y = 0$  corresponds to the case where the parallelogram is rectangle and the stiffness is the highest in this case. Similar results are obtained for  $\theta_y$  and  $\theta_z$ , which depend on the second PKL.

**Table 1** Parameters of the RAF robot

$C = 1 \text{ Nm}$	$\alpha = \beta = 45 \text{ deg}$
$a = 100 \text{ mm}$	$\mathbf{a}_1 = [-500 \ 0 \ 0]^T$
$d2 = d3 = 10 \text{ mm}$	$\mathbf{a}_2 = [0 \ -500 \ 0]^T$
$E = 200000 \text{ MPa}$	$\mathbf{g}_1 = [-300 \ 0 \ 0]^T$
$\nu = 0.3$	$\mathbf{g}_2 = [0 \ -300 \ 0]^T$
$L2 = L3 = 400 \text{ mm}$	



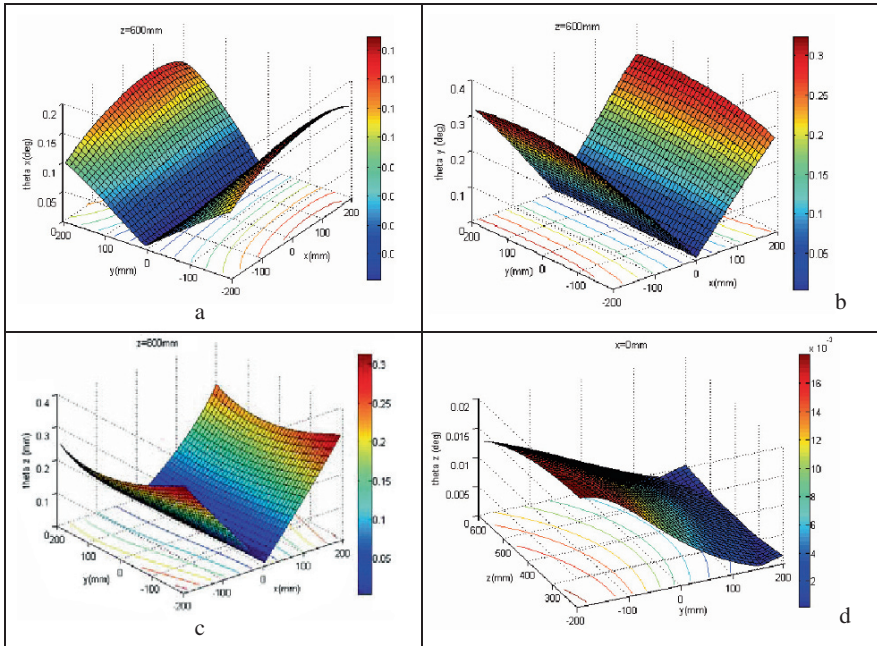


Fig. 7 Mapping of the orientation error on the workspace

## Conclusion

In this work, we derived an analytical model allowing the computation of the orientation error of the RAF robot when the platform is loaded by an arbitrary couple. This result can be a helpful tool in the design and the optimization of this type of manipulators or the evaluation of the orientation error within the workspace.

## References

1. L. Romdhane, Z. Affi and M. Fayet “Design and Singularity Analysis of a 3 Translational-DOF In-Parallel Manipulator” ASME Journal of Mechanical Design, 2002, Vol. 124, pp. 419–426
2. L. Tsai and S. Joshi, “Kinematics and Optimization of a Spatial 3-UPU Parallel Manipulator”, ASME, Journal of Mechanical Design, 2000, Vol. 122, pp. 439–446
3. T. Huang X. Zhou, and D.J. Whitehouse “Stiffness Estimation of Tripod-Based Parallel Kinematic Machine”, IEEE Transactions on Robotics and Automation, 2002, Vol. 18, No. 1, pp. 50–58
4. W.K. Yoon, T. Suehiro, Y. Tsumaki, and M. Uchiyama “Stiffness Analysis and design of a Compact Modified Delta Parallel Mechanism”, Robotica, 2004, Vol. 22, pp. 463–475
5. M. Ceccarelli and G. Carbone “A Stiffness Analysis for CaPaMan (Cassino Parallel Manipulator)”, Mechanism and Machine Theory, 2002, Vol. 37, pp. 427–439
6. G. Carbone and M. Ceccarelli “A Stiffness Analysis for a Hybrid Parallel-Serial Manipulator”, Robotica, 2004, Vol. 22, pp. 567–576

7. N. Simaan and M. Shoham “Stiffness Synthesis of a Variable Geometry Six-Degrees-of-Freedom Double Planar Parallel Robot” *The International Journal of Robotics Research*, September 2003, Vol. 22, No. 9, pp. 575–775
8. D. Zhang “On Stiffness Improvement of the Tricept Machine Tool”, *Robotica*, 2005, Vol. 23, pp. 377–386

# Sensitivity Analysis of Degenerate and Non-Degenerate Planar Parallel Manipulators

Nicolas Binaud, Stéphane Caro and Philippe Wenger

**Abstract** This paper deals with the sensitivity analysis of degenerate and non-degenerate planar parallel manipulators. First, the manipulators under study as well as their degeneracy conditions are presented. Then, an optimization problem is formulated in order to obtain their maximal regular dextrous workspace. Finally, the sensitivity of the pose of their moving platform to variations in the geometric parameters is analyzed.

**Keywords** Sensitivity analysis · Degenerate manipulators · Regular dextrous workspace · Dexterity

## Introduction

For two decades, parallel manipulators have attracted the attention of more and more researchers, who consider them as valuable alternative design for robotic mechanisms. Parallel kinematic machines (PKM) offer essential advantages over their serial counterparts, i.e., lower moving masses, higher stiffness and payload-to-weight ratio, higher natural frequencies, possibility to locate actuators on the fixed base. However, PKM are not necessarily more accurate than their serial counterparts. On the one hand, variations in the geometric parameters of serial manipulators cannot be amplified. On the other hand, these variations can be either compensated or amplified with PKM [1]. Wang et al. [2] studied the effect of manufacturing tolerances on the accuracy of a Stewart platform. Kim and Tsai [3] studied the effect of misalignment of linear actuators of a 3-Degree of Freedom (DOF) translational parallel manipulator on the motion of its moving platform. Caro et al. [4] developed a tolerance synthesis method for mechanisms based on a robust design approach. Caro et al. [5] proposed two indices to evaluate the sensitivity of the pose of the end-effector of Orthoglide, a 3-DOF translational PKM, to variations in its design parameters.

---

N. Binaud (✉)

Institut de Recherche en Communications et Cybernétique de Nantes, UMR CNRS n° 6597,  
1 rue de la Noë, 44321 Nantes, France  
e-mail: binaud@ircsyn.ec-nantes.fr

Besides, they noticed that the better the dexterity, the higher the accuracy of the manipulator. Caro et al. [6] came up recently with the sensitivity coefficients of 3-RPR planar parallel manipulators (PPM) in algebraic form.

This paper deals with the comparison of the accuracy of two degenerate and two non-degenerate PPMs. First, the degeneracy conditions of 3-RPR manipulators and the manipulators under study are presented. Then, the formulation of an optimization problem is introduced to obtain the regular dextrous workspace of those manipulators. Finally, the methodology introduced in [6] is used to analyze and compare the sensitivity of the pose of their moving platforms to variations in their geometric parameters.

### Degenerate and Non-Degenerate Manipulators

In the scope of this paper, we focus on the sensitivity analysis of two degenerate and two non-degenerate 3-RPR manipulators. First, the parameterization of a 3-RPR manipulator is described in Fig. 1. Then, the degeneracy conditions of such a manipulator are given. Finally, the architectures of the four manipulators under study are illustrated.

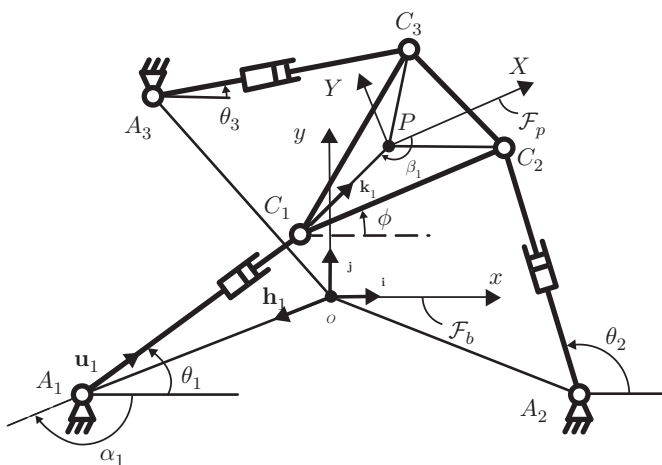


Fig. 1 3-RPR manipulator

### Parameterization

Here and throughout this paper, R, P and  $\underline{P}$  denote revolute joints, prismatic joints and actuated prismatic joints, respectively. It is composed of a base and a moving platform connected by three legs. Points  $A_1$ ,  $A_2$  and  $A_3$ , ( $C_1$ ,  $C_2$  and  $C_3$ , respectively) lie at the corners of a triangle, of which point  $O$  (point  $P$ , resp.) is the center of the circumscribed circle. Each leg is composed of a R, a P and a R joint

in sequence. The three P joints are actuated. For these reasons, the manipulator is named 3-RPR manipulator. The pose, i.e., the position and the orientation, of its moving platform is determined by means of the Cartesian coordinates vector  $\mathbf{p} = [p_x, p_y]^T$  of operation point  $P$  expressed in frame  $\mathcal{F}_b$  and angle  $\phi$ , namely, the angle between frames  $\mathcal{F}_b$  and  $\mathcal{F}_p$ . Besides, the passive and actuated joints don't have any stop.

### Degeneracy Condition

The forward kinematic problem of a parallel manipulator often leads to complex equations and non analytic solutions, even when considering 3-DOF PPMs [7]. For those manipulators, Hunt showed that the forward kinematics admits at most six solutions [8] and some authors proved that their forward kinematics can be reduced to the solution of a sixth-degree characteristic polynomial [9, 10]. The decreasing conditions of the degree of the latter were investigated by [11], [12] and [13]. It turns out that we can distinguish six cases, namely, (i) manipulators with two coincident joints, (ii) manipulators with similar aligned base and moving platforms, (iii) manipulators with nonsimilar aligned base and moving platforms, (iv) manipulators with similar triangular base and moving platforms, (v) manipulators with the three actuated prismatic joints satisfying a certain relationship, and (vi) manipulators with congruent base and moving platforms, of which the moving platform is rotated of 180 deg about one of its side.

In the scope of this paper, we focus on the sensitivity analysis of the fourth and the sixth cases. For the fourth case, the forward kinematics is reduced to the solution of two quadratics in cascade. For the sixth case, the forward kinematics degenerates over the whole joint space and is reduced to the solution of a third-degree polynomial and a quadratic in sequence. Moreover, the sensitivity of two non-degenerate 3-RPR manipulators is analyzed for a matter of comparison.

### Manipulators Under Study

Figure 2(a)–(d) illustrate the four manipulators under study, which are named  $M_1$ ,  $M_2$ ,  $M_3$  and  $M_4$ , respectively.  $M_1$  and  $M_2$  are non-degenerate whereas  $M_3$  and  $M_4$

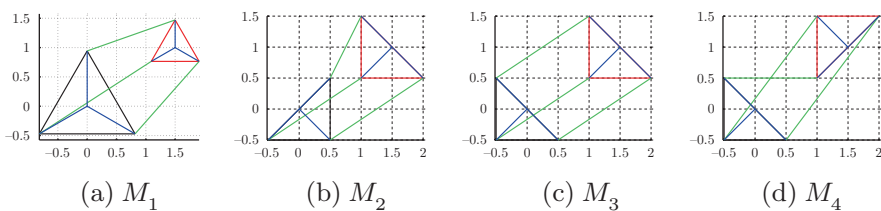


**Fig. 2** The four 3-RPR manipulators under study with  $\phi = 0$  and  $\mathbf{p} = [1, 1.5]^T$ : (a-b) non-degenerate manipulators, (c-d) degenerate manipulators

are degenerate. From Fig. 2(a), the base and moving platforms of  $M_1$  are equilateral. From Fig. 2(b), the base and moving platforms of  $M_2$  are different.  $M_3$  and  $M_4$  illustrate the fourth and the sixth degeneracy cases, respectively. It is noteworthy that the base and moving platforms of  $M_2$ ,  $M_3$  and  $M_4$  have the same circumscribed circle, its radius being equal to  $\sqrt{2}/2$ . As far as  $M_1$  is concerned, the circumscribed circle of its moving platform is two times smaller than the one of the base platform, the sum of their radius being equal to  $\sqrt{2}$ .

### Regular Dextrous Workspace

In order to compare the accuracy of the foregoing manipulators, we first define their Regular Dextrous Workspace (RDW). Then, the accuracy of  $M_1$ ,  $M_2$ ,  $M_3$  and  $M_4$  can be evaluated throughout their RDW and compared. Let us assume that the RDW is a cylinder of  $\phi$ -axis with a good kinetostatic performance, i.e., the inverse condition number of the normalized Jacobian matrix  $\mathbf{J}_n$  of the manipulator based on the Frobenius norm is higher than 0.1 within the RDW, i.e.,  $\kappa_F^{-1}(\mathbf{J}_n) \geq 0.1$ . Therefore, the optimization problem used to obtain such a RDW is formulated below:

$$Pb \begin{cases} \min_{\mathbf{x}} 1/R \\ s.t. \Delta\phi \geq \pi/6 \\ \text{sign}(\det(\mathbf{J}_n)) = \text{constant} \\ \kappa_F^{-1}(\mathbf{J}_n) \geq 0.1 \end{cases}$$

with  $R$  the radius of the cylinder and  $\Delta\phi$  the orientation range of the moving platform of the manipulator within its RDW. Moreover,  $\mathbf{x}$  is composed of the optimization variables and is defined as follows:

$$\mathbf{x} = [R \ I_x \ I_y \ \phi_{\min} \ \phi_{\max}]$$

$I_x$  and  $I_y$  are the Cartesian coordinates of the section of the cylinder.  $\phi_{\min}$  and  $\phi_{\max}$  are the lower and upper bounds of  $\Delta\phi$ , respectively. Figure 3(a)–(d) illustrate the

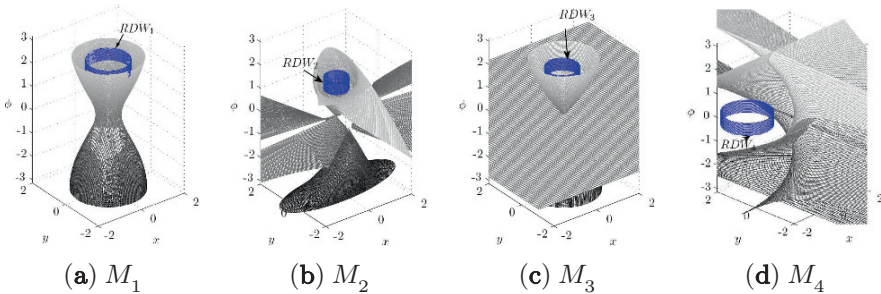


Fig. 3 Maximal regular dextrous workspace

**Table 1** RDW radius of  $M_1, M_2, M_3$  and  $M_4$ 

$R_1$	$R_2$	$R_3$	$R_4$
0.86	0.48	0.67	1.02

workspace, the singularities and the maximal RDW of  $M_1, M_2, M_3$  and  $M_4$ . The RDW of the manipulators were obtained by means of optimization problem  $Pb$  and “Matlab” optimization function  $fmincon$ . Their radius is given in Table 1. We can notice that  $M_4$  has the biggest RDW and  $M_2$  the smallest one.

## Sensitivity Analysis

In this section, the accuracy of  $M_1, M_2, M_3$  and  $M_4$  is evaluated within their RDW for a matter of comparison. First, two global sensitivity indices introduced in [6] are presented to analyze the sensitivity of the pose of the moving platform of a 3-RPR manipulator to variations in its geometric parameters. Then, the contours of these indices are plotted in the RDW of  $M_1, M_2, M_3$  and  $M_4$  and the results are analyzed.

### Global Sensitivity Indices

Let  $v_p$  and  $v_\phi$  be the global sensitivity indices of the position and the orientation of a 3-RPR manipulator, respectively. From [6], they can be defined in algebraic form as follows:

$$v_p = \frac{\|\mathbf{v}_i\|_2}{\det(\mathbf{A})} \sum_{i=1}^3 (1 + |q_i| + |r_i| + |s_i| + |t_i|) \quad (1)$$

$$v_\phi = \frac{|v_i|}{\det(\mathbf{A})} \sum_{i=1}^3 (1 + |q_i| + |r_i| + |s_i| + |t_i|) \quad (2)$$

with

$$q_i = \rho_i(\mathbf{u}_i^T \mathbf{h}_i \cos \alpha_i - \mathbf{u}_i^T \mathbf{E} \mathbf{h}_i \sin \alpha_i) \quad (3a)$$

$$r_i = \rho_i(\mathbf{u}_i^T \mathbf{h}_i \sin \alpha_i + \mathbf{u}_i^T \mathbf{E} \mathbf{h}_i \cos \alpha_i) \quad (3b)$$

$$s_i = \rho_i(\mathbf{u}_i^T \mathbf{k}_i \cos \beta_i - \mathbf{u}_i^T \mathbf{E} \mathbf{k}_i \sin \beta_i) \quad (3c)$$

$$t_i = \rho_i(\mathbf{u}_i^T \mathbf{k}_i \sin \beta_i + \mathbf{u}_i^T \mathbf{E} \mathbf{k}_i \cos \beta_i) \quad (3d)$$

and

$$\det(\mathbf{A}) = (m_1 \rho_2 \rho_3 (\mathbf{u}_2 \times \mathbf{u}_3) + m_2 \rho_3 \rho_1 (\mathbf{u}_3 \times \mathbf{u}_1) + m_3 \rho_1 \rho_2 (\mathbf{u}_1 \times \mathbf{u}_2))^T \mathbf{n} \quad (4a)$$

$$v_1 = \rho_2 \rho_3 (\mathbf{u}_2 \times \mathbf{u}_3)^T \mathbf{n} \quad (4b)$$

$$v_2 = \rho_3 \rho_1 (\mathbf{u}_3 \times \mathbf{u}_1)^T \mathbf{n} \quad (4c)$$

$$v_3 = \rho_1 \rho_2 (\mathbf{u}_1 \times \mathbf{u}_2)^T \mathbf{n} \quad (4d)$$

$$\mathbf{v}_1 = \mathbf{E} (m_2 \rho_3 \mathbf{u}_3 - m_3 \rho_2 \mathbf{u}_2) \quad (4e)$$

$$\mathbf{v}_2 = \mathbf{E} (m_3 \rho_1 \mathbf{u}_1 - m_1 \rho_3 \mathbf{u}_3) \quad (4f)$$

$$\mathbf{v}_3 = \mathbf{E} (m_1 \rho_2 \mathbf{u}_2 - m_2 \rho_1 \mathbf{u}_1) \quad (4g)$$

$$\mathbf{n} = \mathbf{i} \times \mathbf{j} \quad (4h)$$

with matrix  $\mathbf{E}$  defined as

$$\mathbf{E} = \begin{bmatrix} 0 & -1 \\ 1 & 0 \end{bmatrix} \quad (5)$$

and

$$m_i = -r_2 \rho_i \mathbf{u}_i^T \mathbf{E} \mathbf{k}_i, \quad i = 1, \dots, 3 \quad (6)$$

Besides,  $\alpha_i$  is the angle between vectors  $\vec{O}x$  and  $\vec{O}A_i$ ,  $\beta_i$  is the angle between vectors  $\vec{C}_1C_2$  and  $P\vec{C}_i$ ,  $r_2$  is the circumscribed radius of the mobile platform,  $\rho_i$  is the length of  $i^{\text{th}}$  leg,  $\|\cdot\|_2$  is the 2-norm,  $\mathbf{h}_i$  is the unit vector  $\vec{O}A_i / \|\vec{O}A_i\|_2$ ,  $\mathbf{u}_i$  is the unit vector  $\vec{A}_iC_i / \|\vec{A}_iC_i\|_2$ ,  $\mathbf{k}_i$  is the unit vector  $\vec{C}_iP / \|\vec{C}_iP\|_2$  and  $\mathbf{A}$  is the Forward Jacobian of the manipulator.

## Results

Figure 4(a)–(d) (Fig. 4(e)–(d), resp.) illustrate the isocontours of the maximum value of  $v_p$  ( $v_\phi$ , resp.) for a given orientation  $\phi$  within the RDW of  $M_1$ ,  $M_2$ ,  $M_3$  and  $M_4$ , respectively. It turns out that  $M_3$  ( $M_4$ , resp.) has globally the best positioning (orientation, resp.) accuracy. On the contrary,  $M_4$  ( $M_1$ , resp.) has globally the worst positioning (orientation, resp.) accuracy.

Finally, Table 2 gives an overall classification of  $M_1$ ,  $M_2$ ,  $M_3$  and  $M_4$  with regard to their positioning accuracy, orientation accuracy and the size of their RDW. We can notice that the two degenerate manipulators are the most interesting.



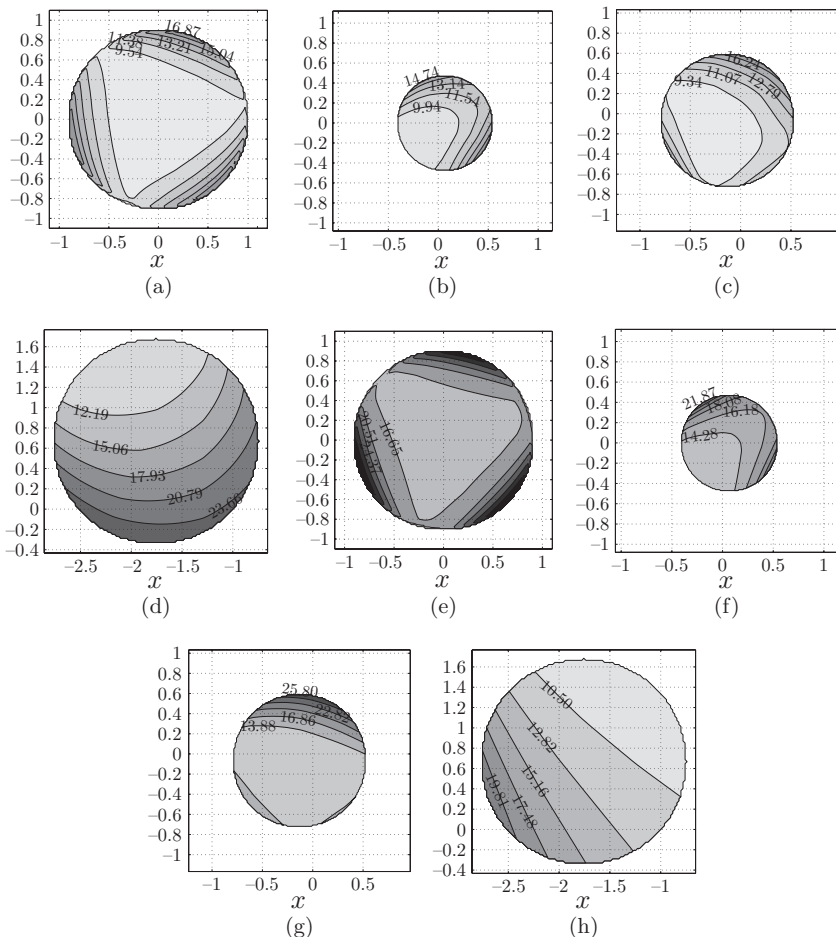


**Fig. 4**  $v_p$  isocontours of: (a)  $M_1$ , (b)  $M_2$ , (c)  $M_3$  and (d)  $M_4$  and  $v_\phi$  isocontours of (e)  $M_1$ , (f)  $M_2$ , (g)  $M_3$  and (h)  $M_4$ , respectively

**Table 2** Classification of  $M_1, M_2, M_3$  and  $M_4$  w.r.t  $v_p, v_\phi$  and the size of their RDW

	$M_1$	$M_2$	$M_3$	$M_4$
<i>RDW</i>	2	4	3	1
$v_p$	2	3	1	4
$v_\phi$	4	3	2	1
Ranking	3	4	1	1

## Conclusions

The paper dealt with the sensitivity analysis of degenerate and non-degenerate 3-RPR planar parallel manipulators. First, the manipulators under study as well as their degeneracy conditions were presented. Then, an optimization problem was formulated in order to obtain their maximal regular dextrous workspace (RDW). Accordingly, the sensitivity of the pose of their moving platform to variations in the geometric parameters was evaluated within their RDW. Finally, it turns out that the two degenerate manipulators are the most interesting in terms of dexterity and accuracy.

## References

1. Wenger, P., Gosselin, C., and Maillé, B., 1999, "A Comparative Study of Serial and Parallel Mechanism Topologies for Machine Tool," *Int. Workshop on Parallel Kinematic Machines*, Milan, Italie, pp. 23–35.
2. Wang, J., and Masory, O., 1993, "On the accuracy of a Stewart platform - Part I, The effect of manufacturing tolerances," *In: Proceedings of the IEEE International Conference on Robotics Automation, ICRA '93*, Atlanta, USA, pp. 114–120.
3. Kim, H.S., and Tsai, L-W., 2003, "Design optimization of a Cartesian parallel manipulator," *ASME J. Mech. Des.*, 125, pp. 43–51.
4. Caro, S., Bennis, F., and Wenger, P., 2005, "Tolerance Synthesis of Mechanisms: A Robust Design Approach," *ASME J. Mech. Des.*, 127, pp. 86–94.
5. Caro, S., Wenger, P., Bennis, F., and Chablat, D., 2006, "Sensitivity Analysis of the Orthoglide, A 3-DOF Translational Parallel Kinematic Machine," *ASME J. Mech. Des.*, 128, pp. 392–402.
6. Caro, S., Binaud, N., and Wenger, P., 2008, "Sensitivity Analysis of Planar Parallel Manipulators," *ASME Proc. of International Design Engineering Technical Conferences*, New York City, August.
7. Hunt K.H., 1978, *Kinematic Geometry of Mechanisms*, Oxford University Press, Cambridge.
8. Hunt K.H., 1983, "Structural Kinematics of In-Parallel Actuated Robot Arms," *J. Mechanisms, Transmissions and Automation in Design*, 105(4); pp. 705–712.
9. Gosselin C., Sefrioui J., and Richard M.J., 1992, "Solutions Polynomiales au problème de la cinématique des manipulateurs parallèles plans trois degrés de liberté," *Mechanism and Machine Theory*, 27; pp. 107–119.
10. Pennock G.R., and Kassner D.J., 1990, "Kinematic Analysis of a Planar Eight-bar Linkage: Application to a Platform-Type Robot," *ASME Proc. of the 21th Biennial Mechanisms Conf.*, pp. 37–43, Chicago, September.
11. Gosselin C.M., and Merlet J-P, 1994, "On the Direct Kinematics of Planar Parallel Manipulators: Special Architectures and Number of Solutions," *Mechanism and Machine Theory*, 29(8); pp. 1083–1097.
12. Kong X., and Gosselin C.M., 2001, "Forward Displacement Analysis of Third-Class Analytic 3-RPR Planar Parallel Manipulators," *Mechanism and Machine Theory*, 36; pp. 1009–1018.
13. Wenger P., Chablat D., and Zein M., 2007, "Degeneracy Study of the Forward Kinematics of Planar 3-RPR Parallel Manipulators," *ASME J. Mech. Des.*, 129, pp. 1265–1268.

# 3D Object Reconstruction Using a Robot Arm

Cesare Rossi, Sergio Savino and Salvatore Strano

**Abstract** A technique for a vision application is proposed by means of which it is possible to obtain the three dimensional reconstruction of surfaces and objects. This technique uses a number of images from a single camera that is moved around the object by a robot arm. In this way the calibration of the video system is no more necessary because the robot kinematics is known. The images are processed by an algorithm that has been developed starting from our previous investigations on computer vision applied to robotics. The reconstruction of the images can be easily used to reproduce the object itself by means of tools installed on a robot arm. Some examples are given.

**Keywords** Kinematics · Manipulators · Vision system · 3D Volume reconstruction

## Introduction

Vision systems represent a very suitable tool in many robotic applications. In some previous investigations [1–6], vision applications to robot arms was investigated. The main aim of these studies was to find a suitable technique by means of which it could be possible to obtain vision system calibration, robot arm mechanical calibration and trajectories recording and planning.

In this paper are presented the early results of three dimensional reconstruction of surfaces and objects by means of a number of images from a single camera that is moved around the object by a robot arm. The main aim of these 3D reconstructions is to obtain, from an object, data files that will be used to make a copy of the object itself by means of a tool fitted on a robot arm or to plan a working cycle for the filament winding manufacturing. Actually, this last technique is generally confined to cylindrical shaped parts; by means of a suitable robot arm, it could be used also for the manufacturing of more complex parts.

---

C. Rossi (✉)

University of Napoli “Federico II”, via Claudio, 21 – 80125 Napoli, Italy  
e-mail: cesare.rossi@unina.it

Generally, 3D reconstruction of objects has become an intensive research topic in Computer Vision. Digital 3D models are required in many applications, such as industrial inspection, biomedical, navigation, objects identification, replication of 3D solid, rapid prototyping, etc.

Usually, high quality 3D models of static objects are obtained using *scanners* systems, generally expensive, but easy to handle. The explosive growth in computer's processing, in terms of computational power and memory storage, and its continuous reducing price, together with the development of more and more sophisticated and affordable digital cameras, allowed the practical use of photogrammetric methods (photogrammetric method determines geometric properties about objects from photographic images) for 3D reconstruction. In fact, they appear now has a low cost and portable alternative to the common 3D reconstruction methods. However, image based reconstruction is still a difficult task, in particular for large or complex objects.

The next subsection will focus on one commonly used image-based reconstruction methods: *Shape From Silhouettes*.

## 3D Reconstruction

### *Shape from Silhouettes*

Shape from silhouettes is well-known technique for estimating 3D shape from its multiple 2D images.

The procedure is divided in three step:

- By the first step the multiple views images of the object are obtained;
- By the second step silhouettes from the images are obtained;
- In the third step 3D reconstruction are implemented in order to obtain data of object shape.

Intuitively the silhouette is the profile of an object, comprehensive of its inside part. In the “Shape from Silhouette” technique silhouette is defined like a binary image, which value in a certain point  $(x, y)$  underlines if the optical ray that passes for the pixel  $(x, y)$  intersects or not the object surface in the scene. Every point of the silhouette, respectively of value “1” or “0”, identifies an optical ray that intersects or not the object (Fig. 1).

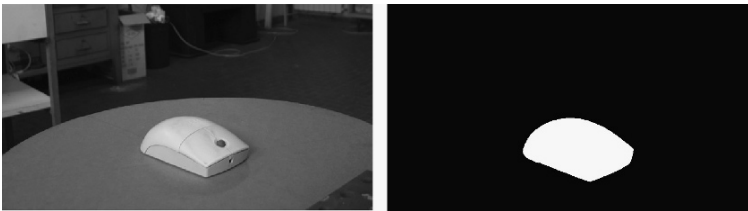
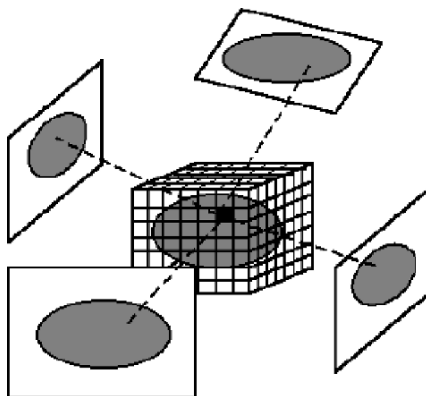


**Fig. 1** A computer mouse: the object acquired image (*left*), the computed object silhouette region (*right*)

**Fig. 2** Space carving technique algorithm scheme



To obtain object volume from silhouettes, we use the space carving technique [7]. A 3D box is modelled to be an initial volume model that contains the object. This box is divided in discrete elements: voxels.

The algorithm is performed by projecting the center of each voxel into each image plane, by means of the known intrinsic and extrinsic camera parameters (Fig. 2). If the projected point is not contained in the silhouette region, the voxel is removed from the object volume model.

By means of this algorithm it is possible to obtain only an approximation of the real three-dimensional object form; particularly it's difficult to reconstruct the object concavities.

The best approximation obtainable from an endless number of silhouette, is denominated “*visual hull*”. It is the maximal form which returns the same silhouettes of the real object for all the external sights of the convex hull of the object [8] (see Fig. 3).

The accuracy of the reconstruction obtained depends on the number of images used, on the positions of each viewpoint considered, on the camera's calibration quality and on the complexity of the object shape.

This justifies the our choice to position the camera on the robot. Infact, in this way we know exactly, not only the characteristics of the camera, but also the position of the camera reference frame in the robot work space. Therefore the camera intrinsic and extrinsic parameters are known without a vision system calibration and it's easy to make an elevated number of photos.

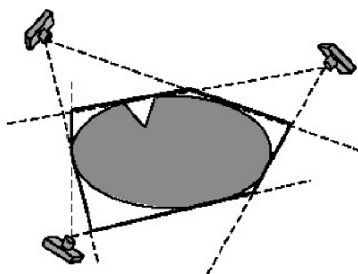


**Fig. 3** Visual hull

Robot positioning errors have no influence on the object reconstruction; this because each photo is acquired and elaborated in a robot configuration that is known by reading the robot feedback signals given by the encoders. With a good robot cinematic calibration the real robot position is known with appreciable precision. For this reason, the robot cinematic calibration [3] becomes very important; in addition, by means of calibration results, it is possible to estimate the vision system extrinsic parameters.

### *Acquisition System*

Our image acquisition system is shown in Fig. 4. One digital camera and a robot prototype, that was designed and built at our laboratory, are used.

The robot performances, like the end-effector (camera) speed or the forces it can exert, aren't limits for the acquisition procedure.

The images have a resolution of  $2592 \times 1944$  pixels and are saved in raw RGB format. The image resolution represents an important parameter for the accuracy in object reconstruction.

By means of a turntable, it is possible to rotate the object, around a vertical axis, of a known angle. These rotations with robot movements allow to capture object images from all its sides and with different angles-shot [9].



**Fig. 4** Acquisition system

### *Implemented Algorithm*

The algorithm is divided in three steps:

1. images analysis and object silhouette reconstruction;
2. calculation of transformation matrix that permits to pass from work space coordinate to each image plane coordinate;

### 3. 3D-solid reconstruction.

Intersections of the optical axes of camera for each positions with  $xy$  reference plane of robot reference system  $Oxyz$ , are evaluated to choose object volume position. Subsequently it is possible to divide the initial volume model in a number of voxels according to the established precision. The centers of voxels are projected into each image plane by means of the pin-hole camera model. In this way it is possible to construct a matrix with the same dimension of image matrix, that has non zero-values only for volume projected voxels. The object silhouette, in the image, is represented by another matrix with non-zero values only for points of silhouette.

The elements of the product among the two matrix that have non-null value are  $ri$ -transformed in the work space and they became the centers of the voxels that must used for the following image.

This procedure is repeated for all images, to obtain the volume object in the robot workspace.

## Experimental Results

The reconstructions of two objects are presented to demonstrate the performance of the algorithm. As displayed in Fig. 5, the test objects are a computer mouse and an mockup head.

For the mouse reconstruction, 8 photos are been used, in Fig. 6 are shown the positions of the 8 frames of camera with the relative images

In Fig. 7 are illustrated the results obtained with the different resolutions that have been chosen; in the figure the reconstructed mouse shape is shown in its position in the workspace of the robot.

The resolution differ in base to the number of voxels in a fixed initial volume, for example to a resolution  $res = n$  correspond  $n^3$  initial voxels. Assuming a initial box with sides length  $x y z$ , the tolerances corresponding to each edge are  $x/res$ ,  $y/res$ ,  $z/res$ .

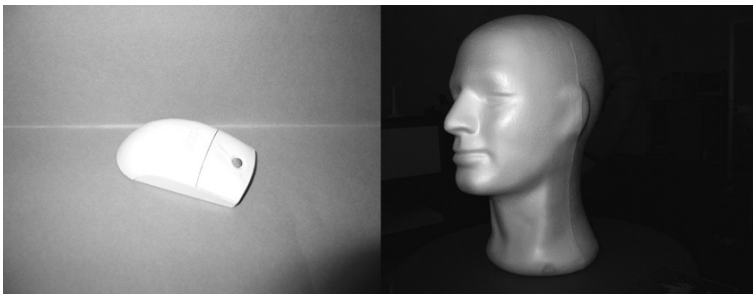
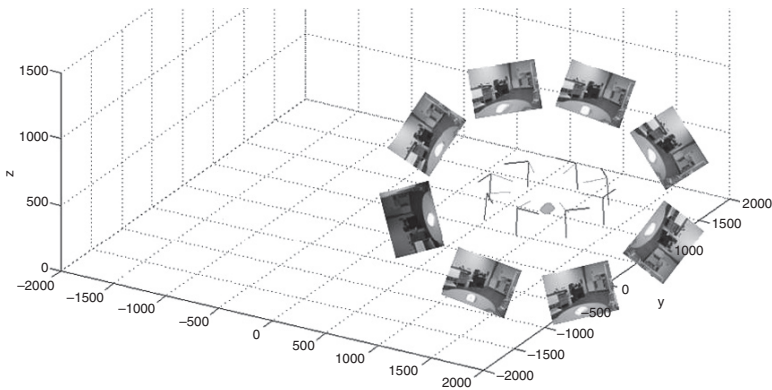
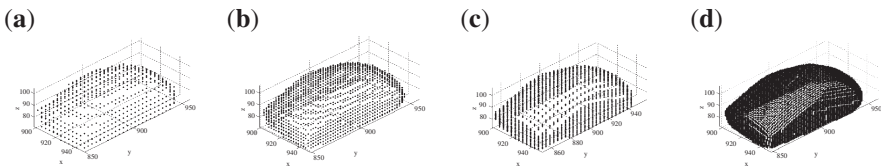


Fig. 5 Test objects



**Fig. 6** Camera positions and relative images



**Fig. 7** Reconstructed computer mouse: (a) res = 50, (b) res = 80, (c) res=100, (d) res = 150

Mouse reconstruction obtained with an initial resolution of  $150^3$  voxels, gives a linear accuracy of 1.33 mm along the direction  $x$ , 1.33 mm along the direction  $y$  and 0.67 mm along direction  $z$ .

The reconstruction resolution influences the time that is necessary for images elaboration. The computing time needed by the implemented software procedure is proportional to initial voxels number, and images number. For example, the reconstruction of the mouse, made with 8 photos and  $150^3$  voxels, was obtained in about 6 minutes. A software optimization is necessary to reduce computing time.

The same test has been carried out on a more complex shape, like a mockup head.

For the reconstruction of the head, 24 photos are been used, in Fig. 8 are shown the results for the various chosen resolutions.

In this case, reconstruction obtained with an initial resolution of  $160^3$  voxels, showed a linear accuracy of 1.875 mm along the direction  $x$ , 1.875 mm along the direction  $y$  and 2.50 mm along direction  $z$ .

Reconstruction with 24 photos and  $160^3$  voxels, was obtained in about 90 minutes.

With the data of object shape, it is possible to plan a robot trajectories to reproduce the object form in any point of the robot workspace, in any position and with any scale factor.

An example of trajectory is a continuous line that is bundled up around reconstructed form, passing for all characterized points. In this way a filament winding



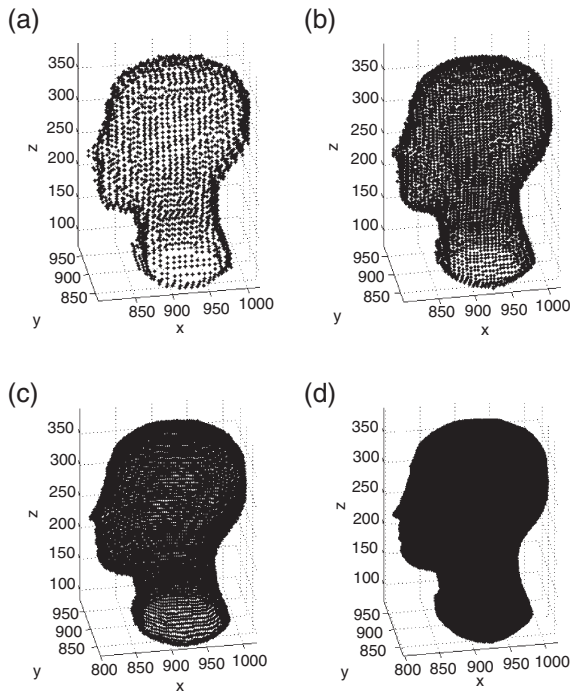


**Fig. 8** Reconstructed head: (a) res = 50, (b) res = 80, (c) res = 100, (d) res = 160

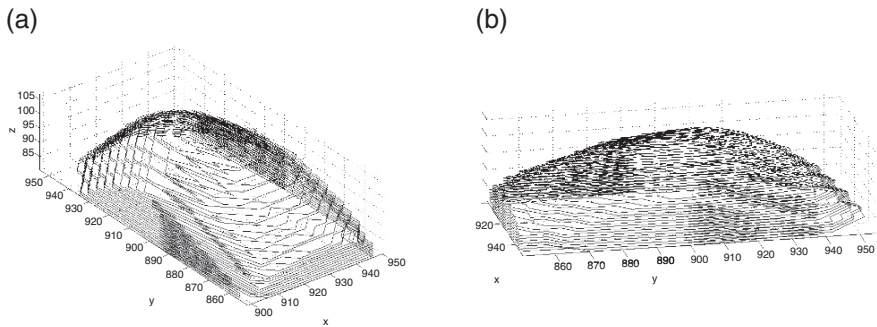


**Fig. 9** Robot trajectory to reproduce the mockup head

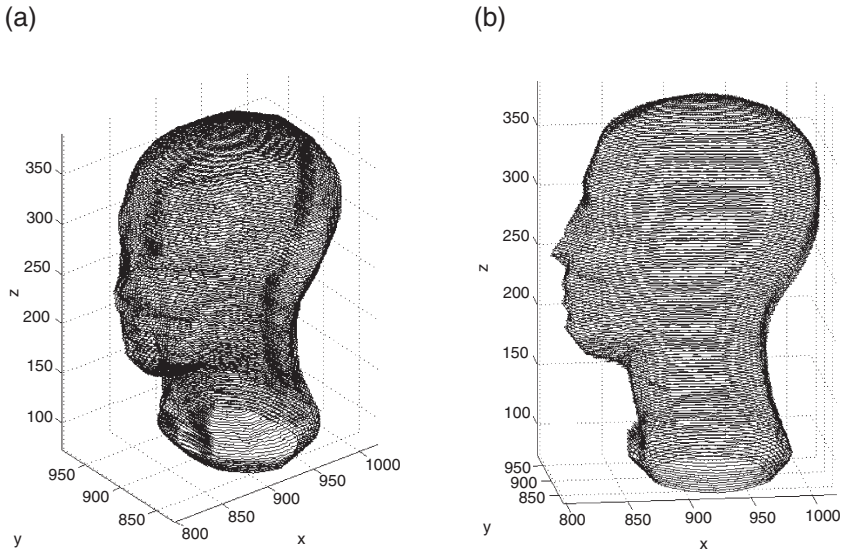
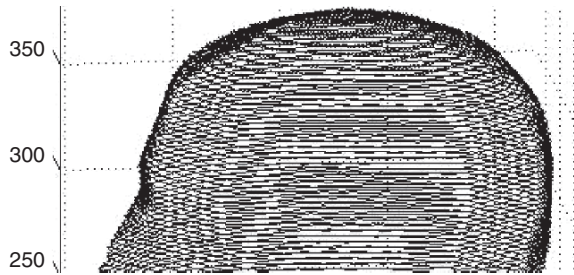


**Fig. 10** Robot trajectory to reproduce the mouse

**Fig. 11** Detail of robot trajectory to reproduce mockup head



process is simulated. In Figs. 9 and 10 are shown this kind of trajectories for computer mouse and for mockup head, respectively.

In Fig. 11 is shown a detail of mockup head trajectory, in which it is possible to observe the continuous line that approximates the 3D path.

## Conclusions

Early results of a 3D reconstruction technique, that use a camera on board of robot, are presented. The technique uses an algorithm that is based on Shape From Silhouettes reconstruction method and space carving method, to obtain the object shape.

The main aim of this activity is to study the possibility to introduce a vision system in robotic application to acquire data of object shape and to plan robot trajectories that can reproduce that shape.

## References

1. V. Niola, C. Rossi “Video acquisition of a robot arm trajectories in the work space”. WSEAS Transactions on Computers, Vol. 4, No. 7, July 2005, pages 830–836.
2. V. Niola, C. Rossi, S. Savino “Perspective transform in robotic application”. WSEAS Transaction on Systems, Vol. 5, No. 4, April 2006, pages 678–684.
3. V. Niola, C. Rossi, S. Savino “A robot arms cinematic calibration method”. WSEAS Transaction on Systems, Vol. 5, No. 4, April 2006, pages 833–838.
4. V. Niola, C. Rossi, S. Savino “A camera model for robot trajectories recording”. Transaction on Computers, Vol. 5, No. 2, February 2006, pages 403–409.
5. C. Rossi, G. D’Orsi, A. Proni, V. Ciccarelli “Early experimental tests on a vision system for robot mechanical calibration”. Proc. RAAD’06, 15th International Workshop on Robotics in Alpe-Adria-Danube Region, June 15–17, 2006, pp. 55–62.
6. V. Niola, C. Rossi, S. Savino “Vision system for industrial robots path planning”. International Journal of Mechanics and Control, 2007, pages 35–45 ISSN: 1590-8844.
7. T. H. Chalidabhongse, P. Yimyam, P. Sirisomboon “2D/3D Vision-Based Mango’s Feature Extraction and Sorting” – ICARCV 2006 (1–6).
8. M. Sabbadini “Ricostruzione volumetrica da sagome”. Tesi di laurea – A.A. 2001-02 Università degli studi di Verona.
9. V. Fremont, R. Chellali, “Turntable-based 3D object reconstruction”. Proc. IEEE Conference on Cybernetics and Intelligent Systems, Singapore, 2004, pages 1276–1281.

# Considerations on Process Performance in Incremental Forming by Inducing High Frequency Vibration

D. Mundo, G. Gatti, G. Ambrogio, L. Filice and G. A. Danieli

**Abstract** The paper is focused on the formability and other specimen characteristics obtained in Single Point Incremental Forming (SPIF) processes. In particular, it is known that friction heavily affects the results because the deformation is very localized at the contact between punch and sheet. Despite the presence of the lubricant, some effects are evident, such as the material wear, the staircase shaping and the geometry torsion.

Finally, it is reasonable to think that the effect is also played on the allowable formability and then, like in other metal forming processes, a high frequency oscillation is imposed to the sheet in order to minimize the friction effect.

The results are accurately discussed in the paper.

**Keywords** Single Point Incremental Forming · Vibrations · Formability · Friction

## Introduction

Incremental Forming processes have been recently introduced in the manufacturing scenario and, for this reason, many aspects related to their mechanics are not well explained, despite the relevant effort spent by several researchers all over the world [1–4].

Among the most interesting aspects, formability plays a strategic role since, in this sense, the process efficiency is very high as compared to the traditional stamping processes. In fact, the strain that the sheet can tolerate is higher than in drawing processes.

In technical literature, many papers focused on material formability and other relevant issues in Incremental Forming can be recognised, and the role of the main

---

D. Mundo (✉)

Dipartimento di Meccanica, Università della Calabria, Via P. Bucci, 87036,  
Arcavacata di Rende (Cs), Italy  
e-mail: d.mundo@unical.it

process parameters is accurately discussed. Among these parameters, friction represents a key-factor since it is responsible for the sheet wear, especially when a small pitch (i.e. the distance between two sequential coils) is selected. This wear can exalt the local material thinning resulting in an early failure.

Furthermore, friction induces a sort of torsion action on the profile that causes a geometrical error on the final obtained geometry. Up to now the friction is reduced as much as possible utilising two ways: the use of punches characterised by a grinded surface and the use of a suitable lubricant, typically mineral oil.

In this paper, a strategy for exalting the lubrication action is implemented, according to other researches which applied an analogue technique to other metal forming processes. The logic is based on the reduction of friction that automatically results in an increasing formability or, anyway, in the improvement of process robustness. In particular, an experimental equipment was set up with the aim to generate high frequency vibrations into the sheet. This method allows the cyclic instantaneous detachment between sheet and tool which induces two immediate advantages: the relaxation of the axial induced stress and the lubricant inflow between working material and tool.

A commercially pure Aluminium Alloy (AA1050) sheet, 0.5 mm thick, was used as raw material. The vibration has been generated using a proper resonator, connected to the sheet, and driven by a wide spectrum function generator. The main results are discussed in the follow.

## Remarks on the SPIF Process

Single Point Incremental Forming is characterized by a peculiar process mechanics which makes such technology very far from conventional sheet metal stamping. Here, in fact, plastic strain is accumulated through the progressive and incremental application of localized deformations at the interface punch-blank.

Several studies were performed with emphasis on assessing and improving the formability in this forming method [5], Iseki and Kumon [6] performed the incremental stretching test for various materials and found that the FLCs are approximately linear. Kim and Park [5] proposed the double-forming technique to improve formability, assuming that only shear deformation occurs in the material. Shim and Park [7] performed a series of experiments and suggested the straight groove test as a method to assess the formability for annealed Aluminum sheet. In addition to these results, subsequently, Kim and Park [8] observed that formability differs according to the direction of the tool movement.

It's quite evident that the total amount of deformation depends on the draw angle  $\alpha$  (Fig. 1), but it is achieved through the "sum" of small localized deformations. The latter, in turn, depends on the size of the step down  $\Delta z$ , between two subsequent loops of the tool. It's obvious that the values of the step down  $\Delta z$  and of the step inward  $\Delta x$  must be combined in such a way to ensure the desired slope, but the size of  $\Delta z$  actually determines the value of the localized deformation applied at each step.

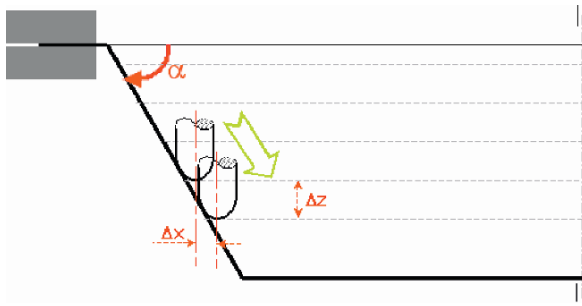


Fig. 1 Single Point Incremental Forming base dimension sketch

At the same time, a relevant role is also played by the process parameters, such as the tool diameter of the tool depth step, utilised during the process, and the friction conditions, due to the continuous sliding on the 3D trajectory. More in detail, on this second topic is focalised the study carried out, aimed to find newer solution to improve the process efficiency reducing the friction negative effects.

### The Experimental Work

An experimental rig was set up in order to support the sheet metal blank properly and induce vibrations into it during the SPIF process.

Harmonic excitation is induced by means of a permanent magnet shaker connected to the sheet using a steel stinger. This allows for in-plane oscillating components to be reduced, so that investigation of out-of-plane vibrations only may be performed [9].

Previous experimental tests showed that, far away from the manufacturing region, material slide during SPIF is negligible and this allows for the vibrating system to be just laid down on the machine base.

In order to select the point of application of the harmonic force excitation and its frequency, numerical simulations are preliminarily carried out on the sheet metal blank.

### Numerical Simulations

Numerical simulations were performed in order to estimate the mode-shapes of vibration and the corresponding natural frequencies [10] in the plastic-undeformed sheet. The FE software Msc-Nastran was used for computation of the structural vibrations. The real eigenvalue analysis was obtained by Nastran solution sequence SOL103. The boundary conditions for the plate are specified as clamped edges [11] and the following geometrical and material properties were used for simulation: plate dimensions  $200 \times 200 \times 0.5 \text{ mm}^2$ , Young's modulus  $Y=70 \text{ kN/mm}^2$ , Poisson's

ratio  $\nu=0.33$ , mass density  $\rho=2700 \text{ kg/m}^3$ . First, second, fourth and fifth mode-shape are shown as fringe contour plots in Fig 2a– 2d. and corresponding natural frequencies are also indicated. Second and third mode-shape are rotated  $90^\circ$  with respect to each other. Figure 2b shows, in fact, results for the second mode only. Due to plate symmetry, natural frequencies for these two latter modes coincide. In Fig. 2a–2d, white zones indicate a null out-of-plane displacement, which corresponds to either a clamped boundary region or a nodal line for the actual mode of vibration.

If the point of excitation is placed at a nodal line, the corresponding mode of vibration is not excited. Besides, if the plate vibrates according to a single mode, no out-of-plane displacement occurs on the corresponding nodal lines.

From the above consideration, it follows that the exciting frequency could be properly selected by focusing on the shape of the vibration mode related to the shape of the final manufactured part.

Mode 1 (Fig. 2a) is axially symmetric, which means that, if the excitation frequency is tuned to the first natural frequency, points laying on a circle centred on the plate will all vibrate harmonically in-phase with the same amplitude. No nodal lines exist for this mode. Exciting the sheet metal blank at that frequency could thus be effective when manufacturing axially symmetric parts. However, most of the energy supplied to the plate by the auxiliary vibrating system will be lost in the most inner region of it, partially affecting the manufacturing process.

On the other hand, mode 5 (Fig. 2d) is characterized by two nodal lines along the plate's diagonals. Maximum energy is located approximately at  $0.2L$  from each

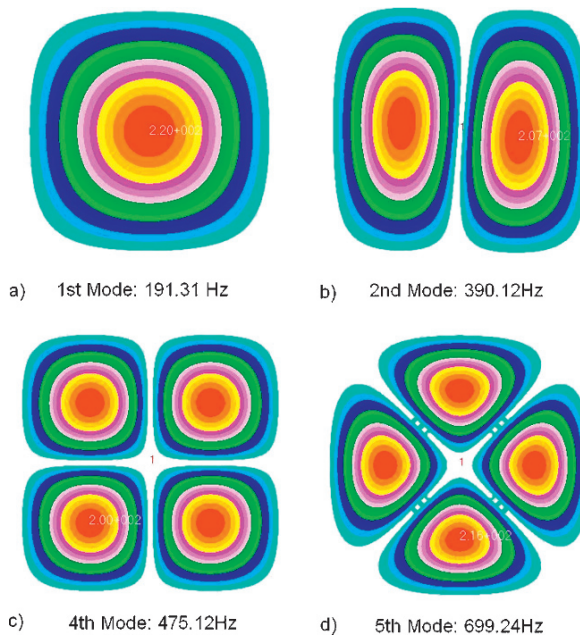


**Fig. 2** Mode-shapes and corresponding natural frequencies for the plate

edge,  $L$  being the dimension of the plate sides. This could be possibly effective when forming squared-section products with vertices on the nodal lines.

Nevertheless, the following consideration are possible. Natural frequencies, as theoretically calculated, are largely affected by the actual structure's boundary conditions, which may be different from the ideal constraints assumed earlier for simulation. Furthermore, the auxiliary wooden die (baking plate), could also affects those results. Mode-shapes are, conversely, only partially affected by boundary conditions' changes, especially at lower frequencies.

It is also worth to notice that results shown in Fig. 2 refer to the sheet metal blank in its plastic-undeformed condition. This means that, as plastic deformation occurs and the product starts forming, mode-shapes and frequencies change. These effects could be investigated in future works.

### ***Experimental Rig***

All the experiments were executed keeping fixed some process parameters ( $D_p=18$  mm,  $p=0.3$  mm and thickness  $s=0.5$  mm and tool rotation speed  $s=120$  r.p.m.) and two pairs of experimental test were planned as follows. In the first pair, the metal sheet was excited at its first natural frequency, while in the second the fifth natural frequency was used. In each pair of test, a rounded-section and a squared-section part are manufactured. Following the discussion in the previous section and with reference to Fig. 2, the point of excitation is selected to be at  $0.5L$  from the lower edge and at  $0.2L$  from the right one. In this configuration either the first or the fifth mode can be effectively excited. A hole is drilled through the baking plate to allow the connection of the shaker stinger to the metal sheet.

A suitable supporting frame was manufactured as shown in the Figs. 3 and 4. A permanent magnet vibration shaker (LDS V201/3) was used to excite the metal



**Fig. 3** Experimental rig



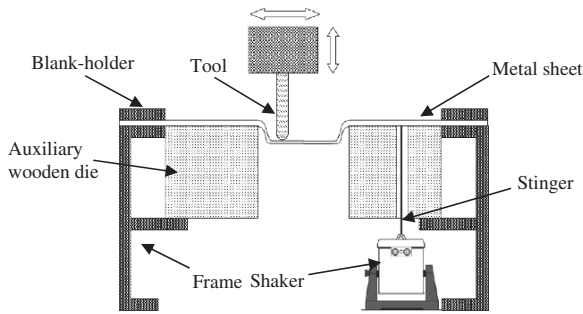


**Fig. 4** Sketch of the experimental rig (vertical section)

sheet through a 15 mm steel stinger placed on its bottom side. Armature resonance frequency of the shaker is 13 kHz and nominal power is 48 W. The signal from a frequency generator is then fed to the shaker through a power amplifier unit.

### *Experimental Validation*

In order to tune the excitation frequency of the shaker to the actual resonance frequency of the sheet, an experiment was conducted to measure its actual vibrational response. The sheet metal blank was mounted in place and fixed by the blank-holder. A modal test was performed using a frequency analyzer (LMS Scadas III), an instrumented impulse hammer (PCB 086C03) and a ceramic shear ICP accelerometer (PCB 333B32). A bandwidth of 1 kHz with 1024 spectral lines was selected for acquisition. With reference to Fig. 2, the response of the plate was measured at point located at  $0.2L$  from the left edge and  $0.5L$  from the lower, while it is excited at a point symmetric to the former. LMS TestLab software was used for signal acquisition and processing. A 5-averaged frequency response function is calculated and the first and fifth resonance frequency of the actual plate are estimated to be 200 Hz and 680 Hz respectively.

### **Results and Discussion**

The two pairs of tests described in Section *Experimental Rig* were performed. Experimental results qualitatively confirm the expectations.

Formability limit can be effectively represented by the maximum slope angle. In the investigated case, in normal conditions, it is more or less  $65^\circ$ , using the given parameters.

Formability increasing is slightly shown even if its amount is limited to about  $2.5^\circ$ . In terms of thinning the increasing is a bit less than 10%, as summarized in Table 1. At the same time, a better surface roughness was obtained, mainly due to the reduction of the wear phenomenon.

**Table 1** Performance of the SPIF process with and without vibrations

	Without vibration	With Vibration
Maximum slope	Up to 65°	Up to 67.5°
Thinning	58%	62%
Torsion effect	Evident	Less evident

Finally, a substantial reduction of the torsion effect due to the torque applied to the specimen by the punch, during the process, was observed.

The latter constitutes a good news in term of dimensional accuracy.

Results are promising and suggest that further investigation could be part of future developments even if the effects are less evident respect to other processes in which the contact surfaces are larger.

In order to overcome the limitation highlighted in Section *Numerical Simulations*, adaptive feedforward and feedback control of vibration could be used to tune the forcing amplitude and frequency in real-time as the manufacturing process develops. Such a control strategy will possibly improve the whole SPIF process further.

## Conclusions

Single Point Incremental Forming processes are heavily affected by the friction at the interface between the forming punch and the sheet. The use of simple lubricant (usually mineral oil), substantially reduces these effects but some consequences remain. The strategy discussed in this study, based on inducing a high frequency oscillation into the sheet, supplies interesting results if some critical issues are considered. In detail, it is possible to summarize the following issues:

- formability slightly increases thanks to the reduction of the localized wear and stress induced by the punch action on the sheet;
- the surface quality is higher as compared to the one obtained in the conventional process;
- the distortion effect on the geometry due to the torsion of the specimen is less evident.

For above reasons, it is possible to state that although more efforts have to be spent in that direction, the use of the proposed strategy seems very promising to improve the overall performance of SPIF process.

**Acknowledgments** This work was funded by Italian Ministry for Education, University and Scientific Research (M.I.U.R.).

The authors would like to thank EP Francesco Pulice for his support during experimental equipment development.

## References

1. Filice, L., Fratini, L., Micari, F., 2002, Analysis of material formability in incremental forming, *Annals of CIRP*, 51/1, 199–202.
2. Kim, T.J., Yang, D.Y., Improvement of formability for the incremental sheet metal forming process, 2000, *International Journal of Mechanical Science*, 42, 1271–1286.
3. Yoon, S.J., Yang, D.Y., 2003, Development of a highly flexible incremental roll forming process for the manufacture of a doubly curved sheet metal, *Annals of the CIRP* 52/1, 201–204.
4. Filice, L., Fratini, L., Micari, F., 2003, Perspectives for enhancing formability and flexibility in sheet metal stamping, *Journal of the Japan Society for Technology of Plasticity*, 44, 397–400.
5. Kim, Y.H., Park, J.J., 2002, Effect of process parameters on formability in incremental forming of sheet metal, *Journal of Materials Processing Technology*, 130–131, 42–46.
6. Iseki, H., Kumon, H., 1994, Forming limit of incremental sheet metal stretch forming using spherical rollers, *Journal of JSTP*, 35, 1336.
7. Shim, M.S., Park, J.J. 2001, Deformation characteristics in sheet metal forming with small ball, *Trans. Mater. Process. J. JSTP*, 113, 654.
8. Park, J.J., Kim, Y.H. 2003, Fundamental studies on the incremental sheet metal forming technique, *Journal of Materials Processing Technology*, 140, 447–453.
9. Lal, R., Dhanpati, Transverse vibrations of non-homogeneous orthotropic rectangular plates of variable thickness: A spline technique, *Journal of Sound and Vibration*, 306(1–2), 203–214.
10. Shu, C., Wu, W.X., Ding, H., Wang, C.M., 2007, Free vibration analysis of plates using least-square-based finite difference method, *Computer Methods in Applied Mechanics and Engineering*, 196(7), 1330–1343.
11. Shimon, P., Richer, E., Hurmuzlu, Y., Theoretical and experimental study of efficient control of vibrations in a clamped square plate, *Journal of Sound and Vibration*, 282(1–2), 453–473.

# Scheduling and Verification of Micro Assembly Processes

Kerstin Schöttler, Arne Burisch, Annika Raatz and Jürgen Hesselbach

**Abstract** This paper presents the scheduling and verification of automated micro assembly processes for which assembly accuracies of a few micrometers are necessary. To reach these accuracies, a relative positioning strategy was used. Possible solutions for the scheduling and verification of two micro assembly processes carried out by a size-adapted assembly system are introduced. These processes reached a positioning uncertainty on the range of 0.5 . . . 1  $\mu\text{m}$  and part dependent assembly uncertainties of 24  $\mu\text{m}$  and 45  $\mu\text{m}$ .

**Keywords** Micro assembly · Relative positioning processes · Size-adapted assembly systems

## Introduction

Micro system technology (MST) is a key technology for emerging markets. The third “NEXUS Market Analysis” has estimated a projected market growth for 1st level packaged Microsystems and MEMS from US\$ 12 billion in 2004 to US\$ 25 billion in 2009 [1].

For hybrid micro systems, assembly accuracies within a range of a few micrometers are required. In order to reach these accuracies, a size-adapted assembly system for sensor guided micro assembly was developed and will be presented in this paper. A relative positioning strategy was used for the micro assembly processes.

Until today, no standardized method for the verification of micro assembly processes exists. This leads to a different understanding of the reached process precision and accordingly to a difficult comparability. In order to bridge this gap, this paper describes the influences on micro assembly processes and defines terms for the quantification of them. The presented process scheduling shows a pre-calculation method for the assembly uncertainty, which is dependent on the geometry of the

---

K. Schöttler (✉)  
Institute of Machine Tools and Production Technology, Technische Universität Braunschweig,  
Langer Kamp 19 B, 38106 Braunschweig, Germany  
e-mail: k.schoettler@tu-bs.de

assembled parts. The scheduling and verification of micro assembly processes with regard to the part geometry will be explained by discussing two examples of assembly processes.

## Size-Adapted Assembly System

The size-adapted assembly system (Fig. 1, left) consists of a serial hybrid robot micabo<sup>f2</sup>, which provides a high positioning accuracy due to its structure, and an integrated 3D vision sensor (Fig. 1, right) using one camera. Additional components are an assembly fixture and part trays for the adjustment of parts inside the robot's workspace. High flexibility is obtained through product specific part trays and diverse grippers, e.g. vacuum grippers with different nozzles and mechanical grippers [2].

### Serial Hybrid Robot Micabo<sup>f2</sup>

At the Institute of Machine Tools and Production Technology (IWF) a size-adapted serial hybrid robot micabo<sup>f2</sup> [2] was developed for precision assembly. The robot has 4 degrees of freedom (DOF) for part handling and 1 DOF for focusing a vision sensor. The workspace measures  $160 \times 400 \times 15 \text{ mm}^3$ ; and according to EN ISO 9283 accuracy measurements, the robot achieved a repeatability of  $0.6 \mu\text{m}$ . This high repeatability is a good precondition for a precision assembly process.

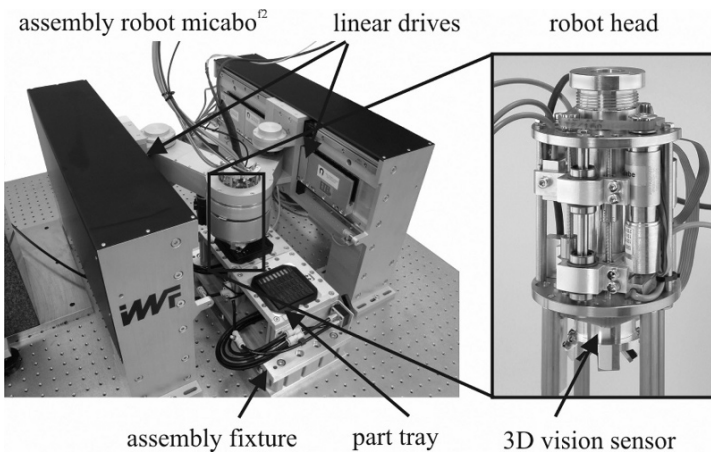


**Fig. 1** Size-adapted assembly system

### ***3D Vision Sensor***

The 3D vision sensor was developed at the Institute of Production Measurement Engineering (IPROM), Technische Universität Braunschweig. As this sensor applies the principle of stereo photogrammetry, it requires only one camera to generate a single image for 3D image processing. This is achieved with a 3-dimensional reconstruction of the objects from the pair of images. The field of vision has a dimension of 11 mm in length and 5.5 mm in width with a resolution of 19  $\mu\text{m}/\text{pixel}$ . Repeatability measurements showed standard deviations of  $\sigma_x=0.22 \mu\text{m}$  and  $\sigma_y=0.29 \mu\text{m}$  [3].

### **Relative Positioning Strategy**

Absolute and relative positioning strategies can be used for sensor guided assembly processes. In absolute positioning processes only one correction step is possible, as the position vectors of the two parts or groups to be assembled are measured in separate positions. After this one correction step, no further position vectors from both parts/groups can be created.

Using a relative positioning strategy offers the opportunity to complete multiple correction steps. This is a result of a simultaneous measurement of both parts/groups with the same sensor system. The relative positioning strategy is used for the latter described automated micro assembly processes, as the multiple correction steps offer an improved assembly uncertainty when compared with the absolute positioning strategy. At present, the relative sensor guidance works according to a so called “look-and-move” procedure. This means that the robot’s movement stops before a new imaging process starts and a new position correction is executed.

Circular positioning marks are used as a feature for the relative positioning process. During the manufacturing of the parts to be assembled, marks are introduced by means of a photolithographic process. These marks are used for quality control of the parts before the process. During the process, these marks are used for the sensor guidance as well as evaluation of the positioning uncertainty. Lastly, these marks provide a way to evaluate the assembly uncertainty after the process has completed.

## **Scheduling of Micro Assembly Processes**

### ***Influences***

The influences on the accuracy of automated micro assembly processes must be known before the process scheduling is executed. The main influences are:

- Tolerances of the assembly robot
- Measurement uncertainties of the vision system
- Stable environmental conditions (temperature, lighting)

- Tolerances in geometry of the assembled parts
- Tolerances in clamping devices and part trays
- Tolerances due to the joining process

### *Definitions for Quantifying Micro Assembly Processes*

The terms positioning uncertainty and assembly uncertainty are introduced to enable quantifiable results of the micro assembly processes. According to DIN ISO 230-2 the positioning uncertainty is the combination of the mean positioning deviation and the double standard deviation. For precision assembly processes, the term positioning uncertainty refers to the reached relative position between the assembly parts before the bonding process is carried out (in this case the handled part is above a fixed substrate part and has no contact).

The term assembly uncertainty describes the relative position between the assembled parts as measured after the assembly process has been completed. This is the combination of the mean assembly deviation and the double standard deviation.

### *Process 1 – Assembly of a Micro Linear Stepping Motor*

In the first process, a micro linear stepping motor [4], which works according to the reluctance principle, has to be assembled. The motor parts were mainly manufactured with micro technologies developed at the Collaborative Research Center 516. One of the assembly tasks is the assembly of guides on the surface of the motor's stator element. In Fig. 2 the assembly group of two guides on a stator is shown.

The circular positioning marks (4 on the stator and 2 on each guide) are measured by the 3D vision sensor and a resulting relative position vector is calculated and given to the control of the assembly system. Inside the controller, the relative position vector is separated into a rotation correction, a correction in  $xy$ -direction, and finally the correction in  $z$ -direction, which places the guide.

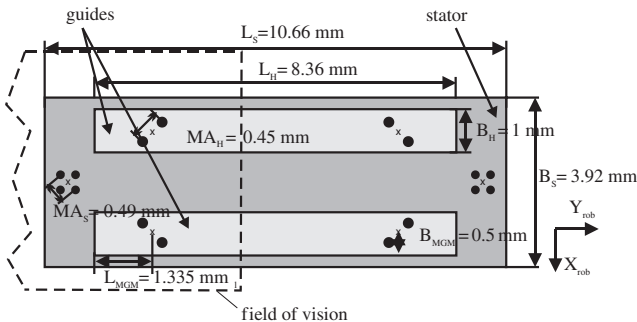


**Fig. 2** Micro linear stepping motor

The assembly steps for both guides are equal. To assemble one guide, the following steps are executed:

1. Marks on the stator are checked.
2. Marks on the guide are checked.
3. Gripping the guide and moving it to a pre-defined position above the stator.
4. Relative positioning process executed.

If the relative positioning vector reaches the pre-defined offset limit value of  $0.2^\circ$  around the  $z$ -axis and  $0.8 \mu\text{m}$  in  $x$ - and  $y$ -direction, a final relative position correction is carried out by moving the robot in the  $z$ -direction (height). This completes one positioning process. Currently the guides are bonded onto the stator element with cyanoacrylate.

During the process only one end of the assembled parts can be measured, as the gripper covers the other half of the guide and stator (see Fig. 3). Therefore the relative positioning device observes only one visible side of the assembled parts. This means that the measured positioning error and the resulting positioning uncertainty are only determined by the visible group of marks on the assembled parts. After the process, both ends of the assembly group can be inspected and the overall assembly deviation can be measured. From the deviation measurements, the assembly uncertainty is calculated.

A small angular deviation leads to a larger positioning error (in  $xy$ -direction) on the side of the part which is hidden during the sensor guided positioning process, than that of the visible side (Fig. 4). To this effect, as the part length increases so will the associated positioning error.

The theoretical reachable assembly uncertainty was pre-calculated regarding the part geometry and the measurement uncertainty of the 3D vision sensor. For the measurement uncertainty of the 3D vision sensor a value of  $MU=0.5 \mu\text{m}$  is

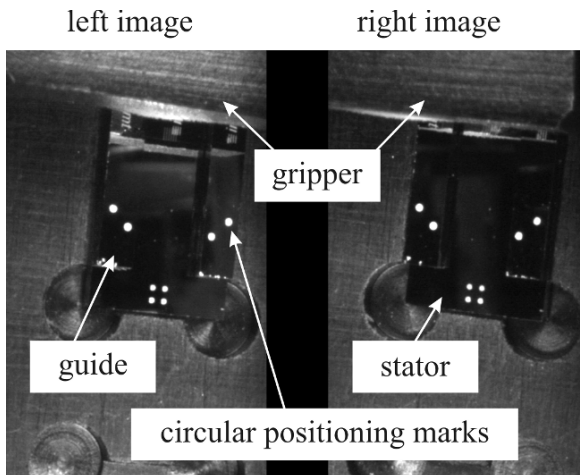


Fig. 3 View from the 3D vision sensor of the micro linear stepping motor



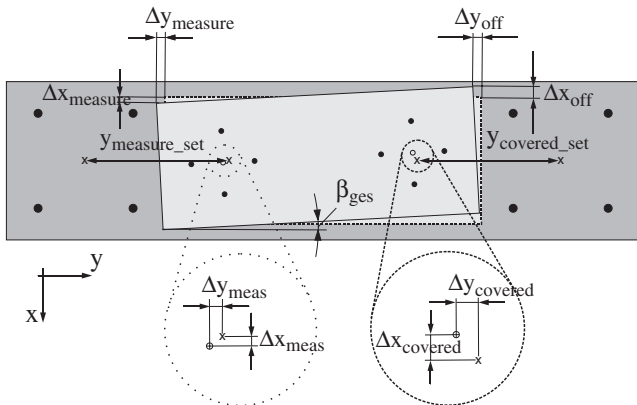


Fig. 4 Errors resulting from geometry

assumed with respect to the former mentioned repeatability measurements. The measurement uncertainty and the small distance between the positioning marks (see Fig. 2) of  $MA_H = 0.45$  mm (guide) and  $MA_S = 0.49$  mm (stator) leads to an angular error of  $\beta_{ges}$  (equation 1). Due to the relative large part length of  $L_H = 8.36$  mm of the guide, an assembly uncertainty of  $30.3 \mu\text{m}$  in  $x$ - and  $2.7 \mu\text{m}$  in  $y$ -direction was pre-calculated with equations 2 and 3.

$$\beta_{ges} = a \tan\left(\frac{2 \cdot MU}{MA_H}\right) + a \tan\left(\frac{2 \cdot MU}{MA_S}\right) \tag{1}$$

$$\Delta x_{off} = MU + (L_H - L_{MGM}) \cdot \sin \beta_{ges} + (B_H - B_{MGM}) \cdot (\cos \beta_{ges} - 1) \tag{2}$$

$$\Delta y_{off} = MU + (L_H - L_{MGM}) \cdot (1 - \cos \beta_{ges}) + (B_H - B_{MGM}) \cdot \sin \beta_{ges} \tag{3}$$

### Process 2 – Assembly of Test Geometries

A relatively high assembly uncertainty was pre-calculated in the assembly scheduling of the micro linear stepping motor. The assembly uncertainty shall be improved with the design of test geometries. These two test geometries (handling device and substrate) are therefore provided with circular positioning marks with a large distance between the marks (Fig. 5). The marks on one side of the two assembled parts almost cover the field of vision of the 3D vision sensor. The parts are designed with a larger width then the guides of the first process.

The assembly steps for the test geometries are similar to the assembly of the micro linear stepping motor. For this assembly process, the relative positioning

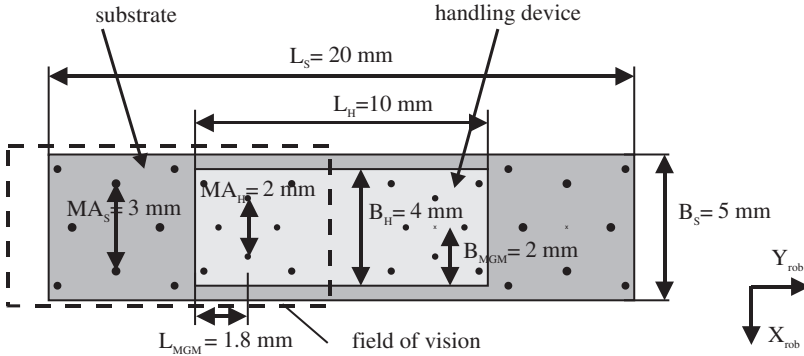


Fig. 5 Test geometries

vector reaches an offset limit value of  $0.05^\circ$  around the  $z$ -axis and  $0.4 \mu\text{m}$  in  $x$ - and  $y$ -directions. When this process is compared to the first, an improvement of a factor of 4 for the angular deviation and an improvement of a factor of 2 for the translational deviation was observed. The reason for this improvement is the enlarged distance between the positioning marks, which enables a more precise angular and translational correction of the relative positions between the assembled parts. These test geometries were also bonded with cyanoacrylate. The reachable assembly uncertainties for the test geometries were pre-calculated to be  $7.3 \mu\text{m}$  in  $x$ - and  $2.2 \mu\text{m}$  in  $y$ -direction. Therefore, an assembly uncertainty in the range of  $10 \dots 20 \mu\text{m}$  is expected regarding further tolerances during the process. If this is an applicable range, it will be verified by the experimental series as well as for the first process.

## Verification of Micro Assembly Processes

The results of two experimental series, each representing one of the described processes respectively are presented. In both cases, the stator or substrate respectively were fixed with a vacuum clamping in the assembly area. The same vacuum gripper and bonding process were used for the processes, to assure comparable processes.

### *Process 1 – Assembly of a Micro Linear Stepping Motor*

For the assembly of the micro linear stepping motor, the experimental series achieves an assembly uncertainty of  $44.88 \mu\text{m}$  and a positioning uncertainty of  $1.06 \mu\text{m}$ . As expected on the basis of the pre-calculation, the assembly uncertainty was much higher than the positioning uncertainty but still in the expected value range. This was the result of the relatively long part size of  $8.36 \text{ mm}$  and the small distances between the positioning marks as mentioned in the description of the assembly planning.

## *Process 2 – Assembly of Test Geometries*

The assembly of the test geometries resulted in an assembly uncertainty of  $24.13\ \mu\text{m}$  and a positioning uncertainty of  $0.53\ \mu\text{m}$ . Compared to the assembly of the micro linear stepping motor, an improvement of 53.77% of the assembly uncertainty has been achieved in the assembly of test geometries. For both assembly processes, the pre-calculated assembly uncertainties were nearly reached.

The verification in this experimental series confirms the former expected enhancement of the positioning and assembly uncertainty due to the enlargement of distances between the positioning marks.

## **Conclusion**

In this paper the scheduling and verification of automated micro assembly processes were presented. A size-adapted assembly system with a workspace of  $160 \times 400 \times 15\ \text{mm}^3$  was used for the automated assembly processes. The system components allow high precision positioning tasks and, using a relative positioning strategy, a positioning uncertainty in the range of  $0.5 \dots 1\ \mu\text{m}$  was obtained.

During the assembly scheduling, the assembly uncertainty was pre-calculated regarding the part geometry and the measurement uncertainty of the 3D vision sensor. On the basis of two experimental series, the scheduled assembly processes was verified. A correlation between the pre-calculated assembly uncertainty and the reached assembly uncertainty was then drawn. The design of test geometries shows that a well directed schedule of the assembly uncertainty is possible.

As the attained assembly uncertainties on the range of  $24\ \mu\text{m}$  and  $45\ \mu\text{m}$  are still too large for micro assembly processes with enhanced requirements on valid deviations, further scheduling and verification steps are necessary to enhance the assembly uncertainty. Therefore, smaller parts in the range of  $1 \times 1\ \text{mm}^2$  to  $3 \times 3\ \text{mm}^2$  with a maximum distance between the positioning marks can be used to give a clear correlation between part size and reachable assembly uncertainty. Furthermore, the influences of tolerances in clamping devices and part trays as well as tolerances due to the joining process can be analyzed by using different process parameters.

**Acknowledgments** The authors gratefully acknowledge the funding of the reported work by the German Research Center (Collaborative Research Center 516).

## **References**

1. Wicht H., Bouchaud J., NEXUS Market Analysis for MEMS and Microsystems III 2005–2009, mst news, Vol. 5, 2005, pp. 33–34.
2. Simnofske M., Schöttler K., Hesselbach J., micabo<sup>2</sup> – Robot for Micro Assembly, Production Engineering, XII(2), 2005, pp. 215–218.

3. Büttgenbach, S., Hesselbach, J., Tutsch, R., Berndt, M., Hoxhold, B., Schöttler, K., Sensor Guided Handling and Assembly of Active Micro-Systems, *Microsystems Technology*, Vol. 12(7), 2006, DOI 10.1007/s00542-006-0088-0, Springer-Verlag, Berlin Heidelberg, S. 665–669.
4. Hahn M., Gehrking R., Ponick B., Gatzel H.H., Design Improvements for a Linear Hybrid Step Micro-Actuator, *Microsystem Technologies*, Springer Verlag, Berlin Heidelberg New York, Vol. 12(7), 2006, pp. 646–649.

# Cambio – A Miniaturized Tool Changer for Desktop Factory Application

Arne Burisch, Christian Loechte, Annika Raatz and Adriano Fabrizi

**Abstract** For desktop factories highly miniaturized assembly robots in conjunction with handling and feeding systems are needed. Thus the size adapted robot *Parvus* was built and tested at the *IWF*. Meanwhile the robot can be equipped with different grippers. For enabling a flexible use of these grippers a tool changer has been designed to extend the functionality of the *Parvus* system. This tool changer, named *Cambio*, is a size adapted system that will allow a complete tool changing within a running assembly process in a future desktop factory.

**Keywords** Miniaturized robot · tool changer · ball coupling system · micro assembly · desktop factory.

## Introduction

Nowadays a trend of miniaturization with regard to product development in several industrial sectors can be observed. The *Nexus III* market study [1] predicts that the market of millimeter-sized MST-products will grow 16% per year. However, an increasing gap can be observed concerning the dimensions and costs between the products and the production systems used. Assembly lines and clean rooms for millimeter-sized products often measure some tens of meters and are mostly too expensive for small- and medium-sized businesses. Thus, many micro-products are assembled by hand, which results in high assembly costs that amount to 20% to 80% of the total production costs [2].

---

A. Burisch (✉)  
Institut für Werkzeugmaschinen und Fertigungstechnik, Technische Universität Braunschweig,  
Langer Kamp 19 b, 38106 Braunschweig, Germany  
e-mail: a.burisch@tu-bs.de

## Miniaturized Robots in Microproduction Systems

Various concepts concerning the reduction of size and costs of micro production systems have been discussed in recent years. Most of these concepts relate to one of the two general groups introduced in the following.

The first group describes small walking micro robots and handling machines that are mostly piezo driven. The second group describes miniaturized robots, or better described as size adapted handling devices, which fill the gap between small walking micro robots and conventional robots. In this case the strategy is to find the highest degree of miniaturization of conventional robot technology using innovative, miniaturized machine parts. With these size adapted handling devices, in the range of several centimeters to a few decimeters, easily scalable and highly flexible production technology can be achieved.

This work is based on the second group, the size adapted robots and desktop factory concepts. They include miniaturized handling systems that are very promising for micro production due to the following assumptions: higher density of functionality, operation in a local clean room cell, higher flexibility of place and configuration, increased accuracies with smaller machine parts, improved dynamic properties due to their reduced mass, lower maintenance costs of small easy manageable systems, lower manufacturing costs of smaller machine parts.

### The Functional Model *Parvus*

The robot *Parvus* is a size adapted handling device and was developed at the *IWF* in cooperation with *Micromotion GmbH*, a manufacturer of micro gears. The *Parvus* is a miniaturized precision industrial robot with the full functional range of larger models.

The robot consists of a hybrid parallel structure, driven by *Micro Harmonic Drive* [3] gears combined with *Maxon* electrical motors. The plane parallel structure offers two translational degrees of freedom in the  $x$ - $y$ -plane. The  $z$ -axis is integrated as a serial axis in the base frame of the robot and moves the whole plane parallel structure in  $z$ -direction. The rotational hand axis  $\Psi$  was designed with a hollow rotational axis as the Tool Center Point (TCP) of the parallel structure. This allows media, such as a vacuum, to be passed along the hand axis. This axis, with a diameter of 2.5 mm, can be equipped with several grippers, e.g. vacuum grippers. Further details are given by the technical specifications in Table 1.

The development of the *Parvus* including its fundamentals, the miniaturized drive systems and the robot design approaches have already been discussed in several previous papers [4, 5].

### Grippers for the *Parvus*

For the first pick-and-place applications the *Parvus* was equipped with two different types of grippers. For gripping glass balls with a diameter of 1.5 mm the *Parvus* used

**Table 1** Technical specifications of the first prototype *Parvus*

Criterion	Value	Unit
Workspace (xy, absolute)	4658	mm <sup>2</sup>
Workspace (max. cubical)	60 × 45 × 20	mm <sup>3</sup>
Footprint	100 × 53	mm <sup>2</sup>
Robot cell	130 × 170	mm <sup>2</sup>
Resolution max. (xy-plane)	< 1	μm
Repeatability (best, worst)	5.9, 14.1	μm
Linear speed	> 100	mm/s
Rotational speed (Ψ axis)	187*/60**	rpm
Angular resolution (Ψ axis)	0.022* / 0.007**	°
Payload	50	g

\*ratio 160:1 / \*\* ratio 500:1

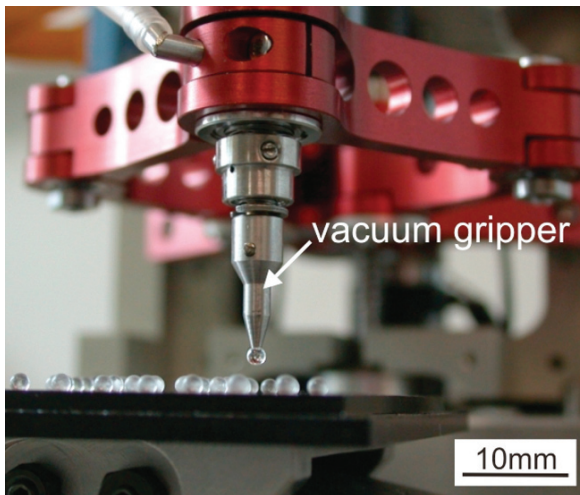


**Fig. 1** Pick-and-place application of glass balls (Ø1.5 mm) with *Parvus*

a typical vacuum gripper. This simple suction nozzle grips the glass balls upper side (see Fig. 1).

The handling of considerably smaller objects is possible with the integration of a mechanical micro gripper into the hand axis of the *Parvus*. The *Institute for Microtechnology (IMT)* at the *Technische Universität Braunschweig* developed this two-jaw micro gripper based on a micro pneumatic actuator manufactured in micro technology [6]. The *IMT* worked in cooperation with the *IWF* to adapt the micro gripper for the *Parvus* (Fig. 2). The jaws of the gripper are guided by a parallel kinematics and are operated by a single channel actuator for both vacuum and pressure. Therefore the gripper is suitable for the single channel axis of the robot. This gripper enables laterally gripping, which allows a camera to observe the gripped objects from the upper side.

Experiments have shown that it is possible to grip small ruby balls with a diameter of 200 μm (Fig. 2). These small objects are greatly influenced by electrostatic

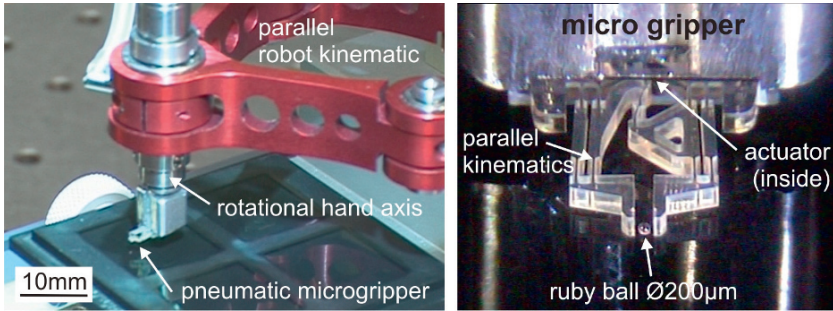


Fig. 2 *Parvus* equipped with a pneumatic two-jaw micro gripper

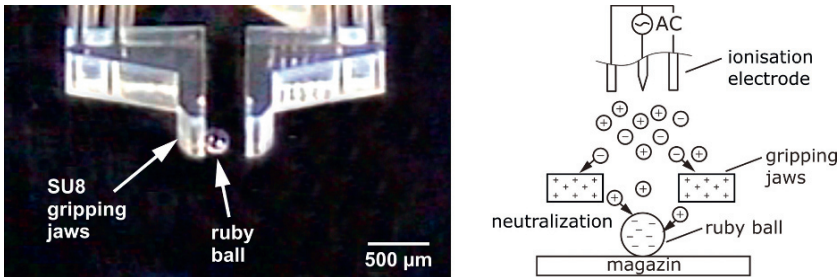


Fig. 3 Placement with adhesion (*left*), method of discharging (*right*) [7]

and Van-der-Waals forces, which in this case cause the ball to stick to one side of the opened gripper (Fig. 3). A solution for this adhesion effect is presented by [7]. Experiments at the *IWF* demonstrated that it is possible to neutralize the electric charge of objects and grippers using ionization electrodes (Fig. 3). Using the proposed method, 94% of the ruby balls were successfully placed without adhesion.

## Tool Changer

To follow up the approach using the *Parvus* as a flexible handling device in a desktop factory, a tool changer has been recently designed at the *IWF*. This tool changer allows the *Parvus* to switch between the previously described tools (and other future tools) during an assembly process. This allows one robot to achieve several different assembly tasks.

Compared to conventional tool changers, such as *RDA's TC-5* [8] or *Schunk's MWS 20* [9], the *Cambio* is a size adapted concept specialized for use in a *Parvus* robot cell. Both of the afore mentioned designs are standardized tool changers, and in this case too big for the small hand axis of the *Parvus*. Additionally, the *MWS 20* needs external forces to be applied to its coupling mechanism to lock and unlock the tool, which could damage the hand axis of the *Parvus*. For locking and unlocking the *TC-5* an external pressure channel within the robot is necessary, which



is currently not available in the *Parvus*. Therefore the coupling mechanism of the *Cambio* is designed for lock or unlock without applying forces to the hand axis of the *Parvus*. Furthermore no changes on the design of the hand axis or additional pressure channels are necessary.

The concept of the tool changer follows the idea of a size adapted micro production system, as described in the second chapter. The footprint covers an area of  $85 \times 64 \text{ mm}^2$  and the height measures 74 mm. Figure 4 shows the tool changer *Cambio* interacting with the *Parvus*.

Compared to the *MWS 20* tool changer system, which operates with a linear tool magazine to store the different grippers, the *Cambio* uses a rotary principle. A revolving tool holder can hold up to six different grippers. This tool holder rotates in both directions, which allows for quicker tool changes. As only one section of the revolving tool holder has to be within the robot's workspace, the *Cambio* has a minimum impact on the workspace.

The stored grippers in the *Cambio* are fixed in their magazine position by vacuum, which is passed through a central vacuum pipe inside the tool changer. The same vacuum exhaust is also used to unlock the coupling mechanism. In contrast to the *Cambio* the *TC-5* tool changer applies air pressure to release the tools from its locking position and the *MWS 20* needs external forces. Though, in this case a further clamping fixture is needed to absorb strains that affect the robot's hand axis. In the *Cambio* no clamping is needed because the tools are fixed by the vacuum in their magazine positions. This enables a compact tool changer design (Fig. 5).

To ensure the interaction with the precision robot *Parvus*, the *Cambio* needs a high resolution and good repeatability. Therefore, the revolving tool holder is driven by a micro motor with a high resolution encoder and a backlash free tooth belt. The angular resolution of the revolving tool holder is  $0.0125^\circ$ . For a safe and reliable exchange, explicit tool magazine positions are detected by additional hall sensors

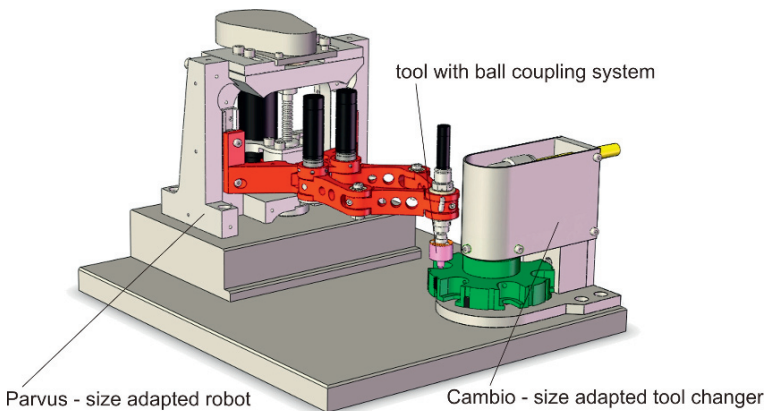


**Fig. 4** *Parvus* with tool changer *Cambio*

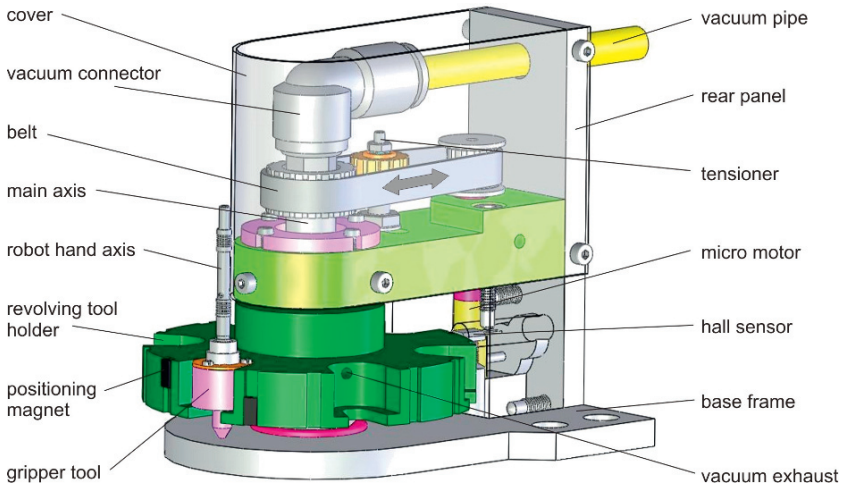


**Fig. 5** Main components of tool changer Cambio

and a positioning magnet. The following figure shows the construction of the tool changer, which is currently under construction.

## Coupling Mechanism of the Tool Changer

As previously described, the hand axis of the *Parvus* should not be loaded with high external forces and torque. To ensure a torque and force free changing of the grippers a ball coupling system is used based on a vacuum exhaust coming from the change station. As illustrated in Fig. 6, three balls lock or unlock the gripper to and from the robot hand axis. Figure 6a shows a simple vacuum gripper, in the locked state without a connected robot axis. The springs push the slide bar down into the locked position. As seen in Fig. 6b, when a vacuum is applied, the slide bar moves up, compresses the springs and the balls are freed. In this state the hand axis of the *Parvus* is inserted into the coupling mechanism. When the axis is in its final position (Fig. 6c), the vacuum is switched off, the springs push the slide ring down and the balls lock the robot hand axis in the gripper. Thus, the gripper is only fixed in axial direction. The rotational fixation is done by a torque connector, which is permanently connected to the robot axis. This concept can be transferred to different types of vacuum driven grippers, as previously described.

## Technical Data of Discussed Systems

In Tables 2 and 3 the performances of the tool changer *Cambio* in comparison with those of other existing systems are shown.

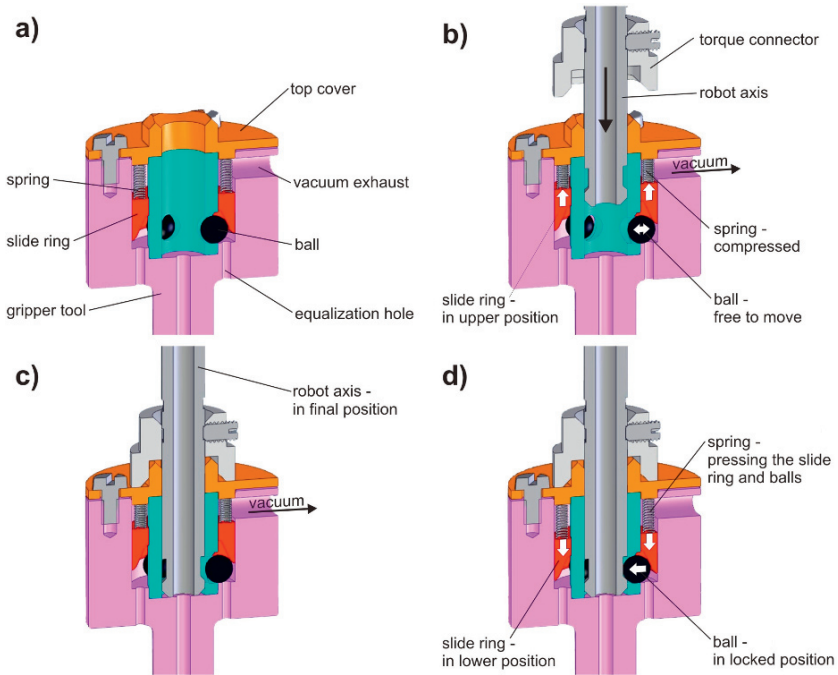


Fig. 6 States of gripper coupling

Table 2 Technical data of locking mechanism

Criterion	IWF Cambio	Schunk MWS 20	RAD TC-5
outer diameter	Ø11 mm	Ø20 mm	Ø49 mm
height (locked)	12 mm	10 mm	48,5 mm
dead weight	3 g (gripper included)	16 g	360 g
feed through	One	six	Six
possible media to pass through	vacuum, compressed	air, vacuum, compressed air, electric contacts	vacuum, compressed air, electric contacts
repeatability	to be measured	5 µm	10 µm
required locking force	none – self locking by springs	7–13 N, mechanical force	690 N at 5.5 bar
unlocking by	Vacuum	mechanical force	pneumatic pressure

Table 3 Technical data of changing station

Criterion	IWF Cambio	Schunk MWS 20	RAD TC-5
footprint	85×64 mm <sup>2</sup>	100×100mm <sup>2</sup>	–
height	74 mm	40 mm	–
principle	rotary moving	linear, not moving	–
resolution	0.0125°	–	–
tool magazine stations	Six	modular extensible	–

## Conclusion and Outlook

For using the size adapted precision robot *Parvus* for several assembly tasks, different gripper concepts have been presented. To enable an automated tool change during the running assembly tasks, the tool changer *Cambio* was designed in particular for the interaction with the *Parvus*. The highly miniaturized *Cambio* system includes the clamping system and handling of six tools.

The robot cell of the *Parvus* extended by the *Cambio* is a further step in building a future desktop factory. The *Cambio* system is currently under construction and will be tested concerning repeatability and reliability. Further various gripper concepts will be adapted for the *Parvus* and the *Cambio* in future time.

**Acknowledgments** The basic development of the coupling mechanism used in the tool changer *Cambio* is based on the master thesis of the fourth author as cooperation with *LARM Laboratory of Robotics and Mechatronics* at *University of Cassino* in Cassino, Italy.

## References

1. Wicht, H.; Bouchaud, J.: NEXUS Market Analysis for MEMS and Microsystems III 2005-2009. In: MST-news, Verlag VDI/VDE Innovation+Technik GmbH, Vol. 5, pp. 33–34, 2005.
2. Koelemeijer, S.; Jacot J.: Cost Efficient Assembly of Microsystems. In: MST-news, Verlag VDI/VDE Innovation+Technik GmbH, Vol. 1, pp. 30–32, 1999.
3. Slatter, R.; Degen, R.; Burisch, A.: Micro-Mechatronic Actuators for Desktop Factory Applications. In: Proc. of Intern. Symposium on Robotics ISR/Robotik 2006 München, p. 137, VDI Wissensforum IWB GmbH, Düsseldorf, ISBN 3-18-091956-6, 2006.
4. Burisch, A.; Raatz, A.; Hesselbach, J.: Strategies and Devices for a Modular Desktop Factory. In: Proc. of Intern. Precision Assembly Seminar (IPAS'2008), Chamonix, France, 10–13 February 2008, S. Ratchev, S. Koelemeijer (Eds.), ISBN 978-0-387-77402-2, pp. 337–344, 2008.
5. Burisch, A.; Wrege, J.; Raatz, A.; Hesselbach, J.; Degen, R.: PARVUS – Miniaturised Robot for Improved Flexibility in Micro Production. In: Journal of Assembly Automation, Emerald, Vol. 27/1, pp. 65–73, ISSN: 0144-5154, 2007.
6. Bütefisch, S.; Brand, U.; Leester-Schädel, M.; Hoxhold, B.; Büttgenbach, S.: Characterisation of Pneumatic and SMA Micro-Actuators with Short Response Times and Large Exerted Forces and Deflections. In: Proc. of Actuator 2006, Bremen, Germany, pp. 483–486, 2006.
7. Wrege, J.: Elektrostatisch unterstützte Handhabungstechniken in der Mikromontage. Dissertation, TU Braunschweig, Institut für Werkzeugmaschinen und Fertigungstechnik, ISBN 978-3-8027-8698-3, Vulkan-Verlag, Essen, 2007.
8. Product catalogue: Tool Changers. Robotic Accessories Division (RAD) <http://www.rad-ra.com>, April, 2008.
9. Haag, M.; Härer, S.; Hoch, A.; Simons, F.: Standardised Interface and Construction Kit for Micro-Assembly. In: Proc. of Fourth Intern. Precision Assembly Seminar (IPAS'2008), Chamonix, France, 10–13 February 2008, S. Ratchev (Ed.), ISBN 978-0-387-77402-2, pp. 353–358, 2008.

# Tensegrity Concept – From Natural Systems to Robots

**Simona-Mariana Cretu**

**Abstract** This paper presents: the tensegrity concept applied to inorganic matter (the construction of the “buckyball” model for water; the tensegrity icosahedron for the hexagonal model of water); a review of the natural tensegrity forms found in living life, from micro to macro level and the different tensegrities which approximate them, including some realisations of the members of the scientific association “Methodology of technical sciences teaching”, from the Faculty of Mechanics, University of Craiova; new trends towards optimally designing mechanisms and mobile robots.

**Keywords** Natural systems · Robots · Tensegrity · Structure

## Introduction

The tensegrity concepts were first put forward by Snelson who in 1948 constructed the X-Piece structure [26]. A tensegrity structure is a prestressed (internal stress prior to application of external force) stable closed structural system, with compressed struts within a web of tensile elements (strings). In tensegrities the compression system and the tension system are always in equilibrium. Initially, Snelson named this kind of structure “Floating Compression”, but later Fuller changed its name into “tensegrity” which represents a contraction of the words “tension” and “integrity”.

In the case of a class I tensegrity structure the struts do not touch one another, but in a class II tensegrity there are struts which may have a common vertex. Another classification of the tensegrities into three patterns – diamond, circuit and zig-zag – was made by Pugh [23].

Tensegrities can be structures or mobile systems depending on whether the flexible elements are cables or elastic elements respectively. Figures 1 and 2 illustrate

---

S.-M. Cretu

Department of Applied Mechanics, Faculty of Mechanics, University of Craiova, 107 Calea Bucuresti, 200512 Craiova, Dolj, Romania  
e-mail: simonamarianac@yahoo.com



**Fig. 1** Tensegrity system built with cables, subjected to a perturbation



**Fig. 2** Tensegrity system built with elastic elements, subjected to a force

what happens when a force is applied to a tensegrity system built with cables and elastic elements respectively: in the first case the structure does not change its shape and in the second it does, because the elastic elements have enough potential energy to modify the shape of the system. When the force ceases its action, the system comes back to its stable configuration due to the energy stored in strings.

Though this theory first appeared in the architectural engineering field, it has rapidly attracted great interest in other fields such as biomedical engineering and robotics and has been the subject of many studies by scientists (i.e. [5]). A large variety of natural systems, inorganic (atoms of carbon [15], molecules of water) and organics (proteins, viruses, cells, human beings), can be understood with the help of the tensegrity concept. The scientists introduced the tensegrity at cellular level and at macro level for modelling the human being. Recently this captivating subject has been used to simulate and design locomotor robots.

## **Tensegrity Theory Applied to Modelling Inorganic Matter**

From ancient times man has known about the structure of water: the Chinese character for water [32] recalls its hexagonal structure (Fig. 3). Dr. Mu Sheik Jhon, a world authority in water research [34], proposed the hexagonal water theory; he sustained

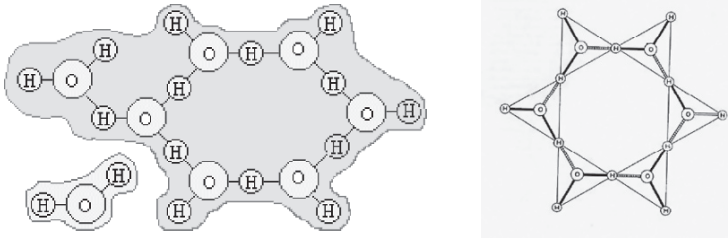


**Fig. 3** Schemes from scientific literature for hexagonal water [33]

that there are three different shapes of water: hexagonal hook-shaped, pentagonal hook-shaped and hexagonal chain-shaped.

During a discussion between Brinzan G.C. and the author about tensegrity and water referring to a paper [4], we noticed that the images of frozen water crystals obtained with a microscope at magnification of 500 times resemble the upper view of a tensegrity icosahedron subjected to a force (Figs. 5 and 6). Until now we haven't found in literature the tensegrity icosahedron model associated to hexagonal water. At the third national seminar on mechanisms SNM'08, in Romania [9], we proposed the tensegrity icosahedron model for hexagonal water. The tensegrity icosahedron has six struts placed in three parallel pairs which are perpendicular to each other (Fig. 4). The twelve vertices of the model are joined together by 24 elastic elements forming in this way twenty triangles (Fig. 4).

The most recent studies present “buckyball” type water clusters (Fig. 7a) [31]. We realised a “buckyball” type tensegrity system with elastic elements and struts after [36] (Figs. 7b and 7c).

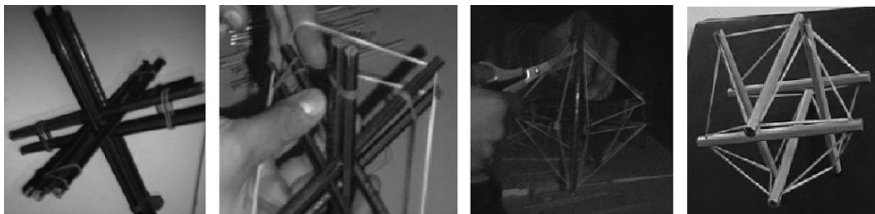


**Fig. 4** The construction of the tensegrity icosahedron, after [35]



**Fig. 5** Tensegrity icosahedron subjected to a force

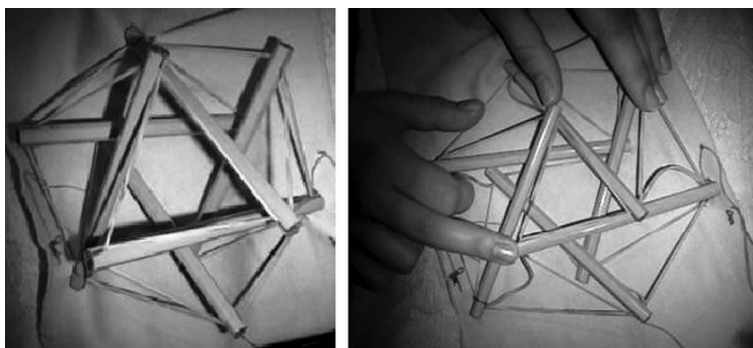


Fig. 6 The *upper view* of the tensegrity icosahedron

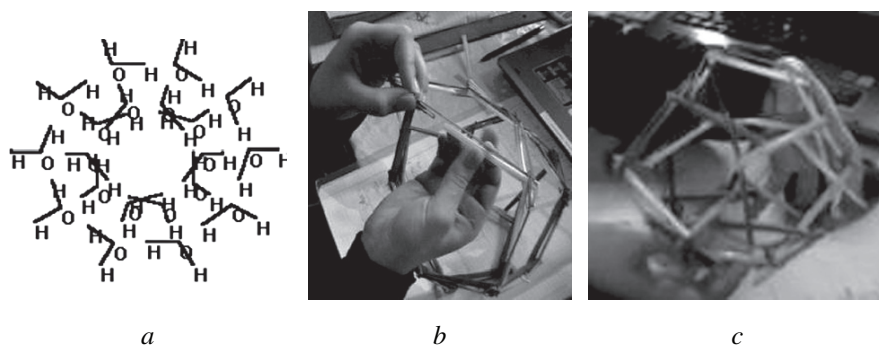


Fig. 7 The “buckyball” model for water clusters

## Tensegrity Theory Applied to Modelling Organic Matter

### *Tensegrity Theory Applied to Living Forms at Micro Level*

The shape stability of many cells depends on the balance between the tension borne by contractile microfilaments and the compression borne by the microtubules [10]. Ingber et al. assumed that the cytoskeleton of the cell is organised as a tensegrity [14]. In the tensegrity model the microtubules of the cell are modelled by struts because they bear the compression forces and the microfilaments and intermediate filaments of the cell are modelled by elastic springs because they bear the tensional forces.

Stamenovic et al. analysed a crude representation of the cell – the icosahedron tensegrity; their study emphasises the cell’s ability to adapt its shape [27] and Wendling et al. [30] determined the relationships between the overall stiffness of the structure and the physical parameters of the constituent elements.



Coughlin and Stamenovic sustained that for the tensegrity models of the cytoskeleton the unilateral behaviour of the microfilaments and the buckling and postbuckling of the microtubules should be considered [7]; this is in contrast to Ingber's model with straight and stiff microtubule-struts.

Volokh et al. give a theoretical explanation of the linear stiffening of living cells by modelling the cytoskeleton as a tensegrity icosahedron with microfilament-cables which allow unilateral mechanical response and microtubule-struts with deep post-buckling [29].

Ingber proposed a model composed of two icosahedron tensegrities, one smaller – like a nucleus, inside the other, bigger, both joined by elastic strings to reproduce the cytoskeletal connections [14] (Fig. 8). We repeat the experiments realised by Ingber to simulate the behaviour of the cell on rigid and flexible supports (Fig. 9).

Canadas et al., using the icosahedron tensegrity with cables considered to behave like viscoelastic Voigt bodies, analysed the structural viscoelasticity of the cytoskeleton [6].

In 2005 a team of researchers presented a mathematical model that explains how the protein skeleton – a net of 33 000 protein hexagons that looks like a geodesic dome in miniature – gives a healthy human red blood cell which can stretch without breaking and can facilitate diffusion of oxygen across its membrane [28].

The tensegrity icosahedron was utilised by Mudana to simulate red blood cells and rod cells [18]. The simulations demonstrated how filopodia, erythrocytes and rod cells acquire their shapes by increasing or reducing the lengths of some struts in their 6-strut tensegrity system.

Because the cytoskeleton architecture is very complex, Baudriller et al. proposed a form-finding method for generating irregular tensegrity shapes, the dynamic relaxation method [3].

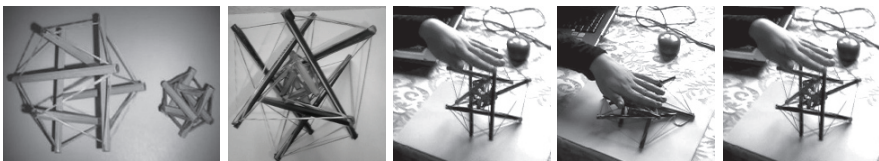


**Fig. 8** The nucleated model of the cell



**Fig. 9** The behaviour of the cell fixed on rigid and flexible supports

## ***Tensegrity Theory Applied to Modelling Anatomical Structures at Macro Level***

At each level of their development the evolving structures are optimized because evolution always gives optimal solutions. Muscles and all other soft tissue elements in the human body are always under tension and bones are compressed. The tensegrity icosahedron is one of the most utilised models in biological musculo-skeletal modelling. Fuller showed that the parallelism of the three pairs of struts to the three axes of the XYZ coordinate system provides tensegrity icosahedra with the capability to link and form infinite periodic arrays [13]. Kroto pointed out that tensegrity icosahedron arrays are hierarchical and evolutionary systems [15].

Levin applied the principles of tensegrity to anatomy and he coined the term biotensegrity. In 1990 he utilised a hierarchically constructed tensegrity icosahedron to model the tensegrity arm with two levels of hierarchy [16] (Fig. 10). He also introduced the tensegrity structure to model the torso, the shoulder, the scapula and the pelvis.

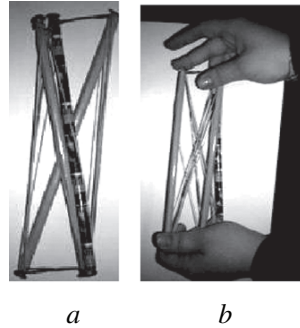
Flemons realised tensegrity models which are abstractions of the body designed for a close match in form and function: an expanded octahedron tensegrity which contracts and expands in the same way the torso does, stellated tetrahedron tensegrities which model the spine, the tensegrity cushions that model the intervertebral discs which act as couplers and a modified expanded octahedron for the pelvis and the knee saddle joint [12]. He proposed chiral tensegrities known as T-prisms – which are single layer and can be clockwise or counterclockwise – in biological musculo-skeletal modelling. They are threefold T-prisms or fourfold T-prisms and describe the forearm, or the weight transfer from the leg to the foot respectively.

Cretu presented the regular polyhedral structures as a base of tensegrities [8]. She proposed a new method of obtaining tensegrity systems by modifying the triangulated primary bodies presented by Plato in his book *Timaeus* [22]. She obtained a model that better approximates the forearm by the transformation of a triangulated platonic tetrahedron into a tensegrity prism model and finally into a tensegrity system like the letter X (Fig. 11a). This tensegrity model follows the geometry and the



**Fig. 10** The modelling of the human arm after Levin

**Fig. 11** Torsion on the tensegrity



kinematics of the forearm. Submitting the tensegrity to torsion will change its form (Fig. 11b) and when the action ceases the system returns to its stable configuration (Fig. 11a), similar to the forearm.

## Tensegrity Theory Applied to Mobile Robots

Arsenault and Gosselin proposed planar tensegrity mechanisms, with 1 and 2 –DOF and studied them kinematically, statically and dynamically [2].

In 2006, Schenk, Herder and Guest introduced a new class of mechanisms, statically balanced tensegrity mechanisms [25] which are considered to be at the limit between structures and mechanisms. In [24] the author presents a statically balanced tensegrity mechanism based on the model of the triangular tensegrity prism.

Because tensegrities firmly resemble both the movable cytoskeleton of the cell and the movable musculo-skeletal systems, they provide a suitable basis for locomotion. A tensegrity system can be of three types, depending on actuation: strut-collocated (the actuators alter the strut lengths), cable-collocated (the effective rest length of the cables is changed) and noncollocated (actuation is applied between two struts, two cables or a strut and a cable). Paul, Lipson and Cuevas introduced the idea of an ambulatory robot based on tensegrity. They simulated two tensegrity robots for locomotion (one based on a triangular tensegrity prism and the other one based on a quadrilateral tensegrity prism) by changing the length of the cables. Evolutionary optimisation was applied to obtain periodic gait controllers for the forward locomotion of these robots [20, 21]. It was concluded that the robots can generate different gait patterns.

Some optimisation approaches were related to design of geometry and forces of tensegrities (i.e. [17, 19]). Aldrich and Skelton realised an approach for control/structure optimisation for minimum-time reconfiguration of tensegrity systems, using a feedback linearisation control law to minimise the norm of the tendon force tracking error while avoiding saturation of the control signals [1]. De Jager et al. introduced the utilisation of optimisation methods for solving nonlinear static response problems associated with large nodal displacements [11].

## Conclusion

In recent years, the captivating domain of tensegrities has been used to simulate and design locomotor robots and most probably its importance will increase. For modelling and designing robots with high performances, the study of optimum living systems will be considered in the future.

**Acknowledgments** I thank my brother, Augustin Cretu, for his contribution to the translation of the papers concerning this subject.

The practical realisations presented in this paper are made by the members of the scientific association “Methodology of technical sciences teaching”, from the Faculty of Mechanics, University of Craiova, Romania: Brinzan G.-C., Cretu S.-M., Pupaza I., Stancu M.

## References

1. Aldrich J. B., Skelton R. E., Control/structure optimization approach for minimum-time re-configuration of tensegrity systems, In: Proceedings of SPIE, Vol. 5049, 2003, pp. 448–459.
2. Arsenault, M., Gosselin, C.M., Kinematic, static and dynamic analysis of a planar 2-DOF tensegrity mechanism, In: Mechanism and Machine Theory, Vol. 41, 2006, pp. 1072–1089.
3. Baudriller H., Maurin B., Canadas P., Montcourrier P., Parmeggiani A., Bettache, N., Form-finding of complex tensegrity structures: application to cell cytoskeleton modelling, In: C. R. Mecanique, Vol. 334, 2006, pp. 662–668.
4. Brinzan G.C., Structura apei si tensegritatea, Concursul national CHIMEXPERT, Satu Mare, 2008.
5. Burkhart RW Jr., A practical guide to tensegrity design, <http://bobwb.Tripod>
6. Canadas P., Laurent V. M., Oddou C., Isabey D., Wendling S., A cellular tensegrity model to analyse the structural viscoelasticity of the cytoskeleton, In: Journal of Theoretical Biology, Vol. 218, 2002, pp. 155–173.
7. Coughlin M. F., Stamenovich D., A tensegrity structure with compression elements: application to cell mechanics, ASME Journal of Applied Mechanics, Vol. 64, 1997, pp. 480–486.
8. Cretu S.-M., Tensegrity as a structural framework in life sciences and bioengineering, In: Modeling, Simulation and Control of Nonlinear Engineering Dynamical Systems, Springer Verlag, Berlin, 2008.
9. Cretu S.-M., Brinzan G. C., Conceptual tensegrity – de la sistemele naturale la roboti, The third national seminar on mechanisms, Craiova, Romania, 2008, pp. 211–227.
10. Danowski B. A., Fibroblast contractility and actin organization are stimulated by microtubule inhibitors, Journal of Cell Science, Vol. 93, 1989, pp. 255–266.
11. De Jager B., Masic M., Skelton R. E., Optimal topology and geometry for controllable tensegrity systems, [http://maeweb.ucsd.edu/~skelton/publications/masic\\_ifac.pdf](http://maeweb.ucsd.edu/~skelton/publications/masic_ifac.pdf), 2004.
12. Flemons T.E., [http://www.intensiondesigns.com/itd-biotensegrity/biotensegrity/papers/geometry\\_of\\_anatomy.html](http://www.intensiondesigns.com/itd-biotensegrity/biotensegrity/papers/geometry_of_anatomy.html), 2006
13. Fuller R. B., Synergetics: Explorations in the geometry of thinking, New York, 1975.
14. Ingber D. E., The architecture of the life, Scientific American, Vol. 278, 1997, pp. 48–57.
15. Kroto H., Space, stars, C60, and soot, Science, Vol. 242, 1988, pp. 1139–1145.
16. Levin S. M., <http://www.biotensegrity.com/>, 1995, 1997, 2002, 2007.
17. Masic M., Skelton R. E., Gill, P. E., Optimization of tensegrity structures, International Journal of Solids Structures, Vol. 43, 2006, pp. 4687–4703.
18. Muddana H. S., Integrated biomechanical model of cells embedded in extracellular matrix. Thesis for Master of Science, Texas A&M University, <http://research.cs.tamu.edu/bnl/papers/muddana.thesis06.pdf>, 2006.

19. Ohsaki M., Zhang J. Y., Kimura S., An optimization approach to design of geometry and forces of tensegrities, IAAS 2005, 2005, pp. 603–610.
20. Paul C., Roberts J., Lipson H., Valero-Cuevas F. J., Gait production in a tensegrity based robot, In: The 2005 International Conference on Advanced Robotics, [http://ccsl.mae.cornell.edu/papers/ICAR05\\_Paul.pdf](http://ccsl.mae.cornell.edu/papers/ICAR05_Paul.pdf), 2005.
21. Paul C., Valero-Cuevas F. J., Lipson H., Design and control of tensegrity robots for locomotion, In: IEEE Transactions on Robotics, Vol. 22, No. 5, 2006, pp. 944–957.
22. Plato, *Timaeus*, 350 BC.
23. Pugh A., An introduction to tensegrity, Berkeley, California, University of California Press, 1976.
24. Rieffel J., Stuk R. J., Valero-Cuevas F. J., Lipson H., Locomotion of a tensegrity robot via dynamically coupled modules, In: Proceedings of the International Conference on Morphological Computation, Venice Italy, [http://ccsl.mae.cornell.edu/papers/MC07\\_Rieffel.pdf](http://ccsl.mae.cornell.edu/papers/MC07_Rieffel.pdf), 2007.
25. Schenk M., Herder J.L., Guest S.D., Design of a statically balanced tensegrity mechanism, In: Proceedings of IDETC/CIE 2006 ASME 2006 International Design Engineering Technical Conferences & Computers and Information in Engineering Conference, USA, September 10–13, 2006.
26. Snelson K., <http://www.kenethsnelson>.
27. Stamenovic D., Fredberg J. J., Wang N., Butler J. P., Ingber D. E., A microstructural approach to cytoskeletal mechanics based on tensegrity, In: Journal Theoretical Biology, Vol. 181, 1996, pp. 125–136.
28. Vera C., Skelton R., Bossens F., Sung L. A., 3-D nano-mechanics of an erythrocyte junctional complex in equibiaxial and anisotropic deformations, In: Annals of Biomedical Engineering, Vol. 33, No. 10, 2005, pp. 1387–1404.
29. Volokh K. Yu., Vilnay O., Belsky M., Tensegrity architecture explains linear stiffening and predicts softening of living cells, Journal of Biomechanics, Vol. 33, 2000, pp. 1543–1549.
30. Wendling S., Oddou C., Isabey D., Stiffening response of a cellular tensegrity model, In: Journal Theoretical Biology, Vol. 196, 1999, pp. 309–325.
31. <http://www.watercluster.com/>
32. <http://www.fsccentre.org/Water,%20the%20Origin%20of%20Life.htm>
33. <http://www.aquatechnology.net/hexagonalwater.html>
34. <http://www.chem1.com/CQ/clusqk.html>
35. <http://www.youtube.com/watch?v=96kz98yEO1w>
36. <http://georgehart.com/virtual-polyhedra/straw-tensegrity.html>

# Laser-Based Structuring of Piezoceramics for Mobile Microrobots

Christoph Edeler and Daniel Jasper

**Abstract** This paper describes the laser-based structuring of piezoceramic actuators used in a mobile microrobot. The actuator has to meet several requirements. Firstly, the achieved positioning accuracy of the mobile platform should be in the single nanometer range. This leads to the use of piezoelectric ceramics, which support this demand. Secondly, as the robot needs to have up to three degrees of freedom (DoF), a complex actuator design is necessary. Thirdly, a small size of the actuator is advantageous in terms of microrobotics. Conventional structuring especially in three dimensions is challenging, due to the refractory properties of piezoceramics and the danger of short circuits or overheating. The presented laser fabrication process uses an Nd-YAG laser and a developed algorithm to structure special actuators. The successful application in a mobile microrobot proves the concept.

**Keywords** Microrobot · Actuator · Laserfabrication · Piezoceramic

## Introduction

Laser processing has been established in macromanufacturing for years in the fields of assembly and separation [1]. Laser processing can be regarded as a key technology for many applications, beginning from welding, cutting or drilling leading to complex micro- and nanoprocessing. Several different materials such as steel, plastics or ceramics can be handled. Accordingly, the laser techniques are as manifold as their applications. The most common advantages of laser processing are the stable and well controllable processing conditions, as little mechanical stress as possible and flexible handling [2]. Therefore, it is beneficial to use a laser to structure ceramics or piezoceramics, respectively. Piezoceramics are the basis for a wide variety of micro- and nanoactuators [3]. As the conventional mechanical structuring of ceramics cannot be used due to the fragile properties, processing ceramics is a challenging

---

C. Edeler (✉)

Division Microrobotics and Control Engineering, University of Oldenburg, Uhlhornsweg 84, 26111 Oldenburg, Germany  
e-mail: christoph.edeler@kisum.uni-oldenburg.de

task. Most of the publications, as far as laser-based structuring is concerned, contain laser-based microstructuring of several materials such as copper, stainless steel or organic polymers, but not ceramics [4]. A problem using a laser to cut piezoceramics in particular is a possible short circuit between the electrodes or surfaces. Because of the structure of the ceramic, conductive metal compounds can occur when the beam heats up the ceramic's edges. These compounds inhibit applying the electric potentials which are necessary for the actuator to work. Because of these problems, there are few publications concerning the laser-based structuring of piezoceramics as in [5, 6]. These deal with the controlled fracturing of ceramics. However, this cannot be a solution for the adequate structuring of microactuators with dimensions in the mm-range.

## Laser Micromachining

The most common applications for lasers in industry are welding and thermal cutting of metals. Both of these processes are based on thermal interactions, and the energy transport into the material can be realized by laser. Today, a wide spectrum of processes can be realized by laser technique: welding, cutting, drilling, hardening, coating, to mention the most important ones. Different beam sources can be used, the most common types being solid-state lasers and gas lasers. A typical solid-state laser is the Nd-YAG (Neodymium-doped Yttrium Aluminum Garnet) laser. It generates a beam with a wavelength of 1064 nm, and has to be optically pumped by a flashlight or laser diodes. A typical gas-laser is the CO<sub>2</sub> (Carbon Dioxide) laser with a wavelength of 10600 nm. A mixture of several gases, mainly carbon dioxide, is used as active medium. CO<sub>2</sub> lasers offer a wide power variety and are very popular. All systems have in common, that they can remove material by the use of thermal phenomena. These can be described by absorption, incitation of electrons, thermal material removal, propagation of shockwaves and interactions and dynamical processes. The absorption defines, which percentage of the beam energy heats the material. The other part of the beam is reflected and is of no further interest. The influence of the electron bond to the working material is similar. If there are few electron bonds, the beam energy (the photons) can easily close the electron gaps in the hull and enable the material atom to be released. Most metallic materials already have completed hulls, so the required photon energy is high. This leads to an increased energy consumption in practical processes. Thermal material removal is based on heating the material over its melting temperature and removing the melted mass. Depending on the thermal conductivity, a part of the thermal energy is dissipated into the material and can change its structure. This effect limits the maximum pulse energy and time. Another important restriction follows from the formation of gas-induced spew. The material is heated to its evaporating temperature and forms quickly expanding gas "bubbles" leading to a very fast removal. This effect can be used to remove the melted mass. Nevertheless, very short pulses and high beam energy are necessary. Due to the dynamic material heating, it expands according to

its thermal expansion coefficient which creates dynamic mechanical stress. This can induce shockwaves, cracks and flaking.

The piezoceramic is delivered in a plate form, 10 mm in square and 0.5 mm thick. The large surfaces have an electrically conductive coating as electrodes for the piezo terminal. These can be structured by laser to generate contact electrodes. The ceramic has a maximum operating temperature of 250°C. This could be a problem because of the thermal removal mechanism. The material could lose its piezoceramic properties or simply decompose.

### Structuring Device

The device Raycutter 3200 [7] is originally designed for marking, but can also be used for further material processing. The key component of the system is a Nd-YAG beam source, pumped by infrared diodes and called beam source in Fig. 1. When the beam leaves the source, it is parallel and unfocused. Therefore a focus lens and a mirror direct the beam to the workpiece and focus it. With this technique, a small beam diameter in the focus of 10 μm is achieved. The focus lens can be moved in z to move the focus point in z, as the arrow indicates. Furthermore, the workpiece is mounted on a stage with an accuracy of 1 μm, which enables the structuring in three DoF with computer numeric control (CNC) capabilities. The system can be programmed with standard G-Code [8].

In the Raycutter, a MESA beam source is used, which is characterized in Table 1. Mainly laser power or diode current, respectively, repetition rate and form feed can be forced. The repetition rate is programmed to be proportional to the stage’s velocity, so a path-dependent generation of laser pulses is reached.

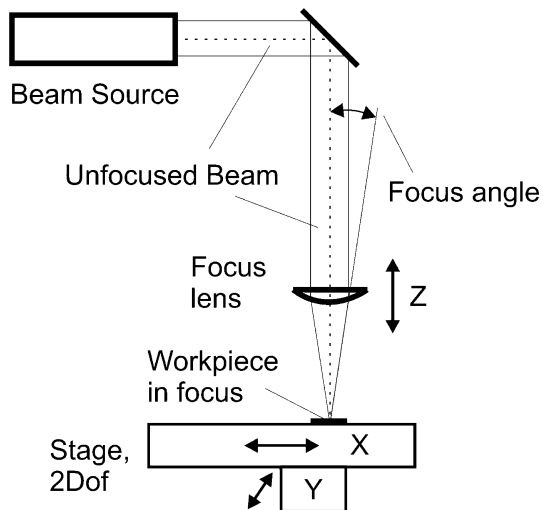


**Fig. 1** The laser structuring device, Raycutter by LaserPlusAG [7]



**Table 1** Data of MESA laser beam source [9]

Beam Source	Nd-YAG
Wavelength	1064 nm
Max. power (CW)	8 W
Pulse duration	>30 ns
Repetitionrate	0-100 kHz
Max. Pulse Energy	1150 $\mu$ J
Focus Aperture	$\sim$ 10 $\mu$ m
Focus Angle	>20 $^{\circ}$
Beam Quality	$M^2 < 1.2$
Polarization	Random

The structuring arranges single material removal points (pulses) in rows to achieve a continuous removal. Preliminary tests showed that defined overlap between the pulses is necessary to enable a residue free removal. The same is the case between several lines, aligned to each other to structure surfaces. So, point and line overlap are important process parameters. The used piezoceramics cannot be modified, i.e. physical parameters such as adsorption or laser incidence angle are given and assumed as constant. Hence, the following parameters have to be identified for a given material in preliminary tests:

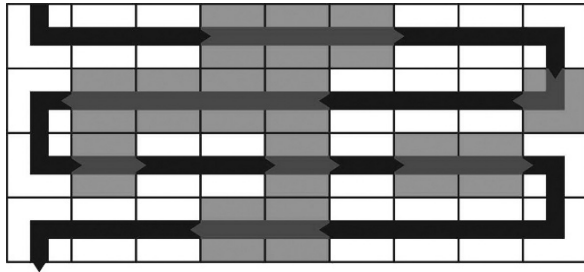
- Laser power
- Repetition rate – Pulse Energy
- Stage form feed
- Point overlap
- Line overlap

Table 2 shows the results for a soft PZT ceramic. The average removal volume per pulse can be calculated. The point overlap indicates a pulse distance of 1.2  $\mu$ m and the line overlap 5  $\mu$ m. The spanned space corresponds to the removal space and leads to 6  $\mu$ m<sup>2</sup>, in combination with the removal depth of 12  $\mu$ m to the removal volume of 72  $\mu$ m<sup>3</sup>. In combination with the repetition rate of 10 kHz a calculated removal rate of at least 0.432mm<sup>3</sup>/min is reached. An important fabrication restriction is the limitation caused by the focus angle (Fig. 1). Cut walls cannot be perpendicu-

**Table 2** Process Parameters for structuring PZT-5H

Material:	PZT-5H
Charge constants	
$d_{33}$	500*10 <sup>-12</sup> C/N
$d_{31}$	-210*10 <sup>-12</sup> C/N
Elastic compliance	
$S_{33}$	19*10 <sup>-12</sup> m <sup>2</sup> /N
Curie temperature	250 $^{\circ}$ C
Poisson's ratio	0.34

**Fig. 2** Principle of the structuring algorithm



lar to the  $x$ - $y$ -plane, they are tilted approximately by the focus angle. This limits the maximum aspect ratio, because the beam is shadowed by the edge. Perpendicular walls could be fabricated by tilting the stage, but the current designs do not suffer from these limitations. An algorithm is necessary which defines where to set laser pulses to obtain the desired geometry. In contrary to conventional milling, laser pulses remove material even when the focus point is above the workpiece due to the long beam waist. Standard G-Code [8] offers the possibility to express geometrical shapes, but appropriate CAM-software is not available and the desired structure is relatively complex. Furthermore, G-Code is less capable of flexible manual adaptation. Using many complex shapes leads to several empty drives during processing, which take time. A simple, but very effective solution is sketched in Fig. 2. It shows a scheme of the workpiece from above, white squares stand for unstructured surface, grey for “material to remove”. The workpiece is moved according to the arrows, beginning in the top left corner. The whole width of the workpiece is processed. Then, the next line is processed until the geometry is complete. The laser is switched on or off dependent on the square colour. The accuracy depends on the square’s size, smaller squares lead to a more accurate structure. As the laser can drive over the whole workpiece in one step, empty drives are reduced to a minimum. Additionally, the overlaps can be integrated easily.

## Laser Structured Actuator

In recent papers, the microrobotic concept of a mobile platform was presented [10, 11]. The principle is based on a piezoceramic element moving ruby hemispheres, which drive a steel sphere by which the mobile platform is supported. The interaction of piezoceramic and ruby hemisphere explains the need for complexly structured piezoceramics. Figure 3 shows the particular part of the platform drive, where the structured piezoceramic is used as an actuator. The ruby hemisphere is fixed to three defined surfaces of the ceramic. In the figure, these are two surfaces for a better understanding. A rotational motion of the ruby hemisphere around its center is essential for the driving principle. This motion can be generated by applying voltages with opposite potentials. The potentials are connected to the surfaces, on which the ruby hemisphere is glued, whereas ground potential can be connected to

**Fig. 3** Principle of the Mobile Platform's Drive

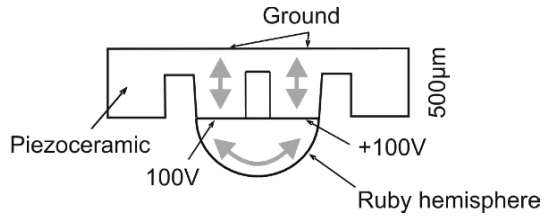


**Fig. 4** Piezoceramic actuator, front (*left*) and back (*right*)



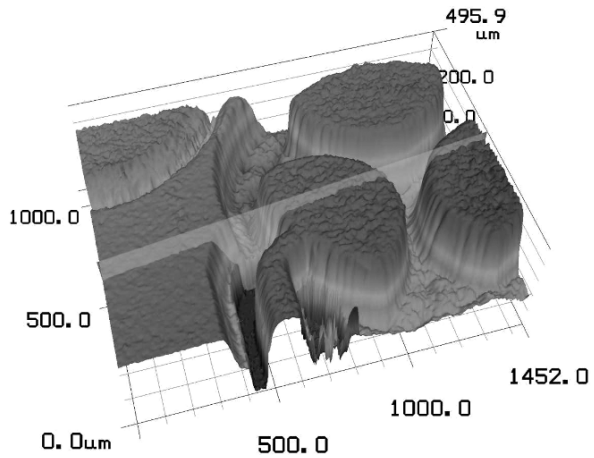
the opposite surface. When applying the voltages, the piezoceramic expands and contracts (grey arrows), and the ruby hemisphere rotates.

Figure 4 shows the front and back of the actuator. The dimensions are  $5 \times 5 \times 0.5 \text{ mm}^3$ . In the front view, three circular shapes can be identified, each separated into three segments. Three ruby hemispheres will be mounted onto these shapes. Each of the nine segments has an electric connection to one of the solder contacts at the actuator's edge. Thus, the surfaces remain unstructured during the process leaving the electrically conductive adhesive intact. The coating of the larger areas is completely removed. The adhesive removal and the structuring of the ceramic on the front (grooves around the nine segments) can be done by laser in one clamping, which reduces geometrical form errors. The laser parameters for removing the coating are similar to those in Table 2. The structuring of the backside is done correspondingly. In Fig. 4, right, three brighter circles mark the back sides of the nine active segments (ground).

## Results and Outlook

The built up mobile platform exhibits great performance, as shown in [10, 11]. The positioning capability is better than 10 nm per step, and the dynamic behavior is advantageous. Control frequencies up to 100 kHz together with amplitudes up to  $\pm 200 \text{ V}$  can be used, leading to a maximum velocity of more than 10 mm/s. The linearity and scalability are very good. These are indicators for the successful concept of the piezoceramic actuator. After producing more than 30 actuators, no problems concerning mechanical damage, short circuits or depolarized piezoceramic occurred.

**Fig. 5** 3D-view of a part of the ceramic



To validate the structured actuator, it was measured with a Keyence 3D laser-microscope. Figure 5 shows a 3D-model of three segments of the actuator including a measuring plane (light gray), which runs through the lower two segments. Figure 6 shows the height profile for this measuring plane. The profile shows two “inverted” peaks. The left peak reaches right through the ceramic where it is completely cut. This corresponds to the grooves which can be seen in Fig. 4, right. The peak on the right shows how deep the grooves between the segments were done. The design prescribes a depth of 300μm, which was fabricated successfully. Similar to wire-based electrical discharge machining, the surface roughness is in the range of several tens of μm.

The successful application in a microrobot proves the concept of structuring functional piezoceramics with a low power and highly focused laser system. In this paper the piezoceramic was used to actuate a microrobot. For further development, there is potential for miniaturizing the structure. Different piezoceramic materials are also available, which could improve the mechanical or dynamical actuator characteristics. Preliminary tests with a mechanically “hard” ceramic were performed, and the laser process could handle these, too. From this point of view the laser fabrication has the potential to become a flexible and valuable tool for further developments.

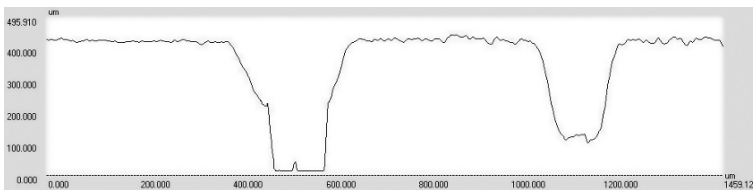


**Fig. 6** Height profile

## References

1. J. F. Ready and D. F. Farson, LIA Handbook of Laser Materials Processing. 12424 Research Parkway, Suite 125, Orlando, FL 32826: Laser Institute of America, Orlando, USA, 2001.
2. M. J. Jackson, Microfabrication and Nanomanufacturing. CRC Press, 2006.
3. S. Fatikow, Mikrorobotik und Mikrosystemtechnik. University of Oldenburg, Lecture notes, vol. 5, 2004.
4. J. A. McGeough, Micromachining of Engineering Materials. CRC Press, 2002.
5. D. W. Richerson, Modern Ceramic Engineering: Properties, Processing, and Use in Design. CRC Press, 2006.
6. C.-H. Tsai and H.-W. Chen, Laser Cutting of Thick Ceramic Substrates by Controlled Fracture Technique, Journal of Materials Processing Technology, vol. 136, no. 1–3, pp. 166–173, 2003.
7. N. LaserPluss, A.G. RayCutter 3200 manual, LaserPluss AG, 2006.
8. I. O. for Standardization, Iso 6983-1:1982 Numerical Control of Machines, 1980.
9. N. N., Datasheet MESA AC IR V, <http://www.ib-laser.com>, IB Lasers, Berlin, Germany, November 2007.
10. C. Edeler, Simulation and Experimental Evaluation of Laser-Structured Actuators for a Mobile Microrobot, IEEE International Conference on Robotics and Automation, 2008.
11. C. Edeler, D. Jasper, and S. Fatikow, Development, Control and Evaluation of a Mobile Platform for Microrobots, International Federation of Automatic Control, IFAC08, 2008.

# Evaluation of Spatial Vibrations Using a Platform with 6 Degrees of Freedom

Jiri Blekta, Josef Mevald and Iva Petrikova

**Abstract** The paper presents the measuring equipment developed for experimental research a sitting human operator subjected to three dimensional vibrations. The simulation model of the platform with six degrees of freedom in software MSC. Adams was created to verification of dynamic properties (stiffness, natural frequencies, mode shape). The operation deflection shape measurement was realized.

**Keywords** Vibration · Dynamic system · Vibration measurement · Human body

## Introduction

The problems of a suitable evaluation of the effects of spatial vibrations on a biomechanical system come into foreground simultaneously with the development and modernization of automobile transport and they result from the requirement to ensure not only sufficient comfort for drivers and car crew or operators of various working machines but also from the requirements on safety of operation. An excess man exposition to vibrations acts adversely on his working ability; it can constitute health and safety risks as the case may be.

To investigate the spatial vibrations, an experimental device has been developed – a platform with six degrees of freedom (Fig. 1) which enables it to identify and after evaluation of particular experiments to judge objectively and evaluate the quality of vibroisolation, i.e., both from the point of view of weighted accelerations in particular points and directions and from the point of view of dissipated energy in the biomechanical system or in the observed vibroisolation degrees (in detail at [1–3]). The aim is to suggest and subsequently verify the suitable methods, complex criteria and procedures for evaluating spatial vibrations on the biomechanical system. Those pieces of knowledge are necessary for the design and manufacture of seats for personal motor cars and namely for lorries, stable or mobile manipulators or

---

J. Blekta (✉)

Department of Applied Mechanics, Technical University of Liberec,  
Studentská 2, 46117 Liberec, Czech Republic  
e-mail: iva.petrikova@tul.cz

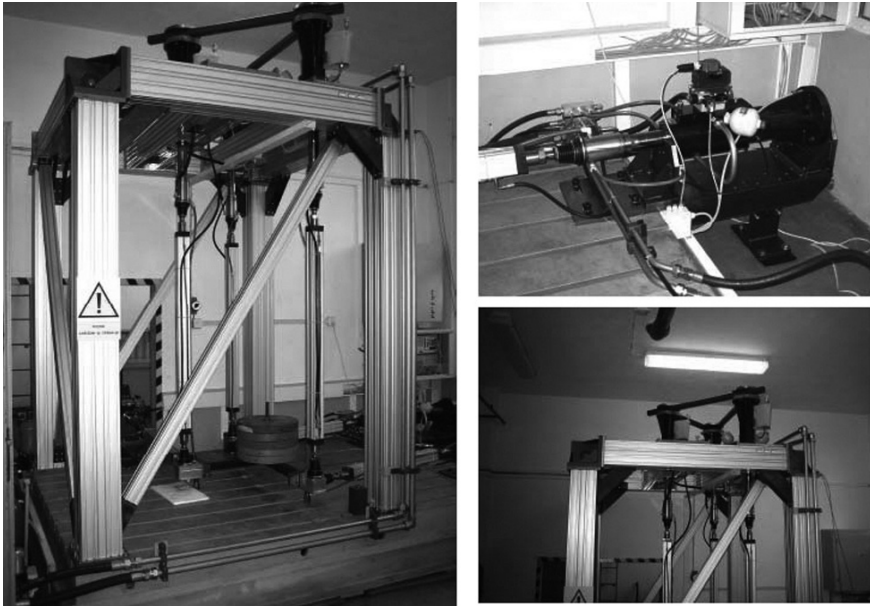


**Fig. 1** Vibration platform with six degrees of freedom in Hydrodynamic laboratory in Technical University of Liberec

for wheel excavators where intensive excitation from all the components of spatial vibrations is in approximately the same intensity and approximately in the same frequency band.

### Description of the Platform with 6 DOF

The technical version of the device should enable to excite the investigated object with harmonic and common signals without considerably distorting the result of dynamical compliance of the device itself. The exciting signals will cover a frequency band of 0–15 Hz with amplitudes dependent on maximum accelerations (excitation frequencies). The maximum mass of the excited object will not exceed 250 kg.

From the point of view of kinematics, the platform with 6 degrees of freedom is a spatial mechanism with six independent exciting elements (Fig. 2). The structure itself can be divided into several basic construction units. The basis of the platform is a steel concrete foundation board (1) with a cast iron anchoring plate (2), which is set up on rubber pads placed along the circumference of the foundation board on the floor of the testing room without any additional anchoring. The platform frame (3) is made from aluminium alloy extruded profiles. Such an execution has been chosen for its easy assembling and supposed good structure damping of 200×200 mm main bearing profiles composed from profiles of 80×80 mm by means of a special coupling profile. The particular bearers of the frame as a whole are connected by means of welded steel nodes and bolts.

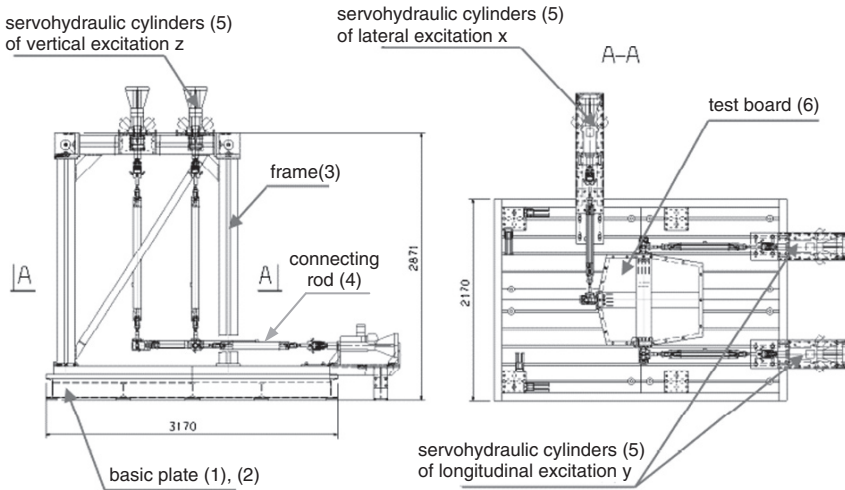


**Fig. 2** Design arrangement of the platform with six degrees of freedom

The platform frame is fastened by the help of bolted connections to the anchoring plate of the platform (2). The connecting rods (4) of the spatial mechanism are also made from aluminium alloy profiles. By means of steel nodes with ball joints, the connecting rods are linked with hydraulic exciting cylinders (5) at the one end and with the test board (6) at the other end. The device is equipped with INOVA servo cylinders (a maximum stroke of 200 mm, a maximum strength of 25 kN) that are fit with REXROTH servo valves, stroke and strength sensors. The hydraulic cylinders ensure kinematic excitation programmable as to particular needs. A test board, which forms a part of the mechanism, serves to fastening objects to be tested. A driver’s seat with a passive or active biomechanical load (human body) will be anchored to the test board. The control of the platform is carried out in the LABVIEW environment by the help of a computer positioned in the control workplace. In contact points of the seat with a load, values of three components of weighted accelerations or force effects are monitored.

### Transformation of the Real Signal into Cylinder Movement

When transforming the real signal into cylinder movement, a transformation algorithm on the principle of matrix operations for general spatial movement is used. The transformation is carried out in three steps. The required signal is transformed into particular coordinates of the position vector of the platform reference point and three appropriate spherical angles.

$$a_{Pi} = f_i(\ddot{r}_{L1}, \ddot{r}_{L2}, \ddot{r}_{L3}, \varphi_1, \varphi_2, \varphi_3, \dot{\varphi}_1, \dot{\varphi}_2, \dot{\varphi}_3, \ddot{\varphi}_1, \ddot{\varphi}_2, \ddot{\varphi}_3) \text{ for } i = 1, 2, 3, \quad (1)$$



$$\alpha = f_{i+3}(\ddot{r}_{L1}, \ddot{r}_{L2}, \ddot{r}_{L3}, \varphi_1, \varphi_2, \varphi_3, \dot{\varphi}_1, \dot{\varphi}_2, \dot{\varphi}_3, \ddot{\varphi}_1, \ddot{\varphi}_2, \ddot{\varphi}_3) \text{ for } i = 1, 2, 3. \quad (2)$$

The attained dependencies  $r_{Li}(t)$  and  $\varphi_i(t)$  for  $i = 1, 2, 3$  are recalculated into appropriate movements of particular cylinders.

The calculated signal will be subjected to a safety test (safe distance of all platform bodies, limiting properties of linear motors, limited size of angular displacements, etc.).

## Simulation Analysis of the Platform with Six DOF

In order to verify the dynamical stiffness of the platform with six degrees of freedom, a simulation model (Fig. 3) in the MSC.ANSYS multibody system programme environment with Vibration module for the calculation of natural frequencies and modes of vibration has been created. In Table 1 there are values of the first eight natural frequencies.

**Table 1** The first eight natural frequencies

Number of modes	Natural frequencies [Hz]	Number of modes	Natural frequencies [Hz]
1	11.6	5.	28.3
2	11.7	6.	35.5
3	13.7	7.	70.3
4	26.8	8.	71.3

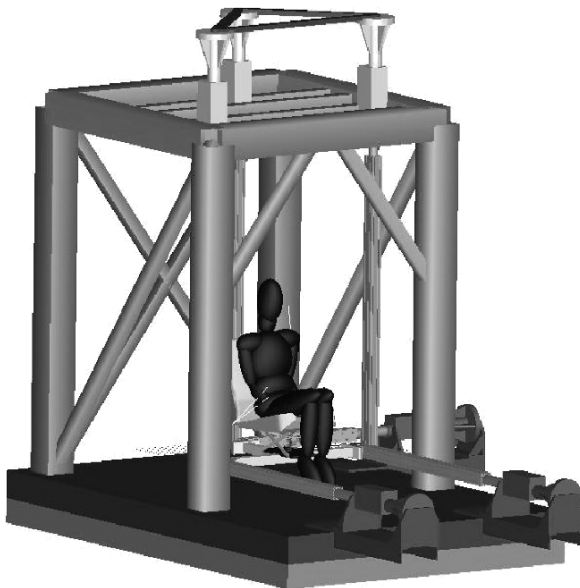


**Fig. 3** A platform model with passive load in the MSC. ADAMS environment

After carrying out a modal analysis of the platform model it was found out that the natural frequency band interferes with the band of considered excitation frequencies. The lowest nonzero natural frequencies have values of 11.6 Hz and 11.7 Hz. The appropriate first two modes of vibration are co-linear with the considered excitation directions. The modal analysis has proved that rubber pads have an in negligible influence on the values of natural frequencies compared with the formerly accepted opinion that structure stiffness is influenced by the stiffness of the platform frame only. That constataion was also confirmed by experimental measuring.

For considering the dynamic properties, accuracy and utilization of the device for experimental research, response simulation to kinematic excitation in time domain in the MSC. ADAMS environment has been carried out.

From the achieved results are, as an example in Fig. 4 (in detail at Dvořák [4]), mentioned responses calculated from acceleration course  $a_y(t)$  by means of FFT during harmonic excitation with a frequency of 5 Hz. It has been shown that when exciting the load with harmonic or periodic signals and their combinations, response courses of the compliant and the absolutely rigid constructions in the area of steady state vibrations (after the transient motion decays) are identical in effect.

Signal courses generated by hydraulic elements, which is just the case of the test platform, are usually distorted with the third harmonic component, relatively small in deflections (3%) that is significant in  $a_y$  acceleration and it still remains after the transient motion decays as it may be seen from the simulation results in Fig. 5.

## Operation Deflection Shapes Measurement

For operation deflection shape measurement, a point contour structure as per Fig. 6 has been chosen on a real device (in detail at Blekta et al. [5] and at Lufinka [6]). Points numbered 10, 11, 12 and 13 correspond to the bottom edge of the foundation

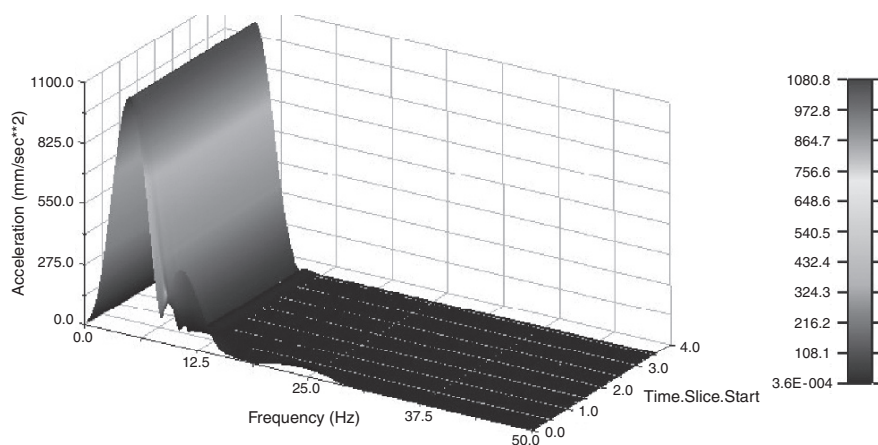


**Fig. 4** The surface of spectra calculated from acceleration course  $a_y$  by the help of FFT

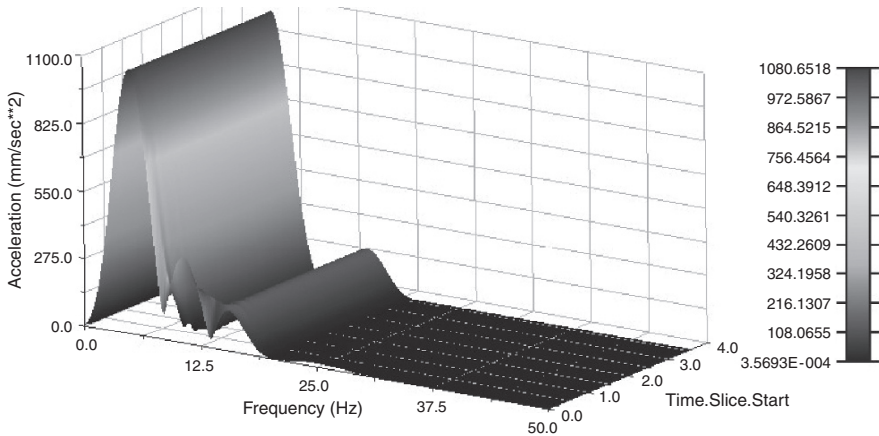


Fig. 5 FFT results of an acceleration signal, the third harmonic component may be observed

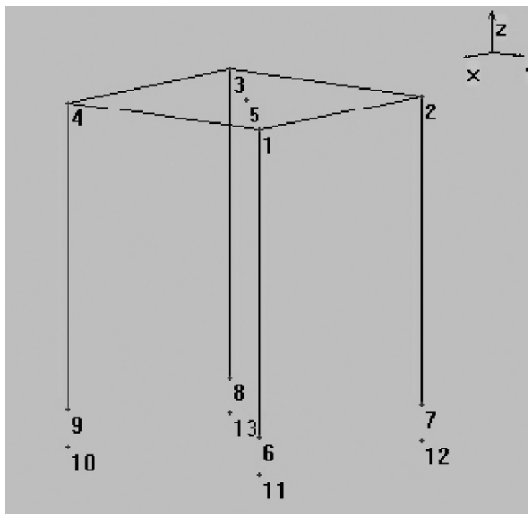


Fig. 6 The structure of points used for operation deflection shape measuring

board of the device; they lie in the close vicinity of the rubber mounting then. Their vibrations confirm the compliance of rubber pads and their part in the total vibrations of the device. Points 1, 2, 3, 4 correspond to the upper nodes of the platform frame and are relevant to the points with significant values of vibration amplitudes. The measurement results are in an acceptable correlation with corresponding simulations [4].

Point 5 corresponds to a central vertical hydraulic cylinder bearing and will serve for evaluating the size of vibration amplitudes of the construction when exciting in z direction.

Those results can be summarized from the evaluated measurements:

- By measuring of operation deflection shapes it has been proved that the foundation board bearing on rubber pads shows significant displacements and decreases unfavourably the total dynamic stiffness of the device.
- The presence of the third harmonic component in exciting signals in measured acceleration spectra has been confirmed.
- By measuring, the size of the device frame deflections at given loading conditions has been determined maximally up to 0,02 mm, which is at a build-up height of approx. 2,9 m and a length of almost 3,2 m more than an acceptable value.
- In the area of the first two natural frequencies (i.e. at 11.6 and 11.7 Hz) in x- and y-directions, a distortion not exceeding 5% occurs due to compliance of the frame; in areas outside resonance, distortion is insignificant.

## Conclusion

The carried out dynamic analysis of a platform model with 6 degrees of freedom in the MSC. ADAMS environment with the Vibration module completed with measuring vibration running shapes has proved a convenient dynamical stiffness of the system in the required range of frequencies. The device will be used namely for evaluating the effects of spatial vibrations on a biomechanical system when establishing the optimum parameters of drivers' seats, for example in research and verification of energy criteria.

## References

1. Barbora J., Mevald J., Energy-based Evaluation Method of Dissipative Properties of a Biomechanical System, Book of Extended Abstracts Engineering Mechanics 2006, Svratka, pp. 18–19.
2. Lundström, R., Holmlund, P., Absorption of Energy During Whole-Body Vibration Exposure, *Journal of Sound and Vibration*, vol. 215(4), 1998, pp. 789–799.
3. Dobry M.W., Energy Analysis of Mechanical and Biomechanical Systems, XX Symposium – Vibrations in Physical Systems, Poznan, 2002.
4. Dvořák B., Dynamic Analysis of Vibration Platform Model with Six Degrees of Freedom. (Ph.D. Thesis), Liberec, 2007.
5. Blekta J., Lufinka A., Dvořák B., Šír M., Some Problems of Car Seats Measurement on Testing Board with Six Degrees of Freedom, In: Book of contribution, Experimental Stress Analysis 2008, Horni Becva, 2008, pp. 23–26.
6. Lufinka, A., The Six Degrees of Freedom Platform, In: Experimental Stress Analysis 2007. Trhanov, 2007.

# Mechanical Design and Optimization of a Microsurgical Robot

M. Miroir, J. Szewczyk, Y. Nguyen, S. Mazalaigue, A. Bozorg Grayeli and O. Sterkers

**Abstract** The tele-operated system with three arms for the microsurgery of the middle ear is composed of an operator console from where the surgeon tele-operates three robotized arms that hold surgery tools with a high level of accuracy. The main difference between these micromanipulators and the conventional minimal-invasive surgery robots is the increased field of vision capacity to carry out complex operational gestures without using dextral tool with intra-body mobility. The method used to design the micromanipulator tool holder is described. A first task consists of analyzing functional specifications. The next step is to define and select a kinematic structure adapted to the task. Finally, a dimensional optimization is carried out by using Pareto front method.

**Keywords** Surgery · Manipulators · Mechanism Design · Kinematics

## Introduction

For more than ten years, important developments in robotized minimal invasive surgery have been carried out in the fields of laparoscopy [1] or cardiac surgery [2]. The goal is to improve the precision, the safety of the gesture and the comfort of the surgeon.

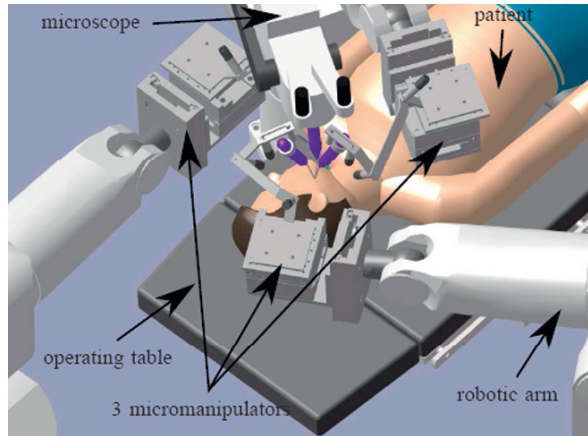
In contrary, the robotic assistance to microsurgery is a recent research domain with many potential applications in the fields of cerebral [3], ophthalmologic [4] or ENT [5, 6] surgery. In this case, the design of a robotic assistance system has to face with specific problems, and nowadays no robotized device dedicated to the microsurgery is used in a clinical context.

Our main objective is thus to develop a robotized system for the microsurgery and particularly the middle ear surgery (Fig. 1). Different robotic systems have already

---

M. Miroir (✉)  
Université Pierre et Marie Curie-Paris 6, FRE-2507, Institut des Systèmes Intelligents et Robotique (ISIR), Paris, Collin SA, Bagneux, France  
e-mail: miroir@isir.fr

**Fig. 1** Overview of a possible assistance robot for the middle ear surgical intervention



been developed and dedicated to this surgery [7–9]. However, these systems do not fully satisfy all the task requirements and in particular the problems of overall size limitation and fabrication costs minimization. Our objective is thus to design a robot for the microsurgery which is:

- Small enough to allow the use of three systems at the same time without cluttering the environment or modifying the ordinary operating layout.
- Dexterous enough to avoid using any intracorporal mobility which leads to significant additional costs in terms of development, fabrication and maintenance.

Our approach will take into account all the technical constraints related to this particular kind of intervention. Moreover, economic and technological requirements inherent to every industrial product will be considered.

In this paper, we first describe the concerned surgical application and characterize the tasks devoted to the controlled device. The choice and the optimal dimensioning of a kinematic structure and of the actuators are then presented. Finally, geometrical parameters of the chosen structure are optimized in regards to the specifications.

## Design Specifications and Expected Performances

The presented system should be able to perform a surgical intervention in the middle ear. In most cases, the considered intervention uses the auditory canal with incision of the tympanic membrane as insertion path for the instrument [10, 11]. The patient's head is oriented on one side and immobilized. The surgeon can observe the operation area only through a microscope placed above the auditory canal at a maximum height's of 300 mm. The tools (three of them can be used during the intervention at the same time) are introduced into the patient's ear through a funnel-shape speculum. Thus, the developed system should include three independent and simultaneously-controlled mandatory micromanipulators, each dedicated to the

manipulation of one tool. These three micromanipulators will be identical, based on the same kinematic and dimension. The surgeon tele-operates the unit using a remote device.

In order to quantitatively specify the task, different measurements were taken. First of all, the manipulator workspace was identified by measuring the anatomy of the ear for ten different patients by means of X-rays and the navigation system Digipointeur<sup>®</sup> [12]. Figure 2(a) presents a geometrical modeling of this workspace. It includes:

- In terms of reachable points: A volume made up of the external auditory canal, and the visible part of the case of tympanum,
- In terms of reachable orientations: All the achievable orientations considering a rectilinear tool introduced into this volume.

The interaction forces between the tool and the bones were measured using an experimental setup (Fig. 2b) including an *ATI nano 43* 6-axis gauge force/torque sensor [13]. We found that the forces applied at the tip of the tool by the surgeon never exceed 3 N. Besides, our clinical partners consider as acceptable a motion resolution not exceeding 5  $\mu\text{m}$  in translation and 1 $^\circ$  in rotation. Finally, a geometrical modeling of the environment was proposed (Fig. 2c) which will be useful to evaluate the obstacle avoidance and vision preservation capabilities of the overall system.

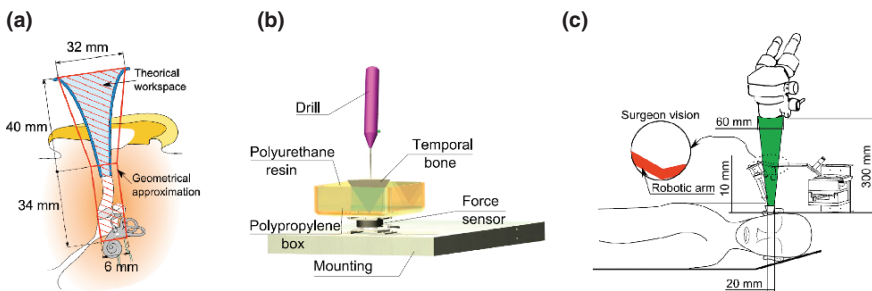
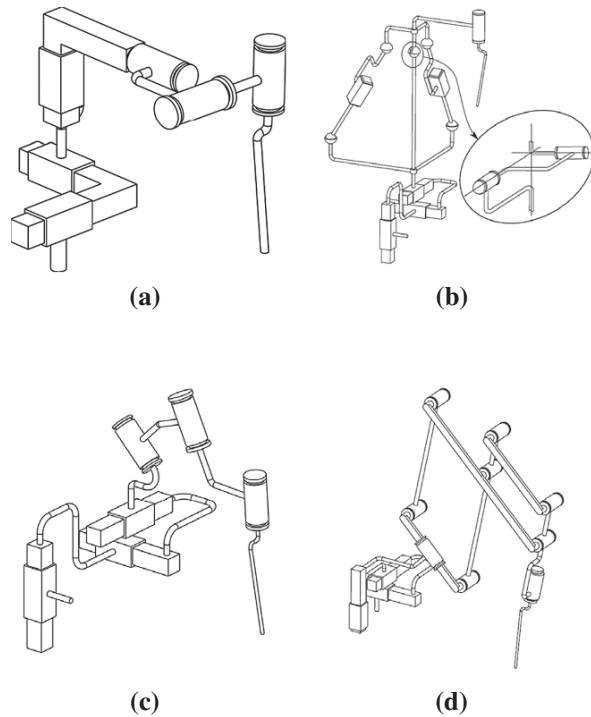


**Fig. 2** From left to right, (a) geometrical approximation of the workspace, (b) experimental setup for measuring the forces, and (c) a global view of the intervention environment

### Topological Structures

Figure 3 shows four candidates of possible kinematic structures. These structures are kinematically non-redundant in order to minimize the complexity and costs. All these structures are mounted on Cartesian “cross tables” in order to decouple translations from rotations of the tool. Moreover, the large displacements along the speculum axis can be entirely supported by the Z-axis of the cross table. In the same way, the four structures have a final rotoid joint devoted to perform large rotations around the tool axis.

**Fig. 3** Kinematic candidates:  
**(a)** 6 dof series, **(b)** 6 dof mixed,  
**(c)** 6 dof series with offset rotation centre (orc),  
**(d)** 6 dof Evans with orc



The kinematics of Fig. 3(a) is a classical serial structure finished by a convergent wrist with orthogonal axes. This kind of structure is relatively simple to design and to control. However, it presents the disadvantage of a rotation centre outside the specified workspace. Indeed, rotating around the tip of the tool would imply in this case very large displacements at the X and Y axis of the cross table. Assuming a tool having a length of 15 cm for example, commanding a  $\pm 20^\circ$  rotation around the tip of the tool in any plane including the workspace principal axis would lead to a more than 10 cm horizontal displacement of the cross table.

The kinematics of Fig. 3(b) has a standard parallel platform well suited for achieving linear and angular displacements with a high accuracy. However, the overall size, weight and complexity are undesirable for the targeted application and it does not have a rotation centre in the workspace either.

The kinematics of Fig. 3(c) has a rotation centre located at the intersection of the three last rotations axis. A clever choice of these axes allows the centre of rotation to coincide perfectly with the end of the handled tool.

The kinematics of Fig. 3(d) also carries out an offset rotation centre by means of a motorized parallelogram (mechanism of Evans). Moreover, it allows an increased rigidity and thereby a higher accuracy. However, this kinematics is complex compared to the previous one and the height of the structure is not compatible with the microscope observation.



In conclusion of this qualitative analysis of kinematics candidates, the design of the micromanipulators will be based on the structure presented on the Fig. 3(c).

Figure 4 shows the selected kinematic structure with its motorized joints. The actuators of the cross table are *Owis* linear motors which provide an impressive stroke/size ratio. The first two actuators have a stroke of 25 mm and the third one has 100 mm. The rotation actuators used for the three rotoid links are *Faulhaber* coreless DC motors selected by their good weight/power ratio.

These actuators guarantee a sufficient displacement resolution at the tip of the tool in regard to the specifications. Indeed, if  $d$  is the axial resolution of the cross table motors, we know that the resolution in linear displacement at the tip of the tool  $d_{max}$  is such that  $d_{max} < \sqrt{3}d$ . If  $d = 2\mu\text{m}$  (as specified by the manufacturer) then  $d_{max} = 3,5\mu\text{m}$  which is lower than the desired resolution  $d_{des} = 5\mu\text{m}$ . On the other hand, if  $q$  is the angular resolution of the chosen rotation actuators, we know that the resolution in angular displacement of the tool  $q_{max}$  will never be larger than  $3q$ . Then, if  $q = 0,2 \times 10^{-3}^\circ$  (as specified by the manufacturer) we will have  $q_{max} = 0,6 \times 10^{-3}^\circ$  which is much lower than  $q_{des} = 1^\circ$ .

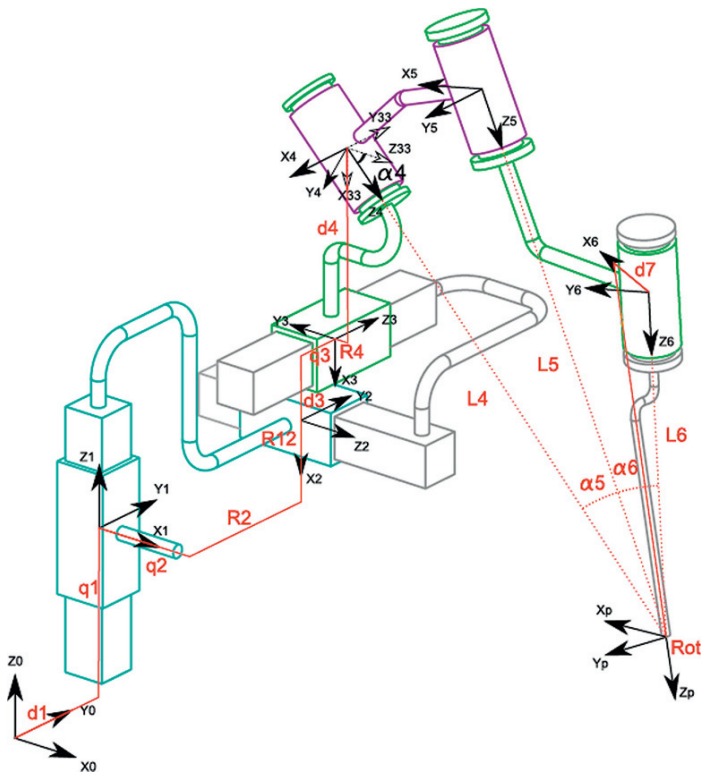


Fig. 4 Equipped kinematics

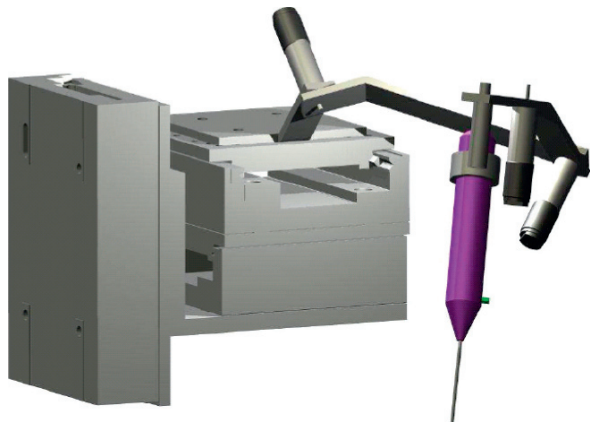
## Geometrical Optimization

Figure 5 shows the joint parameters of the kinematic structure. Five parameters relate to the position of the cross table and are imposed by the dimensions of the chosen linear motors. The other six parameters (Table 1) relate to the position of the three rotoid joints and the relevant dimensions of the manipulator.

The values of these remaining geometrical parameters were optimized with respect to the requirements that have not yet been taken into account at this stage:

- Ability to apply the desired forces,
- Distance to the obstacles,
- Occlusion of the field of vision.

The performances of the 90472 manipulators corresponding to the 90472 sets of parameters indicated in Table 1 were evaluated using a numerical simulation. This simulation consists of calculating all the successive configurations reached by the manipulator when the tool performs a specific 6D trajectory. This trajectory includes an approach path from an initial reference position and an operative path representative of the workspace in terms of angular and linear displacements. During this trajectory, the upper surface of the cylinder is swept by the end of the tool (see



**Fig. 5** Parameters definition

**Table 1** Parameters values related to pivots and dimensions

	$\alpha 4$	$L5$	$\alpha 5$	$\alpha 6$	$d7$	$L6$
mini values	25°	90 mm	25°	15°	5 mm	130 mm
maxi values	55°	140 mm	60°	60°	25 mm	180 mm
pitch	5°	10 mm	5°	5°	5 mm	10 mm

**Fig. 6** Tool representative trajectory used for the optimization process

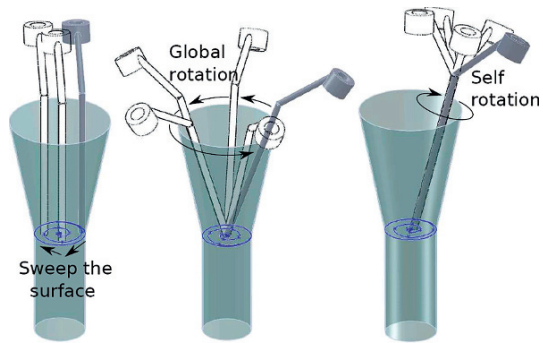


Fig. 6 in 30 steps: 17 for the circle and 13 for the spiral. For each step, the capacity of the robot to produce the maximum slopes of its tool is evaluated in 9 steps. Finally, for each configuration, the capacity of the manipulator to perform a rotation of the tool along its own axis is evaluated with 9 steps.

As rotation and translations are decoupled, it must be pointed out that the accessibility to the other points of the cylinder does not need to be evaluated. Remarkably, the vertical axis of the robot has a sufficient stroke in comparison with the depth of the workspace. The trajectory thus generated is made up of 2433 configurations  $((17 + 13) \times 9 \times 9) + 3$  including 3 for the approach of the tool. For each reached configuration, the simulation computes:

- The forces that the manipulator can apply at the tip of the tool,
- The smallest distance robot/environment,
- The field of vision percentage of the microscope not intercepted by the arm of the robot,
- The stroke imposed to the joint actuators.

Finally, only 4063 candidate manipulators are able to perform the entire trajectory without contacting the environment or going beyond their joints limits and to produce at each step of the trajectory the required tip of the tool forces without exceeding their motors capacities.

Each retained manipulator is represented on Fig. 7 by a point positioned according to its scores in terms of smallest distance to the environment during the trajectory and average percentage of non-obstructed vision.

A Pareto's front made up of eleven non-lower solutions [14, 15] can be highlighted on this graph. This Pareto's front has the characteristics of nearly vertical graphs, all the scores in vision lying between 90% and 93.5%. Logically, we selected the manipulator presenting the best score in terms of distance to the environment. Table 2 presents the geometrical parameters of the eleven non-lower solutions. The last row corresponds to the selected configuration.

**Fig. 7** Acceptable configurations plotted

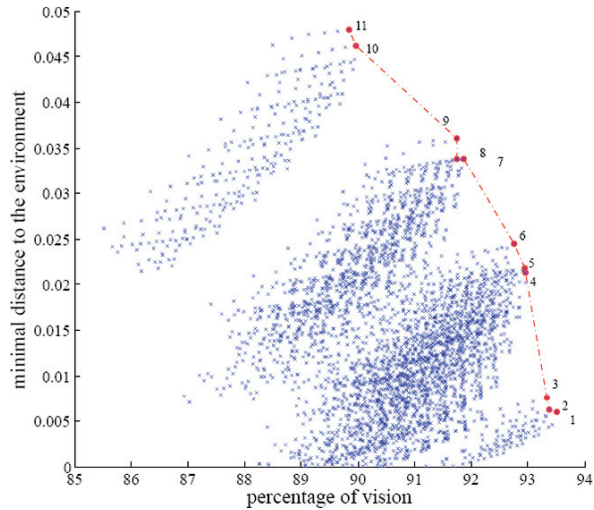


**Table 2** End values for the eleven possible solutions

$\alpha 4(^{\circ})$	$L5$ (mm)	$\alpha 5(^{\circ})$	$\alpha 6(^{\circ})$	$d7$ (mm)	$L6$ (mm)	Vision (%)	Distance (mm)
30	140	60	50	10	180	93.5	6
50	140	50	50	10	180	93.5	6.2
40	140	40	50	10	180	93.3	7.5
40	140	55	45	5	180	92.9	21.3
50	140	45	45	5	180	92.9	21.7
50	140	40	45	5	180	92.7	24.4
35	140	55	40	5	180	91.8	33.8
50	140	40	40	5	180	91.7	33.8
55	140	40	40	5	180	91.7	36.1
35	140	55	35	5	180	89.9	46.2
55	140	35	35	5	180	89.8	47.9

## Conclusion and Future Work

This paper presents a detailed approach for the design of a robotic system in the field of microsurgery. It led to a multi-criteria optimization problem resolution in which constraints such as precision and compactness were taken into account. The implemented optimization method is based on a systematic exploration of the parameters domain and a *MatLab* routine for the constraint evaluations. At this stage, the robot is entirely defined in its geometry and motorization. The robot structure we propose has a compact geometry and allows performing any 6 dof displacements of the tip of the tool into the workspace of the external and the middle ear. Moreover, prototyping this structure will be relatively simple noting that it does not include any miniature intracorporeal mobility. Future work concerns realization and performances test via coworking with the clinical partners.

## References

1. Guy-Bernard Cadière et al. “Feasibility of Robotic Laparoscopic Surgery”, *In World Journal of Surgery*, Vol. 25(11), November 2001, pp. 1467–1477.
2. Nabil Zemiti et al. “Mechatronic Design of a New Robot for Force Control in Minimally Invasive Surgery”, *IEEE/ASME Transactions on Mechatronics*, Vol. 12(2), April 2007, pp. 143–153.
3. P. Di Donato et al. “La neuronavigation : principe et intérêt”, ITBM-RBM 2000, 21:70–7.
4. Natalie Smith-Guerin, “Contribution à l’aide robotisée au geste chirurgical; nouvelle approche en ophtalmologie”, PhD thesis, Laboratoire d’Automatique Industrielle de l’INSA de Lyon, 2000.
5. Russell H. Taylor et al. “A Steady-Hand Robotic System for Microsurgical Augmentation”, *In MIC- CAI '99 : Proceedings of the Second International Conference on Medical Image Computing and Computer-Assisted Intervention*, pp. 1031–1041, London, UK, 1999, Springer-Verlag.
6. Daniel L. Rothbaum et al. “Robot-Assisted Stapedotomy Micropick Fenestration of the Stapes Footplate”, *Otolaryngology Head & Neck Surgery Journal*, Vol. 127(5), 2002, pp. 417–426.
7. Peter J. Berkelman et al. “Performance Evaluation of a Cooperative Manipulation Microsurgical Assistant Robot Applied to Stapedotomy”, *In MICCAI '01: Proceedings of the 4th International Conference on Medical Image Computing and Computer-Assisted Intervention*, pp. 1426–1429, London, UK, 2001, Springer-Verlag.
8. C.-C. Ngan et al. “Hexapod-based cochleostomyhexapod basierte cochleostomie”, <http://www.curac.org/curac06/download/abstracts/18.pdf>.
9. M. Leinung et al. “Robotic-Guided Minimally-Invasive Cochleostomy: First Results”, *In: GMS Current Topics in Computer- and Robot-Assisted Surgery (GMS CURAC)*, Vol. 2(1), 2007.
10. . Pierre Elbaz et al. “L’Otospongiose”, Fondation Adolphe de Rothschild, Paris, 2000.
11. Yann Nguyen et al. “Diode Laser in Otosclerosis Surgery: First Clinical Results”, *Otol Neurotol*. [Epub ahead of print], 28 Feb 2008, PMID: 18317398 [PubMed – as supplied by publisher].
12. Collin ORL, Fabricant et Distributeur de matériel pour l’ORL et la Chirurgie Maxillo-Faciale, [www.collin-ort.com](http://www.collin-ort.com).
13. Daniel L. Rothbaum et al. “Robot-Assisted Stapedotomy Micropick Fenestration of the Stapes Footplate”, *Otolaryngology Head & Neck Surgery Journal*, 127(5), 2002, pp. 417–426.
14. K. Deb et al. “A fast and elitist multi-objective genetic algorithm: NSGA-II”, *In: IEEE Transactions on Evolutionary Computation*, Vol. 6(2), April 2002.
15. Damien Sallé, “Conception Optimale d’Instruments Robotisés à Haute-Mobilité pour la Chirurgie Mini- Invasive”, PhD thesis, Université Pierre et Marie Curie, Paris 6, 2004.

# Multy Mirror Adjustable Space Reflector as the Mechanism with Many Degrees of Freedom\*

Vicktor I. Bujakas

**Abstract** Large precise space reflectors are needed for realization of advanced space projects (JWST (USA) [1], Millimetron (Russia) [2], SAFIR (USA) [3], etc.). To meet high requirements of the projects to the surface accuracy different technological and structural approaches are considered. Among other approaches adaptive methods are proposed to ensure reflecting surface stability in orbit. Statically determinate adjustable structures, which are the subject of the paper, give new interesting possibilities for adaptive approach development.

## Introduction

The primary mirror of large ground-based mm-band telescopes is a large precise reflector formed by high-precision solid panels (modules, facets), which are mounted on a rigid supporting frame (common base). The adjustment or active shape control of reflecting surface are made relative to the frame. It is important that during the adjustment the modules should remain non-deformed, that is, stress-free. In the early space studies the same approach was proposed for large precise space reflectors development. However later it becomes clear that the assemblage of a large rigid common base in orbit is a difficult, expensive technical problem. Therefore it is strongly desirable that in space such multi-mirror designs be used, that on the one hand need no rigid supporting frame, and on the other remain stress – free during shape adjustment.

Such a possibility could be provided by statically determinate adjustable mechanical structures [4–6], which we consider in the paper. We now briefly discuss the approach.

---

V.I. Bujakas (✉)

P.N. Lebedev Physical Institute, Russian Academy of Science, Moscow, Russia  
e-mail: bujakas@yandex.ru

\*The work was supported by RFBR grant no. 07-08-08170-3

## Statically Determinate Adjustable Reflectors

Let us consider two mirrors (solid modules), connected via **S** links (Fig. 1)

If

$$S < 6$$

system is (in general) the mechanism with  $D = 6 - S$  degrees of freedom (Fig. 1a).

If

$$S = 6$$

and links are independent we get a geometrically unchangeable, statically determinate structure (Fig. 1b). **Any link of such structure being free the system transforms into a mechanism with one degree of freedom.** If the link is realized as adjustable the mutual position of the modules – the shape of the structure – may be changed without stress with small forces.

If

$$S > 6$$

– arise statically indeterminate structure (Fig. 1c). In this case the structure becomes strained and modules deformed when some links are changed.

Thus two-mirror statically determinate structures, being between mechanisms and statically indeterminate structures, have the properties very useful for developing adjustable reflectors. Statically determinate multi-mirror designs have the same properties.

Let us consider a structure consisting of **n** modules connected via **S** links. If the Maxwell condition

$$S = 6(n - 1) \tag{1}$$

is fulfilled and links are independent the multi-mirror structure is statically determinate and geometrically unchangeable. **We consider the structures which turn into a mechanism with one degree of freedom the moment an arbitrary link is released.** Therefore if some links are realized as controllable, the mutual position of the modules – shape of modular reflector – may be changed with small forces by variation of adjustable links. Such designs without common base remain stress free during

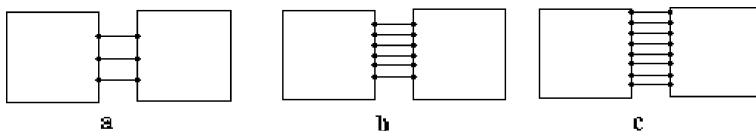


**Fig. 1** Two-mirrors structures (a) mechanism, (b) statically determinate structure, (c) statically indeterminate structure

- assemblage,
- adjustment,
- active shape control,
- not coordinated adjustment of the links.

Different distributions of links (1) within a structure lead to different multi-mirror designs. However if we try to distribute the links between the modules uniformly, the condition (1) will not be satisfied. Therefore we had distributed between additional links some modules. Three types of statically determinate structures are presented in Figs. 2, 3 and 4

Each line between the modules in the figures denotes the link (kinematics constraint), crossed lines denote the adjustable link. In Figs. 2 and 3 additional links are placed between the mirrors on supporting directions  $OA_1, OA_2, OA_3, OA_4$ . The modules lying on support directions form the ribs of rigidity of the structure. In Fig. 4 additional links are placed between periphery mirrors. It can be checked that the condition (1) in figures is fulfilled.

Now we briefly explain the term “link”. The link is a connection between the modules that introduce in the design one kinematics constraint. Such junction may be realized by the rod, connected with the modules by spherical hinges (Fig. 5a). One physical connection between the modules may introduce several kinematics constraints in the system. For example, the rod in Fig. 5c introduce in the system three kinematics constraints and is equivalent to three links.

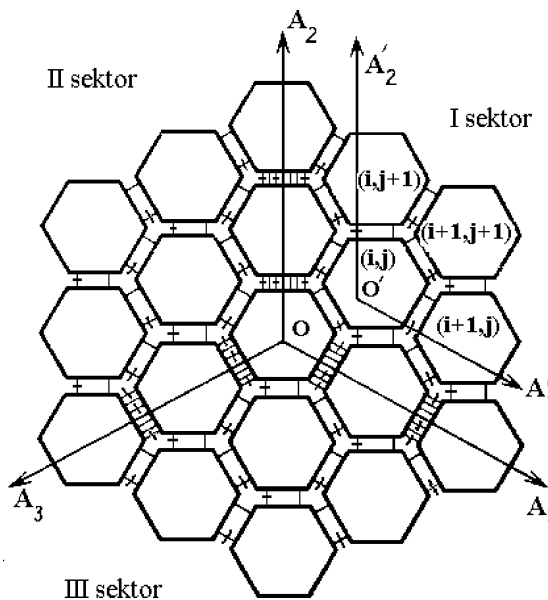


Fig. 2 Multi-mirror adjustable reflector formed by hexagonal modules



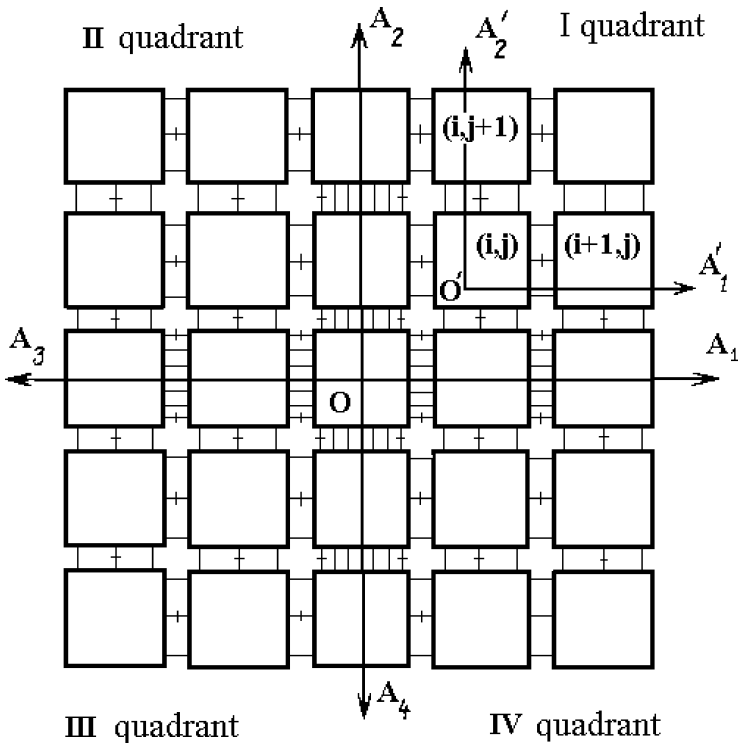


Fig. 3 Multi-mirror adjustable reflector formed by square modules

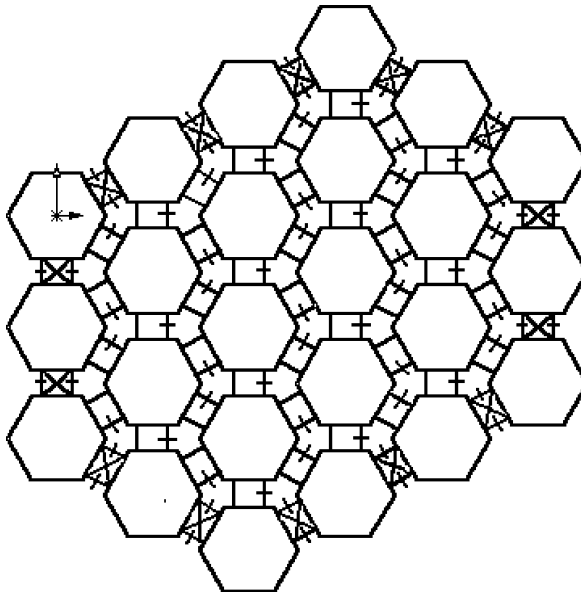
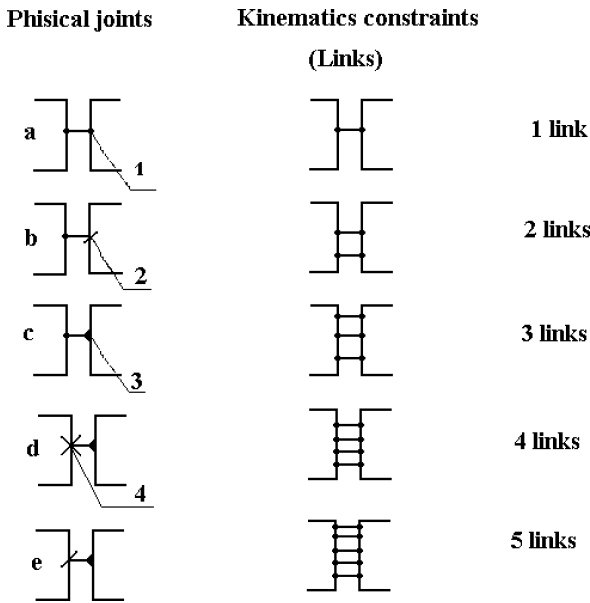


Fig. 4 Adjustable reflector with stiffened periphery



**Fig. 5** Physical joints and mechanical constraints. 1 – spherical hinge, 2 – cylinder hinge, 3 – rigid joint, 4 – cardan joint

### Mathematical Model

Within existing tradition the problem of structure dynamics and the problem of structure shape control are solved separately. It is assumed the shape control of the structure is realized quasistatically, therefore mathematical models describing shape control problems of multi-mirror designs are kinematic, not dynamic.

To describe shape variation of a structure let us introduce two-index numeration of the modules and determine the state of the mirror number (i, j) by the vector  $y(i, j)$ . In statically determinate structures the modules that form the design do not deform during shape control (mutual position of the modules varies only). Therefore the current state of mirror number (i, j) can be described by 6-vector  $y(i, j)$ , which determinate spatial position of the mirror being considered as a solid body. The coordinates of mass center and the angles, which determinate the spatial position of the body in respect to the mass center, may be used as the coordinates of vector  $y(i, j)$ .

Let module (i, j) be connected by a rod and the junction units are realized as spherical hinges. Then for the fixed link we get:

$$||a(y(i, j)) - b(y(i + 1, j))|| - l(i, j, i + 1, j) = 0$$

and for adjustable link we get:

$$\|a(y(i, j)) - b(y(i + 1, j))\| - u(i, j, i + 1, j) = 0$$

Here the vectors  $a$  and  $b$  determine the spatial position of the spherical hinges,  $\|c\|$  is Euclidean norm of the vector  $c$ ,  $l$  is a length of fixed rod,  $u$  is a control variable (length of adjustable rod).

The structures studied are uniform (excluding links in support directions in Figs. 3, 4 and peripheral links in 5). If all the repeating links are taken into account we get a system of equations in a finite differences:

$$F(y(i, j), y(i, j, *), U) = 0 \quad (2)$$

Here the vector  $y(i, j, *)$  describes the spatial position of the modules adjacent to module  $(i, j)$ ,  $U$  is a vector of control variables.

The equations of the links between the modules in support directions in Figs. 3, 4 or between peripheral modules in Fig. 5 setup boundary conditions for system (2). Equation (2) together with boundary conditions describes the shape variation of statically determinate multi-mirror reflector due adjustable links variation.

## Shape Control of Multi-Mirror Reflectors

From control theory point of view statically determinate adjustable multi-mirror reflector is two-dimensional discrete media (distributed system) with distributed control. The numbers (indexes) of the mirrors are the independent variables, dependent variable is 6-vector  $y(i, j)$ , which determinate spatial position of the mirror, parameters of adjustable links play a role of control variables. For studying the kinematics "in a small" the linear approximation of system (2) should be used. Therefore the mathematical formulation of control problem in the vicinity of precise state of the structure leads to the system of linear equations in finite difference with linear control.

## Necessary Conditions of Controllability

Due to the fabrication and assemblage errors and to external disturbances the initial alignment and, in some case, active shape control of reflecting surface are needed. Adjustment or active shape control of statically determinate multi-mirror designs can be realized by regulation of the links. The goal of the control is to remove the mirrors of a disturbed structure in the prescribed positions.

It is strongly desirable that the number of adjustable links be minimized. Two kinds of multi-mirror designs are interesting for applications.

If multi-mirror design operates as a concentrator, two angles, which determine the direction of reflecting beam, should be adjustable. In this case the minimal number **P** of adjustable links (necessary conditions of controllability) is

$$P = 2n - 2. \tag{3}$$

It is supposed that the external forces determinate the position of the central mirror.

For multi-mirror antennas the minimal number of adjustable links is:

$$P = 3n - 3, \tag{4}$$

because the direction (two angles) and the phase of reflected signal for each module had to be controllable. From this point of view the structures in Figs. 3 and 5 are the “antennas” (condition (4) is fulfilled), the structure in Fig. 4 is the “concentrator”(condition (3) is fulfilled).

### Algorithm of Shape Control

Shape control of large mirrors with common base is realized relative to the base. Adjustment of any facet does not change the positions of other modules.

The situation in statically determinate multi-mirror designs without common base is strongly different. If the position of some module is changed, the state of some other modules is disturbed. However, the algorithms of shape control, which transform the disturbed structure in the prescribed precise position, can be built. Different statically determinate structures have different laws of disturbance propagation, and therefore need in different algorithms of shape control.

Let us consider for example the structure in Fig. 4. The structure is symmetric therefore only the first quadrant may be studied. This part of the structure can be successively assembled according to Fig. 6. If two-index numeration of the modules is introduce (Fig. 6, step 8), the assemblage in sequence (0,0), (0,1), (0,2),..., (0,n), (1,0), (1,1), (1,2), . . . , (1,n), (2,0), (2,1), (2,2), . . . , (2,n), . . . , (n,0), . . . , (n,n) is possible. Note that at each step of such an assemblage conditions (1), (2) are fulfilled. Therefore, if the links, which are introduced in the system on each step of assemblage, are independent, the structure remains geometrically unchangeable on each step of assembling.

The disturbance of the links, which connect the (i, j) module with (i - 1, j) and (i, j - 1) modules (i > 0, j > 0) does not affect the modules, which were earlier introduced in the structure, and the modules with the indexes (i, 0), (i, 1), . . . , (i, j - 1), (i + 1, 0), (i + 1, 1), . . . , (i + 1, j - 1), . . . , (n, 0), . . . , (n, j - 1), which are fastened to the non-disturbed part of the structure. So the variation of the links, which connect (i, j) module with (i - 1, j) and (i, j - 1) modules, disturbs the position of the mirrors in the cone A<sub>1</sub>OA<sub>2</sub> (Fig. 6, step 8) and does not affect on the other mirrors of the structure.

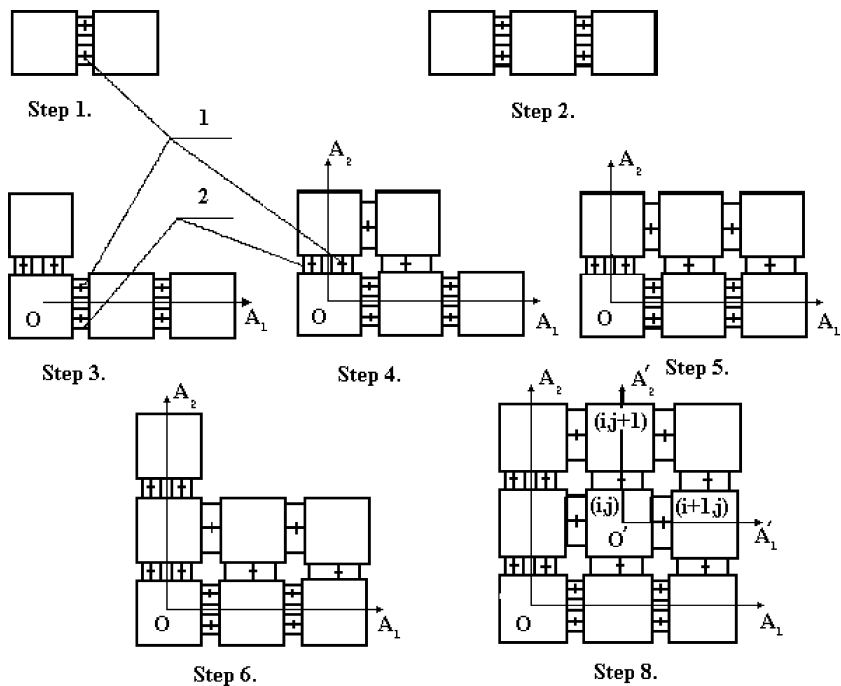


Fig. 6 Successive assemblage of multi-mirror design

The cone  $A'_1OA'_2$  is a discrete analog of the characteristic cone of partial derivatives equations of hyperbolic type.

The successive algorithm of shape adjustment follows from this property. Let us use

- for  $(i,0)$  module adjustment the controllable links, which are placed between  $(i, 0)$  and  $(i - 1, 0)$  modules,
- for  $(0,j)$  module adjustment the controllable links, which are placed between  $(0, j)$  and  $(0, j - 1)$  modules,
- for  $(i,j)$  module adjustment the controllable links, which are placed between  $(i, j)$  module and  $(i - 1, j)$  and  $(i, j - 1)$  modules.

We will regulate the modules position in the sequence  $(0,0), (0,1), (0,2), \dots, (0,n), (1,0), (1,1), (1,2), \dots, (1,n), (2,0), (2,1), (2,2), \dots, (2,n), \dots, (n,0), \dots, (n, n)$ . In this case the adjustment of a current module does not disturb the state of the modules, which were early put in prescribed position. Therefore the alignment of the multi-mirror design will be finished during the finite number of steps.

### Physical Models of Multi-Mirror Controllable Reflectors

To check the approach a physical models of adjustable structures without common base was developed and made. The design in Fig. 7 contains 10 hexagonal modules, which are realized as spatial trusses (Fig. 7a). The size of each module is 500 mm in diagonal. The adjustable joints and actuator are presented in Fig. 7b.

There are three reference points on the surface of each module. The goal of the control is translate the disturbed structure in such position, when all reference

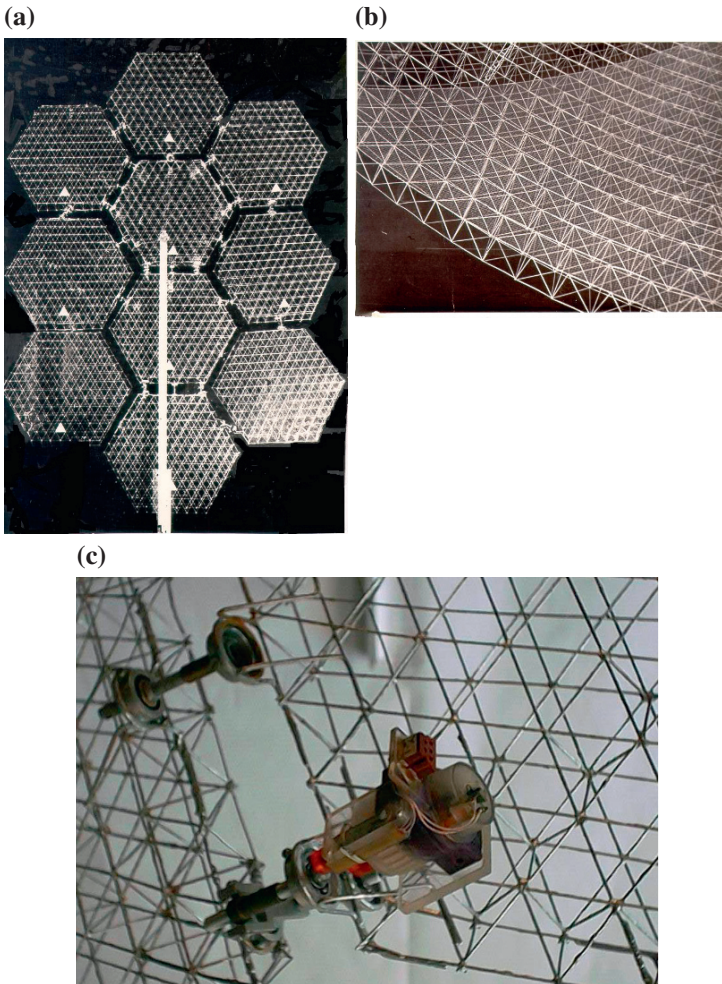


**Fig. 7** Physical model of multi-mirror adjustable reflector (a) the model, (b) the design of the module, (c) adjustable joints and actuator

points lie on prescribed surface (plane, sphere or parabolic). The tests confirm the possibility of stress free assemblage and shape adjustment in the structures without common base.

## References

1. <http://www.jwst.nasa.gov>
2. N.S. Kardashev et al. "Millimetron Project", Proceedings of P.N. Lebedev Physical Institute. Radio astronomical techniques and methods, Vol. 228, pp. 112–128, 2000 (in Russian), <http://www.asc.rssi.ru/millimetron/>
3. <http://safir.jpl.nasa.gov>
4. V.I. Bujakas, "Shape Control and Kinematics Waves in Large Space Statically Determinate Structures", International Journal of Space Structures, Vol. 13, No. 1, pp. 13–22, 1998.
5. <http://www.asc.rssi.ru/radioastron/description/>
6. V.I. Bujakas, A.G. Rybakova, "High Precision Deployment and Shape Correction of Multi-mirror Space Designs", Proceedings of IUTAM-IASS Symposium on Deployable Structures: Theory and Application, pp. 51–57, Cambridge, UK, 1998

# Dynamic Modeling of a Parallel Robot Used in Minimally Invasive Surgery

N. Plitea, D. Pisla, C. Vaida, B. Gherman and A. Pisla

**Abstract** The progresses in engineering and medicine have opened the way for the use of robots in the operating rooms. Robots are useful tools in minimally invasive surgery (MIS), providing benefits such as reduction in hand tremor, navigation, and workspace scaling. In this paper the inverse dynamic model for a parallel robot conceived for MIS using virtual work principle is presented. The dynamic model is obtained by means of the theory of equivalent lumped masses, in order to simplify the given mechanical system from the structural point of view.

**Keywords** Parallel robot · Minimally invasive surgery · Dynamics · Kinematics · Simulation

## Introduction

The parallel robots dynamics requires a great deal of computing as regards the formulation of the generally nonlinear equations of motion and their solution. To establish the motion equations, there are essentially four methods: Newton-Euler equations with impulse and momentum formulation or D'Alembert equations; Lagrange equations of first kind with so-called LAGRANGE multipliers; Lagrange equations of second kind with a minimum number of system coordinates; Virtual work formulation including inertia forces and torques.

Geng and Haynes [1] use the Lagrange formalism to derive the dynamic equations of the parallel robots. Pierrot and Reynaud [2] propose a simplified method for the determination of the dynamic model of the DELTA and HEXA robots in two steps. Codourey [3] proposes the first dynamic model that can be used to control the parallel DELTA robot in real time. Miller and Clavel [4] present the complete dynamic model of the DELTA robot based on Lagrange equations. Guglielmetti and Longchamp [5] present the inverse dynamic model for the DELTA robot in the

---

N. Plitea (✉)

Technical University of Cluj-Napoca, Constantin Daicoviciu 15

RO-400020 Cluj-Napoca, Romania

e-mail: Doina.Pisla@mep.utcluj.ro



analytical form. Tadokorro [6] also explains how dynamic equations can be used in a control scheme closed loop for serial robots. Honneger et al. [7] suggested the use of the dynamic equations in an adaptive control scheme for Hexaglide robot. Tsai [8] presents a dynamic model for a Stewart parallel structure using principle of virtual work. To solve the dynamic model, Merlet [9] uses Lagrange formulas for the direct and the inverse dynamic model for the “*left hand*”, to a prototype accomplished at INRIA based on a KPS kinematic chain structure. Pisla and Kerle [10] propose a generalized dynamic model for parallel robots using first order Lagrange equations on the basis of equivalent masses. Guegain [11] presents a new solution for the dynamics for the Orthoglide using Newton-Euler equations. Itul and Pisla [12] present a comparative study between different dynamic methods for 6-DOF parallel robots.

Ripianu [13] and Hockey [14] have dealt with the problem to replace a mass-loaded rigid body by single rigidity connected mass point (lumped masses) without changing the mass geometry. This theory will be used to solve the dynamics in the paper.

Regarding the application of robots for surgical applications there are some investigators focused on exploring the capabilities of robots in this field [15, 16]. AE-SOP robotic arm, used to guide a tiny camera inside the body, was the first robotic system used in surgery, which was produced by Computer Motion [17]. A competitor of Computer Motion, Intuitive Surgical, the da Vinci<sup>TM</sup> Surgical Robotic System, which became the market competitor of Zeus until 2003 when the two companies merged [17]. Prof. Moshe Shoham has performed extensive studies regarding: the performances of the surgeon in endoscopy, focused on the fulcrum effect [15]; the development of new miniaturized robots which can be mounted on the bones and a research regarding the different methods for scanning and surface recognition of bones before the surgical intervention, [16]. Simaan et al. [18] have developed a new robotic model designed for the MIS of the throat, which could manipulate 2 up to 3 instruments for the suture and handling of soft tissue.

The paper is organized as follows: Section *Paramis Parallel Robot for MIS* is dedicated to the description of the studied parallel robot for MIS. Section *Kinematic Model* deals with the kinematics of the PARAMIS robot. Section *The Inverse Dynamic Model* presents the dynamic model of the parallel robot using the virtual work principle. Some numerical and simulation results obtained from kinematics and dynamics are presented in Section *Numerical Results*. The conclusions are presented at the end of the paper.

## **Paramis Parallel Robot for MIS**

A parallel robot – PARAMIS has been already developed, which could be used for surgical instruments positioning, [19, 20] (Fig. 1). The low-cost robot allows a wider spread of the robot in the OR, an easier acceptance and a better feedback for further improvements.

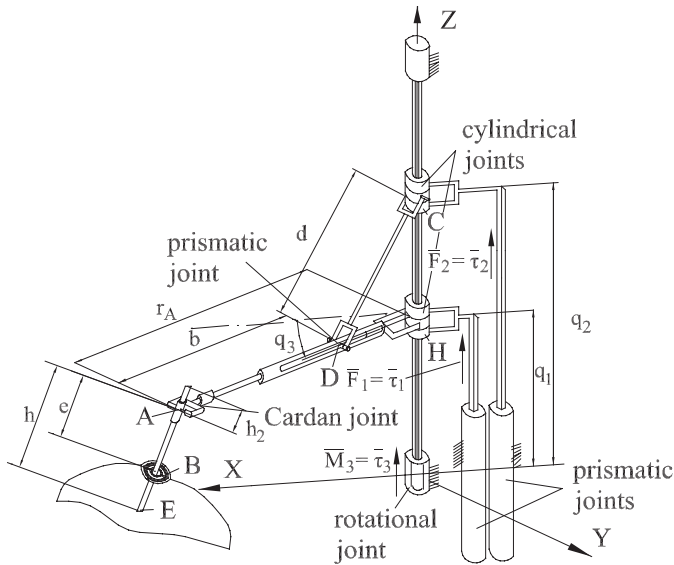


Fig. 1 PARAMIS parallel robot for MIS

The robot has 3-DOF and it consists of three actuated joints (two prismatic and a rotational one). The passive joints are two cylindrical joints, one prismatic joint and one Cardan joint. The particularity of the motion is the fact that the endoscope will move around a fixed point in space, which is the entrance point of the trocar in the abdominal wall of the patient (the point B  $(X_B, Y_B, Z_B)$ ). The geometrical parameters of the parallel robot are represented by  $b, d, h$ ;  $X_B, Y_B, Z_B$  (Fig. 1). The endoscope can be positioned in any point of the abdominal area using the 3-DOF of the robot to offer the surgeon the best possible details of the surgical field.

### Kinematic Model

In [19] the robot geometric models have been already presented.

If  $X_E \neq X_B, Y_E \neq Y_B$  the joint coordinates vector  $q(q_1, q_2, q_3)$  is:

$$q_1 = Z_E + h \cdot \frac{Z_B - Z_E}{\sqrt{(X_B - X_E)^2 + (Y_B - Y_E)^2 + (Z_B - Z_E)^2}}$$

$$q_2 = q_1 + \sqrt{d^2 - \left[ b - \sqrt{\left( X_E + h \cdot \frac{X_B - X_E}{h_1} \right)^2 + \left( Y_E + h \cdot \frac{Y_B - Y_E}{h_1} \right)^2} \right]^2}$$

$$q_3 = a \tan 2 \left[ Y_E + h \cdot \frac{Y_B - Y_E}{\sqrt{(X_B - X_E)^2 + (Y_B - Y_E)^2 + (Z_B - Z_E)^2}}, X_E + \frac{X_B - X_E}{\sqrt{(X_B - X_E)^2 + (Y_B - Y_E)^2 + (Z_B - Z_E)^2}} \right] \quad (1)$$

If  $X_E = X_B, Y_E = Y_B$  the joint coordinates vector  $q(q_1, q_2, q_3)$  is:

$$q_1 = Z_E + h; q_2 = q_1 + \sqrt{d^2 - \left( \sqrt{X_E^2 + Y_E^2} - b \right)^2};$$

$$q_3 = a \tan 2(Y_E, X_E) \quad (2)$$

In [20] the complete kinematic model was presented obtaining the relationships between the driving joint velocities and accelerations and the end-effector velocities and accelerations.

### The Inverse Dynamic Model

The inverse dynamics consists of finding the relationships between the driving torque vector  $\tau$  and the laws of motion for the manipulated object. Furthermore

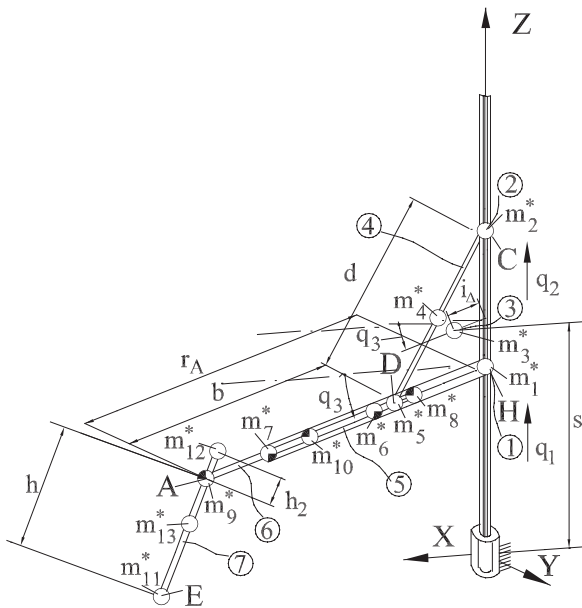


Fig. 2 Dynamic modeling of the PARAMIS robot using lumped masses

we assume that (Fig. 2): the linear motors have the masses  $m_1$  and  $m_2$  and the rotary motor has the mass  $m_3$ ; the driving shaft has the mass  $m_a$ ; the other mechanism links 4, 5, 6, 7 are considered homogenous bars with length  $d$ ,  $l_5$ ,  $l_6$ ,  $h + h_2$  and mass  $m_i$ ,  $i = 4, 5, 6, 7$ ; the joints have the masses  $m_C$ ,  $m_H$ ,  $m_A$ ,  $m_D$ ; all joints are frictionless.

In case the rigid body forms a bar of length  $l_i = l$  with longitudinally and evenly distributed mass  $m_i = m$ , the system is dynamically equivalent to three masses which we may arrange in the following way [13, 14]:  $m_1, 0, 0, l/2$ ;  $m_2, 0, 0, -l/2$ ;  $m_3, 0, 0, 0$ . The mass  $m_3$  is located in the bar centre of mass and the other two masses in the end points of the bar. The equivalent masses are:  $m_1 = m_2 = m/6$ ,  $m_3 = 2m/3$ .

For the dynamic model, the theory of equivalent lumped masses was applied, where the equivalent masses of the system are  $m_i^*$ ,  $i = 1, \dots, 13$ :

$$\begin{aligned} m_1^* &= m_1 + m_H + \frac{m_5}{6}; & m_2^* &= m_2 + \frac{m_4}{6} + m_C; & m_3^* &= m_3 + m_a; \\ m_4^* &= \frac{2}{3}m_4; & m_5^* &= \frac{m_4}{6} + m_D; & m_6^* &= \frac{2}{3}m_5; & m_7^* &= \frac{m_5}{6}; & m_8^* &= \frac{m_6}{6}; \\ m_9^* &= \frac{m_6}{6} + m_A; & m_{10}^* &= \frac{2}{3}m_6; & m_{11}^* &= \frac{m_7}{6}; & m_{12}^* &= \frac{m_7}{6}; \\ m_{13}^* &= \frac{2}{3}m_7. \end{aligned}$$

The coordinates of equivalent mass points  $X_i$ ,  $i = 1, \dots, 13$  depend on joint coordinates  $q_i$ ,  $i = 1, 2, 3$  and through the equations (1) or (2) depend on  $X_E$ ,  $Y_E$ ,  $Z_E$ . The principle of virtual work was applied [8]:

$$\delta W = \delta q^T \cdot \tau + \sum_{i=1}^{13} \delta X_i^T \cdot (T_i^{Tr} + T_i^g) = 0 \quad (3)$$

where  $\delta q^T \cdot \tau$  the virtual work of all driving forces and torques;

$\sum_{i=1}^{13} \delta X_i^T \cdot (T_i^{Tr} + T_i^g)$  -virtual work of all inertia forces and gravity forces from the equivalent system.

From (3) the driving force vector is obtained:

$$\tau = (J_P^T)^{-1} \cdot \sum_{i=1}^{13} -J_i^T \cdot (T_i^{Tr} + T_i^g) \quad (4)$$

where

$$\tau = \begin{bmatrix} \tau_1 \\ \tau_2 \\ \tau_3 \end{bmatrix} = \begin{bmatrix} F_1 \\ F_2 \\ M_3 \end{bmatrix}; J_P^T = \begin{bmatrix} \frac{\partial q_1}{\partial X_E} & \frac{\partial q_2}{\partial X_E} & \frac{\partial q_3}{\partial X_E} \\ \frac{\partial q_1}{\partial Y_E} & \frac{\partial q_2}{\partial Y_E} & \frac{\partial q_3}{\partial Y_E} \\ \frac{\partial q_1}{\partial Z_E} & \frac{\partial q_2}{\partial Z_E} & \frac{\partial q_3}{\partial Z_E} \end{bmatrix};$$

$$J_i^T = \begin{bmatrix} \frac{\partial X_i}{\partial X_E} & \frac{\partial Y_i}{\partial X_E} & \frac{\partial Z_i}{\partial X_E} \\ \frac{\partial X_i}{\partial Y_E} & \frac{\partial Y_i}{\partial Y_E} & \frac{\partial Z_i}{\partial Y_E} \\ \frac{\partial X_i}{\partial Z_E} & \frac{\partial Y_i}{\partial Z_E} & \frac{\partial Z_i}{\partial Z_E} \end{bmatrix}; T_i^{Tr} = - \begin{bmatrix} m_i^* & 0 & 0 \\ 0 & m_i^* & 0 \\ 0 & 0 & m_i^* \end{bmatrix} \cdot \begin{bmatrix} \ddot{X}_i \\ \ddot{Y}_i \\ \ddot{Z}_i \end{bmatrix}; T_i^g = - \begin{bmatrix} 0 \\ 0 \\ m_i^* \cdot g \end{bmatrix}$$

The  $\ddot{X}_i$ ,  $\ddot{Y}_i$ ,  $\ddot{Z}_i$ ,  $i = 1, \dots, 13$  for each equivalent mass are obtained through double differentiation of the corresponding  $X_i$ ,  $Y_i$ ,  $Z_i$  mass coordinates which depend on end-effector coordinates  $X_E$ ,  $Y_E$ ,  $Z_E$ .

## Numerical Results

The kinematic and dynamic models for PARAMIS have been implemented in a MATLAB developed simulation system. The chosen data fit an experimental model (Fig. 3):

$$\begin{aligned} X_B &= 679.209 \text{ mm}; Y_B = 0 \text{ mm}; Z_B = 400.05 \text{ mm}; b = 256.359 \text{ mm}; \\ d &= 493.69 \text{ mm}; h = 270 \text{ mm}; h_2 = 109 \text{ mm}; l_5 = 500 \text{ mm}; l_6 = 256.359 \text{ mm}; \\ m_1 &= 0.955 \text{ kg}; m_2 = 0.955 \text{ kg}; m_a = 5.2 \text{ kg}; m_3 = 0.955 \text{ kg}; \\ m_4 &= 0.123 \text{ kg}; m_5 = 0.714 \text{ kg}; m_6 = 0.572 \text{ kg}; m_7 = 0.353 \text{ kg}; m_H = 0.65 \text{ kg}; \end{aligned}$$

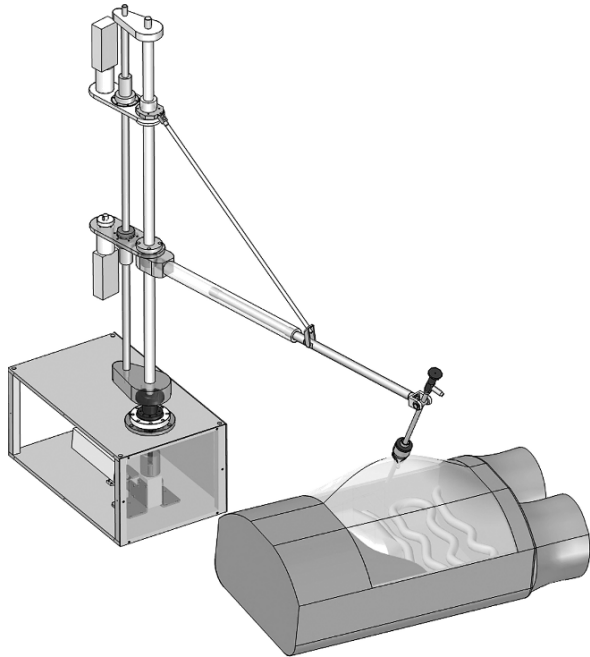


**Fig. 3** The robot experimental model

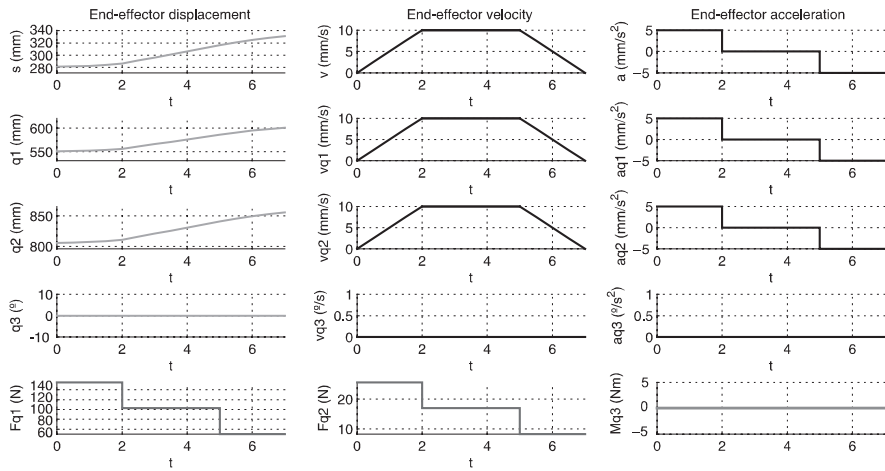


Fig. 4 Kinematic and dynamic results of the dynamic model for PARAMIS

$$m_C = 0.391 \text{ kg}; \bar{m}_D = 0.037 \text{ kg}; m_A = 0.084 \text{ kg}; e_1 = 59.43 \text{ mm};$$

$$e_2 = 387.65 \text{ mm}; r_{\text{rotdrive3}} = 15 \text{ mm}; r_{\text{shaft}} = 30 \text{ mm}.$$

For inverse dynamics, the selected trajectory of the end-effector is a straight line parallel to Z axis starting from  $X_E = 679.2 \text{ mm}; Y_E = 0; Z_E = 281.1 \text{ mm}$  and ending with  $X_E = 679.2 \text{ mm}; Y_E = 0; Z_E = 331.1 \text{ mm}$ , the maximum velocity being  $v_{\text{max}} = 10 \text{ mm/s}$  and the maximum acceleration  $a_{\text{max}} = 5 \text{ mm/s}^2$ . The chosen values for the motion correspond to the MIS procedure requirements.

In the Fig. 4 the time history diagrams for the driving coordinates, velocities, accelerations and driving torques are represented.

Displcmts. and Force ( $F_{q1}$ ) Velocts. and Force ( $F_{q2}$ ) Accelrs. and torque ( $M_{q3}$ )

## Conclusion

In this paper the dynamics for PARAMIS parallel robot used in MIS on the basis of lumped masses has been presented. Starting from mass geometry considerations, which consist in replacing a given multibody system correctly by dynamically equivalent single masses, the method of using virtual work is proposed. The dynamic model has a compact form and offers the possibility of a dynamic study of the PARAMIS robot in order to evaluate its dynamic capabilities and to generate innovative control algorithms.

**Acknowledgments** The authors gratefully acknowledge the financial support provided by the research grants awarded by the Romanian Ministry of Education and Research and the “Institutional Academic Cooperation Research Grant” between the Technical University Braunschweig, Germany and the Technical University of Cluj-Napoca, Romania, awarded by Alexander von Humboldt foundation.

## References

1. Geng Z., Haynes, L.S., On the Dynamic Model and Kinematic Analysis of a Class of Stewart Platforms. *Robotics and Autonomous Systems*, Vol. 9, 1992, pp. 237–254.
2. Pierrot, F. et al., A New Design of a 6-DOF Parallel Robot. *Journal of Robotics and Mechatronics*, Vol. 2, 1990, pp. 92–99.
3. Codourey, A., Contribution a la Commande des Robots Rapides et Precis. Application au robot DELTA a Entraînement Direct. These a l'Ecole Polytechnique Federale de Lausanne, 1991.
4. Miller, K., Clavel, R., The Lagrange-Based Model of DELTA-4 Robot Dynamics. *Roboter-systeme*, Vol. 8, 1992, pp. 49–54.
5. Guglielmetti, P., Longchamp, R., A Closed Form Inverse Dynamics Model of the DELTA Parallel Robot. In *Proc. of Symposium on Robot Control*, 1994, pp. 51–56, Capri, Italia.
6. Tadokorro, S., Control of Parallel Mechanisms. *Advanced Robotics*, Vol. 8(6), 1994, pp. 559–571.
7. Honneger, M. et al., Adaptive Control of the Hexaglide, a Six D.O.F. Parallel manipulator. In *Proc. Of IEEE Int. Conf. On Robotics and Automation*, 1997, pp. 543–548, Albuquerque.
8. Tsai, L.W., Solving the Inverse Dynamics of a Stewart-Gough Manipulator by the Principle of Virtual Work, *ASME J. Mech. Des.*, Vol. 122, 2000, pp. 3–9.
9. Merlet, J.-P., *Parallel Robots*. Kluwer Academic Publisher, 2000.
10. Pisla, D., Kerle, H., Development of Dynamic Models for Parallel Robots with Equivalent Lumped Masses. In *Proc. of 6th International Conference on Methods and Models in Automation and Robotics*, 2000, pp. 637–642, Miedzydroje, Poland.
11. Guégan, S., Khalil, W., Dynamic Modeling of the Orthoglide. *Advances in Robot Kinematics (J. Lenarcic and F. Thomas, Ed.)*. Kluwer Academic, Publication, Netherlands, 2002, pp. 387–396.
12. Itul, T., Pisla, D., On the Solution of Inverse Dynamics for 6-DOF Robot with Triangular Platform. In *Proc. of 1st European Conference EuCoMeS*, Obergurgl, Austria.
13. Ripianu, A., *Mecanica Solidului Rigid*, Bucuresti, Editura Tehnica, 1973.
14. Hockey, B., The Method of Dynamically Similar Systems Applied to the Distribution of Mass in Spatial Mechanisms, *Journal of Mechanisms*, Vol. 5, 1970, pp. 169–180.
15. Ben-Porat, O., Shoham, M., Meyer, J., Control Design and Task Performance in Endoscopic Teleoperation, *Presence*, Massachusetts Institute of Technology, Vol. 9, no. 3, 2000, pp. 56–267.
16. Brown University, Division of Biology and Medicine, 2005.
17. Gluzman, D., Shoham, M. and Fischer, A., A Surface-Matching Technique for Robot-Assisted Registration, *Computer Aided Surgery*, Vol. 6, 2001, pp. 259–269.
18. Simaan, N., Taylor, R., Flint, P., A Dexterous System for Laryngeal Surgery, In *Proc. of ICRA 04*, New Orleans, USA, 2004, pp. 351–357.
19. Plitea, N., Hesselbach, J., Vaida, C., Raatz, A., Pisla, D., Budde, C., Vlad, L., Burisch, A., Senner, R. et al., Innovative Development of Surgical Parallel Robots, *Acta Electronica, Mediamira Science*, Cluj-Napoca, 2007, pp. 201–206.
20. Pisla, D., Plitea, N., Vaida, C. A., Kinematic Modeling and Workspace Generation for a New Parallel Robot used in Minimally Invasive Surgery, In *Proc. of ARK 2008*, Springer, 2008.

# Controlling the Traditional Rigid Endoscopic Instrumentation Motion

D. Moschella and G.A. Danieli

**Abstract** The paper deals with the development of a version of Navi-Robot suitable for controlling the endoscope's and instrumentation's position during a laparoscopic surgery. The basic structure is the same of Navi-Robot, a three arms measuring device where each of the arms bears a 6 DOF self balanced kinematic chain. The central arm is able to pass from passive to active mode upon command, all the arms being lockable in any position. Adding a motor to control rotation of the sixth joint of the lateral arms and another 4 DOF Robot to control the second degree of inclination of the surgical tool with respect to the patient's body surface, as well as penetration, rotation and actuation of the instrument (the first degree of inclination being controlled by the sixth DOF of the lateral arms of the Navi Robot).

Another key element is the way rotation and actuation are controlled. To this purpose two spur gears are used, the first of which is to be fixed to the surgical tool, while the second, fixed to the first gear but free to rotate with respect to it, actuates the handle of the surgical tool using a four bar link and a couple of bevel gears. This pair of spur gears are positioned on a body that allows transmitting the motion through pinions coupled to other bevel gears and universal joints that allow receiving the motion from the non sterile part of the instrument.

Finally two different schemes were studied to control the motion of the instrument, and are described in this paper together with their relative advantages and disadvantages.

**Keywords** CAS Computer Aided Surgery · LIS Least Invasive Surgery

---

D. Moschella (✉)

Dipartimento di Meccanica, Università della Calabria, Via P. Bucci, 87036,  
Arcavacata di Rende (Cs), Italy  
e-mail: d.mundo@unical.it



## Introduction

Least Invasive Surgery is taking more and more momentum as a good method to reduce invasiveness, recovery times and consequently also global costs of surgical procedures, minimizing also related risks [1–7]. In fact, the reduction of the surgeries invasiveness is coupled with their much higher tolerability by the organism, that produces a faster recovery, sometimes even allowing patient's dismissal from the hospital on the same day of the surgery. Instruments used for such surgeries are rigid endoscopes, the most commonly being the laparoscope. This is usually operated by hand by the doctor, that controls its movements, including the actuation of the operating instrument (forceps, scissors, etc.). Two or more further instruments are present, e.g. to inflate the abdomen using CO<sub>2</sub>, and a video camera. Since the instrument control may not be easy, especially if the movements required are very fine, Robots have been introduced [8–16], allowing a finer motion control, that is in any event always actuated by the doctor. These allow also to employ only one medical operator, rather than two or three operators, as it occurs nowadays. Substantially, the system allows a kind of motion deamplification, improving its control. However the cost of these Robots is very high, and also the endoscopic instruments are special, very expensive in the case of da Vinci, and often even disposable. Furthermore the instruments used are of non miniaturized dimensions (>8–10 mm.).

This originated the idea [17, 18] to develop an instrument allowing the same type of actuation with extra fine motion control, using existing endoscopic instruments, which not only should allow a good saving for the hospitals, reutilizing existing instruments, but also to utilize small size instruments (2–3 mm in diameter), which are necessary in neonatal and paediatric surgery, currently not usable in other way than free hand, while precise position control could be more useful, such in the



**Fig. 1** Virtual representation of the Endo-Navi-Robot

case of neonatal laparoscopy, where body structures are miniaturized. Moreover, since during surgeries the doctor is used to feel the effort to accomplish the different operations, an interface will have to be supplied, allowing to feel the physical perception of the force exerted.

The instrument is composed by three arms as the Navi-Robot for Orthopaedics [19, 20], in which the central one will hold the camera, while the lateral will hold each a 5 DOF system to move and actuate the traditional laparoscope, being the entire system controlled via console. Figure 1 presents a virtual prototype of the Endo-Navi-Robot with its three arms, complete with video camera and surgical instruments. It is clear that, should the endoscope have more than three degrees of freedom with respect to the sheet, these will be added to the system controlling the motion of the instruments.

### The Traditional Instrument Actuator

As far as the actuation of the traditional instrument, this is controlled by a mechanism composed by four gears, three of which, hollow gears, are placed around the instrument, as shown in Fig. 2. Gear # 1 (spur) is fixed to the instrument with screws, gear # 2 (spur and bevel) are in one piece, and kept in contact with gear #

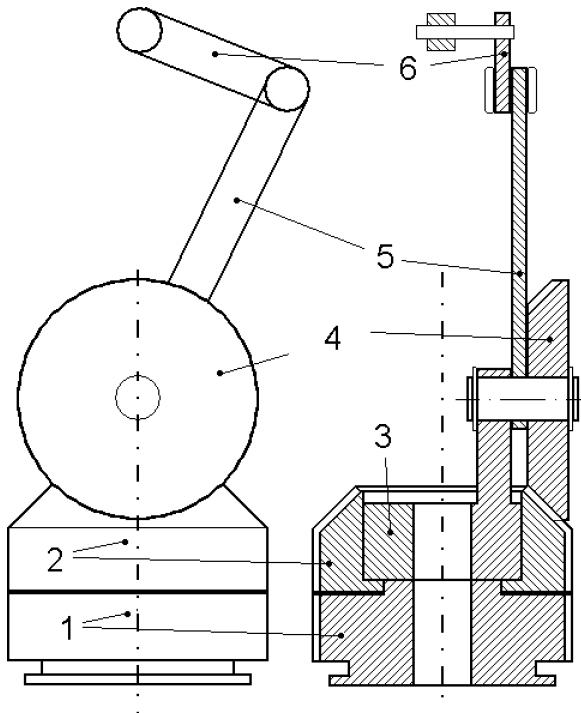
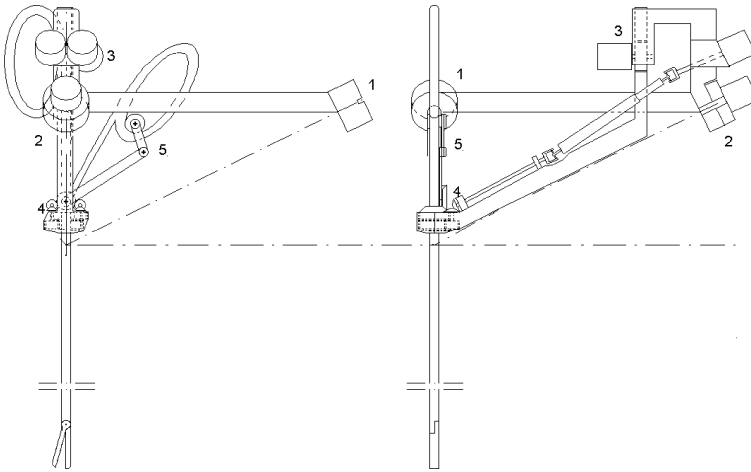


Fig. 2 Scheme of the traditional instrument actuator



**Fig. 3** Scheme 5 DOF instrument actuation system

1 by the element # 3 which also supports the axis of gear # 4 (bevel) which meshes with the bevel portion of gear # 2. Gear # 4 is locked to link # 5 which, through link # 6 commands the handle of the instrument. When desiring a pure rotation of the instrument about its axis, both gears # 1 and 2 should be rotated simultaneously, when wishing to activate the instrument, only gear # 2 should be rotated. Naturally, gear # 1 and 2 are rotated by a couple of small spur gears which are fixed to the two bevel gears shown in Fig. 3, which receive motion from the universal joints. Notice that being the axes of the motors parallel to those of the axes derived from the two bevel gears shown in Fig. 3, transmission is omokinetic and ensured also varying the depth of penetration of the instrument, since a prismatic joint is present between the central forks of the two universal joints.

## Possible Solutions for the 5 DOF System

The five DOF system is designed to allow moving and actuating the instrument as a doctor would do, clearly fixing the point of insertion of the instrument into the patient skin. To this aim, the first two of the 5 DOF allow rotating the surgical instrument, about the point of insertion of the instrument. A third degree of freedom allows the instrument to rotate about its axis with respect to the sheet, while a fourth will control the axial displacement again with respect to the sheet. Finally the fifth degree of freedom will be dedicated to the actuation of the surgical instrument, forceps or scissor or whatever else.

The following Fig. 3 presents a representation of the five degrees of freedom end effector, where is schematically shown the method of control of the instrument rotation about the two axes perpendicular to the surgical instrument. As can be seen, these rotations are obtained using a first hinge (1) whose axis passes through the

insertion point of the instrument in the skin, and by a second hinge (2) whose axis passes through the same point, two axes presenting an angle of  $75^\circ$  between the two. Each axis is originally tilted of  $30^\circ$  with respect to the body surface, when the instrument is perpendicular to it. This causes the fact that in order to obtain a rotation in a direction purely perpendicular to the skin surface, the two rotations are to be combined, which can be easily taken care of via software. In the same figure with (3) is indicated the gear that, acting on a rack, allows axial motion, while gear (4) produces the axial rotation of the entire block, and four bar link (5) activates the surgical instrument.

Now it is desired that, depending on the point of view of the operator (the video camera) moving the joystick up and down he/she should see the tip of the instrument moving on a plane perpendicular to the angle of sight, while moving the joystick left and right the tip of the instrument should move in the direction of sight. Now this is not particularly difficult to do, since in every instant of time the value of the various quadrions representing the position of each joint is known, thus a simple multiple matrix multiplication is needed. However this also requires continuous adjustments in the ratio of the speed of the two motors of joint 1 and 2 of the 5 DOF mechanism. Moreover, the particular geometry of the system limits rather severely this type of adjustments.

An alternative idea came examining what was done in Poland by Robin Hart people [16]. In fact they use of a double four bar link having of equal length the opposite bars (articulated parallelograms), Figs. 4, 5. In fact, since they use an instrument which does not have handles, being the last link also part of the parallelogram, the point of insertion into the patient's skin remains constant for every angle.

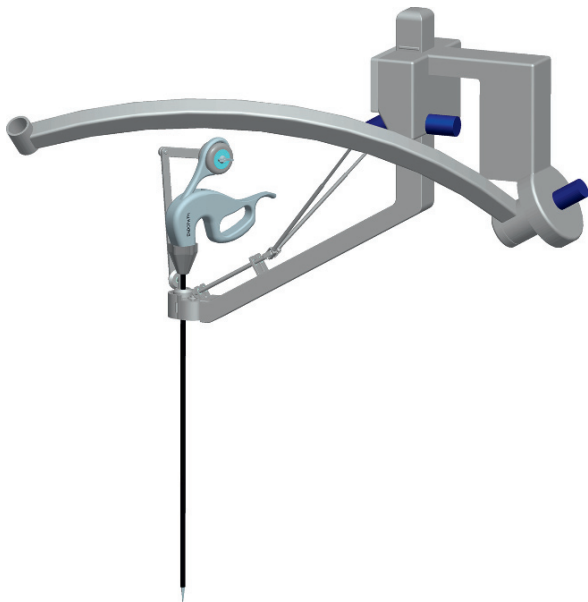
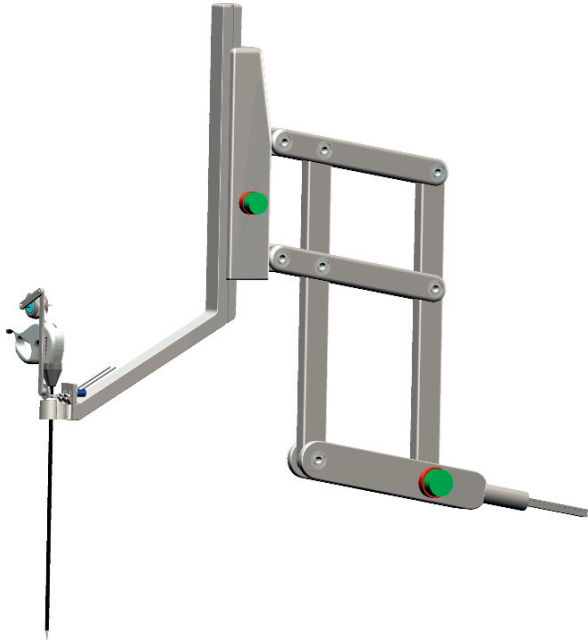


**Fig. 4** CAD model of the above

**Fig. 5** Double four bar link scheme for the 5 DOF actuator



In presence of handles this is not any longer true. The following figure shows this arrangement.

In this case motion control should be simplified, if were not for the fact that, as can be noted in Fig. 6, moving from the 90 degrees position ( $\theta = 0$ ,  $L$  being the distance between the instrument axis and the last bar hinged to the parallelogram) the tip of the instrument moves toward the robot by an amount of:

$$\Delta L_1 = L(1 - \cos \theta) / \cos \theta$$

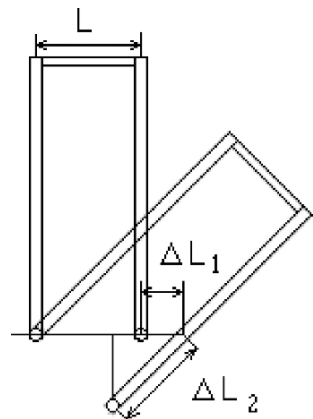


**Fig. 6** Position variation of the instrument's tip as a function of inclination

Even worse the situation in the direction of the links hinged to the frame, were a retraction (penetration) occurs of:

$$\Delta L_2 = L \tan \theta$$

This is shown in Fig. 6.

Now it happens that while control is easier, there is a limit in the inclination of the 4BR, that goes from +30° to almost no limit in the other direction. A limit has been assumed for this angle of -45°, in order to obtain an overall amplitude of 75°. Going back to the problem of controlling  $\Delta L_{1,2}$  this can be obtained both acting on the motors, or with a kind of shape cams made to ensure an automatic purely mechanical compensation.

The idea is to obtain the profile of the cams that will cause the motion of the entire 4BL to nullify both  $\Delta L_1$  and  $\Delta L_2$ . Thus the distance from the origin at which the second hinge must be positioned will be in the two cases:

$$L - \Delta L_1 / \cos \theta = L(2 \cos \theta - 1) / \cos^2 \theta$$

$$L + \Delta L_2 = L(1 + \tan \theta)$$

These profiles have been computed as a function of the angle theta, and the result, rather cumbersome, is displayed in Fig. 7. Basic element is the member in dark grey (1), which is fixed and able to rotate only about its horizontal axis. It contains two horizontal slots, made to allow motion of the shafts in light blue (2) as the member in pink (3) is rotated while the third shaft (4) moves inside the third slot of the first

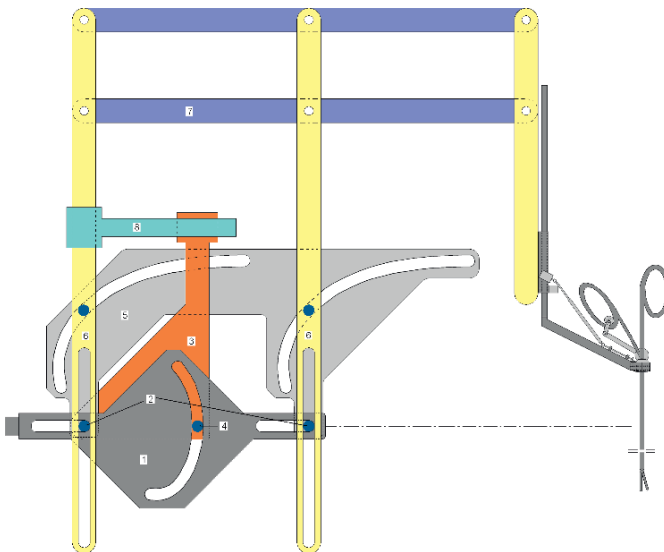


Fig. 7 Mechanism for automatic regulation of changes in  $\Delta L_1$  and  $\Delta L_2$  as function of  $\theta$

member (1) while varying the horizontal position of the member in light grey (5) of  $-\Delta L_1$ . This last member (5) contains two more slots made to allow varying the length of the non horizontal links (6) of the parallel bar four bar link (7) in order to compensate for the variation of  $\Delta L_2$ . Finally a kind of Oldam joint (8) allows transmitting the rotation of member 3 to the 4BL.

Note in fact the when member 3 is rotated in a clockwise direction, member 5 is pulled back while the two bars 7 are rotated of the same angle by the joint 8, while increasing the length of the bars by the factor  $\Delta L_2$ .

## Conclusions

It seem obvious that this mechanism, while undoubtedly solving the problem of automatic mechanical compensation, is much heavier and difficult to build than a system in which, using a simple encoder to measure the angle, a mechatronic control is adopted. However its response time is zero. To solve this problem purely mechanically may be interesting, but probably not practical. Thus a mechatronic solution will also be developed to compare relative performances, and its results and controlling scheme will be presented at the Congress.

## References

1. Dewaele F, Caemaert J et al., Intradural endoscopic closure of dural breaches ion a case of post-traumatic tension pneumocephalus. *Minim Invas Neurosur* 50(3): 178–181 Jun 2007.
2. Watrelot A, Place of transvaginal fertiloscopy in the management of tubal factor disease. *Reprod Biomed Online* 15(4): 389–395 Oct 2007.
3. Nappi C, Di Spiezio Sardo A et al., Prevention of adhesions in gynaecological endoscopy. *Hum Reprod Update* 13(4): 379–394 Jul–Aug 2007.
4. Hernandez-Divers SJ, Stahl SJ et al., Endoscopic orchidectomy and salpingohysterectomy of pigeons (*Columba livia*): An avian model for minimally invasive endosurgery. *J Avian Med Surg* 21(1): 22–37 Mar 2007.
5. Hackethal A, Immenroth M, Burger T, Evaluation of target scores and benchmarks for the traversal task scenario of the minimally invasive surgical trainer-virtual reality (MIST-VR) laparoscopy simulator. *Surg Endosc* 20(4): 645–650 Apr 2006.
6. Nieves MNCY, Haas E, Hollerhage HG et al., Combined minimal invasive techniques in deep supratentorial intracerebral haematomas. *Minim Invas Neurosur* 47(5): 294–298 Oct 2004.
7. Darwish AM, Hassan ZEAZ, Haemodynamic, biochemical and haematological changes during hysteroscopic myomectomy. *Gynaecol Endosc* 11(6): 349–355 Dec 2002.
8. Korets R, Hyams ES et al., Robotic associated laparoscopic ureterocalicostomy. *Urology* 70(2): 366–369 Aug 2007.
9. Tayar C, Karoui M et al., Robot-assisted laparoscopic mesh repair of incisional hernias with exclusive intracorporeal suturing: a pilot study. *Surg Endosc* 21(10): 1786–1789 Oct 2007.
10. Muller-Stich BP, Reiter MA et al., Robot-assisted versus conventional laparoscopic fundoplication: short-term outcome of a pilot randomized controlled trial. *Surg Endosc* 21(10): 1800–1805 Oct 2007.
11. Anderson C, Ellenhorn J et al., Pilot series of robot-assisted laparoscopic subtotal gastrectomy with extended lymphadenectomy for gastric cancer. *Surg Endosc* 21(9): 1662–1666 Sep 2007.

12. Advincula AP, Song A et al., The role of robotic surgery in gynecology. *Curr Opin Obstet Gyn* 19(4): 331–336 Aug 2007.
13. Deloos H, Debacker M et al., European survey on training objectives in disaster medicine. *Eur J Emerg Med* 14(1): 25–31 Feb 2007.
14. Goldstraw MA, Patil K et al., A selected review and personal experience with robotic prostatectomy: implications for adoption of this new technology in the United Kingdom. *Prostate Cancer P D* 10(3): 242–249 Sep 2007.
15. Wang GJ, Barocas DA, Raman JD et al., Robotic vs open radical cystectomy: prospective comparison of perioperative outcomes and pathological measures of early oncological efficacy *BJU Int*, efirst date: 25 Sep 2007.
16. Nawrat Z, Podsedkowski L, Mianowski K, Wróblewski P, Kostka P, PruskiR, Małota Z, Religa Z, Robin Heart 2003 – present state of the Polish telemanipulator project for cardiac surgery assistance. *Int J Artif Organs* 26(12): 1115–1119 Dec 2003.
17. Danieli GA, Riccipientoni G, Robotized System of control and micrometric actuation of an endoscope, PCT/IT05/000486 del 08/08/2005, WO2006016390 A1 of February 16th 2006, EP 05778903.4, IPC A61B 19/00.
18. Danieli GA, Moschella D, Endo-Navi-Robot per il controllo e movimentazione micrometrica di strumentazione endoscopica tradizionale, particolarmente adatto per laparoscopia neonatale. Domanda di Brevetto No. CS2007A000046, depositata 26/10/2007.
19. Moschella D, Gatti G, Cosco FI, Aulicino E, Nudo P and Danieli GA, Development of Navi-Robot, a New Assistant for the Orthopaedic Surgical Room, paper 713, 12th IFToMM World Congress, Besançon (France), June 18–21, 2007
20. Danieli GA, Measuring open kinematic chain able to turn into a positioning Robot. PCT/IT05/000487 del 08/08/2005, WO2006016391 A1 of February 16th 2006, EP 05778744.2, IPC B25J 19/00.



# Use of Substitute of Mechanisms for Tolerance Investigation of Guidance Mechanisms

Mathias Husing and Burkhard Corves

**Abstract** In spite of known methods and available tolerance software there are tolerance investigation problems of guidance mechanisms and especially convertible roof mechanisms that can be suitably solved only with special knowledge of kinematic coherences. A new method will be presented that uses substitute mechanisms to solve special tolerance investigation problems of guidance mechanisms. With the help of an example of use the new developed method will be compared with standard tolerance investigation approaches.

**Keywords** Tolerance investigation · Guidance mechanisms · Convertible roof mechanisms

## Introduction

Manufacturing and also operational errors of measurements of the kinematic parameters cause deviations of the desired nominal motion. In order to get information about motion errors, it is necessary to make a tolerance investigation of the mechanism. Unallowable oversized motion errors are not acceptable, because they risk strongly the quality of the motion or even the function of the mechanism.

For guidance mechanisms especially the deviations of certain nominal positions will be of interest. Thereby two questions concerning positions of joints or coupler points can be distinguished. At one side it is of interest, if the position is inside an acceptable positional tolerance and at the other side what positional deviations can appear in a particular direction.

Especially the second question concerning positional deviations of particular directions for convertible roof mechanisms is important. Nevertheless it is independent, whether the mechanism is for a convertible soft top or a retractable hardtop.

---

M. Husing (✉)

Department of Mechanism Theory and Dynamics of Machines, Eilfschornestreinstr. 18, RWTH Aachen University,  
52056 Aachen, Germany  
e-mail: huesing@igm.rwth-aachen.de

This way of posing a problem can not be handled with existing tolerance analysis software without adding kinematic options. In this paper, a new method will be presented, to handle this problem suitably. This method is based on converting the existing guidance mechanism into a function generator by generation of a substitute mechanism.

## Tolerance Investigation

For the presented problem the influence of clearance is not important, so only tolerances of the design parameters will be considered.

Tolerance investigation can be divided into sensitivity analysis, tolerance analysis, tolerance synthesis and supplementary tolerance management.

The scope of sensitivity analysis is to determine the influence of tolerances on the motion. Suitable parameters describing this are sensitivity factors that represent partial derivations of the motion parameter  $q$  over the tolerance parameter  $p_i$ . Partial derivations can be determined either numerically or analytically [2]. In the meantime there is powerful commercial tolerance software often directly embedded in CAD-systems. Some commercial tolerance software determines the sensitivity factors with partial differentials  $\partial q / \partial p_i \approx \Delta q / \Delta p_i$ . By comparing the sensitivity factors for different design parameters it can be established, which parameters have a very low or a very high influence on the motion error. Thus the design engineer gets information about which design parameter he can tolerate roughly and which he has to keep small, so that the motion error rests within certain limits. Sensitivity analysis plays an important role in design process.

The scope of tolerance analysis is to determine errors of motion parameters. These errors can be exactly estimated as the worst case by approximation or statistics. Different methods are well known [1, 2].

The scope of tolerance syntheses can be divided into two tasks:

1. Determination of insensitive mechanisms
2. Determination of an optimal tolerance distribution.

The first task often violates basic conditions of the motion task and so it will be rarely used in practice. In contrast the second task is of utmost importance. In [2] interesting approaches for both tasks are proposed.

The scope of tolerance management is to consider the assembly and manufacturing processes during the tolerance investigation. Important is to get the best choice of an efficient gauging process during assembly within the sensitivity analysis, the tolerance analysis and the tolerance synthesis.

## Tolerance Investigation of Convertible Roof Mechanism as Guidance Mechanism

The purpose of convertible roof mechanisms is to ensure as guidance mechanism the correct motion of the roof members [3, 5, 6]. Not only with regard to manufacturing

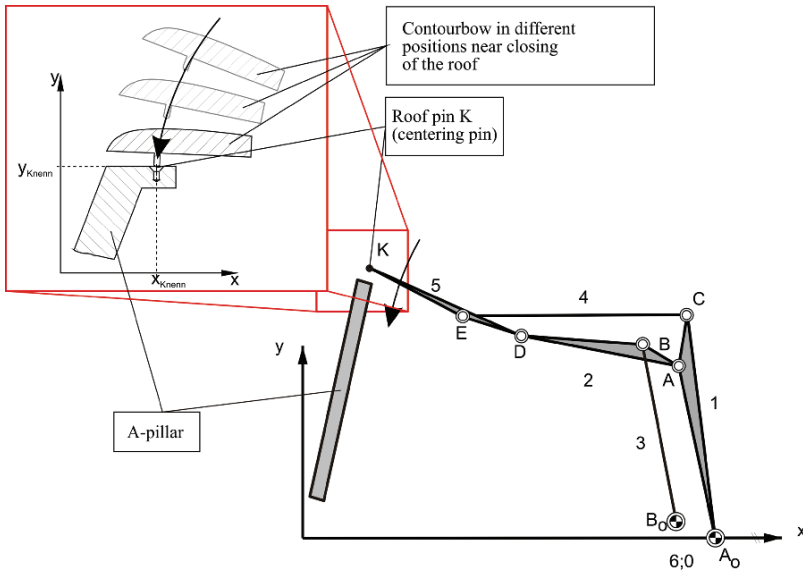


Fig. 1 Closing process of convertible roof

costs but also because of the accurate and precise motion of the roof members a suitable tolerance investigation plays an important role in the design process.

A typical task for roof mechanisms is represented in Fig. 1. It shows a six bar convertible roof linkage near closing of the roof. The roof pin K of the contourbow 5 has to be inserted into the related centre hole of the A-pillar.

Figure 1 represents the motion with nominal dimensions. Because of tolerances of the design parameters motion errors occur. At the level of  $y_K$  the roof pin K can be located between  $x_{Kmax}$  and  $x_{Kmin}$  (Fig. 2). Therefore it is not sure if the roof pin correctly inserts into the centre hole. For convertible roof mechanisms this task is essential.

From the kinematic point of view convertible roof mechanisms are guidance mechanisms. They will be driven at the main linkage 1 (angle  $\varphi_1$ ) with a hydraulic cylinder 7, 8 (length  $l_{HZ}$ ).

Both in publications and in practice sensitivity factors e.g.  $\partial x_K / \partial p_i$  and motion errors e.g.  $\Delta x_K$  are determined with the given drive parameter  $l_{HZ}$  or  $\varphi_1$ . Often two facts are ignored:

- I. The sensitivity factors  $\partial x_K / \partial p_i$  are components of the vector  $\frac{\partial \mathbf{k}}{\partial p_i} = \begin{pmatrix} \frac{\partial x_K}{\partial p_i} \\ \frac{\partial y_K}{\partial p_i} \end{pmatrix}$ .

Therefore  $\partial x_K / \partial p_i$  is not a suitable information about the effects of the tolerance parameters  $p_i$  on the x-coordinate  $x_K$  with **constant** coordinate  $y_K$ , because if the value of parameter  $p_i$  is changed, then not only the x-coordinate  $x_K$  but also at the same time the y-coordinate  $y_K$  changes. In the field of tolerance investigation

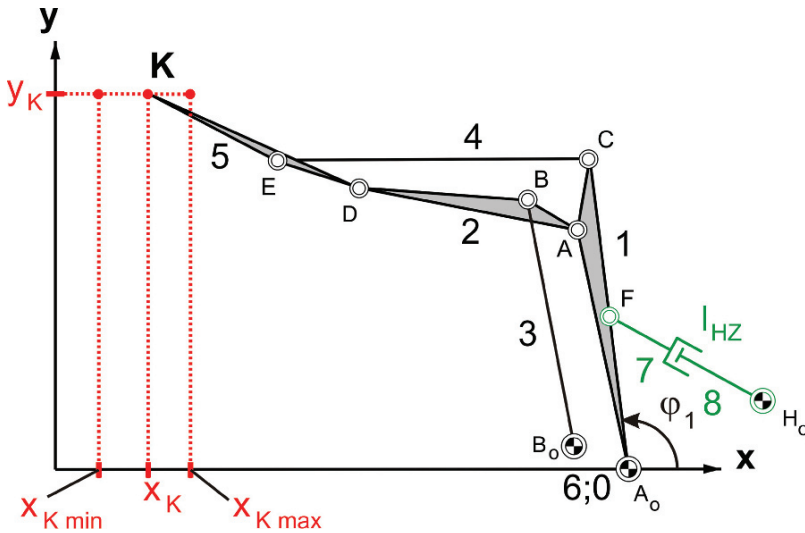


Fig. 2 Tolerance range of roof pin K

a correct estimation of the presented motion task can only be made, if the sensitivity factor describes the effects of the tolerance parameters  $p_i$  with constant  $y$ -coordinate  $y_K$ .

- II. In order to establish the motion task, the extreme positions  $x_{K \max}$  and  $x_{K \min}$  should be known. Thereby it doesn't matter, what values of the drive parameter  $\varphi_1$  this extreme positions  $x_{K \max}$  und  $x_{K \min}$  are reached at.

### Tolerance Investigation with Substitute Mechanisms

In consideration of the two facts I and II mentioned above a suitable tolerance investigation for the present motion task can only be realised by transformation the convertible roof mechanism and guidance mechanism respectively into a function generator. Doing so, the distance  $x_K$  should become the transmission function.

This basic idea causes the use of a first type substitute mechanism as presented in Fig. 3. This substitute mechanism is generated by removing or not driving the hydraulic cylinder 7, 8 and adding a slider 7 as a cylindrical pair. The rectilinear translation axis  $s_1$  of slider 7 is parallel to the  $x$ -axis and crosses through the  $y$ -axis at  $y_K$ . The contourbow 5 is pivoted with slider 7. The position of slider 7 on the translation axis  $s_1$  is described by  $l_x$ .

The degree of freedom of the mechanism in Fig. 2 with  $n = 8$  links and  $g = 10$  joints is  $F_{\text{roof}} = 3(n - 1) - 2g = 1$ . The transformed roof mechanism without hydraulic cylinder presented in Fig. 3 has  $n = 7$  links and  $g = 9$  joints. So this mechanism has the degree of freedom  $F_{\text{substitute1}} = 0$ . It is a truss and not mobile.

But if the design parameters  $p_i$  change their value because of tolerances, then the point K moves on its axis  $s_1$ . For this reason it is possible to realize a tolerance investigation described above. With it the sensitivity factors  $\partial l_x / \partial p_i$  and extreme positions  $x_{K \max} = l_{x \max}$  and  $x_{K \min} = l_{x \min}$  at  $y_K$  can be determined.

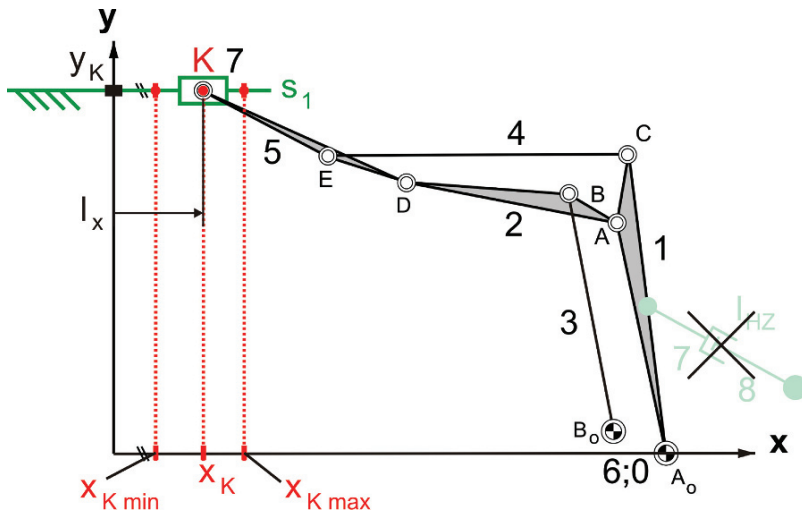


Fig. 3 Substitute mechanism: first type

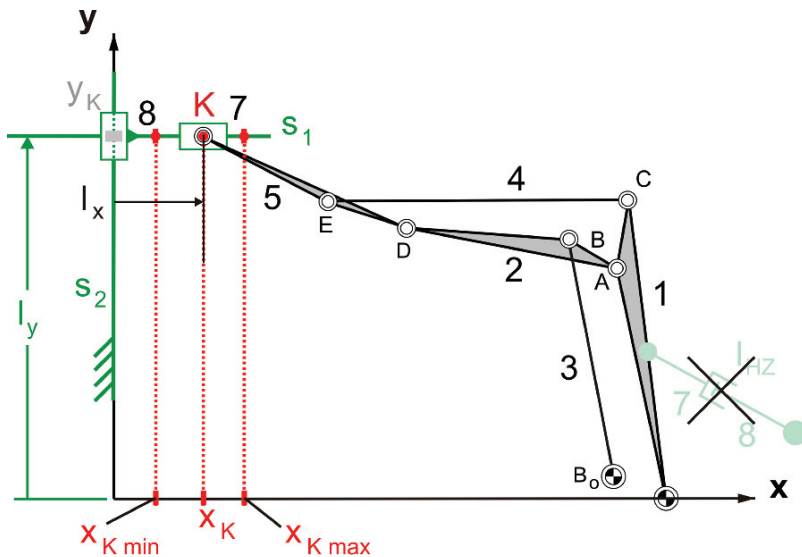


Fig. 4 Substitute mechanism: second type

In order to make a tolerance investigation of the coupler curve of the roof pin K, the first type substitute mechanism in Fig. 3 can be provided with a substitute drive, resulting in a second type substitute mechanism as presented in Fig. 4. Now the translation axis  $s_1$  is connected with a slider 8. Slider 8 moves perpendicular to  $s_1$  on the translation axis  $s_2$ . The new second type substitute mechanism has  $n = 8$  links and  $g = 10$  joints and thus the degree of freedom  $F_{\text{substitute2}} = 1$ .

The described method can be used generally for every guidance mechanism. The orientation of the axes can be orientated arbitrarily, but singularities can occur, if the axis  $s_1$  is parallel to velocity vector  $v_K$  of the roof mechanism in Fig. 2.

### Example of Use: Porsche Boxster

The convertible roof mechanism of the Porsche Boxster is chosen as an example of use. The above presented method of using a substitute mechanism for tolerance investigation will be compared with the standard approach. Figure 5 presents two non-scaled kinematic diagrams of the convertible roof mechanism of the Porsche Boxster: on the left side the original mechanism with the predetermined input angle  $\varphi_1$  and on the right side the second type substitute mechanism with predetermined position  $l_y$  of slider 8.

There are 14 tolerated parameters  $p_i$  ( $I = 1.14$ ): the 10 distances  $B_oG$ ,  $GB$ ,  $AB$ ,  $A_oA$ ,  $AH$ ,  $HC$ ,  $CD$ ,  $DE$ ,  $EK$ ,  $B_oE$  and four frame joint coordinates  $x_{B_o}$ ,  $y_{B_o}$ ,  $x_{A_o}$  und  $y_{A_o}$ . Their sensitivity factors  $\partial x_K / \partial p_i$  for the original mechanism with the predetermined input angle  $\varphi_1$  and  $\partial l_x / \partial p_i$  for the substitute mechanism are presented in Fig. 6. The sensitivity factors of each parameter  $p_i$  differ a lot between the different mechanisms. To understand this difference Fig. 7 presents different curves:

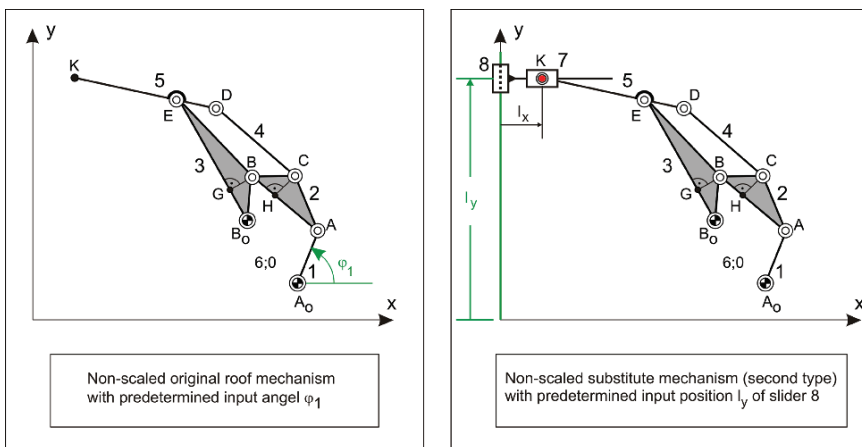


Fig. 5 Kinematic structure of the roof mechanism of Porsche Boxster

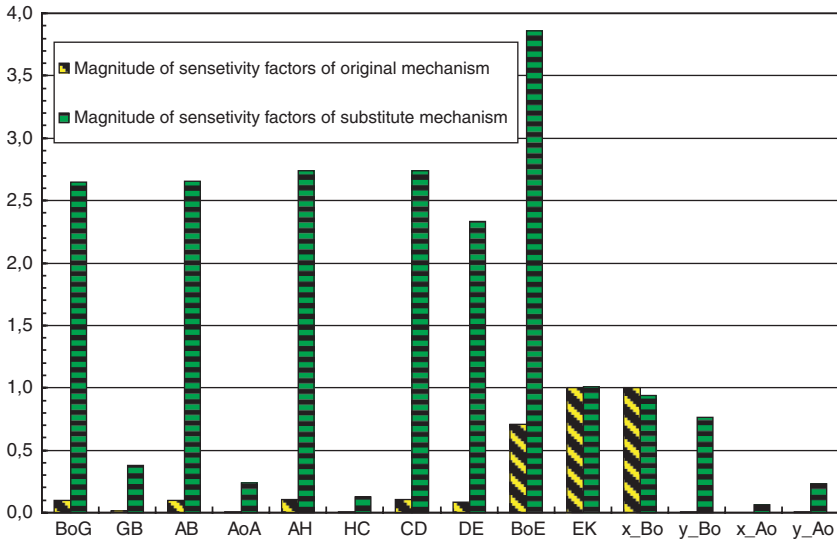


Fig. 6 Sensitivity factors of Porsche Boxster

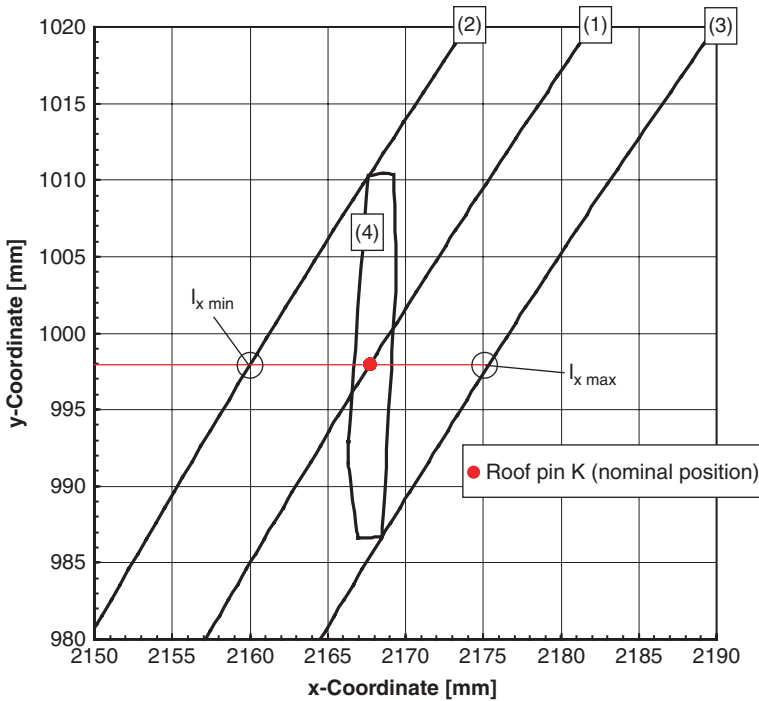


Fig. 7 Sensitivity factors of Porsche Boxster

- Curve (1) represents the coupler curve of roof pin K of the original mechanism for different input angles  $\varphi_1$  just before closing the roof calculated with nominal dimensions.
- Curve (2) and (3) present the minimal and maximal position of roof pin K of the second type substitute mechanism taking into account the 14 tolerated parameters  $p_i$ . The input-coordinate  $l_y$  was varied and the minimal and maximal value of  $l_x$  as the worst case were determined. The curves (2) and (3) represent the tolerance range of the pin position K.
- The roof pin point K of coupler curve (1) is exemplarily picked and marked in Fig. 7. For this point its “tolerance cloud” (4) (tolerance range [4]) is determined. Tolerance cloud means that for a mechanism position  $\varphi_1$  the coupler point K can only be inside a circumferential curve, namely the tolerance cloud (4).

The sensitivity factors  $\partial x_K / \partial p_i$  are a measure for the change of motion (in this case coordinate  $x_K$ ) due to tolerances of tolerated parameters  $p_i$ . On closer examination of the tolerance cloud (4) in Fig. 7 it strikes that in  $x$ -direction the distance between cloud curve (4) and nominal pin position  $x_K$  is much smaller than in  $y$ -direction. Insofar the sensitivity factors  $\partial x_K / \partial p_i$  should be relatively low. This explains the low magnitudes of the sensitivity factors in Fig. 6.

## Conclusion

The standard sensitivity factors and the partial derivations respectively  $\partial x_K / \partial p_i$  are not suitable to characterize the fundamental coherences for tolerance investigation of the presented motion task. Only with the use of the presented first or second type substitute mechanisms suitable sensitivity factors can be determined. Only with this a design engineer is able to find those tolerance parameters, which have the highest tolerance influence on the presented roof closing motion.

It's clear that it is not possible to determine the marked values  $l_{x \min}$  and  $l_{x \max}$  at a predetermined input angle  $\varphi_1$ .

Certain points of the tolerance cloud (4) are tangent to the tolerance range curves (2) and (3). Therewith it is basically possible to determine with a lot of tolerance clouds (4) finally the curves (2) and (3). But it has to be taken into account, that the determination of tolerance clouds is very complex and time-consuming. Following with a suitable algorithm those points have to be determined, which are tangent to the tolerance range curves (2) and (3). Compared to the substitute mechanism method this approach is considered to be unsuitable in practice.

The presented results show that with the use of the substitute mechanism tolerance investigation problems of the described motion tasks can be suitably solved. The main step was to transform the guidance mechanism into a function generator.

It remains to be seen, whether and how commercial programs will generate these substitute mechanisms “automatically”.



## References

1. Hüsing, M.: Cabrio-Verdeckmechanismen toleranzunempfindlich auslegen – Empfindlichkeits- und Toleranzanalyse. In: VDI-FVT (Hrsg.): 8. Internationaler VDI-Kongreß: Berechnung und Simulation im Fahrzeugbau. VDI-Berichte Nr. 1283. Düsseldorf: VDI-Verlag, 1996, S.199–214.
2. Hüsing, M.: Toleranzuntersuchung ebener mehrgliedriger Kurbelgetriebe hinsichtlich ihrer Übertragungsfunktionen. Dissertation RWTH Aachen, Institut für Getriebetechnik und Maschinendynamik, Aachen, 1995.
3. Hüsing, M.: Vorstellung und Vergleich aktueller Cabriolet-Verdeckmechanismen. In: Steinmetz, E. (Hrsg.): Technische Mitteilungen, Organ des Hauses der Technik e.V. Essen. Bd. 91 (1998) Nr. 2, S.78–87.
4. Hüsing, M.: Verdeckmechanismen von Kraftfahrzeugen mit Stoffdach oder mit formstabilen Dachelementen. In: Heinzl, J. (Hrsg.): Kolloquium Getriebetechnik 1999, Technische Universität München, Garching, 20–21 September 1999, S.29–41.
5. Hüsing, M.; Choi, S.-W.; Corves, B.: Cabriolet-Verdeckmechanismen aus der Sicht der Bewegungstechnik. In: VDI-EKV (Hrsg.): VDI-Getriebetagung 2002: Kurvengetriebe, Koppelgetriebe, gesteuerte Antriebe – Problemlösungen in der Bewegungstechnik. VDI-Berichte Nr. 1707. Düsseldorf: VDI-Verlag, 2002.
6. Hüsing, M.; Choi, S.-W.; Corves, B.: Cabriolet-Verdeckmechanismen eröffnen neue Perspektiven – Convertible Roof Mechanisms Open up New Perspectives. In: Konstruktion 55 (2003), Nr. 6, S.37–43.

# Index

## A

Affi, Z., 495  
Agirrebeitia, J., 87  
Aigner, M., 109  
Allotta, B., 201, 287  
Alonso, F.J., 229  
Ambrogio, G., 523  
Amici, C., 479, 487  
Avilés, R., 87

## B

Bartolini, F., 287  
Beomonte Zobel, P., 271  
Binaud, N., 505  
Blekta, J., 567  
Böhm, V., 431  
Bonandrini, G., 77  
Borboni, A., 479, 487  
Bozan, C.A., 405  
Bozorg Grayeli, A., 575  
Bujakas, V.I., 585  
Burduhos, B., 447  
Burisch, A., 531, 541

## C

Cabrera, J.A., 167  
Callegari, M., 313  
Caminero Torija, M.A., 321  
Carabelas, A., 29  
Carbone, G., 139, 149, 191  
Caro, S., 505  
Castejón, C., 139  
Castelli, G., 101  
Castillo, J.J., 167  
Ceccarelli, M., 139, 149  
Choi, S.W., 125  
Chondros, T.G., 11, 21, 29, 369  
Corves, B., 125  
Cuadrado, J., 229

## D

Danieli, G.A., 523, 603  
Davitashvili, N., 159  
De-Juan, A., 175  
Diaconescu, D., 447  
Diaconescu, D.V., 351, 361  
Díaz-Rodríguez, M., 279  
Diez, M., 69  
Dimopoulos, S., 369  
Durante, F., 271

## E

Echávarri Otero, J., 219  
Edeler, C., 559

## F

Fabrizi, A., 541  
Feliu Batlle, V., 321  
Fernández de Bustos, I., 87  
Filice, L., 523  
Flores, P., 305  
Font, J.M., 455

## G

Gabrielli, A., 313  
García Prada, J.C., 139  
Gatti, G., 523  
Gavrilă, C.C., 439  
Gelashvili, O., 159  
Gherman, B., 595  
Golovin, A., 343, 387  
Gori, G., 201  
Guerra Fernández, J., 321

## H

Hernández, A., 69  
Hernandez-Martinez, E., 191  
Hesselbach, J., 531  
Huang, C., 61  
Husing, M., 125

**I**

Incerti, G., 295  
 Iriarte, X., 279  
 Itul, T., 209

**J**

Jaliu, C., 351, 361  
 Jasper, D., 559  
 Jatsun, S., 263  
 Jomartov, A.A., 95, 329  
 Jüttler, B., 109

**K**

Karger, A., 463  
 Kecskeméthy, A., 183  
 Kerle, H., 377  
 Kiper, G., 423  
 Koloc, Z., 337  
 Kovalev, M., 55  
 Kövecses, J., 455  
 Kryczka, P., 237  
 Kyraggelos, P., 29

**L**

Lafitsky, A., 343  
 Lafont Morgado, P., 219  
 Loechte, C., 541  
 Lonij, G., 125  
 Lopez-Cajun, C., 191  
 Lu, Z., 149

**M**

Machado, M., 305  
 Magnani, P.L., 479, 487  
 Malchikov, A., 263  
 Masic, I., 183  
 Mata, V., 247, 279  
 Mazalaigne, S., 575  
 Mendes Carvalho, J.C., 255  
 Merlet, J.-P., 471  
 Mevald, J., 567  
 Mianowski, K., 237  
 Milevskaya, T., 387  
 Mimmi, G., 77  
 Miroir, M., 575  
 Moldovean, G., 405  
 Moschella, D., 603  
 Mourtzis, D., 369  
 Mundo, D., 523  
 Muñoz, J.L., 219

**N**

Nadal, F., 167  
 Neagoe, M., 351, 361  
 Nguyen, Y., 575

**O**

Ortiz, A., 167  
 Ottaviano, E., 101

**P**

Palpacelli, M.C., 313  
 Papadogiannis, A.S., 11, 29  
 Pereira, R., 305  
 Petrikova, I., 567  
 Petuya, V., 69  
 Pfüner, M., 117  
 Pintado, P., 229  
 Pisla, A., 595  
 Pisla, D., 209, 595  
 Plitea, N., 595  
 Pomi, D., 479, 487  
 Popa, V., 447  
 Pugi, L., 201, 287

**R**

Raatz, A., 531, 541  
 Raparelli, T., 271  
 Rindi, A., 201  
 Romdhane, L., 495  
 Rossi, C., 1, 513  
 Rottenbacher, C., 77  
 Rubio, F., 247  
 Russo, F., 1

**S**

Sales Gonçalves, R., 255  
 Sánchez-Peñuela, J.B., 219  
 Sancibrian, R., 175  
 Säulescu, R., 351, 361, 447  
 Savino, S., 513  
 Schöttler, K., 531  
 Schröcker, H.-P., 109  
 Seabra, E., 305  
 Simón, A., 167  
 Simuskhin, A., 343  
 Söylemez, E., 45  
 Stachel, H., 415  
 Sterkers, O., 575  
 Strano, S., 513  
 Stroe, I., 133  
 Suñer, J.L., 247  
 Szewczyk, J., 575

**T**

Täandl, M., 183  
 Tarabarin, V., 37, 397  
 Tarabarina, Z., 397  
 Tsakoumaki, M.C., 11  
 Tsitomeneas, S., 29

**U**

Ualiyev, G., 95, 329

Urizar, M., 69

**V**

Václavík, M., 337

Vaida, C., 595

Valero, F., 247

Velicu, R., 405

Viadero, F., 175

Visa, I., 447

Vitiukov, T., 37

Vyacheslav, D., 263

**W**

Wenger, P., 505

**Y**

Yao, S., 149

Yatsun, A., 263

**Z**

Zentner, L., 431

Zielinska, T., 237